ICECUBE-GEN2 TECHNICAL DESIGN

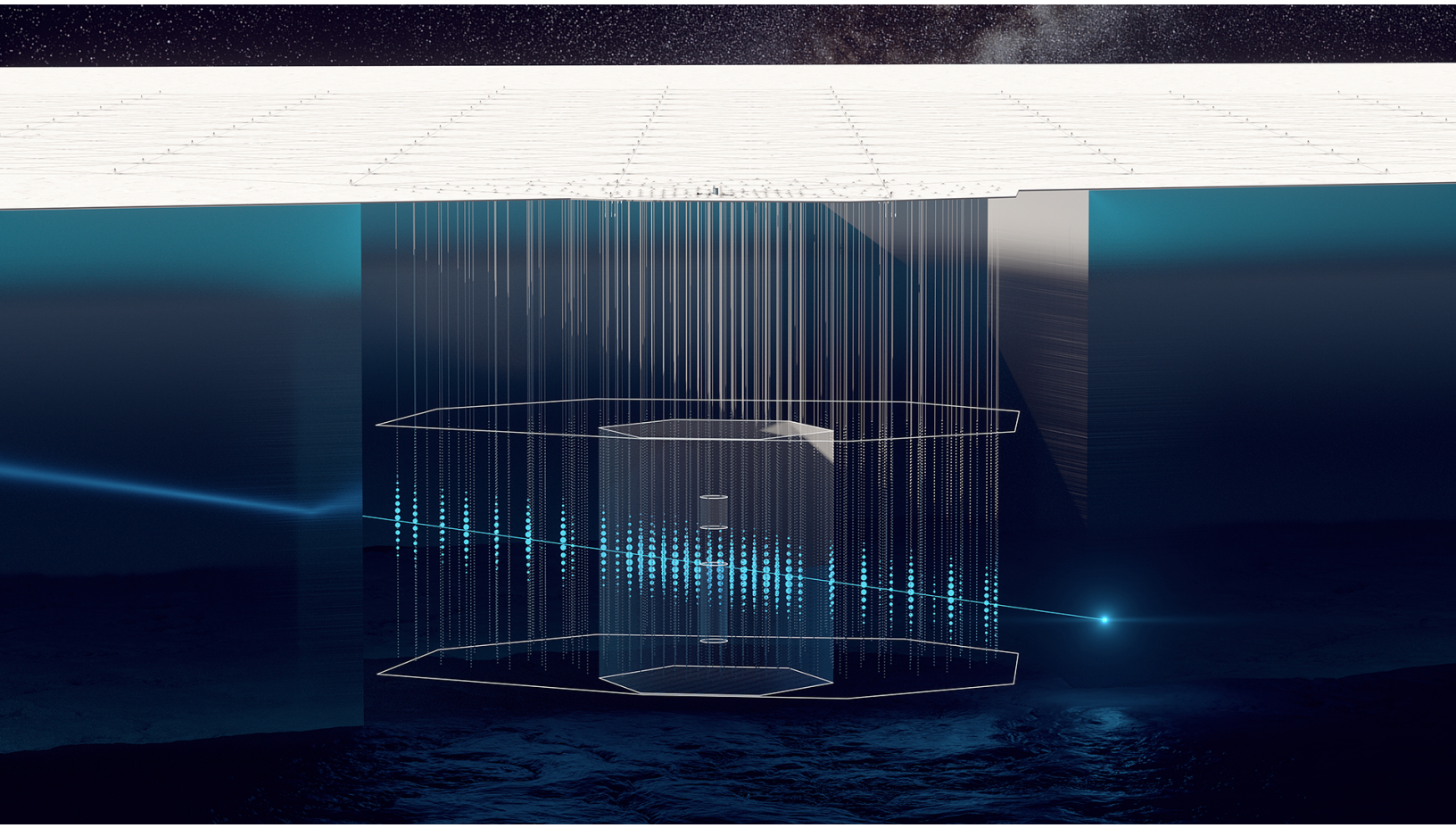

The IceCube-Gen2 Neutrino Observatory

Parts I and II

(Part III will be released at a later time.)

Version: July 27, 2023

IceCube-Gen2 Author List

R. Abbasi,[17] M. Ackermann,[77] J. Adams,[22] S. K. Agarwalla,[48,*] J. A. Aguilar,[12] M. Ahlers,[26] J.M. Alameddine,[27] N. M. Amin,[54] K. Andeen,[51] G. Anton,[30] C. Argüelles,[14] Y. Ashida,[65] S. Athanasiadou,[77] J. Audehm,[1] S. N. Axani,[54] X. Bai,[62] A. Balagopal V.,[48] M. Baricevic,[48] S. W. Barwick,[34] V. Basu,[48] R. Bay,[8] J. Becker Tjus,[11,†] J. Beise,[75] C. Bellenghi,[31] C. Benning,[1] S. BenZvi,[64] D. Berley,[23] E. Bernardini,[60] D. Z. Besson,[41] A. Bishop,[48] E. Blaufuss,[23] S. Blot,[77] M. Bohmer,[31] F. Bontempo,[35] J. Y. Book,[14] J. Borowka,[1] C. Boscolo Meneguolo,[60] S. Böser,[49] O. Botner,[75] J. Böttcher,[1] S. Bouma,[30] E. Bourbeau,[26] J. Braun,[48] I. Brewer,[54] B. Brinson,[6] J. Brostean-Kaiser,[77] P. Bruder,[36] R. T. Burley,[2] R. S. Busse,[53] M. Bustamante,[26] D. Butterfield,[48] M. A. Campana,[61] K. Carloni,[14] E. G. Carnie-Bronca,[2] M. Cataldo,[30] S. Chattopadhyay,[48,*] N. Chau,[12] C. Chen,[6] Z. Chen,[67] D. Chirkin,[48] S. Choi,[68] B. A. Clark,[23] R. Clark,[43] L. Classen,[53] A. Coleman,[75] G. H. Collin,[15] J. M. Conrad,[15] D. F. Cowen,[72,73] B. Dasgupta,[52] P. Dave,[6] C. Deaconu,[20,21] C. De Clercq,[13] S. De Kockere,[13] J. J. DeLaunay,[71] D. Delgado,[14] S. Deng,[1] K. Deoskar,[66] A. Desai,[48] P. Desiati,[48] K. D. de Vries,[13] G. de Wasseige,[45] T. DeYoung,[28] A. Diaz,[15] J. C. Díaz-Vélez,[48] M. Dittmer,[53] A. Domi,[30] H. Dujmovic,[48] M. A. DuVernois,[48] T. Ehrhardt,[49] P. Eller,[31] E. Ellinger,[76] S. El Mentawi,[1] D. Elsässer,[27] R. Engel,[35,36] H. Erpenbeck,[48] J. Evans,[23] J. J. Evans,[50] P. A. Evenson,[54] K. L. Fan,[23] K. Fang,[48] K. Farrag,[44] K. Farrag,[16] A. R. Fazely,[7] A. Fedynitch,[69] N. Feigl,[10] S. Fiedlschuster,[30] C. Finley,[66] L. Fischer,[77] B. Flaggs,[54] D. Fox,[72] A. Franckowiak,[11] A. Fritz,[49] T. Fujii,[58] P. Fürst,[1] J. Gallagher,[47] E. Ganster,[1] A. Garcia,[14] L. Gerhardt,[9] R. Gernhaeuser,[31] A. Ghadimi,[71] P. Giri,[42] C. Glaser,[75] T. Glauch,[31] T. Glüsenkamp,[30,75] N. Goehlke,[36] S. Goswami,[71] D. Grant,[28] S. J. Gray,[23] O. Gries,[1] S. Griffin,[48] S. Griswold,[64] D. Guevel,[48] C. Günther,[1] P. Gutjahr,[27] C. Haack,[30] T. Haji Azim,[1] A. Hallgren,[75] R. Halliday,[28] S. Hallmann,[77] L. Halve,[1] F. Halzen,[48] H. Hamdaoui,[67] M. Ha Minh,[31] K. Hanson,[48] J. Hardin,[15] A. A. Harnisch,[28] P. Hatch,[38] J. Haugen,[48] A. Haungs,[35] D. Heinen,[1] K. Helbing,[76] J. Hellrung,[11] B. Hendricks,[73,74] F. Henningsen,[31] J. Henrichs,[77] L. Heuermann,[1] N. Heyer,[75] S. Hickford,[76] A. Hidvegi,[66] J. Hignight,[29] C. Hill,[16] G. C. Hill,[2] K. D. Hoffman,[23] B. Hoffmann,[36] K. Holzapfel,[31] S. Hori,[48] K. Hoshina,[48,‡] W. Hou,[35] T. Huber,[35] T. Huege,[35] K. Hughes,[19,21] K. Hultqvist,[66] M. Hünnefeld,[27] R. Hussain,[48] K. Hymon,[27] S. In,[68] A. Ishihara,[16] M. Jacquart,[48] O. Janik,[1] M. Jansson,[66] G. S. Japaridze,[5] M. Jeong,[68] M. Jin,[14] B. J. P. Jones,[4] O. Kalekin,[30] D. Kang,[35] W. Kang,[68] X. Kang,[61] A. Kappes,[53] D. Kappesser,[49] L. Kardum,[27] T. Karg,[77] M. Karl,[31] A. Karle,[48] T. Katori,[43] U. Katz,[30] M. Kauer,[48] J. L. Kelley,[48] A. Khatee Zathul,[48] A. Kheirandish,[39,40] J. Kiryluk,[67] M. Kleifges,[37] S. R. Klein,[8,9] T. Kobayashi,[58] A. Kochocki,[28] H. Kolanoski,[10] T. Kontrimas,[31] L. Köpke,[49] C. Kopper,[30] D. J. Koskinen,[26] P. Koundal,[35] M. Kovacevich,[61] M. Kowalski,[10,77] T. Kozynets,[26] C. B. Krauss,[29] I. Kravchenko,[42] J. Krishnamoorthi,[48,*] E. Krupczak,[28] A. Kumar,[77] E. Kun,[11] N. Kurahashi,[61] N. Lad,[77] C. Lagunas Gualda,[77] M. J. Larson,[23] S. Latseva,[1] F. Lauber,[76] J. P. Lazar,[14,48] J. W. Lee,[68] K. Leonard DeHolton,[73] A. Leszczyńska,[54] M. Lincetto,[11] Q. R. Liu,[48] M. Liubarska,[29] M. Lohan,[52] E. Lohfink,[49] J. LoSecco,[57] C. Love,[61] C. J. Lozano Mariscal,[53] L. Lu,[48] F. Lucarelli,[32] Y. Lyu,[8,9] J. Madsen,[48] K. B. M. Mahn,[28] Y. Makino,[48] S. Mancina,[48,60] S. Mandalia,[44] W. Marie Sainte,[48] I. C. Mariş,[12] S. Marka,[56] Z. Marka,[56] M. Marsee,[71] I. Martinez-Soler,[14] R. Maruyama,[55] F. Mayhew,[28] T. McElroy,[29] F. McNally,[46] J. V. Mead,[26] K. Meagher,[48] S. Mechbal,[77] A. Medina,[25] M. Meier,[16] Y. Merckx,[13] L. Merten,[11] Z. Meyers,[77] J. Micallef,[28] M. Mikhailova,[41] J. Mitchell,[7] T. Montaruli,[32] R. W. Moore,[29] Y. Morii,[16] R. Morse,[48] M. Moulai,[48] T. Mukherjee,[35] R. Naab,[77] R. Nagai,[16] M. Nakos,[48] A. Narayan,[52] U. Naumann,[76] J. Necker,[77] A. Negi,[4] A. Nelles,[30,77] M. Neumann,[53] H. Niederhausen,[28] M. U. Nisa,[28] A. Noell,[1] A. Novikov,[54] S. C. Nowicki,[28] A. Nozdrina,[41] E. Oberla,[20,21] A. Obertacke Pollmann,[16] V. O'Dell,[48] M. Oehler,[35] B. Oeyen,[33] A. Olivas,[23] R. Orsoe,[31] J. Osborn,[48] E. O'Sullivan,[75] L. Papp,[31] N. Park,[38] G. K. Parker,[4] E. N. Paudel,[54] L. Paul,[62] C. Pérez de los Heros,[75] T. C. Petersen,[26] J. Peterson,[48] S. Philippen,[1] S. Pieper,[76] J. L. Pinfold,[29] A. Pizzuto,[48] I. Plaisier,[77] M. Plum,[62] A. Pontén,[75] Y. Popovych,[49] M. Prado Rodriguez,[48] B. Pries,[28] R. Procter-Murphy,[23] G. T. Przybylski,[9] L. Pyras,[77] J. Rack-Helleis,[49] M. Rameez,[52] K. Rawlins,[3] Z. Rechav,[48] A. Rehman,[54] P. Reichherzer,[11] G. Renzi,[12] E. Resconi,[31] S. Reusch,[77] W. Rhode,[27] B. Riedel,[48] M. Riegel,[35] A. Rifaie,[1] E. J. Roberts,[2] S. Robertson,[8,9] S. Rodan,[68] G. Roellinghoff,[68] M. Rongen,[30] C. Rott,[65,68] T. Ruhe,[27] D. Ryckbosch,[33] I. Safa,[14,48] J. Saffer,[36] D. Salazar-Gallegos,[28] P. Sampathkumar,[35] S. E. Sanchez Herrera,[28] A. Sandrock,[76] P. Sandstrom,[48] M. Santander,[71] S. Sarkar,[29] S. Sarkar,[59] J. Savelberg,[1] P. Savina,[48] M. Schaufel,[1] H. Schieler,[35] S. Schindler,[30] L. Schlickmann,[1] B. Schlüter,[53] F. Schlüter,[12] N. Schmeisser,[76] T. Schmidt,[23] J. Schneider,[30] F. G. Schröder,[35,54] L. Schumacher,[30] G. Schwefer,[1] S. Sclafani,[23] D. Seckel,[54] M. Seikh,[41] S. Seunarine,[63] M. H. Shaevitz,[56] R. Shah,[61] A. Sharma,[75] S. Shefali,[36] N. Shimizu,[16] M. Silva,[48] B. Skrzypek,[14] D. Smith,[19,21] B. Smithers,[4] R. Snihur,[48] J. Soedingrekso,[27] A. Søgaard,[26] D. Soldin,[36] P. Soldin,[1] G.

Sommani,[11] D. Southall,[19,21] C. Spannfellner,[31] G. M. Spiczak,[63] C. Spiering,[77] M. Stamatikos,[25] T. Stanev,[54] T. Stezelberger,[9] J. Stoffels,[13] T. Stürwald,[76] T. Stuttard,[26] G. W. Sullivan,[23] I. Taboada,[6] A. Taketa,[70] H. K. M. Tanaka,[70] S. Ter-Antonyan,[7] M. Thiesmeyer,[1] W. G. Thompson,[14] J. Thwaites,[48] S. Tilav,[54] K. Tollefson,[28] C. Tönnis,[68] J. Torres,[24,25] S. Toscano,[12] D. Tosi,[48] A. Trettin,[77] Y. Tsunesada,[58] C. F. Tung,[6] R. Turcotte,[35] J. P. Twagirayezu,[28] B. Ty,[48] M. A. Unland Elorrieta,[53] A. K. Upadhyay,[48,*] K. Upshaw,[7] N. Valtonen-Mattila,[75] J. Vandenbroucke,[48] N. van Eijndhoven,[13] D. Vannerom,[15] J. van Santen,[77] J. Vara,[53] D. Veberic,[35] J. Veitch-Michaelis,[48] M. Venugopal,[35] S. Verpoest,[54] A. Vieregg,[18,19,20,21] A. Vijai,[23] C. Walck,[66] C. Weaver,[28] P. Weigel,[15] A. Weindl,[35] J. Weldert,[73] A. Y. Wen,[14] C. Wendt,[48] J. Werthebach,[27] M. Weyrauch,[35] N. Whitehorn,[28] C. H. Wiebusch,[1] D. R. Williams,[71] S. Wissel,[72,73,74] L. Witthaus,[27] A. Wolf,[1] M. Wolf,[31] G. Wörner,[35] G. Wrede,[30] S. Wren,[50] X. W. Xu,[7] J. P. Yanez,[29] E. Yildizci,[48] S. Yoshida,[16] R. Young,[41] F. Yu,[14] S. Yu,[28] T. Yuan,[48] Z. Zhang,[67] P. Zhelnin,[14] S. Zierke,[1] P. Zilberman,[48] and M. Zimmerman[48]

(IceCube-Gen2 Collaboration)

[1] *III. Physikalisches Institut, RWTH Aachen University, D-52056 Aachen, Germany*
[2] *Department of Physics, University of Adelaide, Adelaide, 5005, Australia*
[3] *Dept. of Physics and Astronomy, University of Alaska Anchorage, 3211 Providence Dr., Anchorage, AK 99508, USA*
[4] *Dept. of Physics, University of Texas at Arlington, 502 Yates St., Science Hall Rm 108, Box 19059, Arlington, TX 76019, USA*
[5] *CTSPS, Clark-Atlanta University, Atlanta, GA 30314, USA*
[6] *School of Physics and Center for Relativistic Astrophysics, Georgia Institute of Technology, Atlanta, GA 30332, USA*
[7] *Dept. of Physics, Southern University, Baton Rouge, LA 70813, USA*
[8] *Dept. of Physics, University of California, Berkeley, CA 94720, USA*
[9] *Lawrence Berkeley National Laboratory, Berkeley, CA 94720, USA*
[10] *Institut für Physik, Humboldt-Universität zu Berlin, D-12489 Berlin, Germany*
[11] *Fakultät für Physik & Astronomie, Ruhr-Universität Bochum, D-44780 Bochum, Germany*
[12] *Université Libre de Bruxelles, Science Faculty CP230, B-1050 Brussels, Belgium*
[13] *Vrije Universiteit Brussel (VUB), Dienst ELEM, B-1050 Brussels, Belgium*
[14] *Department of Physics and Laboratory for Particle Physics and Cosmology, Harvard University, Cambridge, MA 02138, USA*
[15] *Dept. of Physics, Massachusetts Institute of Technology, Cambridge, MA 02139, USA*
[16] *Dept. of Physics and The International Center for Hadron Astrophysics, Chiba University, Chiba 263-8522, Japan*
[17] *Department of Physics, Loyola University Chicago, Chicago, IL 60660, USA*
[18] *Dept. of Astronomy and Astrophysics, University of Chicago, Chicago, IL 60637, USA*
[19] *Dept. of Physics, University of Chicago, Chicago, IL 60637, USA*
[20] *Enrico Fermi Institute, University of Chicago, Chicago, IL 60637, USA*
[21] *Kavli Institute for Cosmological Physics, University of Chicago, Chicago, IL 60637, USA*
[22] *Dept. of Physics and Astronomy, University of Canterbury, Private Bag 4800, Christchurch, New Zealand*
[23] *Dept. of Physics, University of Maryland, College Park, MD 20742, USA*
[24] *Dept. of Astronomy, Ohio State University, Columbus, OH 43210, USA*
[25] *Dept. of Physics and Center for Cosmology and Astro-Particle Physics, Ohio State University, Columbus, OH 43210, USA*
[26] *Niels Bohr Institute, University of Copenhagen, DK-2100 Copenhagen, Denmark*
[27] *Dept. of Physics, TU Dortmund University, D-44221 Dortmund, Germany*
[28] *Dept. of Physics and Astronomy, Michigan State University, East Lansing, MI 48824, USA*
[29] *Dept. of Physics, University of Alberta, Edmonton, Alberta, Canada T6G 2E1*
[30] *Erlangen Centre for Astroparticle Physics, Friedrich-Alexander-Universität Erlangen-Nürnberg, D-91058 Erlangen, Germany*
[31] *Physik-department, Technische Universität München, D-85748 Garching, Germany*
[32] *Département de physique nucléaire et corpusculaire, Université de Genève, CH-1211 Genève, Switzerland*
[33] *Dept. of Physics and Astronomy, University of Gent, B-9000 Gent, Belgium*
[34] *Dept. of Physics and Astronomy, University of California, Irvine, CA 92697, USA*
[35] *Karlsruhe Institute of Technology, Institute for Astroparticle Physics, D-76021 Karlsruhe, Germany*
[36] *Karlsruhe Institute of Technology, Institute of Experimental Particle Physics, D-76021 Karlsruhe, Germany*
[37] *Karlsruhe Institute of Technology, Institute for Data Processing and Electronics, D-76021 Karlsruhe, Germany*
[38] *Dept. of Physics, Engineering Physics, and Astronomy, Queen's University, Kingston, ON K7L 3N6, Canada*
[39] *Department of Physics & Astronomy, University of Nevada, Las Vegas, NV, 89154, USA*
[40] *Nevada Center for Astrophysics, University of Nevada, Las Vegas, NV 89154, USA*
[41] *Dept. of Physics and Astronomy, University of Kansas, Lawrence, KS 66045, USA*

[42] *Dept. of Physics and Astronomy, University of Nebraska–Lincoln, Lincoln, Nebraska 68588, USA*
[43] *Dept. of Physics, King's College London, London WC2R 2LS, United Kingdom*
[44] *School of Physics and Astronomy, Queen Mary University of London, London E1 4NS, United Kingdom*
[45] *Centre for Cosmology, Particle Physics and Phenomenology - CP3, Université catholique de Louvain, Louvain-la-Neuve, Belgium*
[46] *Department of Physics, Mercer University, Macon, GA 31207-0001, USA*
[47] *Dept. of Astronomy, University of Wisconsin–Madison, Madison, WI 53706, USA*
[48] *Dept. of Physics and Wisconsin IceCube Particle Astrophysics Center, University of Wisconsin–Madison, Madison, WI 53706, USA*
[49] *Institute of Physics, University of Mainz, Staudinger Weg 7, D-55099 Mainz, Germany*
[50] *School of Physics and Astronomy, The University of Manchester, Oxford Road, Manchester, M13 9PL, United Kingdom*
[51] *Department of Physics, Marquette University, Milwaukee, WI, 53201, USA*
[52] *Dept. of High Energy Physics, Tata Institute of Fundamental Research, Colaba, Mumbai 400 005, India*
[53] *Institut für Kernphysik, Westfälische Wilhelms-Universität Münster, D-48149 Münster, Germany*
[54] *Bartol Research Institute and Dept. of Physics and Astronomy, University of Delaware, Newark, DE 19716, USA*
[55] *Dept. of Physics, Yale University, New Haven, CT 06520, USA*
[56] *Columbia Astrophysics and Nevis Laboratories, Columbia University, New York, NY 10027, USA*
[57] *Dept. of Physics, University of Notre Dame du Lac, 225 Nieuwland Science Hall, Notre Dame, IN 46556-5670, USA*
[58] *Graduate School of Science and NITEP, Osaka Metropolitan University, Osaka 558-8585, Japan*
[59] *Dept. of Physics, University of Oxford, Parks Road, Oxford OX1 3PU, United Kingdom*
[60] *Dipartimento di Fisica e Astronomia Galileo Galilei, Università Degli Studi di Padova, 35122 Padova PD, Italy*
[61] *Dept. of Physics, Drexel University, 3141 Chestnut Street, Philadelphia, PA 19104, USA*
[62] *Physics Department, South Dakota School of Mines and Technology, Rapid City, SD 57701, USA*
[63] *Dept. of Physics, University of Wisconsin, River Falls, WI 54022, USA*
[64] *Dept. of Physics and Astronomy, University of Rochester, Rochester, NY 14627, USA*
[65] *Department of Physics and Astronomy, University of Utah, Salt Lake City, UT 84112, USA*
[66] *Oskar Klein Centre and Dept. of Physics, Stockholm University, SE-10691 Stockholm, Sweden*
[67] *Dept. of Physics and Astronomy, Stony Brook University, Stony Brook, NY 11794-3800, USA*
[68] *Dept. of Physics, Sungkyunkwan University, Suwon 16419, Korea*
[69] *Institute of Physics, Academia Sinica, Taipei, 11529, Taiwan*
[70] *Earthquake Research Institute, University of Tokyo, Bunkyo, Tokyo 113-0032, Japan*
[71] *Dept. of Physics and Astronomy, University of Alabama, Tuscaloosa, AL 35487, USA*
[72] *Dept. of Astronomy and Astrophysics, Pennsylvania State University, University Park, PA 16802, USA*
[73] *Dept. of Physics, Pennsylvania State University, University Park, PA 16802, USA*
[74] *Institute of Gravitation and the Cosmos, Center for Multi-Messenger Astrophysics, Pennsylvania State University, University Park, PA 16802, USA*
[75] *Dept. of Physics and Astronomy, Uppsala University, Box 516, S-75120 Uppsala, Sweden*
[76] *Dept. of Physics, University of Wuppertal, D-42119 Wuppertal, Germany*
[77] *Deutsches Elektronen-Synchrotron DESY, Platanenallee 6, 15738 Zeuthen, Germany*
(Dated: July 27, 2023)

* also at Institute of Physics, Sachivalaya Marg, Sainik School Post, Bhubaneswar 751005, India
† also at Department of Space, Earth and Environment, Chalmers University of Technology, 412 96 Gothenburg, Sweden
‡ also at Earthquake Research Institute, University of Tokyo, Bunkyo, Tokyo 113-0032, Japan

Acknowledgments:

USA – U.S. National Science Foundation, (Office of Polar Programs, Physics Division, EPSCoR program), University of Wisconsin-Madison (UW-Madison Office of the Vice Chancellor for Research with funding from the Wisconsin Alumni Research Foundation, UW-Madison Center for High Throughput Computing (CHTC)), Open Science Grid (OSG), Advanced Cyberinfrastructure Coordination Ecosystem: Services & Support (ACCESS), Frontera computing project at the Texas Advanced Computing Center, U.S. Department of Energy-National Energy Research Scientific Computing Center, Particle astrophysics research computing center at the University of Maryland, Institute for Cyber-Enabled Research at Michigan State University, and Astroparticle physics computational facility at Marquette University; Belgium – Funds for Scientific Research (FRS-FNRS and FWO), FWO Odysseus and Big Science programmes, and Belgian Federal Science Policy Office (Belspo); Germany – Bundesministerium für Bildung und Forschung (BMBF); Deutsche Forschungsgemeinschaft (DFG), the Initiative and Networking Fund of the Helmholtz Association; the states of Baden-Wuerttemberg, Bavaria, Berlin, Brandenburg, North Rhine-Westphalia, Rhineland-Palatinate, and for providing High Performance Computing the RWTH Aachen.Sweden – Swedish Research Council, Swedish Polar Research Secretariat, Swedish National Infrastructure for Computing (SNIC), and Knut and Alice Wallenberg Foundation; European Union – EGI Advanced Computing for research, European Research Council (ERC); Australia – Australian Research Council; Canada – Natural Sciences and Engineering Research Council of Canada, Calcul Québec, Compute Ontario, Canada Foundation for Innovation, WestGrid, and Compute Canada; Denmark – Villum Fonden, Carlsberg Foundation, and European Commission; New Zealand – Marsden Fund; Japan – Japan Society for Promotion of Science (JSPS) and Institute for Global Prominent Research (IGPR) of Chiba University; Korea – National Research Foundation of Korea (NRF); Switzerland – Swiss National Science Foundation (SNSF).

Preamble

The vision of IceCube-Gen2 emerged soon after the IceCube Neutrino Observatory reported the discovery of a cosmic neutrino flux at high energies in 2013. The first conceptual design was presented as early as 2014 at a meeting in Arlington, VA. Since then, we have optimized the design and made significant technical improvements. In addition, the emerging radio detection technology was added to the conceptual design in order to significantly expand the sensitive energy range of the observatory.

This document presents a preliminary design of IceCube-Gen2. Its purpose is threefold, to define a) the science case, b) the technical design to meet the science goals, and c) the approach to the construction at the South Pole. These three goals are laid out in three parts.

Part I, *Science and Conceptual Design*, presents the scientific goals, and the performance and sensitivity parameters. It is based on the IceCube-Gen2 science white paper [1].

In Part II, *Detector and Performance*, readers will find the technical design and performance benchmarks. We present how the technical designs derive from the science requirements for the various detectors used in the IceCube-Gen2 optical, radio, and surface arrays. We also offer solutions for data transfer and processing, as well as calibration strategies.

The readers interested in construction will find that information in Part III, *Detector Construction and Logistical Support Requirements*. We provide a detailed explanation of the challenges of constructing this next-generation observatory with an instrumented volume almost an order of magnitude larger than IceCube. The logistics of transporting 10,000 sensors to the South Pole, drilling 120 holes to 2600 m depth into the most transparent ice, and deploying the surface and a 500 km^2 radio array are laid out. They include cargo and population requirements, as well as high-level information about cost estimation.

The document intends to serve a broad audience for different purposes. The community and collaboration will find here the authoritative reference. Decision-makers and representatives of funding agencies will find a complete definition of IceCube-Gen2. Experimentalists working on other projects may find useful technical approaches in this document.

Contents

I Science and Conceptual Design **3**

1 Introduction **4**

2 IceCube-Gen2 Science: Exploring the cosmic energy frontier **23**

3 IceCube-Gen2 Design Overview **59**

II Detector and Performance **83**

4 The South Pole: an extraordinary platform for astrophysics **85**

5 Optical Array **98**

6 Radio Array **128**

7 Surface Array **155**

8 Surface and Data Acquisition Infrastructure **183**

9 Data Systems and Infrastructure **206**

10 Detector Calibration **227**

III Detector Construction and Logistical Support Requirements **250**

(Part III will be released at a later time.)

Part I

Science and Conceptual Design

Table of Contents

1 Introduction 4
- 1.1 IceCube and the discovery of high-energy cosmic neutrinos 7
- 1.2 Identifying the sources of high-energy neutrinos 8
- 1.3 The energy spectrum and flavor composition of cosmic neutrinos . . . 13
- 1.4 Exploring fundamental physics with high-energy neutrinos 16
- 1.5 Summary of objectives for a next-generation neutrino observatory . . . 17
- 1.6 The IceCube-Gen2 neutrino telescope 18
- 1.7 Global multi-messenger astronomy efforts 20

2 IceCube-Gen2 Science: Exploring the cosmic energy frontier 23
- 2.1 Resolving the high-energy sky from TeV to EeV energies 23
- 2.2 Understanding cosmic particle acceleration through multi-messenger observations 28
- 2.3 Revealing the sources and propagation of the highest energy particles in the Milky Way and the Universe 41
- 2.4 Probing fundamental physics with high-energy neutrinos and cosmic rays 48
- 2.5 Science requirements matrix 56

3 IceCube-Gen2 Design Overview 59
- 3.1 Design considerations 59
- 3.2 Detector design 68
- 3.3 Instrument performance 73

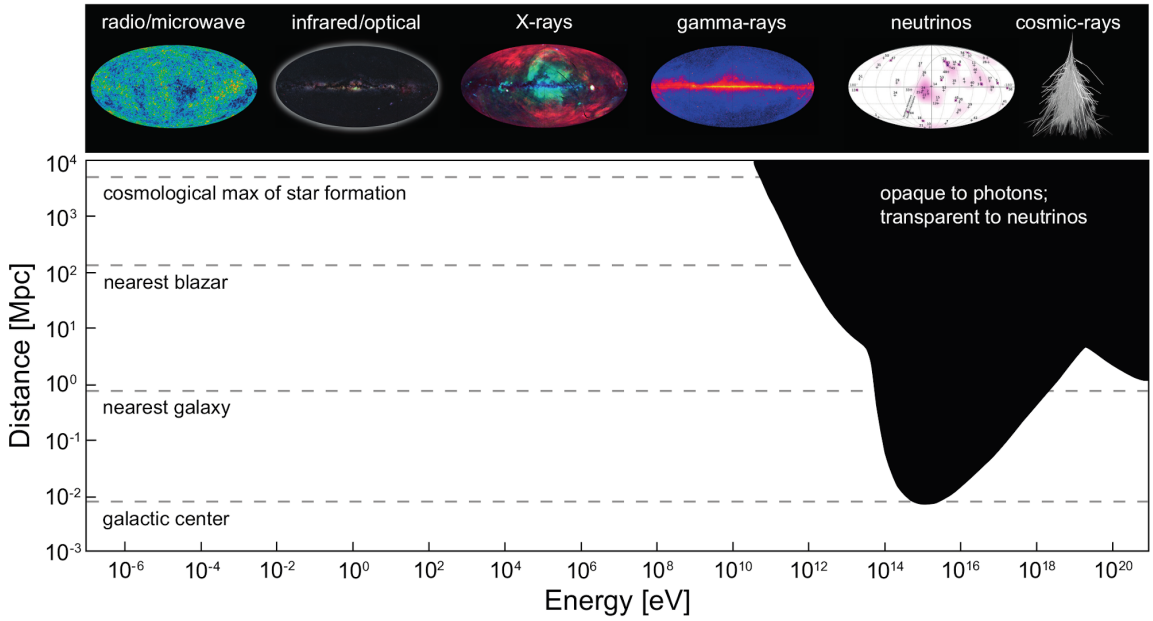

Figure 1: Distance horizon at which the universe becomes non-transparent to electromagnetic radiation as a function of photon energy.

1 Introduction

With the first detection of high-energy neutrinos of extraterrestrial origin in 2013 [2, 3], also called astrophysical or cosmic neutrinos throughout this document, the IceCube Neutrino Observatory opened a new window to some of the most extreme regions of our universe. Neutrinos interact only weakly with matter and therefore escape dense astrophysical environments that are opaque to electromagnetic radiation. In addition, at PeV (10^{15} eV) energies, extragalactic space becomes opaque to electromagnetic radiation due to the scattering of high-energy photons (γ-rays) on the cosmic microwave background and extragalactic background light (EBL, e.g., [4], see also Figure 1). This leaves neutrinos as unique messengers to probe the most extreme particle accelerators in the cosmos - the sources of the ultra-high-energy cosmic rays (CR). There, CR with energies of more than 10^{20} eV are produced, which is 10^{7} times higher than the particle energy reached in the most powerful terrestrial particle accelerators.

CR produce high-energy neutrinos through the interaction with ambient matter or radiation fields, either in the sources or during propagation in the interstellar and intergalactic medium. Unlike the charged CR, neutrinos are not deflected by magnetic fields on the way to the Earth, but point back to their source, thus resolving the long-standing question of CR origin(s). The power of this approach was demonstrated by IceCube and its multi-messenger partners, when a single high-energy neutrino was observed in coincidence with the flaring γ-ray blazar TXS 0506+056, identifying what appears to be the first, known extragalactic source of high-energy CR [5, 6].

IceCube instruments a gigaton of the very deep and clean South Pole ice. It has been taking data in full configuration since May 2011 with a duty cycle of about 99%. With one cubic-kilometer instrumented volume, IceCube is more than an order of magnitude

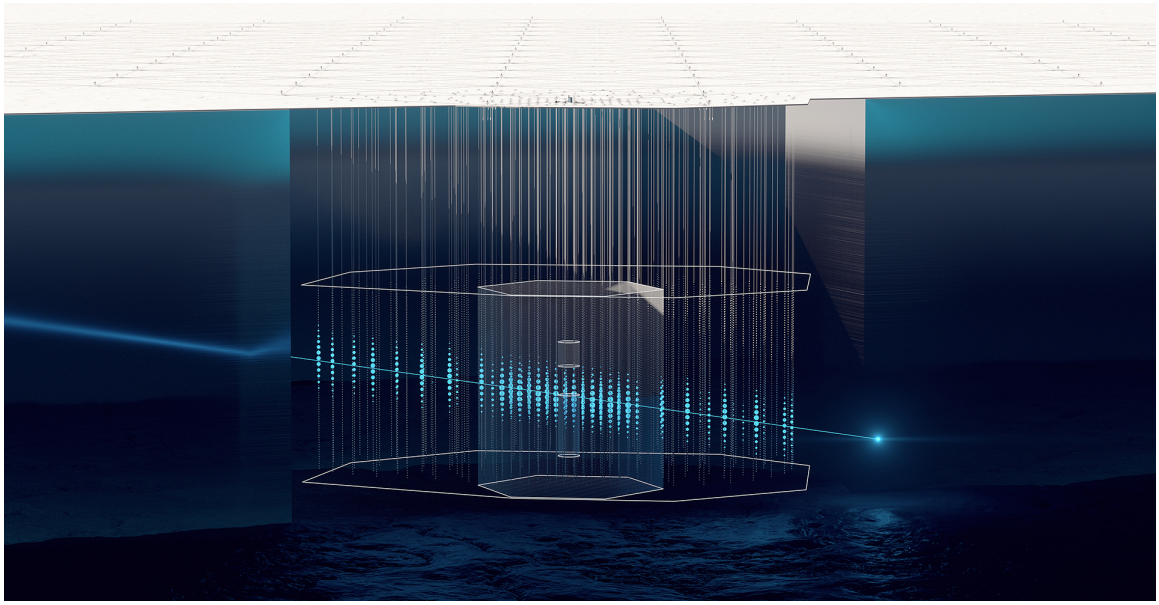

Figure 2: Artistic image of the IceCube-Gen2 facility. The optical array contains IceCube and a densely instrumented core installed in the IceCube Upgrade. A surface array covers the footprint of the optical array. The stations of the giant radio array deployed at shallow depths and the surface extend for several kilometers beyond the optical array.

larger than previous and currently operating neutrino telescopes (Baikal Deep Underwater Neutrino Telescope [7], ANTARES [8], AMANDA [9]). It has collected neutrino induced events with up to 10 PeV in energy, corresponding to the highest energy leptons ever observed and opening new scientific avenues not just for astronomy but also for probing physics beyond the Standard Model of particle physics ([10]). In addition, its high uptime and low detector noise make it a valuable asset to search for and detect the MeV energy neutrinos from a Galactic supernova, thus providing a high-uptime alert system for what is expected to be a once-in-a-lifetime event.

So far, the distribution of the arrival directions of astrophysical neutrinos on the sky indicates a predominantly extragalactic origin with a ~10% contribution from the Milky Way. Given the limited statistics that IceCube collects at the highest energies, the identification of steady sources requires a very long integration time and the vast majority of flaring sources escape detection altogether. Initial associations of high-energy neutrinos of likely cosmic origin with a blazar and tidal disruption events (TDE), and most importantly the clear evidence for neutrino emission from the nearby active galaxy NGC 1068, have been essential first steps. Yet, the sources of the bulk of the cosmic neutrino flux observed by IceCube remain to be resolved (see Section 1.2 for a more detailed discussion of the origin of IceCube's neutrinos). The list of candidates is long; transients such as supernovae (SNe), neutron star mergers, or low luminosity Gamma Ray Bursts (GRBs) — or steady sources such as Active Galactic Nuclei (AGN) or starburst galaxies — are all very well motivated. With almost a decade of IceCube data having been analyzed, the need for new, larger instruments with improved sensitivity is becoming increasingly clear.

With IceCube-Gen2, we propose a detector of sufficient volume to increase the neutrino collection rate by an order of magnitude. Meanwhile, the KM3NeT and GVD detectors

under construction in the Mediterranean Sea and in Lake Baikal respectively, target the size of one cubic kilometer. They will complement IceCube-Gen2 in terms of sky coverage [11, 12], and will achieve astrophysical neutrino detection rates comparable to the present IceCube. Elaborate multi-messenger studies that combine information from other observatories, ranging from γ-rays to radio and also including gravitational waves, continue to provide opportunities for more associations of high-energy neutrinos with their sources.

IceCube-Gen2 (Figure 2) will be a unique wide-band neutrino observatory (MeV–EeV) that employs two complementary detection technologies for neutrinos, optical and radio, in combination with a surface detector array for CR air showers to exploit the enormous scientific opportunities outlined in this document. The IceCube-Gen2 facility will integrate the operating IceCube detector together with four new components: (1) an enlarged in-ice optical array, complemented by (2) a densely instrumented low-energy core, (3) a high-energy radio array, and (4) a surface CR detector array. Construction of the low-energy core has already started as part of the IceCube Upgrade project [13] that is a (smaller) realization of the PINGU concept [14], with completion expected in 2026. Hence, we focus in this document on the science and instrumentation of the IceCube-Gen2 components for the detection of high-energy (TeV–EeV) neutrinos: the optical array, including its surface component, and the radio array.

In Section 1 of this document, we review the contributions of IceCube to neutrino astronomy today, formulate the science objectives for IceCube-Gen2 and discuss its role in the future landscape of observatories relevant for multi-messenger astronomy. We lay out the science opportunities provided through the IceCube-Gen2 project, as well as the requirements on the instrument to achieve these science goals in Section 2. A summary of the conceptual design of the proposed IceCube-Gen2 facility, considerations that led to the choice of this design, as well as the expected performance are presented in Section 3.

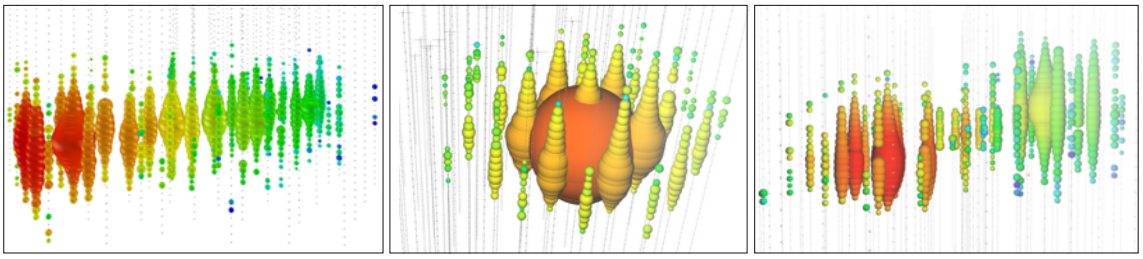

Figure 3: Example event signatures observed by IceCube: a track-like event (left), a shower-like event (middle) and a simulated double-bang event (right). Each colored sphere marks a DOM that records Cherenkov light. The size of the spheres represents the amount of light that was observed. The colors indicate the relative detection time of the photons with respect to each other, starting with red for early photons and progressing to blue for the last photons.

1.1 IceCube and the discovery of high-energy cosmic neutrinos

IceCube was built between 2004 and 2010, financed by a Major Research Equipment and Facilities Construction (MREFC) grant from the U.S. National Science Foundation (NSF) along with contributions from the funding agencies of several countries around the world. IceCube instruments one cubic kilometer of the deep glacial ice near the Amundsen-Scott South Pole Station in Antarctica. A total of 5160 digital optical modules (DOMs), each autonomously operating a 25 cm photomultiplier tube (PMT) in a glass pressure housing [15], are deployed at depths between 1450 m and 2450 m along 86 cables ("strings") connecting them to the surface. The glacial ice constitutes both the interaction medium and support structure for the IceCube array. Cherenkov radiation emitted by secondary charged particles, produced when a neutrino interacts in or near the active detector volume, carries the information on the neutrino's energy, direction, arrival time, and flavor. Digitized waveforms from each DOM provide the record of the event signature in IceCube, including the arrival time and number of the detected Cherenkov photons (measured as charge signals in the PMTs).

IceCube records events at a rate of about 3 kHz, with the vast majority being muons from CR air showers. Only about one in a million events is a neutrino, most of them produced in the Earth's atmosphere, also from CR air showers. This yields an unprecedentedly large sample of neutrinos collected: $\sim 10^5$ yr^{-1}, of which a few hundred per year are of astrophysical origin. Most of the astrophysical neutrinos can only be distinguished from their atmospheric counterparts by statistical methods, searching for excess events, e.g., from point sources. A small fraction, about 10 neutrinos per year, can be identified individually with high confidence as having an extraterrestrial origin. The light deposition patterns from the recorded neutrino events fall into three main event categories. Examples for each category are shown in Figure 3: Track-like events from the charged-current interaction of muon neutrinos; Cascade-like events from the charged-current interaction of electron and lower energy tau neutrinos and from neutral current interactions of all neutrino flavors; More complicated event signatures from very high-energy tau neutrinos, such as the so-called 'double-bang' event shown in the figure, which could be observed in rare cases.

IceCube has collected neutrino-induced events up to at least 10 PeV in energy, corresponding to the highest-energy neutrinos ever observed and opening new scientific avenues not just for astronomy but also for probing physics beyond the Standard

Model of particle physics ([16], see [10] for a review). Evidence for astrophysical neutrinos comes from several independent detection channels, including: cascade-like events [17], events that start inside the instrumented volume [18]; and through-going tracks [19]. IceCube has also observed two candidates for tau-neutrino events [20] that are not expected to be produced in the atmosphere through conventional channels.

The observation of a quasi-isotropic diffuse neutrino flux with cosmic origin has reached a significance that puts it beyond any doubt. A decade of IceCube data taking has demonstrated the means to study the flavor composition of the cosmic neutrino flux via independent channels of tracks, cascades, the tau neutrino candidates, and one observed neutrino candidate at the Glashow resonance of 6.3 PeV [21, 22] (see Section 2.2.6). Clearly to exploit the full potential of all-flavor neutrino astronomy, much larger data samples are needed.

1.2 Identifying the sources of high-energy neutrinos

One of the prime scientific goals of neutrino telescopes is the identification of CR sources through the observation of high-energy neutrinos. To date, the distribution of high-energy track-like astrophysical neutrinos in the sky is largely consistent with isotropy, implying that at least a substantial fraction of IceCube's cosmic neutrinos are of extragalactic origin. The low number of such high-energy cosmic neutrinos, and the moderate angular resolution of $\sim 0.5^\circ$ for track-like events from charged-current muon neutrino interactions and $\sim 10^\circ$ for cascade-like events from all flavors of neutrinos, poses a challenge for the identification of individual neutrino sources. Yet, after over a decade of IceCube operation, strong evidence has been collected for a variety of neutrino sources.

The interactions of Galactic CRs with the interstellar gas of the Milky Way are a guaranteed source of neutrinos (and gamma rays). The gamma-ray emission from such interactions have been extensively studied by the *Fermi* LAT [24] and other instruments up to few hundred GeV. The Tibet AS_γ collaboration has reported the observation of diffuse gamma-rays with energies > 100 TeV from our Galaxy [25]. The observations in gamma rays, combined with CR propagation modeling (e.g., [24, 26]), allow the creation of reliable predictions for the spatial and spectral distribution of neutrinos in the TeV energy range, which can then be tested by IceCube. The Galactic contribution to the astrophysical neutrino flux is predicted to be of O(1 - 10%) above 10 TeV in energy, depending on the modeled CR propagation scenario.

The region of the Galaxy that is expected to be brightest in neutrinos, is predominantly located in the Southern hemisphere of the sky. For this reason, and also for the spatially extended nature of the emission, shower-like events have a superior sensitivity in IceCube compared to track-like events, when searching for TeV neutrino emission from the Milky Way. An analysis of 10 years of IceCube data with an unprecedented efficiency for shower-like events from neutrino interactions, has found strong statistical evidence for diffuse neutrino emission from the Galactic plane. After correcting for trial factors, a Galactic contribution is favored with 4.5σ significance over the null-hypothesis of a purely isotropic distribution of astrophysical neutrinos [23]. Figure 4 shows the all-sky significance map derived from this analysis and indicates the expected neutrino

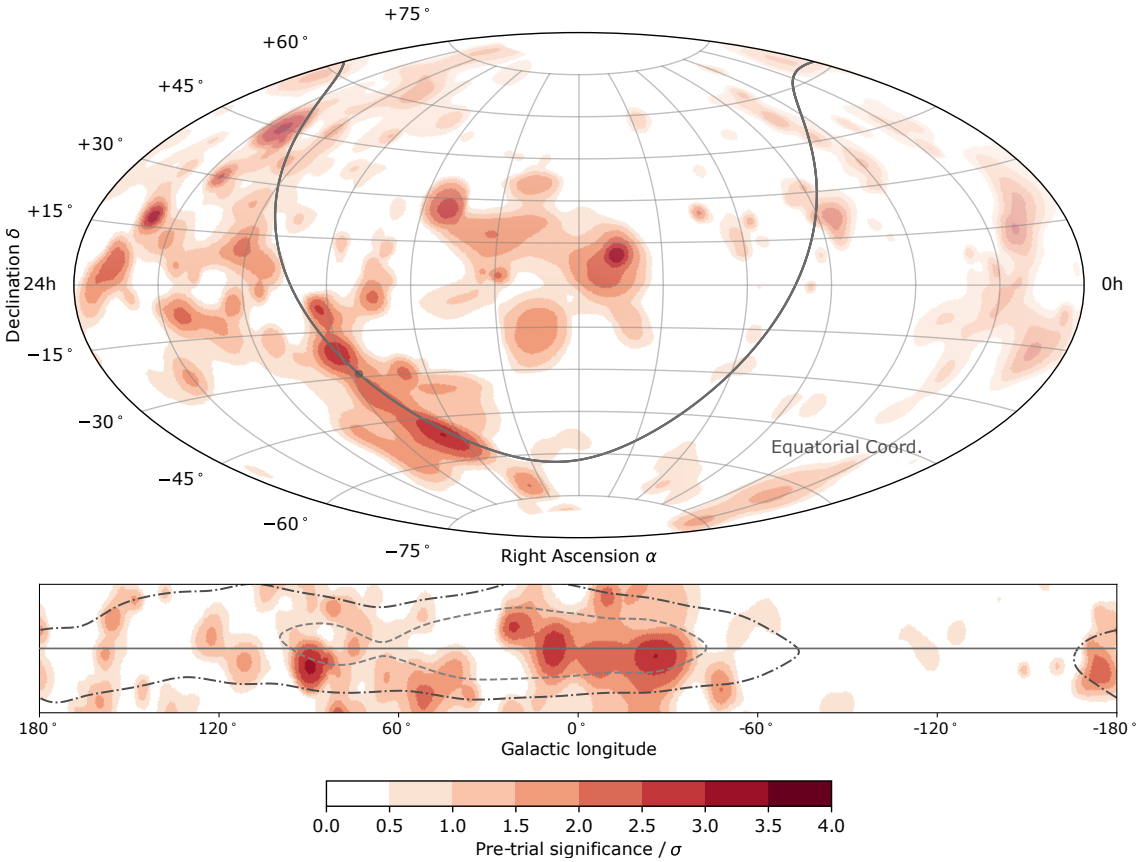

Figure 4: Significance map from a search for neutrino emission using neutrino-induced particle showers. The maps shows the results of the all-sky scan.The Galactic plane is indicated by a gray line, and the Galactic center as a dot. Individual warm spots are consistent with background fluctuations, while a dedicated test with a template for the expected emission of galactic plane yields a 4.5σ (trial-factor corrected) excess over the background-only hypothesis. The template is indicated on the lower map that focuses on the sky region around the Galactic plane: the significance map is compared to the 20% (dashed) and 50% (dashed-dotted) contours of the overall expected diffuse neutrino emission signal. The angular resolution of IceCube has been accounted for in the contours. Figure adapted from [23].

emission from the best-fit template. The measurement implies that 9%–13% of the astrophysical neutrino flux at 30 TeV is of Galactic origin. The observed neutrino flux is consistent with the Tibet AS_γ gamma-ray observations. Given the limited angular resolution of IceCube for shower-type events, both diffuse emission from CR interactions, and individual Galactic neutrino sources might contribute to the measured Galactic emission.

The analysis of IceCube data has also delivered important clues about the origin of the dominant fraction of neutrinos that are of extragalactic origin. There is mounting evidence, that cores and jets of active galaxies are emitting high-energy neutrinos. An analysis of 10 years of IceCube data using the latest detector calibration and reconstruction methods, finds an excess of 4.2σ (after correcting for look-elsewhere effects) for neutrino events from the direction of the nearby Seyfert galaxy NGC 1068 [27]. Figure 5 shows the observed excess of events from the direction of NGC 1068. Assuming

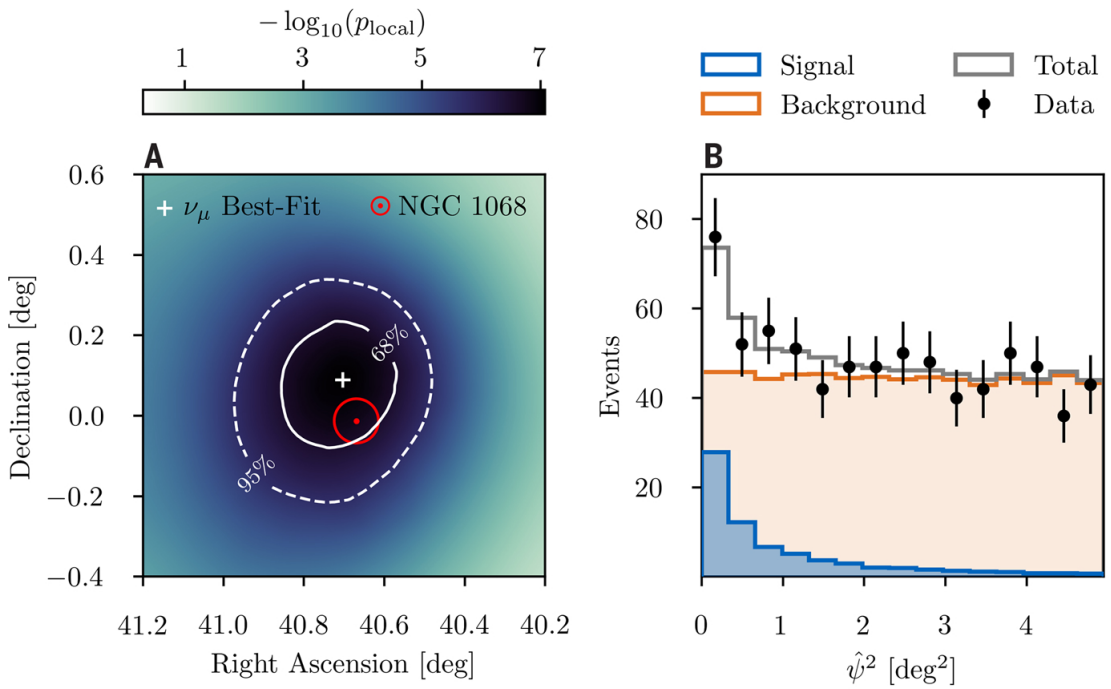

Figure 5: *Left:* Significance map of the sky region around NGC 1068. The point of maximum significance (hot spot) is marked by a white cross, the red circle shows the position of NGC 1068. In addition, the solid and dashed contours show the 68% (solid) and 95% (dashed) confidence regions of the hot spot localization. *Right:* The distribution of the squared angular distance between NGC 1068 and the reconstructed event direction. Background (orange) and the signal (blue) are estimated from Monte Carlo simulation assuming the best-fit spectrum at the position of NGC 1068. The superposition of both components is shown in gray and provides an excellent match to the data (black). Figure adapted from [27].

a power-law spectrum, the spectral index γ of the source is fitted to $\gamma = 3.2 \pm 0.3$ with a ν_μ flux at 1 TeV of $(5.0 \pm 2.1) \times 10^{-11}$ TeV^{-1} cm^{-2} s^{-1}.

For a long time, cores of active galaxies have been speculated to be efficient CR accelerators (see, e.g., [28] for a review). The emission of gamma radiation is considered to be strongly suppressed in the GeV and TeV band, due to absorption in the photon fields and gas clouds surrounding the core region. The assumption of strong gamma-ray absorption is consistent with the best-fit neutrino luminosity of NGC 1068 between 1.5 TeV and 15 TeV that follows from the IceCube observations. It is over an order of magnitude higher than the observed gamma-ray luminosity between 100 MeV and 100 GeV. Consequently, AGN core emission could dominate the neutrino sky at TeV energies, even though non-blazar AGNs constitute only a relatively small fraction of the gamma ray sources and the total emission observed at GeV energies. This is also supported by a different IceCube study, which searches the data for a signature of cumulative neutrino emission from tens of thousands of AGN cores observed in the IR and soft X-ray wavebands. In this study an excess of 2.6σ is found over background expectations, consistent with a contribution of AGN core neutrinos of more than 27% to the total observed extragalactic neutrino flux at 100 TeV [29].

The first compelling evidence for a neutrino point source came from the detection of one neutrino event (IC-170922A) in spatial and temporal coincidence with an enhanced γ-

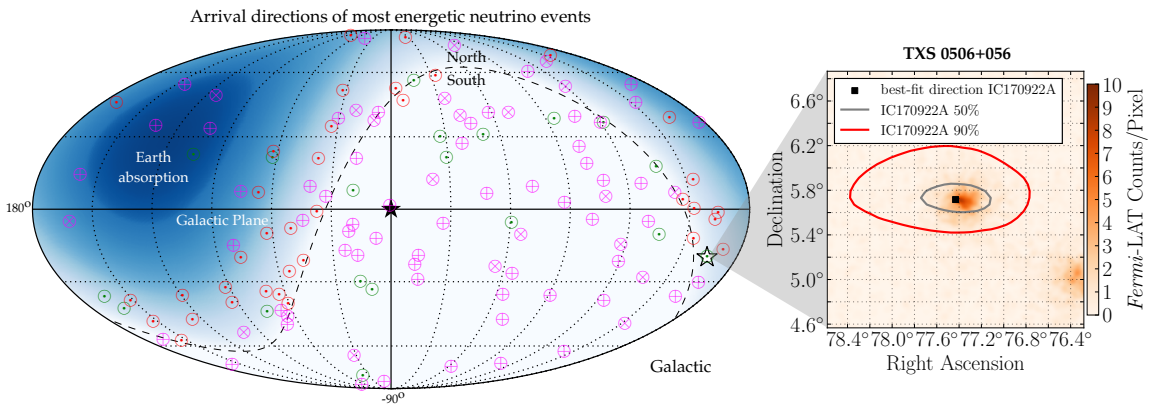

Figure 6: A sky map of highly energetic neutrino events detected by IceCube. Shown are the best-fit directions for upgoing track events [30, 31] collected in 8 years of IceCube operations (⊙), the high-energy starting events (HESE) (tracks ⊗ and cascades ⊕) [18, 32, 33] collected in 6 years, and additional track events published as public alerts (⊙) [34] since 2016. Note that the angular resolution for the different event categories varies from ≲1 deg for high-quality track events to ≳10 deg for cascade-type events. The distribution of these samples of events is consistent with isotropy once detector acceptance and neutrino Earth absorption are taken into account. The location of the first candidate neutrino source, the blazar TXS 0506+056, is marked with a white star. Shown in the inset are the related *Fermi Large Area Telescope* (LAT) measurements of the region centered on TXS 0506+056 around the time that the high-energy neutrino IC-170922A was detected by IceCube (September 2017) [5]. The uncertainty on the reconstructed arrival direction of IC-170922A is shown for reference.

ray emission state of the blazar TXS 0506+056 [5] (see Figure 6), along with a period of enhanced neutrino emission from this source in 2014/15 revealed in a dedicated search in the IceCube archival data [6]. The individual statistical significance of the blazar-neutrino association and the observed excess in the IceCube data alone is 3σ and 3.5σ respectively. Additional events of a similar nature are required to allow definitive conclusions about the production mechanism of neutrinos in blazars. At the same time, it is becoming increasingly clear that γ-ray blazars can not explain the majority of astrophysical neutrinos observed by IceCube: the number of observed coincidences is smaller than expected when compared to the total number of cosmic neutrino events [5, 35]. Further, a comparison of the full set of IceCube neutrinos with a catalog of γ-ray blazars does not produce evidence of a correlation and results in an upper bound of ~30% as the maximum contribution from these blazars to the diffuse astrophysical neutrino flux below 100 TeV [36]. Accordingly, a blazar population responsible for the neutrinos would have to be appropriately dim in γ-rays (see, e.g., [37, 38]).

Another widely considered candidate source population of extragalactic neutrinos are γ-ray bursts (GRBs). Similar to blazars, the non-detection of neutrinos in spatial and temporal coincidence with GRBs over many years has placed a strict upper bound of 1% for the maximum contribution from observed GRBs to the diffuse flux observed by IceCube [41]. In contrast, a larger than expected contribution to the total neutrino flux might arise from a different class of transients, also related to stellar death. Tidal Disruption Events (TDEs) are rare transients that occur when stars pass close to super-massive black holes (SMBHs) and get ripped apart by tidal forces. Theoretical studies

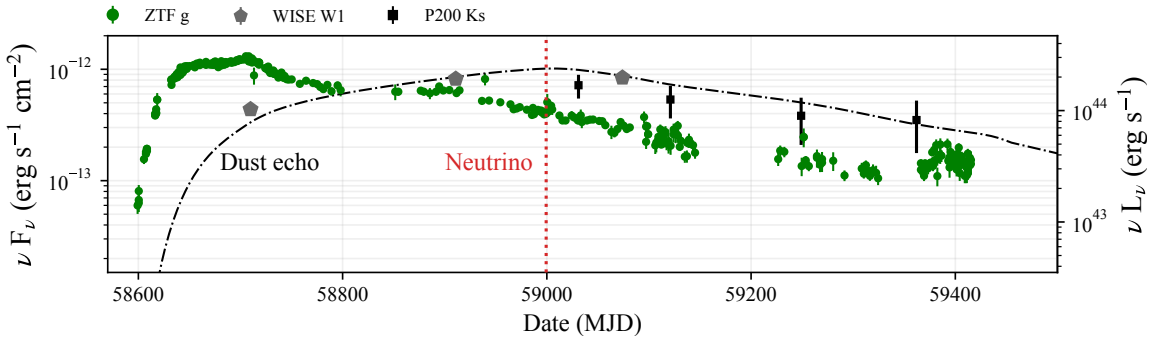

Figure 7: Optical (ZTF) and IR (WISE, P200) light curves of AT 2019fdr in relation to the arrival time of the spatially coincident high-energy neutrino observed by IceCube. The dashed-dotted line corresponds to a simple model of a *dust echo*, i.e., delayed emission from dust heated by the initial UV radiation [39]. Figure adapted from [40].

have suggested that TDEs are sources of high-energy neutrinos and cosmic rays [42–44], including the subset of TDEs with relativistic particle jets [45–48].

The radio-loud TDE AT 2019dsg was identified in spatial coincidence with the high-energy neutrino alert IC-191001A [49] in a follow-up search conducted by the Zwicky Transient Facility(ZTF), an optical survey telescope. The p-value for a chance coincidence of such an object with any of the high-energy neutrinos that were followed up with ZTF observations was determined to be 2×10^{-3} [50]. This first neutrino-TDE association was modeled assuming various emission scenarios (see [51] for a review of the models), confirming that TDEs are conceivable sources of high-energy neutrinos.

After this initial association of the TDE AT 2019dsg with a high-energy neutrino, a second, similar event (AT 2019fdr) — classified as a TDE candidate [52] — was observed in coincidence with a high-energy neutrino [40], following the same procedure as for AT 2019dsg. Observations of a possible dust echo (see Figure 7), combined with host galaxy information, make it plausible that the two TDE events and the observed neutrinos have similar physical origin. Observing both coincidences by chance can be excluded with a significance of around 4σ [40].

Source populations in addition to those mentioned above are anticipated to contribute to the observed cosmic neutrino flux. Starburst galaxies or galaxy clusters are candidates, but no indications for neutrino emission have been observed so far. A stacking search with over one thousand galaxy clusters constrains the flux of neutrinos from massive galaxy clusters ($M_{\rm gc} \geq 10^{14} M_\odot$) to be no more than 5% of the diffuse IceCube neutrino flux at 100 TeV [53]. A parallel stacking search with 75 galaxies showing extreme star-formation rates, so called ultra-luminous infrared galaxies (ULIRGs, $L_{\rm IR} \geq 10^{12} L_\odot$), also does not find any indications for a neutrino flux from such galaxies. This constrains their maximal contribution to the diffuse IceCube neutrino flux to about 10% at 100 TeV, assuming a power-law spectrum with index -2.5 for the neutrino emission from ULIRGs [54].

Galaxy clusters and star-forming galaxies are usually considered transparent to γ-rays produced in the same hadronic interactions as the neutrinos. In addition to the direct neutrino flux upper limits from IceCube searches, indirect constraints on the multi-TeV neutrino flux from such sources exist from the observations of the total extragalactic

γ-ray emission in the GeV band [55] (see Section 1.3), indicating that at least a fraction of the observed neutrinos needs to arise from source classes that are opaque to the γ-rays produced along with the neutrinos. The evidence from IceCube observations for neutrino and CR production in blazar jets, AGN cores and TDE is consistent with this picture.

IceCube has demonstrated that the nature of the neutrino sky is complex, with the question of the CR sources, as well as how and in which environments CR are accelerated to produce the observed high-energy neutrino flux as yet largely unresolved and among the most intriguing unknowns in astronomy. IceCube-Gen2, through its larger size and improved technology (see Section 3.3), is designed to achieve a sensitivity 5 times that of IceCube, bringing within reach the goal of uncovering and disentangling the prospective populations of sources ([56], see also Section 2.1.2).

1.3 The energy spectrum and flavor composition of cosmic neutrinos

The spectrum and flavor composition of the diffuse cosmic neutrino flux, generated by all the sources that cannot be resolved, contain important information about the acceleration mechanisms, source environments, and population properties. A combined analysis of all available IceCube data in 2015 resulted in a spectrum consistent with an unbroken power law with best-fit spectral index of -2.50 $\pm$ 0.09 above 25 TeV [57]. Newer measurements of the spectrum in individual detection channels are consistent with this early measurement. An analysis of cascade-type events of all flavors collected by IceCube between 2010 and 2015 finds a spectral index -2.53 $\pm$ 0.07 above 16 TeV [17], while the analysis of high-energy muon tracks collected over almost 10 years finds a spectral index of -2.37 $\pm$ 0.09 above 15 TeV [58] (see Figure 8). The recent observation of a candidate event from resonant anti-neutrino electron scattering (Glashow resonance, [21]) with an energy of 6 PeV [22] is also consistent with these spectral parameters. While no neutrinos have been observed by IceCube with inferred energies substantially above 10 PeV, searches for ultra-high-energy (UHE) neutrinos in this energy range have already placed significant constraints [59, 60] on the composition of UHE cosmic rays, the redshift evolution of their sources (see also discussion below in this section), and generic astrophysical sources producing such UHE neutrinos (e.g., [61, 62]).

The flavor composition is only beginning to be meaningfully constrained by IceCube data as shown in Figure 9. So far it is compatible with a standard astrophysical production scenario, with neutrinos resulting from decays of pions and muons that have not been subject to significant previous energy loss. A flavor ratio of $\nu_e : \nu_\mu : \nu_\tau = 1 : 2 : 0$ at the source is expected for this case. Neutrino oscillations change this into $\nu_e : \nu_\mu : \nu_\tau \approx 1 : 1 : 1$ at Earth [57].

Measurements of the isotropic neutrino flux (ϕ) are shown in Figure 10, along with the observed isotropic γ-ray background and the UHE cosmic-ray flux. The correspondence among the energy densities (proportional to $E^2\phi$) observed in neutrinos, γ-rays, and UHE cosmic rays suggests a strong multi-messenger relationship. We highlight three areas:

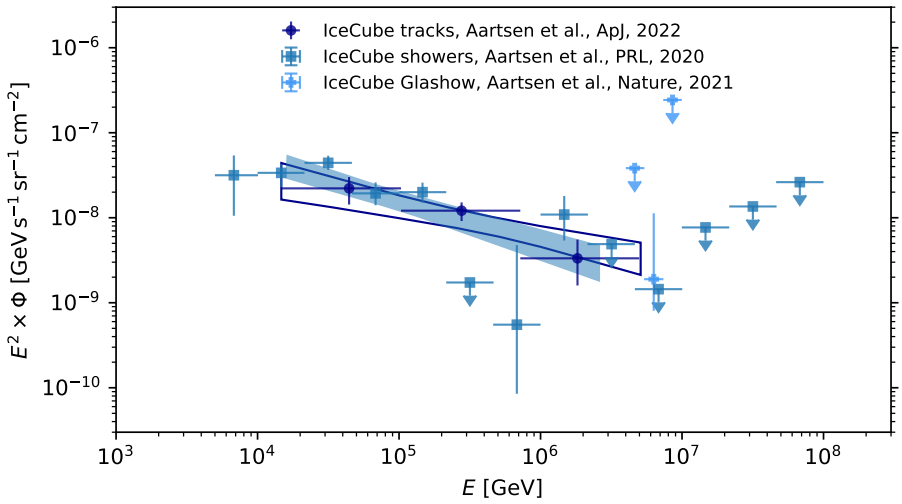

Figure 8: Spectrum of cosmic neutrinos measured in several detection channels [17, 22, 58], The error bars and limits (68% CL) are obtained from a spectral unfolding of the observed events, the shaded regions from fitting the observed events with a power-law spectrum. Φ corresponds to the per-flavor flux assuming a flavor composition of $\nu_e : \nu_\mu : \nu_\tau = 1 : 1 : 1$.

.

A) The multi-TeV range: The simultaneous production of neutral and charged pions in CR interactions, which decay into γ-rays and neutrinos respectively, suggests that the sources of high-energy neutrinos could also be strong 10 TeV – 10 PeV γ-ray emitters. For extragalactic scenarios, this γ-ray emission is not directly observable because of the strong absorption on extragalactic background photons, resulting in e^+e^- pair production. High-energy γ-rays initiate electromagnetic cascades of repeated inverse-Compton scattering and pair production that eventually contribute to the diffuse γ-ray flux below 100 GeV provided the source environment is transparent to such γ-rays. This leads to a theoretical constraint on the diffuse neutrino flux from γ-ray transparent sources [64, 65]. The high flux of neutrinos below 100 TeV implied by the measurement of a spectral index significantly softer than -2.15 indicates that at least some neutrino sources are opaque to γ-rays [66, 67].

B) The PeV universe: Precision measurements of the neutrino flux can test the idea of cosmic particle unification, in which sub-TeV γ-rays, PeV neutrinos, and UHE cosmic rays can be explained simultaneously [68–71]. If the neutrino flux is related to the sources of UHE cosmic rays, then there is a theoretical upper limit (the dashed green line in Figure 10) to the neutrino flux [72–74]. UHE cosmic-ray sources can be embedded in environments that act as “CR reservoirs” where magnetic fields trap CR with energies far below the highest CR energies. The trapped CR collide with gas and produce a flux of γ-rays and neutrinos at PeV energies. The measured IceCube flux is consistent with predictions of some of these models [75–77] (see, however, [78]). The precise characterization of the spectrum and flavor composition beyond the energy range currently accessible by IceCube goes hand in hand with resolving the sources, as the combination of the two will provide novel avenues for understanding the most extreme particle accelerators in the universe.

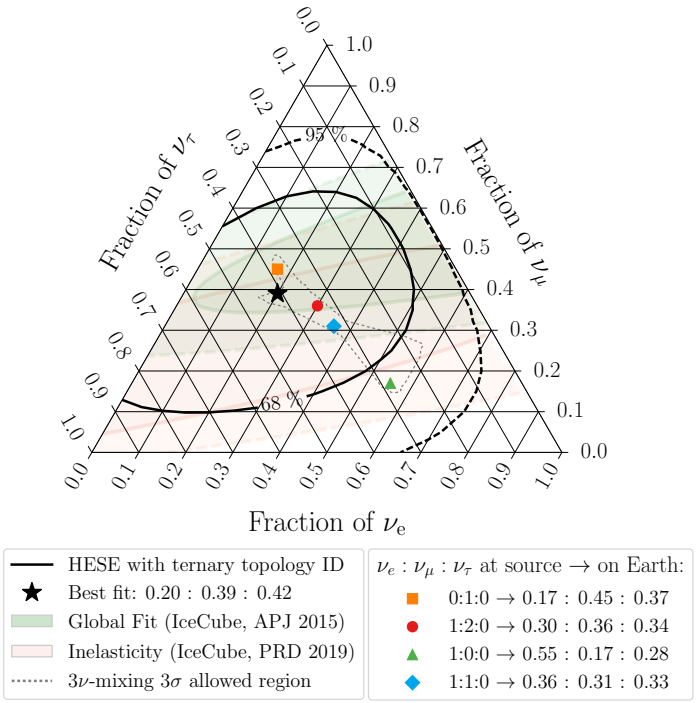

Figure 9: Flavor constraints on the cosmic neutrino flux from various analyses of IceCube data. The constraints from an analysis identifying IceCube's first tau neutrino candidates [20] is shown as black contours. Constraints from earlier measurements, a fit encompassing several IceCube datasets [57] and an analysis of the inelasticity distribution of IceCube high-energy events [63] are shown as shaded regions. They are compared to different scenarios of neutrino production in astrophysical sources and the full range of possible flavor compositions assuming Standard Model flavor mixing (gray dotted region)

.

C) Ultra-high energies (UHE): The attenuation of UHE (E > 10^{18} eV) cosmic rays through resonant interactions with cosmic microwave background photons is the dominant mechanism for the production of UHE neutrinos during the propagation of the CR in the universe. This mechanism, first pointed out by Greisen, Zatsepin and Kuzmin (GZK), would cause a suppression of the UHE cosmic-ray proton flux beyond 5×10^{10} GeV [81, 82] and gives rise to a flux of UHE neutrinos [83] that is shown in Figure 10, but has not yet been detected. The observation of these *cosmogenic* neutrinos in addition to the potential direct identification of astrophysical sources or transients producing neutrinos at ~EeV energies, or a stringent upper limit on their flux, will provide information on the cosmological evolution of UHE cosmic-ray sources and restrict the models of acceleration, spectrum and composition of extragalactic CR (e.g., [64, 83–101]).

To make significant progress on the above questions a future detector should provide several times higher neutrino statistics in the PeV range, flavor identification capabilities, and expand IceCube's energy range to provide sensitivity for neutrinos with 10^{18} eV (1 EeV) at an energy flux level $E^2\Phi < 10^{-9}$ GeV s^{-1} cm^{-2} sr^{-1}. Radio detection techniques are being developed that measure the radio pulses generated in the particle cascades induced by neutrino interactions in the ice to deliver a cost-effective way to explore the EeV energy range. The IceCube-Gen2 radio array component is designed

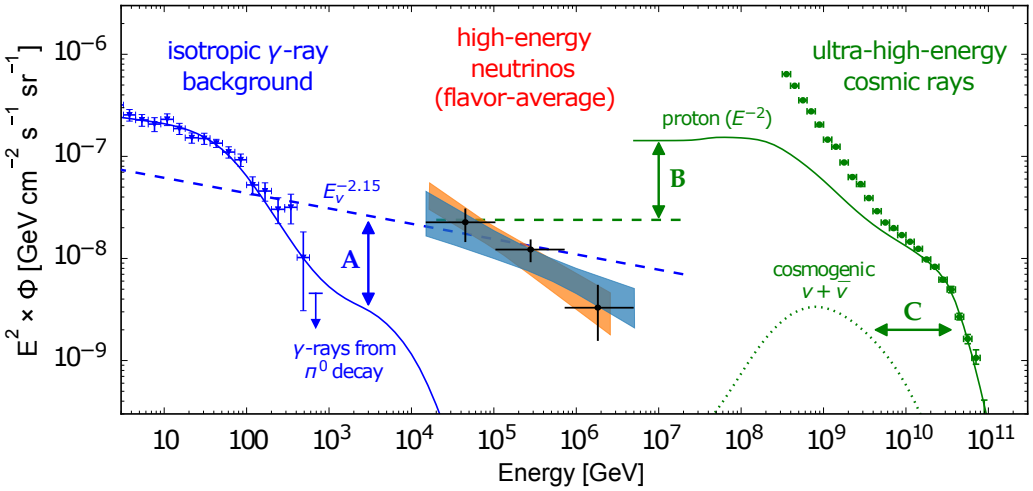

Figure 10: The per-flavor flux (ϕ) of neutrinos [17, 58] (orange and blue bands) compared to the flux of unresolved extragalactic γ-ray emission [55] (blue data) and UHE cosmic rays [79] (green data). We highlight two upper limits on the neutrino flux (dashed lines) predicted by multi-messenger models [74, 80].

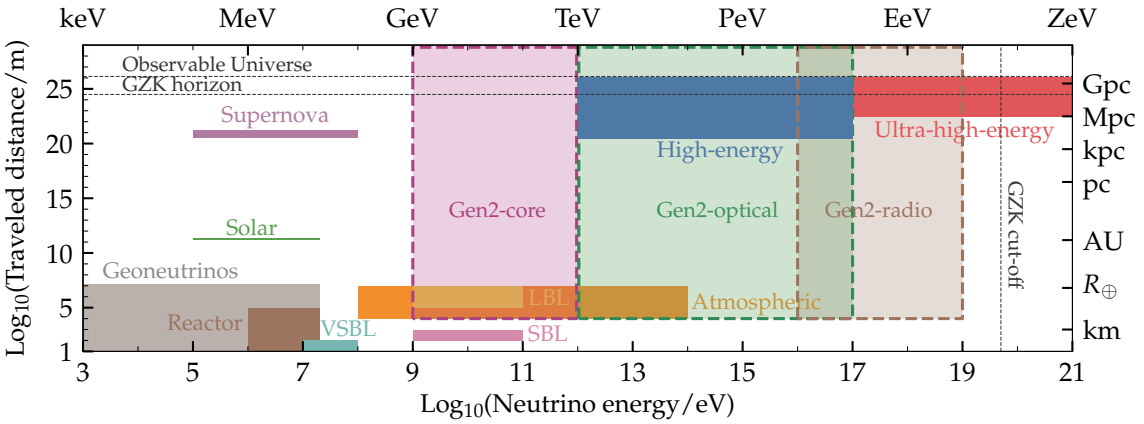

Figure 11: Range of travel distances and energies for neutrinos of different origin that are used for tests of fundamental physics. The IceCube-Gen2 observatory will cover a large range of energies and distances, observing both atmospheric and cosmic neutrinos, the latter indicated by the blue and red bands.

to provide the necessary sensitivity at EeV energies to study the cosmic neutrino flux and astrophysical neutrino sources directly connected to the highest energy CRs. The design of the IceCube-Gen2 optical array component to provide a 5 times higher sensitivity for detecting neutrino sources will increase the rate of detected neutrinos in the PeV range by a factor 10 compared to IceCube.

1.4 Exploring fundamental physics with high-energy neutrinos

The flux of high-energy atmospheric and very high-energy cosmic neutrinos is invaluable, not just for investigations of extreme astronomical sources, but also for probing fundamental properties of the neutrino itself. Often these probes require the observation of neutrinos over specific travel distances (baselines) and in specific energy ranges (e.g., [102, 103]).

The neutrino interaction cross section can be probed indirectly through absorption in the Earth, which depends on the energy and angle dependent matter column. This allows us to test Standard Model predictions, and constrain hypothesized beyond Standard Model (BSM) physics, including new spatial dimensions and leptoquarks [16]. The flavor composition of the cosmic neutrino flux, predicted to lie in a narrow range for various source models and standard neutrino oscillations, probes BSM physics and the structure of space-time itself through propagation effects over cosmic baselines.

Below 100 TeV, the large statistics of atmospheric neutrino events observed by open water/ice detectors yields sensitivity to anomalous oscillation signatures for which some of the strongest constraints originate from IceCube data. These include signatures due to additional sterile neutrinos [104–107], violation of Lorentz Invariance [108], or previously unobserved neutrino production channels such as forward charm production in the atmosphere [30]. In addition, neutrinos are favorable messengers to search for signatures from the annihilation or decays of heavy dark matter with masses beyond about 100 TeV [109–111]. Finally, neutrino detectors are excellent instruments to search for hypothesized exotic particles that would leave distinct traces in the detector, such as magnetic monopoles or other predicted particles in the extensions of the Standard Model (e.g., [112, 113]).

The general requirements for future BSM measurements are similar to those for astrophysics: a much enlarged sample of cosmic neutrinos and an extension of the energy range beyond 10^{18} eV. IceCube-Gen2 is ideally positioned to provide both of these elements through the combination of optical and radio detection methods (see also Section 2.4). Figure 11 shows the unique coverage of both the high-energy and cosmological baseline domains that IceCube-Gen2 will provide.

1.5 Summary of objectives for a next-generation neutrino observatory

The observations described above provide the broader science motivation for a next generation neutrino observatory, and have been discussed within the astronomical community as part of the Astro2020 Decadal Survey. These contributions propose a diverse set of neutrino research topics to pursue, focusing on neutrino astronomy [56], fundamental physics with cosmic neutrinos [102], cosmic ray science [114–116], extragalactic sources [117–119], Galactic sources [120, 121], multi-messenger studies with γ-rays [122–125] and multi-messenger studies with gravitational waves [126–128].

The scientific goals can be grouped according to the following topics:

1. *Resolving the high-energy neutrino sky from TeV to EeV energies:* What are the sources of high-energy neutrinos detected by IceCube? The IceCube-Gen2 sensitivity should allow identifying realistic candidate source populations.
2. *Understanding cosmic particle acceleration through multi-messenger observations:* This involves studying particle acceleration and neutrino emission from a range of multi-messenger sources (e.g., AGN, GRBs, TDEs, SNe or kilonovae). Constraints on the physics within these sources can also come from measurements of the spectrum and flavor composition of the astrophysical neutrino flux.

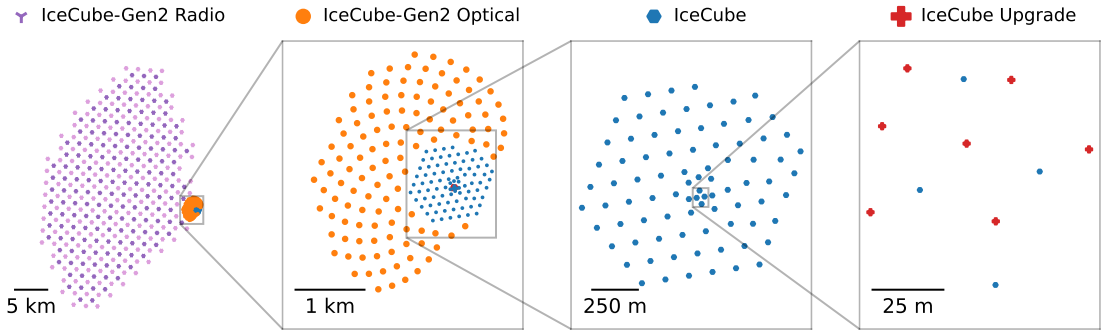

Figure 12: Top view of the envisioned IceCube-Gen2 Neutrino Observatory facility at the South Pole station, Antarctica. From left to right: The radio array consists of 361 stations (shallow and hybrid) in the reference design. The optical high-energy array features 120 new strings (shown as orange points) that are spaced 240 m apart and instrumented with 80 newly developed optical modules each, over a vertical length of 1.25 km. The total instrumented volume of the optical detector in this design is 7.9 times larger than the current IceCube detector array (blue points). On the far right, the layout for the seven IceCube Upgrade strings relative to existing IceCube strings is shown.

3. *Revealing the sources and propagation of the highest energy particles in the Milky Way and the Universe:* This includes studying Galactic and extragalactic cosmic-ray sources and their neutrino emission, cosmic ray interactions in the interstellar medium, the properties of cosmic rays in the galactic-extragalactic transition region above 100 PeV, as well as the propagation of extragalactic cosmic rays through the measurement of cosmogenic neutrinos.
4. *Probing fundamental physics with high-energy neutrinos and cosmic rays:* This entails studying hadronic interactions in the PeV domain, measuring neutrino cross sections at energies far beyond the reach of terrestrial particle accelerators, searching for new physics from neutrino flavor mixing over cosmic baselines, and searching for heavy dark matter particles, monopoles and other particles predicted by SUSY or theories with extra dimensions.

1.6 The IceCube-Gen2 neutrino telescope

The IceCube-Gen2 facility designed to achieve the goals outlined in the previous section will encompass the currently operating IceCube detector, including the 7 new strings in the center of the IceCube array that are scheduled for a 2025/2026 deployment in the *IceCube Upgrade*. Three new components will be added to the existing detector: an in-ice optical array, a surface air shower array, and an extended radio detector array. Figure 12 presents a top view of the IceCube-Gen2 facility, with its various components, each utilizing optimized technologies for the targeted energy ranges. The surface array will be installed on the footprint of the optical array.

The optical array, optimized for the detection of TeV and PeV neutrinos, will feature 120 new strings, each equipped with 80 photosensors that collect 4 times more light than current IceCube DOMs. These 9600 new photosensors will be distributed along each string with a vertical spacing of ~17 m at depths ranging from 1.35 km to 2.7 km below

the surface. The horizontal spacing between strings will be 240 m, about twice the spacing of IceCube strings. Combined, this leads to an instrumented volume of 7.9 km^3 (~1 km^3 for IceCube), increasing the collection rates of neutrinos interacting inside the instrumented volume by almost an order of magnitude. The number of through-going track-like events will increase by a factor of ~4–6 dependent on their direction of incidence*. Together with an improved directional reconstruction, this will allow to detect five times fainter point sources with the IceCube-Gen2 optical array than IceCube is able to.

The entire footprint of the optical array will be covered by a surface array for CR air showers, consisting of scintillator tiles and radio antennas. The surface array serves a dual purpose: as an instrument for studying CRs and their interactions, as well as a veto for the optical array, rejecting particles of atmospheric origin.The scintillator tiles, deployed with a surface filling factor of $2.5{\times}10^{-4}$ will achieve an energy threshold of $\lesssim$500 TeV for CR protons. The atmospheric particle veto acceptance of 8 km^2 sr is 30 times higher than with IceCube's current surface array, IceTop. It's field-of-view will be 20% of the sky, four times the field-of-view of IceTop.

The radio array will target the detection of ultra-high-energy neutrinos in the energy range from 10 PeV to 100 EeV, where no astrophysical neutrino flux has yet been observed due to the limited size of IceCube. Two types of stations for the detection of the radio emission from charged particle showers produced in neutrino interactions are deployed with a spacing of 1.24 km between individual stations. Hybrid stations with antennas near the surface and up to 150 m deep in the ice, and shallow stations with only antennas near the surface complement each other. Together, they form a detector with a footprint of more than 500 km^2 and an effective volume of 1.6×10^3 km^3 sr (trigger level). Such an enormous volume is necessary to achieve a sensitivity that allows the detection of the cosmic neutrino flux in this unexplored energy range in a large number of predicted scenarios.

The science goals and the resulting requirements on the instrument performance that drive the design of IceCube-Gen2 are laid out in Section 2. More details about the reference design of the IceCube-Gen2 facility, the individual sensors and the motivation for various design choices can be found in Section 3. Table 1 summarizes the key instrument characteristics discussed in this section.

*The number of through-going tracks approximately scales with the projection of the instrumented volume on the plane perpendicular to the direction of incidence.

Table 1: Summary of key parameters for the reference design for IceCube-Gen2, in comparison to the existing IceCube detector and the under-construction IceCube Upgrade. The IceCube-Gen2 facility encompasses both, IceCube and IceCube Upgrade. The radio array for the detection of ultra-high-energy neutrinos will be a unique element of IceCube-Gen2, no such array is present in IceCube.

Design parameter	IceCube	IceCube Upgrade	IceCube-Gen2
Optical array			
# of strings	86	7	120[†]
# of optical sensors	5,160	680	9,600[†]
String spacing	120 m	22 m	240 m[†]
Instrumented volume	1 km^3	0.0024 km^3	7.9 km^3
Energy threshold	100 GeV	5 GeV	1 TeV[†]
Surface array			
Aperture	0.25 km^2 sr		8 km^2 sr
Field-of-view	0.63 sr		2.5 sr
Energy threshold (protons)	250 TeV		500 TeV[†]
Radio array			
# of stations			361
Distance between stations			1.24 km
Effective volume (trigger level)			1.6×10^3 km^3 sr
Energy threshold			10 PeV

[†] This value refers to the new instrumentation only.

1.7 Global multi-messenger astronomy efforts

Neutrino astronomy is inherently multi-messenger astronomy. As described extensively in Sections 1.1 and 2, the full picture of the non-thermal universe can be obtained only through the combination of neutrino observations with measurements of the broad-band electromagnetic spectrum, gravitational waves and cosmic rays. Fortunately, IceCube-Gen2 will not stand alone but be embedded in an ever growing global landscape of multi-messenger observatories that is expected to evolve significantly over the next decades.

In the next few years, two km^3-scale Northern Hemisphere neutrino telescopes will complement IceCube. KM3NeT in the Mediterranean and the Gigaton Volume Detector (GVD) in Lake Baikal are both currently under construction. Additionally, a water-based neutrino telescope P-ONE [129] is under development in the Pacific Ocean off the coast of Canada, aiming to deploy by the end of this decade. After completion, they will observe the Southern sky with a sensitivity comparable to IceCube's for the Northern Hemisphere. Taken together, KM3NeT, GVD, P-ONE, and IceCube will therefore have full coverage of the neutrino sky from 100 GeV to energies beyond a few PeV.

The start of IceCube-Gen2 construction is anticipated at a time when KM3NeT and GVD will likely be fully operational. Hence, the build-up of a global network of large neutrino observatories follows a staged approach. After obtaining full sky coverage with the two Northern Hemisphere detectors, IceCube-Gen2 will push for the next level in neutrino astronomy on both the intensity and energy frontiers, expanding the energy range of neutrino telescopes to EeV energies, while improving source sensitivity by a factor of 5, and the source detection volume for transients by a factor of at least 10 (cf. Section 2.1.1).

Once completed, IceCube-Gen2 will be embedded in a network of large-scale observatories surveying the sky from radio to γ-rays, detecting gravitational waves as well as the highest-energy charged cosmic rays. SKA, a radio telescope with a collective aperture of 1 km^2 [130], will give an unprecedented view of the radio sky. New near-infrared sky surveys are scheduled for the next decade by EUCLID [131] and the Roman space telescope [132], in addition to deep observations by the James Web Space Telescope (JWST). The Vera C. Rubin observatory [133], an 8.4 m diameter optical telescope, will perform a deep optical survey of the full sky visible from Chile.

ULTRASAT [134], a UV survey telescope to be launched in the upcoming years will allow fast follow-up of neutron star mergers, tidal disruption events and flares of active galaxies. NASA has recently selected two candidate mid-scale explorer class missions, UVEX [135] and STAR-X [136], one of which will ensure UV survey and follow-up capabilities for the 2030s. In the domain of X-rays, eROSITA [137] is currently performing a full sky survey at soft X-rays that is more than an order of magnitude deeper than previous all-sky surveys. In the next decade, the Advanced Telescope for High Energy Astrophysics (ATHENA) [138] will dramatically surpass imaging and spectroscopy capabilities of today's X-ray telescopes. At high energies, above few tens of GeV, the Cherenkov Telescope Array (CTA), an international γ-ray observatory with both a Southern and Northern site [139] to be completed within this decade, will give us new insights into the γ-ray sky. In parallel, AugerPrime [140] will enhance our understanding of the ultra-high energy CR spectrum and composition.

Technology upgrades of existing gravitational wave detectors such as LIGO [141], VIRGO [142] and KAGRA [143] will allow the detection and improve the localization of more and more sources of gravitational waves over the next decade. Scheduled for launch in 2037, the Laser Interferometer Space Antenna (LISA) [144] will open a window into a new frequency domain for gravitational wave observations. IceCube-Gen2, designed for more than a decade of observations, is also expected to work in parallel to currently planned 3rd generation gravitational wave detectors like the Einstein and Cosmic Explorer telescopes [145, 146].

As the world's most sensitive neutrino telescope, and covering an unprecedented wide range of energies from GeV to EeV, IceCube-Gen2 has a truly unique and essential role in this new multi-messenger world. The high-energy neutrino sources, transients and individual neutrino alerts that will be observed by IceCube-Gen2 can be followed-up across the electromagnetic spectrum with a new generation of telescopes that surpass the performance of today's instruments by a large margin. This follow-up will allow to associate neutrino sources with their electromagnetic and gravitational wave counterparts. Conversely, observations of electromagnetic transients and gravitational waves

can be correlated to the all-sky IceCube-Gen2 observations to measure or constrain the neutrino flux and ultimately lead to a better understanding of CR acceleration mechanisms in these events.

2 IceCube-Gen2 Science: Exploring the cosmic energy frontier

IceCube-Gen2 is designed to observe the neutrino sky from TeV to EeV energies with a sensitivity to individual sources at least five times better than IceCube. It will collect at least ten times more neutrinos per year than IceCube and enable detailed studies of their distribution on the sky, energy spectrum, and flavor composition, as well as tests of new physics on cosmic baselines. In this section, we focus on the expected impact of the IceCube-Gen2 observatory in the young field of neutrino and multi-messenger astronomy. It is structured according to the four key science objectives defined in Section 1.5: resolving the high-energy sky (Section 2.1), understanding the cosmic particle acceleration (Section 2.2), revealing the sources and propagation of cosmic rays (Section 2.3), and probing fundamental physics with high-energy neutrinos (Section 2.4).

All performance estimates and sensitivities in this section are calculated for the reference designs of the optical, surface and radio arrays as described in Section 3. They are based on simulation studies using the IceCube and *NuRadioMC* simulation software frameworks [147, 148], which have been adjusted to the geometries and properties of the proposed IceCube-Gen2 neutrino telescope. Instrument response functions generated from the simulation data for each individual array, are then the input for the calculation of analysis level performance metrics for the combined detector with the *toise* software package [149].

Unless stated otherwise, the figures show the expected combined performance of the IceCube-Gen2 radio and optical arrays, including the surface array veto. An observation time of 10 years is chosen as the baseline for the performance studies, with the exception of transient phenomena, for which individual observation durations are chosen, motivated by the expected duration of the transient. The focus of this document is the description of the science enabled by high-energy (TeV and above) neutrinos. A comprehensive overview of the science case for the study of fundamental neutrino properties with GeV neutrinos in a densely instrumented core was presented in [14, 150].

2.1 Resolving the high-energy sky from TeV to EeV energies

Neutrinos are the only messengers that can directly reveal the remote sites — beyond our local universe — where CR are accelerated to PeV and EeV energies. IceCube has been successful in finding the first evidence for cosmic ray acceleration in active galaxies and neutrino emission from the Milky Way. However, ultimately, it is not sensitive enough to resolve spectral features of the brightest neutrino sources, or to detect populations of less luminous sources.

2.1.1 Detection of persistent and transient sources

The proposed IceCube-Gen2 observatory combines an 8 km^3 array for the detection of optical Cherenkov light originating from neutrino interactions with a 500 km^2 radio array for the detection of ultra-high-energy neutrinos. An angular resolution of 10 arcmin at PeV energies for the optical array and a few degrees above 100 PeV for the

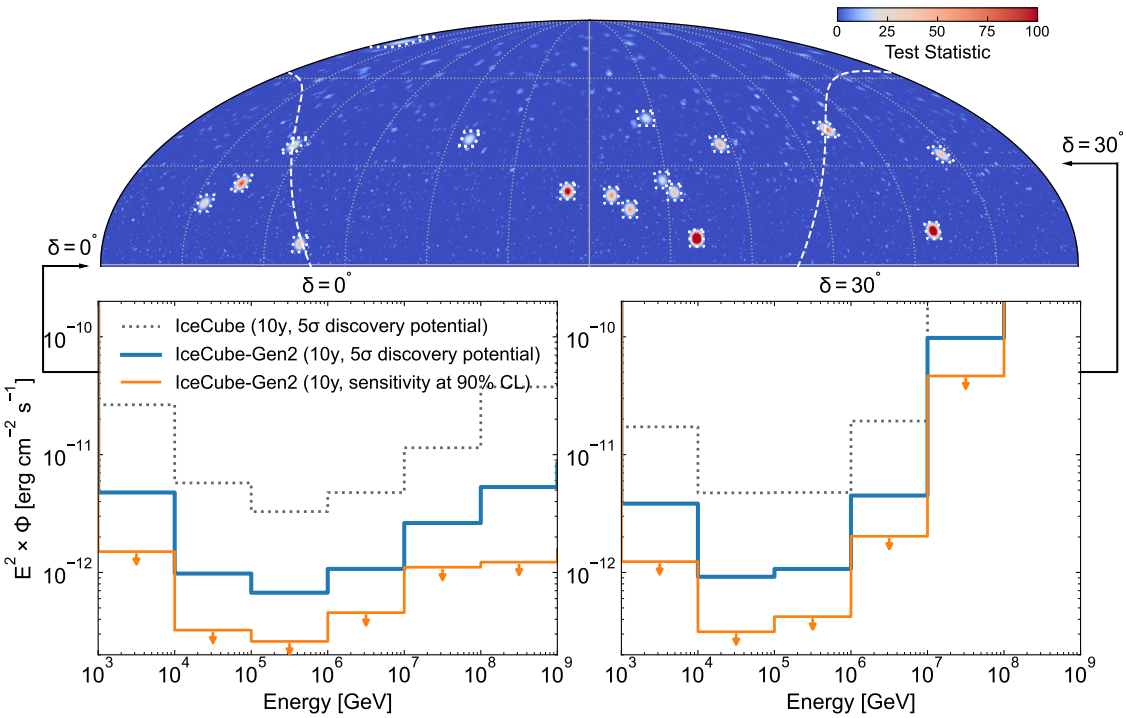

Figure 13: Visualization of source detection capabilities expected for IceCube-Gen2. Source positions on the sky and intensities have been selected randomly from an intensity distribution expected for sources with a constant density in the local universe, and consistent with current IceCube neutrino flux constraints. Shown is the test statistic value determined in a mock-simulation of track-like events that can be obtained at the source position after 10 years of operation of IceCube-Gen2. For better visibility, the region around the sources (indicated by white dotted lines) has been magnified. The position of the Galactic plane is shown as a dashed curve. Below the map, differential sensitivities for the detection of point sources (5σ discovery potential, and sensitivity at 90% CL) are shown for two selected declinations, at the celestial horizon and at $\delta = 30^{\circ}$. Absorption of neutrinos in the Earth limits the sensitivity at PeV energies and above for higher declinations. The IceCube and IceCube-Gen2 sensitivities are calculated separately for each decade in energy, assuming a differential flux $dN/dE \propto E^{-2}$ in that decade only. Neutrino fluxes are shown as the per-flavor sum of neutrino plus anti-neutrino flux, assuming an equal flux in all flavors.

radio array will ensure that individual neutrinos are well localized on the sky and can be correlated with potential counterparts in the electromagnetic spectrum. This will enable more sources to be distinguished from diffuse backgrounds. Details about the instrumentation and performance can be found in Section 3.

IceCube-Gen2 will allow the observation of sources at least five times fainter than those observable with currently operating detectors. An impression of the neutrino sky that can be expected in the IceCube-Gen2 era is presented in Figure 13. It shows a test statistic map obtained from the simulation of the arrival direction of muon neutrinos for a detector as sensitive as IceCube-Gen2 searching for point sources of neutrinos. The neutrino flux of the simulated sources has been chosen randomly from a model extra-galactic source population that has a number density distribution expected of sources having a uniform density and luminosity in the local universe. The intensity of the model sources is consistent with current constraints from IceCube observations. Po-

tential Galactic sources as discussed below in Section 2.3.1 have been added. The differential sensitivity curves in Figure 13 for two selected declinations allow a quantitative evaluation of the source detection potential of IceCube-Gen2. They refer to the sensitivity of the optical array only, as there are large uncertainties on the sensitivity of the radio array for long-duration observations of steady neutrino sources due to the unknown backgrounds at these energies, from, e.g., diffuse astrophysical and cosmogenic neutrinos.

IceCube-Gen2 reaches its peak sensitivity in the region around the celestial equator. Due to the huge atmospheric backgrounds and the increased absorption in the Earth at high neutrino energies, the sensitivity below 100 TeV is largest for events from the Northern Hemisphere, while above a few PeV, mainly the southern sky is observed. Between 100 TeV and 1 PeV the Northern Hemisphere averaged 5σ discovery potential for a neutrino energy flux is 1.3×10^{-12} ergs cm^{-2} s^{-1} — similar to the energy flux level the current generation of high-energy and very-high-energy γ-ray telescopes can detect in the GeV to TeV range.

As γ-rays and neutrinos are produced by CRs in the same interaction processes, their energy fluxes are expected to be similar at production. However, due to absorption of γ-rays in the sources and the intergalactic medium, the photons are reprocessed to the GeV and TeV bands (or absorbed, in which case the neutrino energy flux could be even higher than the γ-ray energy flux). Consequently, IceCube-Gen2 will be able to measure or constrain CR acceleration processes for thousands of known γ-ray sources, as well as searching for cosmic accelerators opaque to high-energy electromagnetic radiation.

Short, second-to-day-scale transients like GRBs, compact object mergers, or core-collapse supernovae (CCSN) explosions are different from persistent sources. Backgrounds from diffuse neutrinos, air showers, thermal and anthropogenic noise are usually negligible when searching for a short burst of neutrinos; therefore, the sensitivity scales differently with effective area, volume, and angular resolution than for persistent sources.

An important performance measure for transient events is the volume within the universe in which they can be observed. Figure 14 shows the observable volume of the universe for IceCube-Gen2 in comparison to IceCube for a generic 100 s burst with equivalent isotropic emission of 10^{50} erg in neutrinos as a function of energy. An order-of-magnitude increase in observable volume is expected for energies up to 10 PeV compared to IceCube, while at energies above 100 PeV the radio array will allow for the first time the observation of a relevant portion of the universe.

2.1.2 Detectability of source populations

IceCube performed the first step towards identifying the sources of astrophysical neutrinos by associating high-energy neutrinos with the highly luminous blazar TXS 0506+056, as well as with the nearby active galaxy NGC 1068. IceCube's capability of identifying sources is limited to high-luminosity neutrino sources that have a low density in the local universe, such as blazars, and neutrino transients with a low rate, such as GRBs. Accordingly, IceCube has set stringent constraints on the contribution of these

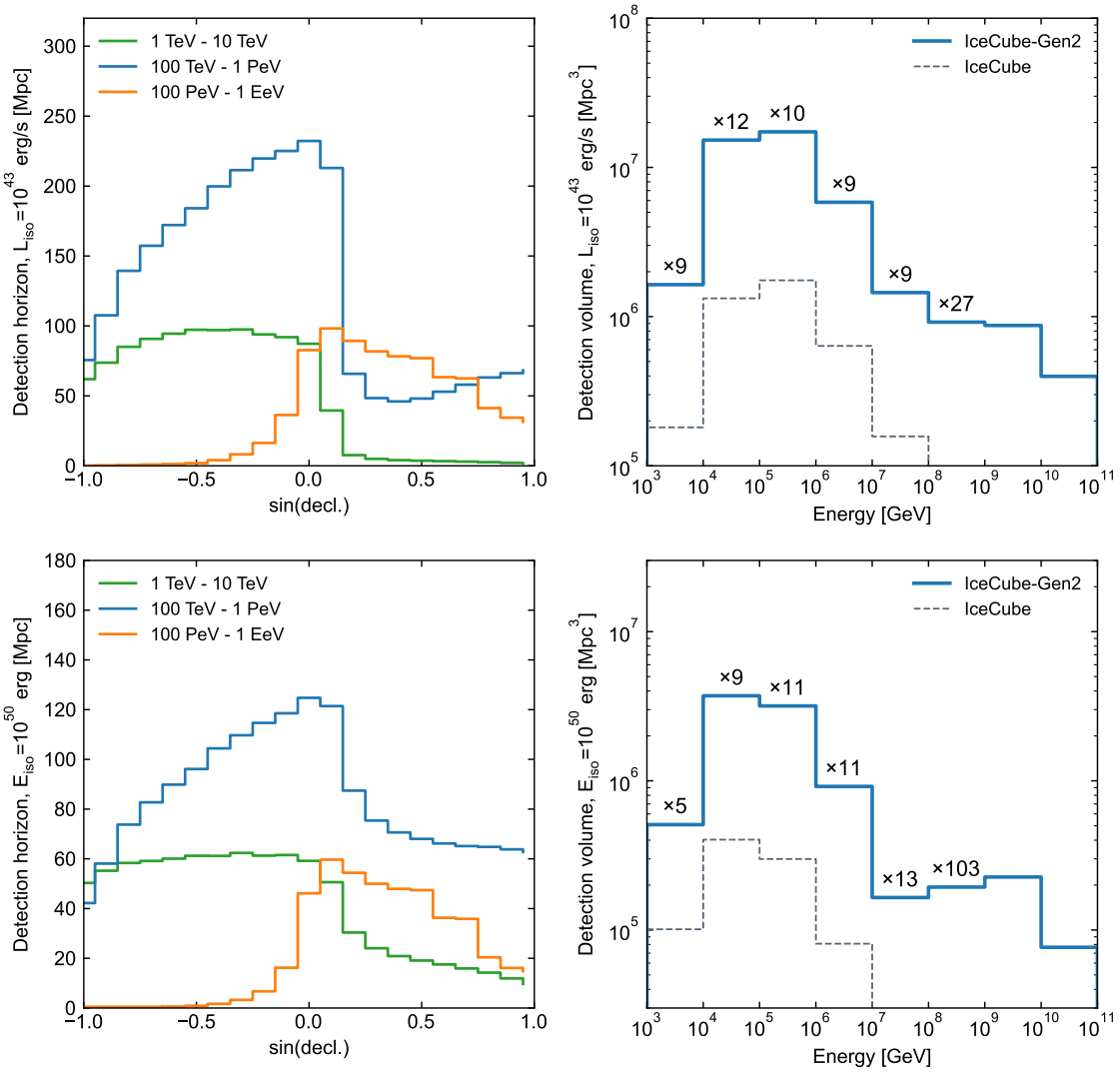

Figure 14: **Left:** Maximum distance at which a persistent source with a luminosity of L_ν =10^{43} erg cm^{-2} s^{-1} can be detected by IceCube-Gen2 if it is observed for 10 years as a function of the source declination for different energy bands (upper panel). The lower panel shows the maximum detection distance for a generic transient with a total energy of E_ν =10^{50} erg and an assumed duration of 100 s. **Right:** Source detection volume derived from the maximum distance as a function of energy. The improvement relative to IceCube is given for each energy band.

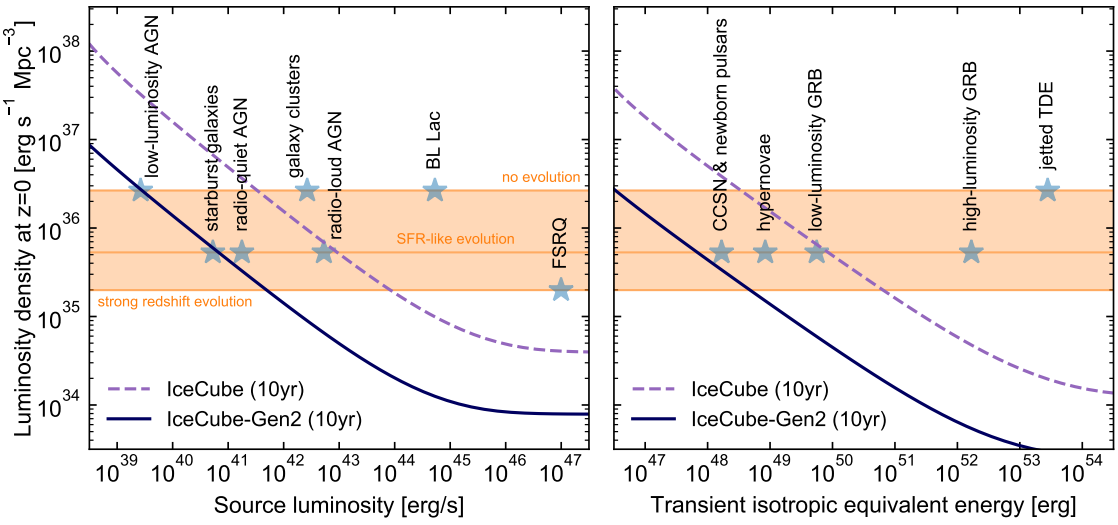

Figure 15: **Left:** Comparison of the effective local density and luminosity density of extragalactic neutrino source populations to the discovery potential of IceCube and IceCube-Gen2. We indicate several candidate populations by the required neutrino luminosity density to account for the full diffuse flux [68] (see also [151]). The orange band indicates the luminosity / density range that is compatible with the total observed diffuse neutrino flux. The lower (upper) edge of the band assumes rapid (no) redshift evolution. The lines indicate the parameter space (above the lines) for which IceCube and IceCube-Gen2 are able to discover one or more sources of the population ($E^2\phi_{\nu_\mu+\bar{\nu}_\mu} \simeq 10^{-12}$ TeV cm^2 s^{-1} in the Northern Hemisphere [152]). **Right:** The same comparison for transient neutrino sources parametrized by their local rate density [153]. The discovery potential for the closest source is based on 10 years of livetime ($E^2F_{\nu_\mu+\bar{\nu}_\mu} \simeq 0.1$ GeV cm^{-2} in the Northern Hemisphere [154]). Only the IceCube-Gen2 optical array has been considered for this figure.

two source populations to the observed cosmic neutrino flux (cf. Section 1.2 and references therein), thus establishing that rather lower-luminosity / higher-density populations must be responsible for the bulk of cosmic neutrinos. Even the brightest sources of such populations are still below or at the detection threshold of IceCube, and the populations can only be firmly identified with a more sensitive instrument. NGC 1068, a non-blazar AGN, observed at the detection threshold of IceCube is an excellent example for the brightest source of such a population.

Figure 15 compares the identification capabilities of IceCube and IceCube-Gen2 for the most common neutrino source and transient candidates. If sources like radio-quiet AGN, such as NGC 1068, and/or low-luminosity AGN, galaxy clusters, starburst galaxies, or transients like CCSNe produce the majority of cosmic neutrinos, they can be firmly identified only with a detector with a five times better sensitivity than currently available such as IceCube-Gen2. In combination with correlation or stacking searches, IceCube-Gen2 can identify a cumulative signal from populations where the closest sources have more than an order of magnitude fainter neutrino fluxes than point sources detectable by IceCube. So their signal remains in reach, even if several of the candidate populations contribute similar fractions to the total observed neutrino flux.

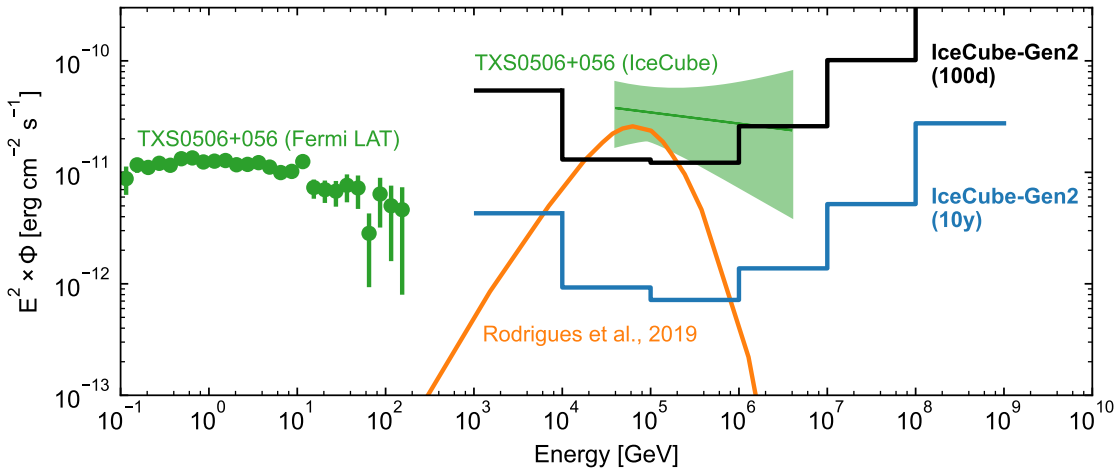

Figure 16: 5σ discovery potential of IceCube-Gen2 for a flux of muon neutrinos in relation to observations of the Blazar TXS0506+056. The black and blue curves correspond to 100 days and 10 years of observations and indicate the sensitivity for neutrino flares and the time-averaged neutrino emission, respectively. The best-fit muon neutrino flux during the 2014-2015 activity period for TXS 0506+056 [6] is shown as a green band, while the green markers show the average γ-ray flux of TXS 0506+056 between 2008 to 2018 observed by *Fermi* LAT [35]. The orange curve corresponds to the predicted neutrino flux from modeling the multi-messenger emission during the flare period in [155].

2.2 Understanding cosmic particle acceleration through multi-messenger observations

Multi-messenger astronomy, the combination of astrophysical observations in CR, neutrinos, photons, and gravitational waves, provides powerful opportunities to identify the physical processes driving the high-energy universe. Astrophysical neutrinos can provide an unobstructed view deep into the processes powering cosmic accelerators. Unlike their counterparts in photons and charged CR, their small interaction cross section and absence of electric charge allow neutrinos to travel the cosmological distances necessary to reach Earth from their sources without absorption or deflection. High-energy astrophysical neutrinos are a smoking-gun signal of hadronic interactions, and will point the way to the sources of the high-energy CR.

2.2.1 Probing particle acceleration in active galaxies

The electromagnetic emission from the high-energy extragalactic sky is dominated by blazars, a subclass of radio-loud active galactic nuclei (AGN) powered by supermassive black holes that display relativistic jets, with one jet pointed near the line of sight of the Earth. The high-energy photon emission from blazars could be explained by the decay of neutral pions from energetic hadronic interactions. Given the extreme luminosity and the potential hadronic origin of their high-energy emission, blazars (and more generally, AGN) have long been believed to be sources of neutrinos and CR [156–158]. Indeed, the observations of high-energy neutrinos from the direction of the blazar TXS 0506+056 [5] (cf. Section 1.2) with IceCube provided strong evidence for a scenario in which CR are accelerated in AGN jets. However, much remains unknown about blazar physics that further observations with neutrinos could help answer, such as the

location of the CR acceleration region in the jet, and the underlying mechanisms driving this acceleration (see, e.g., [159] for a recent review on modeling particle acceleration and multi-messenger emission in blazars).

The larger astrophysical neutrino samples provided by IceCube-Gen2 will enable definitive detection of multiple neutrino flares from a population of blazars. For a TXS 0506+056-type flare with the same best-fit spectral and temporal characteristics as the one identified in 2014–2015, 38 muon-neutrino events would be expected by IceCube-Gen2, compared to the 13±5 events identified in IceCube. As shown in Figures 16 and 17 (left), the improvement in sensitivity would result in a $> 5\sigma$ significance detection of such a flare. A time-averaged or quiescent phase neutrino emission could be detected in 10 years of IceCube-Gen2 if its power is $\gtrsim 10\%$ of the average γ-ray emission observed by *Fermi* LAT. Other blazars usually suggested as neutrino sources, such as Markarian 421 or 1ES 1959+650 [160] will also be within the sensitivity of the IceCube-Gen2 detector during extended flares. Figure 17 (left) demonstrates the improvements for flare detections expected with IceCube-Gen2. Using again the flux and spectral index of the TXS 0506+056 flare as a template the significance of the detection as a function of the duration of such a flare is shown (the flux is assumed constant during the duration of the flare, i.e., the neutrino fluence increases with flare duration). While the modeled flare would need to last for 220 days to be detected with IceCube at 5σ significance, IceCube-Gen2 can already detect the modeled flare if it lasts only 36 days. Hence, IceCube-Gen2 is sensitive to neutrino flares with 6 times lower fluence than IceCube, greatly increasing the range of potentially observable medium term transients.

The blazar detections provided by IceCube-Gen2 will allow the characterization of the neutrino spectrum, and therefore the nature and maximum energy of the particles being accelerated at the source. The detections will also help in determining CR acceleration efficiency for the various sub-classes of blazars. Multi-messenger observations can be used to constrain the spectrum and density of the target photon population involved in the pγ interactions that produce the neutrino emission, the contribution from EM cascading to the observed blazar emission, the structure and Doppler factor of the jet, and other physical parameters [155, 161–164]. As illustrated in these models, electromagnetic broadband observations that are simultaneous with the neutrino detections are crucial in understanding the hadronic emission process. In particular, X-ray and γ-ray observations will be the most sensitive probes for these types of correlated studies.

While the highest-energy neutrinos might originate in the jets of AGNs and be observable predominantly from blazars, a substantial fraction of the observed sub-PeV and PeV neutrinos could be emitted from the AGN core regions, outside the jets [168–170]. The recent observations of IceCube support such a scenario, finding evidence for neutrino emission from the nearby Seyfert galaxy NGC 1068 [27], as well as an excess of events with respect to an isotropic background of atmospheric and astrophysical neutrinos in a search for a cumulative signal from tens of thousands of AGNs [29]. Strong thermal radiation fields can turn the cores opaque to GeV γ rays, thus explaining why the extragalactic TeV neutrino flux is inconsistent with an expectation based on the extragalactic GeV γ-ray flux assuming transparent sources [66].

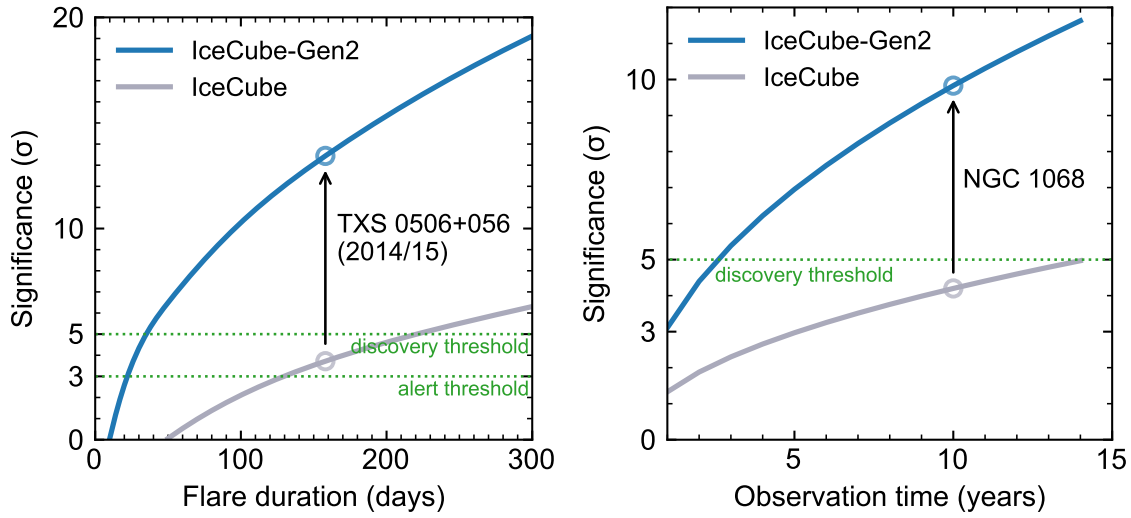

Figure 17: **Left:** Discovery potential of IceCube and IceCube-Gen2 for neutrino flares similar to the one observed for TXS0506+056 in 2014/15 which lasted 158 days. Shown is the projected significance of the observation as a function of the flare duration. The flux and spectral index of the assumed flare are the ones observed for TXS0506+056 (see Figure 16) and assumed constant within the flare duration, i.e., the neutrino fluence increases with flare duration. Green dotted lines mark the 5σ discovery threshold, as well as the lower threshold for sending alerts to partner telescopes for follow-up observations. **Right:** Significance of the observations of NGC 1068 as a function of observation time for IceCube and IceCube-Gen2, assuming the best-fit neutrino flux derived in [27].

IceCube-Gen2 will allow to firmly discover the brightest AGNs on the neutrino sky. Figure 17 (right side) shows the expected significance as a function of observation time for NGC 1068. A detection at 10σ significance is expected after 10 years, allowing a precise measurement of the spectral shape of the neutrino emission that is key to understanding the acceleration processes in the source. Figure 18 shows the differential sensitivity of IceCube-Gen2 in relation to the spectrum of NGC 1068 inferred from the IceCube data, a model of the neutrino emission, and observations of the source in gamma rays, underlining the strong gain in sensitivity with IceCube-Gen2 even for soft spectrum sources. In addition to the direct observations, precise spectrum and flavor ratio measurements (see Section 2.2.6) of the diffuse flux will support the study of the acceleration processes and environmental conditions in AGN cores and/or jets.

2.2.2 Cosmic-ray production in tidal disruption events

Another proposed transient source of high-energy CR and neutrinos is the tidal disruption of stars by supermassive black holes [171–174]. Such TDEs occur when a star is disintegrated by strong gravitational forces as it spirals towards the black hole. TDEs have been detected across a range of wavelengths, and, in some cases, have been observed to launch relativistic particle jets.

Observations of the first coincidences between TDE and high-energy neutrinos open a great perspective for IceCube-Gen2. Figure 19 shows the expected rate of associations between neutrinos and TDEs for IceCube-Gen2, based on current IceCube observations. In combination with the much deeper survey depth that next-generation optical survey telescopes will provide one can expect O(10) coincidences per year. The

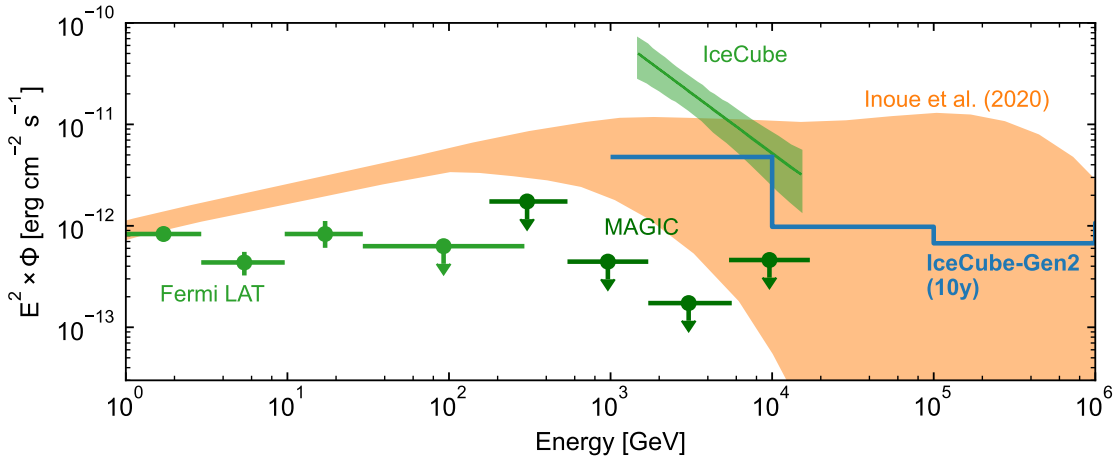

Figure 18: 5σ discovery potential of IceCube-Gen2 for a flux of muon neutrinos in relation to observations of the nearby galaxy NGC 1068. The best-fit muon neutrino flux observed by IceCube in the energy range between 1.5 TeV and 15 TeV with a significance of 4.2σ [27] is shown as a green band, while the green markers show the Fermi LAT observation of the γ-ray flux of NGC 1068 [165] and flux upper limits from the non-detection of the source with the MAGIC telescope array [166]. The orange curve corresponds to the predicted neutrino flux from modeling the multi-messenger emission in [167].

neutrinos probe the regions in the TDE that are inaccessible with electromagnetic radiation and will allow to, e.g., unveil shocks created in jets or the corona or soft X-ray photon seed fields from the forming accretion disk. With just two ingredients, a star and a SMBH, TDEs provide unique conditions to answer questions about key ingredients and mechanisms for particle acceleration related to accretion onto super-massive black holes. By combining multi-wavelength and neutrino data we will also be able to determine the relation of TDE to other neutrino emitting populations, the redshift and luminosity function of neutrino emitting TDE, and the yield and maximum energy of cosmic rays produced in them.

2.2.3 Neutrinos from gamma-ray bursts and core-collapse supernovae

GRBs, either short (lasting <2 s) or long, have been suggested as sources of the UHE cosmic rays and high-energy neutrinos [182, 183]; a prediction usually designated as the *fireball model* and later revised by, e.g., [184]. An alternative sub-photospheric dissipation mechanism for GRBs that also results in neutrino emission has also been proposed [185–187]. Long GRBs (lasting >2 s) are associated with CCSNe that develop relativistic jets and short GRBs are associated with the mergers of compact objects — two neutron stars (NS-NS) and/or a neutron star and a black hole (NS-BH) — that also develop these jets. IceCube has studied 1,172 GRBs and has not found coincident neutrino emission [176]. This implies that GRBs contribute no more than ~1% of the diffuse neutrino flux [188]. Furthermore, in a wide range of scenarios, GRBs are constrained as a source of UHE cosmic rays [177]. Low-luminosity GRBs are potential neutrino and UHE cosmic-ray sources and could contribute significantly to the cosmic neutrino flux [189–191]. IceCube-Gen2 will be able to probe the remaining viable scenarios for neutrino production by GRBs of all types. Figure 20 shows the current best upper limits of IceCube and the expected sensitivity for IceCube-Gen2 for the diffuse

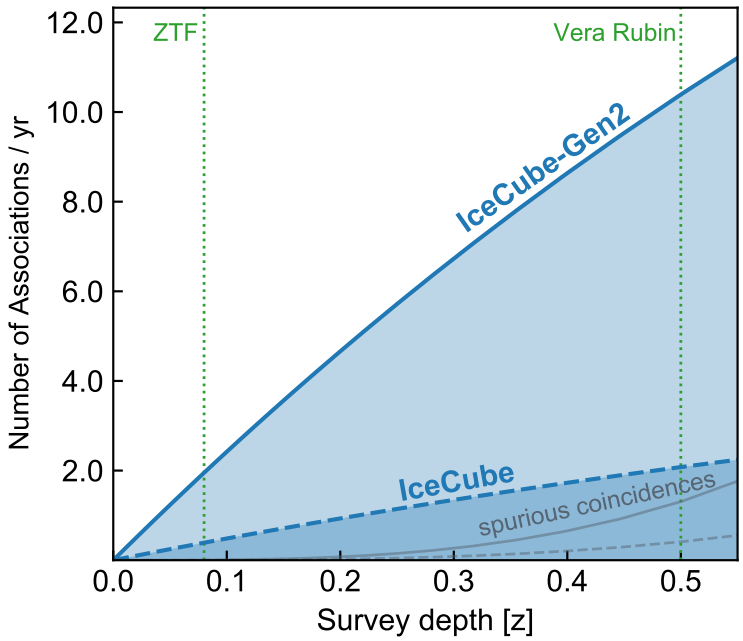

Figure 19: Rate of associations of high-energy neutrinos to TDEs expected from multi-messenger observations with IceCube and IceCube-Gen2. The redshift evolution of TDEs from [175] is used in the calculation, spurious coincidences are marked by thin gray lines. The respective survey depths for the observations of TDEs by ZTF and the Vera C. Rubin observatory are indicated.

flux from GRBs considering 1000-5000 GRBs (assuming 667 bursts/year). This can be compared to three models that assume UHE cosmic rays are produced by GRBs [177]).

Low-luminosity GRBs and relativistic SNe might feature "choked" jets, where the relativistic jet fails to penetrate the progenitor star, and therefore no detectable gamma-ray signal is present. Such jets would provide a unified picture of GRBs and SNe [192, 193]. This scenario could be physically probed by the detection of high-energy neutrinos in coincidence with SNe containing relativistic jets [194, 195]. The neutrino emission is expected in a relatively short time window (~100 s) after core-collapse. Thus, this scenario predicts a high-energy neutrino signal followed by the appearance of a CCSN.

Two complementary search strategies have been applied to identify neutrino emission from CCSNe with IceCube. First, the high-energy neutrino alerts released by IceCube's realtime program [196] are followed up with optical instruments to search for potential optical counterparts of the signatures described above. Second, a catalog of optically detected CCSNe, from instruments such as the All-Sky Automated Survey for Supernovae (ASAS-SN) and the Zwicky Transient Facility (ZTF) [197, 198], has been used to search for the combined neutrino signal from the entire source populations [199].

IceCube-Gen2 will yield about 5 times more alerts from high-energy track-like neutrino events with improved angular resolution than IceCube. The increased pointing accuracy will reduce the fraction of alerts due to chance coincidences between neutrinos and causally unconnected optical transients. Up to 6 coincident detections of high-energy neutrinos and CCSNe can be expected per year from sources with a redshift below $z = 0.15$. High-cadence all-sky observations performed by new survey facilities,

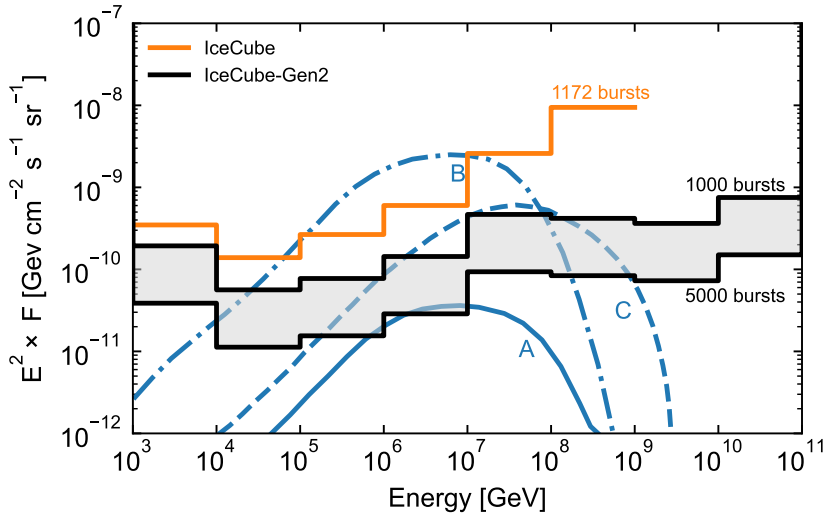

Figure 20: Upper limits from IceCube (rescaled to one energy bin per decade from [176]) and sensitivity of IceCube-Gen2 to the diffuse neutrino flux from GRB. Also shown are three scenarios from [177] in which GRBs produce the UHE cosmic rays (see also [178–181]).

such as ZTF [198] and the Vera C. Rubin Observatory [133] will reduce the uncertainty for resolving the SN explosion time from the current ~30 day window to ~3 days, further reducing the chance coincidence background rate.

2.2.4 Multi-messenger sources of high-energy neutrinos and gravitational waves

LIGO [200] and VIRGO [201] have revolutionized multi-messenger astrophysics with their detection of gravitational waves. The most spectacular observations to date were the joint detections of GW170817 and GRB170817A by LIGO/VIRGO and Fermi-GBM respectively, which confirmed the association of the merger of binary neutron stars with short GRBs. Interestingly, GRB170817A was probably seen off-axis with respect to the relativistic jet. As already discussed, NS-NS and NS-BH mergers are expected to be neutrino sources. The most promising emission scenario from short GRBs is related to their extended emission observed in γ-rays and X-rays that can last up to several hundred seconds [202]. The expected high-energy neutrino emission from neutron star mergers may be higher than inferred from γ-ray observations if the production sites are partially or fully opaque to γ-rays. This can be the case for neutron-star mergers where the dynamical/wind ejecta that produce kilonova emission absorb some of the γ-rays [203], or for core-collapse events where the stellar envelope allows neutrinos to escape but blocks γ-rays [192, 193, 204]. Within a few years, GW from NS-NS mergers will be detectable out to ~330 Mpc [205], with a detection rate of 2.3–71 yr^{-1} [206]. A study of neutrinos in coincidence with GW events complements studies of neutrinos in coincidence with GRBs observed by satellites because the observational biases are different. Compact binary mergers observed with GW may well be relatively dim in γ-rays, but they would be closer to Earth, potentially favoring neutrino detection. A Galactic core-collapse supernova is certain to be a source of MeV neutrinos and is also speculated to be a source of GW and TeV neutrinos.

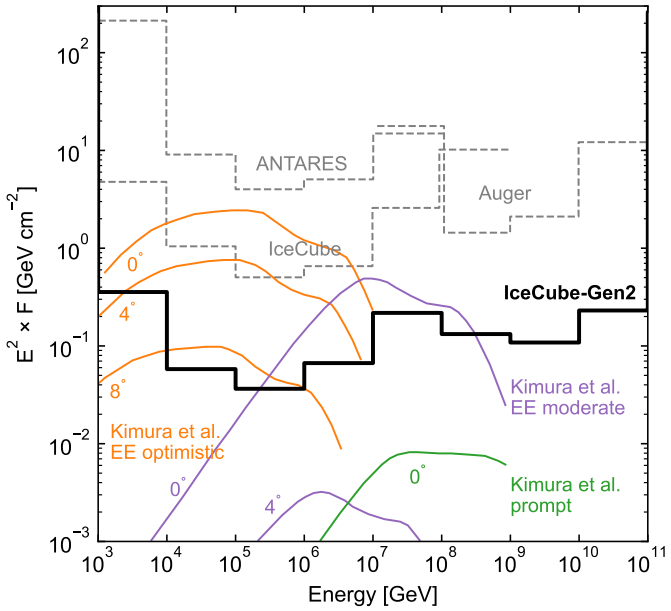

Figure 21: Upper limits (at 90% CL) from various instruments on the neutrino spectral fluence from GW170817 during a ± 500 s window centered on the gravitational wave (GW) trigger time. For comparison, the sensitivity of IceCube-Gen2 (at 90% CL) to an event at a similar position on the sky (solid black line) is presented. Also shown are several predictions by neutrino emission models [216] scaled to a distance of 40 Mpc. Separate curves are displayed for different components of the emission (prompt and extended (EE)), and observation angles relative to the jet axis. See [209] for details. Limits and sensitivities are calculated separately for each energy decade, assuming a spectral fluence $F(E) \propto E^{-2}$ in that decade only. All fluences are shown as the per-flavor sum of neutrino and anti-neutrino fluence, assuming equal fluence in all flavors, as expected for standard neutrino oscillation parameters. Figure adapted from [209].

IceCube and other neutrino detectors such as ANTARES and the Pierre Auger Observatory have searched for neutrino emission in a time window of ± 500 s [207–213]. Starting on November 2016, IceCube began conducting GW-neutrino coincident searches in near-real time [208, 214, 215]. A successful low-latency search for a high-energy GW-coincident neutrino counterpart would enable the well-localized neutrinos to reduce the sky area to be surveyed by electromagnetic telescopes in the follow-up of a GW observation.

IceCube-Gen2 will be able to probe a range of neutrino production scenarios in gravitational wave sources that IceCube is insensitive to, and provide regular multi-messenger detections for some of the (more optimistic) emission channels [203, 216]. It will be particularly interesting to observe 'gamma-dark' high-energy transients where gravitational waves and neutrinos are the only messengers to escape (e.g., [204]). In Figures 21, 22 we show high-energy neutrino observational constraints for the NS-NS merger GW170817, obtained by IceCube, ANTARES and the Pierre Auger Observatory. We also show the results scaled to IceCube-Gen2's sensitivity — an improvement of over an order of magnitude with respect to IceCube. The observation of sources similar to GW170817 during IceCube-Gen2 operation will enable us to probe a broader range of models (e.g. the "moderate" model in [202]) and determine the model parameters.

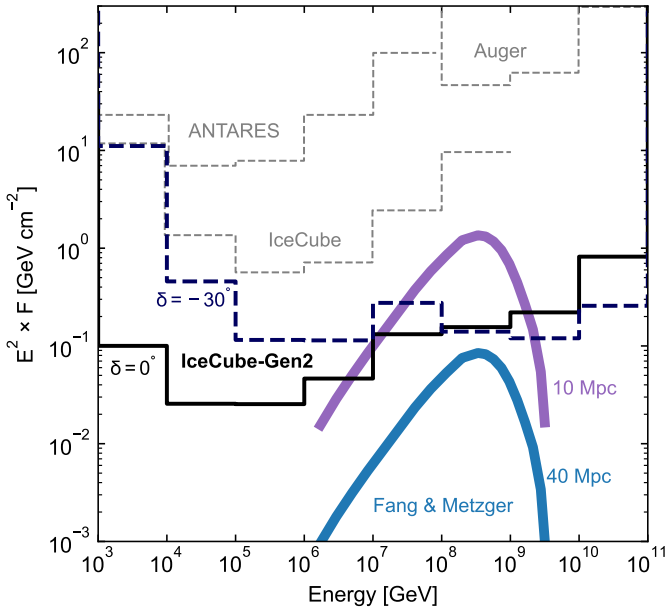

Figure 22: Upper limits (at 90% CL) from various instruments on the neutrino spectral fluence from GW170817 during a 14 day window following the gravitational wave (GW) trigger time [209] . For comparison, we show the sensitivity of IceCube-Gen2 (at 90% CL) for such a time window at the celestial horizon ($\delta = 0^{\circ}$) and at a declination of $\delta = -30^{\circ}$. Also shown are predictions of the neutrino emission model in [203] for an event at 10 Mpc distance, ,and scaled to a distance of 40 Mpc, the distance of GW170817. Limits and sensitivities are calculated separately for each energy decade, assuming a spectral fluence $F(E) \propto E^{-2}$ in that decade only. All fluences are shown as the per-flavor sum of neutrino and anti-neutrino fluence, assuming equal fluence in all flavors, as expected for standard neutrino oscillation parameters.

KAGRA [143] started operations in 2020. Substantial development for gravitational wave detectors such as LIGO A+ [217] and Voyager, with gravitational wave sensitivity range extending up to 1100 Mpc [218], will further increase the detection rate by an order of magnitude. IceCube-Gen2 will be operated in parallel to next generation gravitational wave observatories on the ground (Einstein Telescope [145], Cosmic Explorer [146]) and in space (LISA [144]).

2.2.5 Low-energy neutrinos from core-collapse supernovae

Neutrinos play a major, though not completely understood, role in core-collapse supernovae. In a CCSN, it is estimated that ~99% of the gravitational binding energy of the stellar remnant is converted to $\mathcal{O}$(10 MeV) neutrinos during the core collapse and its aftermath [219]. Core-collapse models also suggest that neutrino-driven heating is crucial to reviving the supernova shock and producing an explosion [220–222].

IceCube-Gen2 will observe CCSN neutrinos via a collective increase in the hit rates in its optical modules during an $\mathcal{O}$(10 s) neutrino burst. While the detector cannot reconstruct individual supernova neutrino events, it is highly sensitive to temporal features in the accretion and cooling phases of the explosion [224, 227]. For CCSN detection, the design of IceCube-Gen2 yields two significant improvements over the current IceCube detector. First, since the hits from CCSN neutrinos are produced by $\bar{\nu}_e$ interactions in the immediate vicinity of the optical modules [224], the increase in total photocathode

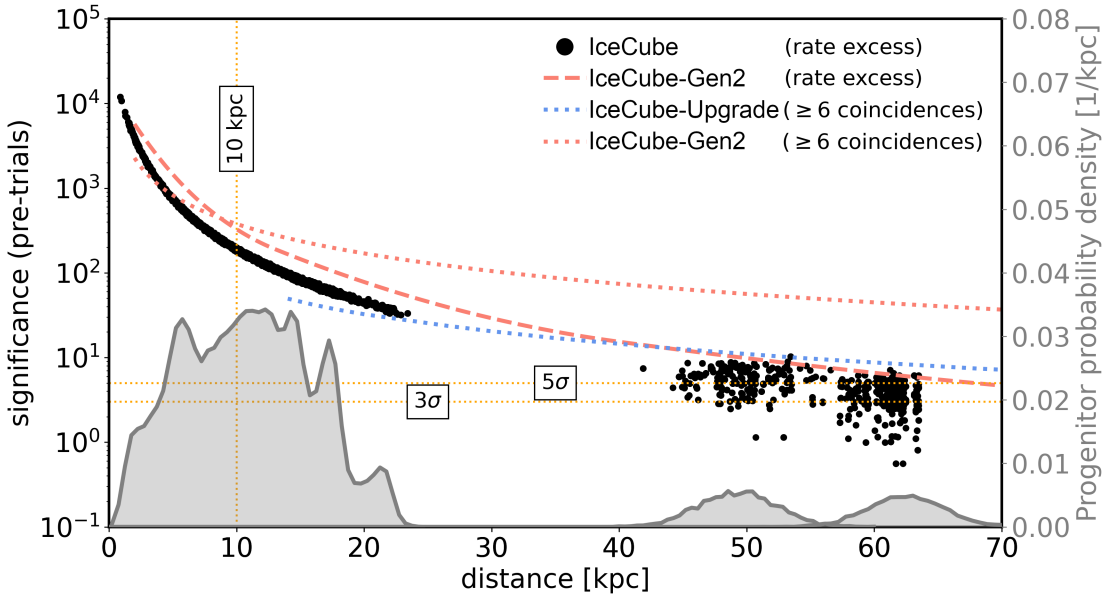

Figure 23: Projected sensitivity to a burst of MeV neutrinos from a nearby CCSN as a function of progenitor distance, assuming a 27 $M_\odot$ progenitor [223]. The sensitivities of IceCube (black points) and Gen2+IceCube (red dashed line) are displayed as the projected detection significance in units of σ, and assume CCSN neutrinos are detected as a correlated increase in PMT hit rates above background [224]. The IceCube Upgrade (blue dotted line) and IceCube-Gen2 (red dotted line) sensitivities are based on an additional coincidence cut that requires > 6 coincident hits per multi-PMT optical module [225]. The coincidence cut provides a substantial gain in sensitivity due to a corresponding reduction in contamination from background hits. The gray histogram indicates the normalized progenitor density as a function of distance from Earth [226], including stars in the Milky Way, LMC and SMC.

area will produce a corresponding increase in the recorded CCSN hit rate. Second, the multi-PMT design of the IceCube-Gen2 optical modules will substantially reduce the rate of accidental coincidences from background hits and improve the sensitivity to CCSN neutrinos.

The projected neutrino flux from a supernova can easily vary by an order of magnitude or more [228–230], with predictions affected by astrophysical uncertainties such as the mass and equation of state of the stellar progenitor [231–233], the distance to the progenitor [224, 234], and the details of supernova simulation codes. Thus, high statistics are crucial to assure sensitivity to a broad range of models and distances. Thanks to its effective volume, IceCube-Gen2 will identify CCSN neutrinos from the Milky Way and the Magellanic clouds at $\gg 5\sigma$ regardless of the details of the explosion (Fig. 23). Moreover, coincident DOM hits in IceCube-Gen2 will improve constraints on the shape of the SN neutrino spectrum by a factor of five compared to the current detector design [225, 235].

The next Galactic supernova will produce copious amounts of electromagnetic radiation, neutrinos, and gravitational waves, providing a unique opportunity for multimessenger observations [236–238]. Phenomena such as standing accretion shock instabililities [239–242] and the rotational modes of rapidly rotating protoneutron stars [243, 244] can produce gravitational waves and imprint temporal oscillations in the

neutrino flux that would be easily observed with IceCube-Gen2. With an annual uptime >99%, IceCube-Gen2 will be a keystone of the SuperNova Early Warning System [245, 246], a global detector network searching for nearby CCSNe. By identifying the onset of the CCSN neutrino burst with an absolute uncertainty of $\lesssim$0.1 ms, triangulation using IceCube-Gen2 and other detectors would enable $<10^{\circ}$ localization for optical follow-up [247–249]. If the core collapse results in the creation of a black hole, the sharp temporal cutoff in neutrino emission will provide even better localization for subsequent identification of the progenitor.

Beyond neutrino and GW astrophysics, CCSNe observations with IceCube-Gen2 would produce key insights into fundamental neutrino physics. Standard MSW mixing in the dense material of a supernova efficiently converts neutrinos into definite mass eigenstates. The final states depend on the mass hierarchy [250, 251], so a CCSN signal in IceCube-Gen2 has excellent discrimination power between normal and inverted mass ordering [224]. Supernova neutrinos also probe unique oscillation effects that occur only at extreme densities and energies not accessible in the laboratory, such as collective oscillations from neutrino self-coupling [252, 253].

Finally, CCSN neutrinos will probe extreme nuclear states and physics beyond the Standard Model [254]. In the interior of the protoneutron star, “pasta-like” structures of nucleons may significantly increase neutrino scattering [241, 255–257]. The increased opacity would produce a corresponding increase in the timescale of neutrino cooling and lengthen the cooling tail well beyond 10 s. The improved backgroud rejection capability of IceCube-Gen2 will be key to exploring this scenario. Beyond the Standard Model searches for axions and axion-like particles (ALPS) will also be readily accessible to IceCube-Gen2. Axions compete with neutrinos to cool the explosion, reducing neutrino emission in the cooling tail [241, 258–265]. IceCube-Gen2 can conduct “neutrino disappearance” searches that are sensitive to axion production [266] and are complementary to gamma-ray appearance searches [267–270]. Searches for sterile neutrinos, even for very small active-sterile mixing angles, are possible due to MSW resonances in a supernova which dramatically enhance sterile neutrino production [271, 272]. IceCube-Gen2 is sensitive via $\bar{\nu}_e$ disappearance; it can also contribute to multimessenger detection of excess gamma rays and daughter $\bar{\nu}_e$ events in the neutrino flux [273, 274].

2.2.6 Spectrum and flavor composition of the astrophysical neutrino flux

Given our current limited understanding of the sources of the cosmic neutrino and the UHE cosmic-ray flux, the processes and environments that lead to such dramatic acceleration of particles remain speculative. However, some key properties of these sources are imprinted upon the observed diffuse flux of astrophysical neutrinos detected by IceCube. The examination of the neutrino spectrum and flavor composition of this signal, in addition to comparisons to signals observed in high-energy γ-rays and CR, can thus be used to elucidate the acceleration mechanisms at work and the environments where the neutrinos are created.

A measurement of the astrophysical neutrino energy spectrum from IceCube along with a projection for IceCube-Gen2 are shown in Figure 24. Currently, the extrapolation of

the neutrino spectrum observed by IceCube up to about 10 PeV, to the energy range of the extragalactic CR with energies of tens of EeV, is not sufficiently precise to firmly establish a link between the two. The unprecedented sensitivity from the combination of optical and radio-detection methods in IceCube-Gen2 will close this gap in energy, allowing us to probe the neutrino energy spectrum with significantly better precision up to energies three orders of magnitude higher than IceCube.

A precise measurement of the spectrum and composition of the diffuse flux of astrophysical neutrinos reveals details about the environment in which CR are accelerated and neutrinos produced. The environment can have significant impact on the spectrum and flavor composition of extraterrestrial neutrinos [275–277], as the presence of sufficiently strong magnetic fields leads to a damping of muons and thus suppression of the flux of electron neutrinos above a critical energy. Interestingly, environments allowing for very efficient acceleration would have the opposite effect [278, 279]. Currently, the constraints derived from IceCube data [57, 63, 280] indicate consistency with the benchmark prediction from complete pion decay of $\nu_e : \nu_\mu : \nu_\tau = 1 : 2 : 0$ which is transformed to approximately 1:1:1 by neutrino oscillations over astronomical distances [281]. While the IceCube constraints are sufficiently strong to rule out that the neutrinos are produced via neutron decay, they are insufficient to probe muon-damping scenarios [57, 282].

The diffuse astrophysical neutrino spectrum, measured by IceCube-Gen2 over an unprecedented energy range, can be compared to the extragalactic CR spectrum and composition to firmly establish the connection between the two messengers. Matching spectra would imply that the neutrino sources identified by IceCube-Gen2 also represent the dominant sources of the extragalactic CR.

Moreover, the large samples of neutrinos of all flavors in IceCube-Gen2 will allow us to observe the energy dependence of the flavor ratio over a large energy range, as shown in Figure 25. The sensitivity to detect a changing flavor composition as a function of neutrino energy will allow to distinguish different acceleration scenarios and source environments expected within GRBs, AGN cores, or AGN jets [275].

The unique interaction and decay signatures generated by high-energy tau neutrinos interacting within IceCube's instrumented volume allow for additional handles on the flavor composition of the astrophysical neutrino flux. The primary method of identifying tau neutrinos is to search for high-energy charged-current events with a "double-bang" structure of two nearby cascades, the first one due to the hadronic shower at the interaction vertex and the second one due to the decay of the tau lepton. The density of instrumentation in the IceCube detector limits the rate of observable ν_τ events since the distance between the two cascades is most often much smaller than the distance between two DOMs. So far, only two candidate events could be identified [284]. The measurement of the ν_τ fraction plays an important role in constraining source physics and in ruling out/discovering beyond the Standard Model physics, should the observed fraction be outside of the range expected by standard oscillations. Even though IceCube-Gen2 will be sparsely instrumented, the increase in detector volume will result in an increase of the annual rate of identified tau neutrinos, leading to stronger constraints on the flavor ratio. Studies extrapolating the recent identification of high-energy ν_τ candidates to IceCube-Gen2 show that above an energy of 300 TeV, the yearly rate of identified tau

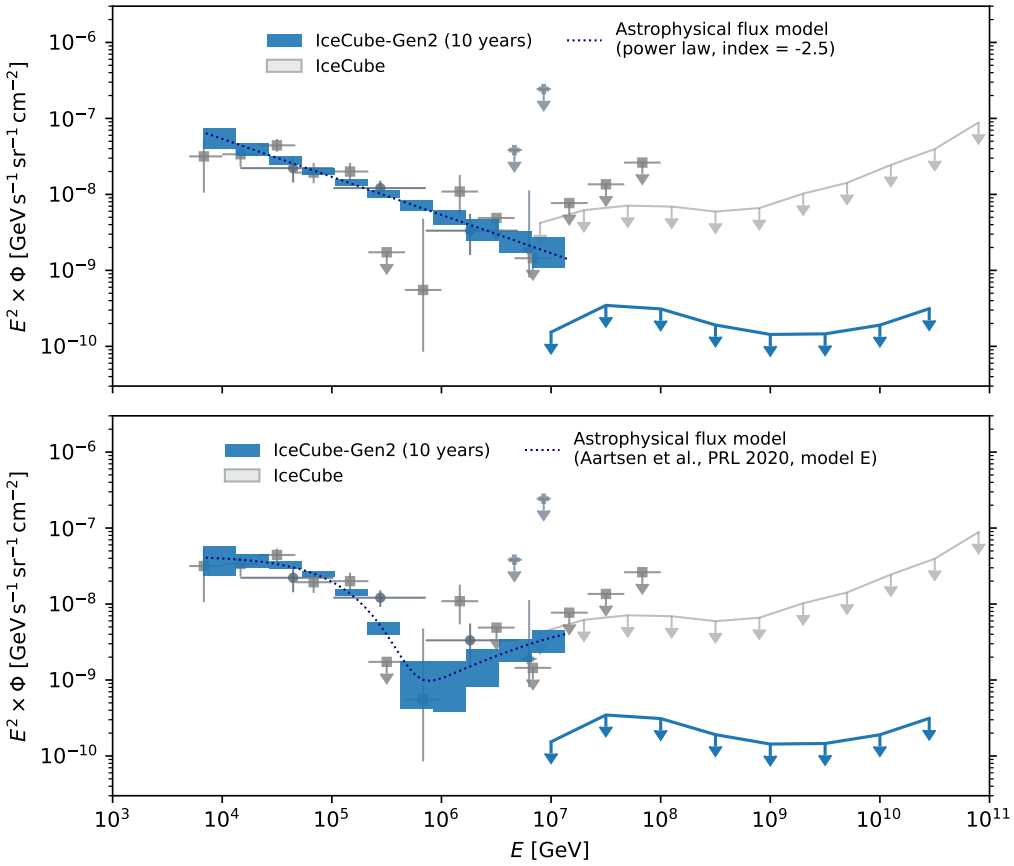

Figure 24: Projections of the sensitivity and precision for the measurement of the diffuse astrophysical neutrino spectrum. For comparison, the current IceCube measurements from high-energy cascades ([17], squares), tracks ([58], circles), a Glashow resonance event ([22], +), and a search for EHE events ([60], line with arrows) are shown in gray. The predicted unfolded diffuse spectrum assuming 10 years of IceCube-Gen2 data is shown in blue with error bands representing 68% confidence intervals up to 10 PeV. The upper panel assumes a single power law model with a spectral index of -2.5. The lower panel assumes a two component spectrum, consisting of a power law with an exponential cutoff at approximately 100 TeV, and a component reflecting a model of the $p\gamma$ emission of BLLac which peaks at tens of PeV. Both models are based on fits to the cascade data [17]. With current data from IceCube, it is not statistically significant to reject either hypothesis. IceCube-Gen2 will provide key measurements to reveal spectral features in the astrophysical neutrino component. Above 10 PeV, the expected differential 90% C.L. sensitivities for the combined optical and radio instrumentation for IceCube-Gen2 are shown in solid blue line. All fluxes are shown as the per-flavor sum of neutrino and anti-neutrino flux assuming equal flux in all flavors.

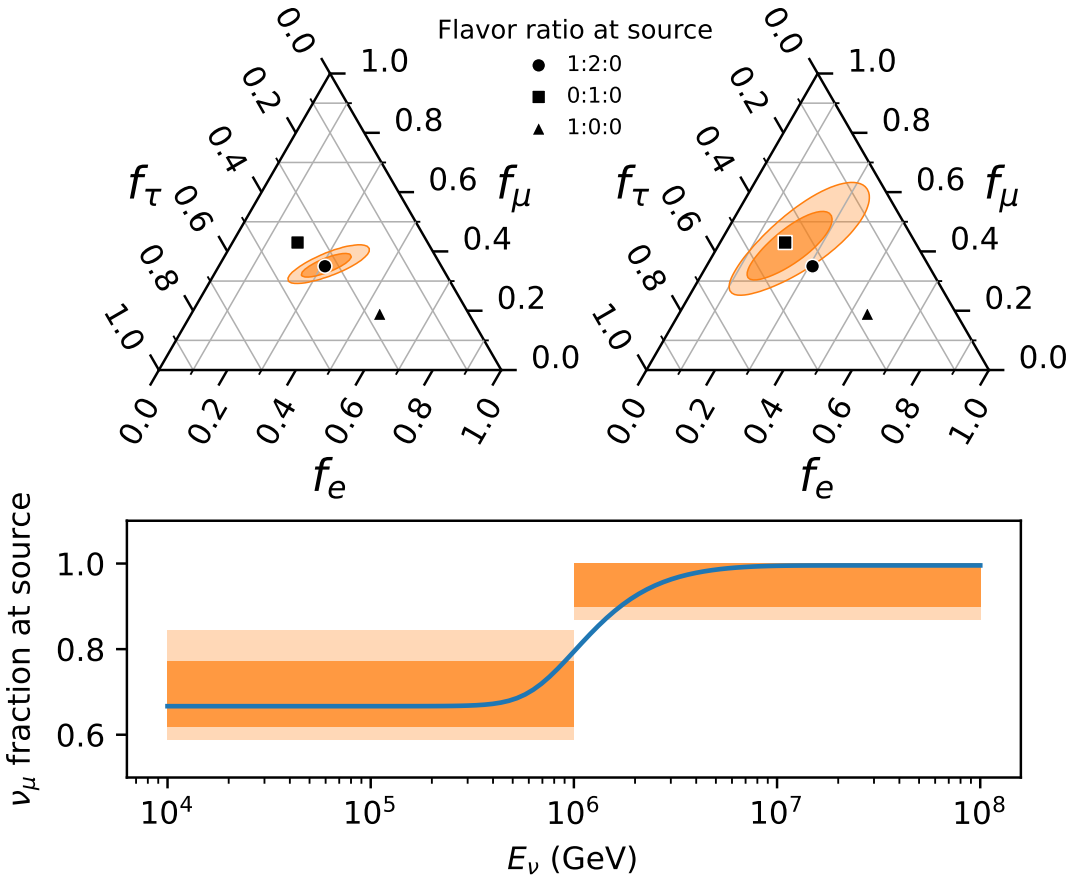

Figure 25: Sensitivity to muon cooling in the sources with IceCube-Gen2. Above a critical energy, the decay time for secondary muons from pion decay exceeds the cooling time, and the flavor ratio at the source changes from 1:2:0 to 0:1:0 [275]. The individual panels show the expected constraints on the flavor composition obtained from 10 years of IceCube-Gen2 observations for an assumed muon critical energy of 2 PeV. The orange contours in the upper panels show 68% CL and 95% CL constraints on the flavor composition at Earth for neutrino energies below and above 1 PeV. The lower panel shows corresponding constraints on the ν_μ fraction at the source as a function of energy, assuming standard oscillations [283].

neutrinos would be equal or greater than 1 event/year in the optical array, a significant increase compared to the current rate of 0.2 events/year in IceCube. Additional tau neutrino identification capability at EeV energies might be provided by the radio array. The flavor composition constraints in Figure 25 include the effects of the predicted ν_τ identification performance.

The fraction of $\bar{\nu}_e$ events observed is another important measurement for understanding conditions within astrophysical sources. When neutrinos are produced in pp collisions, the observed fraction of $\bar{\nu}_e$ events is expected to be 1/6, while in case of $p\gamma$ collisions the fraction is smaller. If only the pion production via the Δ-resonance is considered and the target is optically thin, it is ~1/14 [285]. In a realistic case, however, the fraction of $\bar{\nu}_e$ from $p\gamma$ collisions depends on several parameters, the contributions from multi-pion production, the optical depth of the photon target and the chemical composition of the accelerated beam [286].

Unique sensitivity to the $\bar{\nu}_e$ flux in IceCube and IceCube-Gen2 is available through the 'Glashow resonance' centered at a neutrino energy of 6.3 PeV and a first candidate Glashow resonance event has recently been observed in IceCube [22]. The necessary exposure to distinguish production of neutrinos in pp, $p\gamma$, Fe-γ collisions, low and high opacity targets and other scenarios is discussed in detail in [286]: Many of these production scenarios would require more than 100 years of IceCube exposure to distinguish between them, while a large number of them is accessible to IceCube-Gen2 in $\leq$ 15 years of observations.

2.3 Revealing the sources and propagation of the highest energy particles in the Milky Way and the Universe

There is general consensus that the flux of CR below a few PeV originates from Galactic sources. Around 3 PeV the CR spectrum shows a significant break, the so-called CR *knee*. This spectral feature could be due to Galactic CR sources cutting off at their maximal acceleration energy or to CR escape from the Milky Way becoming more efficient. The energy range from PeV to EeV energies marks the transition region from CR of Galactic origin to CR of extragalactic origin. The nature of the CR in this transition region is not well understood, with potential contributions from heavy nuclei accelerated in the Milky Way, from Galactic super-accelerators, as well as a rising fraction of CR from extragalactic sources that dominate the CR flux above a few EeV.

CR sources, both Galactic and extragalactic, can produce neutrinos at various stages: during their acceleration in the source, while they escape from the source environment and long afterwards during CR propagation in the ubiquitous magnetic fields. Point-source neutrino emission is expected from direct interaction of CR in the sources or from interaction with close-by gas targets (e.g., molecular clouds or galaxy cluster gas). Diffuse emission is expected from the interactions of CR during propagation, which should be correlated with the gas distribution in the Milky Way for Galactic CR, but isotropic for CR of extragalactic origin.

2.3.1 Galactic CR sources and neutrino emission

Many sources in our Galaxy show high-energy (GeV–PeV) γ-ray emission. Such emission has been observed in association with supernova remnants and their interaction with near-by molecular clouds, pulsars and their nebulae, binary systems, and massive star clusters. The observations of high-energy photons indicate the presence of a population of particles in these sources that emit γ-rays via leptonic and/or hadronic processes. The latter implies that the sources accelerate protons and/or nuclei, thus contributing to the Galactic CR. Observation of neutrino emission from these sources would be a diagnostic for such hadronic processes that are often difficult to identify based on γ-rays alone. Indeed, all the above mentioned sources of high-energy γ-rays have also been hypothesized to be continuous or transient neutrino emitters; see, e.g., [287, 288].

It has long been speculated that Galactic CCSNe could be responsible for the majority of the observed CR [289]. These events produce ejecta with kinetic energy of the order of 10^{51} erg per supernova (SN) explosion, at a rate of about 3 per century. Diffuse shock acceleration taking place in remnant shocks could channel a significant fraction of $\mathcal{O}(0.1)$ of this kinetic energy into a non-thermal population of CR. The *Fermi* LAT has observed features in the gamma-ray spectra of the shell-type supernova remnants IC 443 and W44 [290] that can be related to hadronic processes. Neutrino emission from CR acceleration and interaction in supernova remnants has been studied in [291–294].

Pulsars and their nebulae have also been considered as potential sites for CR acceleration [295–299]. However, many details of the proposed mechanisms leading to extraction of rotational energy and acceleration of charged particles at these sites are vague. As with SNRs, the relation between TeV γ-ray and neutrino emission can be exploited to estimate the neutrino flux from pulsar wind nebulae [293, 300, 301].

Pulsars (and other CR sources) born in massive star clusters like Cygnus OB2 or in the Galactic Center region would inject their CR into the near environment, which has enhanced gas densities and an increased magnetic field strength compared to the Galactic average. This could amplify locally the neutrino signal from CR interactions with the interstellar gas [302, 303].

Figure 26 shows a map of Galactic sources detected by the High Altitude Water Cherenkov (HAWC) detector above few TeV in energy. The size of the disk indicates the spatial extension of the source measured by HAWC, for sources with an extension larger than 0.5°. The brightest of these sources will be detectable in neutrinos by IceCube-Gen2 in case all of the observed γ-ray emission originates from hadronic processes. For several more sources, the contribution of hadronic processes to the γ-ray emission can be constrained. In many of these sources the origin of the TeV γ-ray emission is not understood well, sometimes spatially extended, and might encompass different contributions from PWNs, local CR over-densities and molecular cloud interactions. The detection of neutrinos will give essential clues for understanding CR acceleration processes in these sources and regions.

Complementing the multi-messenger mission of IceCube-Gen2, the unique combination of the surface array and the deep optical detectors can also be used to search for PeV photons from the Southern Hemisphere, including parts of the Galactic plane

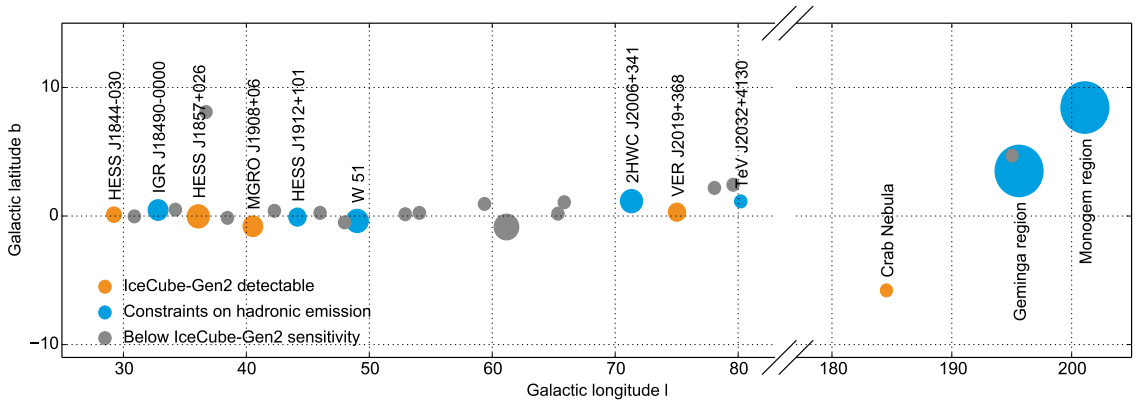

Figure 26: Sensitivity of IceCube-Gen2 to hadronic emission of neutrinos by Galactic sources. Shown are TeV γ-ray sources detected by HAWC near the Galactic plane and in the Northern hemisphere (declination $\delta \geq -5^{\circ}$). The size of the source marker corresponds to the source extension reported by HAWC for sources that are larger than 0.5°. Sources marked in orange will be detected by IceCube-Gen2 if their γ-ray emission originates solely from hadronic processes. For sources marked in blue, the contribution of hadronic emission can be constrained at the 90% confidence level, while sources marked in gray are below the sensitivity of IceCube-Gen2.

not visible by HAWC or LHAASO. Unlike pointed observatories such as CTA, IceCube-Gen2 will continuously observe the entire visible sky using the same triggers for PeV photons as for cosmic rays. As demonstrated for IceCube [304], photon-initiated air showers can be distinguished from cosmic rays based on a comparison of the strength of the surface signal and the number of muons optically detected deep in the ice. PeV photons have recently been discovered from two sources in the Northern Hemisphere by LHAASO [305, 306]. IceCube/IceTop has a similar surface area as LHAASO and has demonstrated gamma-hadron separation with rejection factors better than a few 10^2, where $\mathcal{O}(10^3)$ would be needed to discover a LHAASO-like source with the existing exposure of IceCube. Although IceCube-Gen2 is not designed as a gamma-ray detector and it is not yet studied by how much the gamma-hadron separation will improve, it is fair to say that it has significant discovery potential for PeV photon sources due to its order-of-magnitude larger surface area. Assuming that LHAASO-like photon sources also exist in the Southern Hemisphere, PeV photons thus provide an additional channel to search for the sources of the most energetic Galactic cosmic rays.

2.3.2 Diffuse Galactic emission and the propagation of cosmic rays

The expected diffuse Galactic neutrino flux from interactions of CR with interstellar gas and unresolved CR sources is, averaged over the whole sky, about an order of magnitude lower than the isotropic flux observed in IceCube for $E \simeq 100$ TeV [307–310]. This is in good agreement with the observations of a statistical excess of events correlated with the Galactic plane by IceCube presented in Section 1.2, which is consistent with a galactic neutrino flux of 9% – 13% of the total observed neutrino flux at 30 TeV.

Detailed predictions of the spectrum of the diffuse neutrino flux from CR interactions in our Galaxy depend on the assumptions about the injection and propagation of CRs in the interstellar medium. Extrapolations of the diffuse gamma-ray emission from CR interactions by *Fermi* LAT [24] rely on the assumption that the local CR flux is a good

approximation for the average Galactic CR density. This is not necessarily the case in more complex diffusion scenarios [26, 311, 312], and/or for strongly inhomogeneous source and target distributions in the Galaxy [313–316], as well as time-dependent local CR injection episodes [317]. Such scenarios often predict an enhancement of the hadronic γ-ray and neutrino emissions in the multi-TeV region that can be tested with neutrino telescopes. In addition, the observation of spectral cutoffs in the Galactic neutrino flux at tens of TeV in energy or beyond, would yield valuable information and constraints on the maximum acceleration energy and composition of Galactic CRs.

IceCube's sensitivity enabled a first detection of the Galactic emission at 4.5σ significance using shower-type events. The low statistics and low angular resolution of $O(10^{\circ})$ for these events does not allow to distinguish at high confidence between potential contributions from individual Galactic sources and the contributions from CR interactions with interstellar gas. It also limits the potential for spectral and morphological analysis of the emission to test propagation models and/or observe spectral cutoff features. The order-of-magnitude larger detection volume for shower-like events will improve the spectral measurement substantially. Based on a scaling of the performance of the novel machine-learning approach for the identification of shower-type events[†] that led to the detection of the Galactic plane in neutrinos, we estimate that IceCube-Gen2 will detect the Galactic emission at 11σ confidence, after 10 years of observations.

However, IceCube-Gen2 will be able to significantly observe the Galactic plane not only with shower-type events but also using high-resolution track-like events, allowing a much better localization of the neutrino emission. Assuming the best fit model and flux of the IceCube observations, Ice-Cube-Gen2 will observe an 8.7σ excess in the independent track channel after 10 years of operations as well.

2.3.3 Cosmic rays in the galactic/extragalactic transition region

The sources of the highest energy Galactic cosmic rays are still unknown. Depending on the scenario, the transition to extragalactic CR of even higher energies could start around 10^{17} eV, as a knee of the heavy mass component in the cosmic-ray spectrum has been observed around $10^{16.9}$ eV [318], as well as the 'second knee' around $10^{17.2}$ eV [319–322]. The maximum energy of Galactic CR could be as high as the energy of the 'ankle' around $10^{18.5}$ eV even though extragalactic CR likely start to dominate the flux at a lower energy [323]. Disentangling the cosmic-ray spectrum in the transition region into its Galactic and extragalactic components is an important science goal in astroparticle physics, as this is directly linked to understanding the most energetic particles originating from the Milky Way.

Galactic and extragalactic cosmic rays in this energy range can be disentangled by their mass composition. While extragalactic cosmic rays seem to be dominated by protons and helium until at least 10 EeV, the Galactic CR are presumed to be dominated by nuclei of the CNO group or of even heavier mass such as the iron group [323–325].

[†]Due to the lack of a machine-learning environment specifically trained on IceCube-Gen2 simulation data to identify showers, we rely on the assumption that the relative performance gain of the machine-learning approach compared a conventional shower identification is equal in IceCube-Gen2 and IceCube.

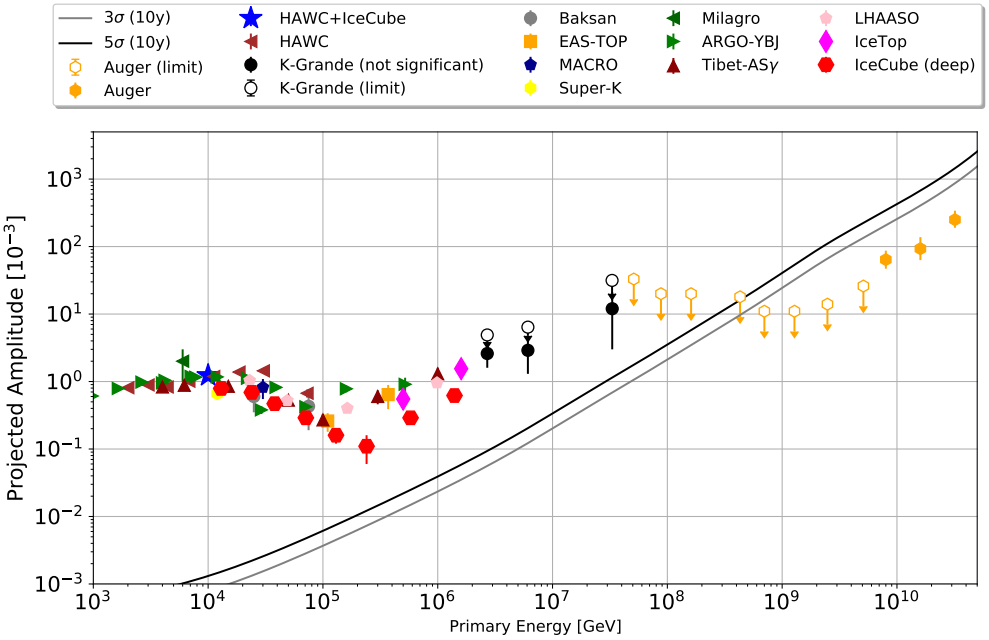

Figure 27: Sensitivity of cosmic-ray anisotropy measurements with IceCube-Gen2 with 10 years worth of data. The expected three and five sigma sensitivities to the equatorial plane component of the dipole anisotropy are shown. IceCube-Gen2 will be far the most sensitive detector for the PeV energy range, extending IceCube's energy range of anisotropies by more than an order of magnitude in energy. In particular, statistically non-significant measurements of the dipole amplitude by KASCADE-Grande [329], if true, can be confirmed at five sigma level. Note that KASCADE-Grande and Auger [330] results are shown with measurements (full symbols) and 90% CL upper limits (empty symbols) [329–343].

Therefore, a high accuracy for the mass of the primary particle is crucial to separate Galactic and extragalactic CR [114, 326].

Next to the study of hadronic interactions, this is the most important reason why the IceCube-Gen2 surface array features elevated radio antennas in addition to scintillation panels: the radio antennas deliver a measurement of the shower energy and the depth of shower maximum [327, 328] which, together with the electromagnetic particles measured by the scintillators and the TeV muons measured deep in the ice, will deliver higher mass accuracy than achieved before in this energy range.

Another observable critical for understanding the transition from Galactic to extragalactic CR is the weak anisotropy of their arrival directions. The phase of the dipole component seems to shift away from the Galactic center starting around 1 EeV, but the complete range from 2 PeV to about 8 EeV currently lacks statistically significant anisotropy measurements, as the KASCADE-Grande measurements in this range are statistically not significant [329] IceCube is already providing the world's most sensitive anisotropy measurements in the low PeV energy range, and the larger exposure of IceCube-Gen2 will extend these measurements towards the energy range of the second knee (Figure 27), which is an extension of more than an order of magnitude in energy.

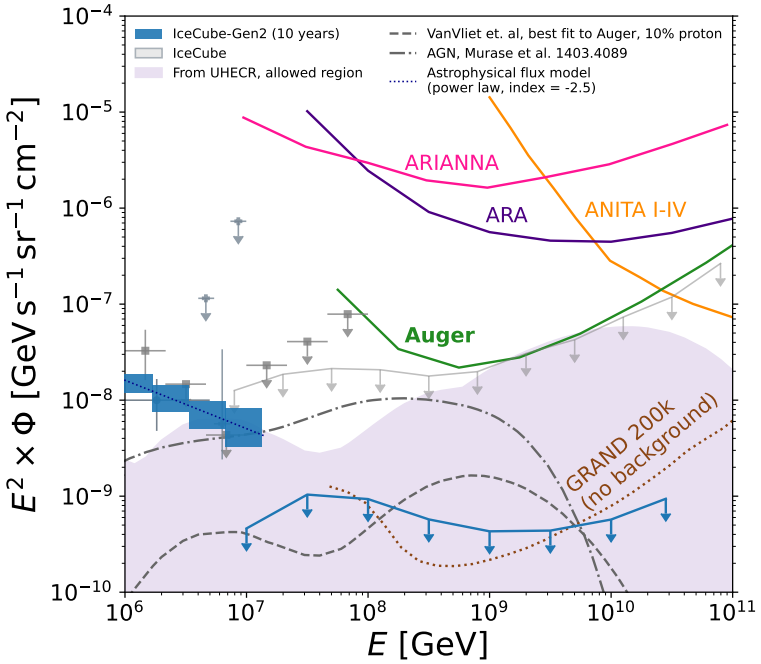

Figure 28: Sensitivity of IceCube-Gen2 at the highest energies in comparison to models [61, 100, 101], existing upper limits [60, 348–351], and the 10 year sensitivity of the proposed GRAND array of 200,000 antennas [352]. The uncertainties on the IceCube-Gen2 radio array sensitivity are $\pm 20\%$, which are uncertainties in the estimated sensitivity of the array, e.g. due to remaining design decisions. The sensitivity for IceCube-Gen2 includes best estimates for backgrounds and analysis efficiency, but likely err on the conservative side. All fluxes are shown as the all-flavor sum assuming equal flux in each flavor.

2.3.4 Cosmogenic neutrinos

At EeV energies all CR are believed to be of extragalactic origin [344]. From CR measurements themselves, we neither know what the accelerators of these UHE cosmic rays are, nor what maximum energies they can reach. Also, particle composition measurements at the highest energies still leave room for various scenarios [326]. While a dominance of iron has been excluded, different and changing ratios of protons and intermediate mass group particles have been reported above EeV energies, all carrying the uncertainties due to the hadronic interaction models [345–347]. Limited knowledge about the Galactic and extragalactic magnetic fields that influence the propagation, further complicates the identification of sources based on CR observations alone. Detecting neutrinos corresponding to these CR energies will provide complementary information to resolve these open questions.

Above EeV energies the CR interactions with the cosmic microwave background and the EBL can produce neutrinos [83]. In addition, unstable atomic nuclei, produced during photo-disintegration or photo-pion production of CR, can produce neutrinos when decaying. All of these neutrinos are referred to as *cosmogenic neutrinos*. So while this secondary flux of neutrinos is extremely well motivated, its level depends strongly on the composition of the CR [353, 354], the cosmic evolution of the sources, the spectral index of the sources, and their maximum acceleration energy [91, 92, 100]. IceCube

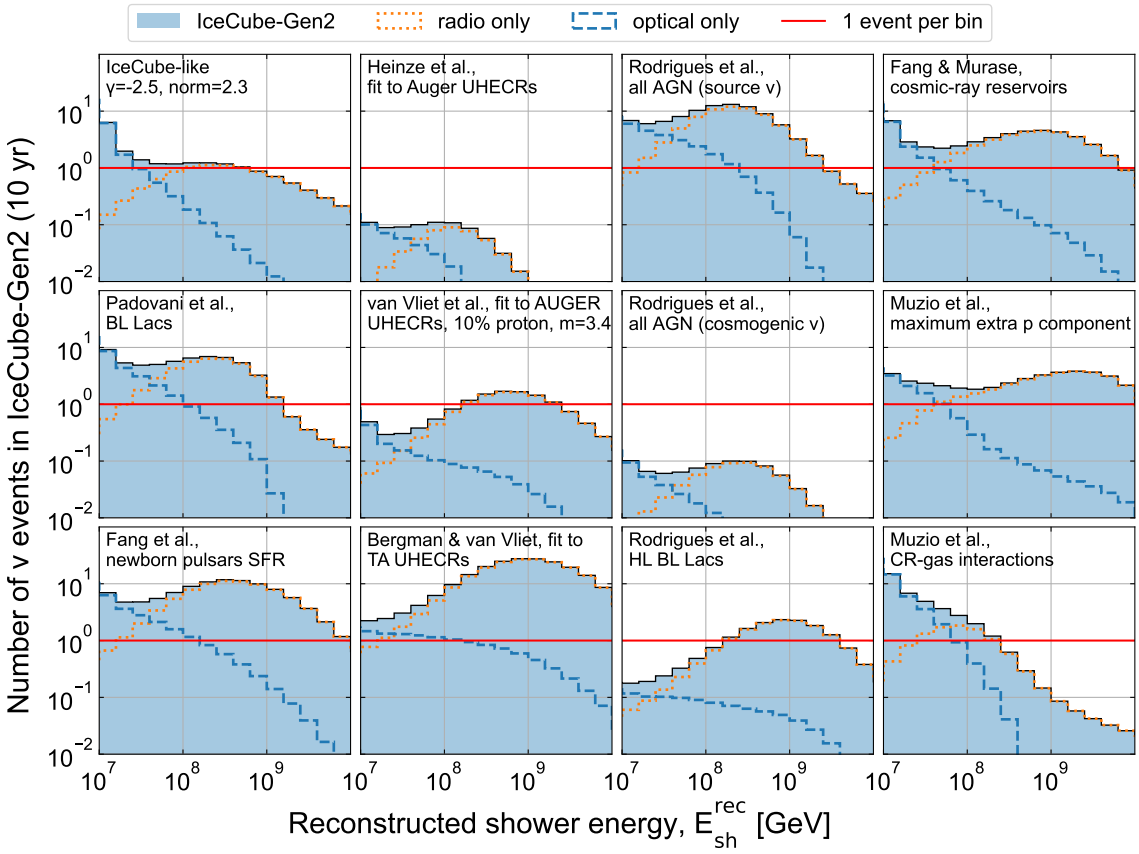

Figure 29: Average expected number of events in IceCube-Gen2, after 10 years of operation, for different predicted diffuse UHE neutrino flux models [62, 69, 101, 356–362], illustrating the variety in the predictions. Shown are the event numbers for optical and radio-only, as well as the total number. The red line highlights one event per energy bin of this analysis.

can already exclude scenarios with a very strong evolution of the CR sources with cosmic redshift [59, 60], but to draw firm conclusions much larger exposures are needed.

The sweet spot for cosmogenic neutrino detection is around 10^{18} eV, since the predicted neutrino flux at these energies depends less strongly on the maximum acceleration energy and spectral index than at the highest energies [93]. The flux at this energy is primarily a function of the proton fraction and even the most conservative flux estimates peak here [100]. The radio array of IceCube-Gen2 will provide excellent sensitivity in the entire energy range relevant for cosmogenic neutrinos (see Figure 28).

With the predicted sensitivity, IceCube-Gen2 will also be able to provide independent evidence for whether the observed cut-off in the flux of UHE cosmic rays is due to the GZK suppression [81, 82] or just due to reaching the limit of acceleration in the sources [355]. The neutrino flux at energies above 10 EeV depends primarily on the maximum energy of CR protons and the spectral index of their power-law spectrum rather than the source evolution parameters [92]. Detecting the corresponding neutrino flux will be a measurement independent of the uncertainties in the modelling of the hadronic interactions in extensive air showers and, thus, complementary to results from air shower arrays.

The IceCube-Gen2 sensitivity would reach the region of current best-fit models to CR data, assuming sources identical in CR luminosity, spectrum and composition, as well as a rigidity-dependent cut-off and thereby essentially no protons at the highest-energies [98, 101]. In an only slightly more favorable scenario of 10% protons, IceCube-Gen2 will detect at least 3 events per year above ~100 PeV, as shown in Figure 29 (subplot 6). The sensitivity of the IceCube-Gen2 optical array will be about 5 times better than the IceCube upper limit shown in Figure 28 and therefore not contribute substantially to the performance of the observatory in the EeV energy range. In the case that no cosmogenic neutrinos are discovered by IceCube-Gen2, the observation would exclude all redshift evolution scenarios[‡] with $m > 0$ for a proton-fraction of more than 20%, thereby excluding many source populations that evolve with the star formation rate, various AGN models, and GRBs as sources of UHE cosmic rays.

Figure 29 shows the average expected number of neutrino-induced events for a large number of diffuse UHE neutrino flux models [62, 69, 101, 356–362], representative of the breadth of theoretical predictions in the literature. Flux models include an extrapolation of the IceCube measurements of astrophysical neutrinos to ultra-high energies (subplot 1), models for neutrinos generated within sources (column 1), neutrinos expected from cosmogenic predictions (column 2), astrophysical and cosmogenic components of a self-consistent model by Rodriguez et al. (column 3), and combined models with self-consistent production of cosmogenic and source neutrinos (column 4). For most flux models, in 10 years, we expect tens of detected events, most of them in the range 10^8–10^9 GeV. For some particularly high flux models, we expect roughly 200 events. The majority of flux models could be discovered decisively within just 5 years of exposure; some, much sooner. After 10 years, it should even be possible to distinguish between most competing flux models, mainly by means of comparing the energy spectra of the events they initiate [363].

2.4 Probing fundamental physics with high-energy neutrinos and cosmic rays

IceCube has been extremely successful in searches for dark matter and other new physics beyond the Standard Model [10] (BSM physics). IceCube-Gen2 will provide new opportunities to study particle physics at energies and baselines well above those accessible at terrestrial accelerators and local natural sources due to increased statistics, extended energy reach and improved flavor identification. This section highlights some of the opportunities that this observatory will provide in probing fundamental physics and searches for new particles.

2.4.1 Hadronic interactions in the PeV domain

The particle physics processes in ultra-high-energy air showers are insufficiently understood, in particular regarding the muon production and the associated atmospheric neutrino production. All state-of-the-art hadronic interaction models predict fewer muons than measured [364–368]. This is difficult to explain with standard physics, and the dif-

[‡] using the customary $(1+z)^m$ parametrization of redshift evolution

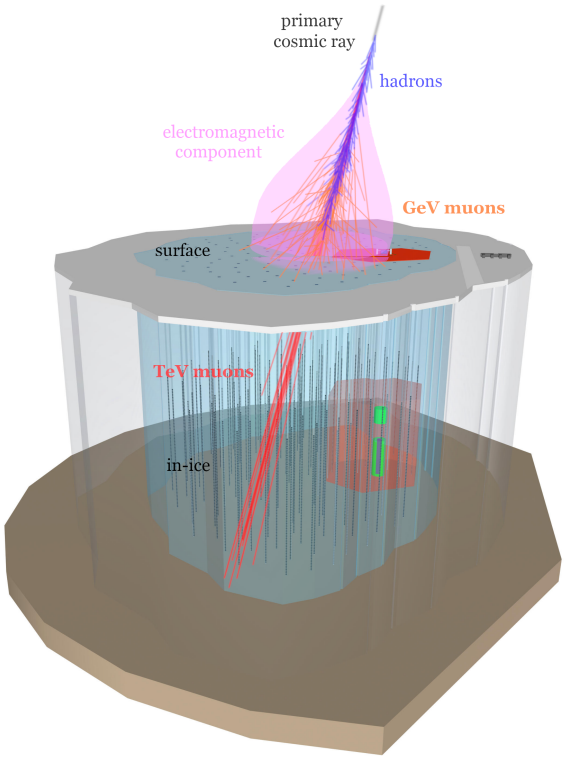

Figure 30: Sketch of an air shower impinging the IceCube-Gen2 surface and optical arrays. While muons of TeV and PeV energy penetrate the ice and will be detected by the optical array, GeV muons and electromagnetic particles can be measured at the extended surface array. In particular, as the muonic component reaches out to further distances from the shower axis as the electromagnetic one. In addition, surface radio antennas can provide a calorimetric measurement of the shower energy and its longitudinal development, all together making IceCube-Gen2 a unique laboratory for hadronic interactions in air showers.

ferent scenarios proposed for the solution need to be tested with more accurate measurements [369]. They predict, e.g., differences in the evolution of the number of GeV muons with energy and different ratios of GeV to TeV muons [370].

Combining the measurements of IceCube's surface array IceTop [371] with those of other experiments indicates that the deficit of GeV muons on ground in the models may start at around 10 PeV cosmic-ray energy [368]. With IceCube-Gen2, these muon measurements will be extended to several 100 PeV providing overlap with the muon measurements of the Pierre Auger Observatory [372]. Also the higher accuracy for the primary cosmic-ray mass in this energy range will help to shrink systematic uncertainties in the interpretation of the muon measurements. With the combination of the surface array measuring the GeV muons and the optical in-ice array detecting the TeV muons of the same air showers [373, 374], we can further scrutinize hadronic interaction models through muon spectroscopy (Figure 30).

Finally, IceCube-Gen2 will provide a unique opportunity to study the flux of PeV forward muons. In particular, the flux of leptons produced by prompt decays is highly uncertain and depends on the mass composition and hadronic physics at multi-PeV energies. IceCube has measured prompt muons [375–377] with its optical array alone,

but without the surface information their interpretation remains uncertain. With the about 30 times larger aperture of IceCube-Gen2 for surface-optical coincidences, we expect several events per year for which we will measure the parent air shower of a PeV muon in the ice. This will also enable new insights in the production of the associate prompt atmospheric neutrinos and reduce uncertainties on their flux at PeV energies and higher.

2.4.2 Neutrino cross sections at high energies

The neutrino-nucleon cross section in the TeV–PeV range was measured for the first time using astrophysical and atmospheric neutrinos in [16, 63, 378], extending previous results [379–383] and measurements that used GeV neutrinos from accelerators [384–386]. The measurements agree with high-precision Standard Model predictions [387]. Future measurements in the EeV range could probe BSM modifications of the cross section at center-of-momentum energies of up to 100 TeV [78, 388–396] and test the structure of nucleons with a sensitivity comparable with colliders [397–399].

IceCube has measured the neutrino-nucleon cross-section with 30-40% uncertainty up to 1 PeV, using only one year of data [16]. Each year of data from IceCube-Gen2 will yield roughly one order of magnitude more statistics. Therefore with this new instrument it will be possible to study the cross-section with significantly higher precision and, in multiple energy bins, to energies beyond 10 PeV. This sensitivity will allow unique tests of BSM physics involving extra dimensions, leptoquarks or sphalerons [380, 396, 400–403]. It would also probe the QCD parton distribution functions (PDFs) at large momentum transfers Q^2 ($Q^2 \approx M_W^2$) and Bjorken-x values down to $\sim 10^{-4}$ [387, 404, 405], where non-perturbative QCD effects are expected to start becoming important. This data will complement results from the FASERnu experiment at CERN, which will use forward neutrinos from LHC interactions to measure neutrino cross-sections at energies centered around 1 TeV [406].

Figure 31 shows the expected sensitivity to the EeV neutrino-nucleon cross section that the radio component of IceCube-Gen2 could achieve after 10 years of operation [407]. We show forecasts for three representative flux predictions from the literature [358, 359, 362]. A measurement of the cross section will be possible under most flux predictions, e.g., [358, 362]; a precise measurement, to within the theoretical uncertainty of the cross-section prediction [404], requires a high neutrino flux, e.g., the flux perdicted in [359]. Measuring the cross section to within an order of magnitude could already distinguish between Standard Model predictions and BSM modifications [378]. This target is achievable with tens of events in the hundreds of PeV–EeV energy range. In the scenario presented in Section 2.3.4, IceCube-Gen2 would record (mostly via its radio detection component) about 3 events/year above 100 PeV just from cosmogenic neutrinos, bringing into reach a test of the Standard Model at these extreme energies [405].

IceCube-Gen2 will enable a measurement of the inelasticity of neutrino interactions (the fraction of energy transferred to the target) over a wider energy range and with higher precision than IceCube [63], using a larger sample of events. This capability will allow us to study a number of new physics topics since the inelasticity is sensitive

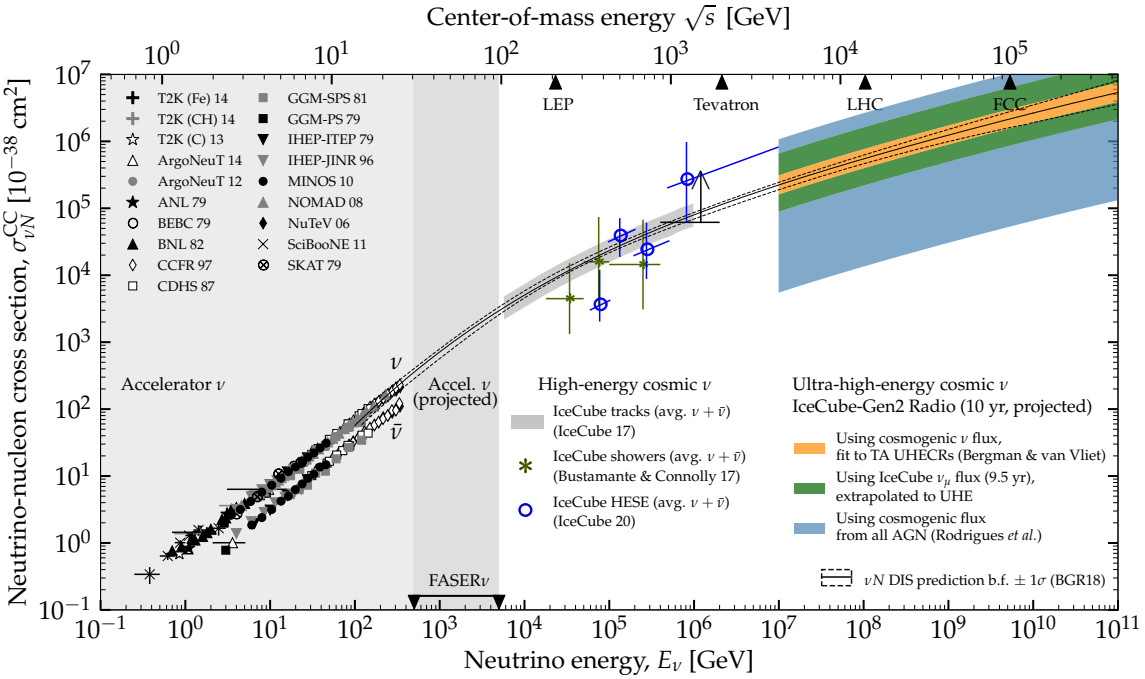

Figure 31: Neutrino-nucleon cross section measurements, compared to deep-inelastic-scattering (DIS) cross section prediction from [404] (BGR18). The forecasts at ultra-high energies are for the radio component of IceCube-Gen2 only, and for three different assumptions of the UHE neutrino flux. For each choice of flux, the cross-section sensitivity forecast accounts generously for the uncertain normalization of the flux prediction. The assumed resolution in shower energy is 10% and the resolution in zenith angle is 2°. Figure adapted from [407]. Please note that the IceCube-Gen2 radio array configuration used in [407] is similar, but not identical to the reference radio array design in this manuscript.

to new phenomena, including non-standard types of interactions, such as 'diffractive' neutrino interactions [408] or BSM physics, e.g., the production of heavy vector bosons. Furthermore, the inelasticity distribution is sensitive to more conventional physics, e.g., the evolution of the PDFs, including nuclear effects like shadowing, which affect both the inelasticity and the cross-section [409].

2.4.3 New physics constraints from flavor mixing

As high-energy cosmic neutrinos oscillate on their way to Earth, the allowed range of each flavor's fractional contribution to the total measured flux is small (see Figure 32), even after accounting for uncertainties in the parameters that drive the oscillations and in the neutrino production process [277]. That is, given a flavor composition at the source and the standard oscillation scenario, the expected flavor ratio at the Earth is quite restricted. However, mixing remains untested at high energies and over cosmological propagation baselines [413]. Even small BSM effects could affect flavor mixing, vastly expanding the allowed region of flavor ratios at the Earth and making the flavor ratio measurement a very sensitive probe of BSM physics [277, 281, 411, 412, 414–421]. Figure 32 shows two examples (ν-decay [277] and Lorentz invariance violation [411, 412]) of how BSM physics effects extend the region of possible flavor composition after cosmological distances. The figure also shows the expected constraints

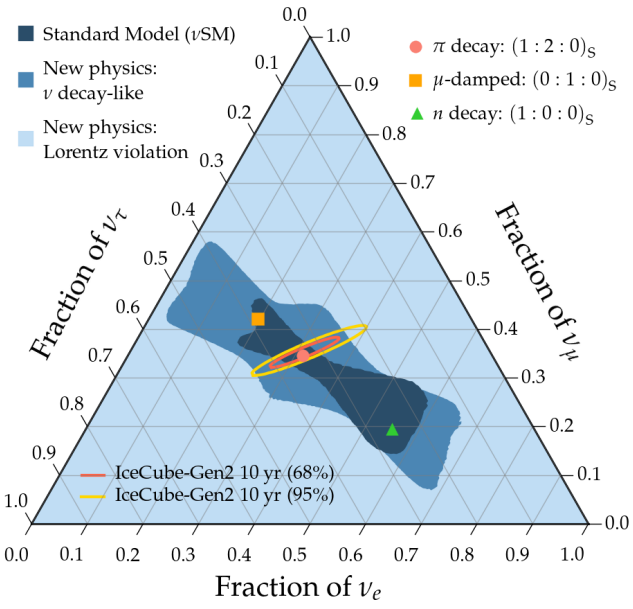

Figure 32: Flavor composition at Earth of high-energy cosmic neutrinos, indicating the "theoretically palatable" [277, 410] regions accessible with standard oscillations, with new physics similar to neutrino decay, and with new physics similar to Lorentz-invariance violation [411, 412]. To generate the colored regions, the neutrino mixing parameters are varied within their uncertainties at 3σ, and the flavor ratios at the sources are varied over all possible values. The colored contours indicate the expected constraints from IceCube-Gen2, if neutrinos are produced with ratios of $(\nu_e : \nu_\mu : \nu_\tau) = (1 : 2 : 0)$ at the source and assuming Standard Model neutrino oscillations. See Figure 9 for an overview of current flavor composition constraints obtained from IceCube data.

from IceCube-Gen2 on the flavor composition of cosmic neutrinos, assuming standard neutrino oscillations and a 1:2:0 production ratio at the sources. IceCube-Gen2 will allow substantially more sensitive searches for, and constraints on, BSM effects using the flavor ratio than the current generation of neutrino telescopes. The improved statistics will also permit searches for a potential energy dependence of mixing (cf. Section 2.2.6), which could also point to the presence of BSM effects [277, 417].

2.4.4 Sterile neutrinos

A detector of the size of IceCube-Gen2 opens the possibility to search for heavy sterile neutrino decay. For example, an active, light neutrino might scatter off a target nucleon producing a heavy, sterile neutrino [422], which has a variety of interesting decay channels [423–425]. Several of these decay signatures will only be observable in the larger instrumented volume of IceCube-Gen2. One such example is the sterile neutrino decaying into pairs of muons; characteristically, this muon pair would be emitted from a secondary vertex that is displaced from the initial neutrino-nucleon interaction.

Such double muon tracks can also point to new physics via neutrino trident interactions [426–428]. This very rare process is mediated by the W, Z, or a virtual photon in the Standard Model. But if it is additionally mediated by a new vector or scalar boson, the final state of a neutrino interaction in the detector—a double muon track and a particle cascade simultaneously produced from the same vertex—would be a very

distinctive signal (although several other interesting signals are also expected [428]). As in the previous case, the size of IceCube-Gen2 will benefit the reconstruction of the double track, or allow the measurement of the unusual light yield of a single track over a sufficiently long lever arm, if the two tracks are not individually reconstructed.

2.4.5 Searches for unexpected neutrino properties and additional species

The extremely long distances that astrophysical neutrinos travel make them a good probe of fundamental neutrino properties. The observation of non-zero neutrino masses opens the possibility of neutrino decay and astrophysical neutrinos can place strong constraints on decay scenarios [429–434]. Additionally, unlike other new physics scenarios, neutrino decay imprints a specific correlation between the energy distribution of the events and the flavor composition [418]. This makes it one of the most predictive signatures of new physics.

The existence of additional neutrino species is of great interest to the neutrino community, specially due to the claims by the MiniBooNE collaboration [435]. Global data allow non-unitarity in the neutrino mixing (PMNS) matrix [436], which may indicate potential mixings of standard neutrinos and sterile neutrinos. The effect of additional sterile neutrino species on the flavor ratio was discussed in [437]. If the initial flavor composition does not contain a significant sterile component its effect is small. This is not the case when the neutrino flux has a large initial sterile component [438] (which can happen for example in the case of decaying dark matter [437]). In this situation the astrophysical neutrino flavor can appear in the tau corner in Fig 32. This is a very striking signature of non-standard neutrino physics as this corner is forbidden by unitary constraints under the assumption of standard production mechanisms [411, 420]. The IceCube-Gen2 flavor composition measurement will be competitive with and complementary to terrestrial high-precision oscillation experiments searching for sterile neutrinos [438].

2.4.6 Tests of fundamental symmetries

Theories allowing for a new spacetime structure at the Planck scale, like quantum gravity, can accommodate violations of symmetries that are taken as fundamental in the Standard Model, like CPT and Lorentz invariance [439]. This has ramifications that can be detected in a neutrino telescope as an anomalous oscillation effect proportional to the neutrino energy, instead of inversely proportional to energy as in standard oscillations [440–451]. Currently, the strongest constraints on Lorentz invariance violation (LIV) with neutrinos come from IceCube, using the high-energy atmospheric neutrino flux [108]. IceCube-Gen2 can add both an increase in statistics of high-energy atmospheric neutrinos, as well as a high-statistics observation of cosmic neutrinos that could provide unprecedented sensitivity to the parameters quantifying the deviation from Standard Model physics [416, 441, 443, 446, 448, 452–459]. The detailed characterization of the extragalactic neutrino flux with the high statistics available with IceCube-Gen2 can be used to set limits to LIV which are complementary to those obtained from the distortion of the oscillation pattern at lower energies. Indeed, the first PeV events detected by IceCube have already been used to set such a limit, under the assumption that they are extragalactic, since such superluminal neutrinos would rapidly

lose energy via bremsstrahlung. The bound obtained from these events is $\delta < 10^{-18}$, where δ is the deviation from the speed of light, orders of magnitude smaller than the previous best limit of 10^{-13} [445, 456]. Additionally, the detection of neutrino flares in cosmic sources, with additional assumptions of the mechanism of neutrino emission, can be used as precise time-of-flight measurements. This exercise was performed on the candidate source TXS 0506+056 [458, 459] resulting in very strong constraints on LIV under the assumption of simultaneous γ-ray and neutrino production; a similar study was performed on a previous candidate source yielding similar strong constraints [460]. As IceCube-Gen2 discovers more high-energy neutrino sources, and our understanding of the emission of γ-rays and neutrinos improves, such studies will yield significantly more robust bounds.

In subluminal LIV scenarios neutrino bremsstrahlung would not be produced, but the expected flavor composition of ultra-high-energy neutrinos would be modified. This can be modeled as a change in the neutrino potential due to its interaction with an ambient LIV field [461]. In general, any new interaction that is not diagonal in flavor will modify the expected flavor composition [411].

At the moment, the astrophysical neutrino constraints have a strong dependence on the details of the production mechanism and the initial flavor composition. It is remarkable, though, that already in some scenarios the astrophysical neutrino constraints are several orders of magnitude stronger than the terrestrial ones. These effective operator bounds apply not only to interactions between neutrinos and the ambient Lorentz violating field, but can be adapted to other kinds of interaction [412]. Further interesting BSM scenarios are coherent interactions between neutrinos and dark matter [462–468]; neutrinos and dark energy [469]; very-long-range $L_e - L_\mu$ and $L_e - L_\tau$ gauged interactions sourced by the universe's electron content [421, 470–472]; and new interactions between high-energy cosmic neutrinos and low-energy relic neutrinos [473–480].

2.4.7 Dark matter searches

Dark matter searches with IceCube have focused on generic thermal relic *Weakly Interacting Massive Particles* (WIMPs), by looking for neutrinos from annihilations (or decays) of dark matter captured in the Sun, Earth, or in the Galactic halo or galaxy clusters [481]. Dark matter candidates with a mass beyond the typical WIMP scale of a few GeV to TeV may also have been non-thermally produced in the early universe [482–484]. Neutrinos offer many advantages to search for annihilation or decays of heavy dark matter with masses beyond about 100 TeV [109–111]. The neutrino interaction cross section increases with energy [387] such that the event rates predicted for heavy decaying dark matter per volume of ice remain constant as function of the particle mass up to several tens of TeV. By contrast, γ-ray signals fall by a factor of $1/m_\chi$ and are further attenuated by the interstellar radiation field [485].

Currently, dark matter lifetimes at the level of 10^{28} s [486] are being constrained by IceCube's highest energy neutrinos, resulting in the strongest constraints on the dark matter lifetime above 100 TeV. These bounds are statistically limited and lifetimes exceeding 10^{29} s could be tested for decay modes which involve neutrinos in the final state.

These searches are expected to be significantly improved by the order-of-magnitude increase in statistics that IceCube-Gen2 will provide.

Beyond the traditional, model-agnostic WIMP scenario, IceCube-Gen2 will also have power to study dark-portal scenarios, where the dark matter is part of a secluded sector [487]. In these scenarios, the dark sector often couples to the Standard Model either via kinetic mixing or neutrino mass mixing. These secluded models can increase the expected neutrino flux from dark matter annihilations in the Sun, reducing the attenuation of the neutrino flux since, for favorable model parameters, the mediator can leave the dense solar interior and decay outside the Sun [488, 489].

It has recently been shown that such dark portal scenarios imprint signatures on the diffuse astrophysical neutrino spectrum [462], as well as on the expected attenuation from a single neutrino source [479]. With the improved characterization of the astrophysical diffuse flux and observation of new neutrino sources expected from IceCube-Gen2, such dark portal scenarios can be further investigated.

2.4.8 Other particle physics searches and exotica

With its unparalleled size, IceCube-Gen2 will have unparalleled sensitivity to searches for new BSM particles and exotica. We have seen that IceCube has produced important physics results in many areas that were either not considered during the proposal, or were too speculative to formally propose. We expect the same for IceCube-Gen2. Here, we list a few planned new-particle and exotica searches, but these are just a sample of what might be possible. New particles can be detected through either their passage through the detector, or by producing unique signatures from interactions either within the detector or outside of it. Magnetic monopoles are one example of the former; relativistic monopoles are notable for their large, but roughly constant dE/dx, without large stochastic fluctuations [490]. Some models of supersymmetry or Kaluza-Klein particles lead to the latter, through the production of pairs of laterally separated particles which may travel upward through the detector [491].

An intriguing possibility is the search for low-scale gravity effects through micro black hole production. If the center-of-mass energy of the interaction of a neutrino with a nucleon exceeds the Planck scale, a microscopic black hole can be produced [392, 393, 492]. In our 4-dimensional world, the Planck scale lies at energies $M_P \sim 10^{19}$ GeV, while the largest terrestrial accelerators only reach TeV center-of-mass energies. But in 4+D space-time dimensions the Planck scale may be much lower, and the interaction of an ultra-high-energy neutrino with a nucleus inside the detector could produce a micro black hole. The evaporation of the black hole through Hawking radiation (in $\sim 10^{-27}$ s) will produce a burst of Standard Model particles that can be detected in a neutrino telescope. Although the free parameters of extra-dimensional models are many and the uncertainties in the predictions large, a detectable signal can be expected in a large volume detector in the most favorable scenarios, taking into account the already existing limits on the ultra-high-energy neutrino flux. Even if the original energy of the incoming neutrinos is not high enough to form a black hole, elastic neutrino-parton scattering through exchange of D-dimensional gravitons could be possible, another feature of low-energy gravity models. In such case the neutrino is not destroyed in the

interaction, as in black hole production, but it continues on its way ready for another elastic interaction after a mean free path which, for a given energy, depends on the number of extra dimensions. The energy lost in each interaction goes into a hadronic shower, producing a very unusual signature in the detector: multiple particle showers without a lepton track between them. Current calculations predict that a large detector could detect a handful of events per year, being able to probe extra-dimensional models with D up to six [493]. The larger size of IceCube-Gen2 will allow to follow such events over a longer lever arm, increasing the identification efficiency. IceCube is just too small to detect several correlated showers.

The atmosphere, acting as a target for UHE cosmic rays, can also be a useful source for searches for physics beyond the Standard Model [494–497]. The interaction of a high-energy CR with a nucleon in the atmosphere can take place at a much higher center-of-mass energy than that achievable in man-made accelerators. Supersymmetric particles can be produced in pairs and, except for the lightest one, they can be charged. Even if unstable, due to the boost in the interaction, they can reach the depths of the detector and give rise to Cherenkov light as they traverse the array. The signature is two minimum ionizing, parallel, coincident tracks separated by a distance of over 100 meters [498]. The interactions of CR with the atmosphere can also be used to probe non-standard neutrino interactions due to TeV gravity effects. At high energies neutrino interactions with matter may become stronger, and the atmosphere can become opaque to neutrinos of energies above a few PeV. A signature in IceCube-Gen2 would be an absence of neutrinos above such energy, accompanied by an excess of muon bundles from the neutrino interactions, mainly at horizontal zenith angles, where the atmospheric depth is larger. The size of the IceCube-Gen2 optical array is of paramount importance for these signatures in order to be able to efficiently reconstruct parallel tracks and/or muon bundles.

2.5 Science requirements matrix

The scientific achievements of IceCube-Gen2 outlined above assume certain capabilities of the facility that can be translated into a set of requirements. In Tables 2, 3 we summarize such performance requirements and indicate to which part of the science program described in sections 2.1 – 2.4 they apply. The performance requirements can be mapped onto technical requirements for the different subsystems, detector arrays and sensors comprising IceCube-Gen2. These technical requirements can be found in Part II of this document, focusing on the technical implementation and expected performance of the individual elements of IceCube-Gen2. Empty fields imply that there is no specific requirement on the performance measure for the respective section of the science program.

Table 2: Science requirements for IceCube-Gen2

Requirement	Resolving the high-energy neutrino sky (Section 2.1)	Understanding cosmic particle acceleration (Section 2.2)	Sources and propagation of cosmic rays (Section 2.3)	Fundamental physics with HE neutrinos (Section 2.4)

Peak sensitivity (5σ discovery potential)

Flux / Fluence / Intensity per flavor and decade in energy, 1:1:1 flavor ratio

	Point Sources		Diffuse flux
	10 y observation [erg cm^{-2} s^{-1}]	100 s burst [GeV cm^{-2}]	10 y observation [GeV cm^{-2} s^{-1} sr^{-1}]
10 TeV	2×10^{-12}	3×10^{-2}	
1 PeV	1×10^{-12}	2×10^{-2}	1×10^{-10}
100 PeV	5×10^{-12}	15×10^{-2}	4×10^{-10}
10 EeV	5×10^{-12}	7×10^{-2}	2×10^{-10}

Source detection volume [Mpc^3]

Power-law flux with index -2, one decade in energy, 1:1:1 flavor ratio

	Point Sources		
	10 y observation L_ν=10^{43} erg/s	100 s burst E_ν=10^{50} erg	
10 TeV	5×10^6	2×10^6	
1 PeV	1×10^7	2×10^6	
100 PeV	5×10^5	1×10^5	
10 EeV	5×10^5	2×10^5	

Angular resolution @ declination $\delta = 0^\circ$ [deg^2]

10 TeV	0.5 (median)		
1 PeV	0.125 (median)	1 (90% CL)	
1 EeV		100 (90% CL)	

Energy resolution

Optical array	30% (E > 100 TeV), 15% (E > 1 PeV)
Radio array	70% (E > 100 PeV)

Table 3: Science requirements for IceCube-Gen2 (continued).

Requirement	Resolving the high-energy neutrino sky (Section 2.1)	Understanding cosmic particle acceleration (Section 2.2)	Sources and propagation of cosmic rays (Section 2.3)	Fundamental physics with HE neutrinos (Section 2.4)
Effective detector volume				
1 PeV			8 km^3	
1 EeV			1.6×10^3 km^3 sr	
Particle identification				
Tracks	x	x	x	x
Showers			x	x
Double showers			x	x
Exotic signatures				x
Timing				
Absolute timing	O(1 s)	O(1 ms)		
Time-to-alert		< 1 min		
CR air shower detection				
Sky coverage	$\theta \lesssim 45$ deg		$\theta \lesssim 65$ deg	
Aperture	$> 8\,km^2$sr for surface-optical coincidences			
Energy threshold	500 TeV (for $\theta < 45$ deg)			
Angular resolution	< 1 deg (median)			
Energy resolution			10 %	
Shower max. resolution			30 g/cm^2 (> 100 PeV)	

3 IceCube-Gen2 Design Overview

The IceCube-Gen2 facility has to meet several performance requirements, outlined in Section 2.5, to accomplish its science goals discussed in Section 2. We describe a reference design that meets these requirements in Section 3.1. We also discuss the physical and practical considerations that have led to the design. All detector sensitivities used to illustrate the science capabilities of IceCube-Gen2 in Section 2 are based on this design. Section 3.2 summarizes the design of the individual detectors and stations in the optical, radio and surface arrays, as well as ongoing R&D efforts. In Section 3.3 we discuss basic performance indicators such as effective area / volume, angular and energy resolution, and how they translate into sensitivities to point sources.

3.1 Design considerations

In the following, we review the most important factors that influence the sensitivity of a large-volume optical-Cherenkov and a radio-based neutrino detector. First, we consider how the constraints that determined the final design of IceCube can be overcome to create a more sensitive facility at comparable cost. Second, we describe the design considerations for the large-volume radio array and developments that inform the design. Finally we review important performance characteristics of the detector facility.

3.1.1 Optical array

Charged-current interactions of electron and tau neutrinos, as well as neutral-current interactions of all flavors of neutrinos produce secondary particles that either deposit all their energy over short distances (electromagnetic or hadronic showers) or decay quickly (tau leptons of low energies). Compared to the average distance between sensors, the Cherenkov light emission region will appear point-like. The rate of events that can be detected is proportional to the instrumented volume of the detection. Tau neutrinos at higher energies produce a double-bang signature, where the interaction and decay vertex — separated on average by (E_τ / 1 PeV) $\times$ 50 m — can potentially be resolved. With a larger instrumented volume, the number of contained double-bang events will increase accordingly at energies $\gg$1 PeV. For IceCube, the separation distance starts to approach the geometrical dimensions of the array at these energies, increasing the likelihood that one of the two vertices lies outside of the instrumented volume.

When a muon neutrino undergoes a charged-current interaction, it produces a muon that can be detected far from the interaction vertex. For example, a 10 PeV (100 TeV) muon will travel on average 17 km (6.3 km) before its energy drops below 10 TeV. This makes the active volume for muon neutrino detection significantly larger than the instrumented volume, and the observable muon-neutrino rate proportional to the projected geometric area of the detector (e.g., the cross-section of the detector for a beam of muons). Muon neutrino events can be separated from the background of penetrating atmospheric muons by direction and energy, and - in the case of astrophysical neutrinos from transients - also by timing. In case of down-going neutrino events with their vertex inside the detector, one can further use the outer layers of the optical array,

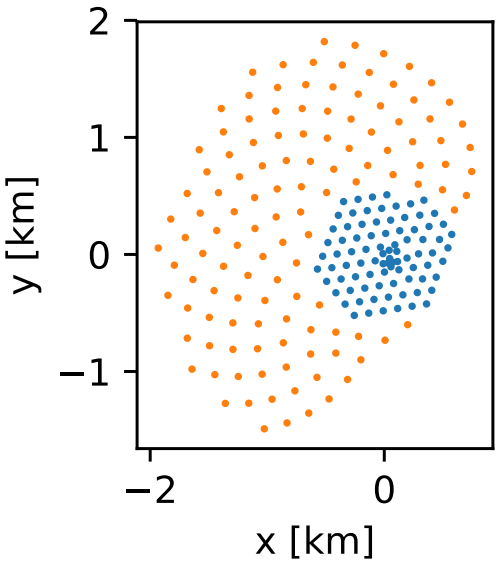

Figure 33: The reference detector string layout (sunflower geometry) has a uniform string spacing of ~ 240 m, with an instrumented volume of 7.9 km^3.

or a CR surface array with sufficiently low threshold, as a veto against atmospheric neutrinos [499, 500].

Geometry considerations: We can increase the neutrino event rate compared to IceCube by expanding the detector. One way to do this is to deploy longer strings. While the strong scattering of light in the South Pole ice at shallow depths is prohibitive for the detection and reconstruction of neutrino interactions, in-situ measurements [501] suggest that the 100 m of ice above and 250 m below the IceCube instrumented volume have adequate optical properties to allow neutrino detection. Instrumenting those would lead to a 35% increase in the geometric area for horizontal track events. The same gain is obtained for the contained volume for cascade events.

Significantly larger gains in effective area and volume are potentially obtained by increasing the string spacing. However, it needs to be ensured that this does not hamper the detector's ability to achieve its scientific goals. For IceCube one of the requirements was that geometry and timing calibration could be done with flashers, a set of LEDs in the upper hemisphere of each DOM that can produce short light pulses. This requirement, along with the requirement to have adequate sensitivity for muons of TeV energy, favored a string spacing of 125 m. However, the ice properties of IceCube, especially in the deep region are significantly better than what was assumed previously. Newer studies performed within the IceCube collaboration support that calibration by flashers can also be performed for a string spacing of 240 m, at least for next-neighbor strings, when using brighter LEDs. In addition, new calibration strategies have become available, including using CR muons [502], acoustic calibration modules [503] and camera systems [504] to calibrate the detector geometry and orientation of the sensors in the boreholes. Finally, the reference geometry for the optical array, shown in Figure 57, results in an energy threshold for through-going muons of ~ 2 TeV. This suppresses the atmospheric contribution that vastly dominates the neutrino flux below few TeV at a

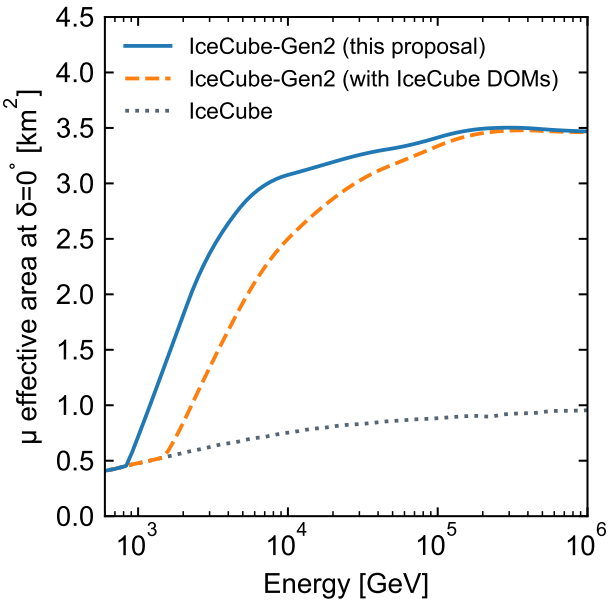

Figure 34: Effective area of the optical array for the detection of muons entering horizontally into the array (declination δ=0°, only events selected for analysis). The reference design is compared to IceCube and a detector design with IceCube high-QE DOMs instead of the new optical sensors developed for Gen2. The factor 3 higher photon detection yield of the Gen2-DOMs improves the effective area in the 1 TeV – 100 TeV energy range significantly, and is particularly important for the detection of soft sources.

negligible cost in sensitivity to the astrophysical flux since the brighter events at higher energies can be reconstructed well even with the larger string spacing.

Typical absorption lengths at a wavelength of ~400 nm are between 50 m and 200 m in the upper half of the current detector, and exceed 200 m in the lower half. Although the optical properties vary with the layered structure of the ice, the average absorption and scattering lengths dictate how far the strings of sensors can be spaced apart without impacting the response of the detector. Studies show that string spacings of ~200 m – 300 m allow us to maintain high efficiency for detecting astrophysical neutrinos and a roughly constant sensitivity to neutrino point sources, where the advantages of a larger volume for the 300 m vs 200 m spacing are offset by a higher energy threshold and reduced directional resolution [505]. Therefore, a string spacing of 240 m is chosen for the reference design, which allows an additional verification of the performance of IceCube-Gen2 with real data, analyzing the light recorded on one out of every four IceCube strings.

Reference design: The reference design for the optical component encompasses 120 new strings that are added to the existing IceCube strings with an average horizontal spacing of 240 m as shown in Figure 12 (second panel from left). Each string hosts 80 modules, totaling 9600 new modules, between 1344 m and 2689 m below the surface, corresponding to the optical array height of 1345 m. Vertical spacing between modules amounts to 17 m, resulting in an instrumented geometric volume of 7.9 km^3. Each module on the string will collect nearly 3 (4) times as many photons as a current IceCube DOM with high-QE (standard-QE) photocathode, using an optical sensor design with

multiple PMTs. This design is derived from the optical modules developed for the IceCube Upgrade, and will be further discussed in Part II of this document. The increased photon collection efficiency leads to a higher muon detection efficiency at energies of few TeV, improving the sensitivity significantly [506], in particular for sources with a soft spectrum and/or a spectral cutoff. This performance increase is illustrated in Figure 34, which compares the muon effective area as a function of energy for IceCube, the reference design of IceCube-Gen2, and a detector with 240 m string spacing, but equipped with IceCube (high-QE) DOMs.

Surface veto: Down-going $\gtrsim$PeV neutrinos can be identified as starting events. But it is also possible to use a surface veto to separate astrophysical neutrinos from background events. A surface veto with air shower detectors eliminates both, penetrating muons and down-going atmospheric neutrinos, as the latter are part of an air shower [499, 500] as well. Downg-going events identified using a surface veto have a very high astrophysical purity. Studies with IceCube and its surface component IceTop [507] suggest that above an energy of 200 TeV to 300 TeV, background can be suppressed to a level lower than the astrophysical flux observed with IceCube, albeit only within the small aperture of 0.26 km^2 sr, covering about 5% of the sky, where the footprints of the detectors overlap. With a surface array covering the footprint of the IceCube-Gen2 optical array, the acceptance for coincident events that can be vetoed increases to ~10 km^2 sr, 40 times higher than with the current surface array. The field of view would correspond to at least 20% of the sky. More details about the surface array and a typical surface veto station to be deployed at the top of each IceCube-Gen2 string are presented in Section 3.2.3.

3.1.2 Radio array

Radio emission is generated in ice by particle showers through the *Askaryan effect* [508]. The electromagnetic component of the shower evolves over time as additional electrons are up-scattered from the ice mostly through the Compton effect and positrons are depleted by in-flight annihilation. This leads to a relativistically moving time-varying negative charge excess in the shower front. As the negative charge excess travels at highly relativistic speeds through the medium, faster than the speed of light or a radio signal, it forms a characteristic coherent emission at a characteristic angle or Cherenkov angle. The emitted frequency range is governed by the shower geometry and the spectrum typically shows the strongest contribution between 100 MHz and 1 GHz [509]. In the time-domain, the emission corresponds to a broad-band nanosecond-scale radio pulse, which has been observed both in accelerator experiments [510–512] and in air showers [513–515].

The fact that radio emission is generated by both purely electromagnetic showers and the electromagnetic component of hadronic showers means that a radio detector is sensitive to all flavors, albeit with different sensitivities. Hadronic showers initiated by all neutrino flavors are detected with the same efficiency. Purely electromagnetic showers, ν_e-induced, are detected with similar efficiency as hadronic showers at energies below EeV. However, due to the LPM-effect [516, 517] the efficiency decreases at higher energies. The LPM-effect describes the reduction of the bremsstrahlung and

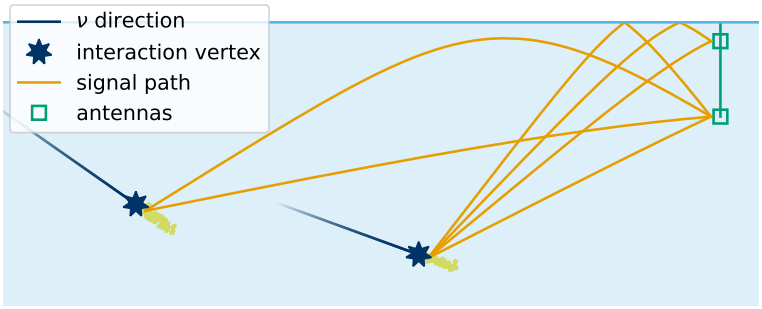

Figure 35: Schematic depiction of the signal trajectories reaching a radio detector from a neutrino vertex. Shown are allowed direct, refracted and reflected trajectories. This schematic assumes an exponentially increasing index of refraction with depth and depicts the effect of the so-called *shadow zones*, in which signals do not propagate and thus do not reach shallow detectors for certain geometries. This schematic also illustrates why the effective volume scales with detector depths.

pair production cross sections at high energies, which leads to large shower-to-shower fluctuations [518], as well as stark differences in shower length [519]. This generally suppresses the high frequency emission and reduces the detection efficiency for purely electromagnetic showers. Given a suitable geometry a radio detector will detect both showers following the interaction of a ν_τ and the τ decay, as well as stochastic energy losses of high-energy τ's or μ's [520]. Taking into account secondary interactions, the radio detection method exhibits roughly equal effective volumes for all three neutrino flavors at the highest energies [521]. The peculiarities imprinted in the radio emission by LPM showers and high-multiplicity energy-losses of secondaries are likely to provide flavor sensitivity [522, 523].

For the same vertex distance, the signal amplitude scales linearly with the shower energy, giving radio detection an energy threshold above the thermal noise floor of a couple of PeV per shower for close vertices, depending in detail on trigger and antenna gain. The attenuation length of radio waves in ice depends on depth and temperature. At the South Pole and other locations with cold ice it is roughly of the order of one kilometer [524], meaning that showers can be viewed from afar. It should be noted that the index-of-refraction profile of naturally occurring ice-sheets follows a typical behavior [525]. Snow accumulating at the surface is compacted and recrystallizes into the so-called *firn* where the density increases with depth. This results in an exponentially increasing index of refraction (n) from roughly 1.30 at the surface to an asymptote of 1.78 at the transition to the ice, reaching 1.77 at a depth of roughly 150 m at South Pole [526, 527]. Due to the exponential profile, the radio signals do not travel in straight lines in the firn, but bend downwards, as shown in Figure 35. This simple model of the firn structure results in zones close to the surface from which signals cannot reach the antennas, as no ray-tracing solution exists, so-called *shadow zones* [524, 525, 528]. Also, the downward refraction of upward moving signals and reflection at the firn-air surface boundary increase the effective volume available to a detector at a certain depth [148, 529].

In order to reconstruct the energy of a shower, resolving the vertex location is key [530, 531]. The amplitude of the radio signal drops as $1/r$ with distance to the vertex. The signal at the detector is furthermore reduced by the attenuation over the path traversed from vertex to detector. Several algorithms can be employed to reconstruct the vertex location. Timing in the wave front can be used to determine the vertex as the origin of a spherical wave. This will be easier the closer the vertex is to the detector. Alternatively, both the direct emission to the receiver and the one refracted or reflected downwards could be measured. The amplitude ratio and the time difference of the two pulses uniquely tag the distance of the vertex [529, 530].

In order to reconstruct the arrival direction of the neutrino, one needs both the arrival direction of the signal at the antenna and information regarding where on the Cherenkov cone the signal was detected. The signal arrival direction can be obtained from timing, given enough antennas, sub-nanosecond time resolution, and a suitable distance between antennas. Using this information alone, the neutrino arrival direction can only be limited to a ring-like region on the sky, a projection of the Cherenkov cone, and limited by the field of view of the detector. However, in addition to amplitude, the electric field also contains information about the polarization and frequency spectrum. Using the fact that the polarization always points towards the shower axis and that the frequency content is determined by the viewing angle relative to the Cherenkov angle, one can determine the arrival direction of the neutrino to within degree-scale precision, given a suitable resolution on both parameters [532–536].

Station geometry considerations: As the radio signal travels long distances in the ice, most prototype radio detectors have chosen a compact station design. A station typically consists of a cluster of antennas and acts independently in both triggering and reconstructing the shower. For an array, radio stations are placed far apart from each other so that they have almost independent effective volumes thereby maximizing the total effective volume. This is different from the approach in the optical detector.

When optimizing station design, various considerations play a role: one would like to use antennas with the highest gain to optimize sensitivity for low-amplitude signals. A higher antenna gain lowers the energy threshold of a given detector and increases the effective volume, as signals of the same strength can be detected at larger distances. Also, one desires the best polarization sensitivity and the broadest frequency response to optimize the input for the arrival direction reconstruction, as discussed above. Such antennas are typically too large to be deployed in deep holes obtainable by drilling, in particular those sensitive to the horizontal component of the electric field vector. One can therefore either stay close to the surface and remain flexible with respect to the antenna configuration, or deploy deeper and accept the limitations given by the borehole geometry. In the latter case, the lack in antenna gain can partly be overcome by phased-array techniques that add signals from several antennas, thereby mimicking an antenna with higher gain [537–539]. However, constructing antennas sensitive to the horizontal signal component remains challenging for borehole-restricted geometries.

It has been argued that air shower signals may create a background for radio detectors of neutrinos, either by catastrophic energy losses from muons in ice [521], refraction of the in-air radio signal into the ice and consecutive reflections off internal-reflection layers [540], or from not fully developed air showers [541]. As such signals are due to

the same emission mechanisms; they are in principle indistinguishable from neutrino-induced signals when detected with a single antenna. Adding antennas sensitive to signals arriving from above at the surface provides every station with a self-veto. Using antennas with a strong sensitivity to horizontally polarized signals, log-periodic dipoles, allows for an excellent reconstruction of the air shower properties, which improves the veto. Furthermore, the footprints of radio signals from air showers are much wider than those from neutrinos (owing to different index-of-refraction profiles and virtually no attenuation in air) and are therefore often detected in multiple stations, which improves the detection efficiency. The signals from air showers also provide detector calibration opportunities and possibly CR science [542, 543].

Antenna depth considerations: At the South Pole—with its large ice sheet with long attenuation length—the deeper the antennas of a station, the larger its effective neutrino volume and sky coverage, as more signal trajectories will be able to reach the detector. For example, at 10^{17} eV a factor of two, and at 10^{18} eV a factor of four can be gained in effective volume when moving from the surface to a depth of 150 m [544]. The respective effective volume is mostly gained away from the horizon, as discussed in Section 3.3. This effect can be understood in the context of ray bending in the changing index of refraction in the firn, as shown in Figure 35, which allows more trajectories for deeper antennas. The index of refraction scales roughly exponentially in the firn and reaches the bulk value at roughly 150 m at South Pole. For radio propagation only macroscopic structures such as over- or under-density layers are relevant, which are found throughout the ice. The event quality will improve with the number of antennas detecting a signal. Given the restricted spatial extent of the Cherenkov ring, the optimal antenna spacing per station is a balance between sparseness to maximize effective volume, veto-capabilities and lever-arm for reconstruction – and compactness to maximize the number of antennas per event with signal above threshold.

Additional considerations are given by the logistics requirements of drilling and a potential closure of the dry boreholes that are currently planned for radio installation; that closure rate depends on the original width and depth of the hole. Overall, in comparison to the optical array, there is little to be gained from great depths and the radio array can always remain comparatively close to the surface.

So far, three experimental approaches have been explored: near-surface shallow stations, deep stations and hybrid stations. Shallow and hybrid stations (similar to those shown in Figure 36) deliver a similar performance in terms of effective volume per unit cost. However, they are, as elaborated above, subject to different systematic uncertainties and risks, which are important considerations for a discovery instrument and a project of the size of IceCube-Gen2. The reference design will therefore includes both types of stations, *hybrid stations* with antennas down to 150 m and *shallow stations*, complementing each other in sensitivity, background rejection and systematic uncertainties.

Station spacing considerations: To maximize the total effective volume, stations should be placed as far apart from each other as needed to no longer have overlapping effective volumes. As shown in [148], the minimal distance is a function of energy and may be as large as 2 km, depending on the depth of the station. However, large distances place a heavier burden on deployment, power infrastructure, and

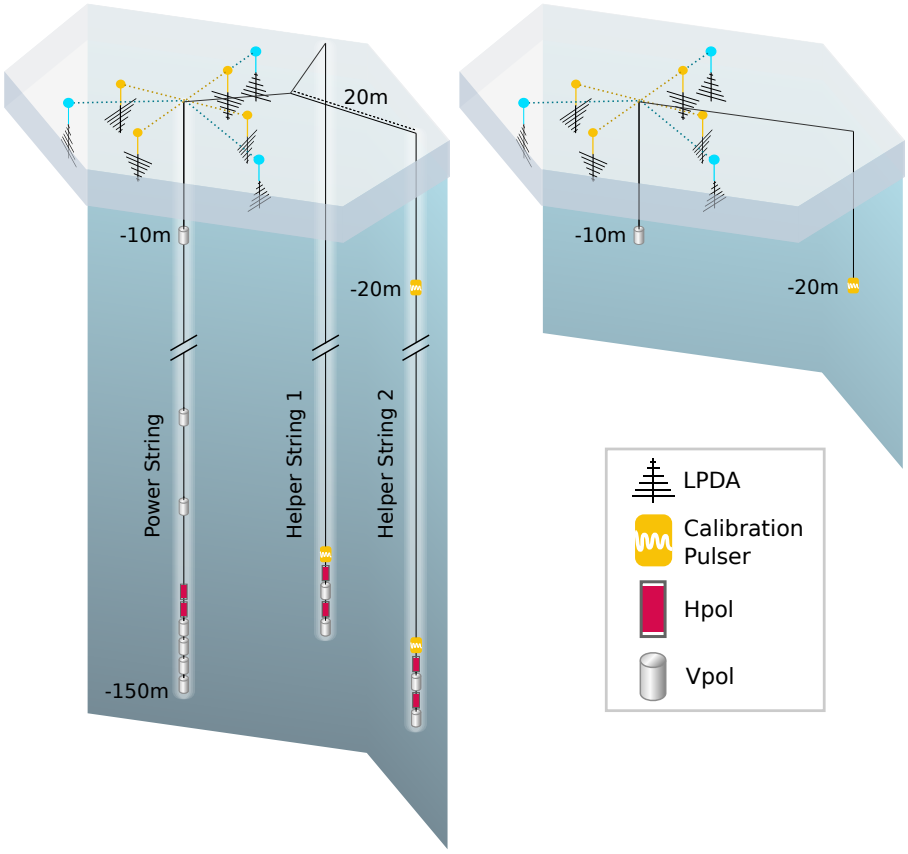

Figure 36: Station layout of the reference design. The shallow stations (right) consist of seven Log-Periodic Dipole Antennas (LPDAs), four downward-facing and three upward-facing, and one dipole antenna at a depth of 20 m. The hybrid stations (left) contain the same shallow component, which is complemented with three strings to the depth of 150 m. One string hosts the phased array trigger using four dipole antennas, sensitive to the vertical signal component (Vpol), as well as additional Vpol antennas to reconstruct the vertex position and slot antennas (Hpol), which are sensitive to the horizontal signal component. Vpol and Hpol antennas on the two other strings allow the reconstruction of the arrival direction and the electric field. Two strings host calibration pulsers to triangulate and calibrate the antenna positions to cm-precision.

operations logistics and coincidences between stations will be helpful in improving confidence in reconstruction methods. A golden sample of events seen in multiple stations will provide extremely high-quality reconstruction and will allow cross calibration, ice calibration, and estimation of systematic uncertainties. For the same spacing, the coincidence fraction increases with energy and station depth. Thus, a target value for the coincidence fraction determines the optimal spacing for a station type, which is larger for hybrid stations than for shallow stations.

The reference design used throughout this document includes shallow-only and hybrid (shallow/deep) stations with antennas down to a depth of 150 m. The stations are deployed on a square grid with a distance of 1.75 km between the hybrid stations and with regularly interspersed shallow-only stations, resulting in a distance of 1.24 km between the nearest-neighbor shallow stations (see Figure 12). The shallow component is identical for both station types. The reference design was selected from a variety of

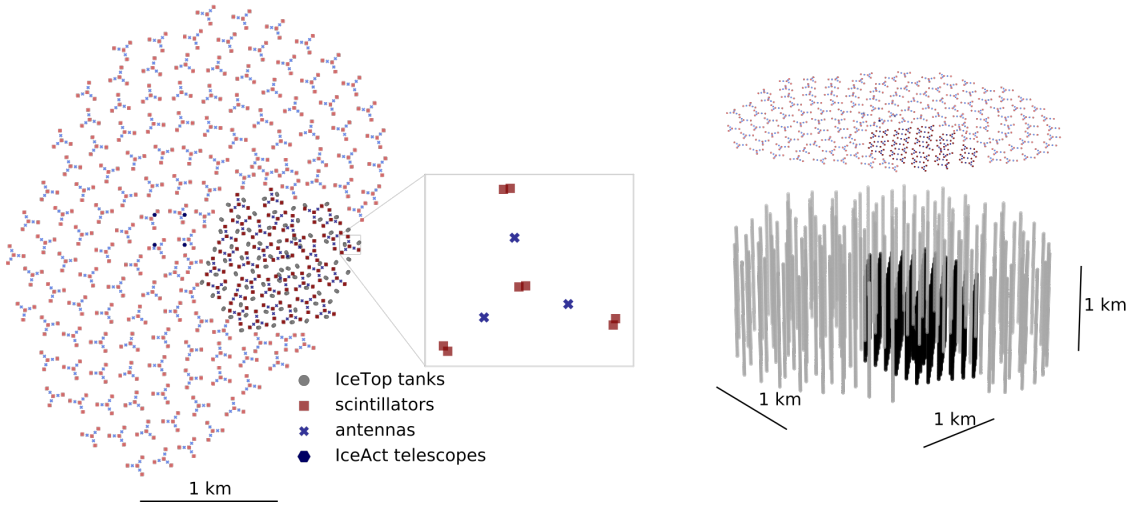

Figure 37: Layout of the surface array reference design. The surface stations on top of each IceCube-Gen2 string encompass 8 elevated scintillation panels (red squares) and 3 elevated radio antennas (blue crosses) per station. Four IceAct stations (purple hexagons) will be deployed in the center of IceCube-Gen2. The existing IceTop tanks are indicated by gray circles.

configurations with different grid patterns and station-type ratios, all with similar sensitivities and logistics requirements.

3.1.3 Surface array

IceCube-Gen2 will be complemented by a surface array above the optical array. Building on the plans for an enhancement of IceTop [507], the surface array will combine elevated scintillation detectors and elevated radio antennas [545]. A prototype station of that hybrid design was installed at the South Pole in 2020 and successfully and regularly measures cosmic-ray air showers [546, 547]. Finally, the planning of the IceCube-Gen2 surface array was informed by a review conducted in May 2021, which provided a strong recommendation to proceed with the design of a hybrid array.

IceAct telescopes will extend the high-accuracy CR measurements to energies below the threshold of the hybrid stations. They are small (55 cm diameter), lightweight telescopes for CR air showers featuring a Fresnel lens and a camera with 61 silicon photomultiplier pixels. Like the hybrid stations, IceAct prototype detectors have successfully operated at the South Pole for several years [548].

Geometry considerations: The surface array is designed to minimize the logistics requirements. It therefore follows the geometry of the optical array, with one surface station per string of IceCube-Gen2 (Figure 37). Additionally, the existing optical array of IceCube will be covered with the same type of surface stations to mitigate the reduced performance of IceTop due to snow that accumulated over the years. A few additional stations will be added for cross-calibration with the radio array and to avoid gaps to IceTop because a smooth coverage is important to achieve the required threshold of 0.5 PeV regardless of the impact point of the cosmic rays.

Table 4: Key properties of the DOM-16 and DOM-18 optical sensors designed for IceCube-Gen2 in comparison to the IceCube Upgrade sensors they inherit from. The effective photon sensitive area, at a representative wavelength of Cherenkov photons after >50 m of propagation in ice, is estimated by a Monte Carlo simulation neglecting the inhomogeneity of the PMT sensitivity over the cathode surface.

Sensor	DOM-16	DOM-18	mDOM	D-Egg
Number of PMTs	16	18	24	2
PMT diameter [inch]	4	4	3.15	8
Module diameter [cm]	31.3	31.8	36	30
Module height [cm]	44.4	54.0	41.1	53.4
Effective photon sensitive area (λ=400 nm) [cm^2]	108	122	100	88

Reference design: The IceCube-Gen2 surface array will consist of hybrid stations with 8 elevated scintillation panels and 3 elevated radio antennas each, sharing one local DAQ in the center of the station. Using the *FieldHub* (see Part II of this document), the DAQ will be connected to the same power, timing and communication infrastructure as the corresponding string of the optical array. For the capability to reconstruct the direction of those showers triggering only a single station, at least three separated detector positions are required per station forming a triangle. With reasonably sized scintillators of 1.5 m^2 sensitive area each, a fill factor of about 2.5×10^{-4} needs to be achieved over the footprint of the optical array to meet the threshold requirement. An additional constraint follows from the need to minimize trenching and is met by exploiting (to the extent possible) trenches prepared for the optical array. An overview of this reference design is shown in Figure 37.

While the radio antennas can provide the measurement accuracy needed at energies above a few tens of PeV, an add-on is needed to provide calorimetric measurements of the electromagnetic shower development at lower energies, too. For this purpose, stations of seven IceAct telescopes each will be installed at four strings in the center of the array. Because of the steeply falling cosmic-ray energy spectrum, the flux is orders of magnitude higher at lower energies. Thus, despite covering only a small part of the array and despite the limited duty cycle, these four stations will be sufficient for the purposes of cross-calibration and measurement of the mass composition in the PeV energy range.

3.2 Detector design

The design of IceCube-Gen2 builds on the experience of constructing and operating the IceCube detector, the sensor R&D and construction effort for the IceCube Upgrade, as well as different radio pilot arrays. It profits from a range of recent technical advances in sensor development. In the following we describe the conceptual design of the sensors, surface detectors, as well as radio components for the reference arrays.

3.2.1 The optical sensor

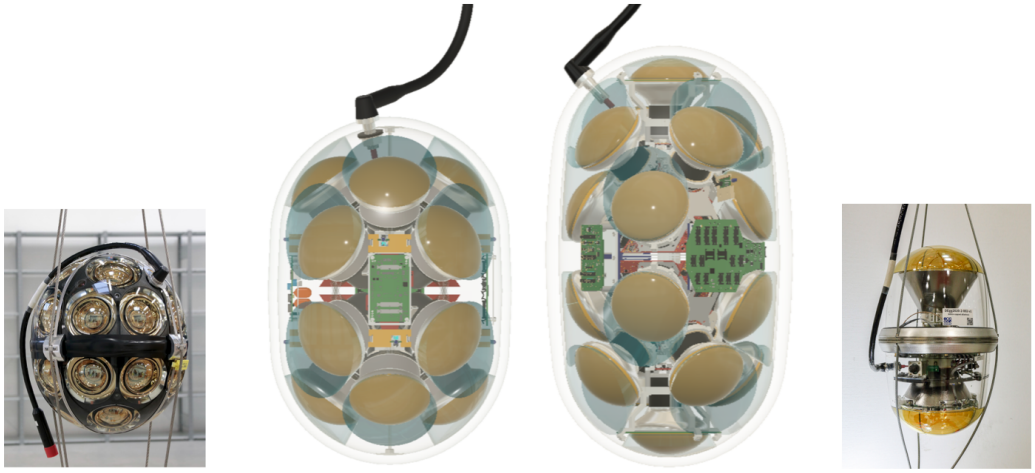

Figure 38: The DOM-16 (middle left) and DOM-18 (middle right) designs for the IceCube-Gen2 optical sensor, framed by their predecessors, the IceCube Upgrade sensors: mDOM (left) and D-Egg (right).

Besides its rich physics program, the IceCube Upgrade project also provides an opportunity to advance the optical sensor technology for the IceCube-Gen2 observatory. Two complementary sensor types have been developed for the IceCube-Upgrade, named mDOM and D-Egg. In contrast to IceCube's single large 10" PMT, the mDOM [549, 550] houses 24 PMT's with a diameter of 3.15" in a 36 cm diameter pressure vessel. The D-Egg [551, 552] houses two 8" PMTs in an elongated pressure housing of 30 cm in diameter. Both sensor types will be deployed for the IceCube Upgrade. Out of 693 sensors deployed along the 7 new strings, 402 will be mDOMs and 277 will be D-Eggs.

The optical sensor module proposed for IceCube-Gen2 is derived from the IceCube Upgrade sensors, optimizing the design for costs, logistics impact and performance. Figure 38 shows renderings of the two variants of the Gen2 sensor (DOM-16 and DOM-18) that are currently developed, together with their predecessors, the mDOM and D-Egg. For a large-scale project such as IceCube-Gen2, it is advantageous to have such alternative designs in the current conceptual phase, avoiding the dependence on single vendors for the most critical components of the optical sensors. However, it is planned to select the most cost effective solution/design that fulfills the science requirements in a later project phase, and deploy identical modules throughout IceCube-Gen2. Both, DOM-16 and DOM-18, inherit the elongated pressure housing design from the D-Egg, with diameters of 313 mm (DOM-16) and 318 mm (DOM-18), respectively. The reduction in diameter in conmparison to the mDOM allows to drill smaller boreholes, saving about 15% fuel and drill time. Instead of 24 of the 3.15" PMTs of the mDOM, the DOM-16 and DOM-18 sensors will utilize 16 and 18 of the 4" PMTs, respectively, that are dedicated designs of the manufacturing companies for this application. This approach combines the advantages of the mDOM, the directional information obtained about the arriving photons from the individual PMTs, and the economy-of-scale benefits of many small-size PMTs over fewer large-sized ones, with a lower power consumption (4W per sensor) and data rate (150 kbps). In combination, the low power and the moderate data rate permit the usage of less complex cables for the communication to the sur-

Figure 39: Individual photo-detection assembly of IceCube-Gen2.The electronics attached to the base of a 4" PMT provide the high-voltage chain for the PMT dynodes, as well as readout, amplification and digitization of the PMT signals.

face, including only 7 wire quads (IceCube: 20 wire quads) even though the individual strings host 80 sensors (IceCube: 60 sensors).

Both variants, DOM-16 and DOM-18 share many common elements. Each individual photo-detection assembly consists of a 4" PMT and a circuit board attached to its base, which combines HV generation, readout and digitization of the PMT signals (see Figure 39). Both designs can work with 4" PMTs of two different vendors. Also the electronics mainboard, providing power and communication for the modules is identical for both variants. The DOM-16 module houses 16 PMTs in a 11 kg pressure vessel of 44.4 cm height, while the DOM-18 module houses 18 PMTs in a 17 kg pressure vessel of 54 cm height (manufactured by a different company). The two extra PMTs in this design point up- and downward. Due to the additional PMTs, the DOM-18 has a 12% higher photon collection efficiency than the DOM-16, albeit at a higher per-module cost. Prototype modules of both variants are scheduled for deployment with the IceCube Upgrade in 2025/2026.

Electronic components are also shared between both variants. The signal from each PMT is read out by circuitry attached to its base. The signal is read in parallel at the anode and at the 8th dynode of the PMT, individually amplified and, after shaping, digitized by a dual channel 60 MHz ADC. The parallel readout enables a large dynamic range from 1 photo-electron (p.e.) to $>10^4$ p.e. that reflects the wide energy range the optical array is designed for (about 10 TeV to above 10 PeV). The digitized waveforms are collected and buffered by flash memory on the sensor mainboard. Summary data or full waveforms are sent to the surface on request from the trigger algorithm. On the surface – on top of each deployed string – the *FieldHub* feeds the data stream into optical fibers connected to the IceCube Laboratory (ICL) which houses IceCube on-site computing. The *FieldHub* was developed for the IceCube Upgrade. Besides relaying the data, it also provides power and timing calibration to strings and surface array detectors (Section 3.2.3).

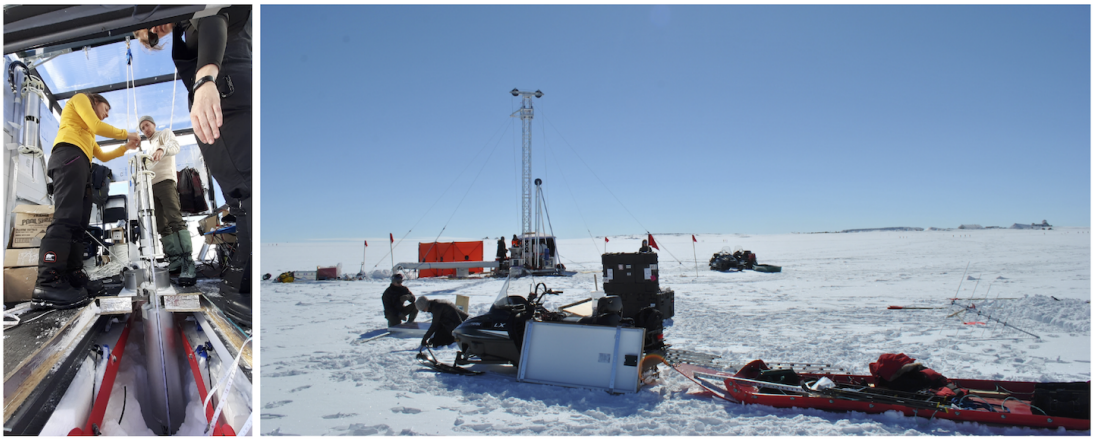

Figure 40: Deployment of RNO-G at Summit Station in 2021. Left: String deployment showing two types of antennas being lowered into the ice. Right: From front to back: Installation of solar panels and log-periodic dipole antennas, the BigRAID drill, and Summit Station.

3.2.2 Radio detectors

The reference design for the radio component of IceCube-Gen2 is informed by both simulations [148] and the experience gained from operating ARA, ARIANNA, and RNO-G [350, 553–556]. It relies on a combination of hybrid and shallow stations (see Figure 36).

The design of the shallow component builds on subsurface log-periodic dipole antennas (LPDAs), both upward-facing (for air shower detection) and downward-facing (for neutrino detection). The LPDAs offer high gain over a wide frequency range and excellent sensitivity to horizontally polarized signals. LPDAs can be custom-made for ease of deployment and installation (as with TAROGE [557]) or obtained commercially (as for ARIANNA and RNO-G). Two pairs of orthogonally placed LPDAs allow a reconstruction of the electric field vector, including polarization. The LPDAs are complemented by a shallow cylindrical dipole antenna at a depth of 10 m that aids in the separation of up- and down-going signatures and improve the reconstruction capabilities [530].

A hybrid station consists of a shallow station plus antennas deployed along three strings down to a depth of 150 m. The core of the hybrid station is a phased array of four closely packed cylindrical dipole antennas (Vpol) that provides the main trigger and is essential for the sensitivity of the station. The phased array technology will be the same as used for RNO-G and in PUEO [558]. It is complemented by additional Vpol antennas on the same string, as well as on two additional strings for reconstruction purposes. For polarization reconstruction, slot antennas (Hpol) are added to the strings, resulting in a total of 24 receiver channels.

In order to reach the overall sensitivity goal, the reference design assumes that 361 stations are deployed at the South Pole, with 164 hybrid and 197 shallow-only stations on a square grid with distances of 1.75 km and 1.24 km, respectively. About 10% of the neutrino events will be detected in coincidence with at least two stations, marking a sample of events with the best reconstructed properties.

Several radio instruments have been built at South Pole, notably the Askaryan Radio Array (ARA). ARA employs a phased-array and has instrumented strings with two different types of antennas down to a depth of 200 meters. The reference design for IceCube-Gen2 foresees deep stations similar to those of ARA. It also foresees shallow antennas, both directly above the deep stations and interspersed between them. These shallow LPDAs provide better polarization sensitivity than the down-hole antennas, thus aiding in event reconstruction. They also ensure a self-vetoing capability of the array against air showers, a concept piloted in the ARIANNA project at Moore's Bay and verified with two stations at the South Pole. In addition to the veto capabilities, these LPDAs provide better polarization sensitivity than down-hole antennas, which will aid the reconstruction.

As compared to the optical detection technique, the radio detection is not as mature. At the relevant energies, no neutrino candidates have yet been detected, and the expected performance has to be extrapolated from previous but different experiments and dedicated simulations. Additional R&D and piloting will happen before the construction of IceCube-Gen2. The deployment of the Radio Neutrino Observatory (RNO-G) has started in 2021 at Summit station in Greenland. The RNO-G stations are similar to the hybrid stations described above. The design of the down-hole antennas for IceCube-Gen2 will be heavily based on experience with RNO-G, with only minor modifications foreseen, in particular for the Hpol antennas.

The station electronics for both kinds of stations – hybrid and shallow – will provide similar functionality and, in most instances, identical components and software. The main DAQ board will be modularized to accommodate 8 channel, as well as 24 channel-stations. The stations will share the same power and communications infrastructure, integrated with the one used for the optical array. The amplifier design of RNO-G has reached a mature state suitable for IceCube-Gen2, with reliable performance at less than 0.5 W per channel.

Deployment opportunities at Summit Station (see Figure 40) reduces the burden on South Pole station logistics and will allow for a fast turnaround in instrument testing, given the easier accessibility. While characteristics of the site influence the science performance and certain specific choices for the instrument, technical challenges will be very similar, paving the way for the radio component of IceCube-Gen2. RNO-G and the radio array at the South Pole will be complementary in terms of their field-of-view, also offering a larger, combined effective volume for diffuse searches.

3.2.3 Surface detector stations

IceCube's surface array IceTop [507] has proved to be a very valuable component of IceCube at a modest cost of approximately 5% of the total investment. Figure 41 shows the layout of an enhanced IceTop station optimized for easy deployment and low maintenance. This is also the proposed design for an IceCube-Gen2 surface station [559, 560].

Each station consists of four pairs of scintillation panels and three SKALA type radio antennas [561, 562] attached to a common local DAQ. Both, the scintillators and the DAQ design have evolved over several years. With the current prototype station regularly

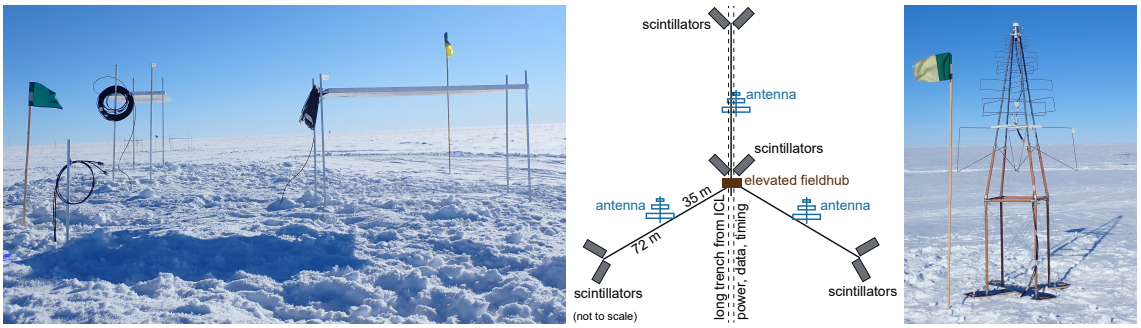

Figure 41: Photos and schematic of the prototype station of the surface array deployed in 2020. Both the scintillators and antennas are on elevated extendable mounts to avoid snow coverage.

detecting cosmic-ray air showers, the design has been successfully tested, pending some minor improvements to be incorporated in the final design (see Section 3.1.3). The radio antennas have been developed for the SKA-low array [563], the leading radio observatory of the coming decade. They feature a particularly low noise level of around $40\,\mathrm{K}$ and a smooth gain pattern with a broad sky coverage and a low backlobe which minimizes systematic uncertainties due to ground conditions, such as the snow level. Although not designed for polar conditions, extensive lab tests and the prototype stations have proven that the SKALA antennas are well suited for continuous operation at the South Pole. After more than two years of operation time until now, no excess snow accumulation has been observed on the ground below the prototype station or on the detectors themselves. Therefore, the prototype station constitutes the reference design for both, the enhancement of IceTop and the IceCube-Gen2 surface array.

3.3 Instrument performance

Section 2 discussed in detail the capabilities of the Icecube-Gen2 facility to address critical science questions in neutrino and multi-messenger astronomy. Here, the underlying instrument performance that enable the science is discussed. We describe the performance of the optical and radio component separately first and conclude with a discussion about the advantages of a combination of both techniques in a single location that goes beyond the sum of the individual parts. All performance studies are based on dedicated simulations and extrapolations of published results, combined in a dedicated framework [149].

3.3.1 Optical array

We characterize the performance of the reference design as shown in Figure 12 by studying simulation and IceCube experimental data. These studies focus on two neutrino detection channels: muons entering the instrumented volume from the outside and isolated cascades within the volume. To estimate the detector performance for throughgoing muons, an isotropic flux of muons entering the detector is simulated, using the standard IceCube simulation chain. IceCube-like sensors are assumed, however each simulated sensor features a 3(4) times larger PMT photocathode area than the actual IceCube high-QE (standard-QE) DOM (approximating the photon collection efficiency

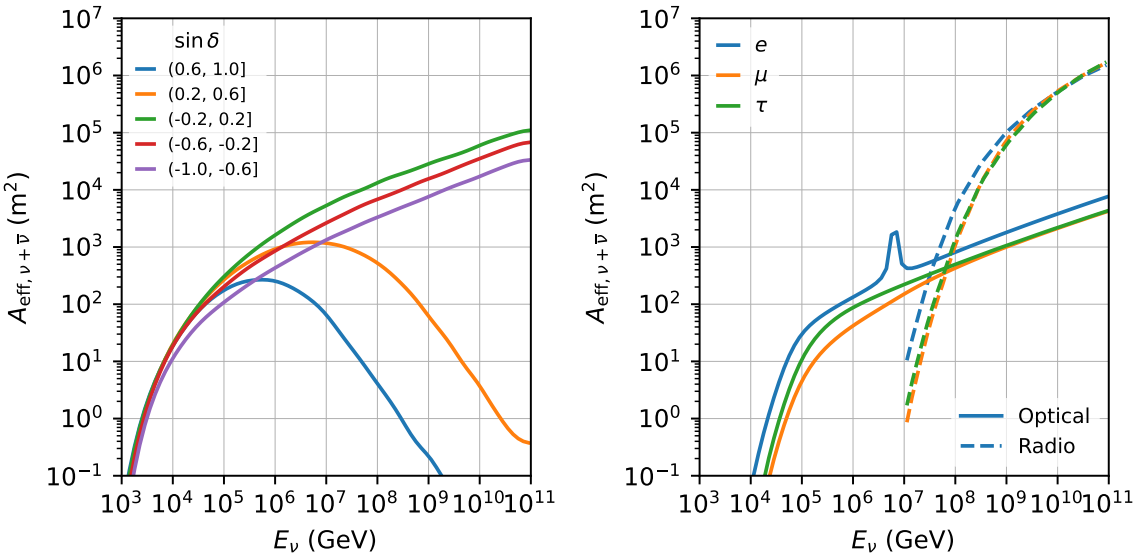

Figure 42: Performance characteristics of the reference design of IceCube-Gen2. Left: Effective area for the detection of tracks as a function of energy for different angular bands. Right: Effective area for the detection of shower-type events as a function of energy for each flavor of neutrinos. Effective areas of the optical and the radio array are shown separately.

of the IceCube-Gen2 baseline sensor). Each muon direction and energy are reconstructed using IceCube's reconstruction algorithms. We then apply a series of quality cuts to these simulated events to remove any whose direction cannot be reconstructed reliably. From the simulated data we derive the muon effective area as a function of energy and zenith angle (Figure 42), and the point spread function (PSF) as shown for the 240 m sunflower layout in Figure 43. These quality cuts are responsible for the difference between the effective and geometrical areas, as, e.g., corner-clipping tracks that cannot be well reconstructed are removed. Note that the PSF is scaled by a factor of 0.8 to account for reconstruction improvements related to pixelated sensors that are not included in the standard IceCube reconstruction chain, and have been studied separately [564].

We characterize the performance for cascades in a similar way. Instead of simulating a flux of incoming muons, though, we simulate single electromagnetic cascades distributed evenly throughout the instrumented volume, and reconstruct each cascade's position and energy. The quality cuts for cascades ensure that the position reconstruction is reliable, and thus that the associated energy estimate is as well. Figure 42 shows the effective areas for cascade detection in the IceCube-Gen2 optical array, and the contributions of individual neutrino flavors to this effective area. The energy resolution achieved in the reconstruction for both cascades and tracks is summarized in Table 7.

To fully characterize the sensitivity to neutrinos, we must also consider the background from penetrating atmospheric muons. IceCube has already demonstrated several successful strategies for removing this background [3, 17, 30, 565]. Here we focus on how to extrapolate these techniques to IceCube-Gen2, with emphasis on the resulting energy threshold. Entering muons from below the horizon are relatively simple to

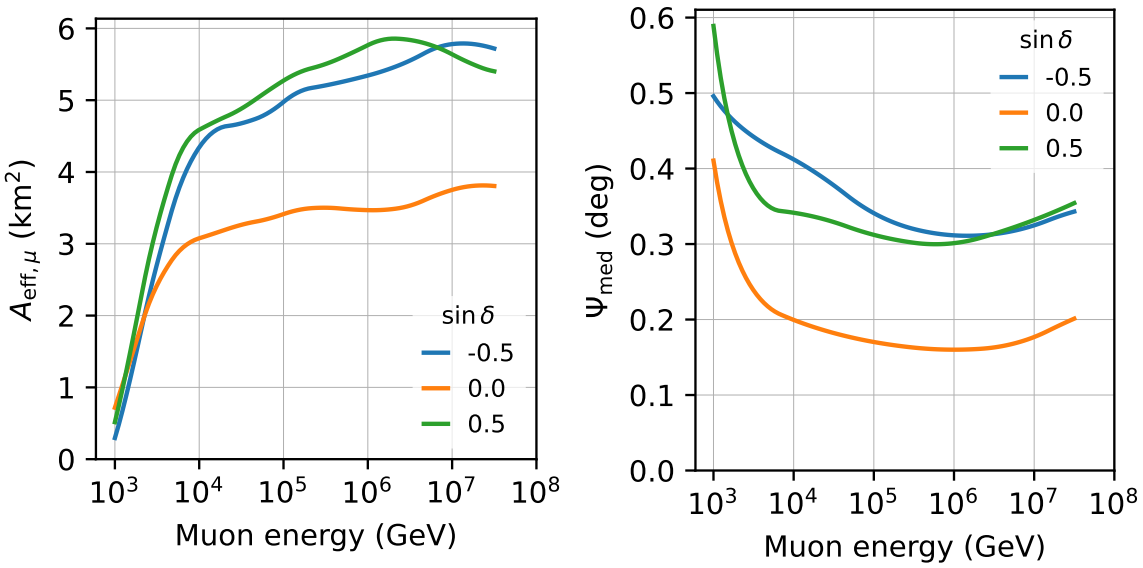

Figure 43: Muon reconstruction performance of the IceCube-Gen2 optical array with 240 m string spacing. *Left:* Effective area for single muons after quality cuts as a function of muon energy for different declination angles δ. *Right:* Median angular error of the directional reconstruction for muons as a function of energy, evaluated at the same angles.

separate from atmospheric muons. Correctly reconstructed up-going muons can only be neutrino-induced, and cuts on the angular reconstruction quality are sufficient to remove all atmospheric muons

Neutrino interactions inside the detector volume are slightly more difficult to isolate, requiring that the outer layer of the detector be used as a veto. We estimate the effective energy threshold of such a veto strategy using a variant of the technique used in [3], where the observation of Cherenkov light in the outer string layer of IceCube above a certain threshold leads to the rejection of the event. The results are shown in Figure 44. First, we identify penetrating atmospheric muon events that first trigger the outer layer of IceCube. We then apply the veto using only the inner detector, with three out of four strings removed to model a detector with twice the string spacing. Compared with a veto using all strings, the energy threshold increases by a factor of ~3. From this we conclude that a high-energy starting event selection in a detector with ~240 m string spacing will be fully efficient and have negligible penetrating muon background above a deposited energy of ~200 TeV, rather than 60 TeV as in IceCube. Figure 44 also shows the projected angular resolution for shower-type events with IceCube-Gen2. It is expected to be similar to the resolution currently achieved by IceCube at energies above few hundred TeV. Please note, that for this projection systematic uncertainties on the optical properties of the ice have been neglected, and the directional information on the photon arrival direction available from the individual PMTs in the IceCube-Gen2 DOMs has not been used.

Figure 42 summarizes the effective areas of the IceCube-Gen2 optical array for tracks and showers. For showers, which can be observed in both, the optical and radio arrays, the radio effective area is indicated as well. The instrument response functions for muon and shower-type events introduced in this section are the basis for the evalu-

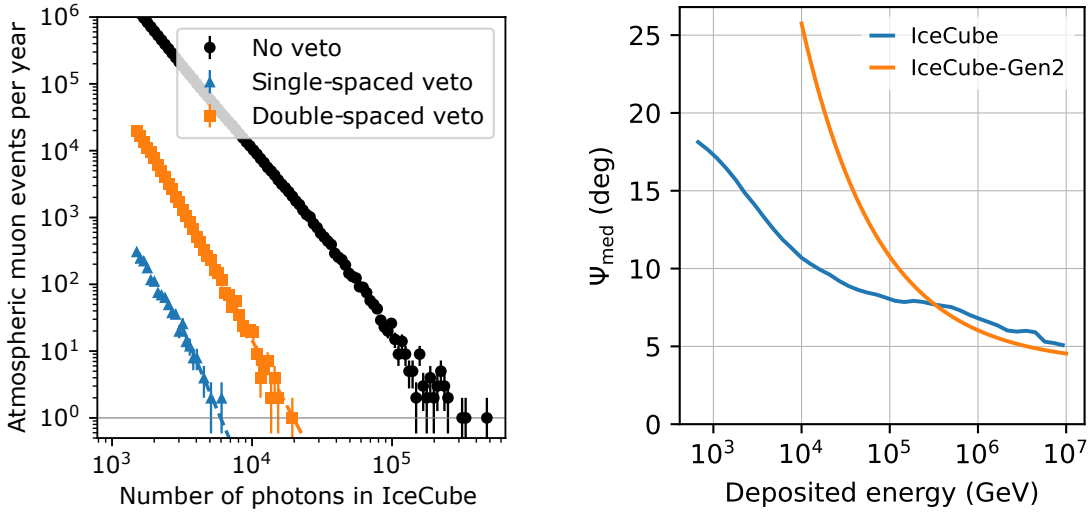

Figure 44: Background rejection performance and angular resolution for shower-type events in IceCube and the IceCube-Gen2 in-ice detector with 240 m string spacing. *Left:* Penetrating muon rejection capabilities of IceCube derived from experimental data and using the information from all strings (blue points) and only 25% of the strings (orange points) equivalent to a detector with ~ 240 m string spacing. The number of collected photons is a proxy for deposited energy. The wider string spacing implies a factor 3 higher energy threshold to ensure an equivalent rejection performance for atmospheric muons as for IceCube. *Right:* Median angular resolution for shower-type events achieved in IceCube and the projected resolution for IceCube-Gen2 as a function of deposited energy.

ation of the science potential of the IceCube-Gen2 observatory presented in Section 2. IceCube-Gen2's efficiency to identify tau neutrinos via their double-bang signature is estimated in two ways. One is with the help of a "sparse" IceCube dataset where only the information from every 4th string is used to model a detector with 240 m string spacing, similar to the procedure described in the last paragraph. In addition, the efficiency for tau identification is estimated from dedicated simulation datasets, produced in the same way as the ones described above to study the detector response to muons. Both efficiencies agree very well, and are included in the estimate of the flavor composition measurement performance discussed in Sections 2.2.6 and 2.4.3.

Table 5 summarizes the yearly event rates expected for track-like events from up-going atmospheric and astrophysical neutrinos in IceCube-Gen2 in comparison to IceCube. Table 6 compares event rates for astrophysical neutrinos of different event categories, shower-type events, double cascades, and tracks starting in the instrumented volume[§]. The event rates are presented for various thresholds in the energy that is deposited in the instrumented volume and assumes an astrophysical neutrino spectrum with a 1:1:1 flavor composition, following a power-law spectrum with an index of -2.5.

[§]To obtain the values in the tables the same set of selection criteria are applied to IceCube simulation data that are used throughout this report for characterizing the IceCube-Gen2 performance. This procedure yields directly comparable rates, however, published IceCube data analysis uses different and often more complex event selection strategies.

Table 5: Rate of upgoing tracks in the IceCube-Gen2 optical array [yr^{-1}]

	astrophysical-ν		atmospheric-ν	
Deposited energy	IceCube	IceCube-Gen2	IceCube	IceCube-Gen2
>1 TeV	1.2×10^2	4.0×10^2	2.9×10^5	3.4×10^5
>10 TeV	16	59	2.4×10^2	5.3×10^2
>100 TeV	1.4	3.8	0.67	0.99

Table 6: Rate of astrophysical neutrinos of various event categories (optical array only) [yr^{-1}]

	shower-type events		double cascades		starting tracks	
Deposited energy	IceCube	IC-Gen2	IceCube	IC-Gen2	IceCube	IC-Gen2
> 10 TeV	6.0	50	0.36	2.4	1.4	21
> 100 TeV	3.6	32	0.3	1.9	0.81	13

3.3.2 Radio array

Based on simulations [148] and experience from radio detectors such as ARA [553], ARIANNA [554], and RNO-G [556], we extrapolate the performance of the in-ice radio array of IceCube-Gen2. Simulations show that the reference stations will be sensitive to emission from neutrino interaction vertices at large distances (~ 5 km at 10 EeV), translating to large geometric volumes per station. As the signal amplitude scales with energy, the visible vertex distances are significantly larger at higher energies. Figure 42 shows the effective area of the reference detector as a function of energy for each neutrino flavor. No astrophysical neutrino flux has been observed above 10 PeV in energy so far. Therefore the expected neutrino rates in the IceCube-Gen2 radio array cannot be estimated from current measurements, but depend on extrapolations of the observed neutrino flux to higher energies, or can be calculated for theoretical predictions of the ultra-high-energy neutrino flux. Such extrapolations and theoretical predictions were discussed in Section 2.3.4, and the expected number of events in the radio-array derived from them were presented in Figure 29.

The energy resolution obtainable with the radio detector depends on both the reconstruction of the energy fluence in the received electric field and the reconstruction of the vertex distance, as discussed in Section 3.1.2. The obtainable resolution of the electric field depends in detail on the antenna design chosen. It has been shown with radio detection of air showers that one can reconstruct the detected radio signal to better than 20% in the absolute energy fluence of the pulse [566–568], with antenna modeling being the driving systematic uncertainty.

The obtainable resolution of the vertex position will strongly depend on the vertex distance. For close vertices, an uncertainty on the resolved vertex distance of the order of tens of meters is likely obtainable, following the location reconstruction of pulser events [527, 569, 570] and simulation studies. For more distant vertices the reconstruction quality will decrease. However, the reconstructed vertex position will be equally good, for the fraction of events in which both the direct and reflected signal can be measured, as was shown by ARA and ARIANNA using pulser signals [530, 569].

Combining the uncertainty of the electric field measurement, with the vertex distance estimate, the energy resolution of a shower will be better than a factor of 2 (see also Table 7). This means that the uncertainty on the neutrino energy will be dominated by the variations of the neutrino energy fraction that is deposited in the shower at the interaction vertex, as shown in dedicated studies for ARIANNA [530] and RNO-G [531, 571]. Systematic uncertainties originate from the limited knowledge of the ice properties such as the attenuation length and index-of-refraction profile. Both will be addressed in calibration campaigns.

The resolution of the neutrino arrival direction is determined by the combination of the signal arrival direction, signal polarization, and the viewing angle with respect to the Cherenkov cone. The obtainable resolution is highly dependent on the event quality, in particular the signal-to-noise ratio in the various antennas.

The accuracy of the reconstruction of the radio signal arrival direction can be extrapolated from the reconstruction of the position of deep pulsers on IceCube strings and those lowered into the SPICE borehole [569, 572, 573], as well as from the reconstruction of the radio signal of air showers [574, 575]. It is expected to be better than 1°.

To obtain the neutrino arrival direction the signal direction has to be combined with information from all antennas to include frequency spectrum and signal polarization. The angular resolution obtainable is also zenith angle dependent due to geometry restrictions imposed by the signal propagation in the ice.

Looking at individual signal components, there is experimental evidence that the polarization is reconstructable to better than 3°, as shown in cosmic ray measurements [543] and deep pulser signals with ARIANNA [535, 573]. The viewing angle to the Cherenkov cone will be reconstructed to better than 2°, extrapolating from frequency slope measurements of CR [533, 542, 576] and dedicated simulations.

Most of the referenced measurements of signal characteristics were obtained with high-gain log-periodic dipole antennas. Simulations indicate a similar performance for the shallow and deep components of the hybrid stations, depending in detail on the number of antennas with signal and the amplitude of the recorded signal [532, 536].

Combining all simulations and previous measurements results in typically asymmetric, curved uncertainty regions for the neutrino direction. Current results indicate that at least 50% of all triggered events can be reconstructed with an angular resolution better than 3° [532, 536]. It is expected that enhanced reconstruction algorithms will improve on this value, especially for those events detected in more than three antennas or in coincidence between two stations.

3.3.3 Surface array

The performance of the surface array has been studied extensively with CORSIKA simulations for a wide range of energies and arrival directions and for different types of cosmic-ray primaries (Figure 45). Compared to IceCube/IceTop, the effective surface area will increase by a factor of 8 to about 6.5 km^2. That increase in area results in a significantly increased range of arrival directions for coincidences between the

Table 7: Energy resolution of tracks and showers in the optical and radio arrays. The numbers define the intervals around the visible energy (energy deposited by charged particles above Cherenkov threshold) of the events in the detector that contain the reconstructed energy for 68% of the events.

Energy range [TeV] E_{min} – E_{max}	Tracks (opt. array)	Showers (opt. array)	Showers (radio array)
1 – 10	27%		
10 – 100	14%	67%	
100 – 10^3	14%	26%	
10^3 – 10^4	13%	14%	
> 10^5	15%	11%	65%

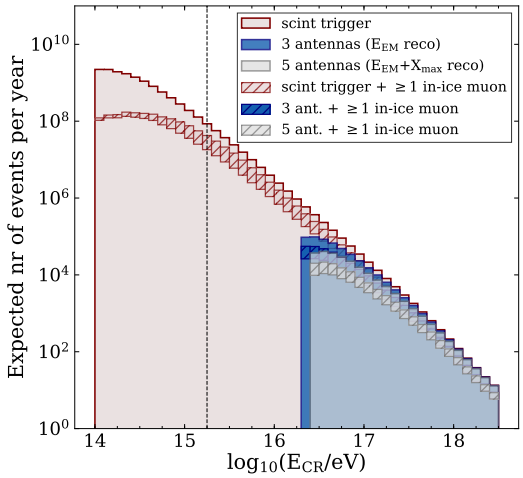

Figure 45: Expected event statistics of the IceCube-Gen2 Surface Array for which scintillator, in-ice optical, and/or surface antenna information will be available. Events in coincidence with the optical array (hatched lines) are the most valuable ones for all science cases (veto, hadronic interaction, cosmic rays, gamma rays) that make use of the surface array.

surface and optical arrays. These events are the most valuable for practically all science cases involving the surface array: its function as veto, the study of hadronic interactions and prompt decays, accurate measurements of the cosmic-ray mass composition, and gamma-hadron separation. The aperture for these coincident events will increase by more than a factor of 30 to about 8 km^2 sr with respect to IceCube/IceTop.

Different parameters are essential to quantify the performance for the various purposes of the surface array:

For the *veto*, the detection threshold for proton induced showers is most important, since atmospheric backgrounds depend on the energy per nucleon; and protons dominate the cosmic-ray flux when expressed as a function of the energy per nucleon (instead of total energy of the primary particle).

For *hadronic-interaction physics*, such as the study of prompt forward leptons, the surface array will be able to provide a precise energy measurement with a resolution of

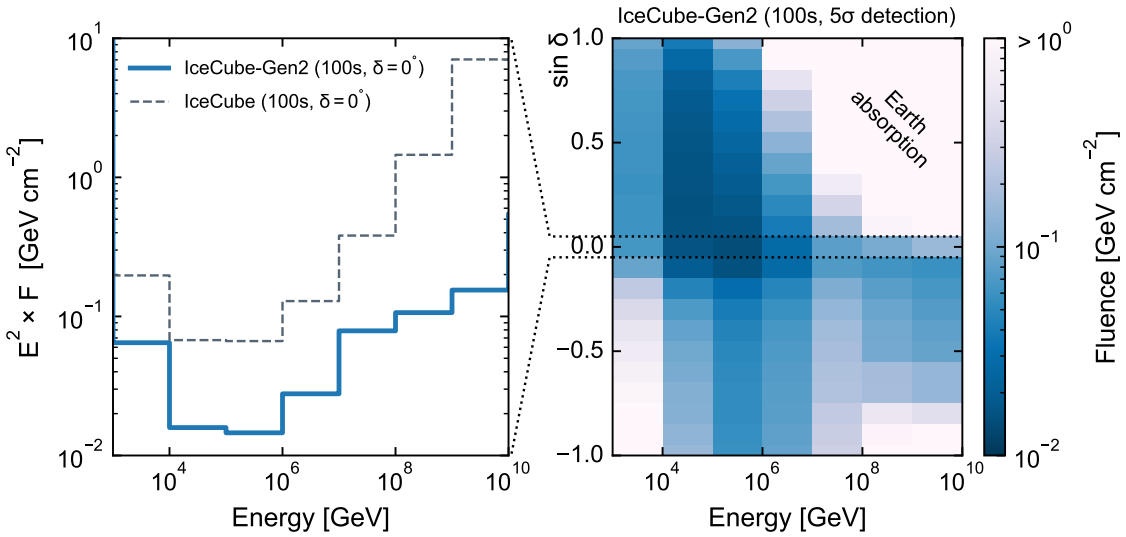

Figure 46: Sensitivity for the discovery (5σ discovery potential) of a generic short neutrino burst of 100 s duration as a function of energy and declination of the source (right panel). The sensitivity at the horizon is compared to the respective sensitivity of IceCube (left panel). IceCube and IceCube-Gen2 sensitivities are calculated separately for each decade in energy, assuming a differential flux $dN/dE \propto E^{-2}$ in that decade only. The neutrino fluence is shown as the per-flavor sum of neutrino plus anti-neutrino fluence, assuming an equal fluence in all flavors.

$\log E = 0.2$ at 1 PeV and $\log E = 0.1$ at 10 PeV for showers with zenith angles up to 30°. This is crucial to study those showers in detail that feature TeV or PeV muons detected in the optical array, and to understand that flux as function of the cosmic-ray energy and mass. Using distant IceTop tanks as muon detectors will provide an additional measurement of GeV muon densities. IceCube/IceTop already plays the leading role in the energy range from few PeV to ~100 PeV regarding the study of the muon puzzle [371], i.e., that state-of-the-art hadronic interaction models predict less muons than measured. IceCube-Gen2 will provide overlapping measurements with the Pierre Auger Observatory at 100–300 PeV.

The surface array will provide unprecedented sensitivity for large-scale anisotropies, boosting investigation of the origin of high-energy galactic cosmic rays. By combining the radio, scintillator, and optical measurements of muons, unprecedented accuracy for the estimation of the primary mass will be achieved. These two measurements combined will help to understand the transition from Galactic-to-extragalactic cosmic rays and shed light on the yet undiscovered origin of the most energetic Galactic cosmic rays.

As a side-goal complementing its multimessenger mission, IceCube-Gen2 will also search for *PeV photons*. With the gamma-hadron separation provided by the combination of the scintillators and the deep optical array together with the largely increased aperture for such events, there is significant detection potential of several high-energy LHAASO-like sources in the southern hemisphere.

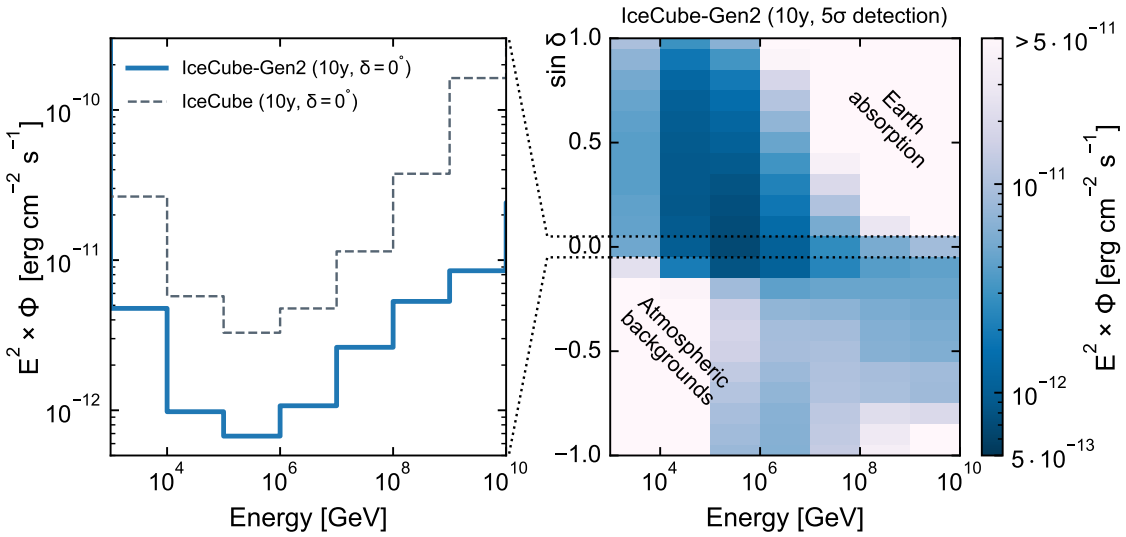

Figure 47: Same as Figure 46, but for persistent point sources and a 10 year observation time. Flux is shown instead of fluence.

3.3.4 Combined performance

The radio and the optical arrays are complementary in their energy range and provide synergistic sensitivity to different detection channels. Combining both techniques will make IceCube-Gen2 a formidable instrument sensitive across a much broader energy range than previously accessible to IceCube. The individual instrument response functions obtained for the radio and optical array, the effective area, the PSF and the energy resolution, are combined to estimate the sensitivity of IceCube-Gen2 to various astrophysical neutrino production scenarios in Section 2. Potential gains from a coincident detection of a subset of events have not been included in these estimates. Figures 46 and 47 give an overview of the differential sensitivities (5σ discovery potential) of the combined detectors as a function of energy and declination δ for generic short bursts (100 s) and persistent sources (10 y). The peak sensitivity of IceCube-Gen2 is around the celestial horizon ($\delta \approx 0^{\circ}$), where both the optical and the radio array have an excellent sensitivity. In the Northern sky ($\delta > 0^{\circ}$), the sensitivity is dominated by the optical array as neutrinos above the detection threshold of the radio array of O(10 PeV) are absorbed in the Earth. In the Southern sky($\delta < 0^{\circ}$), the radio array dominates the sensitivity for persistent sources, as atmospheric backgrounds severely limit the sensitivity to lower-energy neutrinos. For short bursts, both optical and radio array contribute to the sensitivity as the atmospheric backgrounds are not relevant on such short time scales.

The surface array improves the sensitivity of IceCube-Gen2 to sources in the region around the Southern celestial pole significantly. Figure 48 shows the integral sensitivity (5σ discovery potential) of IceCube-Gen2 (optical + surface arrays) to a point source

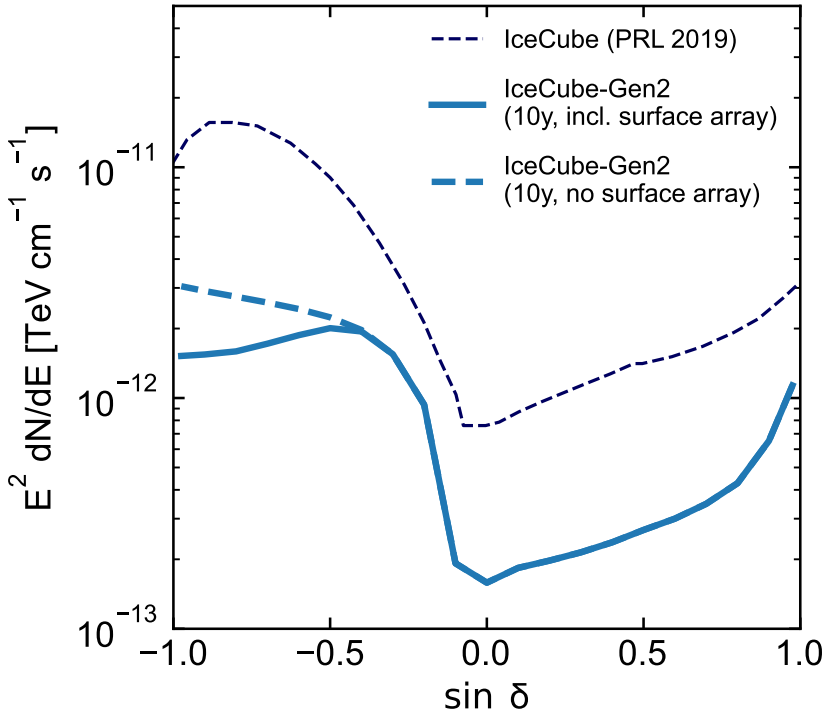

Figure 48: Integral sensitivity for the discovery (5σ discovery potential) of a point source featuring a power-law spectrum with an index of -2, after 10 years of observations. The sensitivity of the optical array is presented as a function of declination, in combination with and without the surface array. The IceCube sensitivity (including the IceTop surface array) from [577] calculated for the analysis of a ten-year dataset is indicated for comparison. The neutrino flux is shown as the per-flavor sum of neutrino plus anti-neutrino flux, assuming an equal flux in all flavors.

featuring a power-law spectrum with an index of -2, after 10 years of observations[¶]. This sensitivity is compared to the corresponding values when not using the cosmic-ray muon veto provided by the surface array. At the celestial pole the sensitivity improves by a factor of ~2, with significant gains in sensitivity for more than 25% of the sky.

[¶]Please note that TeV cm^{-2} s^{-1} is used as the unit for $E^2 \times \Phi$ in this figure instead of erg cm^{-2} s^{-1} to facilitate a comparison to corresponding figures published elsewhere.

Part II

Detector and Performance

Table of Contents

4 The South Pole: an extraordinary platform for astrophysics 85
4.1 Introduction . . . 85
4.2 Site . . . 85
4.3 Existing infrastructure and environment . . . 90
4.4 IceCube . . . 91
4.5 IceCube-Gen2 . . . 95
4.6 Organization of Chapters 5-10. . . . 97

5 Optical Array 98
5.1 Overview . . . 98
5.2 Requirements . . . 100
5.3 Main interfaces . . . 103
5.4 Reference design . . . 105
5.5 Alternatives considered . . . 119
5.6 Additional photon-collection components . . . 121
5.7 Production sites and test plan . . . 123
5.8 South Pole test strategy . . . 125
5.9 Production schedule . . . 125
5.10 Risks and risk mitigation . . . 126
5.11 Summary . . . 126

6 Radio Array 128
6.1 Overview . . . 128
6.2 Requirements . . . 128
6.3 Main interfaces . . . 131
6.4 Reference design . . . 132
6.5 Alternatives considered . . . 146
6.6 Development and production schedule . . . 148
6.7 Test strategy . . . 150
6.8 Risks and risk mitigation . . . 152
6.9 Summary . . . 153

7 Surface Array 155
7.1 Overview . . . 155
7.2 Requirements . . . 156
7.3 Main interfaces . . . 162
7.4 Reference design . . . 163
7.5 Alternatives considered . . . 175
7.6 Development and production schedule . . . 177
7.7 Test strategy . . . 178
7.8 Risks and risk mitigations . . . 180

7.9 Summary 182

8 Surface and Data Acquisition Infrastructure 183
8.1 Overview 183
8.2 Technical requirements 185
8.3 Main interfaces 185
8.4 Reference design 186
8.5 Alternatives considered 200
8.6 Development and deployment strategy 203
8.7 Test strategy 204

9 Data Systems and Infrastructure 206
9.1 Overview 206
9.2 Computing hardware 207
9.3 Online data systems software 212
9.4 Core software systems 217
9.5 Data management and northern computing 220

10 Detector Calibration 227
10.1 Introduction 227
10.2 Optical array 227
10.3 Radio array 234
10.4 Surface array 245
10.5 Summary 249

4 The South Pole: an extraordinary platform for astrophysics

4.1 Introduction

The construction of IceCube began nearly two decades ago. By its completion in 2010, a cubic kilometer of deep South Pole ice had been instrumented with 5,160 photomultiplier tubes, which have continuously monitored the ice for the faint Cherenkov signatures of neutrino interactions. An associated array of surface detector tanks provides a partial cosmic ray veto and, along with the embedded component, a unique three dimensional profile of air showers.

The ice at the South Pole serves as both target volume and Cherenkov radiator. It is some of the best studied ice in the world and has exceptional optical clarity. Extensive calibration programs have been carried out regularly over IceCube's operation, allowing further characterization of the ice and the detector response. This has allowed IceCube to address scientific queries that were well beyond the goals of the original design. The ongoing IceCube Upgrade will expand the calibration program as well as extend the low-energy reach of the IceCube observatory. In the meantime, pioneering arrays colocated at the South Pole have measured the radio frequency attenuation length of polar ice to be the longest recorded anywhere, establishing the South Pole as an ideal location for an antenna array which would allow ultra-high-energy neutrino detection via the Askaryan effect. These endeavors have been made possible by the infrastructure and logistical support provided by the Amundsen Scott South Pole Station.

The extraordinary successes of IceCube's scientific program, as well as the opportunities provided by the proposed IceCube-Gen2 expansion, were outlined in Part I of this document. In Part II, we describe the design of IceCube-Gen2 in detail. We start in the current chapter with a description of the existing IceCube, IceTop, and DeepCore arrays, which will provide the cornerstone of the larger observatory. We also describe the IceCube Upgrade which, while enhancing the scientific reach of IceCube, also provides a platform for the next generation of instrumentation development. Most importantly, we describe the site, in particular the properties of the ice, and why the South Pole is uniquely suited to host a multichannel observatory like IceCube-Gen2.

4.2 Site

The properties of the vast south polar ice cap are perhaps among the best studied in the world. At nearly three kilometers in thickness, the glacial ice near the Amundsen-Scott South Pole Station has been exquisitely mapped over the three decades of neutrino detector operation at the site. In addition, the infrastructure provided by the station as well as an environment largely free of anthropogenic noise make the location ideal for neutrino astronomy. Just as our knowledge of the environment informed the design of the original array, our evolving knowledge of the ice and the surrounding atmosphere, along with our experience in operating the detector, has informed the design of IceCube-Gen2. Here we summarize both the optical and radio-frequency characteristics of the ice as well as the environment.

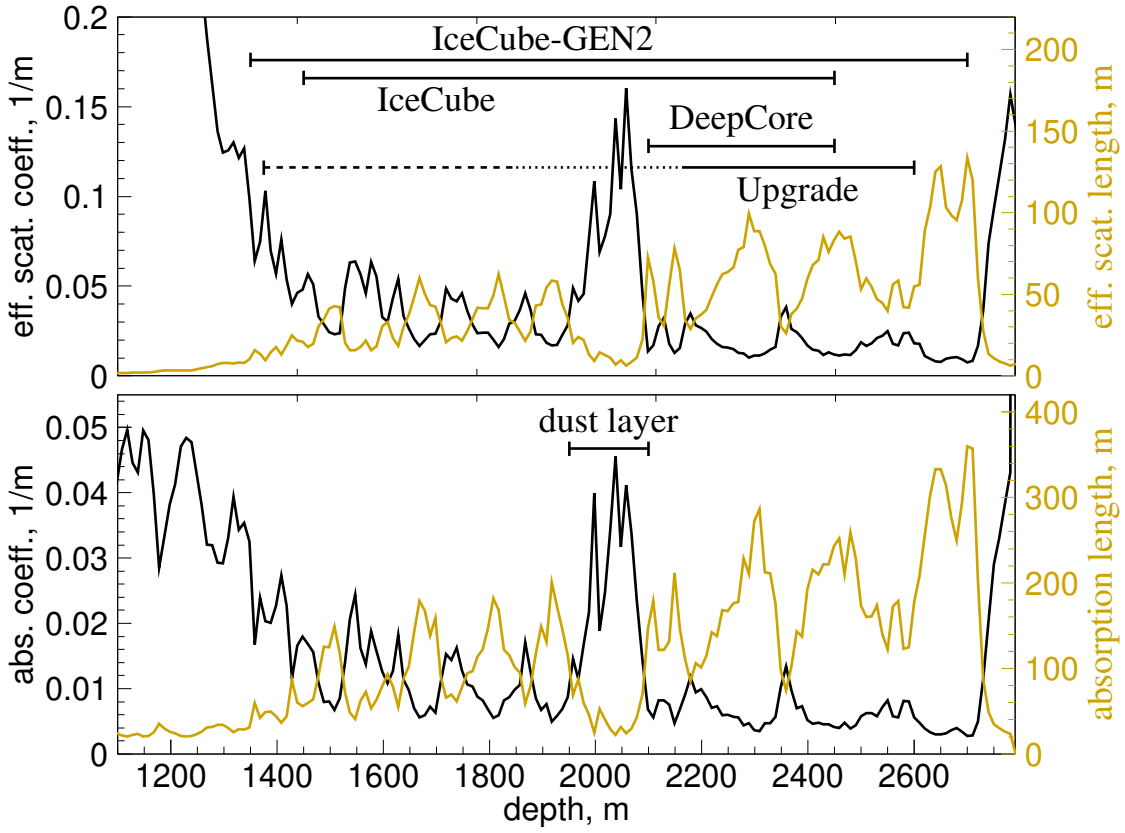

Figure 49: Stratigraphy of fitted absorption and scattering strength. Figure taken from Ref. [582].

4.2.1 The glacial ice as detection medium

Optical properties

The ice within the volume of the IceCube detector was deposited as snow some 40 to 95 kyrs ago [578, 579]. As the snow fell on the surface of the ice, it contained impurities, concentrations of which were determined by the atmospheric conditions at the time. These were influenced by specifics of climate and other major Earth events such as volcanic eruptions. The top 200 m of packed snow, known as firn, has a reduced density compared to the region below, where the packed snow becomes ice with small bubbles of trapped air interspersed. Although the ice at the South Pole has been measured to have an order of magnitude fewer impurities than the cleanest laboratory ice [580], and as such has exceedingly small absorption (with absorption length exceeding 100 m in the cleanest ice in the currently instrumented volume), the air bubbles are a source of very strong scattering, which significantly reduces the propagation reach of photons as well as widens their arrival time distributions so much as to make them nearly useless [581]. At around 1,350 m depth, due to large pressure, the bubbles disappear as the air diffuses into the surrounding ice crystals to create air hydrate clathrates, with a refractive index virtually indistinguishable from that of ice crystals [580].

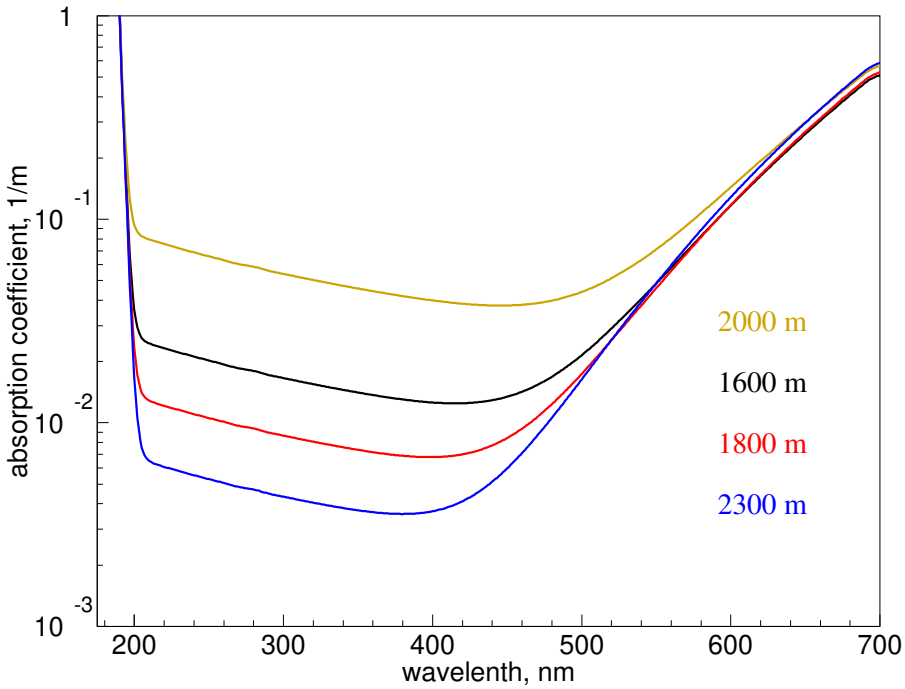

Figure 50: Absorption is shown versus wavelength.

The ice sheet at the location of the South Pole flows at a rate of around 10 m/yr. This, together with the local topography of the underlying bedrock, causes the ice isochrones (i.e., layers of ice that were deposited at the same time and as such have the same dust concentrations and, thus, optical properties) to distort from being perfectly horizontal to varying in depth by as much as 70 m across the IceCube detector near its bottom. The IceCube Collaboration has mapped the changes in depth of these ice layers using a device called a dust logger, which was lowered into eight of the array boreholes after they were drilled and before the main string deployment took place. This dust logger emits a narrow beam of light into the ice and records the returned signal, and it is capable of resolving features 2 mm in width (perfectly resolving the "volcano ash" ice layers). The recorded vertical dust profiles leave characteristic features that have then been successfully matched against dust records collected elsewhere in Antarctica (i.e., Dome C). This allowed us to extrapolate the optical properties of ice measured within the volume of the IceCube detector (described below) to the regions of ice above and below the detector. The ongoing IceCube Upgrade will allow precision measurements of that region.

In the instrumented volume of the IceCube detector, the IceCube Collaboration has measured the optical properties of ice in great detail (scattering and absorption vs. depth is shown in Fig. 49), using the 12 LEDs contained in each optical module. These LEDs can emit brief pulses of light in tandem or individually, and the data received on the surrounding DOMs are then analyzed. By comparing the data with simulations [582, 583], we have obtained the scattering and absorption properties of ice (averaged) in 10-m depth layers as well as discovered a curious effect where more light reaches sensors along the directions closest to the direction of the ice flow (as shown in Figure 51). The

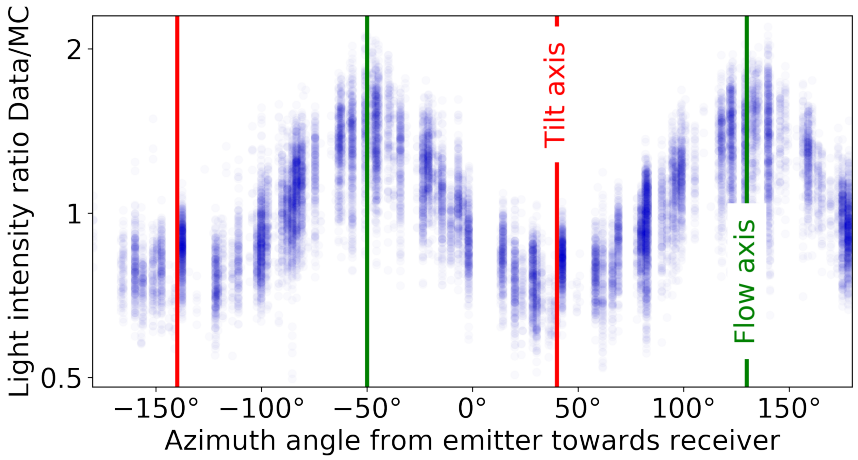

Figure 51: Ice optical anisotropy seen as azimuth-dependent intensity excess in flasher data. Each dot is the observed intensity ratio for one pair of light-emitting and light-detecting DOMs (separated by ~ 125 m) comparing data to a simulation with no anisotropy modeling enabled. The tilt and flow directions are shown for reference.

absorption length is wavelength dependent, as shown in Figure 50. Substantial effort has gone into the investigation and modeling of the photon propagation.

Recently we reinterpreted our calibration data to much better accuracy with a well-known feature of Antarctic ice, namely that the individual ice crystals align perpendicular to the ice flow direction (and, in the deepest ice, it also exhibits a second vertical component in its crystal orientation). Ice crystals are mono-axial, and exhibit a very slight difference in propagation of ordinary and extraordinary rays (i.e., are birefringent). Although this is a vanishingly small effect for a single crystal boundary crossing, because of the large number of such crossings for any typical propagation distance within the IceCube detector (~1,000 crossings per meter), a macroscopic effect emerges where the rays of light bend, on average, towards the flow axis. While this effect competes with the somewhat larger diffuse scattering for directions closest to the flow axis, it still results in more light arriving in such directions, as observed in the flasher data in Figure 51.

RF properties

The ice at the South Pole is extremely cold and is therefore expected to be exceptionally transparent to radio frequency (RF) signals, as the attenuation length of RF emission is expected to increase with decreasing temperature. Figure 52 shows the temperature of the South Pole ice versus depth. Also shown is a hyperbolic fit, which extrapolates to approximately melting temperature at the bedrock, as suggested in a recent model of this data [586]. At the bedrock, the temperature of the ice approaches melting temperature and the RF attenuation is high. This has the advantage that reflected RF signals from the bedrock that could appear as background will be highly suppressed. This makes the cold, shallow ice ideal for RF detection of neutrino induced showers through the Askaryan channel. The air bubbles which scatter visible and ultraviolet light are invisible to to long wavelengths in the radio band. However, the firn, with it's gradually increasing density, presents a varying index of refraction which acts like a mirror, bending the path of rays near the surface. This limits the horizon for shallow

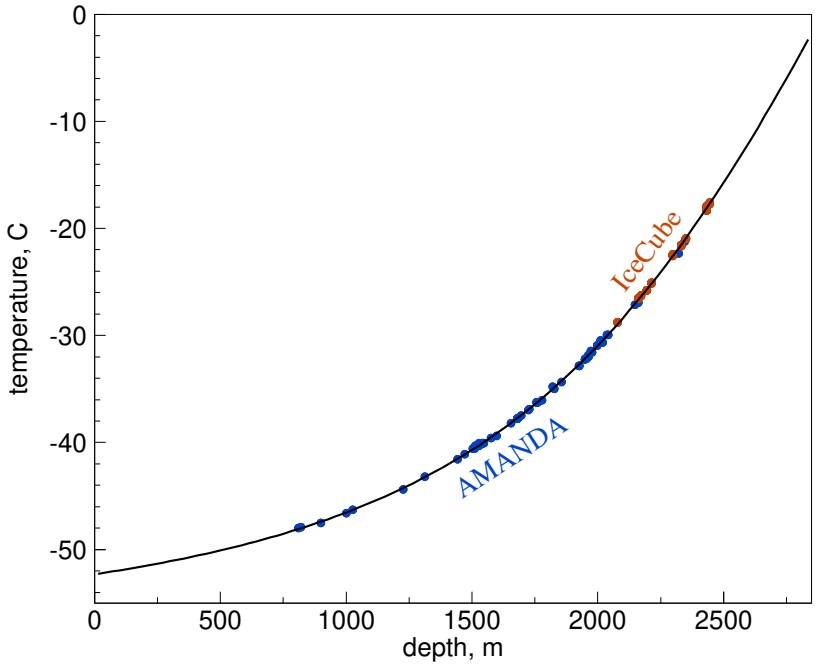

Figure 52: Ice temperature as a function of depth from the surface level at the South Pole. Measurements from IceCube [584] and AMANDA [585].

instrumentation, but also allows a means of estimating the location of the interaction vertex, by comparing the arrival time of rays arriving on a direct versus reflected path.

The radio frequency properties of the ice near the geographic South Pole have been extensively studied through the pioneering efforts of RICE [525] (the Radio Ice Cerenkov Experiment), by a measurement using surface pulsers by Barwick et al. [524] and, in the past decade, the ARA (the Askaryan Radio Array) Collaboration [569]. Also the ARIANNA (Antarctic Ross Ice-Shelf Antenna Neutrino Array) Collaboration installed and operated two stations near the South Pole [573], one of which was powered autonomously. The different experiments studied attenuation length, refractive index as function of depth, and potential birefringent properties.

Dedicated high-voltage radio frequency transmitters were installed on the IceCube strings at depths of 1,450 and 2,450 m, allowing point to point measurements of the signals in ARA receivers located at horizontal distances ranging from 2.2 to 5.4 km, the longest point to point measurements made to date in polar ice. More recently, depth-dependent measurements were made using a retrievable transmitter lowered into a 1,700 m deep borehole drilled for the South Pole Ice Core Experiment located at horizontal distances of 1.2 to 4.1 km from the ARA stations Taken together, these measurements cover a large variety of baselines, depths, and viewing angles. Measurements of the attenuation length are consistent, at > 1 km in the top half of the ice.

Figure 53 compares the RF attenuation length at three sites where RF properties have been extensively studied: the South Pole, Moore's Bay, on the Ross Ice Shelf, and Greenland. The South Pole has an exceptionally large attenuation length of more than 2 km at the surface, which is where the detectors are located.

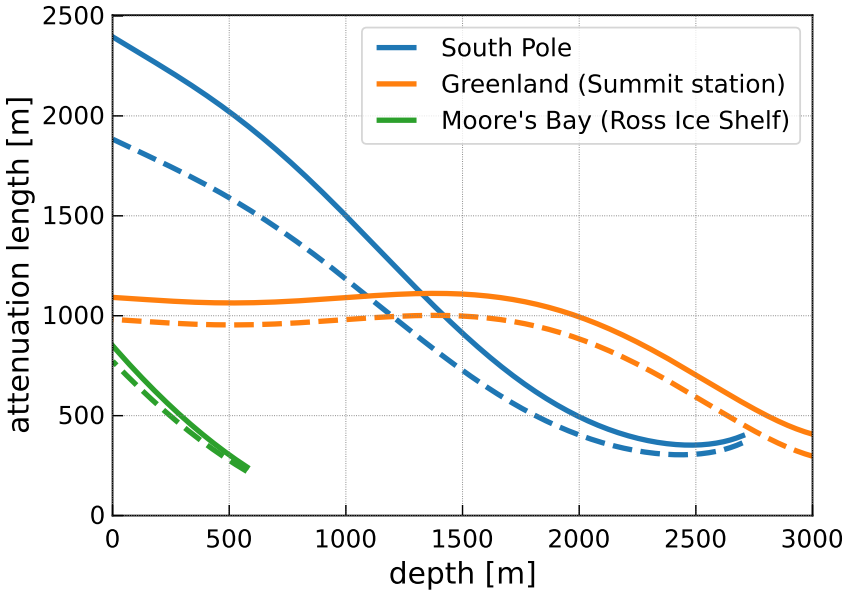

Figure 53: The attenuation length of RF signals is shown versus depth for the South Pole, Greenland, and Moore's Bay. The solid lines show the attenuation length at 200 MHz and the dashed lines at 400 MHz. Figure adapted from Ref. [544].

In addition, the existence of a possibility of a birefringent effect, as seen in the optical, has been investigated [569, 587]. In radio frequencies, this can be measured by comparing the difference in arrival times of the horizontally and vertically polarized components of the incoming signals. An asymmetry has been observed which varies linearly with range and depends on the orientation of the incoming signal with respect to the direction of the local ice flow [569]. Further, both ARA and ARIANNA demonstrated the arrival of two distinct signals, one from the direct path and the other refracted/reflected near the ice's surface, where the loosely compacted firn forms a layer with a varying index of refraction. Depending on the geometry a second signal is either reflected or refracted towards the antennas in the ice.

4.3 Existing infrastructure and environment

The South Pole site offers not only ideal natural conditions, it also is home to the US National Science Foundation's Amundson Scott South Pole Station. The station provides extensive infrastructure, including housing for 160 people during the summer, with a population of more than 30 people during the winter. The winter population also includes scientists who winter over to maintain science programs such as IceCube and the South Pole telescope, which run continually, even during the Austral winter.

Transportation of cargo presents an additional logistical challenge when working in the polar region. During IceCube's construction, all of the instrumentation and fuel required for installation, a total of 9 million pounds of combined cargo, was shipped by LC-130 aircraft. However, transportation by LC-130 aircraft is expected to operate with reduced capacity in the future. An overland traverse, consisting of tractor fleets pulling large sleds, was established over a decade ago and now transports the majority of the fuel

to the South Pole, and has also successfully delivered other cargo. This efficient new mode of transportation should provide an excellent shipping option for Gen2.

The South Pole station provides power to the station as well as the science instruments. However, the current power infrastructure will require an upgrade to support future large experiments. An alternative, which has been investigated by the CMB-S4 project, is to operate future telescopes all year around using entirely renewable energy sources [588].

Data transfer and communication are available via a number of satellites. Due to the polar location, not all satellites are continuously visible. Bulk data transfer via satellite for the station is available at the level of a few hundred GB per day. Communications satellites are available for interactive communication is available for portions of the 24 hour cycle. An Iridium connection exists continuously for interactive work and real time multi messenger alerts.

A more detailed description of the logistical support available can be found in Part III of this document.

4.4 IceCube

IceCube-Gen 2 will be built around the existing IceCube array, with the original IceCube strings forming a high-density core. The simple, modular design of IceCube has proven particularly robust against the difficult polar environment, with failures detected in less than 1% of the installed hardware after more than a decade of continuous operation with nearly 100% uptime. The design of the IceCube-Gen2 array leverages the demonstrated success of IceCube, along with lessons learned about the properties of the ice, and its experience with maintenance, calibration, and data analysis. Here, we give a brief description of the existing hardware.

4.4.1 IceCube in-ice array

The in-ice component of the IceCube Neutrino Observatory is designed to detect photons from charged particles traversing the ice. The deep detector comprises 86 "strings" or cables, with each string supplying power and communications to 60 digital optical modules, or DOMs. Each DOM is composed of a glass pressure sphere containing a downward-facing, 10" photomultiplier tube (PMT) [589], along with electronics that digitize signals, host LED flashers for detector calibration, and provide communication with the surface [590]. Seventy-eight of the strings are arranged on a triangular grid with 125 m spacing, with a hexagonal footprint covering a square kilometer. The DOMs on each of these strings are installed at 17 m spacing extending from 1,450 m to 2,450 m in depth, together instrumenting a cubic kilometer of deep ice. The remaining 8 strings form a low-density core, called "DeepCore," at the center of the detector, with interstring spacing ranging from 41-105 m. The bulk of the DOMs populating the DeepCore strings are arranged 7 m apart in the exceptionally clear ice below the dust layer, which is clearly visible in Figure 49 from 2,150 to 2,450 m deep. The remaining 10 DOMs on the DeepCore strings are arranged with 10 m spacing above 2,100 m. This arrangement is optimized for low-energy studies, with the dust layer providing a light-

tight box and the shallow DOMs acting as a veto to reject background from downgoing atmospheric muons. To this end, the majority of the DeepCore DOMs have photomultiplier tubes with 35% higher efficiency than the standard IceCube DOM. IceCube has a neutrino energy threshold of ≈ 100 GeV, while DeepCore turns on around 10 GeV. The layout of the observatory is shown in Figure 54.

Inside the DOM, digitization is provided by a 4-channel custom ASIC, the Analog Transient Waveform Digitizer (ATWD) [591], set to sample at 300 Msps, with a recording length of 427 ns. To cover the dynamic range of the PMT signals, three channels digitize the signal at gains of 16, 2, and 0.25, while the fourth channel is reserved for calibration. Each DOM is equipped with two ATWDs to reduce deadtime. To capture more faint signals for distant, scattered light, this is supplemented by a continuously sampling fast ADC, which continues to record data for more than 6 μs after the initial trigger, or "launch," which is typically set to commence at a voltage corresponding to 0.25 PE. Dedicated wiring allows a DOM to query its neighbors to recognize coincident hits within a dedicated time window, with nearest neighbor hits designated as a hard local coincidence (HLC). The DOMs send up blocks of data after accumulating data for about a second. Each DOM is capable of running a number of self-calibration tests.

After the DOMs transfer data to the surface, events are built in dedicated servers in the IceCube Lab. The dark noise rates are 560 and 780 Hz, respectively, for standard and high-quantum-efficiency PMTs. Most of the dark noise is due to radioactive decays and subsequent fluorescence in the glass pressure vessel. The fluorescence photons are correlated in time, with a typical correlation time of 1 μs. [592]. The rate from cosmic ray muons varies with depth from 25 Hz to 5 Hz. Algorithms search for causally related HLC hits by searching in a time window determined by the light travel time across the detector. Several software triggers are then run to test consistency with various signal hypotheses. Once the relevant hits for a triggered bundle (an event) are collected, they are combined with calibration data. Data calibration routines are applied to all data, and all triggered events are saved in a compact format known as SuperDST (Super Data Storage and Transfer Format). A set of simple event selections then select interesting events, reducing and compressing the raw event stream of ~ 1 TB per day to 100 GB/day, which is queued for satellite transmission. Additionally, the online data processing contains a series of event reconstruction algorithms that are used to determine the parameters of the event, including energy, direction, and the quality of the event reconstruction. Advanced filters, based on published IceCube analyses, use this information to select interesting events to queue for rapid satellite transmission. These rare events are used to generate alerts to the community when potential astrophysical neutrino events are found [196], or respond to interesting astrophysical transient events observed by others [593].

4.4.2 IceTop: IceCube's surface array

IceTop, the surface array of IceCube, is comprised of ice-Cherenkov detectors and measures cosmic-ray air showers [507]. Each detector features two DOMs frozen into tanks of clear ice (see Figure 55) that detect the Cherenkov light from muonic and electromagnetic air-shower components traversing through and interacting in the tanks.

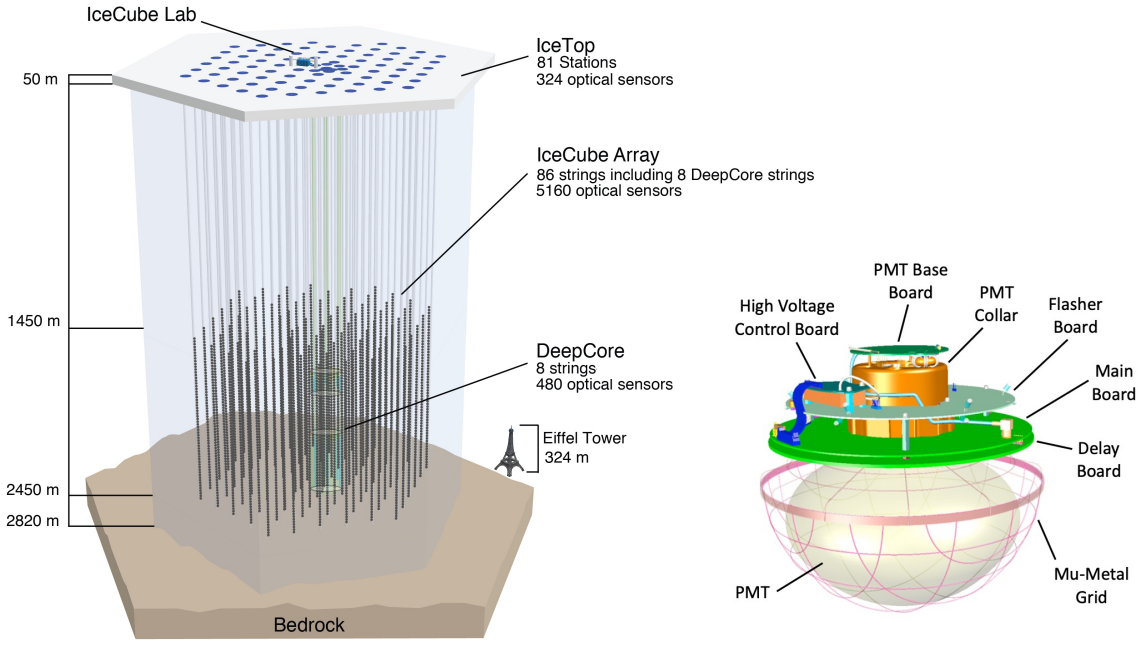

Figure 54: The existing IceCube detector, consisting of 5,160 optical modules installed on 86 cables. Eight of the cables near the center form a high-density core, the remaining cables are installed on a 125 m hexagonal grid. The associated surface array consists of 81 stations of Cherenkov tanks, each read out by four optical modules. A schematic view of an IceCube Digital Optical Module is shown on the right.

The tanks were deployed in pairs, one for each of the 81 strings of the optical array (five strings in the center are without IceTop stations, as the IceTop array is already dense in this region). The DOMs in the two IceTop tanks of a string are connected to the same data acquisition system and share the general infrastructure with the deep array but are treated separately in trigger decisions and in the data analysis. By requiring a coincident signal in both tanks of a pair, low-energy showers and single muons can be suppressed. With the standard trigger requiring at least three pairs of tanks with signal, IceTop efficiently detects showers in the energy range from around $10^{15} - 10^{18}$ eV.

The IceTop signal is generally dominated by the electromagnetic shower component, and muons make up a sizable fraction of the signal at distances of several hundred meters from the shower axis. However, the relative contribution of muons is increasing over the years of operation, as snow accumulation above the IceTop tanks absorbs electromagnetic particles. To date, several meters of snow have accumulated, which has motivated the plans for a surface enhancement consisting of detectors designed to be periodically raised, with a prototype station of elevated scintillators and radio antennas operating successfully for several years. Although the IceTop tanks have proven to be very reliable, this problem of snow accumulation is why the IceCube-Gen2 Surface Array will follow the elevated design of the IceTop enhancement.

The combination of the surface array and the km-scale Cherenkov array below 1.5 km depth allows for unique measurements of air shower parameters with high acceptance: the detailed observation of the electromagnetic and low-energy muon component at the

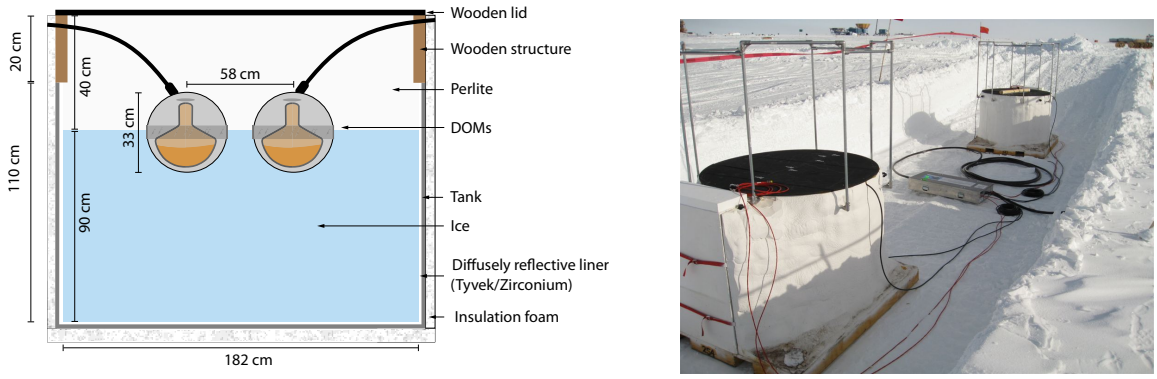

Figure 55: Sketch of an IceTop tank (from Ref. [507]) and photo of a station with its two detectors during construction.

surface and the high-energy muons in the shower core at depth. The three main goals of IceTop have been calibration, vetoing atmospheric muons in neutrino searches, and cosmic-ray physics, all of which are related to and enhance the neutrino astrophysics of IceCube. After deployment of the optical strings, IceTop was used for the purpose of validation, showing the consistency of the reconstructed direction of atmospheric muons with the air showers detected at the surface [594]. Meanwhile, IceTop contributes to the instrument-wide calibration in a wider sense with an in-situ measurement of the cosmic-ray flux responsible for atmospheric backgrounds in the ice. As a veto, IceTop improves the purity of downgoing neutrino samples, such as in starting-track analyses [595], and for high-energy neutrino candidates sent out as real-time alerts [596]. Finally, IceTop has made many contributions to cosmic-ray physics, utilizing IceCube's unique setup combining a surface and a deep detector. These results include the astrophysics of Galactic cosmic rays, solar-heliospheric physics, and hadronic interactions models of air showers, which are also important in understanding the production of atmospheric muons and neutrinos [597].

4.4.3 IceCube Upgrade

The IceCube Upgrade, funded as an NSF mid-scale award with contributions from non-US funding agencies and currently under construction, will add seven additional strings of instrumentation to the center of IceCube's active volume, bolstering the current detector's sensitivity. This first extension of the IceCube detector will include ~730 newly designed optical detectors and calibration devices and will be deployed in the 2025/2026 Antarctic season. The primary goals of the IceCube Upgrade are to improve the low-energy neutrino sensitivity to perform precision studies of neutrino oscillation parameters, deploy a full suite of new calibration devices to more fully characterize the optical properties of the Antarctic glacier, and serve as a testbed for new technologies to enable the realization of IceCube-Gen2.

The seven new strings of the IceCube Upgrade will add optical detectors to the most highly instrumented region of IceCube, as shown in Figure 12. With this addition, a 2-MT volume of clear glacial ice will have a sufficient density of optical modules to detect charged particles from atmospheric neutrino interactions in the ~1-50 GeV energy range and reconstruct them with higher precision (see Table 1). The combination of

improved reconstruction and higher-statistics samples will allow world-leading precision measurements of $\nu_\mu \rightarrow \nu_\tau$ neutrino oscillation parameters. Additionally, the ν_τ flux measurement, in combination with other oscillation results, will enable probes of new physics by examining the unitarity of the Pontecorvo-Maki-Nakagawa-Sakata (PMNS) matrix [13].

These oscillation physics goals are enabled by the 680 multi-PMT sensors that will be deployed on these new strings. Two new types of optical modules will be installed, the multi-PMT digital optical module (mDOM) [550] and the “Dual optical sensors in an Ellipsoid Glass for Gen2" (D-Egg) [598]. These modules are shown in Figure 38 and key parameters are detailed in Table 4. Both of these are designed to have increased per-module photon detection efficiencies when compared to current IceCube DOMs (see, for example, Figure 75). These new multi-PMT designs, already in production and testing for inclusion in the IceCube Upgrade, provide critical input to the IceCube-Gen2 optical array design.

To supplement the new optical sensors, the IceCube Upgrade string will be instrumented with a suite of calibration devices to better quantify the properties of the Antarctic glacier. Each optical module will include fast (~5 ns FWHM) LEDs and fixed-focus charged-coupled device (CCD) camera [599] and illumination board combinations. Additionally, a fleet of stand-alone calibration devices are also included. Wide-angle Precision Optical Calibration Module (POCAM) [600] and narrow-beam (Pencil Beam) [601] light sources, free-focus and zoomable camera modules, and acoustic emitter and receiver modules [503] will all more fully qualify the *in situ* detector response. These improved measurements will address one of the largest sources of systematic uncertainties for IceCube analyses, and will enable improved accuracy in detector simulation and neutrino event reconstruction. Not only will this inform future observations, this improved detector understanding can be applied to over 10 years of existing archival data to greatly improve the detector sensitivity to measurements of the astrophysical neutrino diffuse flux measurements and point source searches.

Finally, many of the design choices made in the IceCube Upgrade were made considering the future needs of IceCube-Gen2. The string power and communication interface design using fieldhubs and IceCube communication modules (ICM) (see Section 8.4) is also being used in the IceCube Upgrade. All calibration and prototype modules being deployed in the IceCube Upgrade are built upon a standard internal electronics stack, known as the "mini-mainboard" (MMB), standardizing the interface between per-module hardware and standardized power and communication hardware. Additionally, several IceCube-Gen2 prototype modules will be deployed in the IceCube Upgrade to evaluate *in situ* design performance and robustness.

4.5 IceCube-Gen2

As described in Part I, IceCube-Gen2 represents the next generation in neutrino astronomy detectors and promises a major leap forward in sensitivity to astrophysical neutrinos and identifying the sources and mechanisms that produce them. The design of IceCube-Gen2, shown schematically in Figure 56, draws from a wealth of experience

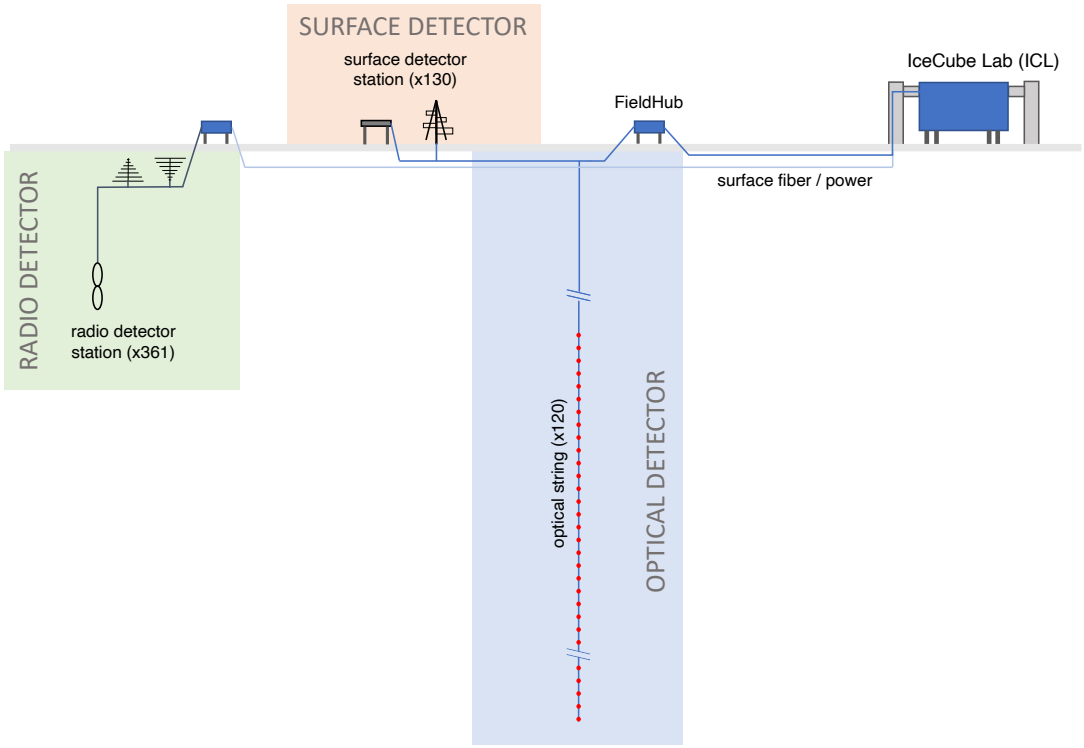

Figure 56: Schematic diagram of the system architecture of the IceCube-Gen2 Observatory. The baseline design includes 120 optical in ice strings, which provide sensitivity to neutrinos of energies up to 10 PeV, 361 radio antenna clusters to extend the sensitivity to EeV energies, and a complementary surface array consisting of 130 scintillator/antenna components for cosmic ray studies and air shower veto. The IceCube laboratory will provide power and communications to for the entire observatory.

gained in the design and construction of IceCube and the IceCube Upgrade as well as from over a decade of detector operation and data analysis.

The 120 optical string enhancement for Gen2 more fully exploits the clear, deep ice, deploying multi-PMT modules to depths of up to 2689 m to expand the total instrumented volume. The strings are arranged in a sunflower pattern with an average of 240 m spacing between them, with the added volume totaling 8 cubic kilometers. Each optical string is associated with a surface station consisting of 3 radio antennas a 8 scintillator panels. The optical string and surface station share a common power, timing and communications infrastructure via a FieldHub, described in Chapter 8. Finally, the in-ice radio component, which provides the sensitivity to ultra high energy neutrinos, takes advantage of the RF clarity of the cold ice nearer the surface, at depths of up to 150 m. The reference design includes a total of 361 antenna clusters will be installed, on a 1.24 m grid.

Like IceCube, the design of IceCube-Gen2 takes into account the constraints presented by working at the South Pole Station. All components must be low power, to minimize power usage at the remote location. All items must be transported to the pole either by plane or traverse, and thus must be modular and straightforward to assemble on site. Due to the harsh weather conditions and the months-long polar night, it is not possible to land planes between February and late October, and during this time, field work is

impossible. During the Antarctic summer, the South Pole station can only house 180 people, a population that is shared with logistics personnel and other scientific efforts. As a result, the efficiency of installation of the instrumentation is a key consideration, as it must be deployed by a limited crew during the short summer seasons. Further details of the logistical requirements - and solutions, including the power, cargo and population can be found in Chapter 12.

4.6 Organization of Chapters 5-10.

In this Part II of the document, we present current details of the technical design for IceCube-Gen2. The description of the current reference design for IceCube-Gen2 is presented in Chapters 5-10, organized along the proposed work breakdown structure (WBS) utilized for cost and planning purposes. This work breakdown builds on the experience from the original IceCube MREFC construction project, completed in 2011, and the current IceCube Upgrade project scheduled for completion in 2026. In Chapters 5, 6 and 7 we describe the three detector array technologies to be deployed: In-ice optical array, in-ice radio array, and surface array, respectively. In Chapter 8 we describe the common data acquisition system (DAQ) used for all three array technologies, which also utilizes a common interface for power and communications. Chapter 9 describes data systems, which include collecting, processing, and transmitting the overall detector data presented by the DAQ, the computing infrastructure in the IceCube Laboratory (ICL), the detector control and monitoring systems, and the core analysis software framework and Northern Hemisphere data warehouse infrastructure. Chapter 10 describes the methods, instrumentation, and systems used to calibrate the detector arrays.

5 Optical Array

In this chapter, we describe the reference design of the optical component of IceCube-Gen2.

5.1 Overview

The reference design for IceCube-Gen2 will add an additional 120 strings of optical modules to the original IceCube observatory. A surface map of the new strings and their locations with respect to the existing array is plotted in Figure 57. IceCube-Gen2 lies entirely within the Dark Sector and encloses the existing IceCube array on three sides, while avoiding the South Pole skiway. In this design, we have departed from the regular hexagonal grid employed by IceCube in favor of a staggered "sunflower geometry." This was chosen to avoid straight-line rows and columns of strings which act as "corridors" through which muons can enter unseen into the detector, mimicking starting events from neutrinos (see, e.g., Ref. [105]). Design constraints included a maximum of 120 strings total to set an upper limit on the total construction time (see Part III). Within those constraints the design was optimized for performance, in particular high effective area and optimal angular resolution in an energy range from 10 TeV to 10 PeV. The string spacing is nearly doubled to 240 m to maximize the effective volume for astrophysical neutrinos.

Figure 58 shows the discovery potential versus the number of sensors on the string. Little improvement is achieved when adding more than 80 modules per string. Therefore, each string will support 80 optical modules while spanning a larger depth range, from 1,344 m to 2,689 m. Overall, the detector will encompass an instrumented volume of nearly 8 km^3. The design of the optical modules themselves has been improved to include multiple PMTs and improved glass transparency of the pressure vessel that, taken together, increase the photon collection rate by a factor of 4. In this section, we will motivate these design choices and quantify their impact on detector performance.

As reviewed in Sec. 3.1.1, the rate of recorded neutrino events with a contained vertex scales with the instrumented volume of the array. The detector hardware and deep drilling are the main drivers of the cost and logistical requirements; thus, for a fixed cost, the science potential will be maximized by reducing the density of instrumentation while increasing the spacing of the boreholes in which the instrumentation is installed. However, in order to fulfill the scientific goals, we must maintain the sensitivity to astrophysical neutrinos as well as the ability to calibrate the detector.

The proposed geometry of the IceCube-Gen2 optical array has been optimized based on our knowledge of the ice properties, which have been mapped in great detail over the three decades that the AMANDA and IceCube neutrino telescopes have operated near the Amundsen-Scott South Pole Station. The scattering and absorption lengths of photons in the South Pole ice have been found to increase with depth, up to ~1,300 m, below which the ice exhibits a layered structure as seen in Fig 49. This motivated the layout of the IceCube detector, whose optical modules are installed in the ice between 1,450 m and 2,450 m depth. The lower portion of IceCube, below a dust layer that

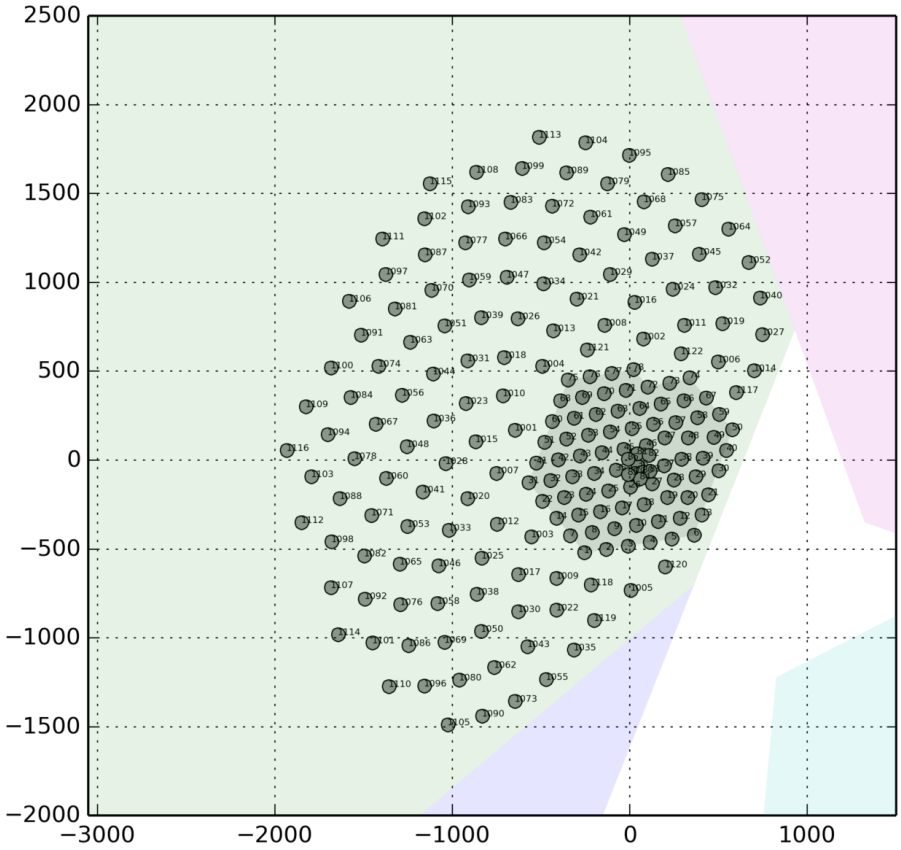

Figure 57: The surface map for the IceCube-Gen2 reference design is shown in relation to the original IceCube array (gray area). The location of the strings is marked with the dark green dots, while the shading orients the layout to the South Pole sector map, with the green shaded area showing the Dark Sector, the pink showing the Clean Air Sector, the white showing the skiway, and the blue outlining the Downwind Sector. The grid shows the distance in meters from the center of IceCube.

spans between 2,000 m to 2,100 m, has been found to have exceptional clarity, with absorption lengths in excess of 200 m.

Because of the improvement in ice characterization, the volume of the IceCube-Gen2 optical array can be increased by installing optical modules from 1,369 to 2,689 m, a vertical range that is about 1/3 longer than for optical modules deployed in IceCube. The deepest part of the ice is known to be highly transparent, therefore including this region is vital. The depth of the shallowest module position of 1,369 m is determined from the ice properties, and the deepest position is determined by the ice-bedrock interface, which is estimated to be around 2,780 m from various measurements [602, 603] in the IceCube-Gen2 region.

The horizontal spacing of the optical modules is increased from IceCube to IceCube-Gen2 by about a factor of 2, which increases the effective detection volume per string; however, the separation length is still close to the photon absorption length. This is important because one of the key calibration tasks, verification of local bulk ice properties, uses LED flashers on neighboring strings (Sec. 10.2.2.3). We have demonstrated that adequate calibration is possible with a string separation of 240 m.

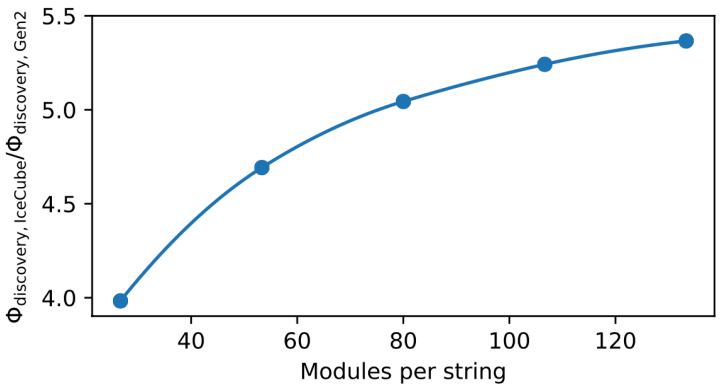

Figure 58: The discovery potential for point sources (E^{-2} spectrum) is plotted vs. the total number of optical modules on the string.

5.2 Requirements

5.2.1 Scientific requirements

To reconstruct complex events, it is essential to record enough Cherenkov photons. Thus, the project requires sensors with good surface uniformity, a wide dynamic range, and a time window that is large enough to capture all detectable photons. The requirements listed in this section ensure the scientific performance of the IceCube-Gen2 optical array outlined in Chapter 2 and Sec.3.1.1.

Photon detection efficiency: In Sec. 3.1.1, it was observed that an increase in photon collection efficiency results a lower energy threshold of a few TeV for throughgoing muons, thus compensating in part for the larger string spacing. (see Figure 34). This principle also holds true for shower-like events. The background veto efficiency near the threshold energy also increases with the photon detection efficiency of each module (or the total photon detection efficiency per string if the number of modules can be varied). Finally the event reconstruction benefits from detecting more photons.

Simulations [506] show a significant increase of the point source discovery potential when increasing the photon effective area beyond IceCube's DOMs. However, the increase is not linear, while the cost per string increases linearly with the number of optical modules. Therefore, we consider the most cost-efficient string design to be the one with 80 modules per string, each module with four times better sensitivity compared to the current IceCube DOM with standard quantum efficiency. With this configuration, we reach the string-wise photon detection sensitivity required to meet the IceCube-Gen2 science goals.

Uniform and directional sensitivity: The current IceCube sensors consist of one PMT pointing downward. One drawback of that approach is that the sensor records no azimuthal information and has reduced sensitivity to photons traveling downward. This results in a loss of information or a bias. For example, in IceCube, we cannot, with a single string distinguish whether a muon passes on one or the other side of that string. Therefore, it is valuable to achieve a reasonable sensitivity in all directions. A directional resolution of $\approx \pm 60^{o}$ adds valuable information to event reconstruction.

Timing precision: The photon arrival timing information is a vital parameter for reconstructing the direction and also the particle identity of an event. For example the characteristic double pulse structure of a tau neutrino interaction with a subsequent decay of the outgoing tau event requires precise tracking of the associated waveforms. The cascade angular reconstruction resolution, which is one of the most challenging reconstruction parameters for IceCube-Gen2, depends on the TTS (transit time spread) of recorded photoelectrons for different cascade energies; however, the dependence is only moderate up to a TTS of 10 ns. This reflects the fact that the substantial separation of the IceCube-Gen2 strings makes the reconstruction resolution less reliant on the timing precision, as many of the photons have undergone scattering in ice before arriving at the DOM surface. On the other hand, the TTS has a relatively minor effect on the reconstruction of muon tracks, as the the event reconstruction relies more on the topology of a large track length crossing the detector.

Time window: Photon time series in a PMT are observed over several hundred nanoseconds for typical events at lower energies. At PeV energies, for tracks or cascades, waveforms may extend to well above 500 ns. It is imperative to capture all the photons associated with a given event of interest for accurate reconstruction or to identify unusual waveforms. To achieve this, we implement a dynamically changing time window designed to capture all the photons until there is a sufficiently large temporal interval between late photons.

Linearity: The generated number of Cherenkov photons correlates nearly linearly with the deposited energy of the events, which for the optical component of the array will operate from TeV to beyond 10 PeV. The number of photons detected also depends not only on the number of photons generated but also on the proximity to the sensors. Indeed, the string closest to a track or the vertex of a cascade will also see the highest quality signals. Thus, a high dynamic range is required. The dynamic range has been a limitation for IceCube's high-energy events. For events above 100 TeV, more than 1/2 of the deposited charge of cascade events is not used because the waveforms are classified as too "bright." Figure 59 shows a waveform recorded by an IceCube DOM at a distance of about 30 m from the shower maximum of a cascade event with 2 PeV deposited energy. The PMT signal is highly saturated. Also shown is the waveform that was obtained based on the best fit of the event. The maximum of the expected or true waveform would have been more than a factor of 30 times larger than the recorded signal. PMT saturation as well as electronics dynamic range made the data from this DOM unusable. To have a faithful record of such signals in IceCube-Gen2, we set the science requirement for linear dynamic range of the sensor to record such rare energetic events of 2 PeV energy at a distance of 30 m from the sensor.

5.2.2 Mechanical requirements

Optical modules for IceCube-Gen2 must survive operations within the deep ice sheet and must be robust to the stresses encountered during deployment and transportation to the Pole. Thus, in addition to demands on optical performance outlined in 5.2.1, the modules must also adhere to the following mechanical specifications.

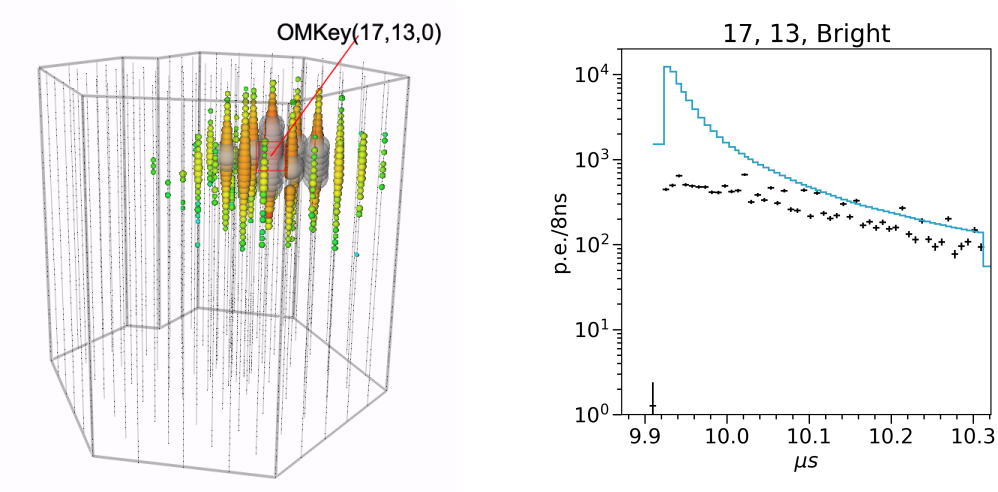

Figure 59: Left: An event display of the 2 PeV shower detected in IceCube with OM 13 on string 17 marked by the red line and box. DOMs that carry greater than ten times the mean total charge across all hit DOMs are classified as "Bright" (gray spheres) and excluded from use in reconstruction. Right: Observed (black) and expected (blue) distributions in time of the number of photoelectrons at IceCube DOM(17, 13), which is about 30 m from the reconstructed shower maximum of a 2 PeV particle shower. The expected distribution overshoots the observed data by a significant amount due to PMT saturation. The DOM is classified as "Bright" and currently excluded from IceCube event reconstruction.

Vibration and mechanical shock: Optical modules for IceCube-Gen2 will be produced at assembly sites on different continents and shipped to McMurdo Station on the coast of Antarctica via cargo vessels traversing the equator. The shipment to the South Pole may include LC-130 cargo aircraft. Alternatively, the modules may be transported overland from McMurdo Station to the South Pole via the South Pole Traverse (SPoT). This logistics stream necessitates that the optical modules meet the mechanical vibration rating (ASTM D4169 section 12.4 Y-axis only truck assurance level II 20min, air assurance level 40min), and the mechanical shock rating (Mil-Std-810F, Method 516.5 procedure II, 10g+,- each 6axis).

Size and weight: Drilling is a large cost driver. Heat transfer simulations [604] were done to minimize the diameter of the ~2,700 m deep holes yet ensure that the holes do not freeze during deployment. The larger the sensor the more effort is needed to drill the holes of the correspondingly larger size. This relationship breaks down for diameters smaller than 30 cm. Based on these studies, we require the sensor to be smaller than 35 cm in diameter and as close as practical to a diameter of 30 cm. Additionally, each module must meet deployment safety regulations, which requires a mass of less than 25 kg per module.

Pressure and temperature shock: In the reference design, eighty modules are installed along each string into a ~2,700m deep water-filled borehole drilled by the hot-water drill. After string installation, the borehole will naturally refreeze around the modules, during which the pressure around the optical modules will reach their maximum. The maximum pressure observed in the in-situ pressure measurements during freeze-in from the original IceCube deployment was over 55 MPa (~8000psi). The water pressure rating of the pressure vessel is therefore set to 70 MPa (~10,000 psi), the same

as for IceCube. Following the depth-dependent temperature profile of the ice (see Fig. 52), the operating temperature range will be between -40°C in the ice and 25°C room temperature, while the storage temperature rating is between -43°C and 50°C, to accommodate possible extremes of storage during transportation and in the ice. The temperature of the ice surrounding the deepest optical modules will be -8°C.

5.2.3 Power, bandwidth, and lifetime

The power budget and the maximum data readout bandwidth of each optical module are 4 W and 150 kbps, respectively (see Section 8). These limitations arise from the architecture of the downhole cable and the infrastructure at the South Pole and thus impose a significant constraint on the electrical system. Another crucial constraint arises from the fact that optical modules will be embedded in the ice, rendering them inaccessible for repair or maintenance after deployment. Survival of the modules during deployment and long-term operation of the observatory is critical to the success of IceCube-Gen2, which aims for a data-taking period exceeding ten years. The survival rate requirement is set similarly to that of IceCube, with a minimum of 95% of DOMs surviving after 10 years of operation. Thus, we estimate that the mean time between failures (MTBF) of the optical modules for IceCube-Gen2 must be 200 years. We note that the actual survival rate of IceCube far exceeds this requirement: Only 6 out of more than 5,000 optical modules were lost in the past 10 years of operation.

5.3 Main interfaces

The following is a brief description of the components and interfaces that form the power and communications pathways from the optical modules in the deep ice array to the IceCube Laboratory (ICL). A schematic view of the optical array and its interfaces is shown in Figure 60. Each of the DOMs has a penetrator cable assemply (PCA) that will deliver power, communication, and signals to and from the module.

- **Ice Communications Module (ICM)**: The ICM handles communications between a given in-ice device (e.g., IceCube-Gen2 optical modules) and the surface. In addition, it provides timing information to the optical module. The ICM handles all the “handshaking” required between the surface and individual in-ice modules such that communications happen transparently.
- **Penetrator Cable Assembly (PCA)**: The penetrator cable assembly is the physical interface between the interior and exterior of the optical module. The DOM’s glass pressure vessel housing has a penetrator hole, and the PCA has a feedthrough (deep sea penetrator) that safely and reliably transmits electrical power and signals through the pressure boundary. Outside of the pressure vessel, the PCA is a 70-MPa pressure-rated cable and connects to the breakout cable assembly (BCA). Inside the vessel, it is connected to the ICM on the main electrical board of the OM.
- **Breakout Cable Assembly (BCA)**: Each group of DOMs communicates through a wire pair in the main cable. Two wire pairs are bundled into a quad, a four-conductor cable that has a twisted quadrupole geometry. The purpose of the BCA

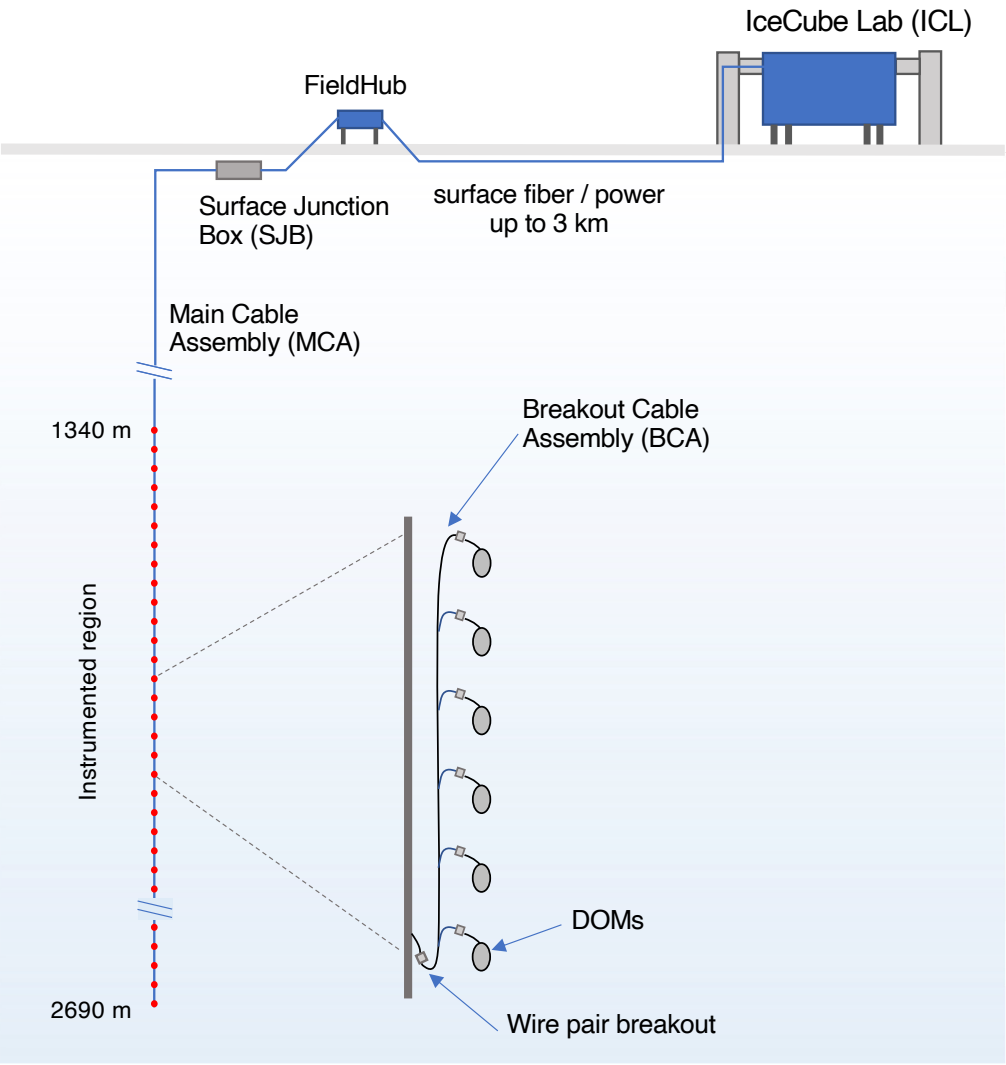

Figure 60: The overall architecture of the optical array is shown.

is to connect one of the wire pairs in the quad cables emerging from a "breakout" of the main cable to a group of 6 DOMs. The BCA has one connector on the main cable side and one connector for each of the 12 DOMs, 6 for each of the two wire pairs. In addition, it contains hardware address jumpers for identifying modules on the wire pair.

- **Main Cable Assembly (MCA)**: The main cable carries power and communications to each in-ice module via the breakout cables and provides mechanical support for all in-ice devices during deployment. The main cable consists of seven quad cables.
- **Surface Junction Box (SJB)**: The SJB is a passive junction box that provides mechanical and electrical connectivity between the MCA quads and the FieldHub. The SJB decouples string deployment from the FieldHub and surface cable installation. The SJB is connected to the FieldHub via short quad patch cables or a quad septet.

- **FieldHub**: The FieldHub can be thought of as a "detector to Ethernet" converter. It provides Ethernet connectivity to the IceCube Lab (ICL) via optical fiber runs and interfaces to both surface and in-ice detectors. It also provides White Rabbit connectivity for timing distribution.
- **Surface Network and Power**: Communications and White Rabbit data are communicated over optical fiber between the FieldHubs and the ICL. Power is supplied from the ICL to the FieldHubs via a copper power cable.
- **IceCube Lab (ICL)**: The ICL houses the computing servers running the data acquisition system, data filtering system, and data handling system along with power supplies, White Rabbit switches, and other networking equipment.

5.4 Reference design

Drawing upon the accumulated experience garnered from the construction and production of IceCube as well as the recent development of optical modules such as mDOMs [549, 550] and D-Eggs [551, 552] for the IceCube-Upgrade (shown in the left and right panels of Fig 38, respectively), we have established a set of optimal combinations of optical module features. One of the distinctive features of IceCube-Gen2 optical sensors is their elongated shape, similar to that of D-Eggs, which is a result of optimization between the required volume for the PMTs, drilling speed, and cost. Another feature is the inclusion of a large number of small PMTs within this confined space, akin to the design of mDOMs.

While we have developed two types of glass vessels and corresponding internal PMT arrangement designs, as introduced in Section 3.2.1, the majority of the developed components are common to both designs. Figure 61 illustrates the main components of the IceCube-Gen2 DOMs: several small PMTs, an electronics system consisting of several electronics boards, optical coupling silicone light guides referred to as “gel pads," a PCA, a glass vessel, several calibration LEDs, and associated internal structures (not shown). In this section, we describe the reference designs of these components to be employed in the IceCube-Gen2 DOMs. We intend to produce approximately 10,000 IceCube-Gen2 DOMs over a period of six years. Given the scale of production, we plan to procure critical components from multiple vendors in different regions to mitigate risk.

5.4.1 Photomultiplier tube (PMT)

Photomultiplier tubes (PMTs) serve as the primary components for the detection of Cherenkov photons in the optical array. The effective area of an optical module is proportional to the sum of the photocathode areas of the PMTs housed within a pressure vessel. To maximize the total photocathode area while ensuring compliance with the mechanical requirements for installation within a water-filled borehole, a likely optimal solution involves the combination of multiple small PMTs while restricting the number of channels to less than 20. This is due to the linear scaling of power and bandwidth with the number of channels.

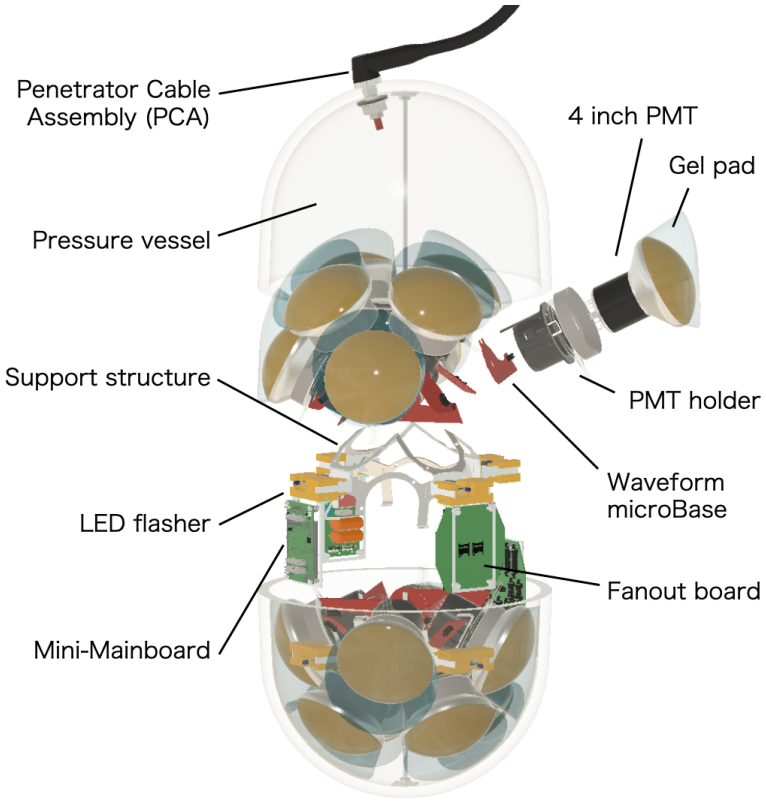

Figure 61: Exploded view of the Gen2 DOM candidate (16 PMT model).

Detailed studies of the internal arrangement show that the deployment of 4-inch PMTs results in cost-efficient optical modules with uniform sensitivity within 12.5-inch diameter pressure vessels. Both variations of the IceCube-Gen2 DOM, described in Section 3.2.1, utilize common 4-inch PMTs. However, the 4-inch PMT must be compact, with a maximum length of 106 mm and a neck diameter not exceeding 55 mm, where the latter includes the thickness of the high-voltage shielding.

The demands for a compact PMT design may result in performance degradation, including a decrease in collection efficiency and an increase in transit-time spread (TTS). To mitigate this risk, we conducted a thorough evaluation of the newly developed PMTs from two manufacturers during the early phase of verification studies. Prototype PMTs from both Hamamatsu Photonics K.K. (HPK) and North Night Vision Technology (NNVT) were studied (Figure 62). Over 50 PMTs have already been delivered, and we have verified that the prototypes meet the mechanical and optical performance requirements. The optical array will require a very large quantity of photomultipliers, approximately 170,000. For a variety of reasons, including things like risk, the project is pursuing a scenario of ideally at least two suppliers of PMTs.

The PMT quantum efficiency (QE) describes the efficiency that a photon hitting the photocathode is converted into an electron. The QE thus directly impacts the overall detection efficiency of the optical modules. Figure 63 illustrates the QE of 4" PMTs from HPK and NNVT, which exhibit different wavelength dependencies, while maintaining an overall efficiency similar to that of the current IceCube DOM. Figure 64 plots the typical transit time distributions of two representative PMTs from each vendor. It is essential to note that, as previously discussed in Section 5.2.1, simulation studies demonstrate that the TTS requirement is significantly relaxed to around $\sigma = 3.4$ ns due to the larger string separations of the IceCube-Gen2 array, as compared to the IceCube DOMs. Therefore, the observed TTS of both PMTs falls well within the required performance for the IceCube-Gen2 optical array.

The deep glacial ice is not only very pure but also exceptionally dark due to the absence of potassium and with it the absence of ^{40}K, the latter of which is a significant source of noise from radioactive decay in sea water. Indeed, the sensors are the primary source of noise followed by the photons generated from cosmic ray muons at a depth

Figure 62: Pictures of the custom designed short neck 4-inch Photomultiplier Tubes. The left photograph is the PMT produced by Hamamatsu photonics, and the right photograph is the PMT produced by NNVT.

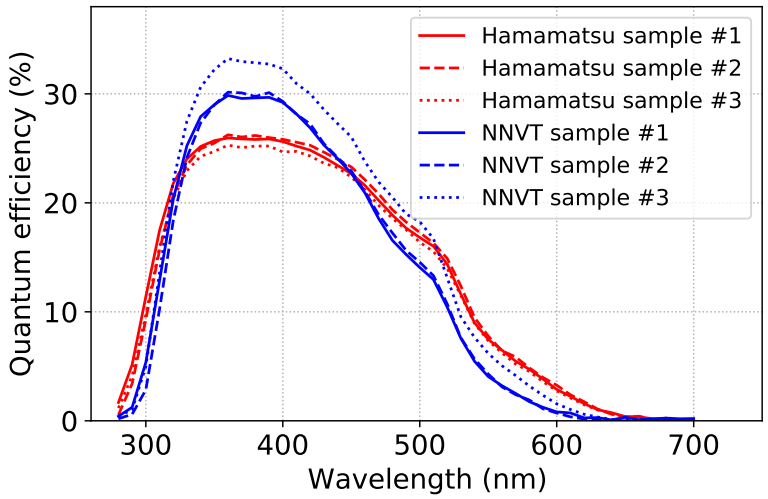

Figure 63: The quantum efficiency of HPK (red) and NNVT (blue) PMTs as a function of wavelength. The measurements were conducted using a laser with a spot size of approximately 70 mm in diameter, covering a significant portion of the 4-inch PMT cathode surface.

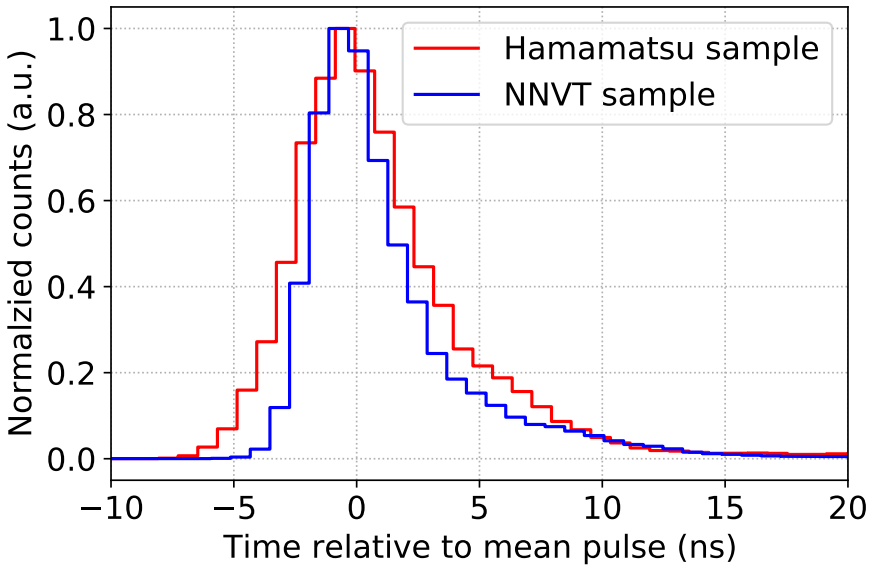

Figure 64: Typical transit time distribution of PMTs from HPK and NNVT. The numerical standard deviations of Hamamatsu and NNVT PMT samples are 3.5 ns and 3.3 ns, respectively, in the range from −8 ns to 16.8 ns.

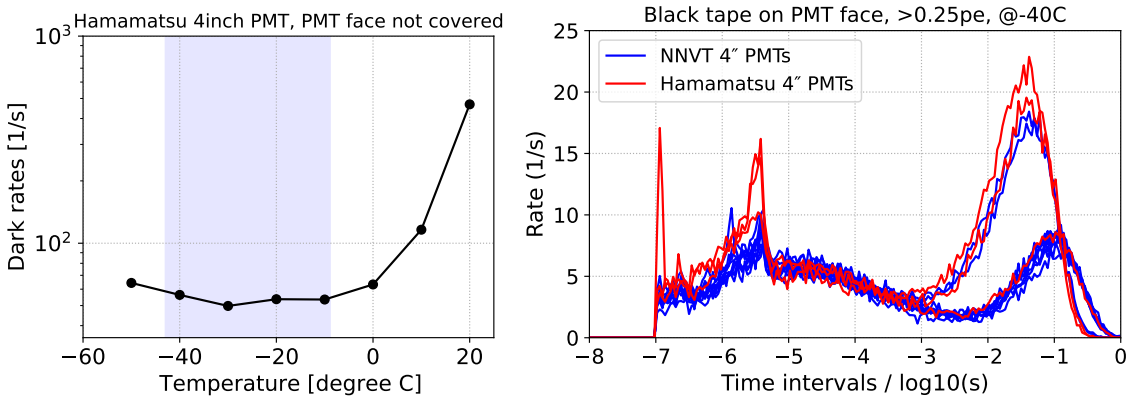

Figure 65: (Left) The dark noise rate of a Hamamatsu 4-inch PMT is shown versus temperature. The dark rate approaches a low value of 600/s and bottoms out in the operating temperature range of IceCube-Gen2 DOMs in the ice (Fig. 52). (Right) Dark rates as a function of the time interval of successive signals at $-40^{\circ}C$ for a threshold of 0.25 PE. Prototype PMTs from NNVT are shown in blue markers and lines, and prototype PMTs from HPK are shown in red markers and lines.

of 2000 m. The cold operating temperature in the deep ice almost entirely suppresses noise from the thermionic emission of electrons from the cathode, which is the dominant source of noise for most PMTs at room temperature.

Our objective is to maintain the dark noise of the PMTs at a level similar to that of the 10-inch PMTs used in IceCube, scaled down to the 4-inch PMTs. In Figure 65, the dark rate at a 0.25 PE threshold is shown as a function of the time interval of successive signals from several prototype PMTs. If the source of dark rate is purely random, the time interval of successive signals follows an exponential distribution with a time constant of the inverse of the total dark rate ($\mathcal{O}(\text{ms})$), and this contribution is called uncorrelated noise. Conversely, if the source is scintillation photons produced due to radioactive decays, the time interval becomes short ($< 10^{-5}$ s) and is referred to as correlated noise. IceCube's 10-inch PMT dark noise rate is 320 Hz with a time interval of $6\mu s$ at $-40^{\circ}C$ [605], representing an uncorrelated noise at the low temperature. This corresponds to 50 Hz for 4-inch PMTs, which is slightly higher than the measured values for the PMTs from both NNVT and HPK.

5.4.2 Electronics

The electronics design of the IceCube-Gen2 DOM requires the digitization of signal waveforms from each individual PMT, followed by low-level processing, buffering at the module level, and communication with surface computers for high-level event triggering and processing.

The PMT base, referred to as "wuBase" (short for waveform microbase), both generates the high voltage for the PMT and digitizes the signal waveform from the PMT. Figure 66 illustrates the PMT base design block diagram, and Figure 67 illustrates a prototype model of wuBase. The high-voltage circuitry is a Cockcroft-Walton generator fed from an LC resonator, with output regulated by the microcontroller, which also controls the duty cycle of the resonator input waveform. It requires 5 mW of power to

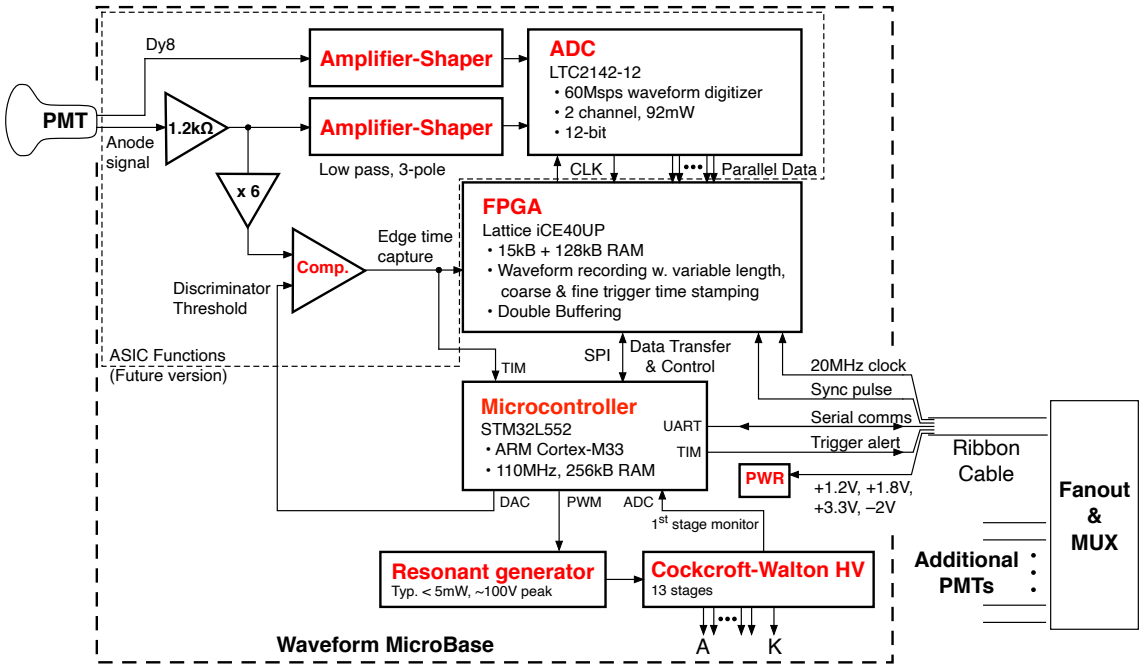

Figure 66: Functional block diagram of the waveform-digitizing PMT base.

achieve a PMT gain of 5×10^6. The same generator, including the feedback and control software algorithm, is also used in the IceCube-Upgrade PMT base (mDOM version).

Digitization is achieved by an onboard 2-channel continuous waveform digitizer, which operates at 60 MSPS. A low-power FPGA captures the digitizer output for intervals flagged by the output of a comparator, set at ~ 0.2 PE, including pre-trigger and post-trigger samples. The recordings have variable length to accommodate waveforms with the typical rich time structure seen in IceCube neutrino events, occurring at a wide range of distances and orientations relative to each module. One digitizer channel records the anode waveform as a series of 12-bit samples where single photons will have peak amplitude of ~45 counts in the final design (90 counts in the current prototype), and observed baseline noise is less than ± 1 ADC count. The other digitizer channel is connected to an intermediate dynode with a lower gain, which will result in a combined linear response from SPE level to $5{,}000$ PE/25 ns, allowing the resolution of important details even for the highest energy events expected (see Fig. 68).

The chosen digitization rate of 60 MSPS is supported by IceCube experience, considering the large string spacing in IceCube-Gen2 and the minimization of power consumption. The waveform is shaped to yield a FWHM of ~ 30 ns, giving a very predictable response to each SPE. Fitting individual SPE responses to a template, the resulting time resolution is $\sigma = 2.6$ ns, dominated by the PMT transit time spread. By deconvolving complex recorded waveforms as sums of SPE waveform templates, the time distribution of arriving photons can be resolved in bins of 10 ns, which helps distinguish energy deposition patterns of different neutrino event types. The first photon arrival time in each event is resolved even more precisely by capture of the comparator output edge in a delay line module in the FPGA. An ARM microcontroller on each PMT

Figure 67: The new PMT base is shown on the left. It includes the HV generator, a 2-channel digitizer for anode and dynode signal and a microprocessor + FPGA. The shape is optimized to accommodate the space requirements inside the DOM. The picture on the right shows two 4-inch PMTs with base attached.

base manages high voltage generation, data buffering and low level processing, and communication with the main controller board.

The optical module block diagram (Fig. 69) shows how the design is distributed between central boards interfacing with the main cable, and individual data-acquisition boards mounted on each PMT. The connections between these are made via intermediate fanout boards, with ribbon cables carrying power and digital signals for data and timing. A major factor driving the distributed architecture is the limited size of spaces available for electronics boards.

The central "mini-mainboard" power and controller sections use circuitry developed for the IceCube Upgrade with different board layouts. The power board connects directly to one wire pair of the main downhole cable, which carries power, communication, and time synchronization signals for up to eight optical modules. The communications and timing signaling are decoupled from power using a passive network, and a DC-DC converter delivers a low-voltage main power bus. The controller board hosts two major components, namely the FPGA-based ICM and an ARM microcontroller. The ICM implements modem functions, processes time synchronization signals, and manages flow of commands and data on the main cable interface to surface computers. The ARM microcontroller collects digitized waveform data from the PMT bases, stores them temporarily in a flash memory (Hitspool) on a fanout board, and sends compressed summary data or full waveforms upon request from surface computers. The ARM microcontroller also manages other optical module level tasks like calibration, including control of LED flasher boards connected by daisy-chain to a fanout board.

The data from PMT bases flows to the mini-mainboard ARM microcontroller over a UART (universal asynchronous receiver/transmitter) serial data interface that is multiplexed to select only one base at a time. This multiplexing happens on the two fanout boards, which are functionally integrated by ribbon cables between them. Each fanout board is connected by smaller ribbon cables to all the bases in the half of the optical module where it is mounted. Besides the UART interface for command and data flow, the PMT base cables carry multiple voltage supply rails, time synchronization signals

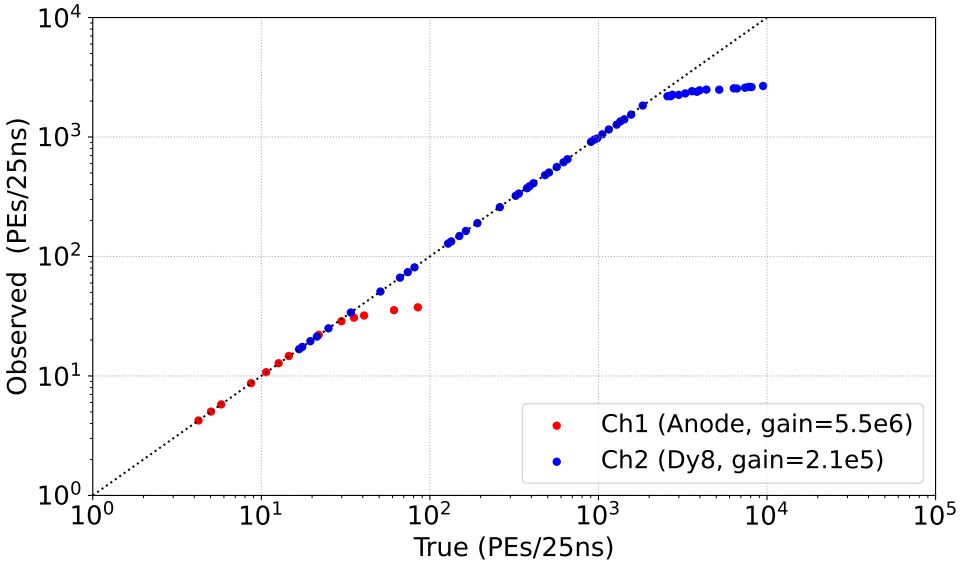

Figure 68: Linear dynamic range of the 4-inch PMT with base (wuBase, prototype design V1.4, mounted on a Hamamatsu 4-inch PMT). The quantity being compared is the peak intensity of a sustained pulse, which departs from linearity when the digitizer range is exceeded. Red markers represent the anode signal channel with full 10 staged amplification in the PMT. Blue points represent the second digitizer channel connected to the 8th dynode with lower gain. The prototype design (shown) provides a combined linear response up to 2,000 PE/25 ns, which can be extended to 5,000 PE/25 ns in an adjusted design using lower amplifier gain.

and a prompt trigger pulse. The fanout board produces the voltage rails from the main power bus and allows independent power control for each PMT base. A common time base is implemented by a 20 MHz master clock plus a synchronization strobe, both originating from the ICM and fanned out to all PMT bases. The prompt trigger signal from each base is a short pulse raised after any photon detection in the corresponding PMT, and these are all fed into an FPGA-based multi-PMT coincidence detector on the fanout board. The coincidence criteria can be programmed from the mini-mainboard microcontroller, which also reads the coincidence information in order to form optical module level triggers, which are forwarded to the surface.

The power consumption of the digitizer dominates the power consumption of each PMT base, which is constrained by the overall optical module power budget of 4 watts. One attractive option would be to replace the on-base DAQ electronics (discriminator, shapers, and digitizers) with a custom integrated circuit (ASIC), shown as a dashed line in Fig 66. An ASIC will significantly reduce the costs, power consumption, and physical size of the base while maintaining compatibility with the development version interface and software. The savings is possible because the ASIC design will be optimized for the IceCube requirements, so some of the power-hungry analog specifications for commercial digitizer chips (e.g., 750-MHz analog bandwidth) can be relaxed. The chip would be designed in well-understood 65-nm technology and would offer an 80% reduction in power for the analog electronics and ADC, from 107 mW/channel to 22 mW/channel. A safe fallback design would offer 30% power savings. These savings will have a ripple-through effect, simplifying power circuitry throughout the project. IceCube-Gen2 will have enough PMTs so that the design costs are amortized among many units, with a

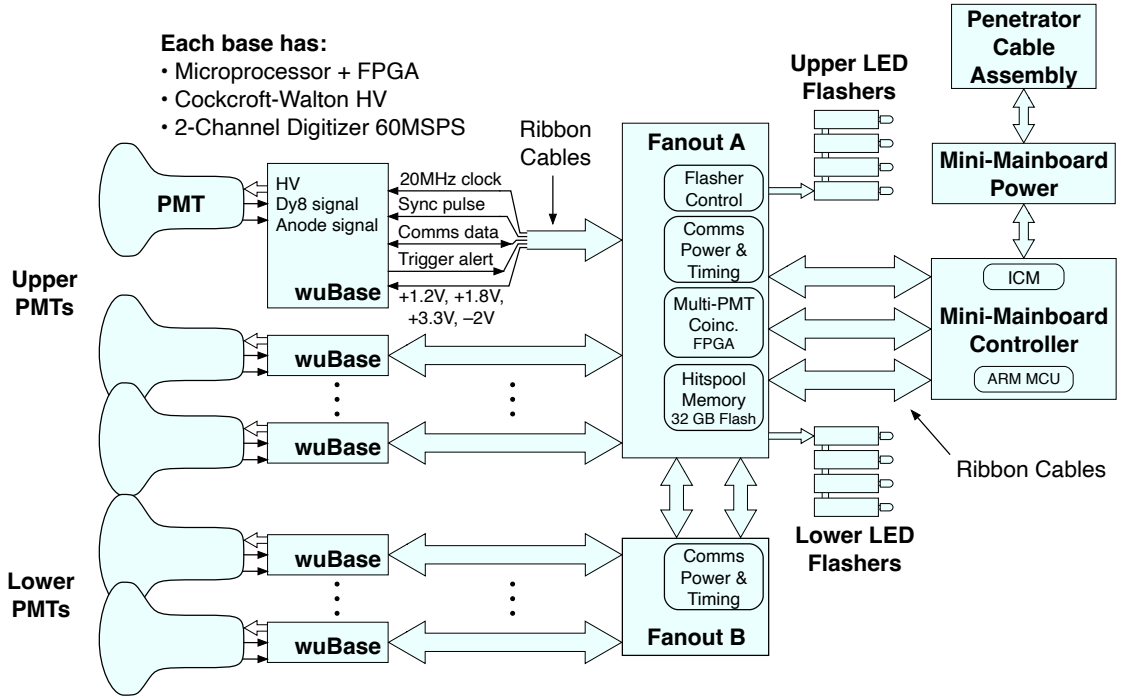

Figure 69: Functional block diagram of electronics in the IceCube-Gen2 optical module.

projected $3.5 M cost savings. It is important to take into consideration that the ASIC approach takes time to design, therefore funding needs to start about 2 years before chip production starts.

5.4.3 Gel pad

Photons propagated through the ice enter the glass vessel and eventually arrive at the PMT cathode surface. Discontinuities in the refractive indexes of materials between the glacial ice and PMT glass must be minimized to efficiently capture Cherenkov photons. The air gaps between PMTs and pressure vessels are filled with UV-transparent conical-shaped silicone elastomers called “gel pads." Figure 70 (left) depicts a picture of the prototype gel pad. The gel pad consists of the same UV-transparent silicone elastomer used in the D-Egg and mDOM, which is a custom-designed silicone for neutrino telescopes. The attenuation of UV photons in the silicone within the relevant wavelength range is negligible, as shown in Ref. [551].

Figure 70 (right) illustrates simulation-based effective areas of IceCube-Gen2 DOMs with and without gel pads. The dotted line represents the case without a gel pad, i.e., air between the vessel and the PMT glass. The dashedline represents the extreme case in which the module is completely filled with gel (this mimics the mDOM design, which features an outer gel layer between the support structure and the pressure vessel; see Ref [606]). The solid black line depicts the performance with the gel pads, which is nearly identical to the gel-filled design. This suggests that the implementation of gel pads results in a significant reduction in the amount of silicone used in a module, making it a cost-effective approach.

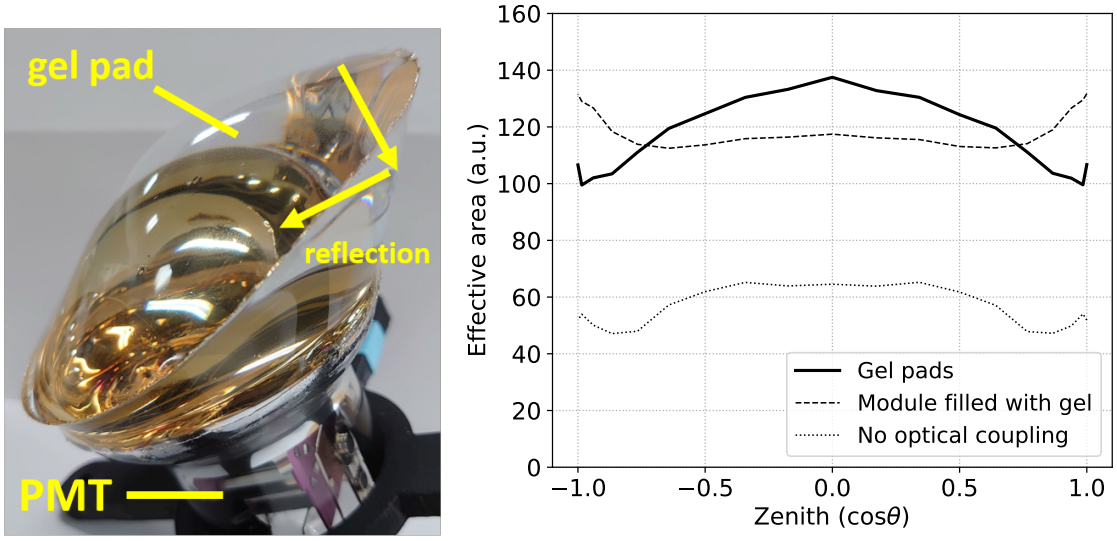

Figure 70: Left: Picture of a gel pad. Photons are internally reflected at the boundary of the air-gel surface. Right: Comparison of the effective areas of a complete IceCube-Gen2 DOM (18 PMT model with Hamamatsu 4-inch PMT) for three different designs: gel pads (solid line), module filled with gel (dashed line), and no optical coupling (dotted line).

The gel pads must be firmly attached to the internal surface of the glass vessel to achieve optimal performance and prevent subsequent detachment. For this purpose, the gel pads have a wall-shaped protrusion along the edge of the front side, which has an open gap for filling liquid gel. Figure 71 shows a schematic diagram of the attachment process, which makes it possible to compensate for unevenness of the glass surface. First, the preformed gel pad is pressed against the inner surface of the pressure vessel, and, afterwards, the liquid elastomer is poured in from above. With this procedure, more than 10 prototype gel pads have been successfully produced so far.

5.4.4 Pressure vessel

Two pressure vessel designs have been developed. Table 8 lists the basic parameters of the two designs, and Figure 72 shows the prototype vessels of the two designs. The Model-16 design can accommodate 16 4-inch PMTs, while the slightly more elongated Model-18 design is optimized to accommodate two additional 4-inch PMTs at the poles.

Both the Model-16 and Model-18 vessels have undergone verification of their pressure rating in a hyperbaric chamber test at a maximum pressure of 70 MPa (10,000 psi) with mechanical compression measured continuously. The measured strain was proportional to the applied pressure and in good agreement with the expected strain from finite element (FE) simulations. The reduction in diameter was measured to be 3 mm and was found to be linear in pressure and fully reversible up to the tested maximum.

The initial prototypes of the Model-16 and Model-18 vessels have been produced by Nautilus and Okamoto Glass, respectively. Nautilus manufactured the mDOM pressure vessel, and Okamoto Glass fabricated the D-Egg pressure vessels for the IceCube Upgrade. Both companies have indicated the ability to manufacture both designs. Thus,

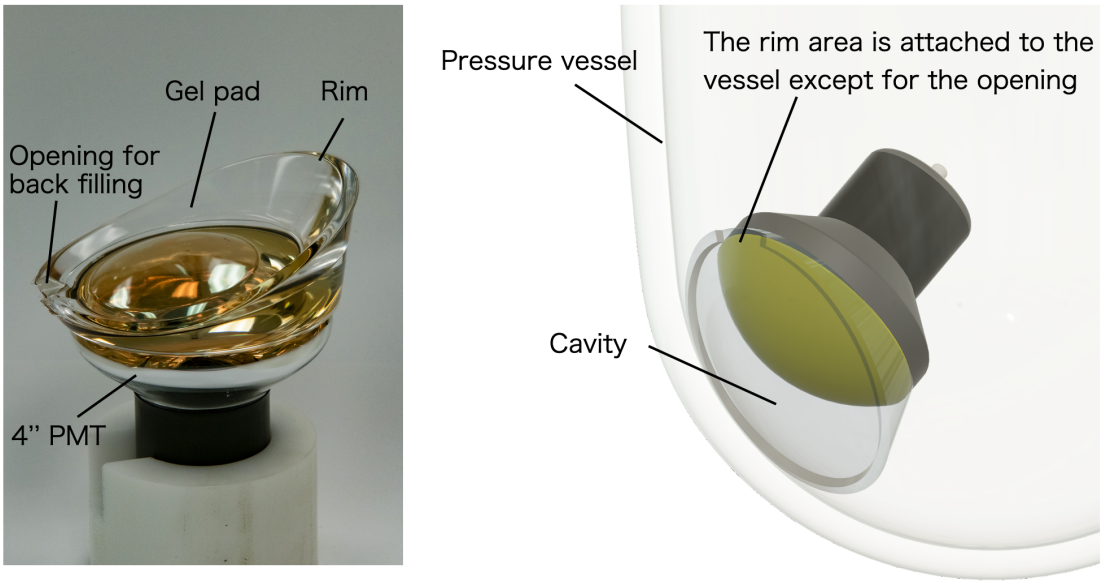

Figure 71: Left: Casted gel pad on a four-inch PMT. Each gel pad has 5 mm width rim to seal the cavity inside for the back filling. An opening on the left is used for the back filling port. Right: The rim of each gel pad is pushed to the pressure vessel to seal the cavity. Additional gel is poured from the opening on the top until the cavity is filled.

	Diameter [mm]	Height [mm]	Wall thickness [mm]	Weight [kg]
Model-16	313	444	12.0 (uniform)	10.8
Model-18	318	540	12.5 (poles) 16.5 (equator)	16.9

Table 8: Basic parameters of the two pressure vessel designs.

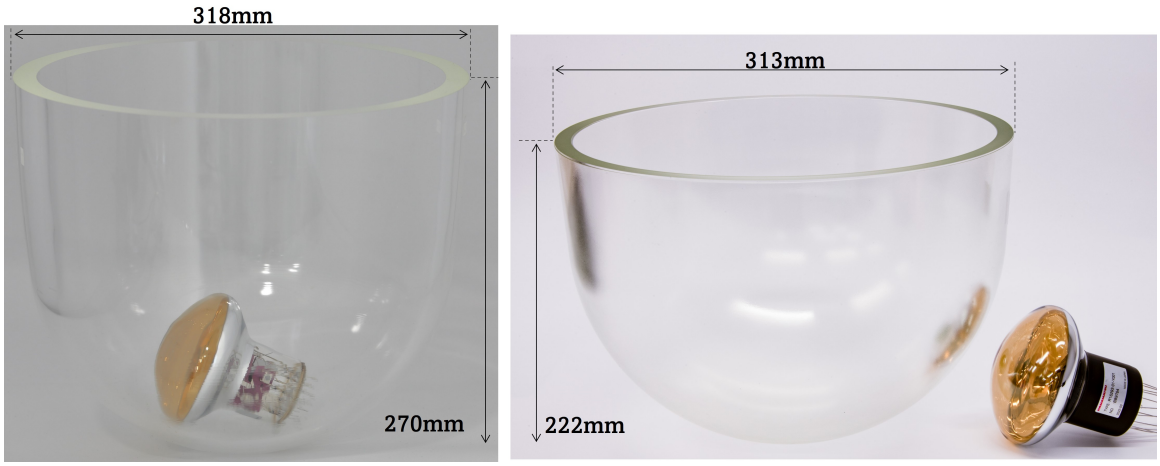

Figure 72: Pictures of two prototype hemispheres of pressure vessels for two variant designs: Model-18 (left) and Model-16 (right) with a 4-inch short-necked Hamamatsu PMT.

	Activity [Bq/kg]	
Isotope / Chain	Okamoto	Vitrovex
K40	2.55	61
U238	0.21	4.6
Th232	0.14	1.3

Table 9: Activities from radioactive decays of K40 and the three natural decay chains. (*) For U235, a concentration of 10% of that of U238 was assumed, as measured in the Vitrovex glass.

we anticipate that both companies will produce glass vessels during mass production once the final design has been selected. This reduces risk and minimizes long-term production and transportation costs.

Nautilus glass from Vitrovex and Okamoto glass possess comparable optical properties, with a transmittance of greater than 50% for wavelengths greater than 320 nm and nearly 100% for wavelengths greater than 370 nm (glass thickness of 12 mm, corrected for reflections) (Fig. 73). The cutoff at shorter wavelengths is consistent with that of the PMTs. In addition to transmittance, optical activity is another crucial property of the pressure vessel. This is a result of the radioactive decays of impurities in the glass, which produce light in the visible range through Cherenkov radiation and scintillation. The radioactive contamination of both glasses has been measured during the development of optical sensors for the IceCube Upgrade.

The Okamoto glass was found to have a reduced concentration of both K40 and natural decay chain isotopes compared to Vitrovex from Nautilus, as shown in Table 9. The increased optical activity in the Vitrovex glass together with any significant contributions from the PMT glass housings will be compensated for by in-module software that filters out temporally correlated signals from radioactive decays. This has proven to be very effective and will already be implemented for the mDOMs in the IceCube Upgrade.

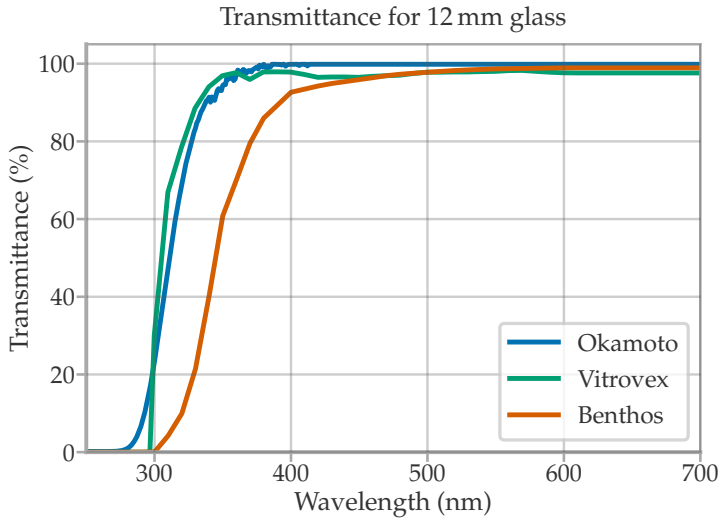

Figure 73: Transmittance for 12 mm thick borosilicate glass from Vitrovex, Okamoto, and the glass used in the IceCube DOM pressure vessels (Benthos) as function of wavelength. The measured values have been corrected for Fresnel reflections.

5.4.5 Internal structure

Within the pressure vessels, a hemisphere contains either eight or nine PMTs and is supported by a structural framework. The support structures for the two pressure vessel designs are based on similar principles. The internal architecture of both designs features a central rod as the point of reference for the internal configuration. A PMT holder, made of folded sheet metal, encases the central rod. The folded metal plate features circular apertures through which PMTs is inserted. In the case of Model-16, the central rod is directly attached to the glass vessel. For Model-18, the rod is supported around the central PMT due to the presence of additional PMTs at the top and bottom of the vessel.

As previously stated, the gel pad features a rim that is firmly pressed against the wall, followed by the injection of silicone gel to ensure firm adhesion. This requires a mechanism that applies constant pressure but is also flexible enough to compensate for the contraction of the pressure vessel by several mm during deployment due to the high pressure. Two mechanisms have been developed for the PMTs to apply outward pressure. The first mechanism uses a bushing bearing to protect the PMT glass from the sheet metal and allows the PMT to move back and forth along its axis. An inflatable bladder is used to move the PMTs outward, and epoxy is pressed into the bladder and cured. Epoxy was chosen instead of a liquid to prevent subsequent leaks from causing the bladder to collapse. The compressible foam collar around the neck of the PMT enables elasticity of the mechanics in response to shrinkage of the module due to outside pressure. The second mechanism is a relatively simple design made of six metal springs. During installation, the spring mechanism is in the retracted position. After release, the springs press the gel pads of the PMTs against the pressure vessel glass. Figure 74 shows the partially integrated prototypes of each model.

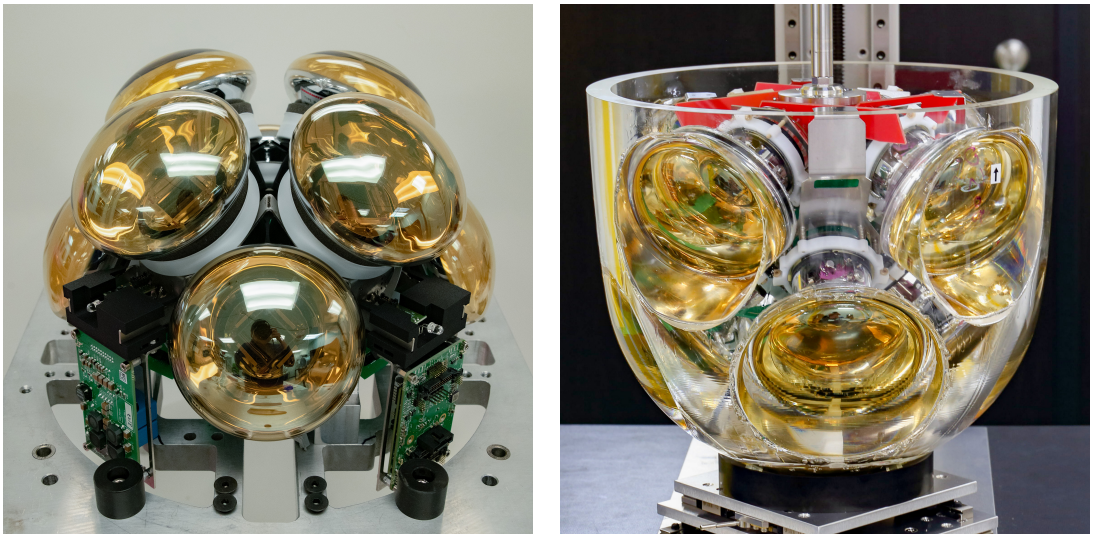

Figure 74: The left photograph shows prototyping of Model-16, where the PMT assemblies without gel pads, electronics boards, and flasher boards are mounted on the metal frame. The right photograph shows a prototype Model-18. All 9 PMTs in a hemisphere are optically coupled to the pressure vessel.

5.4.6 Photon detection performance

Simulation studies were performed to optimize the placement of PMTs and the design of gel pads with respect to uniformity and mechanical constraints. Figure 75 presents effective areas of optical modules of three generations of optical sensors:

1. IceCube DOMs with a single PMT
2. IceCube Upgrade optical modules: D-Egg and mDOM
3. IceCube-Gen2 DOMs in two design variants with 16 and 18 PMTs

The effective area of the optical modules for a given direction is defined by the equivalent physical cross section of the module for which 100% of photons from a plane perpendicular to the direction are detected. We evaluated the effective area of each optical module by using a Monte Carlo simulation based on Geant4 [607]. The simulation flow follows an injection of photons in a given direction to the optical modules. Photons on the surface of the optical module are propagated to the cathode of a PMT. There, they are converted to photoelectrons based on measured quantum efficiencies and angular responses in the laboratory.

The IceCube-Gen2 optical modules have been designed to achieve improved sensitivity compared to the previous IceCube DOMs. In order to quantify the integral gain in the photodetection potential, we consider the entire Cherenkov spectrum and propagate it through the ice. Figure 76 shows the relative gain in photodetection vs. propagation distance compared to a nominal IceCube DOM. Since the spectral sensitivities of the new designs are not fundamentally different—they still use PMTs inside a glass pressure vessel—the relative gain does not depend strongly on the distance.

Model-18, which utilizes 18 PMTs, features an effective area about 4.4 times larger compared to the IceCube DOM (NNVT 4-inch PMTs, propagation distance 50 m),

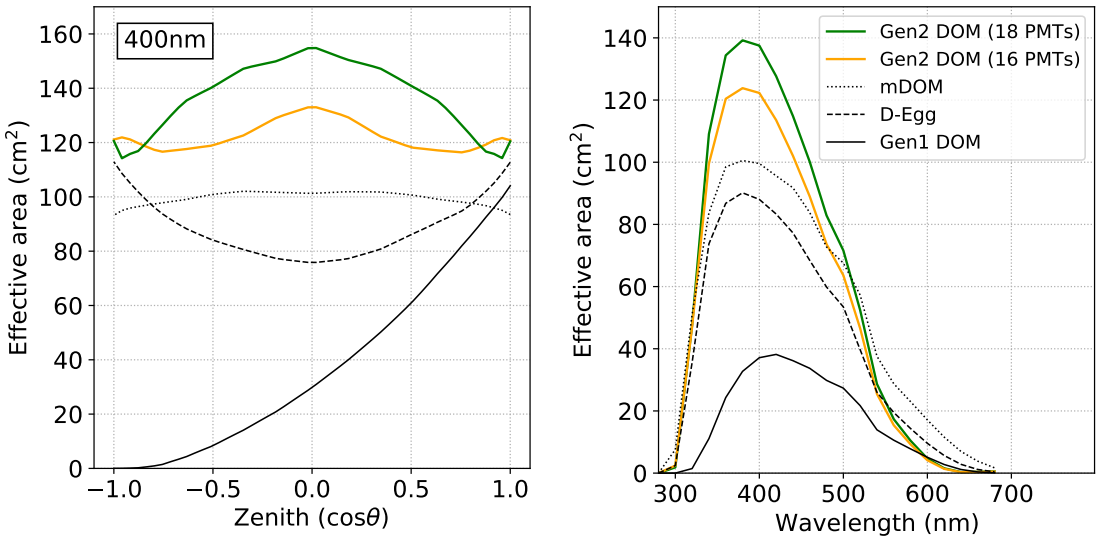

Figure 75: Comparison of the effective area as functions of zenith angle (left) and wavelength averaged over solid angle (right). Results of IceCube-Gen2 DOM candidates, 16 and 18 PMT models are compared to IceCube-Gen1 DOM, D-Egg, and mDOM. For each IceCube-Gen2 DOM candidates, measured quantum efficiency of NNVT 4-inch PMT is assumed.

where both PMT options (see Section 5.4.1) show comparable performances. Model-16 with 16 PMTs has an effective area about 3.9 times larger.

The overall photodetection efficiency gain of a factor of four is a robust basis for the performance and sensitivity studies presented in Chapters 1 and 2.

5.5 Alternatives considered

The success of the IceCube-Gen2 project relies heavily on the performance and reliability of the reference optical sensors, which have been designed based on the experience and knowledge gained from IceCube and more recently from developing the mDOM and D-Egg sensors for the IceCube Upgrade. While the design is well-suited for the project's needs, certain challenges remain, such as the arrangement of 16 or 18 PMTs inside the vessels with a diameter of 313 or 318 mm, as discussed in Section 5.4.5. Additionally, ensuring the optical coupling of the PMTs to the pressure vessel glass is a critical issue, as described in Section 5.4.3. To supplement the reference design, alternative concepts have been considered.

5.5.1 mDOM-like support structure for IceCube-Gen2 optical modules

The mDOM optical sensor employs a half-dome-like support structure made from PA12 to mount the PMTs, as illustrated in Fig. 77. The gap between the pressure vessel and support structure is filled with silicone gel, which is cured to provide mechanical support. To enhance sensitivity, reflectors made of coated aluminum are placed around the PMTs and reflect photons toward the PMTs. This design was no longer pursued for IceCube-Gen2 because of the significant additional costs compared to the sheet

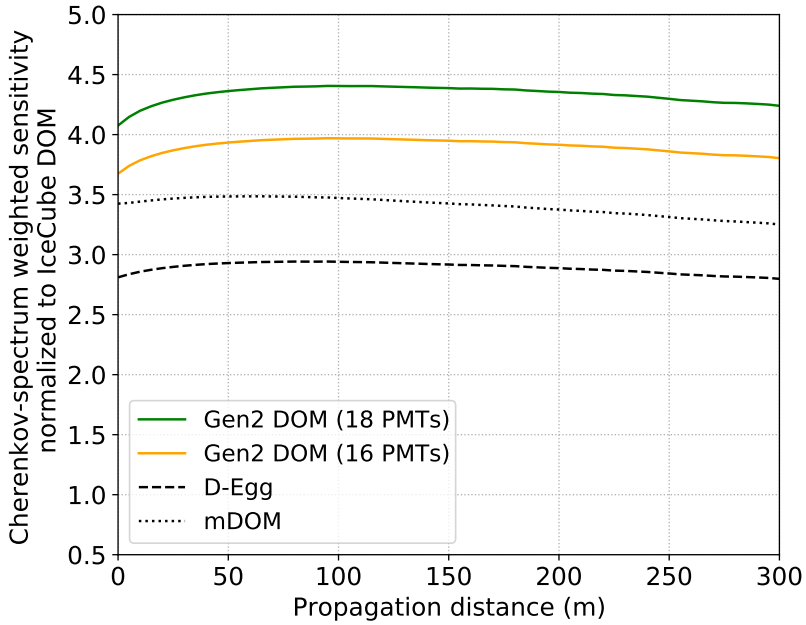

Figure 76: Comparison of Cherenkov-spectrum weighted effective areas of IceCube-Gen2 DOM designs and IceCube DOMs. The vertical axis is effective area normalized to the result with IceCube DOMs, and the horizontal axis is the photon propagation distance from the generation point to the module. Solid lines of IceCube-Gen2 DOM 16 and 18 PMT options represent the results assuming measured quantum efficiency of NNVT 4-inch PMT.

metal approach. Another reason is that the approach requires more gel, which implies greater cost and weight with no benefit. Nevertheless, the mDOM support structure design could be adapted to the IceCube-Gen2 optical module requirements, including its smaller vessel diameter of ≤ 320 mm (compared to the mDOM's 360 mm).

5.5.2 The D-Egg design

The D-Egg (Fig. 78) is based on the IceCube DOM with enhancements made to improve photon detection sensitivity and reduce deployment hole size for cost savings. The D-Egg features two 8" high-quantum-efficiency (HQE) PMTs in a UV-transparent pressure-resistant glass with an electrical readout board in between. Figure 76 compares the effective areas of the D-Egg for Cherenkov light propagated through ice against other designs. For a typical distance of 50 m one can see that the D-Egg has an effective area that is 24% smaller than that of the Model-16 design and 31% smaller than the Model-18 design reference optical modules. This means that a correspondingly larger number of D-Egg optical sensors per string would be required to achieve the same string-wise sensitivity as the reference optical module designs. In addition, the D-Egg design has little directional and no azimuthal sensitivity. Nevertheless, with its narrow shape (diameter 300 mm) the effort to adapt it to the IceCube-Gen2 optical module requirements is expected to be moderate.

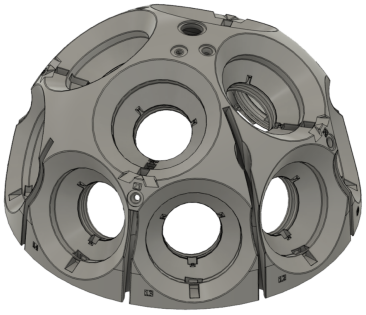

Figure 77: Lower hemisphere of the support structure for the mDOM sensor in the IceCube Upgrade. The PMTs are inserted in the conical openings and fixed with O-rings. Reflectors are mounted in the outer part of the openings to enhance light collection efficiency.

5.6 Additional photon-collection components

While the reference design of the optical modules will satisfy the scientific requirements of IceCube-Gen2, additional low-cost options have been considered as external photon collection component modules. Two strategies that are in an R&D phase focus on taking advantage of the high UV transmissivity of ice by using wavelength shifting approaches.

5.6.1 Wavelength shifting add-ons

One example for such modules consists of a few narrow, meter-long (diameter < 30 cm) photon collection tubes made from a wavelength shifting material (WLS). An optical coupling connector is attached externally to one of the PMTs in the reference optical sensors described in Sec. 5.4. The WLS tube collects and converts UV photons where the Cherenkov spectrum peaks in the ice to wavelengths where the PMT has a higher sensitivity. The optical coupling connector guides the photons to the PMTs inside the pressure vessel of the reference optical sensors. Because this design requires no additional photon sensor, it can be a cost- and power-effective complement. However, the photon time resolution is reduced compared to the reference optical sensors, since the exact impact point on the meter-long tube is unknown.

One of the WLS tube approaches is inherited from the WOM [608, 609]. The WOM has demonstrated high light collection efficiency (>40%) over large tubes. While high collection efficiency can be expected, transporting many long fragile glass tubes may not be feasible. One alternative design is a WLS tube made with WLS fibers surrounding a flexible material for more accessible transportation and integration, with a less efficient photon collection. Another idea that has been considered is the design combined with WLS, dichroic mirrors, and broadband mirrors as described in [610].

5.6.2 Wavelength shifting fiber approach

The fluorescent optical module (FOM) is an innovative light sensor design that is still in an experimental phase. Sensors used for neutrino telescopes, in deep water or ice, typically use pressure vessels which entirely enclose the light collection and electronic

Figure 78: A D-Egg module designed and built for the IceCube Upgrade. The D-Egg sensor is sealed in the UV-transparent glass housing with the waistband around the equator. Each PMT is carefully fixed in place in either an upper or lower glass hemisphere by using a UV-transparent optical coupling gel. Inside are the electronics mainboard, calibration devices (cameras, LED flashers), and magnetic shielding.

signal processing components. In the FOM (fig. 79) the wavelength shifting light collector (WLC) is situated externally to the pressure vessel in direct contact with the ice. The WLC is an assembly of plastic light guides that convert ultraviolet (UV) Cherenkov light into longer wavelengths and guide some of this emitted light to a small light detector within the pressure vessel.

The FOM can use a relatively small (3 inch) photomultiplier tube to collect the WLC output. The WLC comprises plastic lightguides doped with a fluorescent compound having an excitation wavelength optimized for the UV Cherenkov spectrum in ice. The use of wavelength-shifting light guides introduces a significant inefficiency but, because of their low cost, allows the effective light collection area of the WLC to be much larger than the effective light collection area of the PMT collecting its output. Limitations of this approach are attenuation in the light guide and an increase in ambiguity of photon arrival time. Initial measurements and simulations indicate that a FOM with a meter-scale WLC comprised of commercial wavelength-shifting fibers could provide the equivalent detection area of 2-3 IceCube DOMs. Several FOM prototypes will be deployed during the IceCube Upgrade.

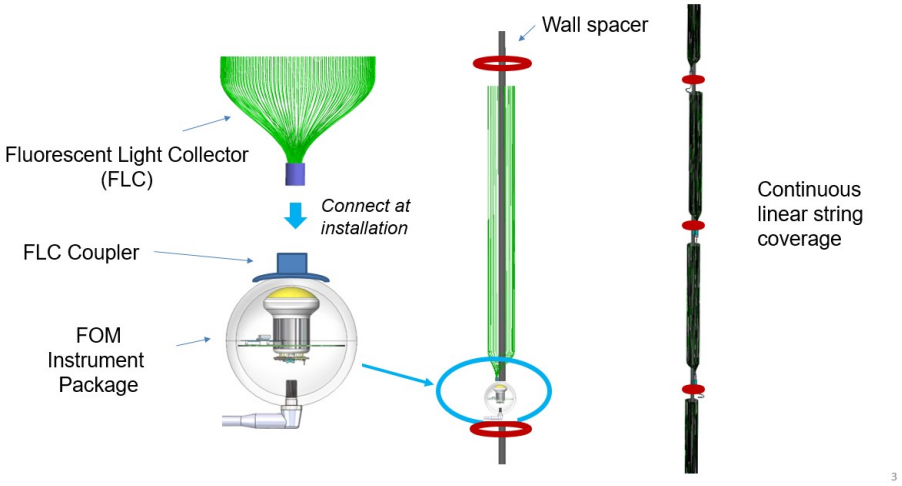

Figure 79: A FOM with the wavelength shifting lightcollector on the string

.

5.7 Production sites and test plan

The IceCube-Gen2 schedule envisions 10,000 sensors produced over a 6 year period. To achieve this, optical modules will be integrated at several production sites located including in Japan, Europe, and the United States. Each site will use the same integration tools and procedures to ensure uniformity among the produced modules. These procedures include not only module assembly, but also common quality control and testing plans. Several facilities have been constructed for production and testing of IceCube Upgrade optical modules, which also feature multi-PMT designs. The same facilities and similar integration procedures can be used for assembly of IceCube-Gen2 modules to leverage the expertise and infrastructure that have been developed at these sites.

5.7.1 Module integration

The reference sensor design for IceCube-Gen2 contains several components that are challenging to repair after integration into the pressure vessel. Therefore, module sub-components will be tested and characterized prior to integration, with the results recorded to a common database for posterity.

Assembly of the waveform-digitizing bases and PMTs will be performed at the PMT production facility. Batches of PMT+base assemblies will then be distributed across various collaborating IceCube-Gen2 institutions, where they will be operated inside large climate chambers over a range of temperatures from 20 to -40°C to ensure that parameters such as the gain stability, dark rates and timing characteristics meet the project design requirements. Dysfunctional assemblies will be analysed further and/or returned to the vendor, while functional assemblies will be shipped to module integration sites.

A production model has been developed on a smaller scale for the IceCube Upgrade. Here we briefly describe some aspects. Module integration will take place in ISO class 7 clean rooms, which allow for temperature and humidity control and tracking. Rooms are divided into stations that focus on a certain set of integration steps, which are connected via a conveyor belt system to facilitate module movement. Assuming 3 production sites, each site will produce approximately 12 modules per week with a workforce of 3 FTE. This production rate will yield approximately 600 modules per site, per year, which is consistent with the required yield over a 6 year period. The time and FTE required for module integration is estimated from prototype development during the R&D phase and experience from integrating mDOMs for the IceCube Upgrade. Throughout the integration process, a QR code on each component is scanned and entered into a production database, so that manufacturing, calibration and testing data collected prior to integration can be tracked to each module.

The first integration station is used for precasting the gel pads onto the PMT+base assemblies. At room temperature, the gel pads cure in approximately 72 hours. Therefore, this step will be performed on a batch of 192 (Model-16) or 216 (Model-18) PMT+base assemblies in parallel with other integration steps, so that enough units are prepared in advance to integrate 12 modules per week. In the next station, all components are integrated into glass hemispheres, with minor differences between upper and lower hemispheres.

In the final station, upper and lower hemispheres are joined together using a dedicated joining tool. This tool uses a vacuum pump-assisted lifting handle to flip the upper hemisphere by 180° so that it can be lowered onto the bottom hemisphere in a safe and controlled manner. Prior to complete closure of the sphere, the fanout board of the lower hemisphere is electrically connected to the mini-mainboard. Both hemispheres are then enclosed in a vacuum container, evacuated and back-filled with nitrogen gas to reach a final internal pressure of about 0.5 bar. The hemispheres are mostly held together with this under-pressure, but are wrapped around the seal with a special putty and cold-resistant tape to prevent inflow of air into the vessel.

5.7.2 Integrated module testing and characterization

After integration, each optical module undergoes a Final Acceptance Test (FAT) to identify failures or sub-optimal performance, and derive necessary calibration parameters prior to shipping and deployment. Each module is placed in a dark climate chamber and operated during several temperature cycles between +20°C and -40°C. This range approximates the operating temperatures that the optical modules are expected to experience. At each temperature extreme, a test suite is performed on each module to ensure operation of all subsystems. Modules are also required to survive a reboot after being cold-soaked at -40°C for several days. Dark noise rates are monitored regularly to catch anomalously high or variable rates. Finally, calibration LEDs are tested for basic functionality at the end of the FAT cycle to avoid exciting the photocathode and therefore biasing the dark rate measurements.

As second component of FAT involves module calibration. These final calibrations on integrated modules are primarily useful as an end-to-end calibration and cross-check of

the full system. The optical sensitivity, linearity, transit time and transit time spread are calibrated using a pulsed 400 nm laser and a filter wheel (for intensity control) coupled to optical fibres that deliver light to each PMT.

FAT will be performed on several dozen modules in parallel, with the exact capacity depending on the test site, and lasts approximately three weeks with a workforce of 2 FTE. Modules that pass FAT are fitted with a harness that attaches to the main cable during deployment and are packaged into individual transport boxes. These boxes are specially designed to allow for easy access to the PCA, such that final communication tests can be performed after transport to the South Pole prior to deployment.

5.8 South Pole test strategy

A South Pole Acceptance Test (SPAT) will be performed to ensure that the optical modules have arrived at the South Pole without damage. Each module is verified for functionality before installation.

Included in the SPAT setup are the hardware and software for performing limited functional testing of the DOMs. All testing at the South Pole implies operation in the harsh temperature, humidity, and pressure of the polar summer environment. Operations in a tent will afford protection from wind. All modules will remain in their shipping containers on transport sleds, with connector access provided by container access holes. The overall concept follows similar procedures developed for IceCube and for the IceCube Upgrade.

Specifically, the SPAT tests will draw from the suite of mature IceCube Simple Test Framework (STF) tests. For each iteration of the SPAT test suite, the framework will identify each module and initiate a series of functional tests for the associated device type. All testing is automated after the modules are mated to the test cable.

Communications and access are verified for each in-ice device component, including hardware, software, and firmware. Functionality of each hardware science sensor is exercised, including analog input channels, photomultiplier tubes, cameras, and other sensors. All science channels are exercised on devices with redundant channels. With this test, the basic functionality of each sensor is verified.

For each test, measurements, pass/fail evaluations with decision thresholds, and the test hardware and software identification data are retained. Information is saved to a local archive and uploaded to the project test and configuration management database.

5.9 Production schedule

The overall construction schedule at the South Pole is driven by the drilling schedule. The DOM production schedule is designed such that there is never a shortage of sensors at the South Pole. The logistics chain of transportation via vessel to Antarctica and then by plane or overland transportation is factored in to derive a production schedule that ensures continued availability of sensors installation at the South Pole. A typical construction field season may need a supply of 20 strings or 1,600 DOMs.

The initial two strings worth of IceCube-Gen2 optical sensors must be delivered to Antarctica by the end of previous year of the first drilling season. This is required so that we are able to proceed to SPAT before a new drilling season starts. In the following drilling years, the number of optical modules just sufficient for the season's activity will be delivered so that there are always two string's worth of extra optical modules on site.

Following the first year production, the production rates are expected to ramp up to 60 DOMs/month at each site which results in 1,800~2,160 modules per year. The production will stay at this rate for approximately 5 years until complete.

5.10 Risks and risk mitigation

Risks are being considered taking into account the experience from IceCube-Gen1 and the IceCube Upgrade project. Because deployed optical sensors cannot be replaced, high reliability requirements are critical. High reliability in was achieved through a range of measures, first and foremost through application of the concept of design for reliability and design for testing. Design for reliability with elevated standards in part selection. Finally, extensive testing programs (Final Acceptance Test or FAT; Sec. 5.7) have been developed over the past twenty years of IceCube and has played an important role in extremely low failure rate of installed optical modules (between 2013 - 2023, only six out of five thousand modules failed). Most failures occur during installation or within weeks of installation, especially during the refreeze process; still 99% of IceCube sensors are in normal operation twelve years after installation.

Additional risks in schedule delay for production are mitigated using proven designs and a long development cycle. Key components may have long lead times, an increased risk in the era of post-COVID19, and securing components early and having multipe sources for critical parts is an important part of risk mitigation. This has been achieved for the highly specialized and critical components: the glass pressure housing (Sec. 5.4.4) and the photomultipliers (Sec. 5.4.1).

Candidate IceCube-Gen2 optical modules are currently under development with the plan to install a small number (approximately 10) of them during the IceCube Upgrade installation.

5.11 Summary

High-energy neutrinos are detected via the Cherenkov radiation induced by the secondary charged particles produced in neutrino interactions in ice. The temporal, directional, and geometrical distributions of the Cherenkov light are measured using a large-scale optical array in the transparent glacial ice to enable precise reconstruction of incoming neutrino properties. The IceCube-Gen2 optical array will extend its volume to eight times that of the IceCube array with only a 50% increase in the number of strings by increasing the string separation. The large detector volume will improve the muon track resolutions. To further optimize point-source sensitivity for IceCube-Gen2, a new optical module design is required, which features high photon detection efficiency within a compact, pressure-tight glass housing while maintaining otherwise similar performance characteristics as the original IceCube design. Two variants of this

module have been developed, utilizing the same methods and technologies but with slight variations in the glass vessels and internal structures.

The key components of the optical modules, the photomultiplier tubes (PMTs) from two manufacturers, meet the requirements for the IceCube-Gen2 DOM. Most notably, we have presented a module design with an increase in sensitivity by a factor of 4 compared to the IceCube DOM allowing for the larger string spacing. The electronic components have undergone significant advancements, transitioning from the single PMT IceCube DOM design to a low-power, low-bandwidth configuration for the IceCube-Gen2 DOM, which accommodates more than 15 PMTs. The high-voltage boards are an evolution of the design for the mDOM, used for the IceCube Upgrade, and have thus undergone extensive validation. The waveform digitization functionality has been incorporated into the HV board design, allowing for optimal utilization of the limited space and power available. The distinctive two-channel readout system allows for a significant increase of the dynamic range. This high dynamic range combined with the use of smaller 4-inch PMT enables the linear detection of photon fluxes almost two orders of magnitude higher than in IceCube. The central electronic board has also been developed for several subdevices of the IceCube Upgrade and has been verified to function effectively. Two variations of the pressure vessels from two suppliers have both been confirmed to meet the requirements and withstand pressures up to 70 MPa.

The extensive experience gained from the construction of the IceCube detector, as well as recent developments and production of optical modules for the IceCube Upgrade, instills confidence in our ability to produce and calibrate the optical modules effectively.

6 Radio Array

The radio array of IceCube-Gen2 targets the discovery and characterization of the neutrino flux above 10 PeV. The radio array is designed to detect the nanosecond-scale radio emission produced in ultra-high-energy particle showers via the Askaryan effect, described in Sect. 3.1.2. The technique is generally sensitive above PeV energies and therefore complements the energy reach of the optical array. Radio emission can be observed from showers from neutral-current interactions (all flavor) as well as charged-current interactions (ν_e) or catastrophic energy losses of secondary leptons (ν_μ, ν_τ).

6.1 Overview

The reference design of the radio array consists of 361 individual stations, each with multiple antennas sensitive to different electric field polarizations, that are capable of forming complementary triggers; waveforms recorded by the antennas allow reconstruction of the incoming neutrino. The individual stations, taken together, comprise the full array that then delivers the necessary neutrino effective volume.

The array will combine two different types of stations. 197 so-called *shallow stations* comprise 8 channels/antennas, mostly log-periodic dipole antennas, close to the surface. The other station design is the *hybrid station*, which has the same shallow component as the shallow stations, but adds a phased array of antennas at $150\,\mathrm{m}$ depth with additional antennas on the same string and two additional strings for event reconstruction and background rejection. 164 of these hybrid stations with 24 channels/antennas will be built. As discussed in Sec. 6.5.1 several combinations of different numbers of shallow and hybrid stations reach a similar science performance.

Radio detector stations can be deployed relatively close to the surface, due to the kilometer-scale attenuation length of the glacial ice at the South Pole [524]. By design, only a small fraction of neutrino events is detectable in more than one station, such that the total effective volume is (approximately) the linear sum of the per-station effective volume.

While the first generation of IceCube did not include a radio component, the array proposed herein builds on experience from the pioneering in-ice array RICE [528] and its successor (ARA [553]), both at the South Pole, as well as ARIANNA [554] near the coast of Antarctica, with two stations at the South Pole. The technology also draws from experience with the ANITA balloon experiment [611] flown at high altitudes over Antarctica. RNO-G, currently under construction in Greenland [556], also serves as technology demonstrator and informs the design, as the proposed IceCube-Gen2 stations are very closely related in geometry and technology.

6.2 Requirements

6.2.1 Effective volume

The science requirements for IceCube-Gen2 are summarized in Table 3, with the radio component providing the sensitivity at the highest energies. Since neutrinos have not

been observed above 10 PeV, the most important of these requirements is a sufficient effective volume and livetime to accumulate the exposure required to discover neutrinos in this energy range. As discussed in Sec. 2.3.4, there are a wide range of predictions for neutrinos at EeV (10^{18}) energies. A reasonable target for the neutrino effective volume is one that allows the observation of cosmogenic neutrinos in a scenario in which at least 10% of the UHECR at the highest energies measured with the Pierre Auger Observatory are protons, with five years of data, e.g., see Ref. [100]. This diffuse flux at 2×10^{-10}GeV cm^{-2} s^{-1} sr^{-1}is also what 30% protons in the flux of UHECRs at 30 EeV, following the standard range of stellar composition models [612] or the nuclear cascades in UHECR sources [171, 612], yields.

This target is by an array with effective volume of $\mathcal{O}(200\,\mathrm{km}^3\mathrm{sr})$ at 0.1 EeV and $\mathcal{O}(1600\,\mathrm{km}^3\mathrm{sr})$ at 1 EeV at trigger level, with a livetime of at least 90%.

6.2.2 Triggering

We require that the DAQ electronics can handle a rate of at least 1 Hz of triggering on the earliest read-out level, where all stations form their triggers individually on waveforms very close to thermal noise. We expect that advances in triggering will allow us to lower the trigger rate forwarded without loss of science. The upper end of the trigger rate is bound by set limits on the throughput of the communications system and data read out speed, where no requirement beyond the minimum rate is set. Furthermore, we require minimal system dead-time after a trigger (or double buffering) to provide the capability to record all neutrino pulses from all antennas, their potential reflections off the surface, and signals from air shower backgrounds. Given the geometry of the stations in the reference design, this requires a recording of a continuous waveform of at least 850 ns, ideally 1300 ns.

6.2.3 Timing precision

In order to correlate neutrinos with sources and aid in the flux reconstruction and its interpretation, we require the detector to have angular reconstruction capabilities; ideally a high-quality single-station event should reconstruct to better than $3\,\mathrm{deg}$, which requires antenna position accuracy of $10\,\mathrm{cm}$ and relative timing between channels at DAQ-level of at least 5×10^{-10} s. There is no hard requirement on interstation timing. A value of 1×10^{-7} s is more than sufficient in order to correlate the signals between events that are observed in two stations.

6.2.4 Broadband coverage and polarization

While timing alone can be used to determine the incoming signal arrival direction, it is not sufficient to determine the incoming neutrino arrival direction. In order to reconstruct the incident direction of the neutrino, one also needs information regarding where on the Cherenkov cone the signal was detected. A full reconstruction of the electric field can provide this information, since the polarization always points toward the shower axis. The frequency content can be used to identify the viewing angle relative to the Cherenkov angle. We therefore require that the stations are capable of

measuring different polarization components of the full electric-field vector to be able to reconstruct the polarization of the signal. Furthermore, the stations need to provide an effective bandwidth of at least $150\,\mathrm{MHz}$ to $600\,\mathrm{MHz}$, ideally down to $100\,\mathrm{MHz}$, to be used to reconstruct the viewing angle.

6.2.5 Background mitigation

There are several identified backgrounds that the detector needs to be robust against:

Radio-quietness of instrumentation: The array itself should not emit any detectable radio frequency (RF) noise. Tolerable levels are a maximum of 10% of the ambient thermal noise power in the ice at the full frequency range of 10 MHz - 1 GHz, where the band may be limited by communication frequencies, internal or external to IceCube-Gen2.

Generally, the radio instrumentation should be designed for an effective bandwidth of at least $100\,\mathrm{MHz}$ to $600\,\mathrm{MHz}$, as this is the optimal detection range for neutrino induced radio pulses [539, 613]. In this frequency range, the instrument needs to provide a system noise temperature that is below the external thermal noise and the diffuse Galactic emission. The detector is also subject to the constraints on RF emissions of other experiments at the South Pole, such as the CMB telescopes.

Anthropogenic and environmental noise: Past experience with anthropogenic noise suggests that building a detector at remote locations will simplify the data analysis and that anthropogenic noise can, in principle, be handled on an analysis level. However, wind-induced (triboelectric) background is unavoidable and must be mitigated in the data [614]. This will require continuous wind velocity measurements for several positions within the radio array. It should be noted that the surface antennas are expected to be more subject to anthropogenic/environmental noise than the deep trigger, which will have to be taken into account for the total trigger budget [570, 615].

Air showers: The least quantified physics background stems from air showers. This includes the in-air signal refracted into the ice, the signal from a partially developed air shower entering the ice, and from $>1\,\mathrm{PeV}$ atmospheric muons propagating in the ice, undergoing stochastic energy losses [521, 541]. The expected rates strongly depend on the cosmic ray composition at EeV energies as well as hadronic interaction models, which are both subject to significant uncertainties at the moment. Furthermore, it is currently unclear how much reflective layers or horizontal propagation of signals [526, 540, 616] will contribute to detectable backgrounds. Therefore, the detector must have the capability of tagging air showers through their in-air radio signal. Work both at RNO-G and in theoretical studies will improve our understanding of these backgrounds before construction of IceCube-Gen2 begins.

6.2.6 Power and livetime

In order to facilitate the powering of the stations across such a large area, the target power consumption is less than $25\,\mathrm{W}$ per hybrid station and less than $12\,\mathrm{W}$ per shallow station, including the capability to operate in lower power mode. The experiment is designed for a life cycle of at least 20 years. This requires that all components be

designed to last for 20 years and need a minimal amount of maintenance (if any) during this period. The latter is particularly important given the large area that will be covered by the radio array. Furthermore, the detector should be designed for a livetime of at least 90%.

6.2.7 Calibration

In order to obtain absolutely calibrated signals (i.e., voltage calibration, which is a requirement for energy reconstruction) within a reasonable calibration envelope, we require individual component uniformity in the RF chain to within 15% in amplitude, an absolute calibration of the system (excluding the antenna) of better than 15% in amplitude, and antenna systematics and uniformity to better than 30% in amplitude.

A golden sample of events seen in multiple stations will be helpful in improving confidence in reconstruction methods. Such coincidences will provide extremely high-quality reconstruction and will allow cross calibration, ice calibration, and estimation of systematic uncertainties. For fixed spacing, the coincidence fraction increases with energy and station depth. To obtain a meaningful sample of events, we require *at least* a 10% overlap in effective volume. We note that the current reference design has a larger coincidence fraction.

6.2.8 Reliability

The radio detection technology is less mature compared to the optical detector, so close attention will be paid to the reliability of the instrument. Ongoing experience with the RNO-G array, which is similar in design, will provide confidence that the hardware is robust and allow any potential maintenance challenges to be identified. We aim for a design with minimal maintenance needs (if any) for the radio array. Embedding the radio detector under the IceCube umbrella, with its excellent track record in constructing and operating the IceCube Observatory, will ensure design verification and quality control.

6.3 Main interfaces

The radio array is comprised of autonomous stations, each capable of both self triggering and fully reconstructing an event. In fact, in order to maximize the effective volume, the spacing of the stations in the reference design is chosen such that the majority of events will be observed in only a single station. Since the trigger decision and event building is performed locally, and not at the central counting house, each station relies on a local GPS for timing (and does not require White Rabbit). The radio station interfaces will therefore only need to provide power distribution, communication, and the transmission of complete events to the counting house where they enter the IceCube-Gen2 data stream. These interfaces are described in more detail in Sect. 8.4.2.

6.4 Reference design

The reference design of the radio array is based on two different types of stations as outlined in Sec. 6.4.3, which are combined to the full array as described in Sec. 6.4.1. Each station is capable of self-triggering and provides sufficient data to fully reconstruct an event. As discussed in Chapter 3.1.2, the depth of the antennas determines the effective volume of the stations, with deeper antennas viewing more ice, while shallower antennas are easier to install. A number of array geometries with different ratios of shallow and deep stations, discussed in Sec. 6.5.1, were considered, all with similar sensitivities and logistics requirements. The reference design was positively reviewed by an external panel in 2021.

6.4.1 Array layout

Hybrid stations combine deep strings of antennas deployed at a depth of down to $150\,\mathrm{m}$ with shallow antennas deployed near the surface of the ice. Shallow-only stations include antennas only near the surface and are identical to the shallow component of the hybrid stations. The stations are spaced on a square grid of $1.24\,\mathrm{km}$, and alternate between shallow and hybrid stations. This results in a spacing of $1.24\,\mathrm{km}$ between shallow components and $1.75\,\mathrm{m}$ between deep components.

As stated in the requirements, at least 10% of the neutrino events will be detected in multiple stations, comprising a sample of events with significantly enhanced reconstruction. The array layout for the reference design is shown in Fig. 80 and achieves a 30% overlap in events at 10^{18} eV in energy. The overall dimensions are chosen to be within the Dark Sector at the South Pole to minimize radio interference and comply with agreements from other experiments. The station positions have not yet been optimized for coincident measurements of air showers with the surface array (see Sec.7), which would allow for a detailed cross calibration of the two detector responses.

6.4.2 Antennas

Three types of antennas are used in the radio array for IceCube-Gen2. There are high-gain, log-periodic dipole antennas (LPDAs) used at shallow depths and two types of azimuthally symmetric antennas: fat dipole antennas (Vpol, vertically polarized signal content) and quad-slot antennas (Hpol, horizontally polarized signal content). Both downhole antenna types are cylindrically symmetric and designed to fit within the 11.2-inch diameter holes of the BigRAID drill (see Sec. **??**).

Antennas deployed at shallow depths should be directional so that some channels can point upward, monitoring downgoing cosmic rays and above-surface backgrounds, and some can point downward, monitoring both the ice for neutrino signals and the near-surface radio backgrounds. Directional antennas also have the advantage that they are naturally high gain; they are however also typically large. LPDAs are typical directional antennas that achieve a high gain along the axis of maximum gain (boresight gain), high front-to-back ratio, and are broadband because of their self-complementarity. The LPDAs are similar to commercially available antennas CLP-5130-2 from the Creative Design Corporation (CREATE, Japan), as used in the ARIANNA and RNO-G experi-

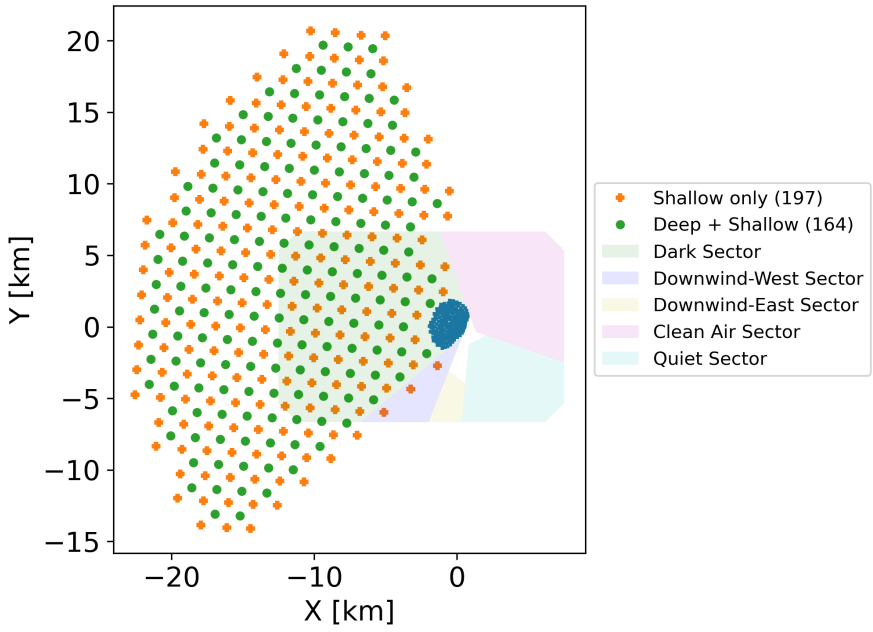

Figure 80: The locations of the radio array stations on South Pole sector map, with the Dark, Downwind, Clean, and Quiet Sectors also shown. The shallow-only stations are shown in orange crosses, while the hybrid stations are shown as green circles. The stations are spaced on a 1.24 km square grid. All stations have a shallow component, while alternating stations are hybrid stations which have additional antennas installed at 150 m depth.

ment. The reference design for IceCube-Gen2 antennas will be custom-built, similar to what has been used for the TAROGE and TAROGE-M experiments [617]. These custom antennas, shown in the left panel of Fig. 81, do not require as much assembly as the CREATE antennas and can be made compact for transport. For IceCube-Gen2, we are also considering a more cost-effective design using high-power laser cutters, shown schematically in the right panel of Fig. 81. The operational bandwidth of these antennas, defined by the range over which the Voltage-Standing-Wave-Ratio (VSWR) is lower than 2, is 100 MHz to greater than 1 GHz.

At depth, omnidirectional antennas are preferred as radio signals from the neutrinos can arrive from above or below. Both Hpol and Vpol antennas antennas are 60 cm tall, made of aluminum cylinders, have PCB antenna feeds, and are well suited for mass production. The Vpols are shown in Fig. 82, and the Hpols are shown in Fig. 83.

The Vpol antennas are 5-inch diameter fat dipoles similar to the original RICE design [528] and used most recently in RNO-G [556]. In ice, they have a usable bandwidth of 150-800 MHz and gain of 2-4 dBi across the band. The Vpols are used in phased array triggering at depth [537], as reconstruction antennas, and as calibration pulsers. Similar Vpols built for RNO-G and their performance are shown in Fig. 82.

The Hpol antennas are 8-inch quad-slot antennas based on the RNO-G designs. Slot antennas radiate like dipoles due to Babinet's Principle and multiple slots arranged around the outer edge of a cylinder can approximate a uniform beam pattern. The Hpol antennas have a boresight gain of -2 dBi over 350-750 MHz in glacial ice. Because the Hpol antennas are used for reconstruction rather than triggering, the narrower band-

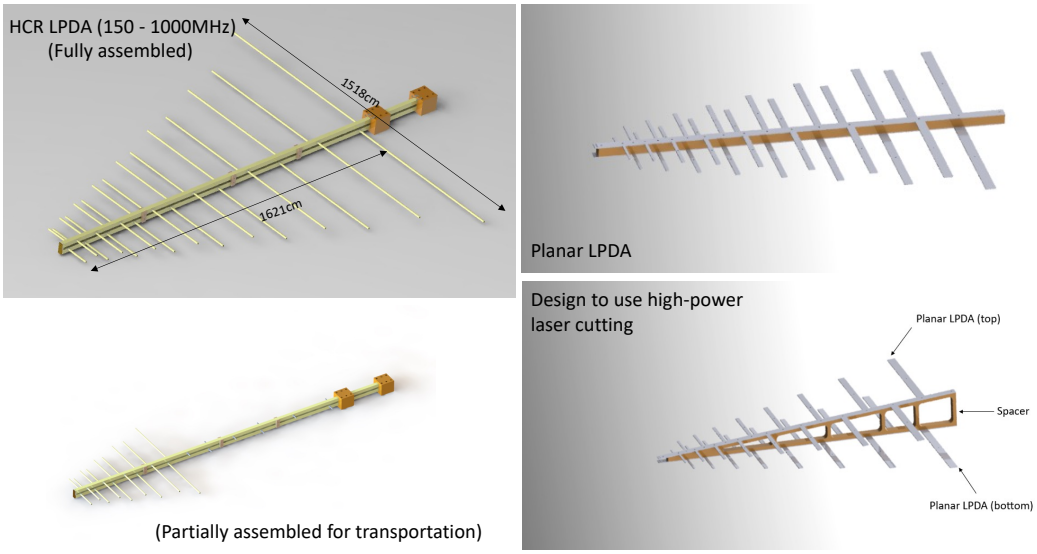

Figure 81: Options for the LPDAs and manufactured specifically for neutrino experiments. Left: The HCR LPDA both fully assembled and partially assembled for transport. These antennas have been used in Antarctica [617]. Right: For IceCube-Gen2, a more cost-effective design using high-power laser cutters is being considered.

width of the Hpols compared with the Vpols is acceptable. The details of the Hpols is shown in Fig. 83.

The performance of the three types of antennas is compared in Table 10.

6.4.3 Station layout

The stations layouts are shown in Fig. 84. Shallow-only stations are composed of seven high-gain log periodic dipole antennas (LPDAs) $3\,\mathrm{m}$ below the surface of the ice and a vertically polarized dipole antenna at $10\,\mathrm{m}$ depth. All eight channels are connected via coax cables to the central channel data acquisition system (DAQ) box. At least one calibration pulser will be also installed at 20 m depth which will enable a continuous measurement of the snow accumulation [530]. Additional pulsers may be considered for some stations to continuously measure the index-of-refraction profile [618]. Three antennas point upward to monitor cosmic ray rates and uniquely tag anthropogenic noise. The remaining four LPDAs point down to provide neutrino sensitivity and are oriented to cover two orthogonal horizontally polarized directions (North-South and East-West). The shallow-only stations trigger on the coincidence of the downward facing LPDAs over the low-frequency portion of the band [613]. In parallel, a coincidence of

Antenna	Configuration	Polarization	Boresight Gain (dBi)	In-Ice Bandwidth (MHz)
LPDAs	Shallow	Hpol	11 to 13	105-1300
Fat dipole	Shallow, Hybrid	Vpol	2 to 4	150-575
Quad-slot	Hybrid	Hpol	-2 to 2	350- 750

Table 10: Comparison of the performance of the three types of antennas used in the radio array.

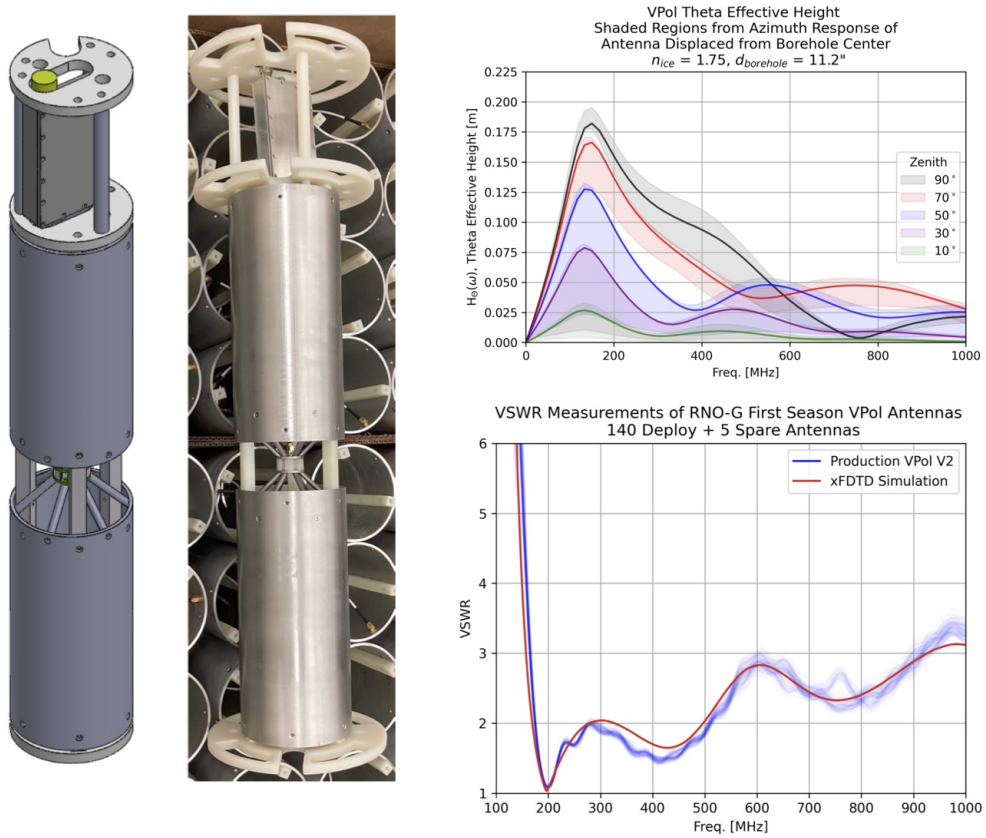

Figure 82: Fat dipole vertically polarized antennas as planned for IceCube-Gen2, based on the RNO-G design. Antenna modules include the amplifiers and RF-over-fibre mounted directly to the top of the antenna. Left: CAD model and example antenna. Right: Effective height for a variety of zenith angles (top) and the performance in terms of VSWR (bottom).

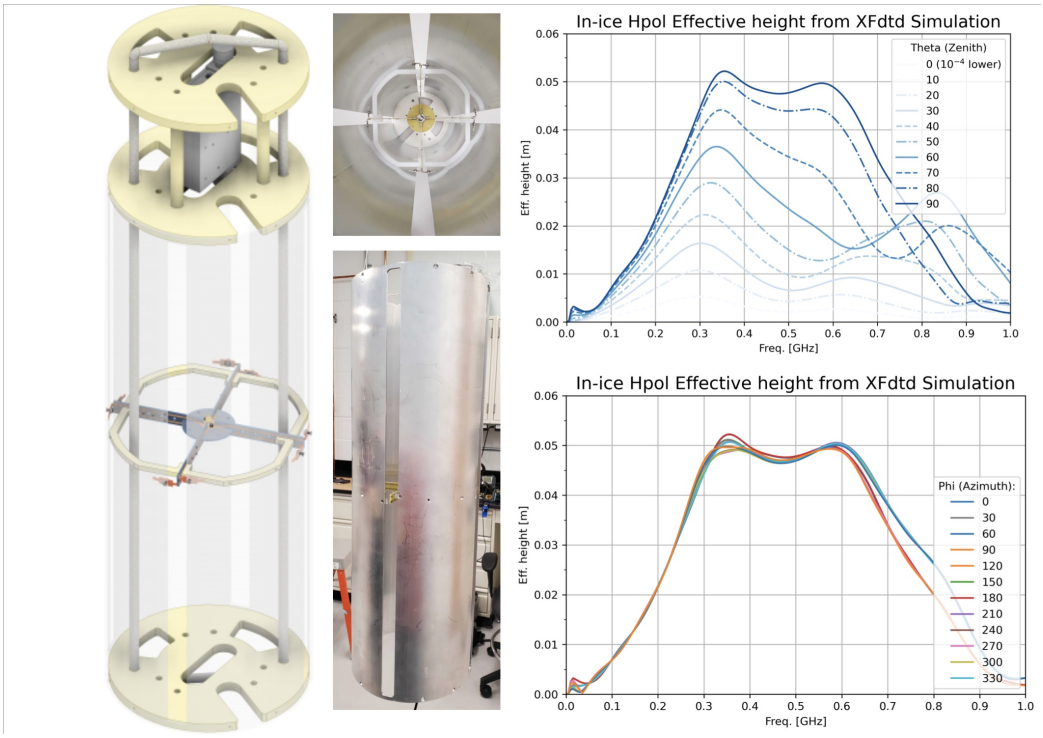

Figure 83: Quadslot horizontally polarized antennas planned for IceCube-Gen2, based on the RNO-G design. Antenna modules include the downhole amplifiers and RF-over-fiber units mounted directly to the top of the antenna. Left: CAD model and example antenna. Right: Effective height for a variety of zenith angles (top) and azimuthal cut planes (bottom, on boresight).

the upward facing LPDAs is sensitive to cosmic ray events [619], as demonstrated in ARIANNA [542]. The dipole aids with event reconstruction by registering both the direct and refracted ray path in the same waveform as shown in Fig. 35. The amplitude ratio and the time difference of the two pulses uniquely tag the distance of the vertex [529, 530].

Hybrid stations have a deep component and a shallow component, both connected to a centralized 24-channel DAQ. As in the shallow-only stations, there are seven LPDAs installed just below the surface. The remaining 17 channels are installed in three strings lowered in boreholes extending to a maximum depth of $150\,\mathrm{m}$. The deep antennas are cylindrically symmetric antennas, each sensitive to either the vertical component (Vpol) or the horizontal component (Hpol) of the electric field.

One string, the *power string*, includes a compact array of four Vpol antennas that together form a phased array [537]. The phased array tests the observed waveforms for consistency with several hypotheses for the incoming signal direction, coherently summing the signal observed on the four antennas together in multiple beams that point in the full solid angle for neutrinos, from -60° to 60°. This beamforming increases the voltage signal-to-noise ratio of a given event by factor of two (= $\sqrt{N}$ where $N = 4$ is the number of antennas in the phased array), enabling a low trigger threshold. The phased array trigger will be the main trigger of the instrument. The phased array technique was pioneered for neutrino detection by the ARA collaboration [539] and analyses have been shown to reconstruct weak events with high efficiency [615]. The power string also includes one Hpol antenna installed directly above the phased array, as well as three additional Vpol antennas spaced to maximize the variety of baselines for reconstruction of the neutrino vertex and arrival direction.

Each of the other two strings, the *helper strings*, include two Hpols and two Vpols as well one calibration pulser. They are required to obtain an arrival direction for each incoming neutrino, by allowing triangulation of the signal arrival direction from the vertex and the polarization and frequency content of the signal [532, 553]. The spacing of the strings is a trade-off between larger baselines for reconstruction and smaller baselines for detectable signals [620].

6.4.4 RF signal-chain electronics

Block diagrams of the signal chain for each station type are shown Fig. 85. It shows the signal flow and the individual components of the electronics as discussed in the later sections. For reference, the RNO-G version of the whole station electronics enclosure is shown in Fig. 86. By contrast, the IceCube-Gen2 system will not include batteries and will have a different DAQ board.

The RF signal-chain is responsible for amplifying the antenna output to a measurable voltage level with minimal added electronics noise or other signal distortions. Assuming a system operating in the 150-800 MHz band at 50Ω, viewing $-40\,^\circ$C ice, the thermal noise level is approximately 2 pW, or $\sim 10\mu V_{\mathrm{rms}}$ before amplification. The data acquisition system requires at least a few $\sim V_{\mathrm{rms}}$ at the digitizer boards for accurate digitization of the thermal noise signal, yielding a requirement on the gain of the RF signal chain of

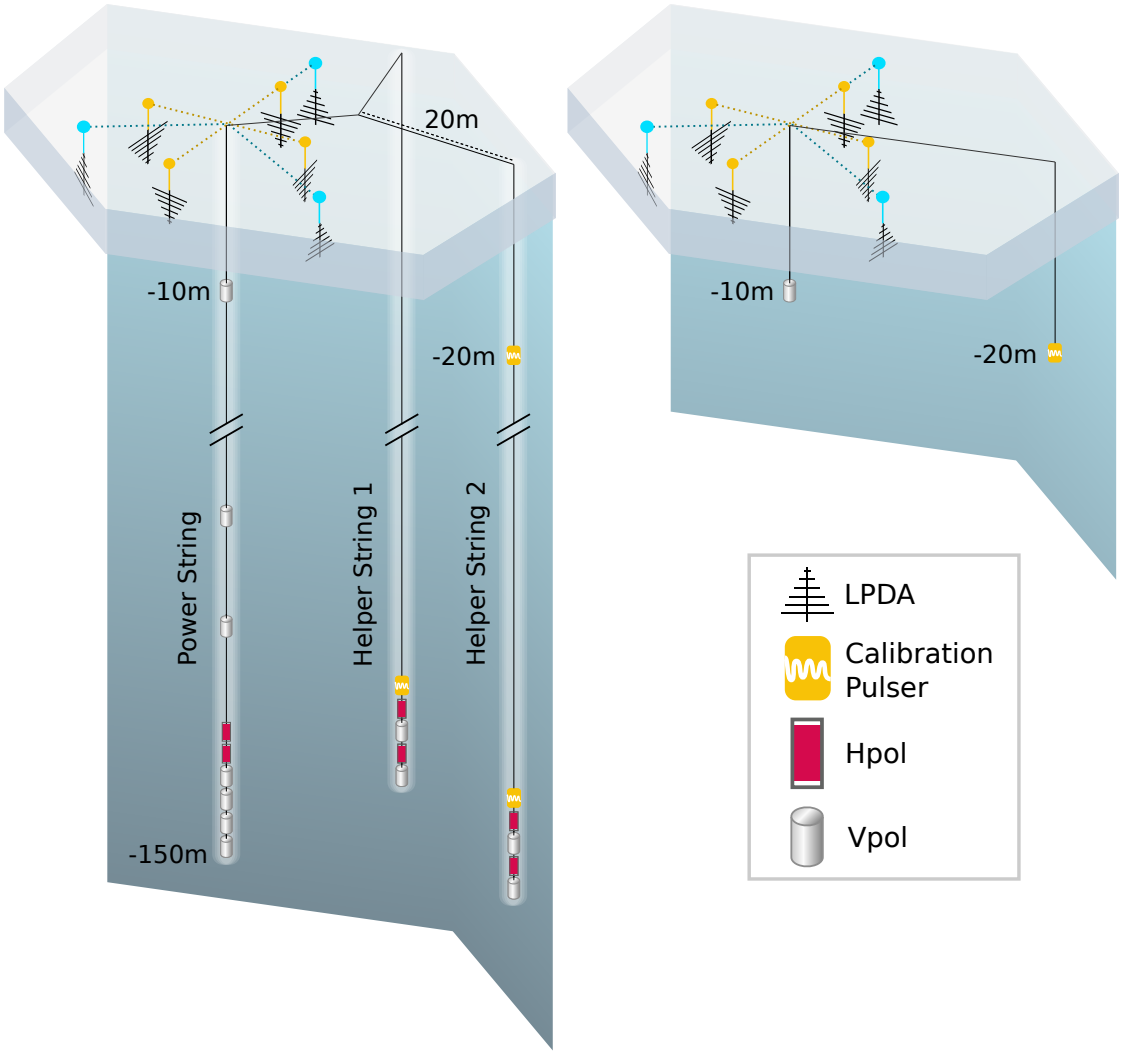

Figure 84: Station layout of the reference design. The shallow stations (right) consist of seven Log-Periodic Dipole Antennas (LPDAs), four downward-facing and three upward-facing, and one dipole antenna at a depth of 10 m. The hybrid stations (left) contain the same shallow component, as well as three strings to the depth of 150 m. One string hosts the phased array trigger using four dipole antennas, sensitive to the vertical signal component (Vpol), as well as additional Vpol antennas to reconstruct the vertex position and slot antennas (Hpol), which are sensitive to the horizontal signal component. Vpol and Hpol antennas on the two other strings allow the reconstruction of the arrival direction and the electric field. Two strings host calibration pulsers to triangulate and calibrate the antenna positions to cm-precision.

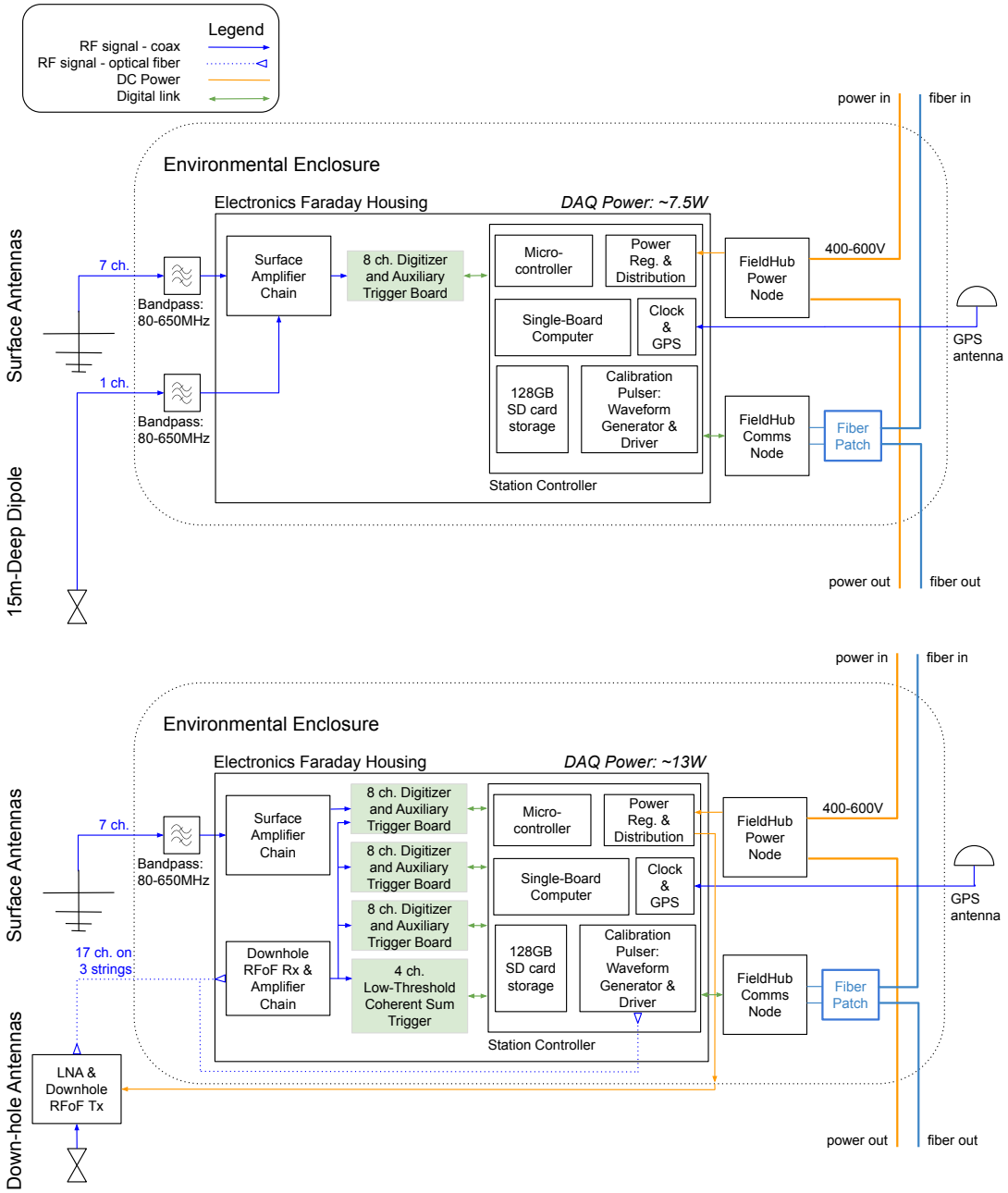

Figure 85: Block-diagram of the station signal chain for the shallow stations (top) and the hybrid stations (bottom).

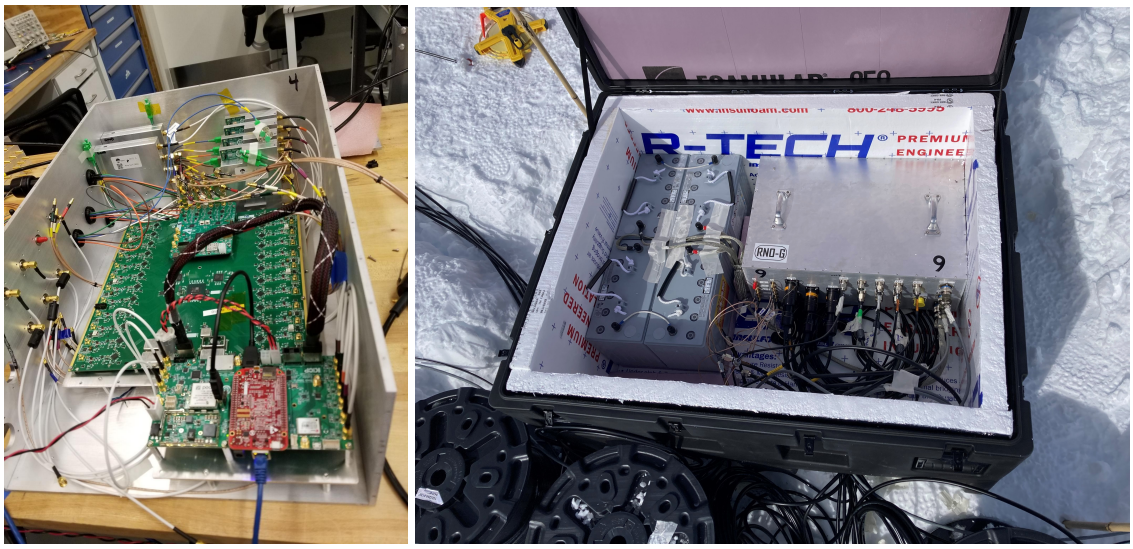

Figure 86: Instrumentation boxes (left: DAQ box in lab, right: vault in field) of RNO-G, for illustration purposes. The DAQ box for IceCube-Gen2 will be built as shown schematically in Fig. 85 and Fig. 88. In the field, the metal DAQ box is in an environmental enclosure with cable feedthroughs for power, communication, and signal cables. The IceCube-Gen2 vault will be smaller since the stations will not require batteries.

at least 60 dB. The RF signal chain components should incorporate a low power design, as the power consumption will scale with the number of channels in each station.

The baseline RF signal chain will be the same design that has been developed and deployed for the RNO-G experiment, in which over 150 channels have already been installed and operated in the field. There are two distinct RF signal chains that will be used, one for the downhole antennas, and one for the near-surface antennas.

Because of the long distances between the downhole antennas and the DAQ box, the downhole channels employ a two-stage frontend amplification system and transmit data over optical fiber, i.e. a radio-frequency-over-fiber (RFoF) transmitter and receiver pair. Using a module mounted directly over the antenna, signals from the antennas are first amplified using a 50Ω-matched low-noise amplifier (LNA), then conditioned with a bandpass filter, and finally transmitted to the surface via a custom low-power RFoF transmitter design. This first stage is a single-channel device that is housed in an EMI enclosure directly above each borehole antenna in a deployable packaging called the *antenna unit*. Each antenna unit has a through power connection over an N-type coaxial cable connector and a single-mode fiber connection on the EMI enclosure using a FC/APC bulkhead connector. The RF signal is sent to the second stage amplifiers in the instrumentation box over military-style tactical fiber bundles that connect to EMI-rated multi-channel fiber bulkhead connectors on the instrument box.

The second stage receiver system is housed within the instrument box. Each quad-channel receiver has the RFoF photodiode receiver, which converts the optical signal back to a 50Ω electrical signal, as well as the final stage of filtering and amplification.

The shallow channel RF signal chain is similarly housed in the instrument box, but due to the short distances between the antennas and the instrumentation box, there is only one stage of amplification. Each shallow antenna will be routed to the instrument box

Chain	Median Gain	Bandwidth [-3dB]	Noise Temp [<400MHz]	Pwr/ch
Downhole	61dB	80-620 MHz	<140 K	0.24 W
Shallow	62dB	80-650 MHz	<110 K	0.26 W

Table 11: Measured performance of the RNO-G RF signal chains, used as reference design for IceCube-Gen2. As noted in the text, the bandwidth parameter is adjustable to the requirements of the radio array of IceCube-Gen2.

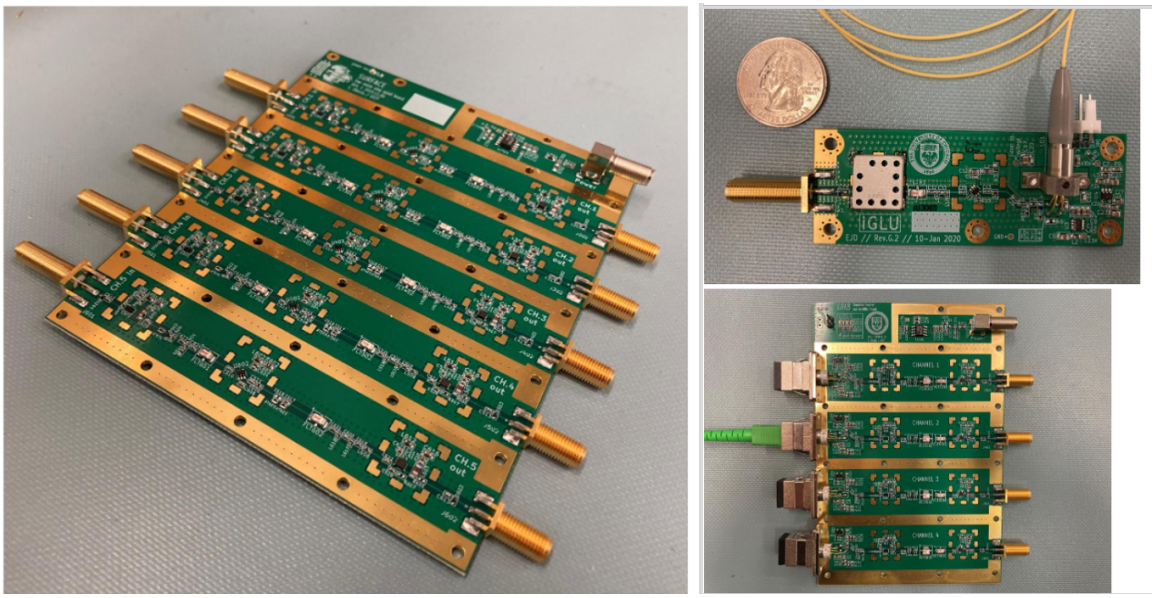

Figure 87: RNO-G 5-channel surface channel amplification and signal conditioning board is shown on the left. The downhole-antenna low-noise amplification and RFoF pair is pictured on the right, (top: downhole antenna end, bottom: surface concentrator unit). These boards are installed in full-metal enclosures for installation.

over low-loss coaxial cable, which connects to the input of an amplification board. This board uses the same 50Ω board-mount LNA at the input as the downhole channels, and each RF channel is followed by two stages of bandpass filtering and further amplification. The amplifier boards for the shallow channels are designed as compact 4-channel devices with an EMI housing that isolates each channel to better than 70 dB over the band.

The basic parameters of the RF signal chains are shown in Table 11, as measured using the RNO-G signal chains. Images of the boards for RNO-G are shown in Fig. 87 which are representative of the boards that will be used in IceCube-Gen2. The output of the RF signal chain is sent to the digitizer and trigger boards.

The amplifiers are packed in full iridited aluminum enclosures that both shield any potential noise and protect them for installation. The downhole amplifier units will be packed directly on the antennas and they are thereby exposed to the environment. The second-stage downhole receivers and shallow amplifier units will be in the environmental enclosure of the system.

6.4.5 Cables and fibers

The antennas close to the surface will be connected to the station DAQ with LMR-400 coax cable. This has been used in several radio experiments and has shown good in-field mechanical and electrical performance.

The down-hole fibers are planned to be similar to the fibers used for RNO-G. Custom-made military grade fiber bundles (e.g., Optical Cable Corporation, D series, Mil-Tac) are used to connect all antennas on a string in the correct distances. Since they are custom-made they required calibration before installation with respect to timing.

6.4.6 Triggering and Data Acquisition (DAQ)

The radio data acquisition system (DAQ) is based on a flexible architecture that can be applied to both hybrid and shallow stations. The DAQ is managed by a back-end remote-station controller board, which hosts an industrially-rated single-board computer (SBC), local data storage using industrially-rated SD card(s), a system clock reference, a timing GPS receiver, housekeeping and low-level station control with an on-board microcontroller, and external interfaces to the array power and communications grid. A pair of digitizer- and trigger-board designs perform the RF signal acquisition / triggering functions and transfer data to the controller SBC using a commonly-defined communications link. The controller can accommodate up to four digitizer or trigger boards as shown in the DAQ block diagram in Fig. 88.

The DAQ waveform acquisition and triggering is split between two board designs: the ‘digitizer’ board, which houses a custom switched-capacitor array (SCA) transient-recording ASIC to sample the full-band waveforms at up to 2 GSa/s with a single-event record length of 2048-samples, and the ‘trigger’ board, which uses a commercial 8-bit pipeline ADC sampling at 500 MSa/s and uses an FPGA to create low-threshold trigger decisions on the lowest 250 MHz of the RF signal bandwidth. The digitizer boards receive 8-channels each and consume 2W/board; the trigger boards are 4-channels each and draw roughly 3W each. Each board links to the controller board using the common communications link, and each run off a single +5V supply rail. These two boards are depicted in Fig. 88.

A custom 4-channel ASIC will be implemented on the digitizer board, which will provide ‘snapshots’ of the triggered events at up to 2 GSa/s. From the required system bandwidth of 100 MHz - 600 MHz, the Nyquist criterion relates this to at least 1.2 GSa/s. This ASIC will use the SCA topology that is a common architecture for similar low-power sampling chips used in this field and elsewhere, such as the SST[621], LAB4D [622], and PSEC4A [623] devices. The chip will be designed with two 2048-sample arrays per channel, to allow for multi-event buffering for close-in-time events to avoid significant latency. Once triggered, the chip will digitize the analog-captured waveform at 12-bit resolution and readout the region-of-interest event. Each event data packet is roughly 30kB for a 24-channel station. The chips will be controlled by an on-board FPGA, which will also manage the digitizer-to-controller interconnecting link.

The **trigger board** design will be directly taken from the RNO-G low-threshold system: the FLexible Octal Waveform Recorder (FLOWER) board. This board uses two

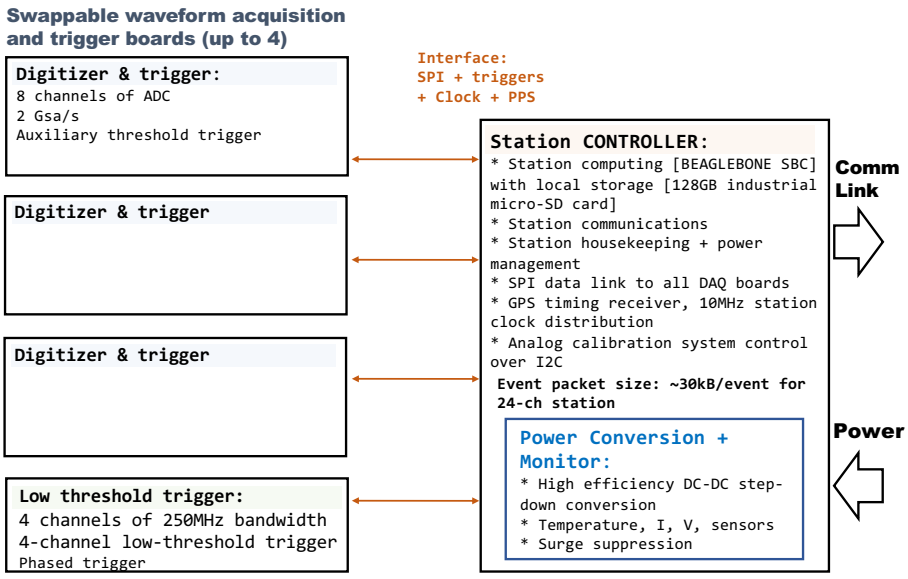

Figure 88: Block diagram for the flexible radio data acquisition system. The waveform recording is handled by a 8-channel board housing a custom ASIC with 2048 samples/buffer capable of at least 2.0 GSa/s sample rates. The low-threshold trigger board is inherited from the RNO-G experiment and allows a low-power trigger formation on streaming ADC data on 250 MHz of signal bandwidth. Both boards communicate to the remote station controller board over a common interface, which includes an SPI link for data transfer, as well as trigger, clock, and PPS signals. The remote station controller also includes a GPS timing receiver for inter-station time syncing, 128GB of local storage on a low-power industrial-rated and field-proven single-board computer, and interfaces to the array power and communications grid.

instances of the Analog Devices HMCAD1511 ADC, each nominally in dual-channel mode. The input is low-passed at 250MHz to prevent aliasing, and the ADC output is streamed to the FPGA to build smart trigger decisions to lower the neutrino-energy threshold at the hardware level. The basic planned FPGA operation is to form coherent sums based on incoming plane-wave hypotheses for different zenith angles from a compact array of Vpol antennas on one of the borehole strings. Once generated, a trigger signal will be sent back to the controller board, which distributes to the other devices in the DAQ system with very low latency. Simulations and measurements show that a trigger threshold of 2σ on the thermal noise baseline are achievable with this trigger board strategy, which corresponds to waveforms very close to thermal noise.

In addition, the DAQ will have **on-board triggering options**. Although, by definition, the trigger board will serve as the primary trigger, the digitizer board will have per-channel discriminators that are fed to the digitizer-board FPGA. These discriminators are based on simple and economical Schottky-diode transient power detectors, each of which are fed to the one-side of a differential input on the FPGA and compared to a voltage threshold. These will not reach the low threshold capabilities provided by the trigger board, but allow the system to generate triggers, for example, using coincidence detection in the shallow antennas for cosmic ray detection. The DAQ may also be used to form more complicated trigger decisions that may combine the streaming trigger generation on the trigger board with these auxiliary discriminators – the trigger board has the capability for buffering (bandwidth-limited) waveform data on the FPGA for up to 100 μs.

The IceCube-Gen2 radio **controller board** design is closely inherited from the RNO-G back-end remote-station controller that has proven operation in the field. For the RNO-G controller, an industrially-rated BeagleBone Black has served as the single board computer (SBC), which uses an AM335x 1 GHz ARM processor and includes 512MB of RAM, a micro-SD slot, and an on-board 4GB eMMC flash storage chip. The Linux operating system is loaded on both the micro-SD card (128-256 GB) and the on-board flash storage, allowing the system to fall-back to the on-board flash in case of an unexpected corruption of the SD card, which serves as the primary boot device. The BeagleBone Black SBC has shown good reliability in the field and low-power performance, but other more modern single-board computing options may be also considered for IceCube-Gen2. The SBC works together with the on-board microcontroller, each which have an independent link to the array communications grid. The microcontroller can toggle or re-boot the SBC, enable power to down-stream subsystems, and also records local voltages, temperatures, and other station-health information. The microcontroller firmware will be based on the established and field-tested RNO-G microcontroller code.

The command and data-transfer between the controller and to the digitizer / trigger boards are performed on a commonly-defined link. Data are sent over a 4-wire serial-peripheral interface (SPI) at up to ~30Mbps. The controller serves as the host for SPI links and the digitizer and trigger boards as the client devices. The controller also houses a system clock, which is a 10 MHz temperature-controlled crystal oscillator (TCXO) with a frequency stability of better than 0.25ppm over a temperature range -40 to 85C. This system clock, in addition to a GPS-derived pulse-per-second (see

Sec. 6.4.7), are sent from the controller to each device, ensuring that the individual digitizer and trigger boards are fully synchronized. Two general-purpose I/Os and a global trigger signal are also included on this interconnect link.

The local +5V and +3.3V power supply rails are generated on the controller board using high-efficiency and EMI-filtered DC-DC converters. The +5V rail is capable of providing up to 6A, which is supplied to the digitizer / trigger boards and to the SBC, and the +3.3V is used for the RF signal-chain power and can provide up to 3.5A. A small +3V DC-DC converter is used to power the microcontroller independently, in case the other power rails need to be reset, or the if station needs to go into a low-power operation mode (<10 mW) in which only the microcontroller and its immediate peripherals remain powered. This local-power generation and distribution scheme has worked well on the RNO-G controller system and is field proven, both in terms of reliability and mitigation of any associated EMI from the DC-DC switching supplies.

The power consumption of the DAQ is a major design consideration. At full operation, each digitizer board consumes ~2W. each trigger board ~3W, and each controller takes ~3.5W with all the peripherals on-board enabled and managing four digitizer / trigger board devices. For a 24-channel DAQ that serves a hybrid station, the DAQ power consumption is roughly 13W. For an 8-channel DAQ equipping a shallow-only station, including a trigger board, is approximately 7.5W.

6.4.7 Timing system

To maintain accurate absolute timing, each station will have a timing GPS (e.g. u-blox ZED-F9T or LEA-M8T) which emits a pulse per second (PPS) with an absolute accuracy of better than 10 ns to the GPS second. The digitizer boards, which have a nominal $\mathcal{O}$(100 MHz) internal clock (e.g. Si5538), will record the clock cycle at the time of each PPS, allowing for precise mapping of board clock cycles to times referenced to GPS seconds. This implied <10 ns timing accuracy is very much above what is needed for the purpose of determining if triggers from different stations are coincident in time as well as basic inter-station reconstruction. The GPS will be connected to the station SBC over UART, and the PPS will also be made available to a digital input on the computer. Therefore, the SBC time will also be derived from GPS, providing improved timing accuracy over NTP or even PTP.

The station control microcontroller has its own independent real time clock, derived from a crystal. However, as it is only used to time tag slow-changing housekeeping data, it need not be very precise and can be synchronized to the desired precision from the SBC over UART (or, in the wireless/autonomous power alternative, over LoRaWAN).

6.4.8 On-station calibration system

The radio DAQ includes a calibration-driver board, which is controlled by the SBC. The calibration-driver board comprises both a fast (~1 ns, 5V) impulse generator circuit and sine-wave outputs at two in-band frequencies (nominally 188 and 400 MHz). A pro-

grammable RF-signal attenuator is in-line with the output signal that allows amplitude scans in the receiver antennas and *in situ* interrogation of the detector trigger-threshold.

The output calibration waveform is sent to a bank of RF switches with a total of four outputs. Two are sent to the downhole transmitting antennas and the other two are sent to coaxial connectors for surface transmitters. The downhole channels use the same RFoF system used in the RF receivers to transmit the signal to the deep calibration-transmitter antennas. There is an RFoF receiver and restoration amplification stage at each of these antennas. Each calibration transmitter unit draws ~0.1 W.

The output signal waveform, the output path selection, and the signal amplitude are fully remote-controllable over an I2C bus. The calibration-driver board can also be fully disabled and put in power-down mode. The fast impulse is nominally triggered by the GPS pulse per second, though it can also be pulsed at higher rates using a secondary trigger passed through the general purpose I/O on the SBC.

6.4.9 Power and communications

Cabled power and communications are distributed from the ICL to FieldHubs within the radio array, and the FieldHubs distribute power and communications to the surrounding clusters of radio stations. Details of the cabling layout are described in 8.4.3.2.

6.5 Alternatives considered

Major alternatives were considered for the array design itself, antennas, power and communications, and the DAQ system. For all other systems, evolutions rather than alternatives are considered.

6.5.1 Alternative array designs

The decision to combine shallow and deep antennas is chosen as strategy to provide the most robust discovery experiment, given different ways to detect neutrinos with different systematic uncertainties. However, there are a number of options of how one can combine shallow and deep antennas.

A number of trade-studies have been conducted in the past [624] to establish the best performing array. It is known how effective volume and coincidences scale with depth and trigger threshold. In principle, there are many possible combinations, even assuming that installation time and population are the limiting parameters. The shallower a hole, the shorter it takes to drill, but also the smaller the effective volume. Or in other words, every hybrid station can be replaced by a number of shallow-only station for the same total effective volume.

For the purpose of this document, the performance of a total of four arrays, similar in hardware and installation costs, were simulated and compared. In addition to the reference design shown in Fig. 80, the three arrays arrays considered are shown in Fig. 89. The initial estimates of costs of installation were subject to large uncertainties, which will be refined in future work.

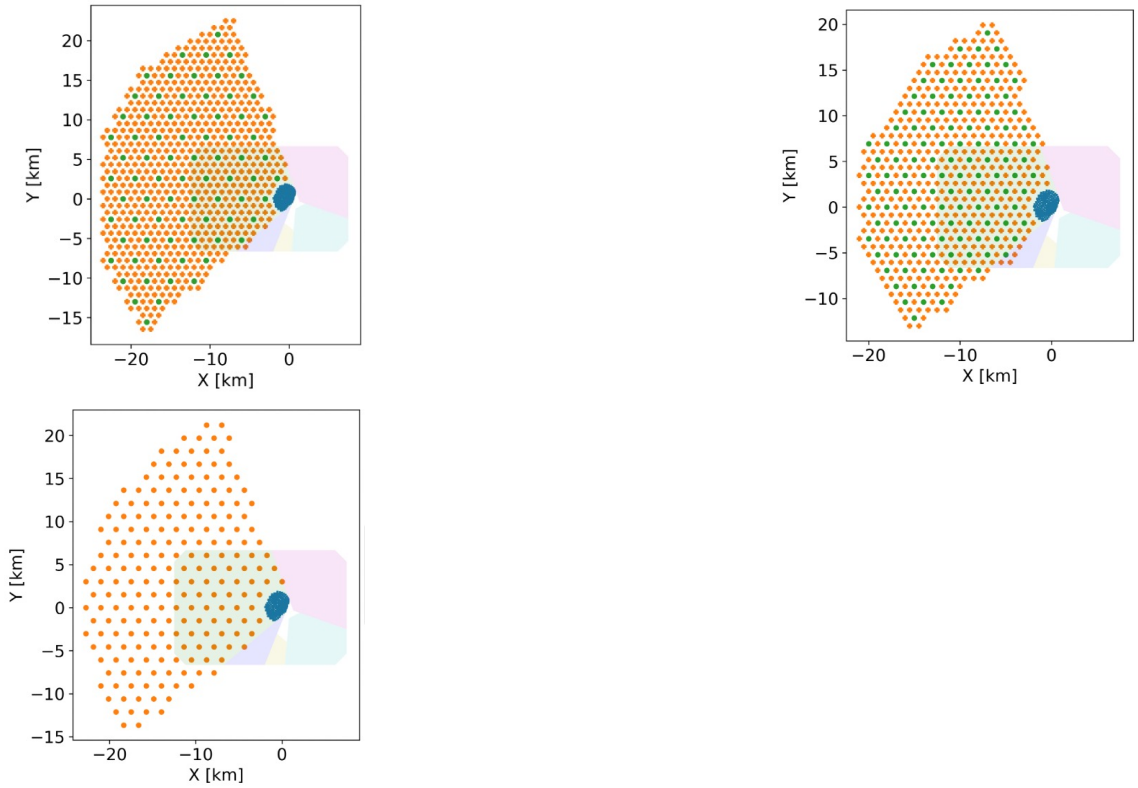

Figure 89: Alternative array layouts considered for the radio array. The orange markers show the locations of shallow stations, while the green dots show the locations of hybrid stations. From left to right: the "shallow heavy" array features 628 shallow stations and 76 deep stations, the "hexgrid-array" features 414 shallow stations and 123 hybrid stations on an hexagonal grid, and the "hybrid only" array has 208 hybrid stations. For comparison, the reference design (Fig. 80) has 197 shallow stations and 164 deep stations on a square grid.

Simulations indicate that the resulting scientific performance with respect to neutrino effective volume is similar. However, it should be noted that there are smaller differences in aspects such as sky coverage and effective volume as function of energy that are different between the arrays. Also, the estimated coincidence rate between stations, varies slightly, leaving room for optimization in a future simulation study.

Overall, in the choice of an array design, there seems to be a rather broad optimum in which many configurations nominally achieve the same scientific performance. This means that there may be room to optimize on the basis of other considerations such as the ease of installation logistics. It is important to note that this is a good situation from a risk mitigation perspective: should one of the components not perform as anticipated, this can always be counteracted by re-balancing the number shallow-only and hybrid stations.

6.5.2 Antennas

Alternatives for antennas are to use the commercially available antennas CLP-5130-2 from the Creative Design Corporation (CRE-3335 ATE, Japan), as used in the ARIANNA and RNO-G experiment for the LPDAs. These antennas are more expensive

and require pre-assembly as opposed to the custom-design, but have shown good long-term performance.

It is conceivable that the RNO-G design for the Vpol and Hpol antennas may evolve slightly, but this is considered an evolution rather than an alternative. These antennas are already an evolution of antennas installed at ARA. There are no commercially available antennas that fulfill the requirements of fitting in the borehole, matching the frequency band and providing sufficient gain.

6.5.3 DAQ

The reference design builds on a custom ASIC specifically designed for the in-ice radio array of IceCube-Gen2. This is an item that carries significant risks, however, the opportunities are also large.

Alternatively, the DAQ could built on existing designs from RNO-G (built around the LAB4D chip [622]) or the ARIANNA DAQ (built around the SST chip [625]). Both designs, however, would require modifications to use for IceCube-Gen2.

The SST chip record length is not long enough to accommodate hybrid stations, simply due to the signal travel time. It would therefore have to be further developed to be use-able for both the shallow and the hybrid stations, essentially resulting in a new chip design building on the existing one. The LAB4D chip, in turn, is a single channel chip, which leads to very large and complex boards as it is the case for RNO-G. For hybrid and shallow stations, one would have to design two systems in parallel, which is why this is only considered as alternative design. That said, both are existing systems that have been field-tested and their performance is well-known, which makes them viable alternatives.

Finally, there is R&D ongoing into DAQ systems that provide continuous digitization making use of very recent developments in digital electronics (e.g. ADC: TI ADC12QJ1600-EP), which may also provide opportunities in advanced real-time triggering.

6.5.4 Power and communications

Alternative designs that eliminate the cabled power and communications network have also been considered. In particular, wireless communication to/from the radio stations is described in Sect. 8.5.5, and autonomous station power is detailed in Sect. 8.5.6.

6.6 Development and production schedule

The production plan is reported in Table 12 for the two station designs. This production schedule is based on experience extrapolated from mid-scale production done for RNO-G, while also leveraging experience with the ARIANNA station production for the shallow-only stations.

The first year we will produce all hybrid stations needed for two deployment seasons. Following the first year, the production rate will ramp up to a maximum of 30 hybrid and 36 shallow stations per year.

	Hybrid station		Shallow station	
	units	time [day]	units	time [day]
VPols	14	1.6	2	0.3
HPpols	6	0.9	0	–
LPDAs	7	0.15	7	0.15
8ch-digitizer + trigger boards[¶]	3	3	1	1
Amplifier boards	24	4.2	2	0.4
Controller boards[¶]	1	1	1	1
Cables (fibers and coax)[¶]	station	0.5	station	0.04
Enclosures (DAQ boxes)	1	1	1	0.8
Integration	station	1	station	0.5

Table 12: Time needed to produce, test, integrate, and calibrate the components of one hybrid and one shallow station.

For components produced by contracted manufacturers, the production time for 1 unit is difficult to estimate since components will be produced in a batch and only spot tests will be performed. In this case the second column in Table 12 only indicates the time needed for calibration, which will be performed by the project.

The following assumptions are made to build the table:

- The shallower VPol of the hybrid station as well as the one in the shallow station are deployed at a depth of $10\,\mathrm{m}$. For this channel, no RF over fibre amplifiers are foreseen.
- We assume all boards from a manufacturer will be produced and tested in 2 months.
- We assume all LPDAs will be produced and tested in 2 months.

Most of the components (digitizer, controller and amplifiers boards as well as the DAQ boxes) will be produced and tested by a contract manufacturer and sent back to collaboration institutions for calibration and integration. Table 13 shows the number of units to be produced per year, starting two years before the first deployment season. Dedicated spare stations will be produced in PY1 as indicated in the table.

All hardware will be produced and tested at several production site and integrated and calibrated at a single facility. This distributed effort works well for the RNO-G project, and can be used as a model for the radio array for IceCube-Gen2. As long as commercial parts are available, the production schedule can easily be adjusted in the event that changes need to be made in the deployment schedule.

At the final integration site, a number of calibration measurements will be performed at low temperatures, as described below in Sect. 6.7.1, and all parts will be integrated into a station. The DAQ box will be shipped fully integrated, as all connections are made as such that they cannot loosen due to shaking during shipment. Cables and antennas are shipped separately and will be integrated again during deployment in the field using

[¶]Components produced by manufacturer

Project year	PY1	PY2	PY3	PY4	PY5	PY6	Total
hybrid stations	20+2	24	30	30	30	30	**166**
shallow stations	16+2	34	34	37	37	39	**199**
VPols	344	404	488	494	494	498	**2722**
HPols	132	144	180	180	180	180	**996**
LPDAs	280	406	448	469	469	483	**2555**
8ch-digitizer + trigger boards	102	140	158	164	164	168	**896**
Amplifier boards	604	702	852	861	861	867	**4747**
Controller boards	40	58	64	67	67	69	**365**
Enclosures (DAQ boxes)	40	58	64	67	67	69	**365**

Table 13: Table summarizing the production plan for the whole radio array split up by project year (PY).

the environmental enclosure, which will be installed when power and communications are provided from the Radio FieldHubs (see Sec. 8.4.2).

6.7 Test strategy

The testing and commissioning of the radio detector of IceCube-Gen2 benefits from long-standing experience with ARA, ARIANNA and RNO-G as well as with radio detectors for cosmic rays such as the radio detector of the Pierre Auger Observatory, LOFAR, Tunka-Rex etc. that have similar procedures. IceCube-Gen2 has members from all these experiments which guarantees the transfer of existing knowledge and best practices. The commissioning plan for Gen2-radio is the following:

6.7.1 Testing during production and predeployment verification

All individual components (e.g., amplifiers, DAQ boards, etc.) will be cold-stress tested (multiple temperature cycling) at their individual production sites to ensure that all parts perform according to specifications. In particular, the S parameters of the full signal chain will be measured, and the components will be tested at the low temperatures (approx -50 °C) expected at the South Pole.

The Pre-Deployment Calibration Plan includes:

- *Component-level testing* Component-level testing is done at the institutions that procure and assemble the individual components. The RF-signal chain gain and noise figure will be measured. These tests are performed both for stability over time and through several thermal cycles. The power delivered to all boards over time and through multiple thermal cycles will also be measured. Each component will be stress-tested and qualified for deployment in the cold. Components that are deployed above the surface will be evaluated for mechanical stability and their ability to withstand extreme weather conditions, including thermal cycles and wind. The return loss of each antenna will be measured and compared to a standard for quality control. Data acquisition chips will be scanned for reliability and channel gain variations using thermal noise and injected calibration pulses. Board-level timing will be calibrated with standard techniques using zero-crossings of sine waves.

- *Integration, Testing, and Validation* All subsystems will be integrated into a custom-machined Faraday Housing that consists of an RF-tight, monolithic instrument 'box'. Integration-level testing is performed after all component-level subsystems are delivered and constructed, comprising the station instrument boxes. Testing includes verifying that the connections are sound among components of the DAQ. It also includes live- and control-tests of all instrument subsystems after integration to ensure full range of operational capabilities and interconnections, and confirmation of nominal power consumption for all subsystems. Validation of the integrated instrument includes: validation of the communication links, the RF signal chain, the timing synchronization, the trigger threshold, RF shielding, and 100 hours of instrument burn in. Each fully integrated instrument box is tested in full operating mode in a thermal chamber at -50°C over a 24 hour period.
- *Calibration Databases* Calibration data will be stored in a database for up-to-date access on station performance metrics.

6.7.2 South Pole acceptance tests and commissioning

Once a station is installed and connected and while the deployment team is still at the station, a series of short tests are performed to verify basic station operation. The station electronics will be directly connected to the central DAQ in a special *test* mode that allows operating the station remotely and to immediately check the antenna readouts. A scientist either sitting at South Pole station or even off the continent, in case a good internet connection is available, will run the following tests and will report back to the deployment team via Land Mobile Radio (locally) or Iridium satellite phone (remotely):

- *periodic detector readouts*: The voltage traces from all antenna channels allow verification of electrical continuity. The measured noise level and, in particular, the frequency spectrum allow verification of proper functionality and connection of all components of the signal chain.
- *calibration pulser run*: The station is configured to trigger on the sequential impulsive signals generated by the station calibration pulsers. This test verifies trigger functionality, whether all channels are connected correctly, i.e., not swapped, and, by analyzing the pulse arrival times, if all antennas are at their nominal positions.

It is important that any issues be rapidly identified so that the on-site deployment team can perform any required troubleshooting in real time. Execution of the first two tests should require $\mathcal{O}(10)$ minutes.

In addition, more in-depth tests will be performed for commissioning that need $\mathcal{O}(1)$ day. They include:

- *calibration pulser run*: The measured pulse shapes and their amplitudes are compared to expectation and predeployment laboratory standards, which tests the signal chain more thoroughly, i.e., antennas, amplifiers, RF over fiber, filters and connectors.
- *Test run in neutrino mode*: The trigger thresholds are tuned (through a fast on-board tuning process) to yield the design trigger rate of $1\,\mathrm{Hz}$. Then, the station is

run in *neutrino mode*. The triggered voltage traces are analyzed and compared to expectation (amplitude distribution, frequency spectrum, ...) for the dominant thermal-noise background.

These two tests benefit from increased statistics, and potential issues are likely to be more subtle if a station passed the first two tests already. Twelve hours of data-taking should provide an adequate triggered event sample size, such that a final assessment of nominal station operation can be performed. Once hardware functionality has been validated, the station is added to the central DAQ for nominal operation. Clearly written procedures will be provided to the deployment crew identifying which failures are recoverable and which need immediate on-ice repair.

In addition to the testing program described above, an extensive postdeployment radio calibration program is planned to provide a precise survey of the geometry after deployment, the long-term monitoring of the DAQ and antenna response, and further measurements of the properties of the ice. Those activities, as well as the instrumentation and procedures required to complete them, are described in detail in Chapter 10.3.

6.8 Risks and risk mitigation

Lacking large scale, long-term performance experience with the planned hardware. The in-ice radio array is builds on either very small detectors (ARA, ARIANNA) or the recently installed RNO-G. This risk will be mitigated by the growing experience with RNO-G. By the time construction starts for IceCube-Gen2, RNO-G will have operated for several years. However, this timeline may make changes later in the project necessary, and the design has to remain more flexible than potentially ideal.

Limited experience in mass production and reliability of electronics for radio arrays. For the radio array production has to be scaled up by a factor of 10 even compared to what will been achieved for RNO-G. A large fraction of participating institutions have experience in large scale production and management of large projects from IceCube and other experiments. Knowledge will have to be transferred between the experts in radio and experts in large-scale production to mitigate this risk.

Supply chain issues for electronic components and the related potential delay of RNO-G. Before the large-scale production of the electronics for IceCube-Gen2 begins, it is anticipated that supply chains for electronic components will have stabilized. However, RNO-G is currently experiencing procurement challenges, and RNO-G is an important field-test for all components. Nonetheless, this should have a minimal impact on the in-ice radio array of IceCube-Gen2, as the RNO-G schedule is decoupled from the IceCube-Gen2 radio array schedule. RNO-G is currently scheduled to install additional stations in 2024, 2025, and 2026. Parts have been secured for a large portion of the required hardware, and the collaboration has been pursuing gray market purchasing with good success. In addition, alternative testing sites and electronics components will be explored for IceCube-Gen2.

Discovery experiment. To date, no neutrino has been detected with the radio technology. Early, pioneering efforts, while demonstrating the technical feasibility of radio

arrays, have nonetheless lacked sufficient effective volumes to detect the small flux of neutrinos expected at ultrahigh energies.

In fact, the radio array of IceCube-Gen2 may be the first instrument to detect neutrinos at EeV energies. Thus, the array design has to be guided by neutrino simulations. There may be unknown backgrounds, unknown large scale ice effects, or unknown signal characteristics that cannot be accounted for in these simulations. With a potential discovery in mind, the detector has been carefully designed to differentiate backgrounds and provide redundant detection channels to verify a potential discovery. In parallel, the collaboration is pursuing a significant calibration effort. This is a risk inherent to any discovery experiment.

Drill performance untested on large scales. The BIGRaid Drill is constructed by world experts at the British Antarctic Survey (BAS), but has only been field-tested on a limited basis at RNO-G (2021, 2022) and has not yet been optimized to meet the operating requirements. The drilling of holes is an important limiting factor in the installation, and nominal speeds are required to meet the installation schedule. However, by the time construction for the radio array starts, the drill will have been tested and further developed in several field seasons in Greenland for RNO-G. A close collaboration of BAS with the drilling experts within IceCube-Gen2 has also already started, which transfers mass production and reliability expertise to the drill development. Additional testing is also foreseen for the South Pole, and once deployment begins, the drilling schedule will ramp up slowly. The track record of BAS and experience with the IceCube drills suggests a likely successful outcome. Should drilling performance not be reached, the ratio of shallow to hybrid stations can be adjusted to compensate for the performance issues.

Providing reliable power and communications over 550 km^2. The footprint of the radio array will be larger than anything ever constructed at South Pole or other parts of Antarctica. Still a $> 90\%$ up-time in communication and power distribution is the target, which is a tight requirement. However, our reference design employs a technology proven at IceCube and the IceCube Upgrade. A mitigation strategy is to switch (a part) of the array to renewable power (wind-turbines and solar panels per station), however this mitigation switch will need to be made early in the project. Solar power is a proven technology in polar environments, but it limits the operation to 50% of the year. Wind-turbines are needed to bridge the gap, but they are not proven yet and need to be developed in parallel. The installation of wind-turbines is foreseen in Greenland for the coming RNO-G field seasons.

6.9 Summary

The radio array of IceCube-Gen2 provides the coverage of the highest neutrino energies, in particular improving over IceCube at EeV energies. It consists of two types of stations combined to a large array that reaches an unprecedented sensitivity to neutrinos above $10\,\mathrm{PeV}$ in energy. Shallow stations use high-gain log-periodic dipole antennas just buried below the surface. At the surface they view a smaller volume of the ice, but are considerably easier to install. More complex hybrid stations provide a larger field-of-view and thus more effective volume per station by combining antennas

installed down to a depth of $150\,\mathrm{m}$ with shallow antennas at the surface Both station types are complementary in terms of risks and signal robustness, which is essential for a discovery experiment; no prior detection of EeV neutrinos has been reported to this date. The radio array combines 197 shallow with 164 hybrid stations and meets the science requirements as described in Chapter 2.

The technology builds on many pathfinder experiments (RICE, ARA, ARIANNA, ANITA), and most prominently on RNO-G which is currently being installed at Summit Station in Greenland. By the time, the production will start for IceCube-Gen2, a robust design will have been field-tested over several seasons and will further guide the design of the array for IceCube-Gen2. Site-specific tests will also be carried out at South Pole, either as part of the ARA experiment or with dedicated set-ups.

7 Surface Array

The surface array complements the optical array of IceCube-Gen2 in the same way as IceTop has been complementing the deep detector of IceCube. Building on the success of IceTop as well as on lessons learned from IceTop, we have developed a design of the surface array that optimizes the total science output of IceCube-Gen2. The surface array will consist of stations comprised of elevated scintillation and radio detectors on top of and connected to each string of the optical array.

7.1 Overview

The surface array supports and enables a number of IceCube-Gen2's science goals by detecting cosmic-ray air showers up to energies of $\gtrsim 10^{18.5}$ eV. For those air showers whose axis intersects the optical array, IceCube-Gen2 constitutes a world-unique setup: the surface array measures the electromagnetic shower component and low-energy muons while the optical array detects TeV and potentially PeV muons produced by the same air shower. As major advantage over IceCube, which only provides surface-deep coincidences for near-vertical events, the range of zenith angles for geometries of coincident surface and optical events is significantly increased in IceCube-Gen2 (cf. Figure 30 in chapter 2). The combination of the larger area of the surface array and the enlarged range of zenith angles for in-ice coincidences, results in roughly 30 times larger aperture for such events.

An important function of the surface array, thus, is to provide a veto that reduces the background of atmospheric muons in samples of astrophysical neutrinos from the southern sky. Moreover, the surface array is essential for a better understanding and estimation of atmospheric backgrounds from all arrival directions, including up-going atmospheric neutrinos. In particular at PeV energies, the atmospheric muon and neutrino fluxes are dominated by prompt decays. Due to uncertainties in hadronic interaction models, uncertainties in the proton fraction as well as in the energy scale and absolute flux of the cosmic rays, calculations of these prompt backgrounds come with significant uncertainties. The surface array will improve on all of these aspects. Furthermore, cosmic-ray measurements are a science target by themselves, as accurate measurements with high statistics are necessary to understand the most energetic Galactic cosmic rays and their transition to extragalactic cosmic rays.

One of the most important lessons learned from IceCube is that the surface array needs to be designed in a way that facilitates snow maintenance. Therefore, all detectors are elevated and easily raisable, minimizing the yearly maintenance effort. Other design aspects of IceTop are kept. As IceTop did, also the IceCube-Gen2 surface array follows the design of the optical array and shares its power and communication infrastructure. This enables building the surface array with just a small fraction of the total budget.

Finally and importantly, the design builds on several years of experience, with individual prototypes tested at the South Pole for more than five years, and a complete prototype station operating above IceCube since 2020. For the layout of the surface array, an overview of the station design, and photos of the detectors of the prototype station, please see chapter 3, especially figures 37 and 41.

7.2 Requirements

The science goals of the surface array include neutrino and cosmic-ray objectives, and PeV photon search as a target of opportunity. On the neutrino side, the surface array will

1. *Veto:* provide a veto for the atmospheric muons that make up the primary background for down-going astrophysical neutrino events.
2. *Atmospheric leptons:* characterize the production of atmospheric leptons in air showers which governs the background muon production for the optical and in-ice radio arrays, in particular, prompt muons.
3. *Background fluxes:* provide a better understanding of atmospheric-neutrino background fluxes in the optical array, as these depend not only on the hadronic interactions, but also on the absolute flux and mass composition of cosmic rays.

On the cosmic-ray side, the surface array will contribute to both the particle physics and astrophyics of cosmic rays using the combined information from the surface and optical detectors. Specifically, the array can

4. *Primary mass composition:* conduct a measurement of the primary mass composition and its variation with energy, which can improve our understanding of the highest-energy Galactic sources. In the energy of the Galactic-to-extragalactic transition, the accuracy should be higher than those of previous arrays.
5. *Hadronic physics:* study hadronic physics in air showers by exploiting surface-optical coincident measurements. A better characterization of hadronic interactions will enhance the interpretation of IceCube's measurements but also the data analysis for all indirect cosmic-ray experiments.
6. *Galactic cosmic-ray anisotropy:* extend the energy range of Galactic cosmic-ray anisotropy measurements by one or two orders of magnitude in energy depending on the physics scenario, and search for a mass dependence of the anisotropy.

Some science goals, e.g., extending the energy range of anisotropy can be reached almost automatically with the larger size and statistics of IceCube-Gen2, but other science goals set particular requirements on the design of the surface array regarding its threshold and accuracy for the energy and mass composition of cosmic rays. In particular, while all science goals profit from a low detection threshold, the veto objective as well as the goal to measure prompt muons in coincidence with their parent air showers demand a high efficiency for the detection of primary protons above 0.5 PeV. Moreover, if PeV photon sources similar to those detected by LHAASO [306] exist in the field of view of IceCube-Gen2, there is a significant discovery potential due to the gamma-hadron separation provided by combining the surface with the optical array.

7.2.1 Science requirements and flow down

The primary background for astrophysical neutrino sources from the southern hemisphere is from that of high-energy, $\mathcal{O}$(TeV - PeV), atmospheric muons, created in the first few interaction lengths of air showers. This background sets the threshold for sev-

eral science cases described in section 2, particularly those related to point source searches and multi-messenger astronomy. The flux of background from cosmic rays is approximately equal to the astrophysical neutrino flux at ≃ 300 TeV [30]. We therefore require a surface array with a detection efficiency at commensurately low energies to effectively veto the background. A ≃ 90% detection efficiency at 300 TeV would enable a more precise measurement of the diffuse flux of muon neutrinos over a wider range of energies. An additional lowering of the veto to the few tens of TeV energy ranges can also enhance the veto capabilities, increasing the TeV energy astrophysical neutrino rate. A very high detection efficiency (≥99%) at 1 PeV would significantly improve multi-messenger studies in the *southern* sky, which currently start at few PeV [626]. Enabling this also requires the largest possible aperture for *coincident* detection with the optical array to be most effective.

Exploiting the unique setup of IceCube-Gen2 with its deep and surface detectors, one can study the production of PeV energy forward muons, in particular, muons originating from prompt decays of charmed and unflavored mesons. The flux of such prompt muons (and the corresponding prompt atmospheric neutrinos) currently has large uncertainties. A better understanding is not only important for a more accurate modeling of the atmospheric backgrounds of astrophysical neutrinos, but also an important science goal in itself. Assuming proton initiated air-showers, these prompt muons are produced mainly by cosmic rays from roughly 0.5 PeV to a few PeV energies [627]. With the large enough aperture of IceCube-Gen2, first measurement of the prompt muon component in coincidence with a measurement of the parent showers at the surface will become possible. In addition to the veto, this is another reason to require full detection efficiency for protons above 0.5 PeV.

It is also worth noting that the hadronic interaction models are necessary to interpret the mass of cosmic rays, generally done via air shower simulation codes. On one hand, modern hadronic interaction models disagree on the production of muons at the level by ≈ 20% [374]. On the other hand, current measurements indicate that all simulations under-produce muons, generally, by a few 10% in the production of hadrons, with the largest discrepancy observed at the highest cosmic-ray energies [368]. Any error in the simulations translates into a systematic bias on the mass and energy assignments of cosmic rays and results in a systematic uncertainty for neutrino measurements. Making significant progress towards resolving this problem requires a detector that can provide strong constraints on hadronic interaction models via precise and complementary measurements for the electromagnetic (γ and $e^{\pm}$) and muonic components of individual air showers. Uncertainties in the hadronic interaction models also translate to systematic effects in the self-veto capabilities of neutrinos event selections, especially for the southern sky TeV astrophysical neutrinos. Precision measurements of 10-500 TeV energy air showers can significantly reduce the impact of this systematic. These goals necessitate that the surface array includes multiple detection methods with complementary sensitivity to both components. The energy assignment must be relatively precise (absolute uncertainty of ≲ 10%) and primary masses must be separable into individual species or at least into heavy and light groups. The hadronic interactions are imprinted in the muon distributions within the air showers and therefore the observatory should include sensitivity to muons, preferably over a wide range of energies (GeV up

to PeV). Also, extending the measurements of muons for primary cosmic ray energies above 100 PeV will cover the gap existing between the measurements at IceCube [628] and at the Pierre Auger Observatory [629].

Several technical challenges must also be met by the detector and readout hardware design. The coincident showers that are detected by the surface and optical arrays require a hardware scheme where both arrays can trigger readout of each other. This can be accomplished by including buffers for the surface and optical detectors which can store the readout data long enough for a trigger request to be sent, $\mathcal{O}$(seconds), depending on the details of the trigger scheme. Although only $\mathcal{O}(10^6)$ air-shower events per year above a threshold condition of at least three scintillator panels with signal strengths of more than 0.5 MIP are expected, the data acquisition system (DAQ) must be able to handle a much higher trigger rate: the dead time needs to be $\ll 0.1$ ms to cope with the $\mathcal{O}$(kHz) trigger rate of individual scintillator panels due to secondary muons originating from low-energy cosmic rays. This is necessary for the efficient functioning of the surface array as a veto. The overall event rate over the complete surface array will depend on the exact trigger implementation and can likely be $\sim \mathcal{O}$(kHz). Finally, the calibration of the detectors must be accurate enough to achieve a $10\,\%$ systematic uncertainty on the energy. For the scintillation detectors, the main uncertainty from the hardware will be determined from the calibration of the minimum-ionizing particles (MIPs) and is expected to be as precise as the $3\,\%$ calibration uncertainty of the IceTop tanks ([507]). For the radio antennas, the primary uncertainty will be driven by the absolute gain pattern. The gain patterns are available from the SKA collaboration and can be crosschecked in an anechoic chamber to directly measure the gain pattern to an accuracy better than 0.5 dB. Given the recent improvements in calibration techniques for radio arrays, the target accuracy of $\mathcal{O}(10\,\%)$ seems feasible. The orientation of each antenna can be measured using traditional surveying techniques that regularly happen at the South Pole. As shown with the prototype station, this is easily possible to an accuracy level that is more than sufficient for the overall goal of $10\,\%$ absolute accuracy of the radio amplitude measurement.

7.2.2 Expected Performance

The reference design of the surface array includes 130 (120 + 10) stations with eight scintillator panels and three radio antennas, as shown previously in Figure 37 (162 total stations together with the surface enhancement of IceTop). One station is located near the top of each IceCube-Gen2 optical string, and eight additional stations are added to fill the gaps between the surface array footprint of IceCube and IceCube-Gen2. Two more stations are foreseen for cross-calibration with the radio array, making a total of 162 surface stations together with the 32 stations of the surface enhancement of IceTop, as it is important for the science goals to have the complete surface area covered with the same type of stations.

This spacing, station layout, and the number of detectors is set by the 0.5 PeV energy threshold needed for protons to achieve an efficient veto. A cosmic-ray veto is possible by registering three panels with signal above threshold, coincident with a track-like signal in the optical detector. The left panel of Figure 90 shows the expected event

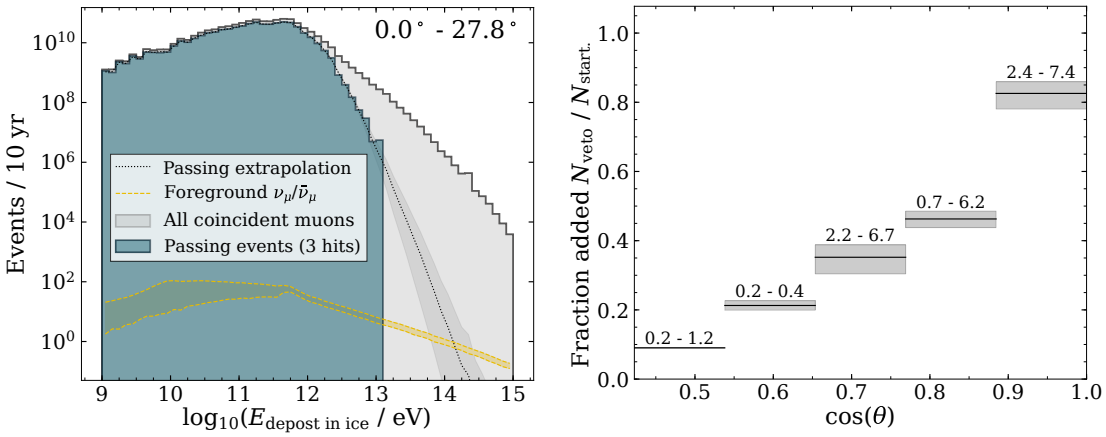

Figure 90: Left: Rate of cosmic ray events which will produce muons (gray) and those which cannot be vetoed (blue) as a function of the energy deposited in the optical detector volume by muons, simulated using SIBYLL 2.3d. Only trajectories that are contained on the surface and in-ice are considered. An extrapolation, based on the rejection rate of CR events, is shown by the black dashed line. The foreground from $\nu_\mu/\bar{\nu}_\mu$ is shown based on the flux measured in [362]. Right: for various zenith angles, the relative increase in the number of neutrinos that will be detected due via the surface veto w.r.t. the use of a self-veto. The numbers indicate the 1σ range for how many additional neutrinos will be detected for each angular bin after 10 years of operation.

rates of muons, produced by air showers, with a trajectory that passed through the surface array and optical volume. The rate is given by the amount of energy deposited by muons in the volume of the optical detector. A suppression of roughly 5 to 8 orders of magnitude of the background is required to reveal the muon neutrino flux. The surface veto enables a significant reduction of the background above $\mathcal{O}(10\,\text{TeV})$ in deposited muon energy, resulting in a background level lower than the astrophysical neutrino rate above $\mathcal{O}(100\,\text{TeV})$. For PeV muon tracks, the surface veto will enable a background-free measurement of down-going astrophysical neutrinos for all geometries intersecting the surface array. Figure 91 shows the fraction of high-energy neutrinos added through the surface veto as a sky map, where the largest benefit is for near-vertical down going events. Such a veto would increase the number of neutrinos detected at these energies by up to $80\,\%$ in the southern sky, see Figure 91, and would amount to $11.0^{+6.2}_{-3.3}$ additional neutrinos over 10 years.

The cosmic-ray energy threshold is shown in the left panel of Figure 92, requiring at least five hit scintillator panels in the array. The trigger efficiency reaches $98\,\%$ at $670\,\text{TeV}$ for all primaries with zenith angle up to 45°. More important for the key science goals of the veto and the study of prompt muons is the trigger efficiency for protons, which meets exactly the requirement of $500\,\text{TeV}$ for vertical air showers. The surface antennas will be sensitive to the coherent emission produced in air showers and will be externally triggered by the scintillator panels. The reconstruction of events with radio antennas will be possible for air showers beginning at a few $10\,\text{PeV}$, as shown in the right panel of Figure 92. The 18° inclination of the geomagnetic field at the South Pole mainly governs the detection efficiency at various shower inclinations with larger zenith angles producing stronger amplitudes in the radio signal.

The main strength of the IceCube-Gen2 design is the coincidence detection with the in-ice optical array. The increased lateral size of the surface array results in a geometric

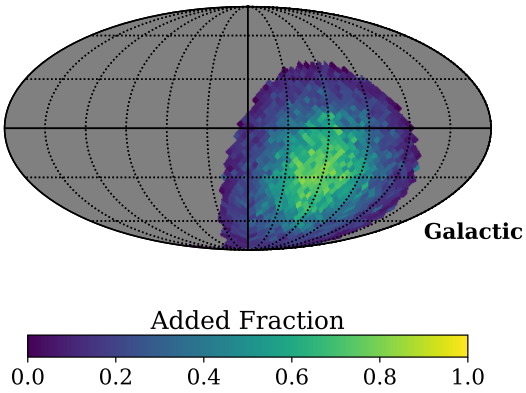

Figure 91: Sky map showing the added fraction of high-energy neutrinos which can be identified with the surface veto relative to having only the in-ice self veto. The surface veto provides the strongest improvement for those areas of the sky which otherwise would feature the lowest sensitivity of the optical array alone, i.e., near-vertical down-going neutrinos.

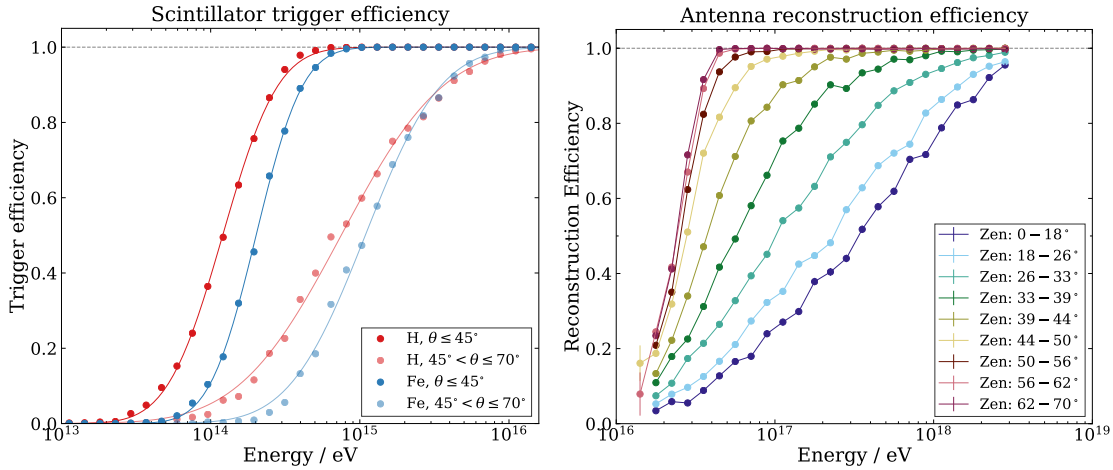

Figure 92: Left: The trigger efficiency of the scintillator array with the condition of at least 5 hit detectors. Simulations are shown in two zenith angle bands for proton and iron primaries using SIBYLL 2.3d [370] as a hadronic interaction model. Right: The reconstruction efficiency for at least 3 surface antennas, assuming noise that is dominated by Galactic emission [630], is shown for various zenith angles.

aperture of $8\,\mathrm{km}^2\,\mathrm{sr}$ (currently $0.26\,\mathrm{km}^2\,\mathrm{sr}$) and includes possible coincident trajectories up to 68° (currently 38° with IceTop). This increased aperture will boost the event rate of coincident detection by a factor of $\simeq 30$, despite the factor of $\simeq 7$ increase in instrumented area. A plot with the expected event rate is shown in Figure 45 for various combinations of detection modes. We expect 10^8 events per year with both scintillator and optical signals at $1\,\mathrm{PeV}$ and 10^4 events per year with scintillator, antenna, and optical signals at $100\,\mathrm{PeV}$.

The *simultaneous* detection of the high energy ($\gtrsim 300\,\mathrm{GeV}$) muons with the surface and optical arrays will result in much stronger constraints on the hadronic interaction models. Preliminary studies using the existing IceCube/IceTop detectors have indicated that there is an inconsistency with the high and low-energy muons [374]. The increase in aperture will allow for such tests in muon production from cosmic rays up to an energy of 10^{19} eV as a result of the improved statistical uncertainty by a factor of $\sqrt{30}$.

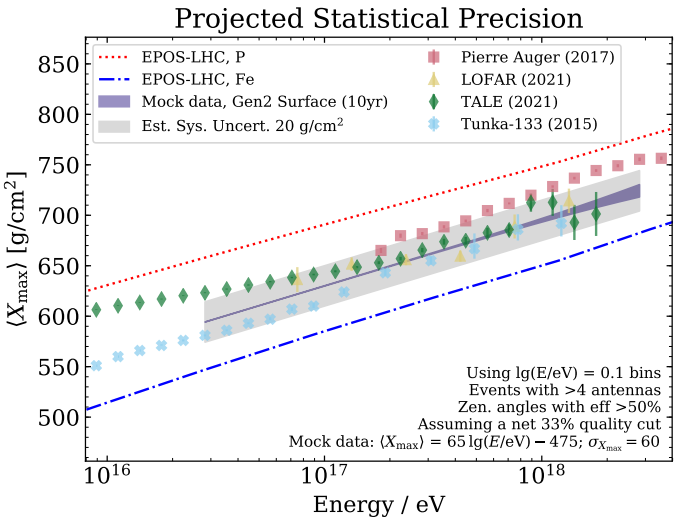

Figure 93: The statistical precision to which X_{max} can be measured using the surface antennas after 10 years of operation is shown. This is compared to the expected systematic uncertainty of $20\,\mathrm{g/cm^2}$. The measurements and statistical precision of several other experiments are shown for comparison [631–633].

For cosmic ray energies above 30 PeV, additional studies can be performed using the electromagnetic measurements from the surface antennas. The depth of air shower maximum, X_{max}, includes significant composition information. Figure 93 shows the expected statistical precision after 10 years of operation , based on the results of other radio arrays. The current tension in the hadronic models is most clearly demonstrated by the disagreement between the X_{max} and the muon production [368]. The construction of an observatory that can make direct measurements of the muon production as well as the electromagnetic content will result in the strongest constraints on the development of hadronic interaction models in the field.

With the inclusion of such corrections to the hadronic interaction models, we will be able to reconstruct the cosmic-ray mass from IceCube-Gen2's measurements with unprecedented accuracy, especially with the inclusion of the surface and in-ice information. Also, as an advantage over IceTop, the direct measurement of X_{max} will provide an accurate absolute mass scale that is independent of the muon problem in these models. Both panels of Figure 94 show the advantage of simultaneous measurements of the electromagnetic and muonic components of air showers using several observables measured with the surface array. While each quantity (the number of ≥ 500 GeV muons, the surface electron-muon ratio for muons of this energy, and X_{max}), individually, includes some separation power, the combination of them for individual air showers increases the mass-discrimination even more. The right panel shows a figure-of-merit FOM where values higher than 1.5 can be interpreted as a good event-by-event mass separation of the primary particle [635]. With the inclusion of more accurate reconstruction uncertainties, especially at higher energies, it is expected that the FOM will be around 2 for the complete energy range of interest, i.e., the proton and iron distribution will be separated by approximately two sigmas (for reference, the AugerPrime upgrade of the Pierre Auger Observatory has been designed to increase the FOM for proton-iron separation to 1.5 [636]). It is also plausible that the mass separation

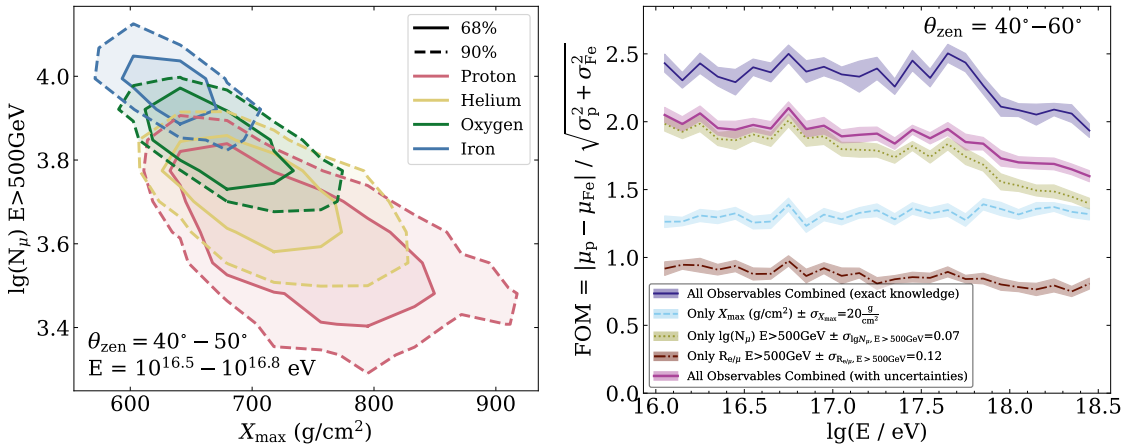

Figure 94: Left: Two air shower observables that will be most important for mass separation, number of ≥ 500 GeV muons and X_{max}, are shown for four primaries, simulated using SIBYLL 2.3d [370] as a hadronic interaction model. The number of muons has been corrected using the Heitler-Matthews scaling [634] of $\beta = 0.85$. Right: The figure-of-merit (see text) describing the separation power of proton and iron primaries as a function of simulated energy. The relative importance of X_{max} in addition to muon measurements increases with energy.

will improve even more by the time IceCube-Gen2 goes into operation, e.g., by the development of machine learning techniques considering further information from the contributing detectors. Consequently, by combining surface particle, surface radio, and in-ice muon measurements, IceCube-Gen2 will be capable of an unprecedented level of accuracy for the cosmic-rays mass in the energy range around 100 PeV and higher, i.e., for the most energetic Galactic cosmic rays. With an extended energy threshold down to 0.5 PeV, the full range of measurements will cover four orders of magnitude in energy.

7.3 Main interfaces

Most surface-array stations will be located on top of an in-ice string of the IceCube-Gen2 optical array, except for the stations over the deep detector of the current IceCube (i.e., the IceTop enhancement and a few stations filling gaps to the IceCube-Gen2 surface array). Thus, for most of the surface stations, the central fieldhub for each station will also be used to house the electronics for the optical string. For infill stations without in-ice strings, the same design will be used in order to simplify the production, i.e., for those few stations the fieldhub will only host the surface electronics. For more details on the fieldhub see section 8.4.2.

Each fieldhub is connected to three radio antennas through 50 m LMR-400 coaxial cables which carry the analog radio-frequency (RF) signals from the antennas to the DAQ and 5 V DC from the DAQ (called TAXI) to the antenna low-noise amplifiers (LNAs). Also each fieldhub is connected to eight scintillator panels through 90 m CAT6 cables which carry power and timing to the panels and digitized data back to the DAQ. Both the antenna and scintillator cable lengths include 5 m slack on each end, which permits more than two decades of operation by raising the detectors by about 1 m approximately every five years (the lifetime can be prolonged beyond 20 years through extension cables). The fieldhub is also connected to the IceCube Laboratory through a 150 V power

cable and an optical fiber for data transfer, communication and timing. The total power consumption in the current prototype station is around 60 W for the complete station including the DAQ and all radio and scintillation detectors of the station. For more details on the DAQ interfaces, see section 7.4.3. The IceAct stations are connected to the field hub with 2 optical fibers(one for WR timing and one for communication) and a 150V power cable. The total power consumption in the IceAct stations is on average around 350 W (with 400W peak power consumption during startup) including the telescope DAQ, communication box, WR timing and lens heating. As the IceAct stations are only running for 1/3 of the year, the overall power budget per year is less than 120 W per station per year.

7.4 Reference design

The design of the surface array makes use of the infrastructure put in place for the optical array. Each optical string will feature one surface station consisting of four pairs of elevated scintillation panels and three elevated radio antennas. While the scintillation detectors fulfill the low detection threshold requirement (full efficiency for protons above 0.5 PeV), the radio antennas provide the needed accuracy for the measurement of cosmic ray energy and depth of the maximum of the electromagnetic shower component. Compared to the in-ice radio array, where a high number of antennas is critical to maximize the discovery sensitivity, the requirement is different for the surface array. Since measurement accuracy for cosmic rays above 100 PeV is a critical requirement for the surface array, antennas of high quality are required, which combine a wide sky coverage with low systematic uncertainties ($< 10\,\%$ on the measured radio amplitude). Four IceAct stations along with the scintillators and radio antennas additionally provide sensitivity to air showers from TeV energy cosmic rays.

Like the scintillators, the antennas are also elevated, which successfully mitigates the problem of snow coverage, one of the central problems of IceTop. Therefore, the same design of surface stations for the surface enhancement of IceCube is planned to be deployed on top of IceTop. This will not only mitigate the deteriorating threshold of IceTop due to snow accumulation, but also ensure that the complete optical IceCube setup is covered by a unified design of surface stations (the DAQ electronics of stations of the IceTop enhancement can be updated to the same version that will be used in IceCube-Gen2). It is important to note that a unified surface array over the complete optical footprint will enhance the science of both the existing deep array and the IceCube-Gen2 optical array. Thus both optical arrays, i.e., the IceCube and IceCube-Gen2 optical arrays, will benefit from the increased sky coverage of a unified surface array.

In order to deploy a surface array able to achieve our science goals, while located at one of the most extreme places on Earth, the surface detectors need to fulfill some basic requirements that are summarized in the table below.

Requirements for Surface Detectors	
Shared requirements	
Elevated at more than 1 m	Raisable by 1 m every 5 years
Resist temperature to -70°C	Resist wind max 100km/h [637]
Easy assembly at the site	Weight < 50 kg per detector
No snow accumulation around detectors	Affordable
Scintillator specific	**Radio specific**
Leveling accuracy better than 1°	Leveling and orientation accuracy better than 1°
Light-tight design	No metal in contact with the antenna
Can be lifted by two people	Metal parts no larger than 10 cm

7.4.1 Elevated scintillators

The eight scintillation detectors of each station are connected via $90\,\mathrm{m}$ long CAT 7 cables to the central DAQ, which provides power, timing and communication. Each scintillation detector has an active area of $1.5\,\mathrm{m}^2$ and a total weight of <$50\,\mathrm{kg}$. This enables transport and assembly by two people.

The active area consists of 16 extruded plastic scintillator bars, made of polystyrene with doping of $1\,\%$ PPO and $0.03\,\%$ POPOP and coated with a 0.25 ± $0.13\,\mathrm{mm}$ thick reflective layer of TiO_2. Each bar has the dimensions $1\,\mathrm{cm} \times 5\,\mathrm{cm} \times 187.5\,\mathrm{cm}$ and has two holes with a diameter of ≈ $2.5\,\mathrm{mm}$. Wavelength-shifting fibers, Y-11(300) with a diameter of $1\,\mathrm{mm}$, are fed through these holes to collect and guide the light produced by an energetic particle crossing the scintillator. All fiber ends of a scintillation detector are read out by a single light sensor, a silicon photo-multiplier (SiPM) of type 13360-6025PE with an active area of $6 \times 6\,\mathrm{mm}^2$, see Figure 95. The fiber ends are bundled into a cookie and end ≈ $1\,\mathrm{mm}$ above the surface of the SiPM. The gap allows the illumination of all SiPM pixels, thus increasing the dynamic range. It is filled with the optical glue "EJ-500", providing robustness and long term stability.

The inside of the scintillation detector is wrapped in opaque polymeric foil to ensure light-tightness. An aluminum housing of the scintillators provides sufficient mechanical stability and enables an elevated mounting on poles (see Figure 96) that can be easily extended in height every few years. Several years of operation of a prototype station at the South Pole have shown that this design avoids any additional snow accumulation beyond the usual about $20\,\mathrm{cm}$ per year, and the occasional small snow accumulation on top vanishes reliably each summer. Due to lessons learned from prototypes, minor improvements regarding the riveting of the corners and the exact design of the poles and hooks have been incorporated into the final design, which is now ready for mass production and deployment.

The hits from the scintillation detectors are received at the local station DAQ in 8 independent data streams, one from each panel. These are then merged into events by using a microsecond sliding window. In order to make the directional reconstruction possible, events with less than 3 hit panels are rejected (in the prototype station these are the three panels of the station; for the IceCube-Gen2 surface array, timing windows will be adjusted for array-wide coincidence).

Figure 95: Schematic (top) and photos (bottom) of the assembly of a scintillation detector, from left to right: routing of optical fibers through the scintillator bars of the detector to the cookie that interfaces to the SiPM; Styrofoam cover of the scintillator bars; light-tight foil cover. In a final step not shown in these photos, the scintillation detector is closed by an aluminum sheet.

The charge deposited in the scintillators is read out in ADC units. To use these charges for reconstruction, they need to be compared to the average charge from a single minimal ionizing particle (MIP). However, a robust conversion from ADC to MIP units is not straightforward due to the SiPM gain dependence on temperature. Because the SiPM gain also depends on the bias voltage, the bias voltage can be adjusted during operation to correct for temperature effects. For details on the calibration procedure, see Sec. 10.4.

The SiPM signals are read out by custom-designed electronics, the scintillator uDAQ. The uDAQ is a microprocessor-based DAQ board which captures the SiPM pulse charge and start time. Using a clock speed of $180\,\mathrm{MHz}$, times are resolved to $\sim 1\,\mathrm{ns}$ by using delay lines with eight taps individually captured in the microprocessor. The uDAQ also generates the SiPM bias voltage and facilitates low level calibration, including pedestal recordings once per second and histogramming of signals. A temperature sensor close to the SiPM is read out by the uDAQ, which allows adjustment for the effects of temperature variation. Time calibration signals from the central DAQ are used on the uDAQ to match its time base to the chosen standard.

The uDAQ board amplifies the SiPM signal by three different gains in parallel, yielding a wide dynamic range of 1150 MIP in the first version planned for the surface enhancement of IceTop and approximately 3000 MIP planned in the final version. Note that for very rare ultra-high-energy showers the scintillation panels of the surface enhancement will go into saturation earlier, which does not become a concern for such air showers from large zenith angles. However, for the large flux of PeV cosmic rays there will be no essential difference. The high-gain channel enables straightforward SiPM gain calibration by separation of individual N-photon peaks, while simultaneously revealing the MIP peak position. The amplifier circuitry also shapes SiPM pulses for sample-and-

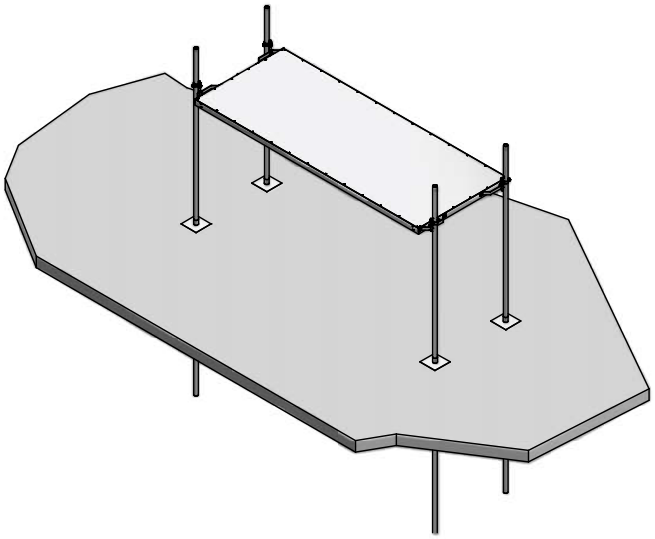

Figure 96: Schematic drawing of the mount of the scintillation panels. The panel rests on four poles hammered to about 1 m depth into the firn. The poles can be extended to lift the panels by about 1 m approximately every five years.

hold ADCs in each gain channel, which capture the pulse at a suitable delay after the input rises above a programmed trigger threshold. The recorded signals are proportional to the deposited charge in a time window 50 ns following the trigger. The final version can be adapted to record both a prompt time window and an extended one, as appropriate. Digitized charge and time information is accumulated in a circular data buffer on the uDAQ board and regularly transferred out in batches under control of the central DAQ.

Additionally, when the signal crosses the trigger threshold, a prompt pulse is sent on the cable to the central DAQ, which is used to trigger the readout of the radio antennas. The length of the trigger pulse sets the length of the coincidence window and can be changed via software. By this design, all scintillator signals are recorded for all air-shower events. The readout of the radio signals is directly triggered inside the local DAQ for stations with a high multiplicity of scintillator signals, whereas the radio signals from all other stations (even those without any coincident scintillator signals) will be obtained from a buffer after a global trigger request from the central DAQ.

7.4.2 Elevated surface antennas

7.4.2.1 Antennas SKALA-v2 The antenna foreseen for the surface array of IceCube-Gen2 was developed for the Square Kilometer Array (SKA) [561, 563], the leading low-frequency radio telescope of the coming decade. Instead of using a custom made design, as for the scintillation detectors, we can benefit from the long-term professional antenna development performed for the SKA. The SKA antenna is based on the Log Periodic Dipole Array (LPDA) antenna family, with a variety of improvements over a simple LPDA design. Except for the low temperatures at the South Pole, the SKA design requirements generally exceed the requirements for the IceCube-Gen2 surface array.

As the second version of the SKA antenna, named SKALA-v2, is already in use by the prototype station of the surface enhancement array since more than three years, we have demonstrated that it can be reliably operated under South Pole conditions. Minor optimizations done on the SKALA design after v2 are all not important for the purpose of air shower detection, so we can reduce the risk by sticking to v2 in the reference design. Particular versions of the SKALA are available commercially upon request. As an added advantage, v2 is slightly simpler than later versions and more economic. Therefore we plan to use the SKALA-v2 as antenna type for the surface enhancement of IceTop as well as for the complete IceCube-Gen2 surface array.

The SKALA-v2 antenna is operable in the SKA-low design band of 50 to 350 MHz (and is sensitive to even higher frequencies, up to 650 MHz), and provides a smooth and wide sky coverage. This is important, as a high measurement accuracy is needed for the complete zenith angle range from 0° to 68° of coincident events between the surface and optical arrays. Figure 97 shows the gain pattern of the antenna at several frequencies. According to [638], including the band of 100-190 MHz at the South Pole maximizes the signal-to-noise ratio and hence optimizes the detection threshold of cosmic-ray induced air showers. Ideally, the radio signal is not limited to that band, but recorded also at lower and higher frequencies, as the reconstruction accuracy of $X_{\max}$ benefits from a wider band.

As the SKALA-v2 includes the desired bandwidth and extends beyond, it is ideal for the surface array, without the hurdles of developing a new antenna. Reusing this well-studied and optimized antenna is a key ingredient towards achieving the accuracy goal of 10 % for the energy and, thus, for the radio amplitude. This accuracy goal is the main reason why a more sophisticated antenna is needed than for the in-ice radio array. The latter is mainly optimized on the detection threshold and has less strict requirements on the accuracy. The in-ice radio array can still benefit from the cross-calibration with the more accurate radio measurements of the surface array.

Although the antenna can receive at frequencies up to 650 MHz, a low-pass filter is installed directly in the analog signal line to filter out frequencies above 350 MHz. The main reason behind that design choice is a communication channel at the deployment site which uses the 360.2 MHz band. This would have significantly increase the noise level in the signal traces [639]. Generally for radio detectors, limiting environmental noise is essential. Although even the dark sector at the South Pole is not free from radio interferences, the prototype station shows that these are limited to certain frequencies and can be digitally filtered.

Receiving elements of the antenna are soldered on a common metal pole to build one arm, see Figure 98. The antenna is composed of four arms disposed symmetrically around the center of the antenna. Two arms face-to-face form one polarization, and the two other arms form the second independent, perpendicular polarization.

A new supporting structure for the antenna was developed in order to be deployed at the IceCube site. Details are described below.

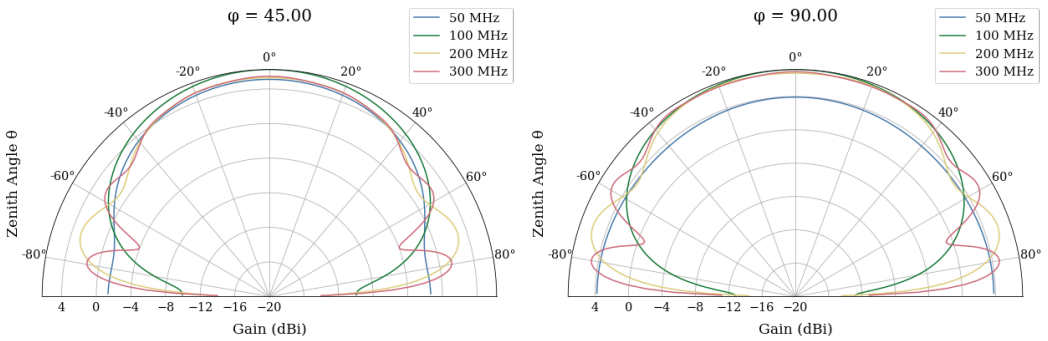

Figure 97: Gain patterns of the SKALA-v2 antenna for fixed azimuth cuts of 45° and 90°. The wide sky coverage enables air-shower detection over a wide range of zenith angles, and the low backlobes reduce systematic uncertainties due the details of the surface, such as the snow level.

7.4.2.2 Low-Noise Amplifier (LNA) Each of the antenna polarizations comes with a low-noise amplifier (LNA) directly attached at the top. The close proximity of the LNA to the antennas helps to reduce noise.

The LNA pre-amplifies the radio signal of about 40 dB and converts the balanced signal to a single-ended signal. Coaxial copper cables transmits the RF signal from the LNA to the central DAQ, which provides a 4.5 V DC voltage over the same cable to power the LNA. Two coaxial cables connect to each antenna, one for each polarization channel, which each consist of two parts: short 1.5 m LMR-240 coaxial cables are used to connect the LNAs to the 50 m long LMR-400 cables leading to the fieldhub.

The resulting system noise is as low as 40 K, which lies below the external galactic noise in the frequency band of interest [562]. This was also confirmed by an in-situ measurement of the galactic background noise as shown in [640].

7.4.2.3 Antenna Mounting Structure One of the challenges for installing and operating an array of detectors at the surface of the Antarctic continent is the harsh weather to which it will be exposed over the years. Another important requirement of the surface array is the raisability of the structure, which enables a continuous elevation of the detectors. The snow height at the site increases of about 20 cm per year. As learned from IceTop, accumulation of snow above particle detectors reduces the capabilities of the detector, and removing it is maintenance intensive.

Also for the radio antennas, snow above the antenna would constitute a hard to control systematic uncertainty, as snow changes the propagation of the radio waves. For some antenna types, even the height of the snow level below the antenna would need to be monitored. To avoid this complication, with the SKALA-v2 an antenna type with low backlobes of the gain pattern has been chosen. Except for very inclined events beyond the target zenith range until 69° of possible surface-optical coincidence, no significant impact of the snow level under the antenna is expected on its gain.

However, snow would become a problem when starting to reach the height of the lowest antenna elements. While snow coverage is tolerable for the antennas of the in-ice radio array, as these have a lower requirement on the accuracy, snow accumulation needs to

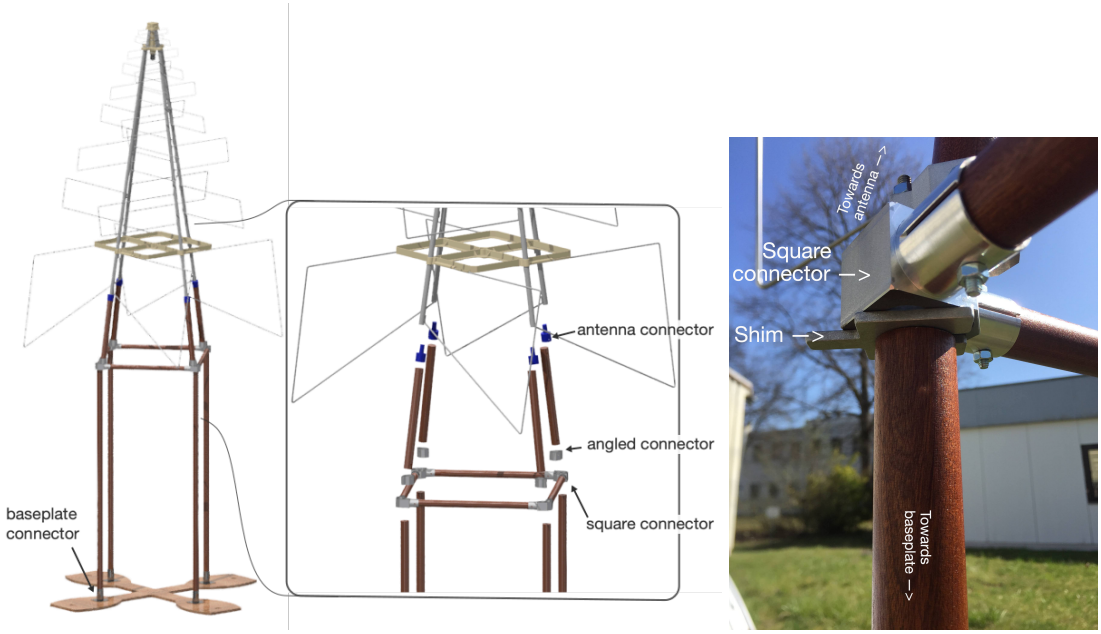

Figure 98: On the left, a CAD assembly of the antenna and the mount with a zoom-in on the mount parts. On the right, a photo of the leveling system using a shim inserted under the connector. The design is raisable by adding extension poles, and the shims allow for leveling with 0.5° accuracy, roughly twice better than required.

be avoided on top of the antennas of the surface array. Hence, the antennas need to be elevated and raised in the same intervals as the scintillators.

In order to fulfill the requirements in tab. 7.4, wood was selected as the most suitable option for the structural skeleton as it is affordable and relatively impervious to cold temperatures. This is especially valid considering the dry air and the freezing point temperature at the site. In general, wood will not expand or contract once installed at the South Pole, and to further enhance the stability of the wood, sapele mahagony (*Entandrophragma cylindricum*) wood was chosen because of its low water content, its hardness and the overall good properties that it exhibited during climate chamber tests. All metal connectors are smaller than 10 cm and made of aluminum or stainless steel.

The structure does not have cross reinforcement by wooden beams, but optionally through a thin polymer rope to avoid the risk of extra snow accumulation at the antenna locations. Four 1.20 m snow spikes are hammered in the snow from the baseplates of the structure, which represent around 50% of the total length of the detector. This fixes firmly the structure to the ground. Figure 98 shows a CAD drawing of the mount.

The first version of the structure is standing at the South Pole since January 2020, and no structural issues have been reported. Small modifications, mainly on the connectors were done to improve the deployment assembly for a second version. The latter was tested during a year in weather and wind condition of Karlsruhe, Germany, which has a similar wind load as at the Amundsen–Scott South Pole Station, and was installed successfully at the South Pole early 2023. In case any major structural stability problems would be reported, a system of ropes could (as in version one) complement the structure and provide increased cross-stability.

All the connectors are designed with two grooves for the acceptance of the loose tolerances on the wood dowel's diameters as well as to allow different temperature-dependent expansion and contraction of the metal and the wood. These grooves allow the connector to bend slightly around the wood when the bolts are tighten and hence secure them firmly. As the baseplates comprise the majority of the weight of the mount: in order to reduce weight while ensuring the strength, a finite element simulation was done to optimize the weight/strength ratio.

Finally, a system of shims, that can be inserted under the square parts, was developed to obtain an accuracy on the leveling of 0.5° (a factor of two better than the minimum requirement), which can be seen in Figure 98. A misalignment of a SKALA-v2 in zenith angle of 0.5° translates to a maximum error of around 0.35 dB and an overall mean of 0.04 dB. Those values are lower than the maximum 10 % (0.8 dB) uncertainty needed for the measurement of the radio amplitude of air showers.

No particular alignment in azimuth is required, but the orientation needs to be known for each antenna in order to correctly reconstruct the electric field vector from the measured radio signals. An uncertainty of a few degrees can be tolerated for this azimuthal orientation, as a misalignment of 1° would cause errors of only 0.08 dB on the measured radio amplitude. As demonstrated with the prototype station, the azimuthal orientation can easily be attained by a GPS survey to $< 1^\circ$, i.e., much better than required.

7.4.2.4 Cables As mentioned before, the LNAs are powered and transmit the RF signal over coaxial copper cables. A 1.5 m LMR-240 cable [641] is connected via a SubMiniature version A (SMA) connector to the LNA and hangs from the antenna center (tow cables in total, one of each of the two polarization channels of the SKALA-v2). A 50 m LMR-400 cable [642] is rolled around the antenna's structure and attached via N-type connectors to the LMR-240 cable at one end and to the central DAQ at the other end. The 50 m cable includes 5 m slack on each end, sufficient for four extension of the mount, for a total lifetime of more than 20 years (approximately 5 years initially, and 5-6 years per extension). The LMR-400 are proven to work well at the prototype station, but are very stiff in the cold environment of the South Pole, and we will consider using the ultraflex version of these cables as an optional improvement. Eventually, to increase the lifetime, extension cables could be added to the surface detectors. The cable was carefully chosen to survive the cold weather as well as delivering only small attenuation of the signal over the 60.5 m of propagation. The longest cable gives an attenuation of around -3.8 dB at 350 MHz, and exponentially smaller attenuation for lower frequencies.

These cables were used before at the South Pole, e.g., by the ARA collaboration and have been successfully tested with the prototype station.

7.4.2.5 Radio specific electronics The LNAs are complemented by a custom radio board attached to the local DAQ electronics in the fieldhub. Those boards provide the power for the LNAs via a bias tee, give a further 2-3 dB gain and a passive filtering of the traces to $70 - 340$ MHz to reduce the impact of noise. The boards also split the

radio signal of each polarization channel four times, to provide four times the identical signal input to the DRS4 chips of the TAXI DAQ (see next section).

Although the electronics, detailed in the next section, will undergo some improvements for IceCube-Gen2, especially regarding the size of the buffer, the conceptual design of this board will be used as basis for radio pre-processing electronics. It satisfies the 10% amplitude fluctuation needed for accurate cosmic-rays observation, has an only slight dependence on temperature, and works at temperature as low as -70°C.

7.4.3 DAQ

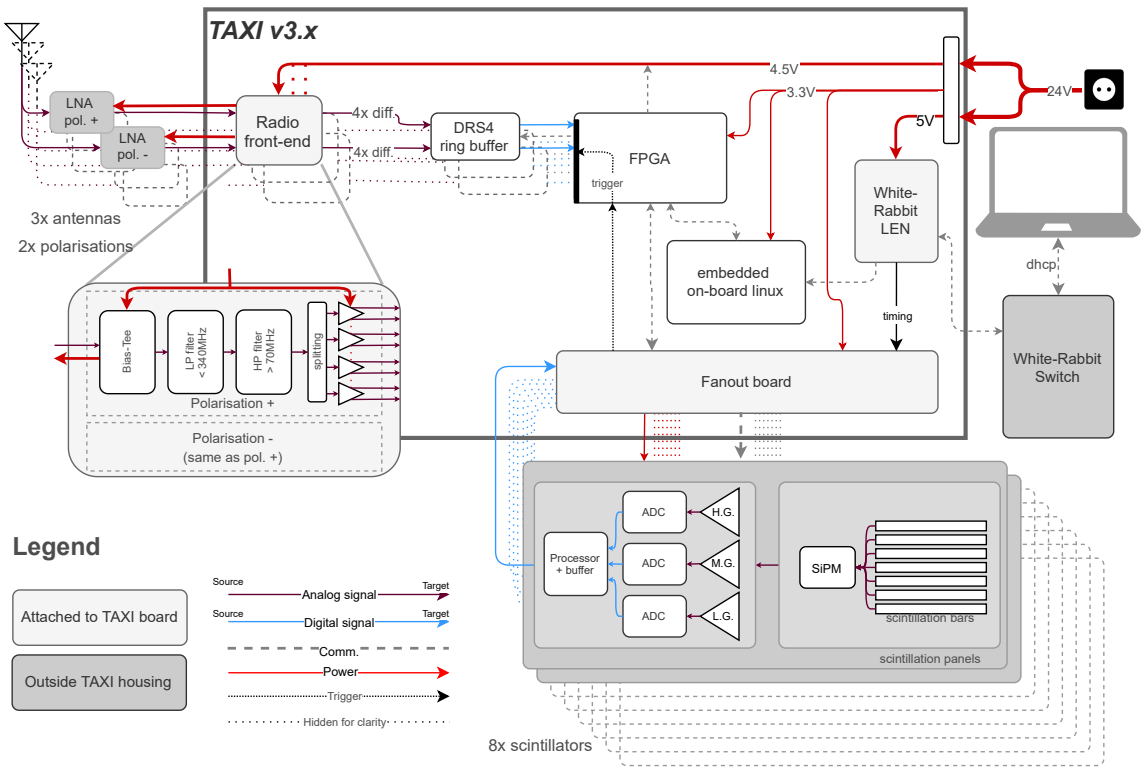

Figure 99: Schematic diagram of the DAQ electronics [640].

The design of the IceCube-Gen2 surface array data acquisition system is heavily based on the experience acquired from the development and deployment of the DAQ for the prototype station of the IceCube surface array enhancement. This prototype station is being operated at the IceCube site and has been acquiring diagnostics, calibration and physics data since January 2020. The control, communication and data acquisition for the station is being performed by a central DAQ, the TAXI v3 module [640]. During the operations of the prototype station some shortcomings of the initial TAXI 3.0 design have been identified and an improved TAXI 3.2 module has been developed. The prototype station has been upgraded with the TAXI 3.2 electronics in January 2022 and the TAXI 3.2 design is planned to be used for the surface enhancement of IceTop. For a schematic of the DAQ, see Figure 99.

The TAXIv3 system consists of an ARM-based microcontroller, an FPGA, 3x8 analog input lines, readout and digitization components, a serial communication interface and a White Rabbit timing system.

One TAXI module can read-out the analog signals arriving from three radio antennas with two polarizations each. Each of the analog signals are filtered through a 70-340 MHz band-pass filter, split through a 4-way splitter and amplified. The signals then go through one of the three DRS4 chips [643] which contain a 1024-cell switched capacitor arrays and can handle up to eight input lines, each with 1 GHz sampling frequency. The signals are then digitized by separate 14-bit ADCs. This results in a total length of the radio traces of 1024/1GHz=1024ns. However, since each of the input lines is split 4-ways and read out separately, a delay between the readouts can be introduced and the traces can be combined later to receive a 4096 ns long trace for each polarization of each antenna. The maximal dynamic range of the ADCs is 1 V.

A Spartan 6 FPGA on the TAXI board is responsible for low-level DAQ operations, as well as the readout of the ADCs. The TAXI microcontroller is a Stamp G45 module running an embedded on-board Linux and is responsible for the high-level control of the DAQ, configuration of the FPGA and the scintillator electronics, collection of the data, as well as the transfer of all the data to a central server located in the IceCube Lab.

The timing of the system is provided by a White Rabbit system. A central White Rabbit switch receives the time from GPS satellites and communicates it to the White Rabbit LENs, one of which is contained in each TAXI system. The White Rabbit LEN generates a precisely timed 10MHz signal and a PPS signal containing timestamps. Both of these are split-up and distributed to each of the scintillation panels connected to the TAXI system, as well as to the FPGA which uses it to tag each digitized trace. The White Rabbit system uses the Precision Time Protocol and is capable of achieving sub-nanosecond timing accuracy.

In the TAXI v3 design, the limiting factor to the timing accuracy of the system is the precision with which the FPGA clock and the DRS4 readout clocks can be synchronized between several stations. With the TAXI 3.2 system we expect to achieve a timing accuracy of 1 ns, although that value still has to be confirmed in situ. A relative timing accuracy of a few nanoseconds is sufficient for the data analysis of the air-shower measurements, including $X_{\max}$ reconstruction. Nonetheless, in the new DAQ, an internal sub-nanosecond timing is preferable, as it enables a slightly lower detection threshold for the radio antennas through interferometric analysis methods (up to $\sqrt{3}$ lower when combining the three antennas of one station). However, a lower threshold is only an asset and not essential, as the main purpose of the radio antennas is to provide the needed accuracy for air showers at high energies.

TAXI 3.2 offers several other improvements in performance compared to the earlier TAXI 3.0 version. Most notably, the analog signal chain has been optimized to obtain a more uniform gain and timing between the different channels and for various frequencies. Moreover, the TAXI system runs on an input voltage and steps the voltage down through several DC-to-DC converters, which were a significant source of self-induced

radio interference in TAXI 3.0. This issue has been improved with the TAXI 3.2 design by introducing additional shielding and filters.

Due to the expanded scientific objectives of the IceCube-Gen2 surface array, the TAXI design has some shortcomings that will affect the measurement accuracy of some high-energy air showers with the radio antennas of the surface array: saturation may occur at some antennas for multi-EeV air showers, and radio signals extending to stations without scintillator signals will not be recorded due to the missing scintillator trigger. Furthermore, some of the electronics which are currently mounted on separate peripheral boards will be integrated into the main TAXI board in order to simplify the production and assembly processes. Solving the shortcomings is not critical for the core science requirements, but will further enhance the science output in the energy range of the Galactic-to-extragalactic transition region, as the accuracy of the shower observables increases with the number of non-saturated radio antennas. Another iteration of the TAXI system might improve on the dynamic range, but implementing a deep enough buffer for reading out antennas at distant stations is beyond the capabilities of the TAXI design, and requires a different concept than the switched capacitor arrays of the DRS4 chips. Thus, a more in-depth redesign is desirable, though not required, which is why we plan the reference design with the existing TAXI system operating successfully at the prototype station.

Ideally, we would like to design a new DAQ system with the same basic functionality, power consumption ($40 - 60$ W per station), costs and reliability as the TAXI system, but with some improved features that would allow it to unlock additional scientific objectives. With a more careful design of the timing system, sub-ns timing accuracy should be achievable for the three antennas of each station. Depending on the technical development of ADCs in the next few years, ideally on the dynamic range on the new DAQ ideally would be upgraded from 14-bit to 16-bit in order to allow for the observations of high energy showers without saturation even at the antennas with the strongest signal.

The main upgrade will be the inclusion of an approximately 10 seconds long ring buffer for the radio data to enable an external trigger by both, the optical and surface arrays. The sampling can be reduced from 1 GS/s to about 800 MS/s, which still is above the Nyquist frequency, but reduces memory requirements and may slightly lower the power consumption. The buffer then will require 32 GB of fast RAM per antenna, i.e., 96 GB per station. With the TAXI system, the readout of the radio antennas is only triggered if a certain number of scintillators observe a signal in the same station. However, with the long buffer we could introduce a global trigger where the radio read-out can be triggered by other surface stations or even by the in-ice detectors.

The feasibility of this new DAQ system is currently under investigation, along with its costs and power requirements. If these investigations turn out to be promising, we would proceed with the new design, otherwise we would fall back onto the more conservative TAXI 4.0 option. Because the fieldhubs will remain accessible after deployment, it is also an option to start with the TAXI 4.0 for the first strings, and later change to a new DAQ electronics. Likewise, the DAQ systems of the surface enhancement covering the area of the current IceCube can be updated, so the full surface array will operate in a uniform way with the same DAQ electronics.

7.4.4 IceAct - air Cherenkov detector stations for low energy coverage

To enable highly accurate measurements of the cosmic-ray flux also at lower energies, IceAct telescopes will be added at four of the optical strings at the center of IceCube-Gen2 (see Figure 41), which maximizes the coincident event rate with the other detector components. This helps in boosting the veto capabilities and the hadronic interaction studies at tens of TeV to a few PeV. IceAct telescopes are cost-effective, with material costs at around $\$10$ k, lightweight (~ 25 kg), and compactly built around a fiberglass barrel with a diameter of 55 cm to withstand the harsh conditions at the South Pole [644]. An IceAct station consists of 7 telescopes in a fly's eye configuration: six telescopes which are tilted approximately 13° outwards are placed around a center telescope that points straight up. This increases the total field of view to 36°.A schematic of the telescope can be seen in Figure 100. The distance of approximately 200 m between the stations allows for events to be detected in more than one station.

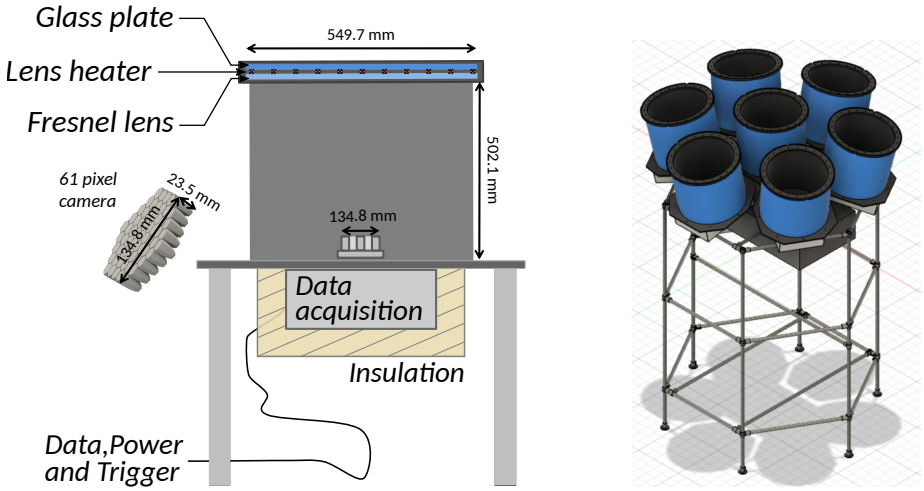

Figure 100: Left: Technical drawing of the IceAct telescope. Right: Schematic of a station setup consisting of seven telescopes.

On top of the barrel is a thin glass plate to protect a UV transparent Fresnel lens from snow and ice. A self-regulating heating wire is installed between the lens and the glass plate in an aluminum frame to keep the glass plate snow and ice-free. The camera is positioned 50.2 cm behind the lens and consists of 61 silicon photomultipliers (SiPMs) (*SensL-FJ-60035*). A solid PMMA light guide is glued to each SiPM, which increases the opening angle for each pixel to 1.5°, and gives the telescope a total field of view of 12°.

The camera is controlled and read out by a *TeV Array Readout Electronics with GSa/s sampling and Event Trigger* (TARGET) module [645], as shown in Figure 101. The TARGET module can digitize 64 channels and controls 16 SiPM bias voltages. Therefore, the camera is divided into 16 groups of each four pixels. Each group forms its own trigger signal and is supplied with its own bias voltage according to the measured temperature.

To account for different light conditions, such as the moon phases and auroras, the trigger threshold is set by providing a target trigger rate per pixel group. A trigger scan

is performed in regular intervals by decreasing the trigger threshold for a single group until its trigger rate has fallen below the target trigger rate. A trigger signal is sent when a group's signal decreases below the trigger threshold. The readout of the camera is triggered when two neighboring groups send a trigger signal within 8 ns. In addition to these threshold runs, "pedestal" runs are recorded to account for different temperatures of the readout DAQ.

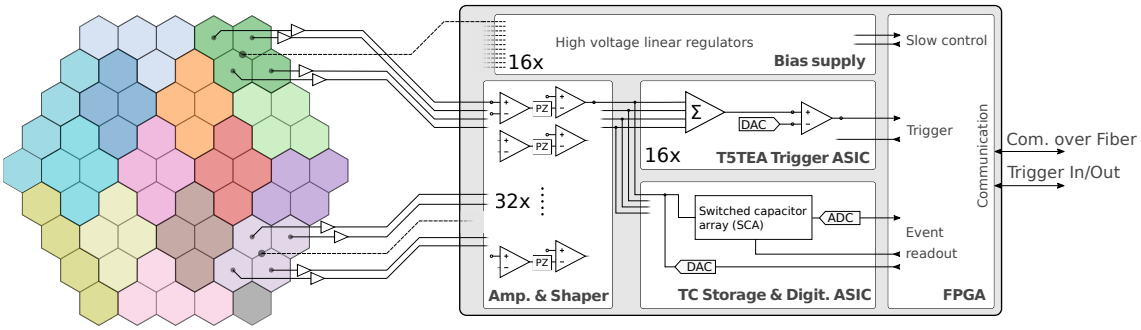

Figure 101: Schematic of the trigger path and DAQ readout of the *TeV Array Readout Electronics with GSa/s sampling and Event Trigger* (TARGET) [645] module. The hexagons represent the SiPM pixels on the IceAct camera board, the colors represent the 16 trigger groups. The SiPMs are grouped for a shared bias supply and read-out individually.

The power distribution, communication and trigger relay for each station are handled by a surface box which provides the functions similar to that of the fieldhub. This surface box contains the network infrastructure, DCDC converter, relays, an FPGA trigger board and a custom white rabbit (WR) node to achieve ns precision for the event time stamps. The power supplied by the fieldhubs is converted with a DCDC converter to the required voltages for the communication, the DAQ, the WR node and the heating. The FPGA trigger board sends trigger signals for a full station readout and external trigger output.

The effective area of the array provides enough stereo reconstruction capability to perform several scientific goals, including hybrid detector cross-calibration for air showers detected by the other surface and in-ice detectors, high energy gamma-ray search and cosmic-ray mass composition studies. We expect the average trigger rate for a single telescope to be below 10 Hz, depending on the light conditions, with an average of around 3 Hz. For each station, we expect a trigger rate below 50 Hz which leads to a data rate of 100 MBits/s per station. It is expected that the station will have a duty cycle of ≈ 20% on average.

7.5 Alternatives considered

The arrangement of the surface detectors is determined by the in-ice string locations. We would not propose changing this geometry, however, we have considered alternatives where the number of detectors per station is increased or decreased. Using CORSIKA simulations, we have studied alternative scenarios and found that the design-critical detection threshold for protons is approximately inversely proportional to the number of scintillators per station. For example, a reduction to 4 panels per sta-

tion would double the proton detection threshold to around 1 PeV for zenith angles up to 45°, clearly missing the requirement of 0.5 PeV. Any reduction below 8 panels per station would thus reduce veto capabilities in a crucial energy region of around 100 TeV muon energy and impact our ability to understand the flux and production of prompt muons. Conversely, an increase in the number of scintillators per station would further improve the veto performance. We have chosen a reference design of 8 panels per station as this is the minimum number configuration needed to comply with the threshold requirement.

For the number of antennas per station, the argument is simpler: 3 antennas is the minimum required for directional reconstruction of the incoming radio signal at a station. For radio detection, due to the coherent nature of the radio emission, the threshold only improves with the square root of the number of antennas. Thus, deploying more than 3 antennas per station would only slightly improve the threshold. It would still improve the reconstruction accuracy, as 5-6 antennas with a signal are required for a precise X_{max} reconstruction. In the reference design, this requires at least two stations, and being able to measure X_{max} with one station would be particularly valuable for near-vertical events. Thus, if additional resources were available, doubling the number of antennas per station is a possible improvement to be considered.

We have investigated several options on how to arrange the stations and the panels within a station. Because the impact on the detection threshold is small, the design is driven by logistics requirements. We have therefore chosen a design that minimizes the required trenching and deploys up to three of the four scintillator pairs along a main trench of the optical array. This is a small deviation from the optimal layout of a perfect triangular station shape.

Another alternative with a modest additional investment would be an infill array of stations at the IceAct telescopes or at the existing IceTop infill. This would extend the energy range to lower energies and provide overlap to direct measurements of cosmic rays. A significant improvement of the veto would require a major additional investment, e.g., deploying a significant number of additional stations for a substantially denser surface array. Because of the overall low cost of the surface array, such an alternative could be considered to enhance certain science cases such as the search for high-energy neutrinos from the Galactic center.

As discussed in section 7.4.3, two options are considered for the surface array DAQ. One option is to go with a TAXI DAQ, a design very similar to what will be used for the IceCube surface array enhancement. This design has already been tested at the Pole and more testing will be done for the surface enhancement, however, this design lacks the option of a global trigger for the readout of the radio antennas. As preferred alternative, a new DAQ design is being explored that would improve on these points while keeping the reliability of the TAXI system without a major increase in cost or power consumption. A prototype of this new DAQ system will be developed and tested for feasibility, and if the new system cannot meet the DAQ specifications, the proven TAXI design will be used. As the fieldhubs remain accessible after deployment, a later electronics upgrade is also an option if warranted by scientific merits.

The capability of the scintillator array to veto air showers and suppress the atmospheric background for neutrino studies by several orders of magnitude was demonstrated in section 7.2.2. This was studied in the context of showers with trajectories that are contained within the surface array footprint and for zenith angles up to 69°. A possible extension of the veto, targeting $\gtrsim 100$ PeV showers could be constructed using the surface antennas. The radio emission of air showers with zenith angles between 70° and 85° extends out to $\simeq 0.5$ to 1 km from the shower axis and therefore covers several square kilometers at ground level. Guard-ring(s) of surface antennas centered around the optical detector could be built to veto such showers and suppress the background for the highest energy neutrinos that are expected to be observed by the optical array.

For the functioning of the IceCube-Gen2 surface array it is important that the complete area including the surface above IceCube is covered by the same type of surface detectors. Assuming that the planned surface enhancement of IceTop by the same type of scintillators and radio antennas will be completed before IceCube-Gen2, a few extra stations filling gaps between the surface enhancement and the IceCube-Gen2 surface array are sufficient to ensure a smooth coverage with the full-efficiency threshold at 0.5 PeV. However, if the surface enhancement of IceCube would not be built in its full size, the remaining area will need to be completed as part of the IceCube-Gen2 surface array to ensure a complete and smooth coverage of the entire surface area above both the IceCube and IceCube-Gen2 optical arrays.

7.6 Development and production schedule

The schedule of the surface array will lead the schedule of the optical array by approximately one year. In the year before drilling, the fieldhub for the string will be deployed together with the associated surface instrumentation. Because of the minimal effort required to deploy the scintillators and radio antennas, the deployment plan is flexible and can easily be adjusted if needed.

In order to meet the deployment schedule, the scintillator panels and antennas need to be fully produced and tested at least half a year before their deployment. The production process is already established for the surface enhancement, and only minor improvements have been developed based on the lessons learned from the prototype station (e.g., we have implemented mechanical design improvements for the mitigation of small light leaks that appeared in the prototype scintillation panels after one year). Thus, no further developments are foreseen for the scintillation panels or the radio antennas.

Further development is being planned for the data-acquisition as described above, with the backup option of continuing to use the TAXI system currently running at the prototype station. The DAQ development schedule is not critical: because the fieldhubs remain accessible, an electronics upgrade to the alternative DAQ supporting a global trigger is possible even after the deployment has started.

The 4 IceAct stations are planned to be deployed in PY2 and PY3, with 2 stations per year. In order to meet this deployment schedule the stations have to be produced and fully tested at least half a year in advance. The production process of the telescopes is already established and tested.

Deploying the surface instrumentation at the same time as the other surface structures enables to exploit synergies with the deployment of the fieldhub. Trenches made for the fieldhubs can also be used for the surface instrumentation cables. We envision that a 2-person team deploying the fieldhub and its cables and a 3-person team deploying the surface instrumentation can mutually support each other in the field and deploy up to three surface stations per week.

7.7 Test strategy

All DAQ systems of the surface array are tested and calibrated in a temperature chamber to ensure reliability and accuracy. Testing is done for temperatures between 30℃ and -70℃ in steps of 5℃. For each temperature, the DAQ boot up sequence and basic communications are tested. Additionally, at each step the onboard temperature sensors and analog radio inputs are calibrated. The calibration of the radio inputs is done by feeding in known signals at various frequencies, digitizing them, and comparing the result to the known signals. The communication protocols and data transfer between the DAQ and the scintillator panels are also tested. A photograph of the climate chamber with two DAQs being tested can be seen in Figure 102. This configuration allows for testing and calibration of up to 2 stations per week.

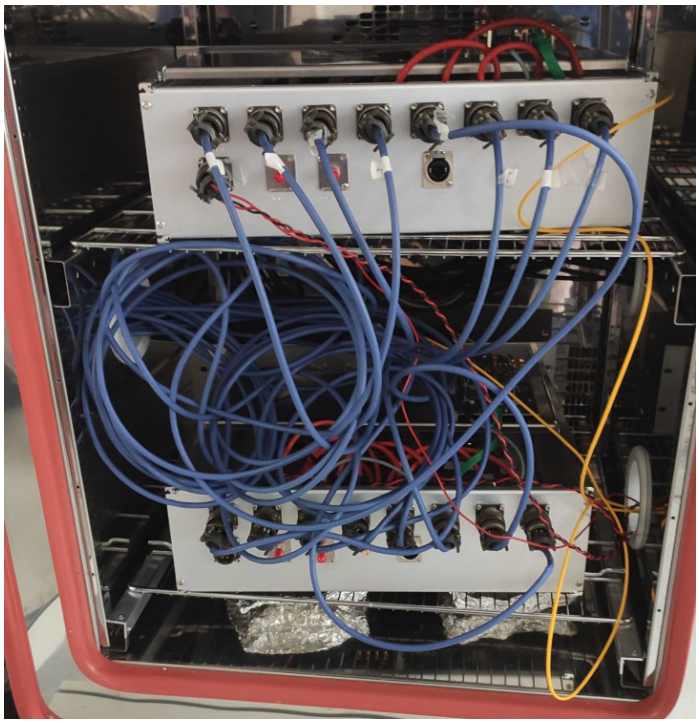

Figure 102: The climate chamber setup with two TAXI DAQs being tested.

Before gluing the scintillation panel SiPMs to the optical fibers, they are tested in a dark chamber called SPOCK [646], using the Ice-ARM readout boards developed during the prototyping stage of the scintillation detectors. The dark spectrum, temperature output, and the IV characteristics of the SiPMs are studied during these preliminary tests. A schematic of the test setup is shown in Figure 103.

Following these preliminary tests, the scintillators are assembled and subjected to another two step testing. In the first step, a setup with the DAQ electronics equivalent to that at the South Pole, consisting of a TAXI powered by a 24V power supply, and a WR switch for timing synchronization is used to test the scintillator output (Figure 104). The objective of this setup is to check communication with the uDAQ and the SiPM, as well as carry out hitbuffer and histogram measurements to examine the functionality of the scintillator panel. In the second step, the panels are tested in a muon tower checking for production errors and investigating uniformity and efficiency of the scintillator by means of spatial resolution. This is achieved by placing a scintillator panel between Limited Streamer Tubes panels which already have a spatial resolution of $1\,\mathrm{cm}^2$ (Figure 105).

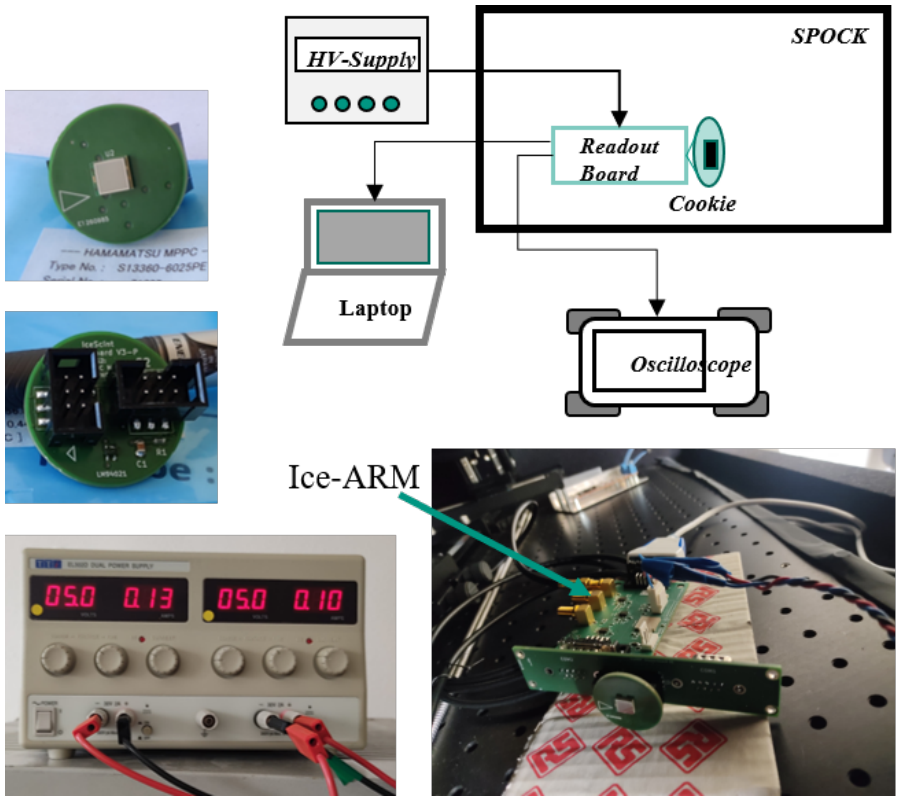

Figure 103: Top: The schematic for the preliminary tests of the SiPM boards (cookie boards) and pictures of the SiPM board are presented. Bottom: the readout board, Ice-ARM powered by a $\pm 5V$ supply. The board provides three amplification levels for a greater dynamic range for the SiPM readout.

Each LNA is calibrated by measuring its gain with a vector network analyzer. A testing setup, developed for the surface array enhancement, will be further improved to allow systematic uncertainties of less than 0.3 dB. Similar to the DAQ system, the temperature chamber is used to calibrate the temperature dependence of the LNAs. This has already been successfully done (see Figure 106). It was shown that the LNAs are fully functional at South Pole temperatures, with a slight increase of the gain towards lower temperatures.

Since the antenna impedance and the impedance of the testing setup are not equal, the gain of the deployed system will differ from the gain measured in the lab. Therefore, the individual calibration measurements are mainly performed to sort out any pro-

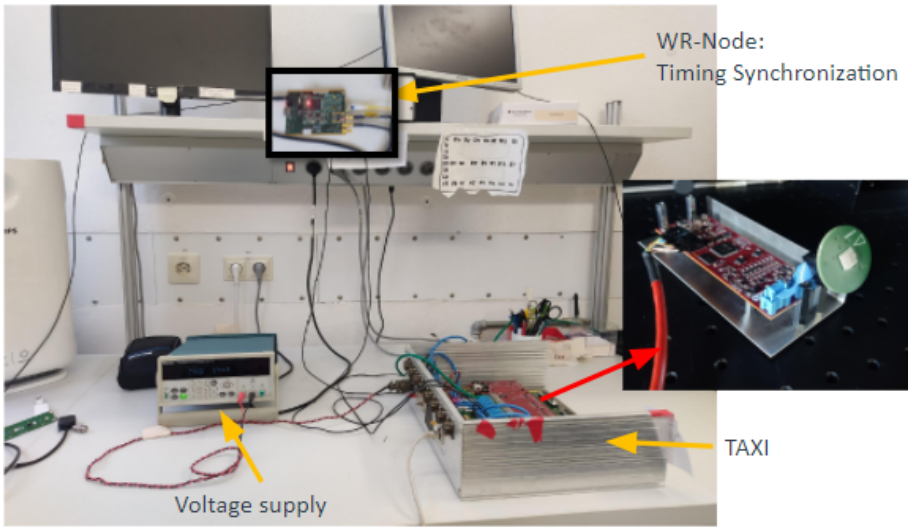

Figure 104: Setup for the lab tests of the assembled scintillation panels. The TAXI is powered by a $24V$ power supply, and the timing synchronization is provided by a WR node. The TAXI is then connected to the uDAQ on the panels which reads out the SiPM (shown in inlay for clarity).

duction outliers or malfunctioning LNAs. The total gain of the overall radio setup will be calibrated continuously in-situ using Galactic noise, which is an established technique [647].

7.8 Risks and risk mitigations

As the layout of the surface array follows the optical array, there are only a few risks specific to the surface array. In particular, there are no specific deployment risks as no drilling is required and the work can easily be interrupted at any time in case of emergencies.

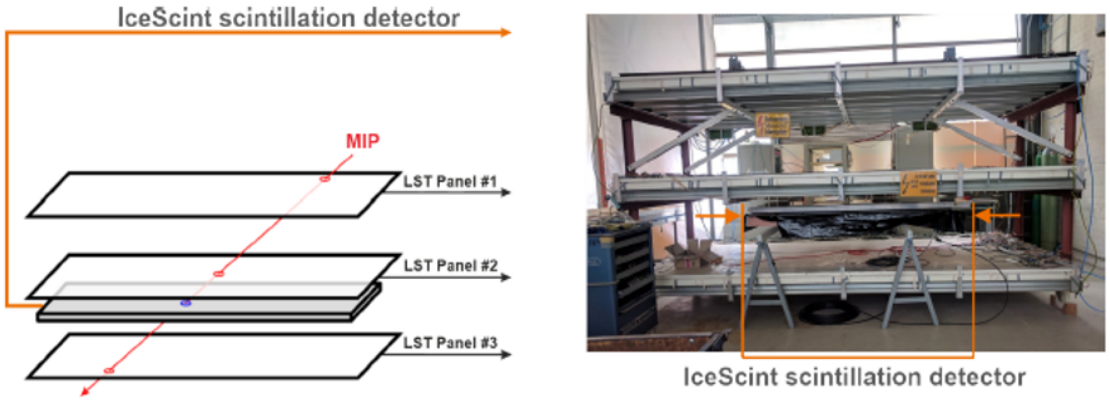

Figure 105: Left: Schematic for the calibration and efficiency measurements with the muon tracking detector; Right: Photo of the setup.

There are however specific risks regarding the operation of the detectors and regarding the production of the surface detectors. For the surface array, the majority of the detectors are pledged to be produced in Germany and, thus, depend on support from the Helmholtz association. Although that support is critical for the surface array, the risk is considered small because the Helmholtz association has been proven to be a reliable partner.

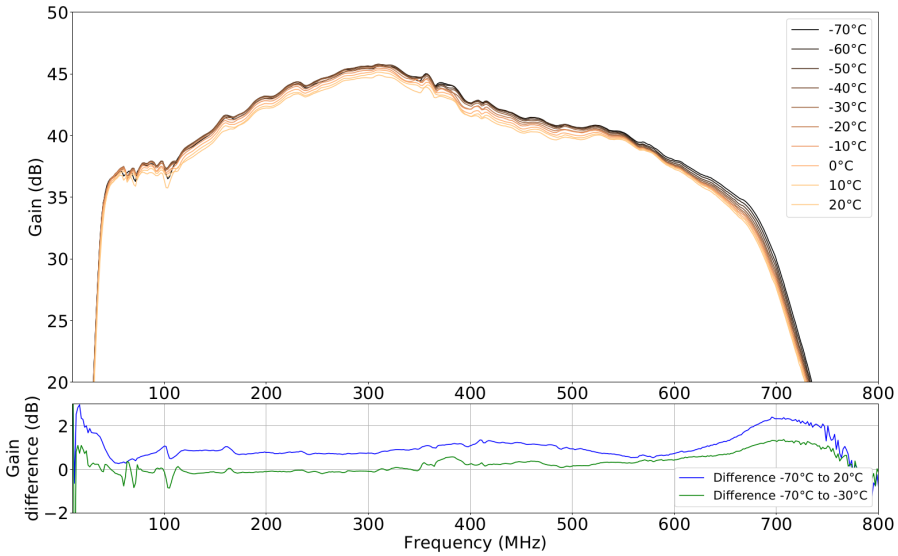

Figure 106: S21 measurements of the LNA at different temperatures from $+20^{\circ}$C down to -70°C. The lower plot shows the difference in gain between the measurements at -70°C, to the measurements at -30°C (green) and $+20^{\circ}$C (blue). Figure is taken from [648].

Regarding the antennas, the reference design uses the SKALA v2 instead of the newest version (currently v4) because v2 already fulfills all requirements and has been tested successfully at the South Pole. However, the SKALA v2 is available from a single manufacturer and only upon request. That risk is mitigated by the backup option to simply switch to the by then newest version of the SKALA that will be mass produced for the SKA and available in large quantities.

Regarding the 4 IceAct telescope stations, deployment is possible as soon as the field hub of the string is in place at the foreseen position. The telescopes will be produced and tested in Germany and the USA. The telescope hardware has been tested successfully at the South Pole over several seasons. There are no specific deployment risks as no drilling is required and the work can easily be interrupted at any time in case of emergencies.

Detector specific risks mostly concern the large range of operating temperatures. Unlike the deep instrumentation, the surface instrumentation will be exposed to a wide range of temperatures, weather, and seasonal changes. Nonetheless, the prototype station and the prototype IceAct telescopes have been operating successfully under these conditions for more than three years as of the time of writing. Therefore, the risk of failure of detectors is considered small. Additionally, unlike the deep detectors, the surface instrumentation will remain accessible over the full runtime of IceCube-Gen2. Thus, even if some surface detectors fail during the lifetime of IceCube-Gen2,

replacements and maintenance are feasible, and a modest overproduction of additional detectors is foreseen as spares to mitigate this risk.

7.9 Summary

The surface array consists of elevated scintillators and elevated radio antennas connected to the same fieldhubs put in place for the optical array. Four complementary IceAct stations are also included in the surface array for added advantage at lower energies. Using established instrumentation and making use of the infrastructure of the optical array adds up to a cost and effort effective method to build the surface array, and the surface array represents only a few percent of the total budget of the IceCube-Gen2 project.

The surface array contributes in various ways to IceCube-Gen2's core mission. The array's veto function enables purer astrophysical neutrino measurements by directly reducing atmospheric backgrounds, and its unique measurements of the cosmic-ray flux and of hadronic interactions enable a more accurate understanding of these backgrounds. Furthermore, the combination of the surface and optical array constitutes a unique setup to study the particle physics related to cosmic-ray air showers. Finally, the cosmic-ray measurements and photon searches could contribute to explaining the origin of the highest energy Galactic cosmic rays.

As it is critical for the science mission of IceCube-Gen2, the surface array builds on proven techniques. In particular, a prototype station has been operating successfully at the South Pole for more than three years, which provides confidence that the technical requirements as well as schedule and budget needs are well in hand.

8 Surface and Data Acquisition Infrastructure

8.1 Overview

The data acquisition (DAQ) and surface infrastructure systems are responsible for collection of data from the various sensors and communication of those data to a central counting house for high-level triggering and further processing. In addition to communications, the surface infrastructure also distributes power and timing networks to the instrumentation. The DAQ and surface infrastructure employ successful, field-tested elements of IceCube, the IceCube Upgrade, and the IceTop surface array enhancement, while adapting the topology to support the larger footprint of IceCube-Gen2.

The original IceCube DAQ is based on digital communications over copper cabling. In IceCube, devices are up to 3 km from the IceCube Laboratory (ICL), including the in-ice depth. The 96 VDC power feed is directly routed from the ICL to the DOMs. Reciprocal electronic pulses are sent through the copper power cable to synchronize the devices, and the digital communications protocol is also transmitted through the copper power cable on the same wire pair. This concept works well for IceCube but becomes problematic at larger scales. IceCube-Gen2 optical devices can be up to 5 km from the ICL when accounting for the in-ice depth. Higher voltage is required to mitigate resistive power loss, and digital communication becomes unreliable due to signal attenuation.

Scaling the design of IceCube and the IceCube Upgrade to the larger IceCube-Gen2 presents several challenges [649]. At a high level, the scaling issue is solved by simply extending the optical fiber White Rabbit [650] network used in the IceCube Upgrade out of the ICL and physically moving the custom DAQ electronics (the FieldHub, Sect. 8.4.2) to the top of the string. A similar strategy is already in use for the IceTop surface array enhancement. This evolution of timing and communication topology from IceCube to IceCube-Gen2 via the IceCube Upgrade is shown in Figure 107.

Key components of IceCube-Gen2 are shown in Figure 108. A central FieldHub provides the main interface between the surface cabling, the DOMs, and each cosmic ray surface array station. Each in-ice string is serviced by a single FieldHub. The downhole cabling (Sect. 8.4.1) connects to each of the DOMs via a passive surface junction box (SJB), using cabling technology from IceCube and the IceCube Upgrade. The string interface electronics in the FieldHub convert between the custom timing and communications protocol on the downhole cable and the surface network. The data acquisition electronics of the surface array station are described in Sect. 3.2.3 and are housed in the FieldHub enclosure. The radio array stations trigger autonomously (Sect. 6.3), so the Radio FieldHubs are simplified compared to the optical and surface array FieldHubs. The Radio FieldHubs distribute power and Ethernet over copper cables and optical fiber to the stations; no DAQ elements are needed.

The surface communications, power, and timing system consists of a network of surface cables connecting each FieldHub to the central counting house as shown in Figure 120. Power is distributed from the counting house to the FieldHub via high-voltage DC cabling, with DC-DC conversion to various levels within the FieldHub for the electronics (Sect. 8.4.3). Communications and timing is distributed using White Rabbit [651,

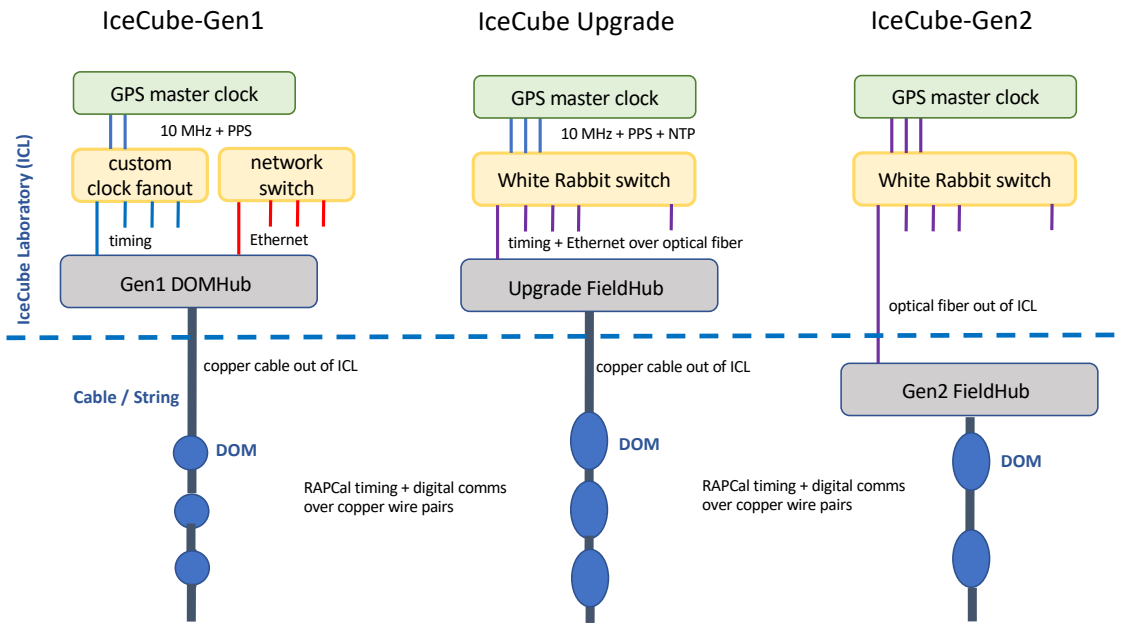

Figure 107: Evolution of the timing and communication networks and topology used in the IceCube DAQ from IceCube and the IceCube Upgrade to IceCube-Gen2.

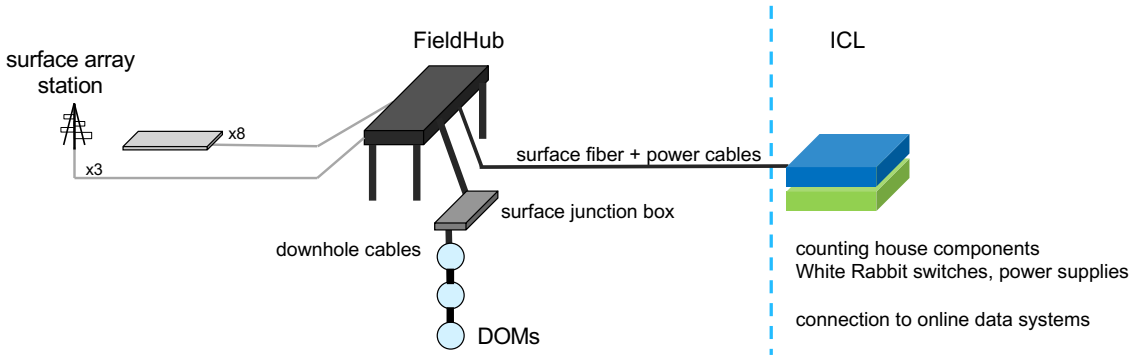

Figure 108: Key components of the data acquisition and surface infrastructure for the optical and surface arrays. A central FieldHub connects each in-ice string and surface array station to the surface cable power and communications network.

652] which provides general data transfer and sub-nanosecond time accuracy over Ethernet. The White Rabbit switch located at the counting house transmits the GPS time reference (and general data) via single-mode optical fiber and is received by a custom White Rabbit node at the FieldHub, as part of the FieldHub Timing Node. White Rabbit uses Precision Time Protocol [653], Synchronous Ethernet [654], and a phase-locked loop (PLL) to synchronize the FieldHub Timing Node clock and correct for cable delay. Within the ICL, the White Rabbit switches also provide network connectivity to higher-level online data systems (Sect. 9) using standard Ethernet.

The DAQ systems also provide the necessary firmware and software to read out and control the optical instrumentation, surface instrumentation, and the various electronics within the FieldHub (Sect. 8.4.4). This includes software/firmware support for both operational data-taking modes as well as instrumentation design verification, acceptance testing, characterization, and calibration. The instrumentation software provides an API to communicate with the higher-level online data systems for triggering, event readout, control, and monitoring.

8.2 Technical requirements

As an intermediary subsystem that supports instrumentation data-taking, the DAQ and surface infrastructure requirements are primarily technical in nature. These high-level requirements are shown in Table 14. Data readout bandwidth and power delivery to the DOMs are set by the downhole cable architecture, discussed in more detail in Sect. 8.4.1. Timing accuracy is provided by a combination of White Rabbit (on the surface), the IceCube RAPCal protocol on the downhole cables, and integrated GPS for the radio stations. Maintainability of surface infrastructure is ensured by using elevated instrumentation that is not buried in the snow, combined with sufficient cable slack to enable periodic raises.

Category	Optical Requirement	Surface Requirement	Radio Requirement
Readout data rates	150 kbps / DOM	10 kbps / station	0.5 Mbps / station
Power delivery	4W / DOM	50W / station	25W / station
Timing precision	2.5 ns	1 ns	10 ns
Long-term maintainability	n/a	20 years	20 years
Target uptime	99%	99%	99%

Table 14: High-level technical requirements for the optical, surface, and radio infrastructure. The target radio detector uptime refers to the baseline cabled array design.

8.3 Main interfaces

The DAQ and surface infrastructure serves as the primary communications, power, and timing (CPT) interface between the optical, surface, and radio instrumentation (Sects. 5, 6, and 7) and the data systems in the counting house (Sect. 9).

The interfaces to the optical array include mechanical support of the DOMs during deployment and electrical connection through a breakout cable assembly (BCA) to the

downhole cable, providing wire pair communications, power, and timing using IceCube's standard protocols. The DAQ software and firmware in the DOMs provides the control, monitoring, and data readout interface for higher-level software, as well as support for device design verification and testing (DVT) and final acceptance testing (FAT).

The interface to the surface array includes providing physical space and CPT connections in the FieldHub for the surface array DAQ electronics. The FieldHub provides a copper gigabit Ethernet link to the surface array DAQ, along with timing signals from the White Rabbit system for local timestamping. The DAQ software and firmware in the surface array electronics, as with the software in the DOMs, provide the control, monitoring, and data readout interface for higher-level software.

The interface to the radio array includes providing communications and power to the Radio FieldHubs and distribution from the Radio FieldHubs to the surrounding radio stations. The timing requirement for the radio array is less strict and White Rabbit sub-nanosecond time accuracy is not required. Instead, integrated GPS at each radio station is used for timing as described in Sect. 6.4.7.

The interface to data systems is physically through the White Rabbit network, which in the counting house is a set of specialized network switches. The White Rabbit switches connect via the counting house local-area network to standard rack-mount servers, the DataCollectors. The DataCollectors serve as the data interface between the instrumentation and the higher-level trigger and event builder components of the DAQ. The instrumentation software and firmware provides an API for control / configuration, monitoring, and data readout of the instrumentation through the FieldHub, using defined data structures with common timestamps from the White Rabbit system. Data systems also provides the rack space and power delivery to the CPT components in the counting house, in particular the power supplies and White Rabbit switches.

The interface to drilling and installation is via the downhole and breakout cables. The downhole cable provides the primary mechanical support during deployment and must physically interface with the deployment tower, crescent, and winch. The downhole cable must also provide support for a pressure sensor that must be read out during deployment, along with any surface electronics needed to interface with this sensor while the string is being deployed.

8.4 Reference design

The reference design for the DAQ and surface infrastructure builds upon existing technologies from IceCube, the IceCube Upgrade, and the IceTop surface array enhancement. The general architecture is similar to that of the IceCube Upgrade, with the following optimizations for IceCube-Gen2's larger footprint:

- the string interface electronics are moved from the counting house to the field, in the FieldHubs;
- the power and fiber optic cabling to the FieldHub is extended from the counting house to the FieldHubs in trenched surface cable runs;

- the FieldHub adds components to support a surface array station, as in the IceTop enhancement; and
- the trigger and readout scheme for the optical array has been optimized to allow for a simpler downhole cable design.

The FieldHub concept, where instrumentation is connected to an elevated, insulated enclosure that contains DAQ, communications, power, and timing electronics, has been demonstrated in the IceTop surface array enhancement prototype station and successfully operated continuously through several South Pole winter seasons. Elevating the enclosure ensures access to electronics for maintenance during the summer season, as instrumentation on the polar surface becomes buried in snow over time. Improvements to the prototype FieldHub design include better management of the cable slack needed for periodic raises and improved thermal management.

The FieldHub concept is particularly beneficial to IceCube-Gen2's larger footprint where cable cost and power transmission loss are significant factors. Power transmission losses are minimized by running high-voltage from the counting house to the FieldHub. At the FieldHub the high voltage is converted to the lower voltages required by the nearby devices. The number of optical fibers required for communications and timing is minimized via the FieldHub concept. The timing node within the FieldHub distributes communications and timing to the attached devices.

Surface cabling to the prototype FieldHub and IceCube-Gen2 FieldHubs is similar, using cold-rated optical fiber bundles and a separate, shielded copper power cable. While the original prototype optical fibers were terminated on site, the IceCube-Gen2 fibers will be pre-terminated for ease of installation and improved reliability.

Both the IceCube Upgrade and the IceTop surface array enhancement use White Rabbit to synchronize distributed detector elements connected to the fiber optic network to the sub-nanosecond accuracy level. While previous installations have used commercial equipment, the White Rabbit node in each FieldHub will be a custom component in order to optimize cost and improve reliability. Commercial White Rabbit equipment comes with proprietary firmware which the user is unable to modify, while a custom component will allow the user full control over the firmware development, optimization, and maintenance. Commercial White Rabbit nodes consume 5-6 W while the target power consumption of the custom node is 3-4 W. The custom White Rabbit node will be developed and tested in the IceTop surface array enhancement as a pathway to usage in IceCube-Gen2.

The downhole cable cost and complexity scales with the number of quads (two wire pairs) needed to connect the DOMs. In the IceCube Upgrade, the number of DOMs per wire pair is limited to three by both power delivery and bandwidth constraints, although up to 8 devices per pair are supported by the communications protocol. For IceCube-Gen2, both of these issues are solved in order to allow a downhole cable design with only one third of the conductors of the IceCube Upgrade cable and up to six DOMs per wire pair. A significant reduction in DOM power and increasing the voltage removes the power delivery constraints. To resolve the bandwidth issue, the DAQ architecture is changed so that instead of sending every detected photon ("hits") to the counting house, only coarse timestamps of PMT-coincident hits are sent for triggering purposes,

and then only once a trigger is formed by the higher-level DAQ are other hits read out from the DOMs (Sect. 8.4.4). This eliminates a large fraction of bandwidth previously consumed by PMT dark noise.

A summary of the key technological components and their readiness for IceCube-Gen2 is presented in Table 15.

Component	Demonstrator	Readiness
surface-to-DOM cables	IceCube / Upgrade	same design, fewer quads
breakout cable assemblies	Upgrade	same design, more DOMs
string interface electronics	Upgrade	same design, fewer quads
FieldHub enclosure	IceTop surface array	deployed, new version
surface power + fiber	IceTop surface array	deployed, new versions
White Rabbit timing	IceTop surface array, Upgrade	deployed
FieldHub timing node	Upgrade	new custom design
FieldHub power systems	IceTop surface array, ARA	new design
firmware / software	Upgrade	some new development

Table 15: Key DAQ and surface infrastructure technologies planned for IceCube-Gen2.

8.4.1 Optical detector downhole cables

The downhole cables for the optical detector provide the electrical connection from the DOMs and other in-ice devices to the FieldHub, as well as mechanical support during deployment and freeze-in. The downhole cables consist of a primary Main Cable Assembly (MCA) and secondary Breakout Cable Assemblies (BCAs) that connect to each DOM and other in-ice devices.

The Main Cable Assembly is a bundle of four-conductor copper quads, with each pair in the quad supporting multiple devices. A key improvement in IceCube-Gen2 is the ability to connect more devices to each wire pair, significantly reducing cable complexity and cost. Specifically, up to 6 DOMs can be connected to each pair, compared to 3 in the IceCube Upgrade and two DOMs per pair in IceCube. The primary specifications for the MCA are presented in Table 16.

Property	IceCube-Gen2	IceCube
Length (m)	up to 2800	up to 2600
# of quads	7	20
# of devices / pair	6	2
Conductor diam. (mm)	0.9	0.9
Breaking strength (kN)	25	55
Outer diameter (mm)	25	46
Weight/length (kg/m)	0.54	2.0
Total weight (kg)	1500	5200

Table 16: High-level IceCube-Gen2 optical array Main Cable Assembly specifications. The original IceCube cable specifications are shown for comparison.

The reference MCA design consists of a 7-quad "septet", shield, and Kevlar-reinforced outer mantle (Figure 109). There are regularly spaced breakouts to access each wire pair, which is connectorized and attaches to a Breakout Cable Assembly (BCA).

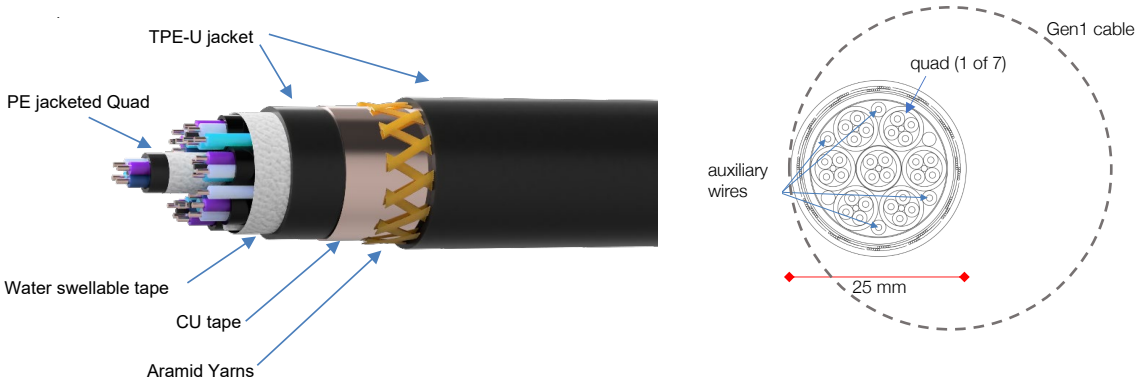

Figure 109: Diagram (left) and cross section (right) of the downhole Main Cable Assembly. The size of the original IceCube cable is shown for reference.

The individual quad design and electrical requirements are identical to the IceCube Upgrade, as are the DOM communications and timing protocols. The IceCube Upgrade MCA consists of 3 septet sub-assemblies, while the IceCube-Gen2 MCA consists of only one septet. This simplification solves some of the manufacturing challenges present with the larger IceCube Upgrade MCA design. One operational difference from the IceCube Upgrade design is that the deployment pressure sensor does not have a dedicated quad, requiring either that the pressure sensor communicate using the IceCube protocol during deployment or that the four individual auxiliary wires within the cable are used.

The BCA fans out from the MCA breakouts to each DOM or other in-ice device, connecting up to 6 devices per wire pair as seen in Figure 60. Different BCA variants can be used for specific device arrangements. The BCAs have watertight connectors at both the MCA end and DOM end in order to facilitate operation in water, both during deployment and before freeze-in. As in the IceCube Upgrade, electrical jumpers in the BCA-to-DOM connector set the wire pair communications address of each device, as represented in Figure 110, as well as automatically enable electrical termination of the last device on each wire pair, to avoid reflections.

8.4.2 FieldHubs

FieldHubs distributed throughout the arrays support the IceCube-Gen2 instrumentation by providing power, communications, and for the optical and surface array, timing. The optical and surface arrays share a FieldHub for each string and surface array station. This FieldHub contains DAQ, power, and timing electronics. Each Radio FieldHub contains communications and power electronics for a cluster of radio array stations.

Each optical and surface FieldHub will connect to a nearby passive surface junction box (SJB) and then to the downhole string cable, which provides maximal flexibility in the surface array and string deployments without the need to synchronize FieldHub deploy-

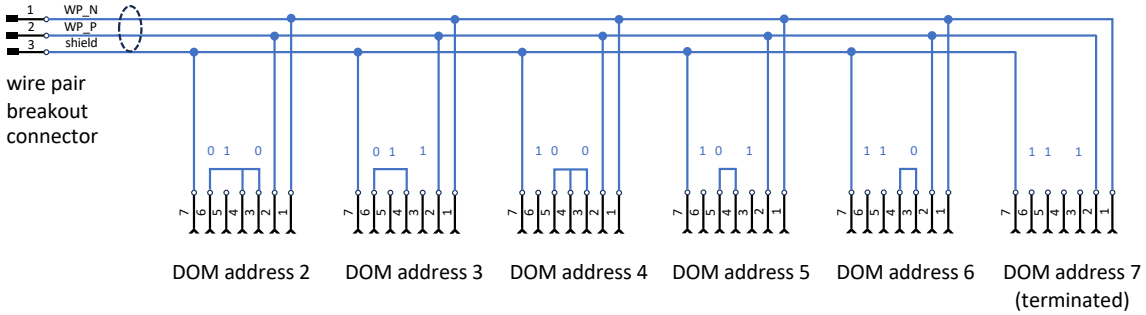

Figure 110: Schematic of the BCA-to-DOM wiring and electrical jumper addressing. Each DOM's communications address is set by jumpers in the BCA connectors, and address 7 is auto-terminated in the DOM. Up to eight devices per wire pair are supported by the communication protocol.

ments with string deployments. Each FieldHub will connect the surface instrumentation including the three radio antennas via coaxial cables, four pairs of scintillator panels via CAT6 cables, and connect to the ICL via a 400-600V power cable and an optical fiber for data transfer, communication, and timing (see Figure 111). Each FieldHub will contain a number of subcomponents, including FieldHub Surface DAQ, FieldHub String Interface, FieldHub Power Node, and a FieldHub Timing Node.

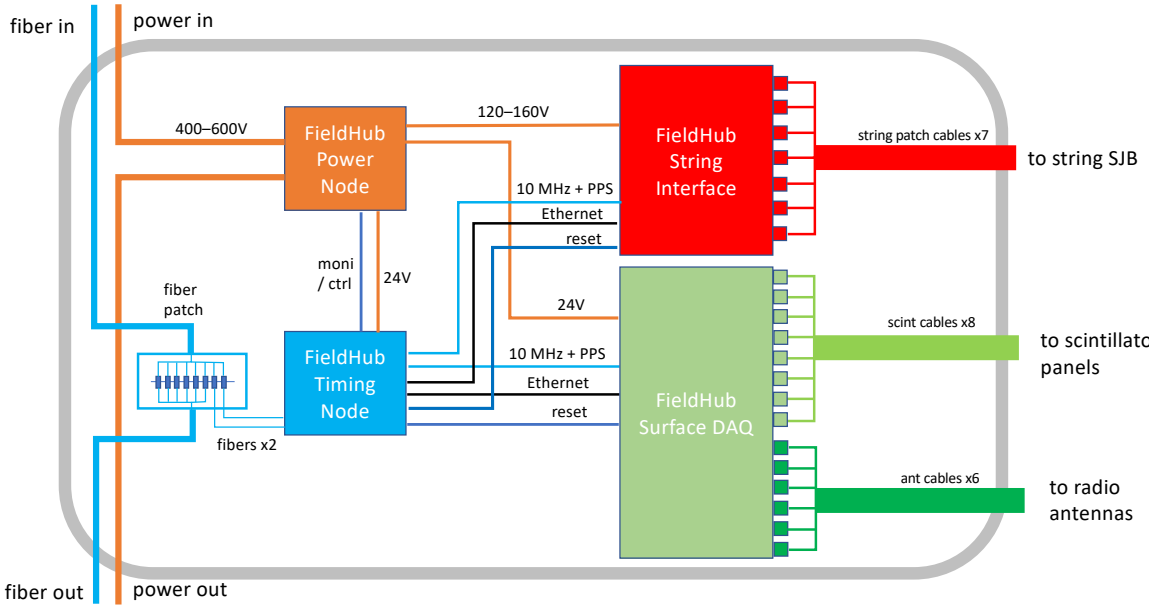

Figure 111: Block diagram of the IceCube-Gen2 FieldHub, including external and internal interfaces.

The FieldHub enclosure is an insulated metal box that is elevated on steel legs 1.5m above the snow surface at the time of installation (see Figure 112). With an expected annual snow accumulation of 20-30 cm, enclosures will need to be raised periodically to avoid being buried in the snow. Cable slack is managed using service loops below the FieldHub in a cable slack box. Raising of the FieldHubs can be performed with a two-person crew within about 10 min. The insulation is designed, based on the power dissipation of the internal components, to maintain an approximately 30 degree

temperature rise above the ambient South Pole temperature ($-82\,^{\circ}$C to $-12\,^{\circ}$C) during normal operation. During an extended power outage, the components may equilibrate to outside temperatures, in which case a cold restart may be required. If needed, a supplementary resistive heater in the FieldHub Power Node can warm the primary DC-DC converters in such a case.

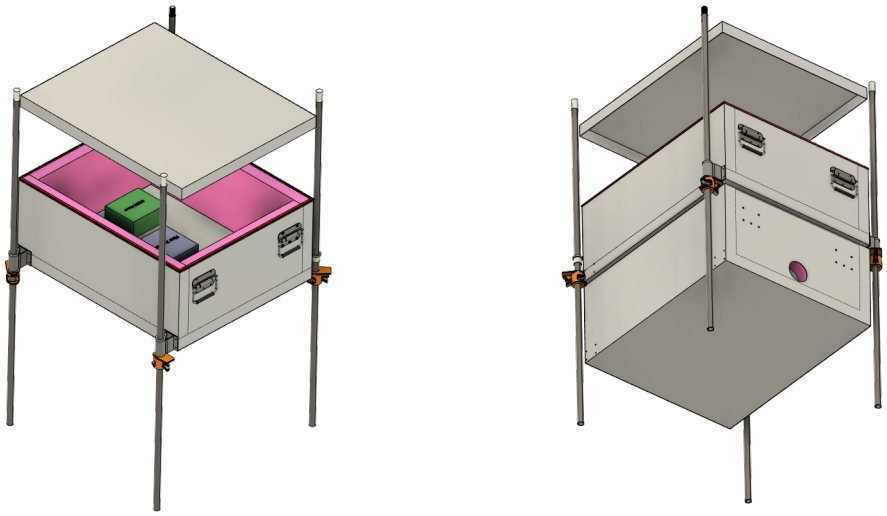

Figure 112: FieldHub enclosure CAD drawing. Left: top view of insulated electronics enclosure, with lid open. Right: bottom view, also showing cable slack box.

The FieldHub String Electronics provide the CPT interface to the downhole cable and are closely based on the IceCube Upgrade FieldHub, except with a reduced number of cable quads. A block diagram is shown in Figure 113. The primary component of the electronics is the FDOR card (Figures 114 and 115) provide the interface to the downhole cable via the patch cables and the SJB; each FDOR card connects to two quads (four twisted pairs), and each twisted pair connects to up to 6 DOMs. The FDOR uses the same communication and timing protocol on the cable as the IceCube Upgrade. A controller board (FCON) hosts the primary single-board computer (SBC) and timing fanout from the input 10 MHz and IRIG-B clock signals to the FDOR cards. The service board (FSEB) hosts the internal electronics DC-DC converters along with components for external reset, power control, and low-level monitoring such as line voltages, component temperature, and power status.

The FDOR card communicates over the downhole wire pair with a dedicated module in each DOM, the Ice Communication Module (ICM). By optimizing the communications packet size and bundling data transfers efficiently, up to 1.5 Mbps data throughput per wire pair can be realized (Figure 116). This is more than sufficient to support 6 DOMs per wire pair using the optimized IceCube-Gen2 architecture of buffering raw hits on the DOMs themselves until a trigger is formed at the surface.

Precision timing to each DOM is provided by IceCube's standard RAPCal scheme [15], which allows translation of hits timestamped in each DOM's clock domain to the clock domain on the FDOR card using pulses transmitted down and back up the cable to/from each device and timestamped at either end. The clocks of all FDOR cards across the

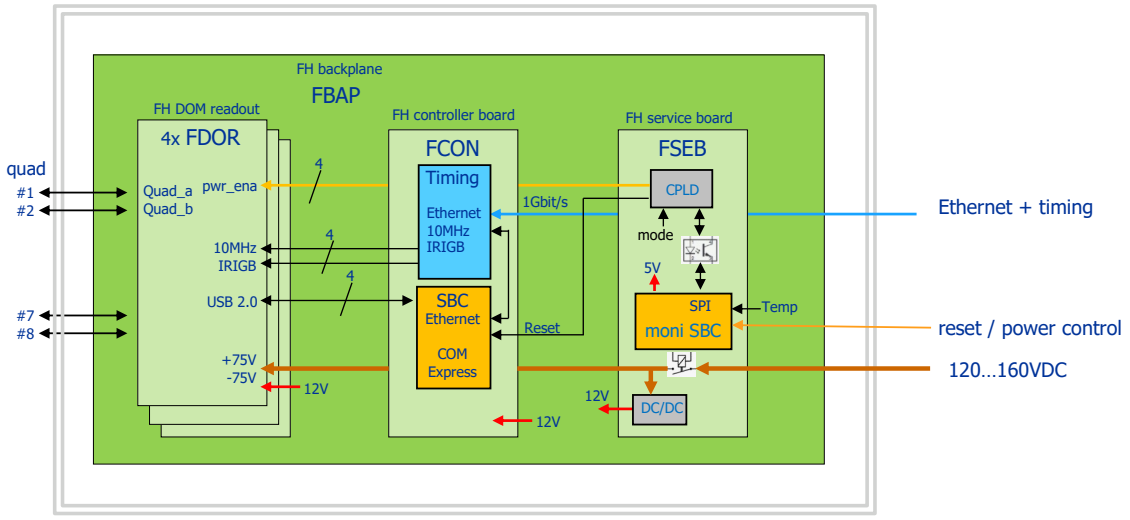

Figure 113: FieldHub String Interface electronics block diagram. The FDOR cards connect to the downhole cable quads via patch cables and the SJB, while two central controller (FCON) and service (FSEB) boards host the central single-board computer (SBC), clock fanout, and other monitoring and control functions.

detector are synchronized using the 10 MHz clock distributed on the White Rabbit network, and translation of each FDOR timestamp to UTC is allowed using the pulse-per-second (PPS) and IRIG-B time string. RAPCal pulses transmitted over a 2.8 km cable in the IceCube Upgrade Northern Test System (NTS) have a round-trip time spread of 300 ps (see Figure 117). The total timing resolution of the RAPCal procedure is sub-nanosecond in the lab using IceCube Upgrade DOM mainboards (see Figure 118) and 1.2 ns over deployed IceCube cables [15].

The cosmic ray surface detector electronics are described in detail in Sect. 7.4.3. The FieldHub Power and Timing Nodes, described in Sect. 8.4.3, provide similar timing and communications interfaces to the surface DAQ as to the string electronics described above.

The FieldHub is connected to the downhole cable through the surface junction box (SJB). While not strictly required, this allows decoupling the installation of the FieldHub from the installation of the string, nominally the season after the FieldHub has been installed. The SJB is used both in IceCube and the IceCube Upgrade, and is essentially a passive patch panel in a metal enclosure. The SJB is installed in a shallow pit and can be buried after the downhole cable is connected and basic connectivity tests are complete, as long-term access for maintenance is not required. For the winter between FieldHub and SJB installation and deep drilling, a temporary wooden vault will be put in place to allow easy access the following summer.

Each radio detector station is connected to the ICL via a Radio FieldHub. Each Radio FieldHub distributes power and communications to a cluster of 48 stations. Main trunks of copper and optical fiber distribute power and communications from the ICL to eight Radio FieldHubs (Sect. 8.4.3.2). Figure 119 shows a simplified diagram of the power and communications distribution scheme for the radio array.

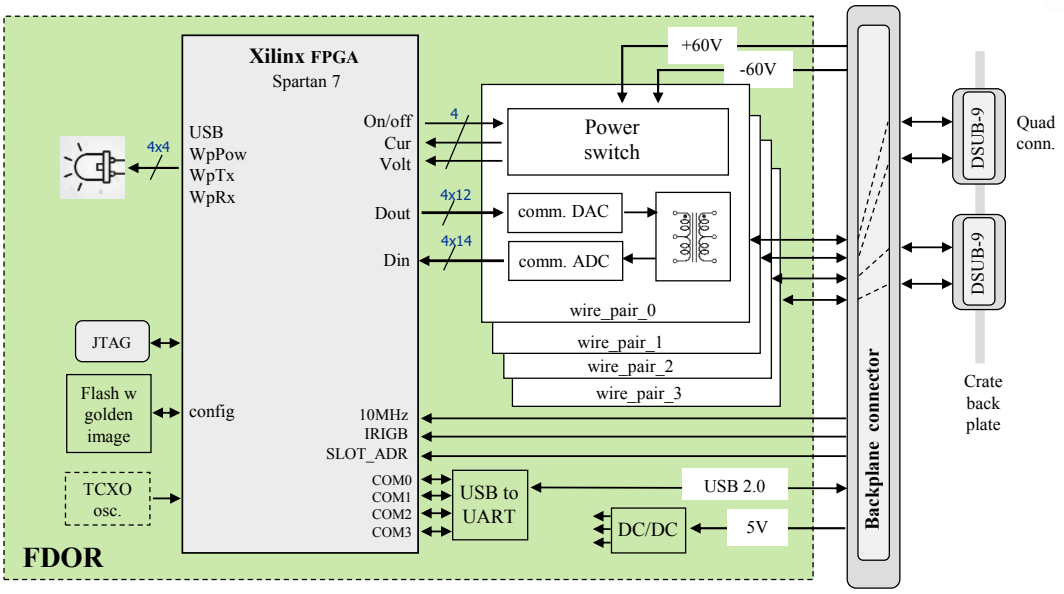

Figure 114: Block diagram of the FDOR card, the primary component of the FieldHub String Interface electronics. The FDOR provides the interface to DOMs on two quads (four pairs) of the downhole cable.

At the FieldHub, redundant DC-DC converters will step down the main trunk cable voltage to 150 VDC for distribution to the radio stations. DC-DC conversion at the radio stations will step down the supplied 150 VDC to the voltages required by the radio DAQ. The radio DAQ at each station is housed within a radio surface junction box (rSJB), a sub-surface insulated enclosure (e.g. a Pelican case) that connects back to each Radio FieldHub. The rSJB will be deployed along with the surface cabling and will be in place at a station location before radio instrumentation installation, allowing commissioning of new stations immediately.

A standard optical network switch at the FieldHub will distribute communications to each radio station via redundant single-mode optical fiber operating in bidirectional mode (100Base-BX). Each radio station will receive two dedicated optical fibers operating in active redundancy mode. A transceiver at the radio station will convert the optical signal to Ethernet over copper to interface with the radio DAQ.

8.4.3 Surface communications, power, and timing

A network of surface cables connect the optical, surface, and radio arrays to the central computing systems of the ICL via the FieldHubs.

8.4.3.1 Optical and Surface Detector Communications, Power, and Timing Communications, power, and timing (CPT) are distributed from the IceCube Laboratory (ICL) to the FieldHubs via cold-rated, direct-burial cable. Power is distributed via shielded, 3-conductor, 12 AWG copper cable. This gauge of wire is chosen to keep resistive power losses below 20 percent. Communications and timing are distributed via single-mode optical fiber using 1 Gbps bidirectional transceivers. These 1 Gbps transceivers are fairly standard and surpass the data bandwidth requirements. The optical fiber is

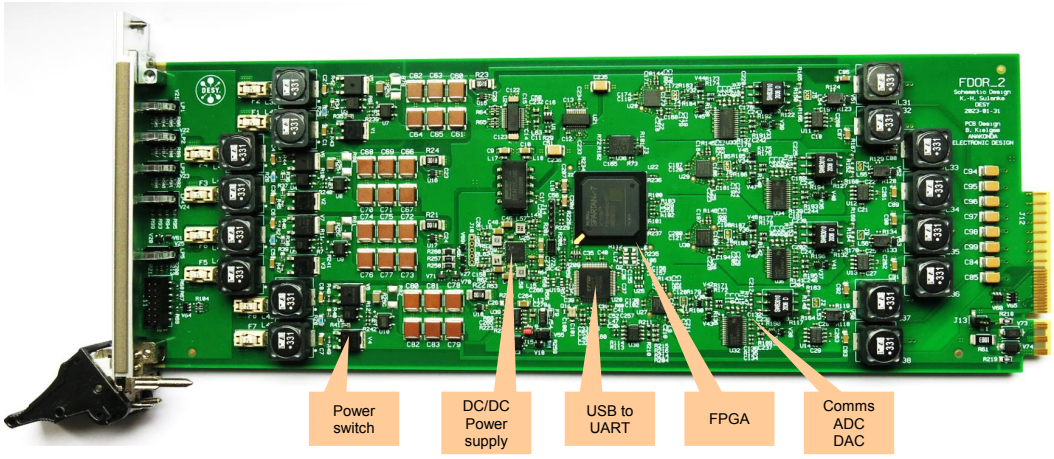

Figure 115: The FDOR interface card for the IceCube Upgrade. The FDOR electronics can support the IceCube-Gen2 optical array without modifications.

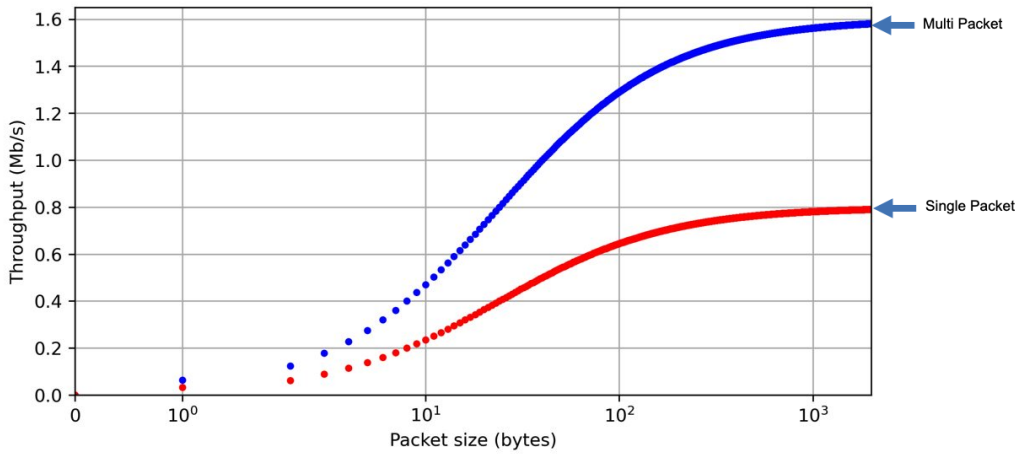

Figure 116: Data throughput on a wire pair with IceCube Upgrade hardware and communications protocols. By using a larger packet size and bundling packets, a throughput of at least 1.5 Mbps is achievable.

cold-rated and preterminated with connectors in order to simplify deployment. IceCube-Gen2 CPT cables extend from the ICL to the perimeter of the original IceCube footprint via 4 main trunks to minimize trenching. Beyond this, cable is routed along the 18 branches of IceCube-Gen2 optical and surface instrumentation as seen in Figure 120. All surface cabling is trenched a minimum of three feet below the surface using an industrial trenching tractor that simultaneously creates the trench and unspools the power cable into the trench. Another vehicle will make a second pass along the trench and unspool the optical fiber into the trench. The cables will breach the surface at the FieldHubs.

Each of the 18 branches of IceCube-Gen2 instrumentation has a dedicated 5 kW power solution in the counting house, allowing each branch to operate autonomously. Each power solution contains N+1 power supply redundancy and UPS backup rated to 10 minutes of power reserve. Slow control and monitoring of the power solutions is pro-

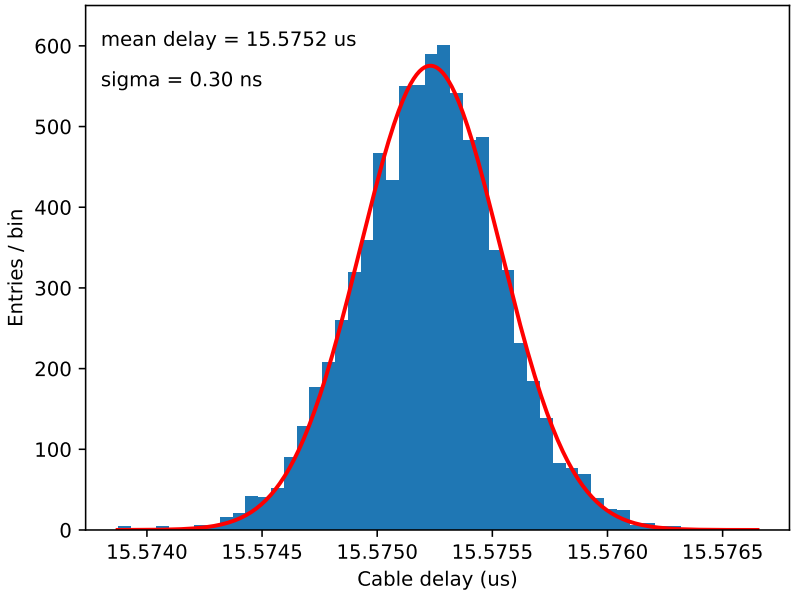

Figure 117: RAPCal round-trip cable delay over a 2.8 km cable in the IceCube Upgrade Northern Test System.

vided over Ethernet. The power solutions require single-phase 208 VAC input and output 600 VDC. Power is distributed to each branch via 3-conductor 12 AWG cable with copper foil shield.

At the FieldHub, the FieldHub Power Node performs the first-level DC-DC conversion from the surface cable high voltage to the voltages required by the FieldHub electronics and the downhole cable voltage of 150 VDC. These DC-DC converters are redundant, since maintenance during the austral winter is generally not possible. A monitoring / control link between the FieldHub Timing Node and Power Node allows power to individual components to be switched remotely, without the need to power down an entire branch.

Communications and timing is distributed by White Rabbit which provides general data transfer and sub-nanosecond time accuracy over Ethernet. Each branch of instrumentation has a dedicated fiber cable containing 18 fiber cores and is cold-rated to -55 C. Each FieldHub has dedicated primary and backup optical fibers both operating in bi-directional (BiDi) mode at 1 Gbps.

The proposed IceCube-Gen2 CPT distribution scheme is based off the experience and success of the deployed prototype surface array station [655]. The station incorporates a central FieldHub with CPT delivered via copper conductors and optical fiber. The station has been in operation since January 2018 and continues to perform as required.

8.4.3.2 Radio Detector Communications and Power

The power and communications distribution scheme for the radio detector is similar to the optical/surface detector. Main trunks of copper and fiber distribute power and communications from the ICL to 8 FieldHubs within the radio array as seen in Figure 121. Each Radio FieldHub has a dedicated ~2 kW power solution located at the ICL. Each power solution contains N+1

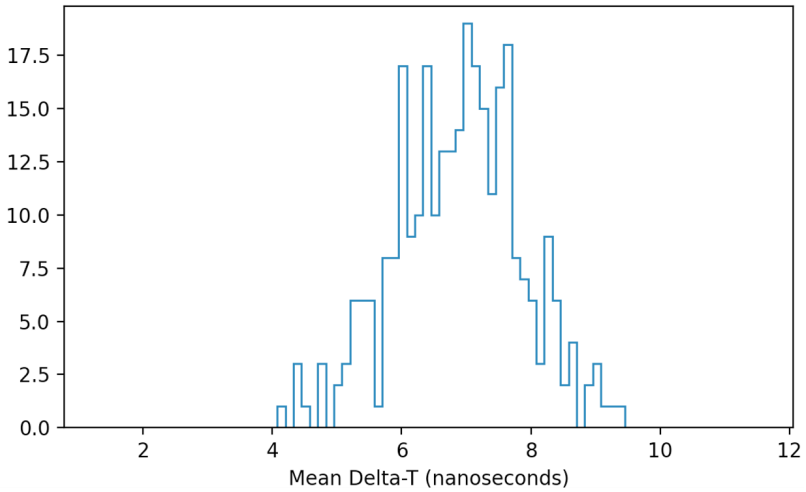

Figure 118: Time difference between two IceCube Upgrade DOM mainboards as measured by RAPCal in the lab. The width of the distribution corresponds to an underlying RAPCal time resolution of ~700 ps.

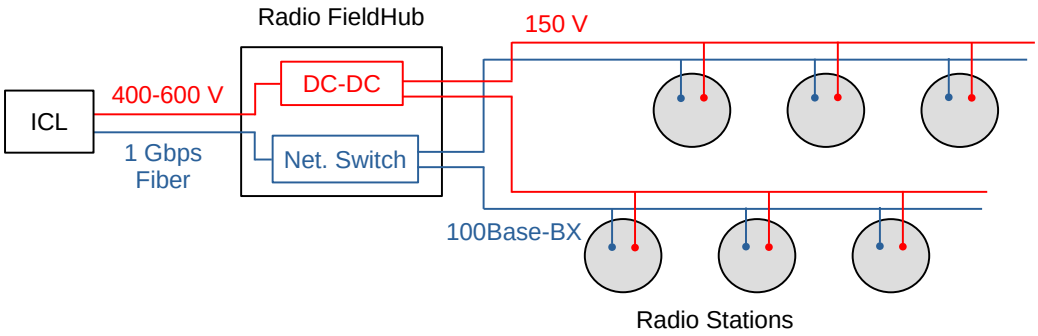

Figure 119: A simplified diagram of the radio array power and communication interfaces from the radio station, through the Radio FieldHub, and to the central computing system at the ICL.

power supply redundancy and UPS backup rated to 10 minutes of power reserve. Slow control and monitoring of the power solutions is provided over Ethernet.

Each FieldHub will distribute communications and power to 48 surrounding radio stations. At the FieldHub, redundant DC-DC converters will step-down the main trunk cable voltage to 150 VDC for distribution to the radio stations. DC-DC conversion at the radio stations will step down the supplied 150 VDC to the voltages required by the radio DAQ.

A standard optical network switch at the FieldHub will distribute communications to each radio station via redundant single-mode optical fiber operating in bidirectional mode (100Base-BX). Each radio station will therefore receive two dedicated optical fibers operating in active redundancy mode. The radio DAQ will incorporate a transceiver at the radio station to convert the optical signal to Ethernet over copper, as detailed in Sect. 6.4.6.

The timing accuracy requirement for radio is 10 ns, and each radio station will use integrated GPS for timing (Sect. 6.4.7) instead of White Rabbit. The optical fiber dis-

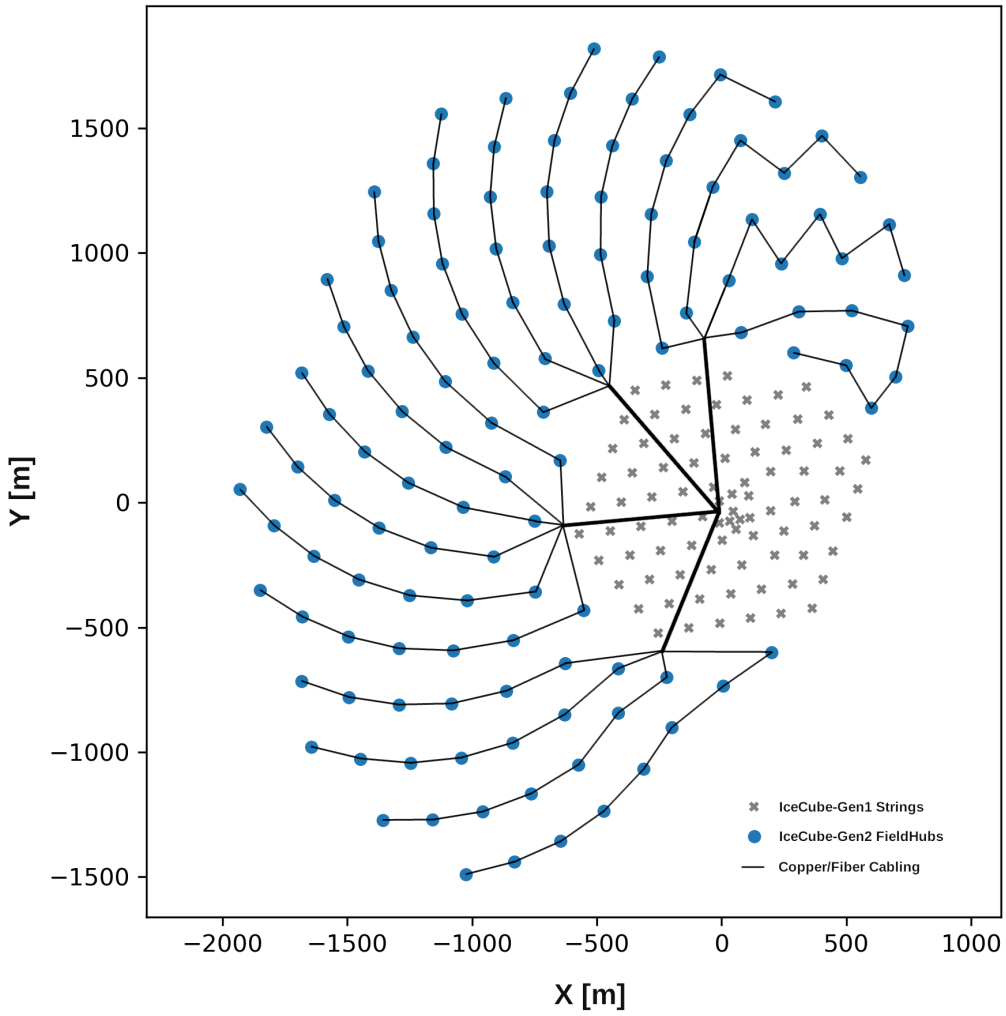

Figure 120: Surface cable layout and trenching from the ICL to the Optical/Surface detector FieldHubs. The black traces represent the copper/fiber cable runs from the ICL to the FieldHubs.

tribution scheme is simplified by not requiring White Rabbit, and the communications power budget is significantly reduced.

8.4.4 Instrumentation software & firmware

Embedded firmware and software running on FPGAs and microcontrollers (MCUs) in the instrumentation is developed by IceCube and is responsible for much of the functionality of each device. Much of the firmware and software for IceCube-Gen2 is based on similar devices in the IceCube Upgrade.

The IceCube-Gen2 DOM contains an FPGA and a MCU on each PMT base (the waveform microbase, or wuBase; see Sect. 5.4.2) and a central MCU on the control board, shown in Figures 69 and 66. Firmware on the wuBase FPGA primarily controls the waveform digitization ADC and is responsible for waveform triggering, timestamping, and buffering. Software on the wuBase MCU reads waveform data from the FPGA and

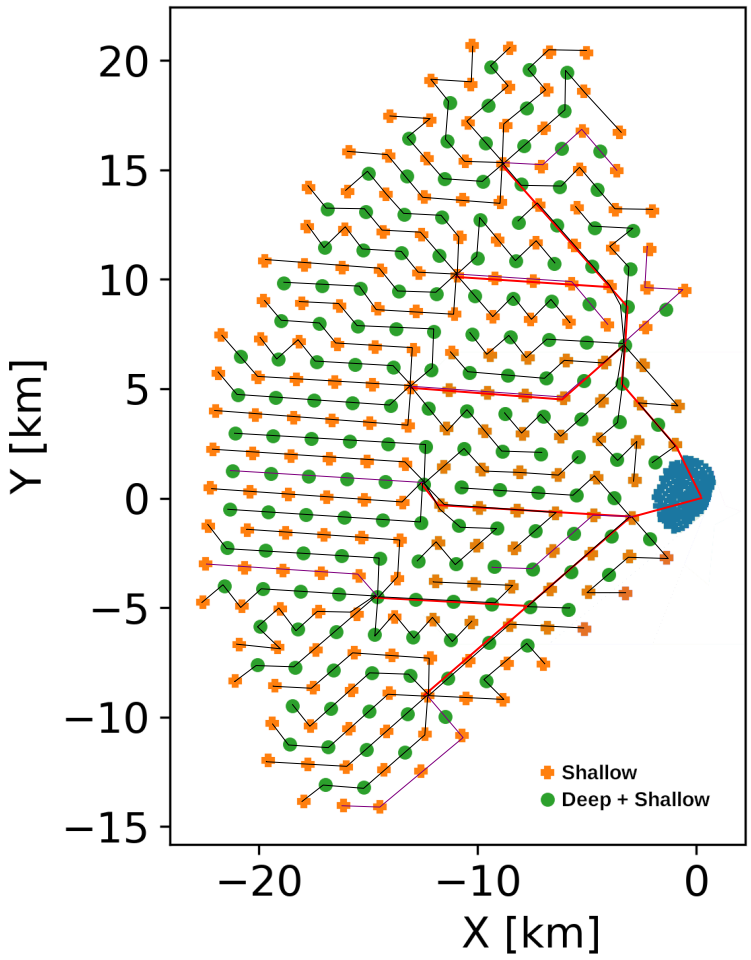

Figure 121: Surface cabling layout and trenching from the ICL to the radio detector FieldHubs and stations. The red traces represent the main backbone copper/fiber cable runs from the ICL to the FieldHubs. The black traces represent the copper/fiber cable runs from the FieldHub to radio stations.

compresses it. Waveforms from single photoeelctrons are feature-extracted, and the corresponding ADC data are discarded. Only the extracted charge and arrival time of the photoelectron are kept. This data is bit-packed into a record of approximately six bytes. More complex waveforms from multiple overlapping photoelectrons are instead losslessly compressed using a standard IceCube algorithm and are unfolded during processing and filtering, described in 9.3.2. The wuBase MCU software additionally controls and monitors the PMT high voltage.

The DOM central MCU reads waveform records from each wuBase. The sum of the hit record data rates from all wuBases on the IceCube-Gen2 DOM is anticipated to be approximately 500 kbps. The DOM central MCU is additionally responsible for controlling calibration hardware, programming the wuBase FPGA and MCU, and running test and calibration software.

Communications between the DOM central MCU and the IceCube DAQ or other surface software are facilitated by the DOM ICM and the FieldHub. Firmware on the

ICM FPGA exchanges messages with firmware on the FieldHub FDOR using one wire pair of the quad. The ICM and FDOR firmware implement a physical data link using amplitude-shift keying to transmit each bit and 8b/10b encoding of bytes, providing a data bandwidth of 1.5 Mbps. The ICM and FDOR firmware also provide packet error detection/retransmission and multiplexing between devices sharing the wire pair.

Since the ICM is responsible for communications, a known good boot image of the ICM firmware is written to the ICM before the DOM is sealed, and then the image is write-protected. The ICM boots this version of the firmware at power-up, and this firmware provides the ability to upload and boot to updated ICM firmware runtime images. If communications to the DOM are lost by e.g. a problematic or corrupt ICM firmware image, communications are recovered by power-cycling the wire pair, automatically booting the protected firmware image. The ICM firmware also is responsible for programming the DOM central MCU. In addition, the FDOR firmware is responsible for controlling the power state of each wire pair and monitoring wire pair voltages and currents.

Finally, a central responsibility of the ICM and FDOR firmware is time calibration. The ICM and FDOR firmware keep 60 MHz clock counters for time reference. The FDOR firmware receives 10 MHz and IRIG-B timing signals from White Rabbit, and therefore the FDOR clock counter is synchronized with the GPS clock and other FDOR cards. The ICM clock counter is driven by a local oscillator with a drift relative to the surface clock. Since DOM waveforms are timestamped with the local ICM clock counter, a calibration must be done to translate the local ICM clock timestamp into global GPS time. This calibration is performed by the FDOR and ICM firmware using the IceCube RAPCal algorithm [15]. This allows the ICM to also provide triggers to calibration hardware with precise timing.

Software running on the FieldHub SBC communicates with firmware running on each of the FDOR cards. This software creates an Ethernet server socket for all potential devices on each wire pair connected to the FieldHub. The IceCube DAQ, or any other client, connects to the Ethernet socket to establish serial communications with the corresponding device. The software also provides a request-reply interface to access other functions of the FDOR/ICM firmware. For example, the request-reply interface allows the user to turn on/off the wire pair power, initiate RAPCals, view the status of all devices on a wire pair, and reset any individual device MCU.

The FieldHub is also responsible for processing data from the Surface DAQ. Details on the Surface DAQ firmware and software are presented in section 7.4.3.

Significant changes are introduced into the overall data flow in IceCube-Gen2 instrumentation, shown in Figure 122. In IceCube and the IceCube Upgrade, all hit records are sent to the surface DAQ. The anticipated total data rate of six IceCube-Gen2 DOMs sharing a wire pair is 3 Mbps, exceeding the wire pair bandwidth of 1.5 Mbps. Instead of transmitting all hit records to the surface, the IceCube-Gen2 DOM central MCU "spools", or buffers, the hit records onto a 32 GB or larger flash memory operated as a ring buffer, providing approximately one week of storage. This deep buffer allows readout of all untriggered hits in the detector in the case of a delayed, external alert from the wider astrophysical community.

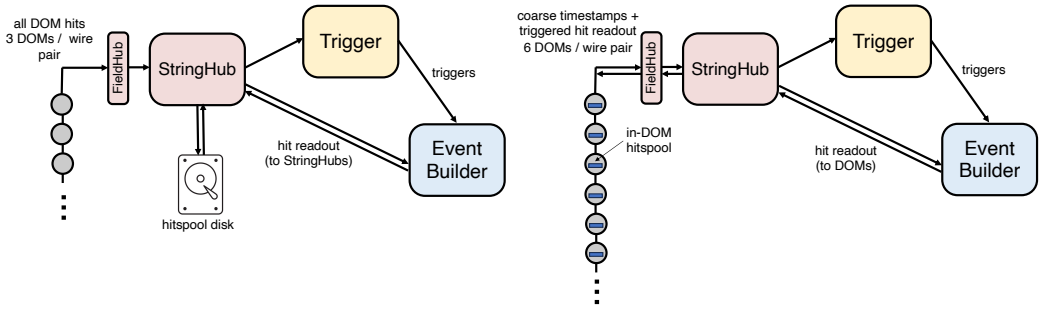

Figure 122: Left: data flow for the IceCube Upgrade. All hit/waveform records in both IceCube and the IceCube Upgrade are sent to the surface DAQ and spooled on disk. Right: data flow for IceCube-Gen2. All hit records are spooled in flash memory inside the DOM. Coarse timestamps are sent to the surface DAQ if coincidence is observed between multiple PMTs in the DOM. Hit records are only sent to the surface in response to readout requests from the surface DAQ.

When the central MCU identifies records in coincidence with those from other PMTs in the same DOM, coarse timestamps are sent immediately to the surface DAQ and are used in trigger calculations, discussed further in Sect. 9.3. When the IceCube surface DAQ issues a trigger, each DOM is queried for all records in a time window relevant to the associated event, including those without coincidence. By transmitting only hit records associated with surface DAQ event readout, the total wire pair data rate is significantly reduced and expected to be well under 1.5 Mbps.

8.5 Alternatives considered

8.5.1 Optical detector cabling

A primary alternative to the infrastructure design presented here is simply to scale up the design of IceCube, with multi-quad copper surface cables similar in design to the surface-to-DOM cables supplying both power and communications from the counting house to the DOM. This has several disadvantages. First, the cost is significantly higher due to the increased cost of a complex, custom copper surface cable for communications versus commodity optical fiber. Second, the increased cable length from $\approx$ 3 to 5 km becomes technically problematic, not only from increased attenuation of the communications signals, but also from resistive losses for power delivery. This scheme has the advantage of not requiring active components in the field for the string interface electronics; however, since active electronics are required at each string to support the surface array station, a FieldHub is already required, and the IceCube Upgrade electronics are already designed for extended temperature range operation.

Deploying optical fiber for downhole communications to the DOMs in the optical array has been considered but is disfavored. Some strings in the AMANDA detector used optical fiber, but some failures were observed during deployment / freeze-in. Because of the changes in the DAQ architecture for IceCube-Gen2, the higher bandwidth provided by optical fiber is not needed. Copper connections to the DOM would still be required in any case for power distribution, although using fiber for communications would simplify the electrical requirements. This benefit, however, is not seen as worth the added risk given the limited experience with downhole fiber since AMANDA.

8.5.2 FieldHub design

An alternative design to the elevated FieldHub is a FieldHub that is located below the snow surface inside a covered cylindrical tube that extends to a depth of about 5 m and extending 1.5 m above the surface at the time of installation. This mini-tower design has several advantages over the elevated field hub concept by avoiding having to cope with significant temperature variations over the year, which would be a major advantage in dealing with temperature control, especially in the event of a power loss. In addition this system might be less susceptible to wind loading. The tower design promises a more efficient cable slack handling and raising procedure. The components of the FieldHub are stacked vertically in a tube of 19”x16.5” inside the tower, insulation is added to ensure stable operations, and the FieldHub rests on a pan with strain relief for the incoming cables from below. The thermal profile inside the tower can be well characterized and avoids large temperature swings encountered above the surface. The FieldHub is operated below the snow surface and can be raised via a pulley system for maintenance or to extend the tower periodically following snow accumulation. The tower would contain at least one loop of the incoming cables from the surface array and string and naturally provides sufficient slack to raise the FieldHub for 30+ years. Tower sides are shielded via a tube of 30” diameter. The tower can be extended by a new tube section, which gets assembled in place by connecting two tube halves, for easy handling and transport.

A second alternative to the reference elevated FieldHub is a pole-mounted FieldHub. The inner enclosure design of the FieldHub would be identical to the reference design, but the enclosure is mounted vertically on a pole. Cables exit the enclosure at the bottom of the enclosure and are contained in a zipper tube. The zipper tube is hung on the pole with sufficient slack so that it stays above ground even following snow accumulation. To raise the FieldHub the pole is extended and the FieldHub and cable slides up on the pole, by loosening holding brackets. Thermal control can be managed similar to the reference design, or the outside of the pole could be insulated, such that it thermally couples the FieldHub to the ground via the inner pole. The thermal coupling of the FieldHub to the ground would allow for a much better temperature control.

For the initial installation, a 5m deep hole would need to be drilled using a tractor-mounted auger or the IceCube firn drill. For the latter option, the firn drill usage gets coupled to the FieldHub installation, allowing for scheduling conflicts and contributing to scheduling complexity. The approximate maximum diameter of a custom firn drill head is 36”, which would be sufficient for the holes. Snow accumulation due to the tube section above the surface needs to be evaluated.

8.5.3 Power distribution

For power distribution to the FieldHubs, AC power distribution from the station grid is considered but raises concerns. There is an elevated risk of AC neutral being at a significantly different voltage potential relative to virtual ground, and this presents a serious shock hazard, especially in the field. Extra precautionary measures must be taken to ensure AC neutral and virtual ground remain at the same potential, but this can cause significant power transmission losses and requires further evaluation.

8.5.4 Optical detector DAQ architecture

Regarding the DAQ architecture, we also consider the approach used in IceCube of transmission of all DOM hits to the counting house. This approach is disfavored due to the costs and complexity associated with providing the necessary bandwidth. The proven wire pair bandwidth would support transmission of all hits for two DOMs. This would require a main cable with at least 20 quads to support an 80-DOM string, an additional 13 quads relative to the reference design. While a main cable of this size has been used for the IceCube Upgrade, the smaller IceCube-Gen2 cable is much simpler to manufacture. Additional costs in FieldHub hardware for DOM readout would also be incurred.

8.5.5 Radio detector wireless communications

A technically viable alternative communications solution that meets bandwidth and power requirements is an 850-MHz LTE cellular network, with a 900-MHZ backup LoRAWAN network. LTE is a mature technology with readily available low-power parts. LTE may operate over a number of different bands, but for our purposes LTE Band 26 (uplink 814-849 MHz, downlink 859-894 MHz) is the most practical, as it is the lowest frequency US LTE band available that is above our instrument band. LTE has been successfully deployed in Greenland for RNO-G, albeit at a slightly different European band (the 900 MHz Band 8), without any apparent interference with the science instrumentation. The client half of an LTE deployment uses LTE modems, which are readily available with industrial rating and will typically use about $1\,\mathrm{W}$ on average under normal use. An LTE modem may transmit at up to $23\,\mathrm{dBm}$ $(200\,\mathrm{mW})$. Readily available commercial band-pass filters prevent output at other frequencies that may interfere with science instrumentation.

While a communications design using LTE is practical, and the basic design has been demonstrated in Greenland, the Dark Sector near the South Pole is meant to be free of radio transmissions. While there are many advantages to this alternative, in particular with respect to installation, the requirement to avoid radio interference with other experiments in the Dark Sector, particularly the cosmic microwave background (CMB) experiments, makes this alternative riskier and less attractive. Should the boundary requirements of the CMB experiments change in the near future, the choice of communications method should be revisited.

8.5.6 Radio detector autonomous power

Autonomous power for the radio detector stations would be a particularly attractive if wireless communications were to become a viable option, as it would obviate the need for cabling the array. The decreased load on the limited South Pole power resources and smaller environmental impact would be additional benefits. Solar panels and wind turbines have been considered as alternative power sources.

Solar panels have been extensively used by many polar installations. Of particular interest for the in-ice radio array of IceCube-Gen2, is the autonomous ARIANNA station at South Pole. This station successfully hibernated during two polar nights, coming

back to normal operation in the polar morning. If only photo-voltaic panels are used for power then approximately 5 months of operation per year can be expected at the South Pole, assuming reasonable panel power and battery size.

Wind power is a more challenging technology, and the relevant experience is more limited. Wind turbines in arctic conditions are frequently successfully used for different autonomous instruments (e.g. UNAVCO [656]), albeit often with different environmental conditions and power levels than required by IceCube-Gen2. Wind power for radio detectors have been tested in a few studies. The most relevant were those from the ARA collaboration, that reported on autonomous renewable power stations installed at the South Pole [553]. These tests were extended in [657]. In addition, the ARIANNA Collaboration operated four commercially available turbines at Moore's bay on the coast of Antarctica, with a rated power of $150\,\mathrm{W}$ [554]. Furthermore, several wind-turbines have been and will be installed as part of RNO-G.

Renewable power sources can, as described above, be used for fully autonomous stations, but they can also be used in combination with a cabled power network. The latter option would offset part of the central power production needs for the stations and for losses in the network. Such a system can be designed without batteries. In both cases, solar power and wind turbines offer a viable and attractive alternative. To realize a reliable, low maintenance system for the specific environmental and instrumental requirements would naturally require some time for system design studies and *in-situ* verification.

8.6 Development and deployment strategy

Development for the DAQ and surface infrastructure follows the technical readiness of key components as described in Table 15. Components requiring new development in particular are the FieldHub Power and Timing Nodes, and revised version of the FieldHub enclosure. Integration and field testing of prototype IceCube-Gen2 FieldHub components is possible using the IceTop surface array prototype station(s) as a testbed. The following activities are foreseen in preparation for full-scale production readiness:

- Development of a custom/customized White Rabbit node
- Development of a prototype FieldHub power system
- Development of a prototype FieldHub enclosure
- Deployment of upgraded surface cables at the prototype surface array station
- Integration and deployment of the above items at the prototype surface array station
- Procurement of a full-length downhole cable prototype
- Development of IceCube-Gen2 DOM firmware and software, via IceCube-Gen2 DOMs installed in the IceCube Upgrade

The deployment strategy for the surface infrastructure leads the optical deep drilling by one year, so that the optical strings can be commissioned immediately after deployment. In order to support this schedule, production of FieldHubs, surface cables,

etc. will be required. The radio array FieldHubs and radio surface junction boxes will also be installed before the stations to enable prompt commissioning. In particular, the first field season will include: deployment of the backbone surface cabling out of the IceCube array footprint for both the optical and radio arrays; deployment of 3 optical/surface FieldHubs corresponding to the first 3 optical strings; and installation of radio backbone cabling to at least one Radio FieldHub site.

8.7 Test strategy

The downhole cable will be tested using prototypes and the production assemblies to ensure that all mechanical and electrical requirements are satisfield. Pull tests will ensure the downhole cable has sufficient mechanical strength for the loads during string deployment. Electrical tests on the cable will include inter-quad and intra-quad crosstalk (NEXT/FEXT), insulation resistance, continuity, and pairwise capacitance measurements. After the downhole cable breakouts are installed and the cable is fully connectorized, production tests will ensure correct installation.

A central integration center will receive the FieldHub subcomponents (incl. surface DAQ, string interface, and timing node) and parts, such as Power Node, fiber patch panel, cables, enclosure and support structure. The subcomponents, as well as the assembled FieldHub, will be functionally tested at multiple stages during their production. The FieldHub enclosure and mechanical support structure for elevation will consist of off-the-shelf and machined parts and assembled at the integration center. Each subcomponent will be individually tested prior to transportation to the integration center. After the validated subcomponents are received at the integration center, they will be inspected and subjected to a set of standardized tests before being installed into a FieldHub. After integration, the entire FieldHub assembly will be subjected to an additional series of standardized tests. These will include functional, electrical, mechanical, temperature and cold testing of each fully assembled FieldHub. Once fully tested, the completed FieldHub will be crated and prepared for shipping. Test result reports and certifications will be included with each FieldHub and recorded in an electronic database for future reference.

Bare mainboards and assembled DOMs are functionally tested at multiple stages of production, described in section 5.7. DOMs are also tested on-ice before deployment (section 5.8) and after deployment in the ice. The bulk of functional testing is carried out by the Simple Test Framework (STF), a modular testing framework developed for the IceCube Upgrade and inspired by existing IceCube software. STF is a software framework that communicates with the MCU of a single DOM and provides the context to execute a set of modular scripts that each tests a specific functionality. Before each test in the set, STF re-initializes DOM hardware to prevent dependencies on the ordering of individual tests. STF passes the serial communications stream and configuration parameters to each test, and then executes the test. Configuration parameters are often either an expected range of a quantity to be measured, an amount of data to be used in the test (e.g., number of waveforms to collect), or a channel number or other identifier indicating the particular piece of DOM hardware to test. The test collects data and returns it to STF. The STF framework then compares quantities measured by the

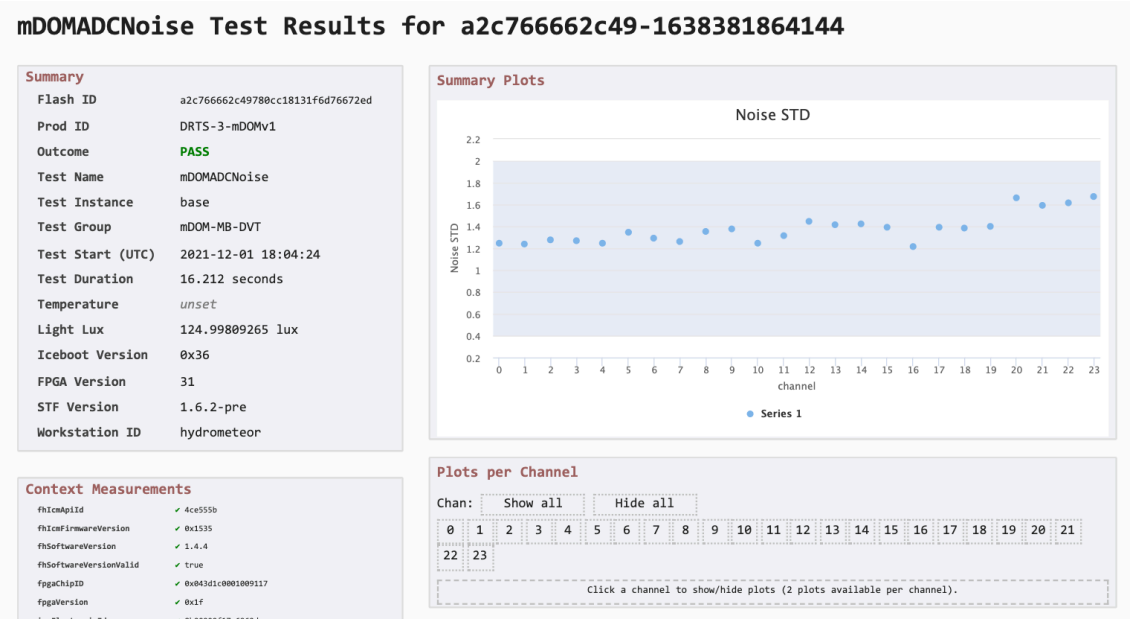

Figure 123: Example STF web interface page for one specific IceCube Upgrade test result.

test against expected ranges for that quantity and issues a pass/fail determination for the test. The STF framework prints pass/fail results to the screen for the test operator and records values and the pass/fail determination in a database for later analysis. A web interface to this database, shown in Figure 123, provides easy access to results for any instance of a given test and simplifies the process of understanding test failures.

9 Data Systems and Infrastructure

9.1 Overview

This section encompasses the hardware and software systems starting inside the South Pole IceCube Laboratory (ICL) including the existing StringHubs (computers that collect the hit data from the in-ice DOMs), and their equivalent DataCollectors in the IceCube-Gen2 detector additions, through to the Northern Hemisphere data center. Specifically, it is responsible for the final stage of online triggering, event building, processing and filtering clients using offline IceTray software framework, realtime alerts and data stream, data storage at South Pole, data movement over satellite to the northern data center and the overall experiment control and monitoring system. The existing IceCube detector online system is shown in Figure 124. It is also responsible for the core IceTray software and database systems used in online processing & realtime system, offline physics reconstruction and analysis and simulation. It is responsible for the purchase, installation and commissioning of all computer systems in the ICL. This includes the DataCollectors, although custom DAQ software installed on the DataCollectors is in DAQ responsibilities. Finally it is responsible for the needed additional infrastructure to store and make available data and simulation at the northern hemisphere data center.

The bulk of the design and development effort will be in requirements for hardware and software systems integration of the new detector instrumentation deployed in the IceCube-Gen2 project (Figure 125). These new systems include not only new in-ice optical modules that will require extensions to the hardware and software systems but also new surface detector technologies as well as in-ice radio components that will be a larger effort to integrate into the existing IceCube data systems. The red text in the figure indicates needed effort and hardware. The existing top level box will need modest hardware and software additions and updates to accommodate the new subsystems of IceCube-Gen2. While the lower box indicates completely new hardware and software systems needed for readout and control of the new systems (i.e. in-ice, surface and radio). To the right near ICL is the indication that the new systems of IceCube-Gen2 will require major upgrades in infrastructure for power and space to accommodate the new hardware. The infrastructure requirements for power and space for the ICL are indicated in this section, while the possible solutions, cost, schedule and logistics are in the Logistics and Infrastructure section.

Shown in Table 17 are the current and expected data rates for the completed IceCube-Gen2 facility. The IceCube rates come from current data and facilities in place, while the expectations for the IceCube Upgrade and IceCube-Gen2 are from simulations studies of the detector designs. These estimates are used for the architecture of the technical designs for the South Pole Computing, Online and Realtime, Data Transfer, and Data Handling systems to accommodate the completed IceCube-Gen2 facility.

IceCube's unified high-level scheme for sub-detector triggering and readout is described in Sect. 9.3.1. The estimated optical detector rate assumes a trigger based on multi-PMT in-DOM coincidences and a multiplicity condition across the array. The surface array trigger is based on scintillator panel coincidences at the station level,

and surface radio antenna readout is limited to higher energy events and in-ice coincidences in order to keep the data rates manageable. The radio neutrino detector data rates are based upon a station trigger adjusted to a 1 Hz station-level thermal noise rate. Satellite transfer estimates shown in Table 17 are not fixed and can be adjusted with various filter selection criteria (see Sec. 9.3.2).

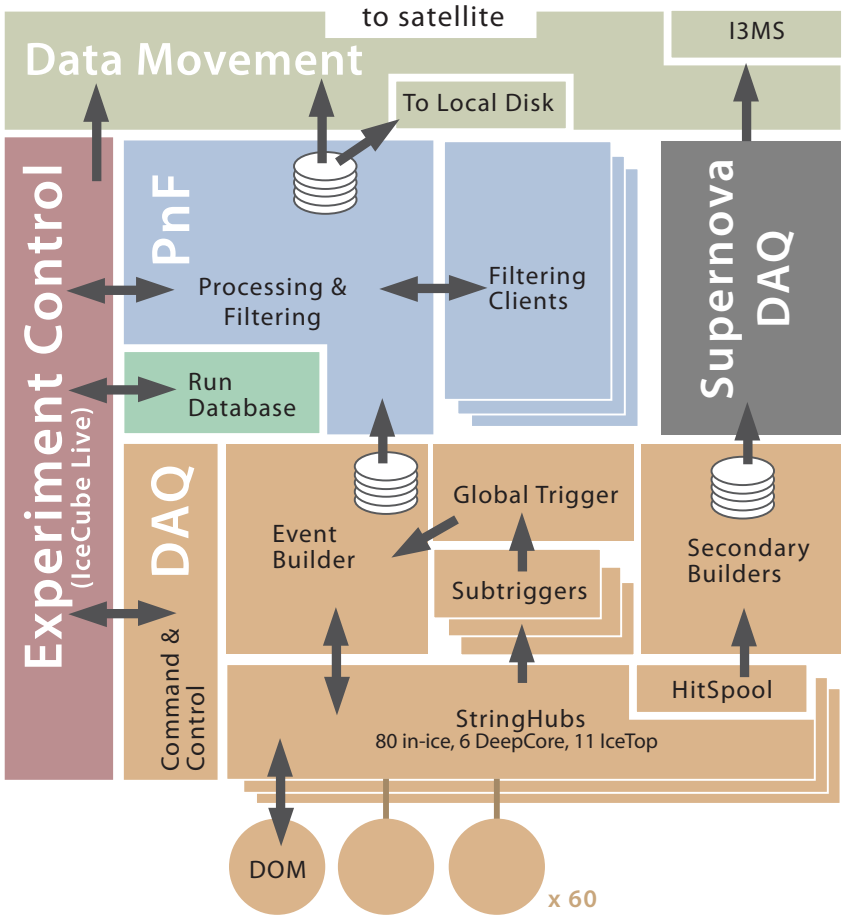

Figure 124: Diagram of the current IceCube Online Data Systems. Data Systems is responsible for the computing hardware and IT infrastructure, Online Specific Software and Core IceTray Analysis Software for everything after the StringHubs [DAQ] and needs to be extended to include new Gen2 instrumentation. This includes in-ice optical, surface station and in-ice radio.

9.2 Computing hardware

This section describes the computing infrastructure design for the local counting house at South Pole as well as for the associated test and development systems in the Northern Hemisphere. IceCube-Gen2 compute systems will be integrated transparently into the existing IceCube compute infrastructure and will follow a similar overall design that focuses on a high level of redundancy and high availability to achieve maximum detector uptime. This includes redundant networking, battery-backed power for all critical data read-out and processing systems, as well as redundant, multi-copy archiving of science data. Remote systems management tools (remote controlled power distribu-

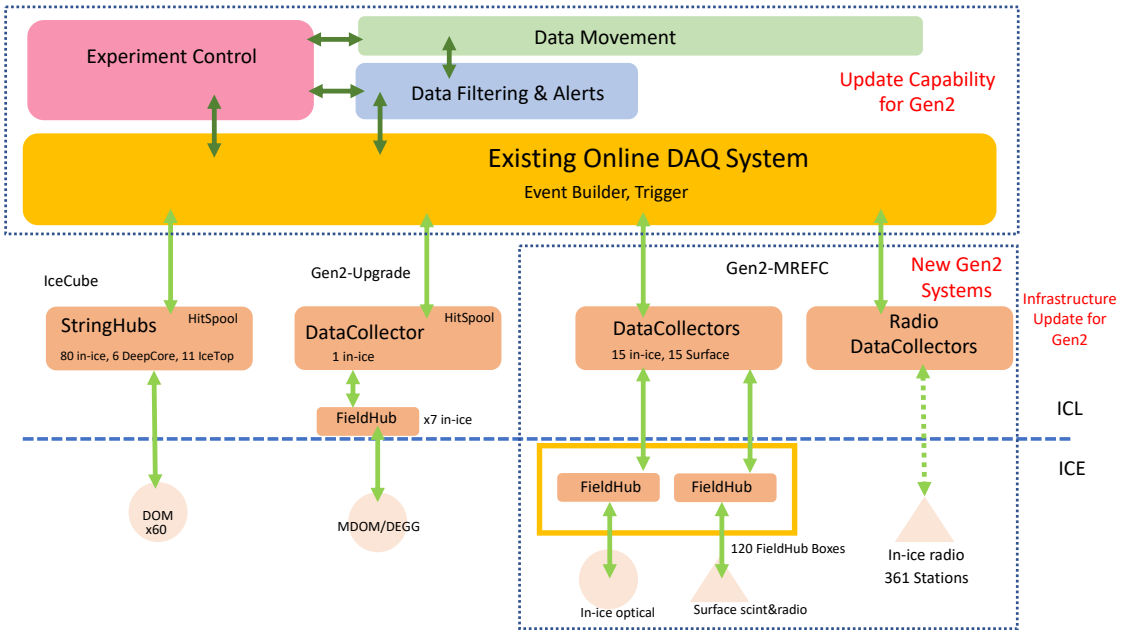

Figure 125: integration of new components for IceCube-Gen2. The red text indicates needed effort and hardware. The existing top level box will need modest hardware and software additions and updates to accommodate the new subsystems of Gen2. While the lower box indicates completely new hardware and software systems needed for readout and control of the new systems (i.e. in-ice, surface and radio). To the right near ICL is the indication that the new systems of Gen2 will require major upgrades in infrastructure for power and space to accommodate the new hardware.

Detector Component	DAQ(MB/s)	Archive(TB/yr)	Satellite(GB/day)
IceCube			
In-ice/Icetop	10-12	375	145
IceCube Supernova	1.2	40	5
	Subtotal	415	150
Upgrade			
In-ice	2.1	56	18
	Subtotal	56	18
Gen2			
In-ice	12	322	104
Surface	11.5	308	15
Radio	11	350	15
	Subtotal	980	134
	Total	**1451**	**302**

Table 17: Current and expected data rates for IceCube facility. The DAQ column represents the rate of raw data from the detector components, Archive represents the formatted and compressed data physically stored for archival purposes and for transport north during austral summer, Satellite is the filtered and compressed primary data stream for analysis sent north by satellite.

tion units, independent management chips, keyboard/video/mouse switches, etc.) will

allow operators to address most data center issues remotely without having to be physically present in the server room.

A homogeneous compute approach for all subdetectors (deep in-ice optical, near surface radio, and surface) will greatly reduce maintenance effort and costs. A common hardware platform will be identified as the base for all compute in the counting house, with specialized one-off hardware to be added on a case-by-case basis as requirements warrant. A similar approach on the software and operating system side will maximize system interoperability and software portability. All compute systems will be running on the same operating system (currently based on RedHat Linux) and will be maintained through a central configuration management system (currently Puppet). Required software packages outside of the core operating system context will be provided to target systems as needed, minimizing the amount of software required on any individual system, therefore increasing system security, reducing upgrade and maintenance efforts, and minimizing the time required to install a system. A fully automated system installation routine ("Kickstart"), together with the central management system, will ensure that any number of servers can quickly and reliably be re-installed from scratch to a known state at any time.

The existing IceCube compute infrastructure at the IceCube Laboratory is exclusively based on CPUs. With new algorithms and, in particular, machine learning approaches becoming more and more utilized in our analysis, parts of our on-site data processing might need to be moved to GPU computing. The requirements for GPU computing in the counting house need to be assessed as we move forward into the final design process.

9.2.1 South Pole computing and infrastructure

The data center at South Pole presents unique challenges. The facility is only accessible for significant upgrades for a few months during the austral summer. A maintenance window of about 3 months per year allows IT experts a very limited time period to perform on-site data center work. For the remaining 9 months of the year, the data center can only be visited by two year-round on-site operators (winterovers). The winterover operators are matched based on their technical abilities and experience, but overall levels of operator skills can vary greatly from year to year. Hence it is crucial to provide a robust, reliable, and easy to maintain data center infrastructure with a high level of automation, detailed system and environmental monitoring, and a reliable notification system that informs operators and experts in the North alike of any problems in the data center so that proper action can be taken quickly and detector downtime be minimized or avoided. All communication between South Pole and the North is based on satellite communication and very limited. Satellite connectivity is unreliable, and having multiple communication channels is critical. The current IceCube data center infrastructure therefore utilizes a multitude of communication tools, including satellite email, VoIP phone, Iridium-based 24/7 chat messaging, as well as Iridium 24/7 email and telephone. New technologies, including commercial offerings (StarLink, etc.) are currently being evaluated to be added to this list for IceCube-Gen2. The IceCube-Gen2 data center will be physically connected to the United States Antarctic Program's (USAP)

network. As such, we follow government-mandated cybersecurity rules and ensure the required security mechanisms are in place. This includes network security via a pair of NextGen firewalls, separating IceCube network traffic from USAP traffic, and periodic system update and patch management on all IceCube data center machines. All electrical power at South Pole is provided by diesel generators. These generators are operated under extreme conditions, and power delivery to the data center can sometimes be unreliable. In order to provide stable and clean power to our sensitive equipment, incoming power needs to be filtered and stabilized via dual-conversion UPS systems which will also provide battery backup power in case of power failures. As with current IceCube infrastructure, UPS and battery power will be designed to provide at least 5 minutes of battery-supported detector runtime for IceCube-Gen2. Network connectivity inside the counting house needs to be able to sustain an estimated ~ 400 Mbit/s of incoming data rate. Dual 1Gb/s Ethernet network connectivity from each server to two independent network switches will provide redundant networking for each system and 2Gb/s of throughput capacity All network switches will be connected via multi-path 10Gbit/sec ethernet, providing 10-20Gbit/sec of throughput. A redundant fiber link will provide network connectivity between our data center network and the USAP-maintained station network (required for science data satellite upload and remote data center access from the main station). Proper cooling needs to be provided to the data center to avoid any temperature related damage to our equipment and the data center will need to be fitted with a clean agent fire suppression system. To avoid interference to the science data read-out, the data center needs to resemble a Faraday cage and provide a good common "ground."

The total estimated power budget for IceCube-Gen2 detector hardware in the counting house is around 114 kW; a detailed breakdown of all components is provided in table 18. To ensure reliable data acquisition and to keep critical detector components powered if main power goes out, the counting house UPS system needs to support at least 90 kW. The schedule of power requirements versus string deployments are shown in the infrastructure section of Part III in Figure **??**)

Table 19 provides an overview of the physical rack space required to support IceCube-Gen2 hardware in the data center. A baseline of 119U for the actual detector hardware translates into 2.5 standard 47U racks, but an additional 2U of space per rack will be required for basic rack infrastructure components. Assuming that no extra rack space has to be allocated for special cabling, connectors, or adapters, the basic IceCube-Gen2 compute infrastructure should comfortably fit into 3 standard 19" racks.
However, additional rack and/or floor space will be required for the UPS backup power infrastructure. IceCube detector hardware is currently spread out over 19 racks and utilizes two rack-mountable, 6kVA UPSs per rack to provide a maximum of redundancy, battery run time, and user serviceability. The overall power footprint of Gen1 is around 65kW. While a similar approach is still feasible for IceCube-Gen2, the much higher power density of IceCube-Gen2 (3 racks 90kW) makes a rack UPS based design more challenging. A more cost and space efficient solution can be found in modular, expandable, tower UPSes. Depending on the overall design and model, an additional 2 racks worth of space will be required to support 90kW in a redundant fashion. New battery technologies can further help reduce the UPS footprint but potentially presents

logistical challenges when it comes to shipping large quantities of lithium-ion batteries to Antarctica.

Component	Target Power (in kW)
Optical	46.3
Radio	9.3
FieldHubs	14.4
Distribution	9.5
Surface Array	6.5
ICL AC/DC conversion	12.9
ICL compute	12.0
ICL networking / timing	3.4
Total	**114.3**

Table 18: Estimated power consumption for Gen2 detector hardware inside the counting house.

Component	Number of components	Rack space each (in U)	Total rack space (in U)
White Rabbit Switch	7	1	7
Fiber patch panel	11	1	11
Fieldhub power supply	41	1	41
DataCollector Server	16	2	32
Radio interface server	1	2	2
Radio processing server	10	2	20
Surface trigger	1	2	2
Optical trigger	0	2	0
Event builder	0	2	0
Secondary builder machine	0	2	0
Processing & filtering node	2	2	4
		Total	**119**
Rack infrastructure			
network switches & PDUs	2	1	2

Table 19: Estimated rack space requirements to support Gen2 detector hardware inside the counting house. An additional 2U per rack will be required for basic rack infrastructure.
Numbers provided by J.Kelley, M.Kauer

9.2.2 Northern test system

The existing IceCube detector operates at >99.9% uptime. Such a high level of uptime can only be achieved by ensuring that hardware and software components are thoroughly tested and evaluated prior to any deployment at the production site. Furthermore, due to the short maintenance window at the data center at South Pole, all upgrade procedures and system modifications need to be properly exercised step-by-

step prior to roll-out at the detector site. For this purpose, IceCube currently maintains two testing sites dedicated to South Pole testing and development.

The South Pole Test System (SPTS) at UW Madison provides access to actual photosensors, several hours worth of raw detector replay data, a full processing and filtering farm, a one-to-one replication of all data acquisition (DAQ) systems, and a full-scale copy of the data archiving system (JADE). A full-length 2km spool of IceCube in-ice cable, large-scale freezer units to cool equipment down to -50C, and a replica of the full data center infrastructure that we have at the South Pole allow for end-to-end hardware and software development. The SPTS system at Madison also provides an ideal training environment for winterover operators.

The Northern Test System (NTS) at Michigan State University is transparently integrated into the SPTS system and provides access to IceCube-Gen2-type FieldHubs and IceCube Upgrade/Gen2 in-ice cables for integration testing and serves as a general testing site for potential next-generation off-the-shelf data center hardware, like networking equipment, UPSes, and servers.

IceCube-Gen2 will consist of several different subsystems (in-ice, surface, radio) that will share hardware and software resources both in the counting-house and in the field. The test systems in the North will be upgraded and expanded to provide adequate resources for integration testing of all systems and development work for all detector components.

9.3 Online data systems software

Online data systems covers the software for data acquisition and processing in the counting house. This includes all subdetectors: IceCube (in-ice, DeepCore, IceTop, IceCube Upgrade), and IceCube-Gen2 optical detector, radio array detectors, and surface array extensions. The objective is for a unified, single detector approach in which various streams of data are processed by a single high-level DAQ and a single data filtering system. The integrated approach enables cross-subdetector physics.

Major components of online data systems are: DataCollectors and Radio DataCollectors, High level DAQ, Experiment Control and Online Monitoring, the Supernova DAQ, and processing, filtering and realtime alerts. Most of the online data systems have a strong inheritance from IceCube. Since, for IceCube collaborators, the least experience is with radio-neutrino detection, a specific subsubsection is called out detailing how to integrate these efforts into online data systems.

Inputs to the online data systems are primary detector data (IceCube-Gen2 DOMs, scintillators, surface array antennas, radio-neutrino stations), as well as secondary streams of data for detector monitoring.

9.3.1 Triggering and data acquisition

`pDAQ` is IceCube's high-level DAQ. Figure 124 shows, in orange shade, the existig subcomponents of the high-level DAQ. `pDAQ` will be expanded to handle Upgrade and Gen2 needs. Gen2 needs benefit by inheritance of work on the Upgrade. It is assumed that

pDAQ can be modified to handle data rates that are $\sim 2-3$ times higher than IceCube, though testing is required.

Gen2 data arrives at the counting house (physically) and to the high-level DAQ (virtually) via the DataCollectors and Radio-DataCollectors. These systems are mostly pass-through from either Gen2 field hubs or radio-neutrino stations. Data streams that are siphoned by the DataCollectors and Radio-DataCollectors includes: IceCube-Gen2 DOM hit data, secondary streams, IceCube-Gen2 DOM hitspool data, and radio-neutrino station data.

Several subtriggers can be formed by the trigger system. Subtriggers are defined for each subdetector, and there can be more than one type of subtrigger per subdetector. As an example, Gen2-Optical simulations currently include a Single Majority Trigger and a Volume Trigger.

Preliminary studies of the IceCube-Gen2 optical trigger allow validation of the triggering and readout architecture as well as estimation of the data rates on the cables (see Chapter 8) and for higher-level event building and filtering. By requiring $N_{\rm PMT}$ multiple-PMT coincidences within a IceCube-Gen2 DOM before hits are sent via the downhole cable to the higher-level trigger in the counting house, data rates on the cable from module dark noise can be controlled. The simulated implementation of array-level Simple Multiplicity Trigger, requires $N_{\rm DOM}$ modules hit within a time windows set by the particle travel time across the array. Figure 126 shows the simulated rates for a single DOM as a function of the number of PMTs that record a photoelectron in a time window of 500 nsec. The noise rates created caused by radioactivity in the glass of the PMT and the pressure housing drops below the physics rate when requiring $N_{\rm PMT} \geq 3$. However, placing the threshold at $N_{\rm PMT} \geq 2$ is sufficient to send trigger messages within the bandwidth budget. We introduce one additional condition that we call a string cluster, $N_{\rm SC}$, to obtain a high trigger efficiency for neutrinos while limiting the bandwidth requirement due to noise. A string cluster requires that at least 2 out of any 5 neighboring DOMs have a signal within 500ns. This condition can be implemented at the surface. The resulting trigger rates and efficiencies for background cosmic-ray muon simulation are shown in Figure 127; the preliminary benchmark trigger assumed is $N_{\rm PMT} \geq 3$ and $N_{\rm DOM} \geq 12$ and $N_{\rm NSC} \geq 1$.

Radio-neutrino stations operate as neutrino detection units are already provided at the Radio-DataCollector level triggered data. The global trigger combines all time-coincident subtriggers into a single global trigger.

A minimum bias subtrigger, with a to be defined small rate, should be designed for each subdetector.

Global triggers, and the information of each subtrigger is sent to the Event Builder, which assembles events on their appropriate read out time windows. For Gen2-Optical IceCube-Gen2 DOM hit data is gathered from the DataCollectors. The event builder writes out data for use of the data filtering system. The event builder includes a decision tree for the readout of various subdetectors whenever another subdetector is triggered. It may be necessary to have joint readouts to be more fine grained than subdetector level. Case in point, only for nearby radio-neutrino station triggers, a Gen2-Optical readout should be considered.

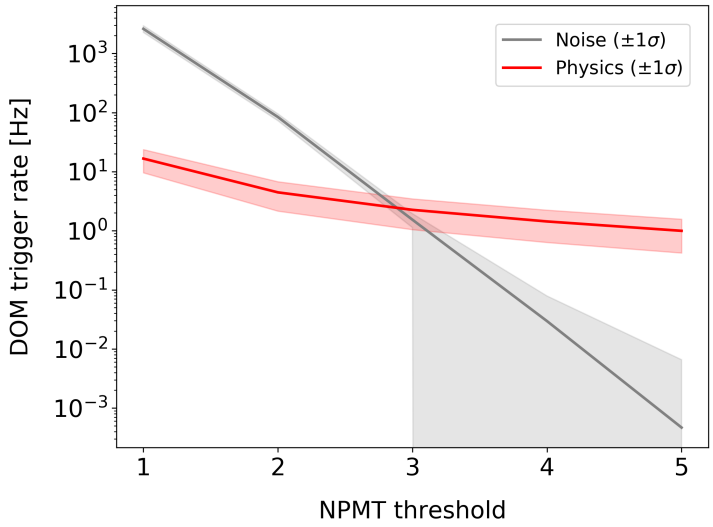

Figure 126: The trigger rates of individual DOMs is shown as a function of the number of PMTs that are required to have signals in conincidence (<500 nsec). The DOM noise rate drops below the physics rate for $\geq 3PE$

A secondary builder continuously reads detector level (IceCube-Gen2 DOM, scintillator, radio station, etc.) monitoring data and writes out this information for use, e.g. of Experiment Control and Online Monitoring.

At specific instances, e.g. in automatic response to a supernova alert, the high-level DAQ can request hitspool data directly from IceCube-Gen2 DOMs and writes it to disk.

During the construction phase of IceCube-Gen2, it will be necessary at times to operate two instances of the high-level DAQ. This will allow new detectors, e.g. new optical strings to become operational within the high-level DAQ, while maximizing the uptime for IceCube. Special provisions will be made to minimize the DAQ level downtime for supernova detection mode.

9.3.2 Data filtering and real-time alerts

The IceCube processing and filtering (`PnF`) is responsible for the correct calibration, processing and filtering all DAQ triggered events. This system distributes events to a large farm of parallel processing compute systems, each running identical processing chains in the IceTray data analysis framework (9.4.1). Results from this processing are returned to a central server, and written to files that are passed to the data handling system (9.5.1). As part of this realtime processing of each DAQ event, this system also hosts the IceCube realtime alert system, and ensures these critical alert messages are transmitted north via the I3MS system (9.3.3). For IceCube-Gen2, this realtime processing and filtering of data is planned to continue with some needed system architecture changes to support the IceCube-Gen2 data volumes and heterogeneous data types.

The `PnF` system (Figure 128) accepts as input all triggered events from the IceCube DAQ, IceCube-Gen2 DAQ, calibration and configuration information from the I3Live DB systems, and a set of filter and realtime alert configurations that are determined by the

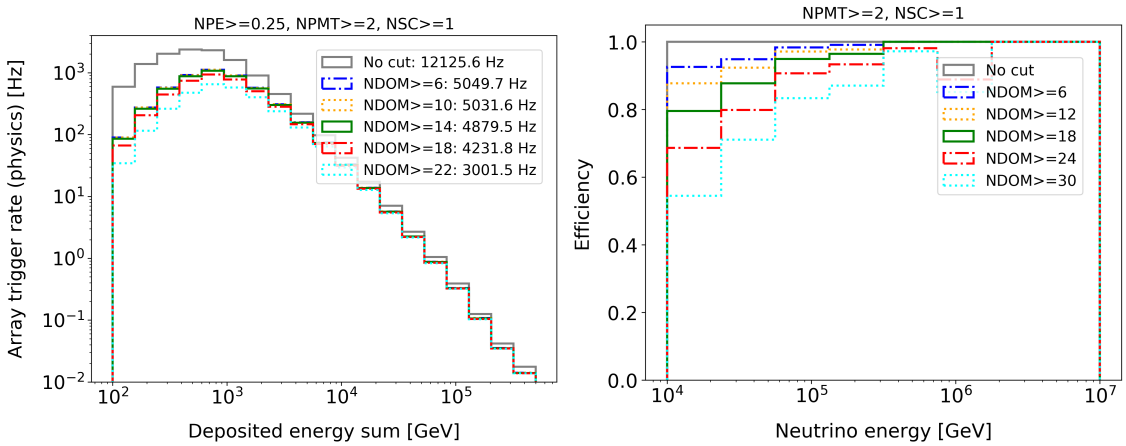

Figure 127: Simulated in-ice optical trigger rates are shown for background cosmic-ray muons as a function of deposited energy (left). The trigger efficiency for injected neutrino events is shown on the right. The trigger condition requires 2-PMT coincidences, at least one "string cluster" and a given number of DOMs.

IceCube collaboration ahead of each operational season. After processing each event through the needed processing software, generating a filter result and monitoring information for each event, the system produces up to three output formats of the data. The first, saved as an archival copy, preserves all DAQ events as read from the detector. The second copy preserves a hit-reduced copy every event from IceCube, where online calibration and feature extraction routines are used to replace the raw waveforms produced by IceCube OMs with series of time/amplitude pairs, vastly reducing the size of the data. Finally, a third copy preserves just the events, realtime alert information, and online monitoring information that can be immediately transmitted North and accommodated into IceCube satellite bandwidth. Presently, the current IceCube detector has updated the event processing so that minimal filtering is required at South Pole, instead, all hit-reduced trigger level data is sent via satellite and is filtered and reconstructed in the northern hemisphere. Here, `PnF` continues to be responsible for producing hit-reduced data, detector monitoring and selection of real-time alerts.

For IceCube-Gen2, `PnF` will be expanded to handle additional data streams from the heterogenous detector types produced by the DAQ: in-ice optical, surface array and radio-neutrino detectors. It is observed that `PnF` can handle a data rate of ~2 times that of IceCube within the current design. A higher data rate, as potentially created by IceCube Gen2, would necessitate the redesign of the `PnF` components in charge of writing archival data to disk. The alerts system is already highly configurable and extensible (see [196]), and, for example, after initial observation of >PeV neutrinos with the radio-neutrino detector, the system will be upgraded to send realtime radio-detection neutrino alerts.

Currently `PnF` uses a fairly standard configuration of multi-CPU cores. Software will need to be modified to take advantage of GPU/TPU and their application for machine learning classification/regression tools, and would be done as part of a larger upgrade of the IceCube offline software system.

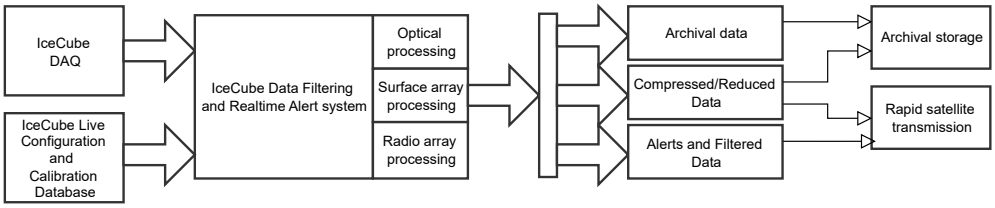

Figure 128: IceCube online filtering and realtime alerts system will process event data from the IceCube DAQ, using calibration and configuration information from the IceCube Live databases and apply per-detector specific data processing algorithms to each event. Several output data streams will preserve the raw data in archival formats, reduced and/or filtered data streams for archival storage and satellite transmission. Depending on size and satellite bandwidth available the full compressed/reduced data set (hit-reduced) can either be written to archival disk or sent north via satellite.

9.3.3 Experiment control and online monitoring

Experiment Control and Online monitoring inherit the structure of IceCube's `i3Live`. This system will be expanded to include Gen2 subsystems, including IceCube-Gen2 optical, the surface array and radio-neutrino stations.

Experiment Control will have the same functionality as it currently has in IceCube. In particular radio-neutrino stations will need to adapt their operations such that the "run lifecycle" matches the expectations of experiment control.

Monitoring is to have a first implementation phase during early construction and a commissioning phase towards end of construction. Only operational experience can provide the appropriate information for the commissioning version of online monitoring.

Similar to IceCube, Experiment control will take advantage of existing IceCube 24/7 fast messaging infrastructure available at South Pole. This system is currently based on Iridium, which limits the bandwidth significantly. Emerging technologies that use fleets of low Earth orbits satellites, e.g., Starlink, will be explored.

9.3.4 Radio array systems integration

IceCube has an existing software structure used for online readout and processing, experiment control and monitoring and offline analysis. For IceCube-Gen2 we plan to integrate new subsystems, including radio detection, into the existing framework in order to maintain a single IceCube-Gen2 software ecosystem.

The architecture of the radio neutrino array, consisting of clusters of antennas installed on a sparse grid, allows each cluster or station to operate autonomously. The design was optimized to achieve the largest effective area possible at low cost. In the reference design 20% of the events are expected to be observed by more than one cluster or station for an injected single power law $E^{-2.3}$ energy spectrum. Each station can form a trigger, and reconstruct the direction of the event independently. Events with coincident observation will allow event reconstruction with very high fidelity. As de-

scribed in the radio detector chapter, triggers are formed in a "phased array" of closely spaced, colinear antennas whose signals are summed with time delays corresponding to several directional hypotheses (or "beams") as a test of coherence. The time delay corresponding to the largest signal enhancement provides a coarse estimate of the elevation angle of an incoming event.

The data rates shown in Table 17, assume a trigger rate of 1 Hz per station for a 366 station array. The data rates can be modulated by adjusting the signal to noise ratio. Alternate modes of operation are also possible. For example, the beamforming trigger allows the trigger threshold to be temporarily dropped to increase sensitivity for a particular incoming signal direction. A similar measure can be applied in the shallow stations. This "burst mode" is envisioned in response to localized real time alerts. Once the data has reached the counting house, events selected by the PnF system will be transmitted via satellite, while the entirety of the triggered data will be written to disk.

Once a radio station is installed, a series of operational and commissioning tests will be run. Once the station is commissioned, it will be integrated into the DAQ and monitored via `i3Live`.

9.3.5 SuperNova DAQ

The Supernova DAQ inherits from the structure of IceCube's `SNDAQ`.

The supernova system has two major components. The main system monitors counts from scalers on each PMT on each IceCube-Gen2 DOM. Existing `SNDAQ` monitors detector-wide rise in the rate of PMTs. In IceCube, hitspool data, which has all the hits in the detector for ~1 week is stored in StringHubs. A high-significance `SNDAQ` trigger results in hitspool for the relevant data period to be requested.

In IceCube-Gen2, the new DOMs will also have scalers with similar capabilities as in IceCube. Current scalers in SNDAQ are ~1 ms. However, for participating in SNEWS, it is required that the absolute timing of a supernova alert has an uncertainty of ~0.1 ms. This can be accomplished with finer-binned scalers, which result in a higher data-rate Supernova stream, or by online (within the supernova DAQ) fitting of the rise time of detector-wide PMT rate.

In IceCube-Gen2, hitspool data will reside in IceCube-Gen2 DOMs with a buffer of ~1 week. Similarly to IceCube, a supernova DAQ trigger will result in the request of hitspool data.

9.4 Core software systems

The unified software framework for analysis of IceCube data, both online and offline, is the IceTray framework. In order to smoothly integrate the new detector systems of IceCube-Gen2 into this existing framework, a significant amount of software engineering is needed to extend the IceTray framework for accommodation of these new systems.

9.4.1 The IceTray framework

The IceCube experiment uses a dedicated software framework known as IceTray [147]. The IceTray framework is a modular interface used for all processing between readout from the DAQ until final analysis levels. Simulation, background rejection, and reconstruction tasks are all handled within this framework in IceCube.

IceTray provides a stable basis for IceCube-Gen2 software, but substantial upgrades and extensions are necessary. First among these changes will be improved efficiency for when handling large numbers of PMTs. Many software plugins contained in the IceTray framework will require checks and improvements to properly handle IceCube-Gen2 DOM segmentation. While much of this work is already underway for the IceCube Upgrade, an expansion of these efforts will be needed to extend these changes to higher energies. New efforts will be devoted to exploring parallelization in IceTray, allowing expensive reconstruction tables and GPU resources needed at high energies to be more efficiently shared across processes and reducing software memory requirements.

In addition to updates to legacy codes, IceCube-Gen2 will require new tools to support expansion into machine learning. Work in IceCube has shown significant reconstruction improvements using dedicated neural networks [658], highlighting the potential improvements soon within reach for the larger IceCube-Gen2 detector. Centralized support for new machine learning models in IceTray will accelerate simulation and reconstruction tasks, increasing the rate by which IceCube-Gen2 can deliver high-quality astrophysical neutrino candidate events for analyses.

Additionally, IceTray will require updates and extensions to accommodate the radio array component of IceCube-Gen2. New classes and modules will need to be designed to handle the radio data, including the calibration of digitizers and deconvolution of the system responses. After the data is calibrated and ready for analysis, algorithms to reconstruct the signal direction and polarization, the neutrino vertex location, etc. will also need to be implemented. The radio community—including ANITA, RICE, ARIANNA, ARA, and RNO-G—has a long heritage of analysis frameworks which handle both the calibration and later analysis of data. This includes, for example, the ANITA AnitaAnalysisFramework [659], ARA's AraRoot [660], or the community supported software utilized by RNO-G, NuRadioReco [533]. These frameworks are generally modular and operate on an event-by-event basis, and it should therefore be possible to adapt or incorporate them into IceTray. Because those tools are written in a variety of different languages (C++, Python, etc.) and some are specific to the each experiment's proprietary data structures, dedicated effort is required for their adaptation. We note that the surface detector component of IceCube-Gen2 will also have antennas, and so development of software for radio purposes can jointly leverage new infrastructure specific to radio, such as the handling of antenna geometry files, Fast Fourier Transform (FFT) methods, etc.

9.4.2 Simulation software

Centrally produced simulation is necessary for characterizing signal and background expectations for analyses and for developing reconstruction algorithms, in particular, the training data sets required for deep learning. The goal of simulation and Monte Carlo generation is to efficiently generate realistic high energy signal events—neutrinos, muons, and other exotica, such as magnetic monopoles—and backgrounds, which are mostly comprised of cosmic ray air showers and noise. Further, systematic variations of the simulations, such as in the ice model, detector response, etc., are required to derive uncertainty estimates. This can be a time consuming and computationally expensive process—for example, in IceCube, generating 10 years of livetime worth of Monte Carlo required 6M CPU hours for signal (muons) and 30,000 CPU *years* for background (cosmic rays with CORSIKA) [661]. Because of these enormous computational times, centralized and coordinated production efforts, with dedicated personnel, are required. In IceCube, this has partially been handled by the IceProd [662] production system. Because these simulation sets are such a substantial time and computational investment, resources are needed to vet and document them so they are available for general collaboration use.

For the optical component of IceCube-Gen2, the IceTray framework provides these tools, covering particle Monte Carlo generation, propagation of leptons and photons, PMT- and DOM-simulation, and triggering. These tools, currently being generalized for the IceCube Upgrade, will be maintained for all of the various subdetectors IceCube-Gen2. For radio instrumentation, three actively maintained simulation frameworks are available for *in-situ* instruments (AraSim [663], PyREx [664], and NuRadioMC/NuRadioReco [148, 533]). All of these frameworks model the entire neutrino interaction and detection process from beginning to end, including specifying of the initial neutrino and interaction properties, the signal generation and propagation, as well as the detector response (antennas, digitizers, filters, etc). It was shown that the results from the three codes are compatible at the 10% level when configured with the same physics inputs, and in NuRadioMC an automated test suite verifies that results stay consistent with new features and code improvements. Therefore, the TDR document was completed with the NuRadioMC package [148, 533] which offered the most flexibility to define the different arrays, station designs, and triggers, includes the most extensive treatment of secondary interactions of muon and tau leptons, and has a more comprehensive modeling of the LPM effect [521, 522].

Already, optical and radio simulations can be combined “offline" by sharing the properties of the initial neutrino interaction. Long-term, the desire is to integrate the detector and trigger simulation into IceTray which will naturally provide access to the channel-by-channel detector response and calibration constants for simulation of the “as built" detector. Dedicated effort is also needed for general framework maintenance and upgrading, so that e.g. new physics can be added, such as tau regeneration through the earth, improvements in modeling of ice propagation, etc.

9.4.3 Reconstruction tools

For most planned analyses, the reconstruction of most-likely particle interaction properties is necessary. For IceCube-Gen2, this will take the form of three types of reconstruction.

First-pass reconstructions, designed to be performed analytically in 10 ms or less, will be necessary for low level filtering. These reconstructions generally will not include detailed modeling of glacial effects or module segmentation. The primary goal of these first-pass reconstructions is identifying obvious backgrounds from atmospheric air showers visible in the optical or surface arrays.

A separate fast reconstruction method using neural networks will also be used. These methods require significant simulation for training, but provide accurate modeling of all detector effects. Work in IceCube has shown that these reconstructions can be used to identify both particle properties and uncertainties quickly.

After reduction based on first-pass reconstructions, more complex likelihood reconstructions incorporating knowledge of the IceCube-Gen2 DOM segmentation and ice properties will be used to refine directions and energies of events. To include ice properties, calculations of PMT charge expectations will be needed. Charge expectations traditionally be calculated using pre-existing tables will be generalized to accept neural networks or other new prediction methods.

Segmented sensors can improve event reconstruction in two main ways. First, knowledge of the individual PMT orientations within each OM gives additional information on the arrival direction of Cherenkov photons. Second, PMT saturation effects can be mitigated thus preserving information on the number of photons incident on each OM. These two components should improve the positional and directional reconstruction performance as compared to Gen1 sensors.

For cascades, reconstruction performance is strongly dependent on photon statistics, and thus on the distance between source and the nearest string. The photon density drops off approximately as $\exp(-r/\lambda)/r$ while scaling linearly with energy. As the IceCube-Gen2 string spacing is approximately twice that of IceCube's, the exponential fall off tends to dominate over the linear scaling making cascade reconstruction more of a challenge. Preliminary studies indicate possible improvements with segmented sensors for cascades close to its nearest string, but for cascades farther away than 60m from its nearest string the improvements are less substantial.

9.5 Data management and northern computing

The cyberinfrastructure in the Northern Hemisphere is a key piece in the pipeline from data taking to science results. IceCube and IceCube-Gen2 science goals are inextricably linked, requiring that any IceCube-Gen2 cyberinfrastructure project, such as data warehousing, has to support IceCube cyberinfrastructure as well. At the end of construction, IceCube-Gen2 will have to support nearly **four decades** of data and simulation, and the infrastructure needed to analyze this data.

All of the estimates that folow are conservative. Cyberinfrastructure is undergoing multiple technological transitions at the moment. On the CPU side, Dennard scaling, Moore's Law, and Koomey's law are slowing or coming to an end. This makes it harder to predict how much CPU performance increases over time we can anticipate. With the rise of machine learning and artificial intelligence and the long-term performance scaling concerns for CPUs, specialized computing hardware, mainly accelerators like GPU, FPGAs, or ASICs, are emerging as the source for increased computational performance, see expansion of accelerators in high performance computing. This transition increases development cost. Accelerators do not have the same level of support as CPUs in operating systems, and have accelerator- or vendor-specific program paradigms and software development kits (SDKs). Increased effort is needed to support and port algorithms across various platforms, esp. in a heterogeneous computing environment like IceCube's. Separately, risk of vendor lock-in over the course of the IceCube-Gen2 project is high.

On the storage front, electro-mechanical storage media, i.e. hard drives, have been the only economical choice for large-scale and user-friendly storage. Hard drives have hit a technological roadblock and the cost per unit storage has plateaued in recent years. Best estimates are that new technology may emerge between 2023-25 and that cost per unit storage will decrease again, but the overall picture remains unclear. Replacing electro-mechanical storage media with flash-based storage media is currently cost prohibitive. The cost per unit storage of flash-based storage is currently 5-10$\times$ compared to electro-mechanical storage. The cost per unit storage of flash-based storage has been decreasing more quickly than electro-mechanical storage. Yet, it is unclear whether flash-based storage will reach the same economies of scale. There are also concerns with the longevity of flash-based storage for certain applications compared to electro-mechanical storage. It will require investigation whether flash-based storage could be an economical choice.

Machine learning and artificial intelligence have changed the calculus of cyberinfrastructure investment significantly. The requirements and demand vary widely with application. Yet, they also provide immense opportunity for acceleration and reducing overall cost. We will need to carefully investigate which parts of and how the IceCube and IceCube-Gen2 workflow could be accelerated with machine learning and artificial intelligence.

Public cloud resources have the potential to mitigate some of these risks. This comes at a considerably higher cost than today. IceCube has explored using public cloud resources. Working with researchers at the University of California San Diego and the San Diego Supercomputing Center, and with additional funding from NSF and Internet2's Exploring Clouds for the Acceleration of Science (E-CAS), IceCube generated the largest GPU pool in history using cloud resources from three major vendors: Amazon Web Services (AWS), Google Cloud Platform (GCP), and Microsoft Azure. We determined that IceCube would be able to utilize future exa-scale resources, and that the cloud would be too expensive to use for IceCube's computing needs. Cloud cost are anywhere from 5-20$\times$ higher than comparable hosting cost at UW-Madison.

9.5.1 Data management, access, and organization

Data transfer from South Pole: The pattern of IceCube-Gen2 data handling from the South Pole will generally be the same as for IceCube. There will be three major data paths to the North:

- Real-time and interactive 24h data communication via Iridium satellite for detector status data, communication with winterovers, and MMA real-time alerting;
- Primary science data, a reduced data set of filtered data transmitted via TDRSS or TDRSS-like satellites on a daily basis: This data stream is the basis for regular science data use by the collaboration.
- Bulk data transfer of highest fidelity (raw) data by physical transport of permanent storage media, such as disk drives during the Austral summer: This data stream provides a backup in case there is a need to access and reprocess raw data.

The current IceCube-deployed cyberinfrastructure for data transfer from South Pole, including software and hardware, is scalable to accommodate the increased data rates. Thus, the planning will rely highly on a well developed and functioning data eco-system. The rates outline in Table 17 will require to double the currently allocated satellite bandwidth for IceCube.

The construction of IceCube-Gen2 will be carefully coordinated with ongoing IceCube operations. New detector systems will be integrated and produce data as they come online. While the current cyberinfrastructure is scalable and can accommodate the rise in data rate, it will require continued maintenance during the course of construction and operation of the evolving IceCube Neutrino Observatory. While the regular operations need to be coordinated, they are outside the scope of IceCube-Gen2 construction.

Data archiving: Archival data storage provides long-term storage of all IceCube data. This is separate from the normal data stream used for analysis by the collaboration and is primarily an emergency long-term backup system. Archival data storage is a function of detector operations and not generally a part of the construction project, but we address it here for completeness in describing the overall plan.

Currently, IceCube uses DESY and NERSC for data archiving. With the substantial involvement of DESY in the construction project, it is assumed that DESY will continue to contribute cyberinfrastructure for archival data storage to IceCube-Gen2. In case of changes, alternative archival strategy will be identified by IceCube operations.

Data warehouse:

We are estimating 60-70 Petabyte of storage being needed at the end of IceCube-Gen2 construction, assuming the data rate summarized in Table 17. This is a 6-7× expansion compared to today. The largest portion of this is due to the needed simulation during the construction of IceCube-Gen2, the continued operation of IceCube, and the operation of partially completed IceCube-Gen2 sub-detectors.

Over 15 years of experience with IceCube have shown us that there is significant potential for improvement in how data is cataloged/curated, organized, and made accessible to researchers. IceCube with its seven sub-detectors (IceCube in-ice array, Deep-

Core array, IceCube Upgrade array, IceTop surface array, IceCube-Gen2 in-ice array, IceCube-Gen2 radio array, and IceCube-Gen2 surface array) at the end of construction of IceCube-Gen2 will expand on IceCube's impressive and broad science program. It will also generate a wealth of new and different data types and analyses that need to be supported during and after construction.

Expanding upon and continuing with the IceCube data warehousing concept in IceCube-Gen2 is probably unsustainable and would build larger then possible costs for maintenance. Therefore, we plan on building an extensible system, capable of the larger data requirements and more cost effective to maintain, that is based on current and near future technologies. The IceCube model was practical and appropriate during the construction and initial operation phase of IceCube. With a decade of additional data, an expanded science portfolio, changes in the data analysis culture within IceCube, and emergence of the FAIR (Findability, Accessibility, Interoperability, and Reusability) [665] scientific data principles, the shortcomings of the IceCube model compared to modern data warehousing techniques have become apparent. With the increasing diversity of IceCube-Gen2 data sources and analyses, it is essential to modernize the data warehousing strategy.

The data warehousing for IceCube-Gen2 will be based on the the FAIR scientific data principles as best as possible within the established cyberinfrastructure framework, needs, and funding for IceCube-Gen2. Making IceCube-Gen2 data truly FAIR would require significant investment, which may not be warranted. For example, in IceCube outside researchers have only requested access to high-level data products; making low-level data products in IceCube-Gen2 accessible, inter-operable, and reusable for outside researchers may not be needed as long as the high-level data products are. Additionally, the low-level data products require significant and detailed knowledge that the collaboration may not have the resources to make public.

A limitation of the IceCube model within the FAIR data principles is "finding" the data. Machine- and human-accessible metadata is key to making data easy to find. IceCube does not have a true single source metadata catalog. Rather there are currently several distinct sources of metadata: websites, databases, data warehouse structure, files, wiki pages, email threads, etc. A single source, user-friendly metadata catalog would alleviate a significant hurdle for researchers in finding (first step of any data analysis task), understanding (second step of any data analysis task), and more importantly *interacting* with the data.

Implementing a metadata catalog would also allow a separation of details of the data organization, i.e., how and where the data is stored. This creates an opportunity for long-term efficiency and scalability gains compared to the IceCube model. The underlying storage technology, e.g. distributed storage system or data access pattern, can be "hidden" from the user, such that the user would not notice whether the data is local or remote to them. Divorcing the researchers from the underlying storage technology would allow operators to store the data more efficiently. For example, currently multiple copies of the same data are stored across the Gen1 data warehouse. This consumes large amounts of storage unnecessarily. Allowing operators to "de-duplicate" data would use storage more efficiently over the long-run. Similarly, the data would not have to be stored at a single location or storage tier, but could be distributed or stored

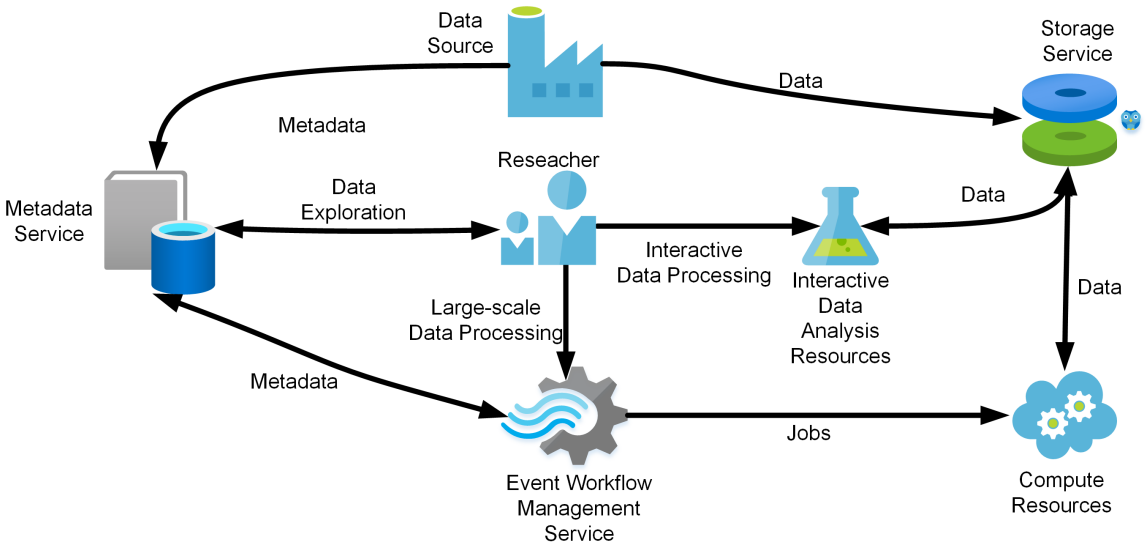

Figure 129: High-level diagram of the Observation Management Service.

in various tiers with different cost. For IceCube-Gen2, we propose to build an integrated data warehousing, metadata catalog, and workflow management system called the **Observation Management Service** (OMS). OMS will be the backbone of the Gen2 data warehousing and workflow management strategy. We have integrated the workflow management system into the data management system, as these two aspects are deeply intertwined in large-scale data-driven projects like Gen2. At the same time, we want to lower the barrier-of-entry for researchers to efficiently run large-scale scientific workflows across a wide variety of computing resources.

9.5.2 Northern computing

IceCube-Gen2 data analysis computing will utilize both interactive and batch infrastructures. The interactive infrastructure will be used for high-level data analysis and finalizing data analyses. Given the data rates in Table 17 and the transition to more machine-learning- and artificial-intelligence-based methods that the infrastructure will need to expand 2-3× (18-27 servers) compared to today and add ML-specific hardware. Today we would increase the number of interactive GPU nodes, but this could change in the near- to medium-term future as the demand from researchers evolves as they explore machine-learning- and artificial-intelligence-based methods in Gen1.

The IceCube-dedicated batch infrastructure would consist of a high-throughput computing (HTC) cluster located at UW–Madison and a globally distributed resource pool. The current IceCube HTC cluster consists of nearly 200 servers providing a total of about 4000 CPU and 300 GPU job slots. Given the data rate and the increased resource requirements of Gen2 simulation, we expect an expansion of 4-5× required for Gen2. These dedicated resources are not sufficient to ensure timely data processing and simulation production for Gen1. To increase overall capacity, Gen1 relies on distributed resources available at collaboration institutions, opportunistic computing consortia, such as Partnership to Advance Throughput Computing (PATh)'s Open Sci-

ence Pool, and allocation-based high-performance computing (HPC) consortia, such as XSEDE. We expect a 4-5× demand increase in the need for external computing resources.

The current capacity plan foresees providing 10% of the CPUs needed for simulation at the UW–Madison data center, 15% at DESY-Zeuthen, and 75% at other collaboration sites and compute consortia. For GPUs, the plan is to provide 50% of the needs through Gen2-funded resources and 50% at other collaboration sites and compute consortia. A majority of the Gen2-funded resources will be hosted at UW–Madison. We have hosted Gen1 cyberinfrastructure at MSU and UMD. We will look into expanding this model depending on demand. Gen2 will continue to seek collaboration sites and compute consortia to procure additional resources.

9.5.3 Cybersecurity

The information security program was developed and implemented and is maintained to provide an organizational environment to ensure appropriate information security and acceptable levels of information-related risk. This program entails ongoing activities to address relevant policies and procedures, technology and mitigation, and training and awareness.

A risk-based approach will be used to secure IceCube-Gen2 systems. Information systems are evaluated in terms of sensitivity of information and availability requirements of the asset. Security controls are selected and implemented to reduce risk to acceptable levels. In addition, we inherit security controls from ASC for information systems at the South Pole station and UW security controls for information systems operated at UW–Madison.

Asset protection The detector will be the single most valuable asset. As such, the primary concern is securing and maintaining the operational capability of the detector as well as day-to-day operations and data collection. This is followed closely by the data collected by the detector.

Access to the detector and its subsystems is restricted to IceCube personnel with a need to work on the detector itself. Remote access is limited to a small set of machines in the Northern Hemisphere. These machines are protected by IceCube-operated, network-based firewalls in the north and south. In addition, any access to the systems at the station must also pass through network firewalls and other security systems operated by ASC. Changes to station security controls are coordinated with ASC via the annual support information package process.

The data collected by the detector is the foundation of all science output. To avoid missing unique events, it is critical to collect and preserve this observational data as they are created. To reduce the likelihood of data loss, two copies of the raw data are written to disk at the Pole. These disks are shipped to UW–Madison during the austral summer. A filtered copy is written to disk at the Pole and a reduced data set, about 10%, is transferred north via satellite daily. The reduced data set is replicated to DESY in Germany daily when it reaches the north. The raw data are read from disk when

they arrive at UW–Madison, where they are then replicated to NERSC. One copy is also physically stored offline in Madison.

The science data collected and maintained are not sensitive or regulated, and indeed are eventually published. In the course of operating the center, other information is generated and stored. This information is intended for internal use only. We only generate and retain the data necessary for executing administrative processes. This information is stored separately from all computing and research systems and uses normal IT controls to ensure the confidentiality of the data.

Where widely accepted security practices and standards are not workable, compensating controls are adopted to maintain an appropriate security level. For example, stateful, network-based firewalls have unacceptable performance impacts on large research data flows, and therefore data moving machines are frequently placed outside of such protections. To mitigate the risk, a ScienceDMZ architecture [666] is applied as a compensating control to apply equivalent protections.

Cybersecurity standards and adherence We follow standards, practices, and guidance from TrustedCI [667] that are consistent with operations of NSF major facilities as well as UW–Madison campus policies and ASC policies at the station. IceCube participates in and contributes to NSF security communities via TrustedCI and the large facilities security team.

Cybersecurity breach reporting policy ICNO maintains an incident response plan which includes escalation and notification procedures. To summarize, breaches will be reported to the appropriate parties in a timely manner in accordance with the severity. For incidents with a scope beyond the home institution, external incident response staff will be engaged immediately. For breaches that may impact resources at the South Pole station, ASC, and NSF program officers will be notified immediately. Significant breaches will be reported to NSF program officers within 24 hours. UW security personnel will be notified in a manner consistent with UW reporting policy.

ICNO maintains a list of security contacts for all collaborating institutions to facilitate notifications within the collaboration.

10 Detector Calibration

10.1 Introduction

The primary purpose of calibration is to ensure the accurate translation of raw data to reconstructed physics quantities (time, position, direction, and energy), which has proven to be critical for the performance of the detectors at analysis level. IceCube-Gen2 draws on extensive calibration experience from IceCube, previous surface air shower arrays and in-ice radio detection. While surface and optical array calibration is very mature and well understood, the radio array presents a unique challenge due to its size and the lack of observed radio neutrino signatures as well as the lack of natural calibration signals from cosmic rays.

10.2 Optical array

The main calibration steps performed as part of the optical array calibration are the final detector geometry calibration, and characterization of the detector medium, which is sub-divided into two main objectives consisting of the calibration of the ice model for the bulk ice and the refrozen ice in the drill hole. Detector geometry calibration and ice measurement are described in the following sections. The precise characterization of the optical sensor modules themselves is described in section 5.7. Time calibration is handled by the RAPCal protocol as described in Sec. 8.4.2.

10.2.1 Geometry

The impacts of uncertainty in the relative position of each sensor module in the array—that is, uncertainty in the geometry knowledge—have been derived from the expected impact on muon reconstruction as well as from known constraints from other subsystems.

The impact on reconstructions was assessed using a method first developed in Ref. [668], where an ensemble of events is reconstructed using either the true geometry used in simulation or a set of geometries that have been perturbed under certain assumptions. For the IceCube-Gen2 geometry, current IceCube reconstruction algorithms, and energies ranging from TeV to PeV, the median opening angle between true and reconstructed arrival directions increases by about 0.1° given a perturbation where each string is displaced assuming 1 m standard deviations in both lateral directions.

Offset errors in the DOM-to-DOM timing calibration, which are constant over timescales of an event or longer, affect reconstructions similarly to a geometry uncertainty. Given the known performance of the IceCube time-synchronization system [15] and the LOM electronics design, an overall relative offset error of 2 ns is expected. Taking into account only the refractive index of the ice and neglecting further delays from scattering, this is equivalent to a length-scale uncertainty of about 0.4 m. This would correspond to uncertainties in the lateral and vertical geometry of 0.32 m and 0.25 m, respectively, if geometry uncertainty is not to affect the reconstruction more than uncertainty in timing.

10.2.1.1 Drilling and Deployment The first measurement of the geometry of the sensors is obtained during the drilling and deployment process via a navigation package. The package includes accelerometers and a compass that allow measuring the tilt of the entire drill in the x and y axes (where the z axis is the vertical) as well as the horizontal direction of a fixed reference point on the drill. For absolute positioning, the x-y position of each borehole on the surface will be surveyed. During IceCube drilling operations, horizontal deviations from the vertical of up to ~1 m were observed. The vertical distance between neighboring sensors on a string will be measured during the deployment with a laser ranger, and the final depth of the deployed instrumentation is determined with a pressure sensor at the bottom of the string.

10.2.1.2 Mainboard Slow Control Sensors Even with the geometry of the hole known, the absolute orientation of the sensors cannot be fixed prior to deployment since the string can twist during deployment. Additionally, modules can come to rest in a tilted position with respect to the hole axis. Therefore, each module mainboard is equipped with a set of sensors to measure the azimuthal orientation (compass or magnetometer) and tilt (accelerometer).

10.2.1.3 Flashers LED flashers were used extensively in IceCube to verify the detector geometry. The first measurement, done after deployment, was to verify the final depth of strings, especially in cases where the pressure sensor had failed and the final depth was uncertain. Based on extrapolation from IceCube, the geometry should be able to be measured to within 2.4 m by flashers. It is expected that the drill navigation package will perform better than this, but the flashers will serve as a cross-check.

10.2.1.4 Acoustic The most precise part of the geometrical calibration system will be an acoustic system that consists of multiple so-called acoustic modules (AMs), which emit and receive acoustic pulses. The acoustic modules are currently being developed for the IceCube Upgrad,e in which ten of them will be deployed [669] [670]. The design is based on a piezoelectric transducer that serves as sender and receiver of acoustic signals. Results from the IceCube Upgrade will help to further understand the ice properties and to improve the system for use in the IceCube-Gen2 detector.

The baseline IceCube-Gen2 design (see Figure 130) is to attach two AMs to each string—one in the upper and one in the lower half. The z positions of these modules are varied uniformly within ± 100 m to increase the accuracy of the geometry calibration along the z axis. The AMs will serve as precisely located anchor points from which the position of DOMs can be interpolated with an accuracy of a few tens of centimeters. The measured propagation time allows determining the distance between each emitter and receiver pair, and the geometrical positions of each AM can then be reconstructed by means of trilateration. With the known positions of the AMs attached to the strings, the positions of optical modules are then determined by interpolation along the strings.

Acoustic signals have a long range of several hundred meters in Antarctic ice. The attenuation length has been measured by the South Pole Acoustic Test Setup (SPATS) to be $300\,\mathrm{m}\ \pm 20\,\%$ [671]. Also, propagating as a wave, acoustic signals are only geo-

metrically attenuated by $1/r$. This makes acoustics an ideal technique to probe large distances reaching the km scale. With this range the network of AMs will not be limited to nearest neighbors but will allow for an over-constrained and thus robust geometry calibration. Unlike optical calibration systems, acoustic signals are not affected by optical properties of the ice such as scattering, and the operation of the system is optically dark which means that calibrations can be performed in parallel to the normal operation of the detector. With the large spacing of optical strings and particularly for regions in the ice at which the optical absorption is high (e.g., in the dust layer) the acoustic calibration system provides an important complement to the optical calibration devices. Simulation studies predict an accuracy of about five centimeters for the localization of the AMs [669]. Figure 131 shows the accuracy result of these simulations for the baseline configuration in IceCube-Gen2.

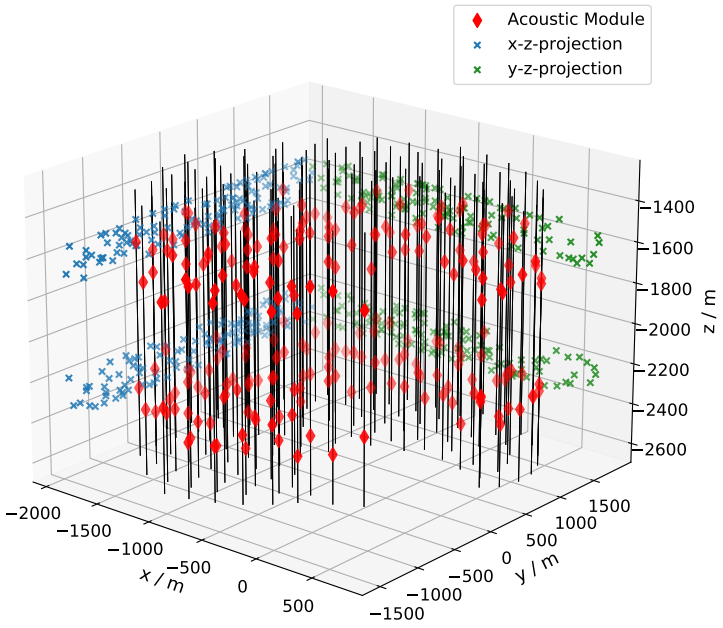

Figure 130: Distribution of acoustic modules in the IceCube-Gen2 detector. Each string is equipped with one AM in the upper and one in the lower half. The heights are varied within ± 100 m to improve the accuracy in z-direction.

10.2.2 Bulk ice

IceCube and its predecessor AMANDA have pioneered measurements and modeling of ice optical properties [501, 672], described in Sec. 4.2.1. Most recently the birefringent polycrystalline microstructure of the ice has been incorporated into the modeling [673] to explain an observed anisotropy in the light attenuation, such that the ice model now overall yields a very precise agreement to data. The IceCube Upgrade will further improve the ice knowledge by studying the detailed shape of the scattering function at short distances, increasing the depth granularity of the employed stratigraphy and probing remaining anisotropy scenarios [674].

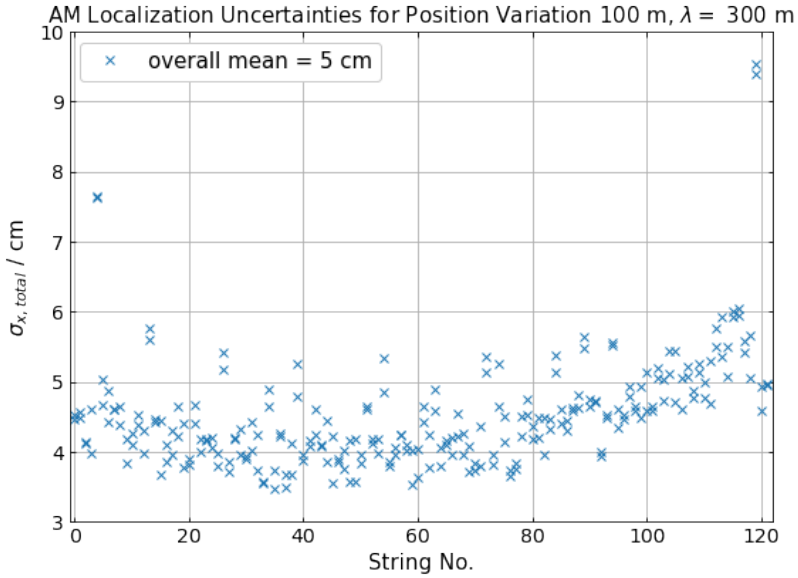

Figure 131: Simulation results for the localization uncertainty of individual AMs for an attenuation length of $300\,\mathrm{m}$. Larger values at the lowest (highest) string numbers result from the fewer number of direct neighbors of these AMs. The mean of all values is 5 cm.

Given the detailed understanding obtained to-date and refined by the time of IceCube-Gen2, studies of the bulk glacial ice in IceCube-Gen2 will primarily be limited to extrapolating the known stratigraphy to the entire footprint of the array and cross-checking homogeneity.

This requires knowledge about the undulation of ice isochrons, layers of ice which have been deposited at the same time and thus feature identical properties, which have become distorted through the underlying bedrock and ice flow. A requirement on this so-called "tilt" has been derived by demanding that the resulting systematic uncertainty shall at most result in a 10% cascade energy uncertainty. As a result the tilt shall be known with an uncertainty of at most 5 m at any point in the detector.

10.2.2.1 IceCube Upgrade This will include a variety of calibration devices intended to characterize the optical properties of the ice with unprecedented precision. The Upgrade will include devices which were not available in IceCube, or which were only available in very limited numbers. Because the baselines in the Upgrade are shorter than the optical scattering length in ice, it will allow more detailed studies than were possible in IceCube. The calibration goals of the Upgrade are to determine the *in situ* absolute DOM optical efficiency to better than 3%, to reduce the uncertainty in the modeling of the hole ice by a factor of 2, and to determine the source and depth dependence of anisotropy in optical scattering in bulk ice. Calibration instrumentation will be deployed to a depth of 2600 m, measuring the ice at IceCube-Gen2-relevant depths.

- All optical modules in the Upgrade will include LED flashers and fixed cameras. The cameras will explore hole ice and the local environment of every module.

- An isotropic light source called the Precision Optical CAlibration Module (POCAM) will measure the optical efficiency of modules as well as the hole ice.
- A collimated, steerable light source called the PencilBeam will study the scattering function in the ice and the effect of birefringence on the anisotropy in the ice optical properties observed in IceCube.
- A small number of steerable cameras in their own pressure vessels will be deployed to complement the fixed focus cameras and study the properties of the hole ice.
- Acoustic modules will be deployed to measure the acoustic properties of the deep ice and test acoustic geometry triangulation, which is planned as the most precise geometry measurement method in IceCube-Gen2 (Sec. 10.2.1.4).

Several revamped IceCube optical modules, called pDOMs, will be included for cross-calibration of the IceCube PMT with the new calibration devices. Additionally, light from some calibration devices will be detected by nearby IceCube modules, since the Upgrade is deployed near the center of the existing detector. The Upgrade will complete our knowledge of the bulk properties of the ice, and the primary bulk ice measurement in IceCube-Gen2 will be the tilt of the dust layers as described in Sec. 10.2.2.2.

10.2.2.2 Dust Logger Laser dust logging is a well-established technique for measuring the stratigraphy and tilt of dust layers in the glacial ice at the South Pole [675–677]. Dust logs are recorded in the boreholes made by the hot water drill, several hours before permanent instrumentation is lowered into the ice for freeze-in. The logger consists of a 1 m cylindrical pressure vessel containing a laser line source, which emits pulsed light in a thin fan-like pattern; onboard pressure and orientation sensors; a PMT photosensor; and brush baffles which span the diameter of the borehole, blocking the photosensor from observing direct light from the laser [676]. An armored cable is used to mechanically support the logger and provide power and communication from a control station on the surface.

Laser light entering the bulk ice is scattered by bubbles, volcanic ash, and dust. A small fraction of the scattered light reenters the borehole, where it is recorded by the photosensor. By combining the backscatter measurements with depth data from the onboard pressure sensor, the stratigraphy of the dust layers at each borehole is measured with an absolute depth accuracy of about 1 m.

Dust-loggers provide unique ground-truth information about the ice stratigraphy and layer tilt, as well as birefringent scattering. By matching mm-scale dust scattering features across a widely dispersed set of boreholes, it is possible to measure the relative tilt of the dust layers across the detector [677]. The orientation data in the dust logs also enables measurements of the directional anisotropy of light scattered at each borehole. Studies using IceCube dust logs have constrained the optical axis of birefringent scattering in the ice to within $\pm 3^{\circ}$, consistent with the flow direction of the ice sheet [678]. Future logs will extend both types of measurements to the much larger region of ice covered by IceCube-Gen2.

10.2.2.3 Flashers Extrapolation of ice optical properties from those known at a reference location to any other location in the array using the layer undulation assumes the absence of large-scale deviations of ice optical properties over the footprint of the array. While we have no reason to doubt that assumption, we would like to retain the ability to measure the stratigraphy of absolute absorption and scattering coefficients to within 10% for each km^2 subregion of the IceCube-Gen2 footprint. LED flashers with nanosecond-width pulses are the primary workhorse of ice calibration studies performed in IceCube. Having a light source at every location has proven invaluable in IceCube. The primary purpose of LED flashers in IceCube-Gen2 will be the verification of bulk ice properties as well as cross-checks on the geometry and verifying the detector timing. Their capability to fulfill the IceCube-Gen2 requirements has been verified by performing the respective analyses on IceCube data, while only taking into account data from next-to-neighboring strings at a distance of roughly 250 m.

Elevation of ice layers across the IceCube detector can be estimated to better than 1 m uncertainty with the existing flasher data [679]. Skipping every other string to increase interstring spacing to 250 m, to make it similar to IceCube-Gen2, a simplified version of this method was applied, resulting in an estimate of 4.5 m in our ability to estimate with flashers the ice layer elevation in IceCube-Gen2.

The fits to per-layer absorption and scattering coefficients follow the general methodology as described in [501, 582], but with depth resolution achieved simply by binning the emitter DOMs by their ice layer location. The desired 10% accuracy is only obtained in the cleanest ice below the dust layer, while roughly 20% accuracy is achieved for most depths.

To boost the flasher performance compared to the sensitivity studies, the per-flash intensity and repetition rate will be increased compared to the IceCube LEDs. Possible avenues for increasing the intensity include longer duration flashes and the use of laser drivers; the performance of these drivers is currently under study for the Upgrade. A higher repetition frequency compared to the usual operation in IceCube will be possible as each flash generates far less data. Higher intensities per-flash can be achieved through slightly longer duration flashes. Given the large inter-string spacings, these are not detrimental to the sensitivity.

10.2.3 Hole ice

While the dominant part of the propagation of Cherenkov photons happens in the bulk ice, each photon detected by a sensor also has to propagate through the refrozen water in the drill holes, called “hole ice” [680]. Given the drilling conditions in IceCube, the hole ice is believed to feature a central column of strongly scattering, bubbly ice roughly 16 cm in diameter [681]. Images of the hole ice taken by a camera in IceCube are shown in Figure 132.

Depending on the orientation of this central column to each sensor, it affects the optical acceptance of the sensor in different regions. This results in biases, especially in the zenith angle reconstruction. The impact of the hole ice can either be modeled as an effective modification to the angular acceptance function or explicitly taken into account

Figure 132: Sweden Camera images. Left: Camera facing sideways shortly after deployment. The light is seen to scatter the least in the newly refrozen outer hole ice. Right: Lower camera looking straight up at the upper camera, with the hole ice fully developed in the right half of the image. Filament-like outgrowth from the column indicates that the scattering centers are indeed air bubbles.

by accounting for its size, scattering length, and relative position to each sensor during photon propagation in the simulation.

In the Upgrade, the impact of different drilling conditions on the resulting properties of the hole ice will be studied using the segmented photocathodes of the mDOM and D-Egg [682, 683] as well as the camera system [504].

Similar to the bulk ice calibration, efforts in IceCube-Gen2 will mainly focus on verifying our understanding and cross-checking the hole ice properties given the specific drilling conditions.

10.2.3.1 Cameras Each string will contain three camera modules, at the top, bottom, and center to obtain representative measurements of the hole ice topologies and features throughout the entire length of each string.

Each camera module will be contained in a 8-inch diameter pressure vessel. As shown in figure 133, each system will contain two pairs of cameras, one pair pointing upwards and one downwards, that are located at the top and bottom of the pressure sphere, respectively. The cameras will be based on the well tested design for the IceCube Upgrade [599, 684] and have a wide field of view (FOV) of approximately 140 degrees. Camera pairs will have a combined FOV of more than 180° for a full view of the drill hole, and separation of the cameras will provide a stereoscopic FOV for the central drill hole region. Stereoscopic imaging will enable detailed studies of the inner hole topography, which could contain features such as the bubble column.

LED-based illumination systems are installed next to the camera pairs, one pointing directly downward and one directly upwards. The light sources will be useful for both bulk and hole ice measurements as well as for photography. Each LED system will consist of five 1 Watt LEDs covering wavelengths between 300 nm and 700 nm to enable measurements of wavelength dependency of scattering and absorption in the drill hole.

The camera system will be based on the IceCube Upgrade camera [599, 684] with modifications to adapt to IceCube-Gen2 requirements.

10.2.3.2 Flashers In IceCube, the primary analysis of hole ice using LED flasher data [681] takes advantage of two signatures: the diffusion of emitted light when an LED shines directly into the hole ice column, which is primarily used to determine the position of the bubble column with respect to each DOM, and the effective shading of incoming light, which drives the determination of size and scattering length. At the interstring spacing planned for IceCube-Gen2, both kinds of measurements will be restricted to sensors in the cleanest ice layers (similar to section 10.2.2.3) and the available timing information will likely be strongly reduced.

Luckily, the additional photocathode segmentation will aid both in localizing the bubble column (using any light source, potentially even the homogeneous illumination provided by a large set of muons), as well as in determining the optical properties as demonstrated in [682]. Outside the cleanest ice layers, flashers can still be used for same-string illumination scenarios [682] as well as for same-DOM measurements [680].

10.3 Radio array

Calibration of the IceCube-Gen2 radio array logically separates into four closely interconnected tasks, as follows:

1. Pre-deployment calibration, including (frequency-dependent) measurements of
   1.1. antenna gain, group delay and beam patterns in an anechoic chamber,
   1.2. gain, noise figure, group delay and insertion loss for low-noise amplifier, cables and connectors
2. Post-deployment commissioning, including

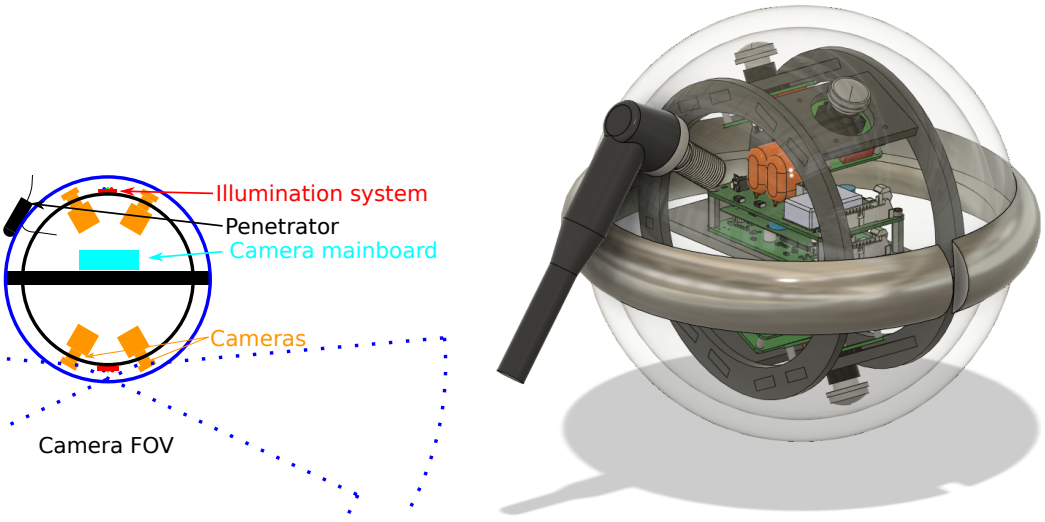

Figure 133: Left: schematic of the camera module for IceCube-Gen2; Right: 3D design of the camera module with basic holding structure

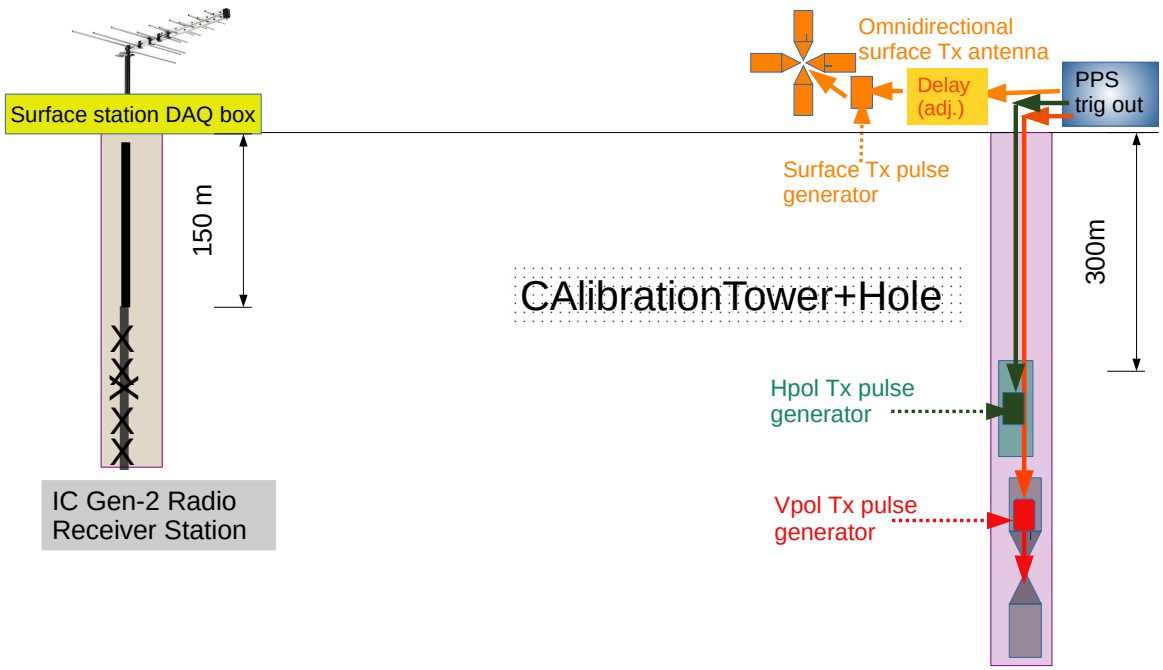

Figure 134: Illustration of proposed calibration scheme of the IceCube-Gen2 radio array. A common high-repitition rate (~100 Hz, corresponding to the maximum estimated data-taking rate of the IceCube-Gen2 radio receiver stations) trigger signal is issued simultaneously to the above-surface azimuthally omnidirectional transmitter antenna, as well as either/both of the signal generators feeding the HPol and VPol in-ice antennas. The above-surface signal passes through an adjustable delay generator (either an off-the-shelf, low-jitter unit, or a pre-defined length of RF optical fiber) to ensure that signals in both the in-ice, as well as the shallow antennas receiver channels are captured approximately simultaneously.

   2.1. re-measurement and verification of front-end and DAQ response required for measurement of radio signals generated in-air (e.g., from UHECR and ultra-high-energy neutrinos (UHEN))

   2.2. Precise surveying of local geometry, as well as global geometry and calibration of system clocks.

3. Longer-term monitoring of DAQ and antenna response, including periodic checks against ‘standard candles’, and monitoring of the possible impact of hole closure.

4. Measurement of the radio frequency ice properties over the full range of possible UHECR and UHEN signal geometries, over the entire effective volume probed by the IceCube-Gen2 radio array. The latter require in-ice calibration sources, either co-deployed in ice-holes drilled for receivers, or in dedicated calibration transmitter holes.

For items 1 and 2.1, the responsibility will be driven by the radio construction and installation efforts (see Sect. **??**), with close coordination to the calibration work-package. That testing program is described in Sect. 6.7. This chapter will focus on tasks 2.2 through 4.

The fact that cosmogenic neutrinos are as yet undiscovered, coupled with the unprecedented scale of the radio array of IceCube-Gen2, requires full characterization of any systematic differences in response across the array.

10.3.1 Pre-existing calibration resources

Several calibration sources, either legacy instrumentation from the Radio Ice Cherenkov Experiment (RICE) or the Askaryan Radio Array (ARA), are already at the South Pole and have been used over the last decade. Two deep pulser radio transmitters (Tx) were installed in IceCube in 2011.

In the near term, we are planning on deploying radio transmitters at depths of 1400, 1800, 2200 and 2600 meters on the IceCube Upgrade strings. Assuming a range of $5\,\mathrm{km}$, those Upgrade transmitters should be visible by a handful of the closest IceCube-Gen2 radio receiver stations. Those four transmitters will be complemented by an array of six additional transmitters on Upgrade strings at a central depth of 1400 meters, with each element separated by 2 meters vertically. Phasing the 6-element transmitter array will yield an effective improvement in output signal by a factor $\sqrt{6}$, which should roughly double the volume illuminated by the Upgrade pulsers.

An estisol-filled, 1700-m deep borehole was drilled for the South Pole Ice Core Experiment (SPICEcore) in 2012-2015. The borehole was used in 2018 and 2019 as a calibration platform. The SPUNK pressure vessel antenna (PVA) transmitter, lowered to a depth of $1700\,\mathrm{m}$, provided data on which published measurements of ice refractive index, attenuation length, and polarization reconstruction (necessary for pointing neutrinos into the sky) were based [569, 573, 685]. As the IceCube-Gen2 radio array is deployed in the future, the SPICEcore hole may again allow ice properties measurements over a wide range of geometries and polarizations.

10.3.2 Calibration hardware planned for the radio array

Guided by experience with co-deployment of radio pulsers on the Upgrade strings, we plan to co-deploy radio pulsers on the IceCube Gen-2 optical strings in order to take advantage of the large depth of those strings. If the Upgrade pulsers are successful, we anticipate a similar number, and layout of radio transmitters on the IceCube Gen-2 optical strings, with geometry maximized for radio receiver illumination.

The primary array calibration of IceCube-Gen2 will be achieved by drilling dedicated interstitial holes to a depth of $300\,\mathrm{m}$. The depth is required for a transmitter to be observed by a 150 m deep receiver separated laterally by $>2\,\mathrm{km}$. As described in Sec. **??**, the same mechanical drill can be used to drill the interstitial hole. A high-power radio transmitter would be placed at the bottom of the hole; a coaxial cable would connect the in-ice transmitter to an above-surface transmitter, thereby facilitating signal averaging of weak and individually subthreshold signals propagating in ice by stacking received signals triggered using the elevated transmitter. The proposed CAlibration Tower+Hole (CATH) is illustrated schematically in Figure 134. The above-surface transmitter→receiver antennas provide the event trigger at the receiver. Assuming an in-ice pulse generator identical to that used for the 2018 SPICEcore tests, and extrapolating from the signal-to-noise ratio observed in those tests, as well as the demonstrated performance of the phased array in ARA, we estimate that approximately 20 seconds of constant triggering would be adequate to yield signals clearly observable above the noise floor.

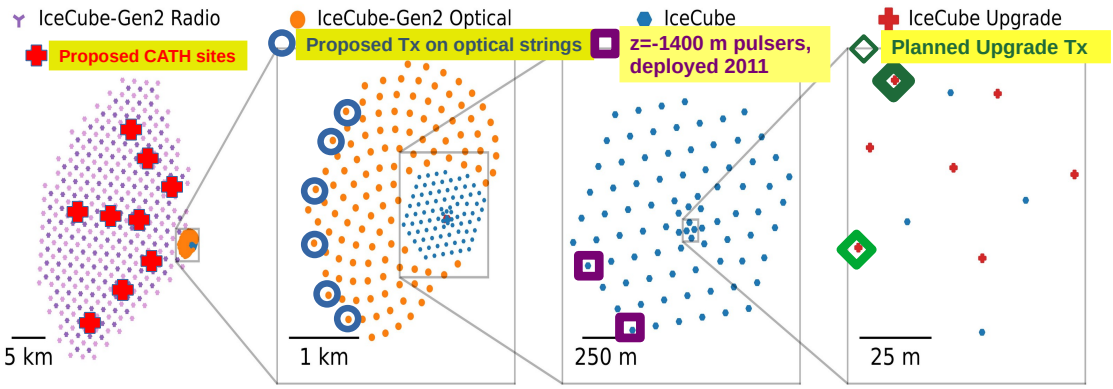

Figure 135: Map of existing, planned, and proposed radio transmitter locations.

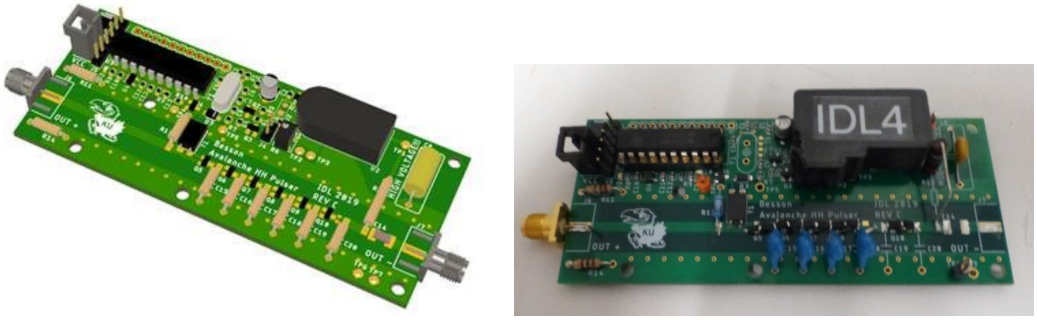

Figure 136: Radio-frequency pulse generator board developed by Instrumentation Design Laboratory (KU).

A summary of the radio transmitters planned for the IceCube Upgrade, proposed location of radio transmitters co-deployed on IceCube Gen-2 optical strings, and the proposed CATH sites, are shown in Figure 135. Transmitter placement is dictated by the desire to a) illuminate as many radio receivers as possible, along trajectories both parallel, and perpendicular to the local ice flow, and b) provide some degree of redundancy, with multiple transmitters reaching some fraction of the radio array.

Although high-voltage radio frequency pulsers are commercially available, deploying multiple transmitters over the large physical scale of IceCube-Gen2 radio would be cost-prohibitive. Alternatively, our calibration strategy favors redundant use of inexpensive custom transmitters, with demonstrated in-field performance during the 2018-19 and 2019-20 SPICEcore calibration campaigns. Transmitter boards are shown in Figure 136.

10.3.3 Drone calibration

Airborne and mobile drones provide a calibration scheme complementary to the calibration of the radio-frequency array using stationary, embedded in-ice transmitters. Such a scheme is particularly valuable to validate system response to radio signals generated

Figure 137: Drone Pulser used for TAROGE-M experiment, and proposed for IceCube-Gen2 radio.

by air showers. A lightweight (total weight less than $1.4\,\mathrm{kg}$) drone-borne pulser system was developed for the TAROGE-M experiment on Mt. Melbourne, Antarctica [686] (Figure 137) to calibrate the performance of the signal event reconstruction, especially for near-horizontal directions. A drone-borne pulser has the advantage of being able to scan multiple directions, which is particularly relevan to understand the systematics of the antenna response. It can also be steered and perform scans in a more controlled way than balloon-borne or manned aircraft-borne pulsers previously used by other experiments (e.g., [687]). The pulser system consists of a differential GPS (DGPS) module for positioning and a pulser module, identical to the model described above (Figure 136), installed on a commercial drone with maximum payload up to $6\,\mathrm{kg}$. A remotely controlled digital step attenuator ensures that the output signals are compatible with the dynamic range of the receivers. The DGPS module consists of a base and a rover units, with the former installed at the station and the latter on the drone, providing measurement of the pulser position with centimeter accuracy. A microcontroller which is clock-synchronized with the pulse-per-second (PPS) signal of GPS triggers the pulse generator, programmed to control the pulse rate and amplitude, and can be easily configured in the field for a stepped amplitude scan for calibration of trigger efficiency. The generated pulses are transmitted by a telescopic biconical antenna in horizontal polarization with about $2\,\mathrm{dBi}$ gain across $180\,\mathrm{MHz}$ to $360\,\mathrm{MHz}$. The system records the pulsing timestamp, position, and strength for later analysis.

Figure 138 illustrates results obtained with the proposed drone calibration system for TAROGE-M [617]. The trigger efficiency was measured by counting the number of received periodic calibration pulses versus the total number transmitted when the pulser was within the main lobe of the antennas. The pulsing power during the drone flights was configured to scan seven steps with a $3\,\mathrm{dB}$ interval, each lasting for $2\,\mathrm{s}$. Within

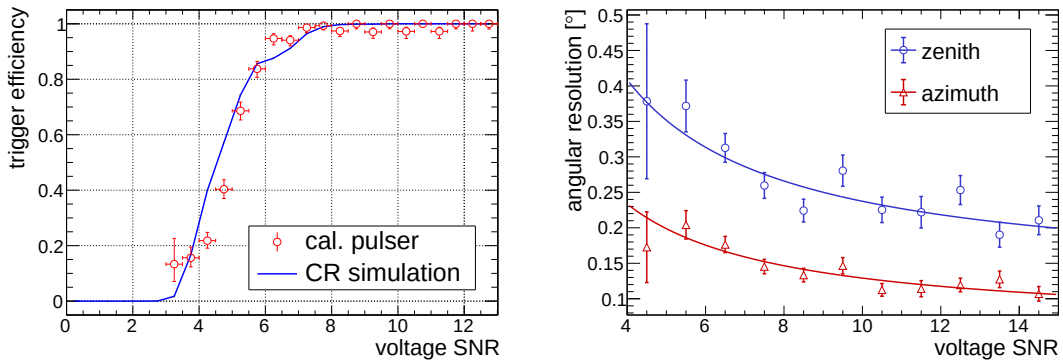

Figure 138: Results obtained with a drone-borne pulser at TAROGE-M. Left: the station-level trigger efficiency as function of average Hpol voltage signal-to-noise ratio measured with the drone pulser (red markers), compared to the results from the simulation of cosmic ray signals (blue curve). The dual-sided trigger threshold during the pulser flights was set at $\mathrm{SNR} \sim 4$. Right: the angular resolution in zenith (blue) and azimuth (red) directions as function of SNR, calibrated by the drone pulser, together with the best-fit curves. Figure from [617].

each step, the average signal-to-noise ratio (SNR) over all events and all Hpol channels was calculated, where the SNR of a waveform is defined as the ratio of its peak voltage to the RMS noise voltage evaluated at the first $50\,\mathrm{ns}$ window that should not be affected by the pulse. The maximum observed SNR is over 25, which amplitudes were used to estimate the true SNR of the weaker pulses in the same cycle by scaling down with recorded attenuation value. TAROGE-M furthermore showed a good agreement between simulated efficiency and acceptance for cosmic ray detections, based on these measurements, and the recorded cosmic rays [617].

10.3.4 Geometry

After initial deployment, calibrating radio-frequency antenna geometry *in situ*, to date, has primarily relied on calculating signal arrival times for radio-frequency pulses broadcast from embedded or surface transmitters. Such measurements, although straightforward in principle, also require disentangling three tightly coupled contributions to signal arrival measurements, namely uncertainties in individual channel cable delays, uncertainties in signal wavespeed as a function of depth, and the antenna geometry itself, taking into account the fact that frequency-dependent antenna group delays may also depend on temperature.

Multi-parameter fit codes have been developed to solve for antenna locations, given a known transmitter location and measured propagation times to an array of receivers, assuming that the cable delays are well-measured. To improve the accuracy of the RF-over-fiber cable delays, optical time delay reflectometry (OTDR) will be done both before and also after deployment, since cable light velocity may vary *in situ*.

10.3.5 *In situ* antenna response calibration

In addition to pre-deployment measurements and simulations of the system response, a full-circuit gain calibration, as a function of frequency and incidence angle, provides

perhaps the most sensitive parameterization. Ideally, transmitter antennas identical to those deployed as receiver antennas are used to illuminate the receiver array over a full range of incident elevation and azimuth angles.

If the signal-to-noise is sufficiently high, then an impulsive, band-limited signal delivered to the transmitter can allow a determination of the antenna gain by calculating in the frequency domain. Alternatively, and perhaps most directly, a continuous-wave sweep (of the type issued by a vector network analyzer) allows a direct determination of the frequency-dependence of the gain, albeit with limited information on the frequency dependence of the group delay. The CATH calibration towers will therefore be equipped with both continuous wave (CW) and impulsive signal generators.

Reconstruction of the neutrino momentum four-vector requires defining the spatial orientation of the radio-frequency Cherenkov cone. Given the relatively small angular fraction comprised by a typical neutrino detector station, the cone itself cannot be imaged; instead the polarization of the Cherenkov electric field vector, coupled with the knowledge that the electric field polarization is perpendicular to the cone itself provides the most powerful constraint on the signal geometry. To extract the polarization orientation, the signal electric field components along two orthogonal axes (vertical- vs. horizontal-) is measured. Reconstructing the electric field from this requires precise knowledge of the response of the antennas to all components of the incoming electric field, which will be obtained through combination of short-baseline data from the on-station calibration system (Sec. 6.4.8) and long-baseline data from CATH transmitters.

10.3.6 Rate vs. threshold calibration: long-term monitoring

Since the neutrino flux is rapidly falling with energy, a quantitative evaluation of the event trigger efficiency as a function of signal strength is critical to an estimate of the detected neutrino rate. In a typical trigger threshold scan, a variable attenuator is used to sweep the output signal amplitude over a broad enough range to observe the evolution from trigger turn-on to 100% trigger efficiency, as previously outlined using the TAROGE-M aerial drone calibration. To accommodate changing trigger criteria, as well as the possibility of understanding possible aging effects, both the in-ice as well as the above-surface CATH transmitters will be equipped with step attenuators to monitor any changes in the trigger efficiency curves, over time.

10.3.7 Ice

As with the optical array, the radio-frequency response of the ice neutrino target largely dictates the sensitivity of any planned experiment. Ideally, ice properties should be both measured, as well as accurately modeled from first-principles, in order that a neutrino detection rate can confidently be estimated. Several attributes are important, as follows:

- The refractive index profile with depth n(z) determines the effective volume at the lowest detectable neutrino energies (10–100 PeV). Deviations from a smooth refractive index profile [688] have been shown to lead to non-classical radio-frequency propagation modes, and may be responsible for so-called 'shadow

zone' signals (see Sec. 3.1.2). As demonstrated *in situ*, polar ice in the radio-frequency band is non-dispersive in the 100-1000 MHz interval of interest, as expected given the frequency separation relative to the ice Debye resonances. In practice, it is easier to measure the ice density, rather than the radio-frequency refractive index dependence on depth and use the proxy that the RF wavespeed depends linearly on density. The density profile dependence on depth should follow an exponential, similar to the atmospheric density profile, derived from the simple assumption that gravity determines the overburden at any given depth. Given the specific gravity of ice at the surface (typically $SG_{surface} \sim 0.4$) and the asymptotic value of the specific gravity of ice below 200 m ($SG_{deep} \sim 0.917$), the refractive index is then completely determined.

- The attenuation length profile with depth and frequency $L_\alpha(z, \omega)$ largely determines the neutrino target volume at the high end of the sensitive energy regime (1 EeV and higher). First-principles calculations of attenuation length require two primary inputs: a) the ice temperature, and b) the concentration of ionic impurities, primarily hydrogen (H+, contributed by water dissociation), chlorine and sodium (CL- and Na+, respectively, and contributed primarily by ocean sea salts blown inland) and species resulting from volcanic eruptions, including potassium, calcium, magnesium and sulfates. Combined with the known activation energies for the impurities, an Arrhenius-like model can then be used to translate the impurity levels into molar conductivities, and therefore, the attenuation length. The frequency dependence of ice attenuation length has been measured directly for laboratory samples and found to be consistent with the expected inverse-frequency scaling.
- Polarization-dependent asymmetries in the refractive index (birefringence) for ice crystals is a well-known property of standard terrestrial ice (see Sec. 4.2.1). In the optical frequencies, as described above, the effect of birefringence is seen in anisotropy in the optical properties of the ice which is aligned with the flow direction of the glacier. At radio frequencies, the effect of birefringence is to cause time delays between different polarization components of the radio signal which can result in amplitude and polarization asymmetries due to interference depending on the geometry. Understanding the polarization asymmetries is important to determine the neutrino direction and energy [587, 689].
- Layered impurities within the ice have long been studied by glaciologists as well as radio-frequency neutrino experiments at the South Pole, and, more recently, Summit Station, Greenland. Only recently, however, has the importance of internal layering vis-a-vis internally reflected surface anthropogenic, as well as cosmic ray backgrounds been quantitatively addressed. Initial efforts suggest that such internal reflection layers may result in background signals virtually indistinguishable from those of neutrinos, depending on the (currently not well-constrained) absolute reflectivity of those internal layers.

Extensive 'first-generation' measurements of the refractive index profile, attenuation length, birefringent asymmetries and layer reflectivities have been made over the last two decades at the South Pole. Currently, however, there are clear areas for improvement, which are, in turn, often systematically limited by the uncertainties in response of the antennas used to make ice properties' measurements.

The real part of the dielectric permittivity for the refractive index profile can be estimated in several ways. A simple ansatz that prescribes a linear dependence of refractive index on ice density (as extracted from South Polar cores), constrained between the limits of the bulk refractive index at depth (n=1.78) and the surface refractive index (n=1.35) provides a reasonable starting point. Such a model should also match the exponential scale height dependence expected for a self-gravitating fluid. The radio frequency refractive index can be directly calculated using *in situ* transit time measurements, although these also uncertainties in antenna surveying and cable delays. Antenna and propagation delay uncertainties can be (largely) removed by measuring the signal arrival time difference between direct and refracted/reflected rays connecting a given transmitter to a given receiver. A range ofrefractive index models have been considered, including a 'standard' scale height exponential, a sigmoid parameterization that gave the best fit to the (refracted - direct ray) time differences observed by ARA for SPICEcore transmitter signals, and also a best-fit model determined using data exclusively from the ARA phased array. The single exponential refractive index profile, although appealing for its simplicity, in some cases, gives a poorer fit to South Polar signal propagation time data than two exponentials, with a transition at a depth of approximately 25 meters. Independent data-fitting at Summit Station, Greenland, led to a similar conclusion. Additionally, meter-scale density 'inversions' at depths of 6–10 meters have been observed at South Pole, as well as Summit Station. South Polar data, in fact, directly observe an inversion using transmitter→receiver propagation time measurements. Thus far, no single model provides a satisfactory fit to all the extant data.

IceCube-Gen2 radio will reduce the refractive index profile uncertainties in three ways: First, neutron-probe monitor measurements will be taken periodically to provide 1% fractional error density values, at 10 cm increments. Second, we will use the pulsers installed at the stations to probe the ice profile. For that we propose active 'pinging' during co-deployment of transmitter and receiver strings. Assuming that transmitter and receiver antennas are at the same depth (to within 5 cm), then the relative refractive index profile can be mapped based on the migration of signal arrival times with depth. Ideally, both the direct and refracted ray would fit within the waveform capture window. This technique cancels uncertainties in cable delays, and also minimizes uncertainties due to ray tracing. Furthermore, the stations the pulsing will happen in-situ on a regular basis. One pulser close to the surface will be used to study snow accumulation. For some stations, two near-surface pulsers will be installed. In combination they can track the development of the profile of the index of refraction. Third, we propose to equip a subset of CATH antennas with a commercially available RF signal generator and power detector, which would not only allow generation of arbitrary CW signals, but also, via the power detector, allow the chip to be used in Network Analyzer mode and return antenna complex impedance Z data, as a function of depth, which will permit a cross-check of the density measurements given the known dependence of Z on the local environmental refractive index. Additionally, an extensive internal layer map, over the entirety of the IceCube-Gen2 footprint will have already been generated by CReSIS surveying, associated with the IceCube Upgrade—this will provide a powerful cross- and consistency-check on the refractive index data taken directly by IceCube.

Extraction of the attenuation length profile typically employs a bistatic radar configuration, with a surface-mounted RF transmitter beaming an impulse down into the ice and observing the bedrock-reflected signal using a surface-mounted RF receiver, horizontally displaced from the transmitter by $\mathcal{O}(10-100)$ m. Such a scheme is experimentally and logistically straightforward, however, only the path-averaged attenuation length can be directly measured. To unfold the depth-dependent $L_\alpha(z)$ requires resorting to temperature and impurity data (largely non-existent at South Pole) coupled with the model described above. Moreover, since the attenuation grows so rapidly with temperature, small uncertainties in the deepest, warmest ice propagate to large uncertainties in the coldest, shallowest ice which provides the bulk of neutrino target.

To date, South Pole measurements of the imaginary component of the attenuation length L_α at radio-frequencies have established that:

- L_α exceeds one kilometer in the upper 1.5 km of the Antarctic ice sheet. This also corresponds to the volume in which 95% of the neutrino detections are expected to occur.
- The magnitude of attenuation tracks the temperature profile, with warmer ice (and therefore higher ionic mobility and absorption) being more RF-absorptive.
- Although having a more favorable (i.e., colder) temperature profile compared to Greenland, impurity conductivity plays a greater role for South Polar ice absorption – correspondingly, first-principles modeling of attenuation at South Pole is more reliant on chemistry analysis from South Polar cores (which are considerably less plentiful than for Greenland, owing to considerably fewer coring campaigns).

Birefringent asymmetries can similarly be measured in bistatic radar measurements [527, 690, 691] however, since the birefringent asymmetry depends on the three-dimensional polarization alignment of a propagating (Cherenkov) electric field vector, horizontally-propagating radio-frequency signals must be measured *in situ*, sampling the entire range of trajectories as putative neutrino signals. An extensive *in situ* data sample has been accumulated by the ARA and ARIANNA collaborations, in response to a radio-frequency transmitter lowered into the SPICEcore borehole. A model assuming linear dependence on both propagation distance and also the opening angle relative to the local ice flow direction has been found to provide a reasonable match to the timing characteristics of compiled experimental data [685]; considerably more data points would help verify this linear model. However, the birefringent models used to explain the timing data are unable to explain the amplitude characteristics of signal polarization measurements [587, 689].

Figure 139, left shows a simple linear fit to the timing asymmetry data. Although birefringence can result in the rotation of polarization vectors, the variation in the measured VPol and HPol signals with depth of a descending transmitter, show in in the right panel of Figure 139, are considerably larger than current birefringent models can accommodate. Although both the HPol and VPol channels show the strong focusing expected as the transmitter emerges from the shadow zone, at a transmitter depth of 600 meters, several features of this plot (the large HPol:VPol signal strength, the large VPol power measured from the nominal shadow zone, and the envelope of the VPol power,

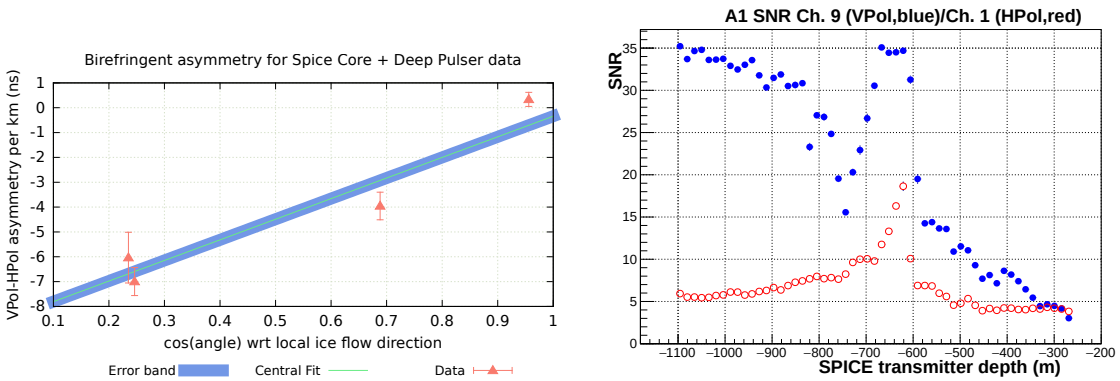

Figure 139: Left: Comparison of measured, birefringence-induced difference of signal arrival times, for orthogonal polarizations (data points), to a simple model, which assumes a linear dependence on signal path length and also signal propagation direction, relative to the local ice flow direction (diagonal line). Right: Received signal as a function of transmitter depth for a transmitter in the SPICEcore borehole sending to ARA vpol and hpol antennas. The asymmetry of the different polarization signals are not explained by the model on the left.

e.g), illustrate our current lack of understanding, and the improved radioglaciological information that IceCube-Gen2 radio will hopefully provide.

The Calibration Tower+Hole strategy outlined above is intended to 'build in' calibration capabilities previously unavailable - namely, signal pulses, of variable shapes, frequency bands, and attenuation, over kilometer-scale horizontal baselines, with multiple receiver stations illuminated by multiple transmitters over a range of signal propagation directions. This should allow a much more extensive data sample with which to simultaneously parameterize attenuation length and birefringent effects over areal scales of hundreds of square kilometers, with nanosecond signal arrival timing resolution.

10.3.8 Cross calibration

The fact that the radio antennas of the surface array and the shallow antennas of the in-ice radio array are sensitive to the same air-shower signals, provides IceCube-Gen2 with a unique opportunity for cross calibration. The surface array is on top of the optical array, which simplifies the cross-calibration between muon signals in the ice and the energy of the primary cosmic ray measured accurately through the radio signal of the shower. Moreover, the radio array and the surface array can benefit from cross-calibration, which is important, e.g., to make use of the extended cosmic-ray aperture provided by the radio array at EeV energies. The radio technique has already been proven to be a suitable tool to cross-calibrate energy scales of different cosmic-ray arrays [576, 692, 693].

Placing an in-ice radio station and a surface station in close vicinity, thereby essentially detecting the same air showers or calibration signals, will allow us to cross-calibrate the absolute scale of the radio instruments, which has been found in the past to be the dominating systematic uncertainty on the energy scale of the cosmic rays measured, see e.g. [694–697]. In addition to the cross-calibration via air showers, there also are synergies by using the same calibration sources for the radio antennas of the radio and

the surface arrays, which will reduce systematic uncertainties in any analysis using both arrays.

Since the radio antennas of the surface array will also be cross-calibrated against the particle signals of the same air showers detected in radio, this will enable an overall minimization of systematic uncertainties of the energy scale across all arrays of IceCube-Gen2. Furthermore, this cross-calibration will allow the instruments to conduct joint air shower studies and provide additional veto capacity for certain types of inclined events. Finally, via the link of the surface array, we will be able to better harmonize our understanding of atmospheric backgrounds to neutrino measurements as well as ice properties across the array.

10.4 Surface array

The calibration of the surface array components is well understood, since as of summer 2021 there are 8 scintillator panels, 3 surface radio antennas and 2 IceAct telescopes running at the South Pole. The calibration process for each component of the surface array is described in the following sections.

10.4.1 Scintillator array calibration

For the scintillator array, calibration of the operational parameters such as the SiPM supply voltage and the trigger threshold, as well as the temperature sensor settings will be done in the lab at different temperatures. Calibration constants for converting digitizer to voltage values will be available to the DAQ during operation.

For *in situ* calibration, a minimum ionising particle (MIP) leaves a characteristic signal in scintillator panels, which manifests as a peak in the charge spectrum above the exponentially decaying background hits. The light yield of panels is measured in units of MIP, and the measured charges are converted to MIP for physics analysis. MIP yield depends on SiPM gain and in turn on temperature. Along with normal data taking, charge histograms as shown in Figure 140 are stored and used for analysis. These histograms are the main calibration tool for the scintillator panels.

Several photoelectron peaks are clearly identifiable near threshold in the highest amplification ADC channel as shown in Figure 141. The SiPM gain can be measured in two ways, either from the distance between the peaks or by taking the FFT of the charge spectrum near threshold. Both methods agree within 2%. The amplification factors between the three ADC channels are determined by comparing the pedestal corrected position of the MIP peak.

The charge histograms are collected every day, and the SiPM voltage can be adjusted when the fluctuations in gain exceeds a preset tolerance value.

Figure 142 demonstrates the linear relation between SiPM voltage, gain (or MIP position), and temperature. A plane fit in the temperature-voltage-gain space describes the data well and will be used for voltage adjustments to keep the light yield of a MIP stable. This method is shown to be successful in keeping the gain stable within 2%.

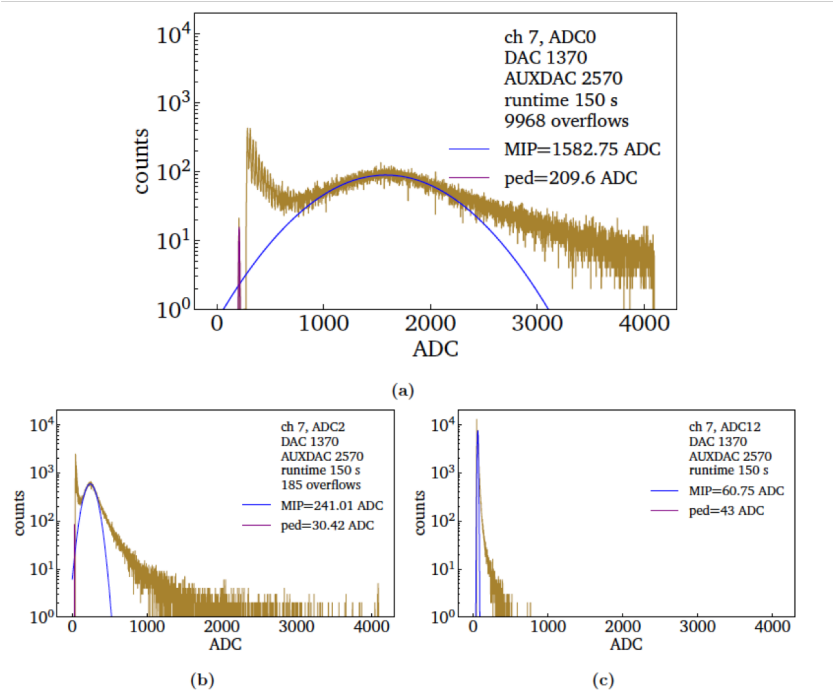

Figure 140: Charge histograms from three ADC channels with high, medium and low amplifications. Pedestal, trigger threshold and the Gaussian fit to the MIP peak are shown for each channel.

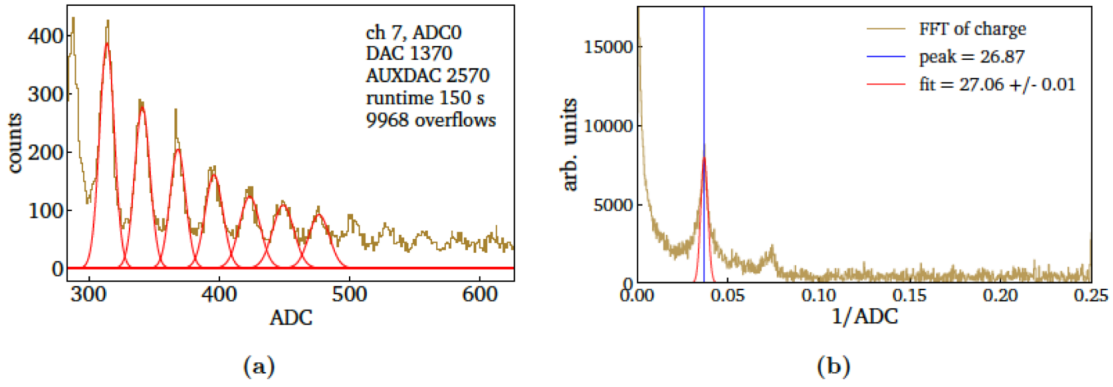

Figure 141: a) The charge spectrum near pedestal of the high-gain ADC channel. The distance between the *p.e.* peaks is used to measure the SiPM gain level. b) The FFT of the same charge spectrum.

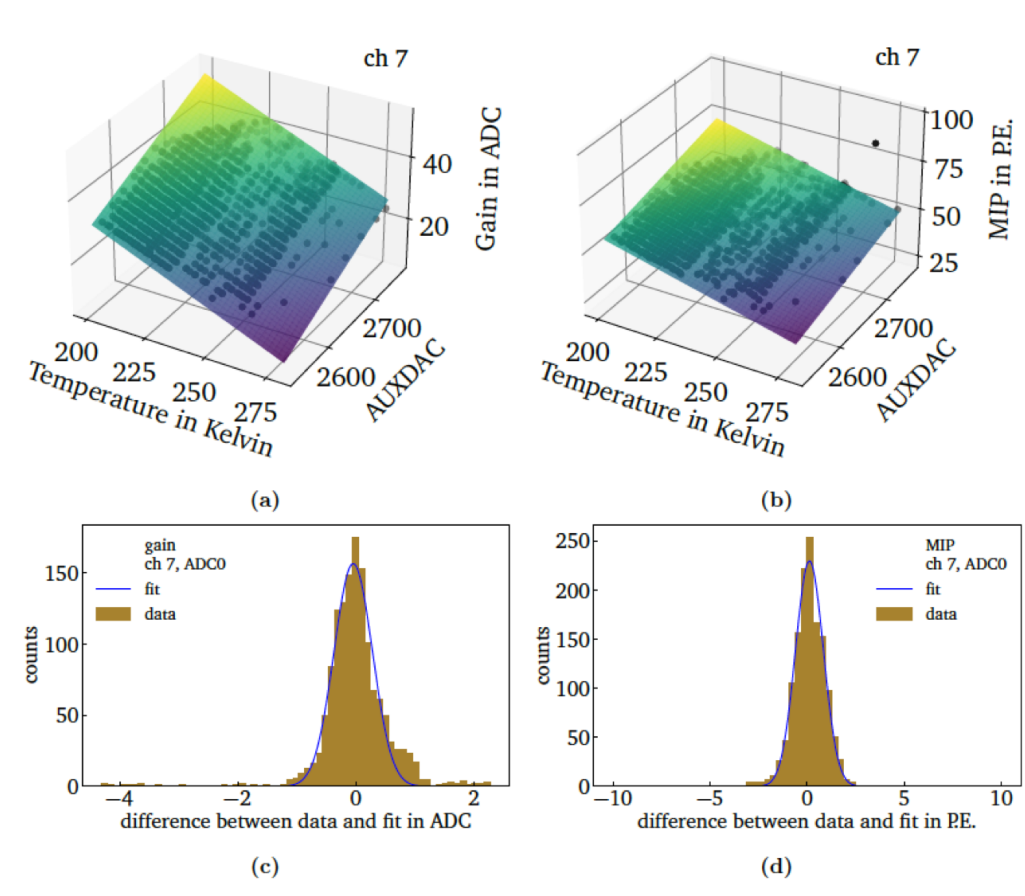

Figure 142: Temperature-voltage-gain relation and plane fits. AUXDAC = specific SiPM bias voltage setting.

10.4.2 Calibration of the surface radio antennas

The calibration of the radio antennas consists of two steps, aiming at a total uncertainty of the absolute amplitude of the order of $10\,\%$.

First, the individual components of the signal chain are tested and calibrated in the lab. This includes in particular, measurements of the attenuation and group delay of the cables and the low-noise amplifiers in the antennas with a vector network analyzer, and the calibration of the DAQ with a function generator which enables an absolute calibration of the voltage. Depending on the differences for each type of component and the impact on the target accuracy of a particular physics analysis, we then can take into account the individual gain and group delay in the data analysis or simply work with an average value.

Second, the absolute energy scale of the surface radio array needs to be calibrated. This is most important, since at least at high energies the surface radio antennas will define the energy scale of IceCube-Gen2 for cosmic rays. By cross-calibration they may also be used to check the energy scales of the optical and radio arrays for cosmic-ray events.

The energy scale will be set by an end-to-end calibration of radio array. This can be done either using Galactic noise as a natural reference source [647], or by using an artificial reference source on a drone [698] or a crane [699]. In the first case, the accuracy is limited by the knowledge of the broadband Galactic radio emission, in the second case by the absolute calibration of the reference source itself. For other experiments, both methods reached a similar level of accuracy with a total uncertainty of the order of $15\,\%$. Since development is going on in the community on both methods, we have thus set a slightly more ambitious target of $10\,\%$ for the uncertainty of the absolute energy for cosmic-ray measurements with the surface radio antennas at IceCube-Gen2. As of now, we plan to use the Galactic noise as primary calibration methods, as it is available 24/7 at no cost. Nonetheless, it is an option to also use a drone if available for the in-ice radio array anyway, so we can cross-check the Galactic Noise calibration for a few antennas.

10.4.3 IceAct calibration

The DAQ system will be fully calibrated at several different temperatures in the lab. For this a calibration of all channels of the trigger chain, the digitizer chain and the full ring buffer will be performed. As the calibration is temperature dependent, the DAQ temperature will be monitored during operation at the South Pole.

The trigger chain is controlled by a digital-to-analog converter (DAC). It needs to be calibrated to determine the conversion factor from DAC counts to voltages and to set a precise and consistent trigger threshold. The two variables which determine the trigger threshold mentioned in Sect. 7.4.4 are the trigger threshold line and the trigger baseline. By varying one of the trigger parameters and keeping the other constant the DAC count value for the trigger threshold line and the trigger baseline can be determined. This is repeated with different voltage amplitudes of a known input signal.

For the ADC digitizer calibration the DC-offset is set to different values and the resulting voltages are measured. This results in a DC-offset DAC to voltage calibration curve. In a second step, pedestal files at different DC-offset values are recorded with no signal provided. The second step is necessary since each cell in the ring buffer has a slightly different gain and offset. Combining both measurements results in a ADC to voltage calibration curve which can be applied to each waveform.

Additionally, the assembled telescopes will be calibrated in the lab using a pulsed laser which sends out signals with very few photons. Plotting the pulse integral of the events in a histogram results in a finger spectrum shown in Figure 143. Each peak also referred to as ”finger” represents a specific number of photons detected in a pixel. This allows for a conversion of measured voltages to the number of detected photons.

During operation the stability of the gain can be monitored using single muons passing through the camera measured in special ”muon runs.” For a ”muon run” the event trigger condition described in Section 7.4.4 is changed to a single trigger signal. As

shown in Figure 143, a single muon traversing through the solid PMMA light guide produces photons. The number of photons produced depends on the length of the muon path through the light guide and results in a characteristic event view with nearly all photons detected in one pixel. Plotting the pulse integral of these events leads to a bump in the histogram. The mean of the bump is determined by the number of photons produced along the average path through the light guide. Since the length of the muon path is constant, shifts of the muon bump show a change of the gain of a single pixel. These measurements will also be directly compared to ”muon runs” taken after the lab calibration.

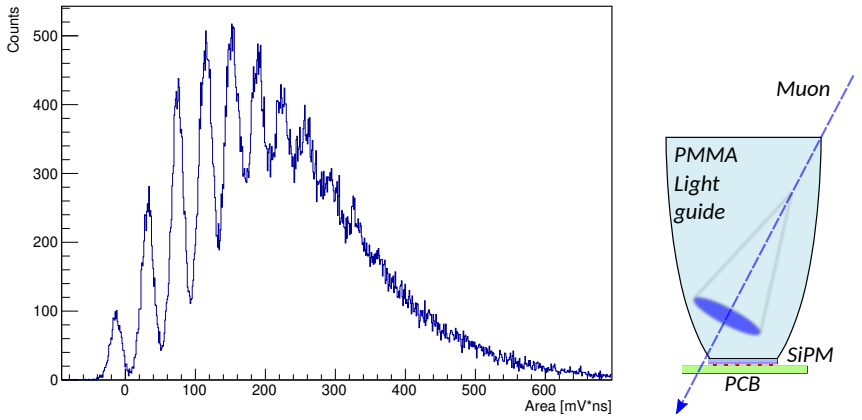

Figure 143: Left: Pulsed laser lab calibration showing single photon resolution. Right: Muons as stable gain calibration source using Cherenkov light created in the solid PMMA light guides.

10.5 Summary

The calibration efforts in IceCube-Gen2 draw on extensive experience from previous detectors and is designed to the specific needs of each component of the detector. Ice properties are more precisely known at optical frequencies than at radio frequencies, which is reflected in the relatively higher-impact radio frequency calibration hardware. The IceCube Upgrade calibration program will provide extensive knowledge and experience which will directly benefit IceCube-Gen2.

Part III

Detector Construction and Logistical Support Requirements

(Part III will be released at a later time.)

References

[1] IceCube-Gen2 Collaboration, M. G. Aartsen *et al.*, "IceCube-Gen2: the window to the extreme Universe," *J. Phys. G* **48** (2021) 060501, 2008.04323.

[2] IceCube Collaboration, M. G. Aartsen *et al.*, "First observation of PeV-energy neutrinos with IceCube," *Phys. Rev. Lett.* **111** (2013) 021103, 1304.5356.

[3] IceCube Collaboration, M. G. Aartsen *et al.*, "Evidence for High-Energy Extraterrestrial Neutrinos at the IceCube Detector," *Science* **342** (2013) 1242856, 1311.5238.

[4] A. Franceschini, G. Rodighiero, and M. Vaccari, "The extragalactic optical-infrared background radiations, their time evolution and the cosmic photon-photon opacity," *Astron. Astrophys.* **487** (2008) 837, 0805.1841.

[5] IceCube, Fermi-LAT, MAGIC, AGILE, ASAS-SN, HAWC, H.E.S.S., INTEGRAL, Kanata, Kiso, Kapteyn, Liverpool Telescope, Subaru, Swift NuSTAR, VERITAS, VLA/17B-403 Collaborations, M. G. Aartsen *et al.*, "Multimessenger observations of a flaring blazar coincident with high-energy neutrino IceCube-170922A," *Science* **361** (2018) eaat1378, 1807.08816.

[6] IceCube Collaboration, M. G. Aartsen *et al.*, "Neutrino emission from the direction of the blazar TXS 0506+056 prior to the IceCube-170922A alert," *Science* **361** (2018) 147–151, 1807.08794.

[7] BAIKAL Collaboration, I. A. Belolaptikov *et al.*, "The Baikal underwater neutrino telescope: Design, performance and first results," *Astropart. Phys.* **7** (1997) 263–282.

[8] ANTARES Collaboration, M. Ageron *et al.*, "ANTARES: the first undersea neutrino telescope," *Nucl. Instrum. Meth. A* **656** (2011) 11–38, 1104.1607.

[9] AMANDA Collaboration, F. Halzen *et al.*, "The AMANDA neutrino telescope," *Nucl.Phys.Proc.Suppl.* **77** (1999) 474–485, hep-ex/9809025.

[10] M. Ahlers, K. Helbing, and C. Pérez de los Heros, "Probing Particle Physics with IceCube," *Eur. Phys. J.* **C78** (2018) 924, 1806.05696.

[11] KM3Net Collaboration, S. Adrian-Martinez *et al.*, "Letter of intent for KM3NeT 2.0," *J. Phys.* **G43** (2016) 084001, 1601.07459.

[12] A. D. Avrorin *et al.*, "Sensitivity of the Baikal-GVD neutrino telescope to neutrino emission toward the center of the galactic dark matter halo," *JETP Lett.* **101** (2015) 289–294, 1412.3672.

[13] IceCube Collaboration, A. Ishihara, "The IceCube Upgrade – Design and Science Goals," *PoS* **ICRC2019** (2020) 1031, 1908.09441.

[14] IceCube, PINGU Collaborations, M. G. Aartsen *et al.*, "Letter of Intent: The Precision IceCube Next Generation Upgrade (PINGU)," 1401.2046.

[15] IceCube Collaboration, M. G. Aartsen *et al.*, "The IceCube Neutrino Observatory: Instrumentation and Online Systems," *JINST* **12** (2017) P03012, 1612.05093.

[16] IceCube Collaboration, M. G. Aartsen *et al.*, "Measurement of the multi-TeV neutrino cross section with IceCube using Earth absorption," *Nature* **551** (2017) 596–600, 1711.08119.

[17] IceCube Collaboration, M. G. Aartsen *et al.*, "Characteristics of the diffuse astrophysical electron and tau neutrino flux with six years of IceCube high energy cascade data," *Phys. Rev. Lett.* **125** (2020) 121104, 2001.09520.

[18] IceCube Collaboration, M. G. Aartsen *et al.*, "Observation of High-Energy Astrophysical Neutrinos in Three Years of IceCube Data," *Phys. Rev. Lett.* **113** (2014) 101101, 1405.5303.

[19] IceCube Collaboration, M. G. Aartsen *et al.*, "Evidence for Astrophysical Muon Neutrinos from the Northern Sky with IceCube," *Phys. Rev. Lett.* **115** (2015) 081102, 1507.04005.

[20] IceCube Collaboration, R. Abbasi *et al.*, "Measurement of Astrophysical Tau Neutrinos in IceCube's High-Energy Starting Events," 2011.03561.

[21] S. L. Glashow, "Resonant Scattering of Antineutrinos," *Phys. Rev.* **118** (1960) 316–317.

[22] IceCube Collaboration, M. G. Aartsen *et al.*, "Detection of a particle shower at the Glashow resonance with IceCube," *Nature* **591** (2021) 220–224, 2110.15051. [Erratum: Nature 592, E11 (2021)].

[23] IceCube collaboration Collaboration, R. Abbasi *et al.*, "Observation of high-energy neutrinos from the galactic plane," *Science* **380** (2023) 1338–1343, https://www.science.org/doi/pdf/10.1126/science.adc9818.

[24] Fermi-LAT Collaboration, M. Ackermann *et al.*, "Fermi-LAT Observations of the Diffuse Gamma-Ray Emission: Implications for Cosmic Rays and the Interstellar Medium," *Astrophys. J.* **750** (2012) 3, 1202.4039.

[25] Tibet ASgamma Collaboration, M. Amenomori *et al.*, "First Detection of sub-PeV Diffuse Gamma Rays from the Galactic Disk: Evidence for Ubiquitous Galactic Cosmic Rays beyond PeV Energies," *Phys. Rev. Lett.* **126** (2021) 141101, 2104.05181.

[26] D. Gaggero, D. Grasso, A. Marinelli, A. Urbano, and M. Valli, "The gamma-ray and neutrino sky: A consistent picture of Fermi-LAT, Milagro, and IceCube results," *Astrophys. J. Lett.* **815** (2015) L25, 1504.00227.

[27] IceCube Collaboration, R. Abbasi *et al.*, "Evidence for neutrino emission from the nearby active galaxy NGC 1068," *Science* **378** (2022) 538–543, 2211.09972.

[28] Y. Inoue, D. Khangulyan, and A. Doi, "Gamma-ray and Neutrino Signals from Accretion Disk Coronae of Active Galactic Nuclei," *Galaxies* **9** (2021) 36, 2105.08948.

[29] IceCube Collaboration, R. Abbasi *et al.*, "A search for neutrino emission from cores of Active Galactic Nuclei," 2111.10169.

[30] IceCube Collaboration, M. Aartsen *et al.*, "Observation and Characterization of a Cosmic Muon Neutrino Flux from the Northern Hemisphere using six years of IceCube data," *Astrophys. J.* **833** (2016) 3, 1607.08006.

[31] IceCube Collaboration, C. Haack and C. Wiebusch, "A measurement of the diffuse astrophysical muon neutrino flux using eight years of IceCube data.," *PoS* **ICRC2017** (2018) 1005.

[32] IceCube Collaboration, C. Kopper, W. Giang, and N. Kurahashi, "Observation of Astrophysical Neutrinos in Four Years of IceCube Data," *PoS* **ICRC2015** (2016) 1081.

[33] IceCube Collaboration, C. Kopper, "Observation of Astrophysical Neutrinos in Six Years of IceCube Data," *PoS* **ICRC2017** (2018) 981.

[34] M. W. E. Smith *et al.*, "The Astrophysical Multimessenger Observatory Network (AMON)," *Astropart. Phys.* **45** (2013) 56–70, 1211.5602.

[35] Fermi-LAT, ASAS-SN, IceCube Collaborations, S. Garrappa *et al.*, "Investigation of two Fermi-LAT gamma-ray blazars coincident with high-energy neutrinos detected by IceCube," *Astrophys. J.* **880** (2019) 880:103, 1901.10806.

[36] IceCube Collaboration, T. Glüsenkamp, "Analysis of the cumulative neutrino flux from Fermi-LAT blazar populations using 3 years of IceCube data," *EPJ Web Conf.* **121** (2016) 05006, 1502.03104.

[37] F. Halzen, A. Kheirandish, T. Weisgarber, and S. P. Wakely, "On the Neutrino Flares from the Direction of TXS 0506+056," *Astrophys. J.* **874** (2019) L9, 1811.07439.

[38] A. Neronov and D. Semikoz, "Self-consistent model of extragalactic neutrino flux from evolving blazar population," *Sov. Phys. JETP* **158** (2020) 295, 1811.06356.

[39] S. van Velzen, A. J. Mendez, J. H. Krolik, and V. Gorjian, "Discovery of transient infrared emission from dust heated by stellar tidal disruption flares," *Astrophys. J.* **829** (2016) 19, 1605.04304.

[40] S. Reusch *et al.*, "Candidate Tidal Disruption Event AT2019fdr Coincident with a High-Energy Neutrino," *Phys. Rev. Lett.* **128** (2022) 221101, 2111.09390.

[41] IceCube Collaboration, M. G. Aartsen *et al.*, "Search for Prompt Neutrino Emission from Gamma-Ray Bursts with IceCube," *Astrophys. J.* **805** (2015) L5, 1412.6510.

[42] G. R. Farrar and A. Gruzinov, "Giant AGN Flares and Cosmic Ray Bursts," *Astrophys. J.* **693** (2009) 329–332, 0802.1074.

[43] L. Dai and K. Fang, "Can tidal disruption events produce the IceCube neutrinos?," *Mon. Not. Roy. Astron. Soc.* **469** (2017) 1354–1359, 1612.00011.

[44] K. Hayasaki and R. Yamazaki, "Neutrino Emissions from Tidal Disruption Remnants," 1908.10882.

[45] G. R. Farrar and T. Piran, "Tidal disruption jets as the source of Ultra-High Energy Cosmic Rays," 1411.0704.

[46] N. Senno, K. Murase, and P. Meszaros, "High-energy Neutrino Flares from X-Ray Bright and Dark Tidal Disruption Events," *Astrophys. J.* **838** (2017) 3, 1612.00918.

[47] X.-Y. Wang and R.-Y. Liu, "Tidal disruption jets of supermassive black holes as hidden sources of cosmic rays: explaining the IceCube TeV-PeV neutrinos," *Phys. Rev. D* **93** (2016) 083005, 1512.08596.

[48] C. Lunardini and W. Winter, "High Energy Neutrinos from the Tidal Disruption of Stars," *Phys. Rev. D* **95** (2017) 123001, 1612.03160.

[49] R. Stein, "IceCube-191001A - IceCube observation of a high-energy neutrino candidate event," *GCN Circular* **25913** (2019).

[50] R. Stein *et al.*, "A tidal disruption event coincident with a high-energy neutrino," *Nature Astron.* **5** (2021) 510–518, 2005.05340.

[51] K. Hayasaki, "Neutrinos from tidal disruption events," *Nature Astronomy* **5** (2021) 436–437, 2102.11879.

[52] S. Frederick *et al.*, "A Family Tree of Optical Transients from Narrow-line Seyfert 1 Galaxies," *Astrophys. J.* **920** (2021) 56, 2010.08554.

[53] IceCube Collaboration, R. Abbasi *et al.*, "Searching for High-Energy Neutrino Emission from Galaxy Clusters with IceCube," 2206.02054.

[54] IceCube Collaboration, R. Abbasi *et al.*, "Search for High-energy Neutrinos from Ultraluminous Infrared Galaxies with IceCube," *Astrophys. J.* **926** (2022) 59, 2107.03149.

[55] Fermi-LAT Collaboration, M. Ackermann *et al.*, "The spectrum of isotropic diffuse gamma-ray emission between 100 MeV and 820 GeV," *Astrophys. J.* **799** (2015) 86, 1410.3696.

[56] M. Ackermann *et al.*, "Astrophysics Uniquely Enabled by Observations of High-Energy Cosmic Neutrinos," *BAAS* **51** (2019) 185, 1903.04334.

[57] IceCube Collaboration, M. G. Aartsen *et al.*, "A combined maximum-likelihood analysis of the high-energy astrophysical neutrino flux measured with IceCube," *Astrophys. J.* **809** (2015) 98, 1507.03991.

[58] IceCube Collaboration, R. Abbasi *et al.*, "Improved Characterization of the Astrophysical Muon-Neutrino Flux with 9.5 Years of IceCube Data," 2111.10299.

[59] IceCube Collaboration, M. Aartsen *et al.*, "Constraints on Ultrahigh-Energy Cosmic-Ray Sources from a Search for Neutrinos above 10 PeV with IceCube," *Phys. Rev. Lett.* **117** (2016) 241101, 1607.05886. [Erratum: Phys. Rev. Lett. 119, 259902 (2017)].

[60] IceCube Collaboration, M. G. Aartsen *et al.*, "Differential limit on the extremely-high-energy cosmic neutrino flux in the presence of astrophysical background from nine years of IceCube data," *Phys. Rev. D* **98** (2018) 062003, 1807.01820.

[61] K. Murase, Y. Inoue, and C. D. Dermer, "Diffuse neutrino intensity from the inner jets of active galactic nuclei: Impacts of external photon fields and the blazar sequence," *Phys. Rev. D* **90** (2014) 023007, 1403.4089.

[62] K. Fang, K. Kotera, K. Murase, and A. V. Olinto, "Testing the Newborn Pulsar Origin of Ultrahigh Energy Cosmic Rays with EeV Neutrinos," *Phys. Rev. D* **90** (2014) 103005, 1311.2044.

[63] IceCube Collaboration, M. G. Aartsen *et al.*, "Measurements using the inelasticity distribution of multi-TeV neutrino interactions in IceCube," *Phys. Rev. D* **99** (2019) 032004, 1808.07629.

[64] V. Berezinsky and A. Y. Smirnov, "Cosmic neutrinos of ultra-high energies and detection possibility," *Astrophys. Space Sci.* **32** (1975) 461–482.

[65] K. Mannheim, R. J. Protheroe, and J. P. Rachen, "On the cosmic ray bound for models of extragalactic neutrino production," *Phys. Rev. D* **63** (2001) 023003, astro-ph/9812398.

[66] K. Murase, D. Guetta, and M. Ahlers, "Hidden Cosmic-Ray Accelerators as an Origin of TeV-PeV Cosmic Neutrinos," *Phys. Rev. Lett.* **116** (2016) 071101, 1509.00805.

[67] K. Bechtol, M. Ahlers, M. Di Mauro, M. Ajello, and J. Vandenbroucke, "Evidence against star-forming galaxies as the dominant source of IceCube neutrinos," *Astrophys. J.* **836** (2017) 47, 1511.00688.

[68] K. Murase and E. Waxman, "Constraining High-Energy Cosmic Neutrino Sources: Implications and Prospects," *Phys. Rev. D* **94** (2016) 103006, 1607.01601.

[69] K. Fang and K. Murase, "Linking High-Energy Cosmic Particles by Black Hole Jets Embedded in Large-Scale Structures," *Phys. Lett.* **14** (2018) 396, 1704.00015. [Nature Phys.14,no.4,396(2018)].

[70] M. Kachelrieß, O. Kalashev, S. Ostapchenko, and D. V. Semikoz, "Minimal model for extragalactic cosmic rays and neutrinos," *Phys. Rev. D* **96** (2017) 083006, 1704.06893.

[71] E. Resconi *et al.*, "The neutrino filter: connecting blazars with ultra high energy cosmic rays and astrophysical neutrinos," *PoS* **ICRC2017** (2018) 1016.

[72] E. Waxman and J. N. Bahcall, "High-energy neutrinos from astrophysical sources: An Upper bound," *Phys. Rev. D* **59** (1999) 023002, hep-ph/9807282.

[73] J. N. Bahcall and E. Waxman, "High-energy astrophysical neutrinos: The Upper bound is robust," *Phys. Rev. D* **64** (2001) 023002, hep-ph/9902383.

[74] M. Ahlers and F. Halzen, "Opening a New Window onto the Universe with IceCube," *Prog. Part. Nucl. Phys.* **102** (2018) 73–88, 1805.11112.

[75] A. Loeb and E. Waxman, "The Cumulative background of high energy neutrinos from starburst galaxies," *JCAP* **0605** (2006) 003, astro-ph/0601695.

[76] K. Murase, S. Inoue, and S. Nagataki, "Cosmic Rays Above the Second Knee from Clusters of Galaxies and Associated High-Energy Neutrino Emission," *Astrophys. J.* **689** (2008) L105, 0805.0104.

[77] K. Kotera *et al.*, "Propagation of ultrahigh energy nuclei in clusters of galaxies: resulting composition and secondary emissions," *Astrophys. J.* **707** (2009) 370–386, 0907.2433.

[78] L. A. Anchordoqui, "Ultra-High-Energy Cosmic Rays," *Physics Reports* **801** (2019) 1 – 93, 1807.09645.

[79] Pierre Auger Collaboration, I. Valino, "The flux of ultra-high energy cosmic rays after ten years of operation of the Pierre Auger Observatory," *PoS* **ICRC2015** (2016) 271.

[80] K. Murase, M. Ahlers, and B. C. Lacki, "Testing the Hadronuclear Origin of PeV Neutrinos Observed with IceCube," *Phys. Rev. D* **88** (2013) 121301, 1306.3417.

[81] K. Greisen, "End to the cosmic ray spectrum?," *Phys. Rev. Lett.* **16** (1966) 748–750.

[82] G. Zatsepin and V. Kuzmin, "Upper limit of the spectrum of cosmic rays," *JETP Lett.* **4** (1966) 78–80.

[83] V. Berezinsky and G. Zatsepin, "Cosmic rays at ultrahigh-energies (neutrino?)," *Phys.Lett.* **B28** (1969) 423–424.

[84] F. Stecker, "Diffuse Fluxes of Cosmic High-Energy Neutrinos," *Astrophys. J.* **228** (1979) 919–927.

[85] C. T. Hill and D. N. Schramm, "Ultrahigh-Energy Cosmic Ray Neutrinos," *Phys. Lett. B* **131** (1983) 247. [, 495 (1983)].

[86] S. Yoshida and M. Teshima, "Energy spectrum of ultrahigh-energy cosmic rays with extragalactic origin," *Prog. Theor. Phys.* **89** (1993) 833–845.

[87] R. Engel, D. Seckel, and T. Stanev, "Neutrinos from propagation of ultrahigh-energy protons," *Phys. Rev. D* **64** (2001) 093010, astro-ph/0101216.

[88] L. A. Anchordoqui, H. Goldberg, D. Hooper, S. Sarkar, and A. M. Taylor, "Predictions for the Cosmogenic Neutrino Flux in Light of New Data from the Pierre Auger Observatory," *Phys. Rev. D* **76** (2007) 123008, 0709.0734.

[89] H. Takami, K. Murase, S. Nagataki, and K. Sato, "Cosmogenic neutrinos as a probe of the transition from Galactic to extragalactic cosmic rays," *Astropart. Phys.* **31** (2009) 201, 0704.0979.

[90] M. Ahlers, L. A. Anchordoqui, and S. Sarkar, "Neutrino diagnostics of ultra-high energy cosmic ray protons," *Phys. Rev. D* **79** (2009) 083009, 0902.3993.

[91] M. Ahlers, L. Anchordoqui, M. Gonzalez-Garcia, F. Halzen, and S. Sarkar, "GZK Neutrinos after the Fermi-LAT Diffuse Photon Flux Measurement," *Astropart. Phys.* **34** (2010) 106–115, 1005.2620.

[92] K. Kotera, D. Allard, and A. Olinto, "Cosmogenic Neutrinos: parameter space and detectabilty from PeV to ZeV," *JCAP* **1010** (2010) 013, 1009.1382.

[93] S. Yoshida and A. Ishihara, "Constraints on the origin of the ultra-high energy cosmic-rays using cosmic diffuse neutrino flux limits: An analytical approach," *Phys. Rev. D* **85** (2012) 063002, 1202.3522.

[94] M. Ahlers and F. Halzen, "Minimal Cosmogenic Neutrinos," *Phys. Rev. D* **86** (2012) 083010, 1208.4181.

[95] R. Aloisio *et al.*, "Cosmogenic neutrinos and ultra-high energy cosmic ray models," *JCAP* **1510** (2015) 006, 1505.04020.

[96] J. Heinze, D. Boncioli, M. Bustamante, and W. Winter, "Cosmogenic Neutrinos Challenge the Cosmic Ray Proton Dip Model," *Astrophys. J.* **825** (2016) 122, 1512.05988.

[97] A. Romero-Wolf and M. Ave, "Bayesian Inference Constraints on Astrophysical Production of Ultra-high Energy Cosmic Rays and Cosmogenic Neutrino Flux Predictions," *JCAP* **1807** (2018) 025, 1712.07290.

[98] R. Alves Batista, R. M. de Almeida, B. Lago, and K. Kotera, "Cosmogenic photon and neutrino fluxes in the Auger era," *JCAP* **1901** (2019) 002, 1806.10879.

[99] K. Møller, P. B. Denton, and I. Tamborra, "Cosmogenic Neutrinos Through the GRAND Lens Unveil the Nature of Cosmic Accelerators," *JCAP* **05** (2019) 047, 1809.04866.

[100] A. van Vliet, R. Alves Batista, and J. R. Hörandel, "Determining the fraction of cosmic-ray protons at ultrahigh energies with cosmogenic neutrinos," *Phys. Rev. D* **100** (2019) 021302, 1901.01899.

[101] J. Heinze, A. Fedynitch, D. Boncioli, and W. Winter, "A new view on Auger data and cosmogenic neutrinos in light of different nuclear disintegration and air-shower models," *Astrophys. J.* **873** (2019) 88, 1901.03338.

[102] M. Ackermann *et al.*, "Fundamental Physics with High-Energy Cosmic Neutrinos," *BAAS* **51** (2019) 215, 1903.04333.

[103] C. A. Argüelles *et al.*, "Fundamental physics with high-energy cosmic neutrinos today and in the future," *PoS* **ICRC2019** (2020) 849, 1907.08690.

[104] IceCube Collaboration, M. G. Aartsen *et al.*, "Searches for Sterile Neutrinos with the IceCube Detector," *Phys. Rev. Lett.* **117** (2016) 071801, 1605.01990.

[105] IceCube Collaboration, M. G. Aartsen *et al.*, "Search for sterile neutrino mixing using three years of IceCube DeepCore data," *Phys. Rev. D* **95** (2017) 112002, 1702.05160.

[106] IceCube Collaboration, M. Aartsen *et al.*, "An eV-scale sterile neutrino search using eight years of atmospheric muon neutrino data from the IceCube Neutrino Observatory," 2005.12942.

[107] IceCube Collaboration, M. Aartsen *et al.*, "Searching for eV-scale sterile neutrinos with eight years of atmospheric neutrinos at the IceCube neutrino telescope," 2005.12943.

[108] IceCube Collaboration, M. G. Aartsen *et al.*, "Neutrino Interferometry for High-Precision Tests of Lorentz Symmetry with IceCube," *Nature Phys.* **14** (2018) 961–966, 1709.03434.

[109] P. Gondolo, G. Gelmini, and S. Sarkar, "Cosmic neutrinos from unstable relic particles," *Nucl. Phys. B* **392** (1993) 111–136, hep-ph/9209236.

[110] K. Murase and J. F. Beacom, "Constraining Very Heavy Dark Matter Using Diffuse Backgrounds of Neutrinos and Cascaded Gamma Rays," *JCAP* **1210** (2012) 043, 1206.2595.

[111] C. Rott, K. Kohri, and S. C. Park, "Superheavy dark matter and IceCube neutrino signals: Bounds on decaying dark matter," *Phys. Rev. D* **92** (2015) 023529, 1408.4575.

[112] IceCube Collaboration, R. Abbasi *et al.*, "Search for Relativistic Magnetic Monopoles with Eight Years of IceCube Data," *Phys. Rev. Lett.* **128** (2022) 051101, 2109.13719.

[113] ANTARES Collaboration, A. Albert *et al.*, "Search for magnetic monopoles with ten years of the ANTARES neutrino telescope," *JHEAp* **34** (2022) 1–8, 2202.13786.

[114] F. G. Schröder *et al.*, "High-Energy Galactic Cosmic Rays (Astro2020 Science White Paper)," *Bull. Am. Astron. Soc.* **51** (2019) 131, 1903.07713.

[115] N. Fraija *et al.*, "Cosmic rays in the TeV to PeV primary energy range," in *BAAS*, vol. 2020, p. 459, May, 2019.

[116] F. Sarazin *et al.*, "What is the nature and origin of the highest-energy particles in the universe?," in *BAAS*, vol. 51, p. 93, May, 2019. 1903.04063.

[117] B. Rani *et al.*, "Multi-Physics of AGN Jets in the Multi-Messenger Era," in *BAAS*, vol. 51, p. 92, May, 2019. 1903.04504.

[118] M. Santander *et al.*, "A Unique Messenger to Probe Active Galactic Nuclei: High-Energy Neutrinos," in *BAAS*, vol. 51, p. 228, May, 2019.

[119] T. Venters *et al.*, "Energetic Particles of Cosmic Accelerators I: Galactic Accelerators," in *BAAS*, vol. 51, p. 396, May, 2019. 1903.04634.

[120] P. Cristofari *et al.*, "Where are the pevatrons?," in *BAAS*, vol. 51, p. 115, May, 2019.

[121] M. Nisa *et al.*, "The Sun at GeV-TeV Energies: A New Laboratory for Astroparticle Physics," in *BAAS*, vol. 51, p. 194, May, 2019. 1903.06349.

[122] J. Vandenbroucke and M. Santander, "Multi-messenger and transient astrophysics with very-high-energy gamma rays," in *BAAS*, vol. 51, p. 553, May, 2019.

[123] J. Holder *et al.*, "Understanding the Origin and Impact of Relativistic Cosmic Particles with Very-High-Energy Gamma-rays," in *BAAS*, vol. 51, p. 267, May, 2019.

[124] R. Ojha *et al.*, "Neutrinos, Cosmic Rays, and the MeV Band," in *BAAS*, vol. 51, p. 431, May, 2019. 1903.05765.

[125] S. Ciprini, S. Buson, C. C. Cheung, and C. Pittori, "Gravitationally Lensed MeV Gamma-ray Blazars," in *BAAS*, vol. 51, p. 427, May, 2019.

[126] E. Burns *et al.*, "A Summary of Multimessenger Science with Neutron Star Mergers," in *BAAS*, vol. 51, p. 38, May, 2019. 1903.03582.

[127] V. Kalogera *et al.*, "The Yet-unobserved Multi-Messenger Gravitational-Wave Universe," in *BAAS*, vol. 51, p. 239, May, 2019. 1903.09224.

[128] K. E. Saavik Ford *et al.*, "AGN (and other) astrophysics with Gravitational Wave Events," in *BAAS*, vol. 51, p. 247, May, 2019. 1903.09529.

[129] P-ONE Collaboration, M. Agostini *et al.*, "The Pacific Ocean Neutrino Experiment," *Nature Astron.* **4** (2020) 913–915, 2005.09493.

[130] C. L. Carilli and S. Rawlings, "Science with the Square Kilometer Array: Motivation, key science projects, standards and assumptions," *New Astron. Rev.* **48** (2004) 979, astro-ph/0409274.

[131] Euclid Collaboration, R. Scaramella *et al.*, "Euclid preparation - I. The Euclid Wide Survey," *Astron. Astrophys.* **662** (2022) A112, 2108.01201.

[132] D. Spergel *et al.*, "Wide-Field InfrarRed Survey Telescope-Astrophysics Focused Telescope Assets WFIRST-AFTA 2015 Report," 1503.03757.

[133] LSST Collaboration, P. A. Abell *et al.*, "LSST Science Book, Version 2.0," 0912.0201.

[134] I. Sagiv *et al.*, "Science with a wide-field UV transient explorer," *Astron. J.* **147** (2014) 79, 1303.6194.

[135] S. R. Kulkarni *et al.*, "Science with the Ultraviolet Explorer (UVEX)," 2111.15608.

[136] W. Zhang *et al.* in *AAS/High Energy Astrophysics Division*, vol. 54 of *AAS/High Energy Astrophysics Division*, p. 108.45, Apr., 2022.

[137] eROSITA Collaboration, A. Merloni *et al.*, "eROSITA Science Book: Mapping the Structure of the Energetic Universe," 1209.3114.

[138] X. Barcons *et al.*, "Athena (Advanced Telescope for High ENergy Astrophysics) Assessment Study Report for ESA Cosmic Vision 2015-2025," 1207.2745.

[139] CTA Consortium Collaboration, B. S. Acharya *et al.*, *Science with the Cherenkov Telescope Array*. WSP, 11, 2018.

[140] Pierre Auger Collaboration, G. A. Anastasi, "AugerPrime: The Pierre Auger Observatory upgrade," *Nucl. Instrum. Meth. A* **1044** (2022) 167497.

[141] LIGO Scientific Collaboration, J. Aasi *et al.*, "Advanced LIGO," *Class. Quant. Grav.* **32** (2015) 074001, 1411.4547.

[142] VIRGO Collaboration, F. Acernese *et al.*, "Advanced Virgo: a second-generation interferometric gravitational wave detector," *Class. Quant. Grav.* **32** (2015) 024001, 1408.3978.

[143] KAGRA Collaboration, Y. Aso *et al.*, "Interferometer design of the KAGRA gravitational wave detector," *Phys. Rev. D* **88** (2013) 043007, 1306.6747.

[144] P. Amaro-Seoane *et al.*, "Laser Interferometer Space Antenna," *arXiv e-prints* (2017) arXiv:1702.00786, 1702.00786.

[145] M. Punturo *et al.*, "The Einstein Telescope: A third-generation gravitational wave observatory," *Class. Quant. Grav.* **27** (2010) 194002.

[146] LIGO Scientific Collaboration, B. P. Abbott *et al.*, "Exploring the Sensitivity of Next Generation Gravitational Wave Detectors," *Class. Quant. Grav.* **34** (2017) 044001, 1607.08697.

[147] T. DeYoung, "IceTray: A software framework for IceCube," in *14th International Conference on Computing in High-Energy and Nuclear Physics*, pp. 463–466, 2005.

[148] C. Glaser *et al.*, "NuRadioMC: Simulating the radio emission of neutrinos from interaction to detector," *Eur. Phys. J. C* **80** (2020) 77, 1906.01670.

[149] J. van Santen, B. A. Clark, R. Halliday, S. Hallmann, and A. Nelles, "toise: a framework to describe the performance of high-energy neutrino detectors," *JINST* **17** (2022) T08009, 2202.11120.

[150] IceCube Collaboration, M. Aartsen *et al.*, "PINGU: A Vision for Neutrino and Particle Physics at the South Pole," *J. Phys. G* **44** (2017) 054006, 1607.02671.

[151] A. Silvestri and S. W. Barwick, "Constraints on Extragalactic Point Source Flux from Diffuse Neutrino Limits," *Phys. Rev. D* **81** (2010) 023001, 0908.4266.

[152] IceCube Collaboration, M. Aartsen *et al.*, "Search for steady point-like sources in the astrophysical muon neutrino flux with 8 years of IceCube data," *Eur. Phys. J. C* **79** (2019) 234, 1811.07979.

[153] K. Murase and M. Fukugita, "Energetics of High-Energy Cosmic Radiations," *Phys. Rev. D* **99** (2019) 063012, 1806.04194.

[154] IceCube Collaboration, K. Meagher, "IceCube as a Neutrino Follow-up Observatory for Astronomical Transients," *PoS* **ICRC2017** (2018) 1007, 1710.01179.

[155] X. Rodrigues, S. Gao, A. Fedynitch, A. Palladino, and W. Winter, "Leptohadronic Blazar Models Applied to the 2014-2015 Flare of TXS 0506+056," *Astrophys. J.* **874** (2019) L29, 1812.05939.

[156] K. Mannheim, "The proton blazar," *Astron. Astrophys.* **269** (1993) 67–76, astro-ph/9302006.

[157] K. Mannheim, "High-energy neutrinos from extragalactic jets," *Astropart. Phys.* **3** (1995) 295–302.

[158] F. Halzen and E. Zas, "Neutrino Fluxes from Active Galaxies: A Model-Independent Estimate," *Astrophys. J.* **488** (1997) 669–674, astro-ph/9702193.

[159] M. Böttcher, "Progress in Multi-wavelength and Multi-Messenger Observations of Blazars and Theoretical Challenges," *Galaxies* **7** (2019) 20, 1901.04178.

[160] A. Reimer, M. Böttcher, and S. Postnikov, "Neutrino Emission in the Hadronic Synchrotron Mirror Model: The "Orphan" TeV Flare from 1ES 1959+650," *Astrophys. J.* **630** (2005) 186–190, astro-ph/0505233.

[161] A. Reimer, M. Böttcher, and S. Buson, "Cascading Constraints from Neutrino-emitting Blazars: The Case of TXS 0506+056," *Astrophys. J.* **881** (2019) 46, 1812.05654.

[162] A. Keivani *et al.*, "A Multimessenger Picture of the Flaring Blazar TXS 0506+056: Implications for High-energy Neutrino Emission and Cosmic-Ray Acceleration," *Astrophys. J.* **864** (2018) 84, 1807.04537.

[163] S. Ansoldi *et al.*, "The Blazar TXS 0506+056 Associated with a High-energy Neutrino: Insights into Extragalactic Jets and Cosmic-Ray Acceleration," *Astrophys. J.* **863** (2018) L10, 1807.04300.

[164] S. Gao, A. Fedynitch, W. Winter, and M. Pohl, "Modelling the coincident observation of a high-energy neutrino and a bright blazar flare," *Nature Astronomy* **3** (2019) 88–92, 1807.04275.

[165] Fermi-LAT Collaboration, S. Abdollahi *et al.*, "$Fermi$ Large Area Telescope Fourth Source Catalog," *Astrophys. J. Suppl.* **247** (2020) 33, 1902.10045.

[166] MAGIC Collaboration, V. A. Acciari *et al.*, "Constraints on gamma-ray and neutrino emission from NGC 1068 with the MAGIC telescopes," *Astrophys. J.* **883** (2019) 135, 1906.10954.

[167] Y. Inoue, D. Khangulyan, and A. Doi, "On the Origin of High-energy Neutrinos from NGC 1068: The Role of Nonthermal Coronal Activity," *Astrophys. J. Lett.* **891** (2020) L33, 1909.02239.

[168] J. Becker Tjus, B. Eichmann, F. Halzen, A. Kheirandish, and S. M. Saba, "High-energy neutrinos from radio galaxies," *Phys. Rev. D* **89** (2014) 123005, 1406.0506.

[169] O. Kalashev, D. Semikoz, and I. Tkachev, "Neutrinos in IceCube from active galactic nuclei," *Soviet Journal of Experimental and Theoretical Physics* **120** (2015) 541–548, 1410.8124.

[170] S. S. Kimura, K. Murase, and K. Toma, "Neutrino and Cosmic-Ray Emission and Cumulative Background from Radiatively Inefficient Accretion Flows in Low-luminosity Active Galactic Nuclei," *Astrophys. J.* **806** (2015) 159, 1411.3588.

[171] D. Biehl, D. Boncioli, C. Lunardini, and W. Winter, "Tidally disrupted stars as a possible origin of both cosmic rays and neutrinos at the highest energies," *Sci. Rep.* **8** (2018) 10828, 1711.03555.

[172] L. Dai and K. Fang, "Can tidal disruption events produce the IceCube neutrinos?," *Mon. Not. Roy. Astron. Soc.* **469** (2017) 1354–1359, 1612.00011.

[173] B. T. Zhang, K. Murase, F. Oikonomou, and Z. Li, "High-energy cosmic ray nuclei from tidal disruption events: Origin, survival, and implications," *Phys. Rev. D* **96** (2017) 063007, 1706.00391. [Addendum: Phys. Rev.D96,no.6,069902(2017)].

[174] C. Lunardini and W. Winter, "High Energy Neutrinos from the Tidal Disruption of Stars," *Phys. Rev. D* **95** (2017) 123001, 1612.03160.

[175] H. Sun, B. Zhang, and Z. Li, "Extragalactic High-energy Transients: Event Rate Densities and Luminosity Functions," *Astrophys. J.* **812** (2015) 33, 1509.01592.

[176] IceCube Collaboration, M. G. Aartsen *et al.*, "Extending the Search for Muon Neutrinos Coincident with Gamma-Ray Bursts in IceCube Data," *Astrophys. J.* **843** (2017) 112, 1702.06868.

[177] D. Biehl, D. Boncioli, A. Fedynitch, and W. Winter, "Cosmic ray and neutrino emission from gamma-ray bursts with a nuclear cascade," *Astron. Astrophys.* **611** (2018) A101, 1705.08909.

[178] P. Baerwald, M. Bustamante, and W. Winter, "UHECR escape mechanisms for protons and neutrons from GRBs, and the cosmic ray-neutrino connection," *Astrophys. J.* **768** (2013) 186, 1301.6163.

[179] P. Baerwald, M. Bustamante, and W. Winter, "Are gamma-ray bursts the sources of ultra-high energy cosmic rays?," *Astropart. Phys.* **62** (2015) 66–91, 1401.1820.

[180] N. Globus, D. Allard, R. Mochkovitch, and E. Parizot, "UHECR acceleration at GRB internal shocks," *Mon. Not. Roy. Astron. Soc.* **451** (2015) 751–790, 1409.1271.

[181] M. Bustamante, P. Baerwald, K. Murase, and W. Winter, "Neutrino and cosmic-ray emission from multiple internal shocks in gamma-ray bursts," *Nature Commun.* **6** (2015) 6783, 1409.2874.

[182] E. Waxman, "Cosmological gamma-ray bursts and the highest energy cosmic rays," *Phys. Rev. Lett.* **75** (1995) 386–389, astro-ph/9505082.

[183] E. Waxman and J. N. Bahcall, "High-energy neutrinos from cosmological gamma-ray burst fireballs," *Phys. Rev. Lett.* **78** (1997) 2292–2295, astro-ph/9701231.

[184] S. Hümmer, P. Baerwald, and W. Winter, "Neutrino Emission from Gamma-Ray Burst Fireballs, Revised," *Phys. Rev. Lett.* **108** (2012) 231101, 1112.1076.

[185] A. M. Beloborodov, "Collisional mechanism for gamma-ray burst emission," *Mon. Not. Roy. Astron. Soc.* **407** (2010) 1033–1047, 0907.0732.

[186] I. Bartos, A. M. Beloborodov, K. Hurley, and S. Márka, "Detection Prospects for GeV Neutrinos from Collisionally Heated Gamma-ray Bursts with IceCube/DeepCore," *Phys. Rev. Lett.* **110** (2013) 241101, 1301.4232.

[187] E. V. Derishev, V. V. Kocharovsky, and V. V. Kocharovsky, "The Neutron Component in Fireballs of Gamma-Ray Bursts: Dynamics and Observable Imprints," *Astrophys. J.* **521** (1999) 640–649.

[188] IceCube Collaboration, M. G. Aartsen *et al.*, "An All-sky Search for Three Flavors of Neutrinos from Gamma-ray Bursts with the IceCube Neutrino Observatory," *Astrophys. J.* **824** (2016) 115, 1601.06484.

[189] K. Murase, K. Ioka, S. Nagataki, and T. Nakamura, "High Energy Neutrinos and Cosmic-Rays from Low-Luminosity Gamma-Ray Bursts?," *Astrophys. J.* **651** (2006) L5–L8, astro-ph/0607104.

[190] K. Murase and K. Ioka, "TeV–PeV Neutrinos from Low-Power Gamma-Ray Burst Jets inside Stars," *Phys. Rev. Lett.* **111** (2013) 121102, 1306.2274.

[191] B. T. Zhang, K. Murase, S. S. Kimura, S. Horiuchi, and P. Meszaros, "Low-luminosity gamma-ray bursts as the sources of ultrahigh-energy cosmic ray nuclei," *Phys. Rev. D* **97** (2018) 083010, 1712.09984.

[192] P. Mészáros and E. Waxman, "TeV Neutrinos from Successful and Choked Gamma-Ray Bursts," *Phys. Rev. Lett.* **87** (2001) 171102, astro-ph/0103275.

[193] N. Senno, K. Murase, and P. Mészáros, "Choked jets and low-luminosity gamma-ray bursts as hidden neutrino sources," *Phys. Rev. D* **93** (2016) 083003, 1512.08513.

[194] M. Kowalski and A. Mohr, "Detecting neutrino-transients with optical follow-up observations," *Astropart. Phys.* **27** (2007) 533–538, astro-ph/0701618.

[195] A. Esmaili and K. Murase, "Constraining high-energy neutrinos from choked-jet supernovae with IceCube high-energy starting events," *JCAP* **12** (2018) 008, 1809.09610.

[196] IceCube Collaboration, M. G. Aartsen *et al.*, "The IceCube Realtime Alert System," *Astropart. Phys.* **92** (2017) 30–41, 1612.06028.

[197] B. J. Shappee *et al.*, "The Man Behind the Curtain: X-rays Drive the UV through NIR Variability in the 2013 AGN Outburst in NGC 2617," *Astrophys. J.* **788** (2014) 48, 1310.2241.

[198] E. C. Bellm *et al.*, "The Zwicky Transient Facility: System Overview, Performance, and First Results," *Publ. Astron. Soc. Pac.* **131** (2019) 018002.

[199] Pan-STARRS, IceCube Collaborations, E. Kankare *et al.*, "Search for transient optical counterparts to high-energy IceCube neutrinos with Pan-STARRS1," *Astron. Astrophys.* **626** (2019) A117, 1901.11080.

[200] J. Aasi *et al.*, "Advanced LIGO," *Classical and Quantum Gravity* **32** (2015) 074001, 1411.4547.

[201] F. Acernese *et al.*, "Advanced Virgo: a second-generation interferometric gravitational wave detector," *Classical and Quantum Gravity* **32** (2015) 024001, 1408.3978.

[202] S. S. Kimura, K. Murase, P. Mészáros, and K. Kiuchi, "High-energy Neutrino Emission from Short Gamma-Ray Bursts: Prospects for Coincident Detection with Gravitational Waves," *Astrophys. J. Lett.* **848** (2017) L4, 1708.07075.

[203] S. S. Kimura *et al.*, "Transejecta high-energy neutrino emission from binary neutron star mergers," *Phys. Rev. D* **98** (2018) 043020, 1805.11613.

[204] I. Bartos, B. Dasgupta, and S. Márka, "Probing the structure of jet-driven core-collapse supernova and long gamma-ray burst progenitors with high-energy neutrinos," *Phys. Rev. D* **86** (2012) 083007, 1206.0764.

[205] LIGO Scientific Collaboration, D. Shoemaker, "Gravitational wave astronomy with LIGO and similar detectors in the next decade," 1904.03187.

[206] V. Baibhav *et al.*, "Gravitational-wave detection rates for compact binaries formed in isolation: LIGO/Virgo O3 and beyond," *Phys. Rev. D* **100** (2019) 064060, 1906.04197.

[207] ANTARES, IceCube Collaborations, S. Adrián-Martínez *et al.*, "High-energy neutrino follow-up search of gravitational wave event GW150914 with ANTARES and IceCube," *Phys. Rev. D* **93** (2016) 122010, 1602.05411.

[208] ANTARES, IceCube Collaborations, A. Albert *et al.*, "Search for high-energy neutrinos from gravitational wave event GW151226 and candidate LVT151012 with ANTARES and IceCube," *Phys. Rev. D* **96** (2017) 022005, 1703.06298.

[209] ANTARES, IceCube, Pierre Auger Collaborations, A. Albert *et al.*, "Search for High-energy Neutrinos from Binary Neutron Star Merger GW170817 with ANTARES, IceCube, and the Pierre Auger Observatory," *Astrophys. J. Lett.* **850** (2017) L35, 1710.05839.

[210] IceCube, LIGO Scientific, VIRGO Collaborations, M. G. Aartsen *et al.*, "Multimessenger search for sources of gravitational waves and high-energy neutrinos: Initial results for LIGO-Virgo and IceCube," *Phys. Rev. D* **90** (2014) 102002, 1407.1042.

[211] ANTARES, IceCube, LIGO, Virgo Collaborations, A. Albert *et al.*, "Search for Multimessenger Sources of Gravitational Waves and High-energy Neutrinos with Advanced LIGO during Its First Observing Run, ANTARES, and IceCube," *Astrophys. J.* **870** (2019) 134, 1810.10693.

[212] B. Baret *et al.*, "Multimessenger science reach and analysis method for common sources of gravitational waves and high-energy neutrinos," *Phys. Rev. D* **85** (2012) 103004, 1112.1140.

[213] I. Bartos *et al.*, "Bayesian Multi-Messenger Search Method for Common Sources of Gravitational Waves and High-Energy Neutrinos," *Phys. Rev. D* **100** (2019) 083017, 1810.11467.

[214] S. Countryman *et al.*, "Low-Latency Algorithm for Multi-messenger Astrophysics (LLAMA) with Gravitational-Wave and High-Energy Neutrino Candidates," *arXiv e-prints* (2019) 1901.05486.

[215] IceCube Collaboration, M. Aartsen *et al.*, "IceCube Search for Neutrinos Coincident with Compact Binary Mergers from LIGO-Virgo's First Gravitational-Wave Transient Catalog," 2004.02910.

[216] K. Fang and B. D. Metzger, "High-energy Neutrinos from Millisecond Magnetars Formed from the Merger of Binary Neutron Stars," *Astrophys. J.* **849** (2017) 153, 1707.04263.

[217] L. Barsotti, L. McCuller, M. Evans, and P. Fritschel, "The A+ design curve," *LIGO-T1800042* (2018).

[218] LIGO Scientific Collaboration, "Instrument Science White Paper," *LIGO-T1900409* (2019). https://dcc.ligo.org/LIGO-T1900409/public.

[219] K. Scholberg, "Supernova Neutrino Detection," *Ann. Rev. Nucl. Part. Sci.* **62** (2012) 81–103, 1205.6003.

[220] H. A. Bethe and J. R. Wilson, "Revival of a stalled supernova shock by neutrino heating," *Astrophys. J.* **295** (1985) 14–23.

[221] H. T. Janka, "Conditions for shock revival by neutrino heating in core collapse supernovae," *Astron. Astrophys.* **368** (2001) 527, astro-ph/0008432.

[222] H. T. Janka, "Neutrino-driven Explosions," *Handbook of Supernovae, Springer* (2017) 1702.08825.

[223] T. Sukhbold, T. Ertl, S. E. Woosley, J. M. Brown, and H. T. Janka, "Core-Collapse Supernovae from 9 to 120 Solar Masses Based on Neutrino-powered Explosions," *Astrophys. J.* **821** (2016) 38, 1510.04643.

[224] IceCube Collaboration, R. Abbasi *et al.*, "IceCube Sensitivity for Low-Energy Neutrinos from Nearby Supernovae," *Astron. Astrophys.* **535** (2011) A109, 1108.0171. [Erratum: Astron. Astrophys.563,C1(2014)].

[225] C. J. Lozano Mariscal, "Sensitivity of multi-PMT optical modules to MeV supernova neutrinos in South Pole ice," in *Proceedings of XXVIII International Conference on Neutrino Physics and Astrophysics (Neutrino 2018)*, June, 2018.

[226] M. Ahlers, P. Mertsch, and S. Sarkar, "On cosmic ray acceleration in supernova remnants and the FERMI/PAMELA data," *Phys. Rev. D* **80** (2009) 123017, 0909.4060.

[227] F. Halzen and G. G. Raffelt, "Reconstructing the supernova bounce time with neutrinos in IceCube," *Phys. Rev. D* **80** (2009) 087301, 0908.2317.

[228] L. Hüdepohl *et al.*, "Neutrino Signal of Electron-Capture Supernovae from Core Collapse to Cooling," *Phys. Rev. Lett.* **104** (2010) 251101, 0912.0260.

[229] K. Nakazato *et al.*, "Supernova Neutrino Light Curves and Spectra for Various Progenitor Stars: From Core Collapse to Proto-neutron Star Cooling," *Astrophys. J. Suppl.* **205** (2013) 2, 1210.6841.

[230] A. Mirizzi *et al.*, "Supernova Neutrinos: Production, Oscillations and Detection," *Riv. Nuovo Cim.* **39** (2016) 1–112, 1508.00785.

[231] E. O'Connor and C. D. Ott, "The Progenitor Dependence of the Preexplosion Neutrino Emission in Core-Collapse Supernovae," *Astrophys. J.* **762** (2013) 126, 1207.1100.

[232] A. Schneider, L. Roberts, C. Ott, and E. O'connor, "Equation of state effects in the core collapse of a 20-$M_\odot$ star," *Phys. Rev. C* **100** (2019) 055802, 1906.02009.

[233] H. Yasin, S. Schäfer, A. Arcones, and A. Schwenk, "Equation of state effects in core-collapse supernovae," *Phys. Rev. Lett.* **124** (2020) 092701, 1812.02002.

[234] IceCube Collaboration, R. Cross, A. Fritz, and S. Griswold, "Eleven Year Search for Supernovae with the IceCube Neutrino Observatory," *PoS* **ICRC2019** (2020) 889, 1908.07249.

[235] IceCube Collaboration, L. Köpke, "Improved Detection of Supernovae with the IceCube Observatory," *J. Phys. Conf. Ser.* **1029** (2018) 012001, 1704.03823.

[236] K. Kotake *et al.*, "Multimessengers from core-collapse supernovae: multidimensionality as a key to bridge theory and observation," *Adv. Astron.* **2012** (2012) 428757, 1204.2330.

[237] K. Nakamura *et al.*, "Multi-messenger signals of long-term core-collapse supernova simulations : synergetic observation strategies," *Mon. Not. Roy. Astron. Soc.* **461** (2016) 3296–3313, 1602.03028.

[238] K. Kotake and T. Kuroda, "Gravitational waves from core-collapse supernovae," in *The Handbook of Supernovae* (A. W. Alsabti and P. Murdin, eds.), ch. 63, pp. 1671–1698. Springer, Cham, Switzerland, 2017.

[239] T. Lund, A. Marek, C. Lunardini, H.-T. Janka, and G. Raffelt, "Fast time variations of supernova neutrino fluxes and their detectability," *Phys. Rev. D* **82** (2010) 063007, 1006.1889.

[240] I. Tamborra, F. Hanke, B. Müller, H.-T. Janka, and G. Raffelt, "Neutrino signature of supernova hydrodynamical instabilities in three dimensions," *Phys. Rev. Lett.* **111** (2013) 121104, 1307.7936.

[241] B. Müller, "Neutrino Emission as Diagnostics of Core-Collapse Supernovae," *Ann. Rev. Nucl. Part. Sci.* **69** (2019) 253–278, 1904.11067.

[242] Z. Lin, C. Lunardini, M. Zanolin, K. Kotake, and C. Richardson, "Detectability of standing accretion shock instabilities activity in supernova neutrino signals," *Phys. Rev. D* **101** (2020) 123028, 1911.10656.

[243] T. Yokozawa *et al.*, "Probing the Rotation of Core-collapse Supernova With a Concurrent Analysis of Gravitational Waves and Neutrinos," *Astrophys. J.* **811** (2015) 86, 1410.2050.

[244] J. R. Westernacher-Schneider *et al.*, "Multimessenger Asteroseismology of Core-Collapse Supernovae," *Phys. Rev. D* **100** (2019) 123009, 1907.01138.

[245] P. Antonioli *et al.*, "SNEWS: The Supernova Early Warning System," *New J. Phys.* **6** (2004) 114, astro-ph/0406214.

[246] SNEWS Collaboration, S. Al Kharusi *et al.*, "SNEWS 2.0: a next-generation supernova early warning system for multi-messenger astronomy," *New J. Phys.* **23** (2021) 031201, 2011.00035.

[247] V. Brdar, M. Lindner, and X.-J. Xu, "Neutrino astronomy with supernova neutrinos," *JCAP* **04** (2018) 025, 1802.02577.

[248] N. Linzer and K. Scholberg, "Triangulation Pointing to Core-Collapse Supernovae with Next-Generation Neutrino Detectors," *Phys. Rev. D* **100** (2019) 103005, 1909.03151.

[249] A. Coleiro, M. Colomer Molla, D. Dornic, M. Lincetto, and V. Kulikovskiy, "Combining neutrino experimental light-curves for pointing to the next galactic core-collapse supernova," *Eur. Phys. J. C* **80** (2020) 856, 2003.04864.

[250] P. D. Serpico *et al.*, "Probing the neutrino mass hierarchy with the rise time of a supernova burst," *Phys. Rev. D* **85** (2012) 085031, 1111.4483.

[251] K. Scholberg, "Supernova Signatures of Neutrino Mass Ordering," *J. Phys. G* **45** (2018) 014002, 1707.06384.

[252] H. Duan, G. M. Fuller, and Y.-Z. Qian, "Collective Neutrino Oscillations," *Ann. Rev. Nucl. Part. Sci.* **60** (2010) 569–594, 1001.2799.

[253] H. Sasaki, T. Takiwaki, S. Kawagoe, S. Horiuchi, and K. Ishidoshiro, "Detectability of Collective Neutrino Oscillation Signatures in the Supernova Explosion of a 8.8 $M_\odot$ star," *Phys. Rev. D* **101** (2020) 063027, 1907.01002.

[254] S. Shalgar, I. Tamborra, and M. Bustamante, "Core-collapse supernovae stymie secret neutrino interactions," *Phys. Rev. D* **103** (2021) 123008, 1912.09115.

[255] I. Sagert, G. Fann, F. Fattoyev, S. Postnikov, and C. Horowitz, "Quantum simulations of nuclei and nuclear pasta with the multiresolution adaptive numerical environment for scientific simulations," *Phys. Rev. C* **93** (2016) 055801, 1509.06671.

[256] C. Horowitz *et al.*, "Nuclear pasta and supernova neutrinos at late times," *arXiv:1611.10226 [astro-ph.HE]* (2016) 1611.10226.

[257] A. Roggero, J. Margueron, L. F. Roberts, and S. Reddy, "Nuclear pasta in hot dense matter and its implications for neutrino scattering," *Phys. Rev. C* **97** (2018) 045804, 1710.10206.

[258] G. G. Raffelt and D. S. Dearborn, "Bounds on Hadronic Axions From Stellar Evolution," *Phys. Rev. D* **36** (1987) 2211.

[259] W. Keil *et al.*, "A Fresh look at axions and SN-1987A," *Phys. Rev. D* **56** (1997) 2419–2432, astro-ph/9612222.

[260] T. Fischer *et al.*, "Probing axions with the neutrino signal from the next galactic supernova," *Phys. Rev. D* **94** (2016) 085012, 1605.08780.

[261] L. Heurtier and Y. Zhang, "Supernova Constraints on Massive (Pseudo)Scalar Coupling to Neutrinos," *JCAP* **02** (2017) 042, 1609.05882.

[262] I. G. Irastorza and J. Redondo, "New experimental approaches in the search for axion-like particles," *Prog. Part. Nucl. Phys.* **102** (2018) 89–159, 1801.08127.

[263] P. Carenza *et al.*, "Improved axion emissivity from a supernova via nucleon-nucleon bremsstrahlung," *JCAP* **10** (2019) 016, 1906.11844. [Erratum: JCAP 05, E01 (2020)].

[264] R. Bollig, W. DeRocco, P. W. Graham, and H.-T. Janka, "Muons in supernovae: implications for the axion-muon coupling," *Phys. Rev. Lett.* **125** (2020) 051104, 2005.07141.

[265] L. Di Luzio, M. Giannotti, E. Nardi, and L. Visinelli, "The landscape of QCD axion models," *Phys. Rept.* **870** (2020) 1–117, 2003.01100.

[266] IceCube Collaboration, S. BenZvi, R. Cross, and T. Nguyen, "Estimating the Sensitivity of IceCube to Signatures of Axionlike Particle Production in a Galactic Supernova," *PoS* **ICRC2017** (2018) 892.

[267] J. W. Brockway, E. D. Carlson, and G. G. Raffelt, "SN1987A gamma-ray limits on the conversion of pseudoscalars," *Phys. Lett.* **B383** (1996) 439–443, astro-ph/9605197.

[268] A. Payez *et al.*, "Revisiting the SN1987A gamma-ray limit on ultralight axion-like particles," *JCAP* **1502** (2015) 006, 1410.3747.

[269] M. Meyer, M. Giannotti, A. Mirizzi, J. Conrad, and M. Sánchez-Conde, "Fermi Large Area Telescope as a Galactic Supernovae Axionscope," *Phys. Rev. Lett.* **118** (2017) 011103, 1609.02350.

[270] N. Bar, K. Blum, and G. D'Amico, "Is there a supernova bound on axions?," *Phys. Rev. D* **101** (2020) 123025, 1907.05020.

[271] S. Choubey, N. Harries, and G. Ross, "Probing neutrino oscillations from supernovae shock waves via the IceCube detector," *Phys. Rev. D* **74** (2006) 053010, hep-ph/0605255.

[272] G. G. Raffelt and S. Zhou, "Supernova bound on keV-mass sterile neutrinos reexamined," *Phys. Rev. D* **83** (2011) 093014, 1102.5124.

[273] C. A. Argüelles, V. Brdar, and J. Kopp, "Production of keV Sterile Neutrinos in Supernovae: New Constraints and Gamma Ray Observables," *Phys. Rev. D* **99** (2019) 043012, 1605.00654.

[274] T. Franarin, J. H. Davis, and M. Fairbairn, "Prospects for detecting eV-scale sterile neutrinos from a galactic supernova," *JCAP* **09** (2018) 002, 1712.03836.

[275] T. Kashti and E. Waxman, "Flavoring astrophysical neutrinos: Flavor ratios depend on energy," *Phys. Rev. Lett.* **95** (2005) 181101, astro-ph/0507599.

[276] P. Lipari, M. Lusignoli, and D. Meloni, "Flavor Composition and Energy Spectrum of Astrophysical Neutrinos," *Phys. Rev. D* **75** (2007) 123005, 0704.0718.

[277] M. Bustamante, J. F. Beacom, and W. Winter, "Theoretically palatable flavor combinations of astrophysical neutrinos," *Phys. Rev. Lett.* **115** (2015) 161302, 1506.02645.

[278] H. B. J. Koers and R. A. M. J. Wijers, "Enhanced high-energy neutrino emission from choked gamma-ray bursts due to meson and muon acceleration," *arXiv e-prints* (2007) 0711.4791.

[279] S. R. Klein, R. E. Mikkelsen, and J. Becker Tjus, "Muon Acceleration in Cosmic-ray Sources," *Astrophys. J.* **779** (2013) 106, 1208.2056.

[280] IceCube Collaboration, M. G. Aartsen *et al.*, "Flavor Ratio of Astrophysical Neutrinos above 35 TeV in IceCube," *Phys. Rev. Lett.* **114** (2015) 171102, 1502.03376.

[281] J. F. Beacom, N. F. Bell, D. Hooper, S. Pakvasa, and T. J. Weiler, "Measuring flavor ratios of high-energy astrophysical neutrinos," *Phys. Rev. D* **68** (2003) 093005, hep-ph/0307025. [Erratum: Phys. Rev. D 72, 019901 (2005)].

[282] M. Bustamante and M. Ahlers, "Inferring the flavor of high-energy astrophysical neutrinos at their sources," *Phys. Rev. Lett.* **122** (2019) 241101, 1901.10087.

[283] M. C. Gonzalez-Garcia, M. Maltoni, and T. Schwetz, "Updated fit to three neutrino mixing: status of leptonic CP violation," *JHEP* **11** (2014) 052, 1409.5439.

[284] IceCube Collaboration, J. Stachurska, "IceCube High Energy Starting Events at 7.5 Years – New Measurements of Flux and Flavor," *EPJ Web Conf.* **207** (2019) 02005, 1905.04237.

[285] A. Bhattacharya, R. Gandhi, W. Rodejohann, and A. Watanabe, "The Glashow resonance at IceCube: signatures, event rates and pp vs. $p\gamma$ interactions," *JCAP* **1110** (2011) 017, 1108.3163.

[286] D. Biehl, A. Fedynitch, A. Palladino, T. J. Weiler, and W. Winter, "Astrophysical neutrino production diagnostics with the Glashow resonance," *JCAP* **2017** (2017) 033, 1611.07983.

[287] W. Bednarek, G. F. Burgio, and T. Montaruli, "Galactic discrete sources of high energy neutrinos," *New Astron. Rev.* **49** (2005) 1, astro-ph/0404534.

[288] M. D. Kistler and J. F. Beacom, "Guaranteed and Prospective Galactic TeV Neutrino Sources," *Phys. Rev. D* **74** (2006) 063007, astro-ph/0607082.

[289] W. Baade and F. Zwicky, "Cosmic Rays from Super-novae," *Proceedings of the National Academy of Science* **20** (1934) 259–263.

[290] Fermi-LAT Collaboration, M. Ackermann *et al.*, "Detection of the Characteristic Pion-Decay Signature in Supernova Remnants," *Science* **339** (2013) 807, 1302.3307.

[291] L. O. Drury, F. A. Aharonian, and H. J. Volk, "The Gamma-ray visibility of supernova remnants: A Test of cosmic ray origin," *Astron. Astrophys.* **287** (1994) 959–971, astro-ph/9305037.

[292] T. K. Gaisser, R. J. Protheroe, and T. Stanev, "Gamma-ray production in supernova remnants," *Astrophys. J.* **492** (1998) 219, astro-ph/9609044.

[293] J. Alvarez-Muniz and F. Halzen, "Possible high-energy neutrinos from the cosmic accelerator RX J1713.7-3946," *Astrophys. J.* **576** (2002) L33–L36, astro-ph/0205408.

[294] M. L. Costantini and F. Vissani, "Expected neutrino signal from supernova remnant RX J1713.7-3946 and flavor oscillations," *Astropart. Phys.* **23** (2005) 477–485, astro-ph/0411761.

[295] R. J. Protheroe, W. Bednarek, and Q. Luo, "Gamma-rays and neutrinos from very young supernova remnants," *Astropart. Phys.* **9** (1998) 1–14, astro-ph/9703045.

[296] P. Blasi, R. I. Epstein, and A. V. Olinto, "Ultrahigh-energy cosmic rays from young neutron star winds," *Astrophys. J.* **533** (2000) L123, astro-ph/9912240.

[297] J. H. Beall and W. Bednarek, "Neutrinos from early phase, pulsar driven supernovae," *Astrophys. J.* **569** (2002) 343–348, astro-ph/0108447.

[298] K. Fang, K. Kotera, and A. V. Olinto, "Newly-born pulsars as sources of ultrahigh energy cosmic rays," *Astrophys. J.* **750** (2012) 118, 1201.5197.

[299] K. Fang, K. Kotera, and A. V. Olinto, "Ultrahigh Energy Cosmic Ray Nuclei from Extragalactic Pulsars and the effect of their Galactic counterparts," *JCAP* **1303** (2013) 010, 1302.4482.

[300] D. Guetta and E. Amato, "Neutrino flux predictions for galactic plerions," *Astropart. Phys.* **19** (2003) 403–407, astro-ph/0209537.

[301] E. Amato, D. Guetta, and P. Blasi, "Signatures of high energy protons in pulsar winds," *Astron. Astrophys.* **402** (2003) 827–836, astro-ph/0302121.

[302] W. Bednarek, "Production of neutrons, neutrinos and gamma-rays by a very fast pulsar in the galactic center region," *Mon. Not. Roy. Astron. Soc.* **331** (2002) 483, astro-ph/0112008.

[303] W. Bednarek, "Gamma-rays and cosmic-rays from a pulsar in cygnus ob2," *Mon. Not. Roy. Astron. Soc.* **345** (2003) 847, astro-ph/0307216.

[304] IceCube Collaboration, M. Aartsen *et al.*, "Search for PeV Gamma-Ray Emission from the Southern Hemisphere with 5 Years of Data from the IceCube Observatory," *Astrophys. J.* **891** (2019) 9, 1908.09918.

[305] LHAASO Collaboration, Z. Cao *et al.*, "Peta-electron volt gamma-ray emission from the Crab Nebula," *Science* **373** (2021) 425, 2111.06545.

[306] LHAASO Collaboration, Z. Cao *et al.*, "Ultrahigh-energy photons up to 1.4 petaelectronvolts from 12 γ-ray Galactic sources," *Nature* **594** (2021) 33–36.

[307] M. Ahlers and K. Murase, "Probing the Galactic Origin of the IceCube Excess with Gamma-Rays," *Phys. Rev. D* **90** (2014) 023010, 1309.4077.

[308] J. C. Joshi, W. Winter, and N. Gupta, "How Many of the Observed Neutrino Events Can Be Described by Cosmic Ray Interactions in the Milky Way?," *Mon. Not. Roy. Astron. Soc.* **439** (2014) 3414–3419, 1310.5123. [Erratum: Mon.Not.Roy.Astron.Soc. 446, 892 (2014)].

[309] M. Kachelrieß and S. Ostapchenko, "Neutrino yield from Galactic cosmic rays," *Phys. Rev. D* **90** (2014) 083002, 1405.3797.

[310] M. Ahlers, Y. Bai, V. Barger, and R. Lu, "Galactic neutrinos in the TeV to PeV range," *Phys. Rev. D* **93** (2016) 013009, 1505.03156.

[311] F. Casse, M. Lemoine, and G. Pelletier, "Transport of cosmic rays in chaotic magnetic fields," *Phys. Rev. D* **65** (2002) 023002, astro-ph/0109223.

[312] F. Effenberger, H. Fichtner, K. Scherer, and I. Busching, "Anisotropic diffusion of galactic cosmic ray protons and their steady-state azimuthal distribution," *Astron. Astrophys.* **547** (2012) A120, 1210.1423.

[313] D. Gaggero, L. Maccione, G. Di Bernardo, C. Evoli, and D. Grasso, "Three-Dimensional Model of Cosmic-Ray Lepton Propagation Reproduces Data from the Alpha Magnetic Spectrometer on the International Space Station," *Phys. Rev. Lett.* **111** (2013) 021102, 1304.6718.

[314] M. Werner, R. Kissmann, A. W. Strong, and O. Reimer, "Spiral Arms as Cosmic Ray Source Distributions," *Astropart. Phys.* **64** (2014) 18–33, 1410.5266.

[315] R. M. Crocker, F. Melia, and R. R. Volkas, "Neutrinos from the Galactic Center in the light of HESS," *Astrophys. J.* **622** (2005) L37–L40, astro-ph/0411471.

[316] J. Candia, "Detectable neutrino fluxes due to enhanced cosmic ray densities in the Galactic Center region," *JCAP* **0511** (2005) 002, astro-ph/0505346.

[317] A. Neronov, D. Semikoz, and C. Tchernin, "PeV neutrinos from interactions of cosmic rays with the interstellar medium in the Galaxy," *Phys. Rev. D* **89** (2014) 103002, 1307.2158.

[318] KASCADE Grande Collaboration, W. D. Apel *et al.*, "Kneelike structure in the spectrum of the heavy component of cosmic rays observed with KASCADE-Grande," *Phys. Rev. Lett.* **107** (2011) 171104, 1107.5885.

[319] Pierre Auger Collaboration, P. Abreu *et al.*, "The energy spectrum of cosmic rays beyond the turn-down around 10^{17} eV as measured with the surface detector of the Pierre Auger Observatory," *Eur. Phys. J. C* **81** (2021) 966, 2109.13400.

[320] IceCube Collaboration, K. Rawlins, "Cosmic Ray Spectrum and Composition from Three Years of IceTop and IceCube," *Phys. Atom. Nucl.* **83** (2020) 280–284.

[321] N. M. Budnev *et al.*, "The primary cosmic-ray energy spectrum measured with the Tunka-133 array," *Astropart. Phys.* **117** (2020) 102406, 2104.03599.

[322] Telescope Array Collaboration, R. U. Abbasi *et al.*, "The Cosmic-Ray Energy Spectrum between 2 PeV and 2 EeV Observed with the TALE detector in monocular mode," *Astrophys. J.* **865** (2018) 74, 1803.01288.

[323] Pierre Auger Collaboration, P. Abreu *et al.*, "Combined fit of the energy spectrum and mass composition across the ankle with the data measured at the Pierre Auger Observatory," *PoS* **ICRC2021** (2021) 311.

[324] Pierre Auger Collaboration, A. Aab *et al.*, "Combined fit of spectrum and composition data as measured by the Pierre Auger Observatory," *JCAP* **04** (2017) 038, 1612.07155. [Erratum: JCAP 03, E02 (2018)].

[325] S. Mollerach and E. Roulet, "Progress in high-energy cosmic ray physics," *Prog. Part. Nucl. Phys.* **98** (2018) 85–118, 1710.11155.

[326] A. Coleman *et al.*, "Ultra-High-Energy Cosmic Rays: The Intersection of the Cosmic and Energy Frontiers," 2205.05845.

[327] T. Huege, "Radio detection of cosmic ray air showers in the digital era," *Phys. Rept.* **620** (2016) 1–52, 1601.07426.

[328] F. G. Schröder, "Radio detection of Cosmic-Ray Air Showers and High-Energy Neutrinos," *Prog. Part. Nucl. Phys.* **93** (2017) 1–68, 1607.08781.

[329] KASCADE-Grande Collaboration, A. Chiavassa *et al.*, "A study of the first harmonic of the large scale anisotropies with the KASCADE-Grande experiment," *ICRC PoS* **34** (2015) 281.

[330] A. Aab *et al.*, "Cosmic-Ray Anisotropies in Right Ascension Measured by the Pierre Auger Observatory," *Astrophys. J.* **891** (2020) 142, 2002.06172.

[331] A. U. Abeysekara *et al.*, "Observation of anisotropy of tev cosmic rays with two years of hawc," *Astrophys. J.* **865** (2018) 57.

[332] V. V. Alekseenko *et al.*, "10-100 TeV cosmic ray anisotropy measured at the Baksan EAS Carpet array," *Nucl Phys B Proc Suppl.* **196** (2009) 179–182, 0902.2967.

[333] M. Aglietta *et al.*, "Evolution of the cosmic-ray anisotropy above 1014 ev," *Astrophys. J.* **692** (2009) L130–L133.

[334] M. Ambrosio and et al., "Search for the sidereal and solar diurnal modulations in the total MACRO muon data set," *Phys. Rev. D* **67** (2003) 042002, astro-ph/0211119.

[335] Super-Kamiokande Collaboration Collaboration, G. Guillian *et al.*, "Observation of the anisotropy of 10 tev primary cosmic ray nuclei flux with the super-kamiokande-i detector," *Phys. Rev. D* **75** (2007) 062003.

[336] A. A. Abdo *et al.*, "The large-scale cosmic-ray anisotropy as observed with milagro," *The Astrophysical Journal* **698** (2009) 2121.

[337] ARGO-YBJ Collaboration, B. Bartoli *et al.*, "Argo-ybj observation of the large-scale cosmic ray anisotropy during the solar minimum between cycles 23 and 24," *Astrophys. J.* **809** (2015) 90.

[338] B. Bartoli *et al.*, "Galactic cosmic-ray anisotropy in the northern hemisphere from the ARGO-YBJ experiment during 2008–2012," *Astrophys. J.* **861** (2018) 93.

[339] Tibet ASγ Collaboration, M. Amenomori *et al.*, "Large-scale sidereal anisotropy of galactic cosmic-ray intensity observed by the tibet air shower array," *Astrophys. J. Lett.* **626** (2005) L29.

[340] IceCube Collaboration, M. Aartsen *et al.*, "Observation of Cosmic Ray Anisotropy with the IceTop Air Shower Array," *Astrophys. J.* **765** (2013) 55, 1210.5278.

[341] M. G. Aartsen *et al.*, "Anisotropy in Cosmic-Ray Arrival Directions in the Southern Hemisphere Based on Six Years of Data from the IceCube Detector," *Astrophys. J.* **826** (2016) 220, 1603.01227.

[342] A. U. Abeysekara *et al.*, "All-sky measurement of the anisotropy of cosmic rays at 10 TeV and mapping of the local interstellar magnetic field," *Astrophys. J.* **871** (2019) 96.

[343] W. Gao *et al.*, "Observation of large-scale anisotropy in the arrival directions of cosmic rays with LHAASO," *PoS* **ICRC2021** (2021) 351.

[344] Pierre Auger Collaboration, A. Aab *et al.*, "Observation of a large-scale anisotropy in the arrival directions of cosmic rays above 8×10^{18} eV," *Science* **357** (2017) 1266–1270, 1709.07321.

[345] Pierre Auger Collaboration, A. Aab *et al.*, "Depth of maximum of air-shower profiles at the pierre auger observatory. ii. composition implications," *Phys. Rev. D* **90** (2014) 122006.

[346] Telescope Array Collaboration, R. U. Abbasi *et al.*, "Depth of ultra high energy cosmic ray induced air shower maxima measured by the telescope array black rock and long ridge fadc fluorescence detectors and surface array in hybrid mode," *The Astrophysical Journal* **858** (2018) 76.

[347] Pierre Auger Collaboration, A. Aab *et al.*, "Evidence for a mixed mass composition at the 'ankle' in the cosmic-ray spectrum," *Phys. Lett. B* **762** (2016) 288–295, 1609.08567.

[348] Pierre Auger Collaboration, A. Aab *et al.*, "Probing the origin of ultra-high-energy cosmic rays with neutrinos in the EeV energy range using the Pierre Auger Observatory," *JCAP* **1910** (2019) 022, 1906.07422.

[349] ANITA Collaboration, P. Gorham *et al.*, "Constraints on the ultrahigh-energy cosmic neutrino flux from the fourth flight of ANITA," *Phys. Rev. D* **99** (2019) 122001, 1902.04005.

[350] ARA Collaboration, P. Allison *et al.*, "Performance of two Askaryan Radio Array stations and first results in the search for ultrahigh energy neutrinos," *Phys. Rev. D* **93** (2016) 082003, 1507.08991.

[351] ARIANNA Collaboration, A. Anker *et al.*, "A search for cosmogenic neutrinos with the ARIANNA test bed using 4.5 years of data," *JCAP* **03** (2020) 053, 1909.00840.

[352] GRAND Collaboration, J. Álvarez Muñiz *et al.*, "The Giant Radio Array for Neutrino Detection (GRAND): Science and Design," *Sci. China Phys. Mech. Astron.* **63** (2020) 219501, 1810.09994.

[353] D. Hooper, A. Taylor, and S. Sarkar, "The Impact of heavy nuclei on the cosmogenic neutrino flux," *Astropart. Phys.* **23** (2005) 11–17, astro-ph/0407618.

[354] M. Ave, N. Busca, A. V. Olinto, A. A. Watson, and T. Yamamoto, "Cosmogenic neutrinos from ultra-high energy nuclei," *Astropart. Phys.* **23** (2005) 19–29, astro-ph/0409316.

[355] Pierre Auger Collaboration, A. Aab *et al.*, "Combined fit of spectrum and composition data as measured by the Pierre Auger Observatory," *JCAP* **04** (2017) 038, 1612.07155. [Erratum: JCAP 03, E02 (2018)].

[356] P. Padovani, M. Petropoulou, P. Giommi, and E. Resconi, "A simplified view of blazars: the neutrino background," *Mon. Not. Roy. Astron. Soc.* **452** (2015) 1877–1887, 1506.09135.

[357] M. S. Muzio, M. Unger, and G. R. Farrar, "Progress towards characterizing ultrahigh energy cosmic ray sources," *Phys. Rev. D* **100** (2019) 103008, 1906.06233.

[358] X. Rodrigues, J. Heinze, A. Palladino, A. van Vliet, and W. Winter, "Active Galactic Nuclei Jets as the Origin of Ultrahigh-Energy Cosmic Rays and Perspectives for the Detection of Astrophysical Source Neutrinos at EeV Energies," *Phys. Rev. Lett.* **126** (2021) 191101, 2003.08392.

[359] Telescope Array Collaboration, D. Bergman, "Telescope Array Combined Fit to Cosmic Ray Spectrum and Composition," *PoS* **ICRC2021** (2021) 338.

[360] IceCube Collaboration, R. Abbasi *et al.*, "The IceCube high-energy starting event sample: Description and flux characterization with 7.5 years of data," *Phys. Rev. D* **104** (2021) 022002, 2011.03545.

[361] M. S. Muzio, G. R. Farrar, and M. Unger, "Probing the environments surrounding ultrahigh energy cosmic ray accelerators and their implications for astrophysical neutrinos," *Phys. Rev. D* **105** (2022) 023022, 2108.05512.

[362] R. Abbasi *et al.*, "Improved Characterization of the Astrophysical Muon-Neutrino Flux with 9.5 Years of IceCube Data," 2111.10299.

[363] V. B. Valera, M. Bustamante, and C. Glaser, "Near-future discovery of the diffuse flux of ultra-high-energy cosmic neutrinos," 2210.03756.

[364] Pierre Auger Collaboration, A. Aab *et al.*, "Muons in Air Showers at the Pierre Auger Observatory: Mean Number in Highly Inclined Events," *Phys. Rev. D* **91** (2015) 032003, 1408.1421. [Erratum: Phys.Rev.D 91, 059901 (2015)].

[365] Pierre Auger Collaboration, A. Aab *et al.*, "Testing Hadronic Interactions at Ultrahigh Energies with Air Showers Measured by the Pierre Auger Observatory," *Phys. Rev. Lett.* **117** (2016) 192001, 1610.08509.

[366] EAS-MSU, IceCube, KASCADE-Grande, NEVOD-DECOR, Pierre Auger, SUGAR, Telescope Array, Yakutsk EAS Array Collaborations, H. P. Dembinski *et al.*, "Report on Tests and Measurements of Hadronic Interaction Properties with Air Showers," *EPJ Web Conf.* **210** (2019) 02004, 1902.08124.

[367] EAS-MSU, IceCube, KASCADE Grande, NEVOD-DECOR, Pierre Auger, SUGAR, Telescope Array, Yakutsk EAS Array Collaborations, L. Cazon, "Working Group Report on the Combined Analysis of Muon Density Measurements from Eight Air Shower Experiments," *PoS* **ICRC2019** (2020) 214, 2001.07508.

[368] EAS-MSU, IceCube, KASCADE-Grande, NEVOD-DECOR, Pierre Auger, SUGAR, Telescope Array, Yakutsk EAS Array Collaborations, D. Soldin, "Update on the Combined Analysis of Muon Measurements from Nine Air Shower Experiments," *PoS* **ICRC2021** (2021) 349, 2108.08341.

[369] J. Albrecht *et al.*, "The Muon Puzzle in cosmic-ray induced air showers and its connection to the Large Hadron Collider," *Astrophys. Space Sci.* **367** (2022) 27, 2105.06148.

[370] F. Riehn, R. Engel, A. Fedynitch, T. K. Gaisser, and T. Stanev, "Hadronic interaction model Sibyll 2.3d and extensive air showers," *Phys. Rev. D* **102** (2020) 063002, 1912.03300.

[371] IceCube Collaboration, R. Abbasi *et al.*, "Density of GeV muons in air showers measured with IceTop," *Phys. Rev. D* **106** (2022) 032010, 2201.12635.

[372] Pierre Auger Collaboration, A. Aab *et al.*, "Direct measurement of the muonic content of extensive air showers between 2×10^{17} and 2×10^{18} eV at the Pierre Auger Observatory," *Eur. Phys. J. C* **80** (2020) 751.

[373] IceCube Collaboration, S. De Ridder, E. Dvorak, and T. K. Gaisser, "Sensitivity of IceCube Cosmic-Ray measurements to the hadronic interaction models," *PoS* **ICRC2017** (2018) 319.

[374] IceCube Collaboration, S. Verpoest *et al.*, "Testing Hadronic Interaction Models with Cosmic Ray Measurements at the IceCube Neutrino Observatory," *PoS* **ICRC2021** (2021) 357, 2107.09387.

[375] IceCube Collaboration, M. G. Aartsen *et al.*, "Characterization of the Atmospheric Muon Flux in IceCube," *Astropart. Phys.* **78** (2016) 1–27, 1506.07981.

[376] IceCube Collaboration, T. Fuchs, "Development of a Machine Learning Based Analysis Chain for the Measurement of Atmospheric Muon Spectra with IceCube," in *25th European Cosmic Ray Symposium*, 1, 2017. 1701.04067.

[377] IceCube Collaboration, D. Soldin, "Atmospheric Muons Measured with IceCube," *EPJ Web Conf.* **208** (2019) 08007, 1811.03651.

[378] M. Bustamante and A. Connolly, "Extracting the Energy-Dependent Neutrino-Nucleon Cross Section Above 10 TeV Using IceCube Showers," *Phys. Rev. Lett.* **122** (2019) 041101, 1711.11043.

[379] V. Berezinsky and A. Y. Smirnov, "Astrophysical upper bounds on neutrino-nucleon cross-section at energy $E \geq 3 \times 10^{17}$ eV," *Phys.Lett.* **B48** (1974) 269–272.

[380] D. Hooper, "Measuring high-energy neutrino nucleon cross-sections with future neutrino telescopes," *Phys. Rev. D* **65** (2002) 097303, hep-ph/0203239.

[381] S. Hussain, D. Marfatia, D. W. McKay, and D. Seckel, "Cross section dependence of event rates at neutrino telescopes," *Phys. Rev. Lett.* **97** (2006) 161101, hep-ph/0606246.

[382] E. Borriello *et al.*, "Disentangling neutrino-nucleon cross section and high energy neutrino flux with a km^3 neutrino telescope," *Phys. Rev. D* **77** (2008) 045019, 0711.0152.

[383] S. Hussain, D. Marfatia, and D. W. McKay, "Upward shower rates at neutrino telescopes directly determine the neutrino flux," *Phys. Rev. D* **77** (2008) 107304, 0711.4374.

[384] J. M. Conrad, M. H. Shaevitz, and T. Bolton, "Precision measurements with high-energy neutrino beams," *Rev. Mod. Phys.* **70** (1998) 1341, hep-ex/9707015.

[385] J. A. Formaggio and G. P. Zeller, "From eV to EeV: Neutrino Cross Sections Across Energy Scales," *Rev. Mod. Phys.* **84** (2012) 1307, 1305.7513.

[386] Particle Data Group , M. Tanabashi *et al.*, "Review of Particle Physics," *Phys. Rev. D* **98** (2018) 030001.

[387] A. Cooper-Sarkar, P. Mertsch, and S. Sarkar, "The high energy neutrino cross-section in the Standard Model and its uncertainty," *JHEP* **08** (2011) 042, 1106.3723.

[388] A. Kusenko and T. J. Weiler, "Neutrino cross-sections at high-energies and the future observations of ultrahigh-energy cosmic rays," *Phys. Rev. Lett.* **88** (2002) 161101, hep-ph/0106071.

[389] J. Alvarez-Muniz, F. Halzen, T. Han, and D. Hooper, "Phenomenology of high-energy neutrinos in low scale quantum gravity models," *Phys. Rev. Lett.* **88** (2002) 021301, hep-ph/0107057.

[390] L. A. Anchordoqui, J. L. Feng, H. Goldberg, and A. D. Shapere, "Black holes from cosmic rays: Probes of extra dimensions and new limits on TeV scale gravity," *Phys. Rev. D* **65** (2002) 124027, hep-ph/0112247.

[391] F. Cornet, J. I. Illana, and M. Masip, "TeV strings and the neutrino nucleon cross-section at ultrahigh-energies," *Phys. Rev. Lett.* **86** (2001) 4235, hep-ph/0102065.

[392] M. Kowalski, A. Ringwald, and H. Tu, "Black holes at neutrino telescopes," *Phys.Lett.* **B529** (2002) 1–9, hep-ph/0201139.

[393] J. Alvarez-Muniz, J. L. Feng, F. Halzen, T. Han, and D. Hooper, "Detecting microscopic black holes with neutrino telescopes," *Phys. Rev. D* **65** (2002) 124015, hep-ph/0202081.

[394] L. A. Anchordoqui, J. L. Feng, and H. Goldberg, "Particle physics on ice: Constraints on neutrino interactions far above the weak scale," *Phys. Rev. Lett.* **96** (2006) 021101, hep-ph/0504228.

[395] D. Marfatia, D. W. McKay, and T. J. Weiler, "New physics with ultra-high-energy neutrinos," *Phys. Lett. B* **748** (2015) 113, 1502.06337.

[396] J. Ellis, K. Sakurai, and M. Spannowsky, "Search for Sphalerons: IceCube vs. LHC," *JHEP* **05** (2016) 085, 1603.06573.

[397] E. M. Henley and J. Jalilian-Marian, "Ultra-high energy neutrino-nucleon scattering and parton distributions at small x," *Phys. Rev. D* **73** (2006) 094004, hep-ph/0512220.

[398] N. Armesto, C. Merino, G. Parente, and E. Zas, "Charged current neutrino cross-section and tau energy loss at ultra-high energies," *Phys. Rev. D* **77** (2008) 013001, 0709.4461.

[399] A. Yu. Illarionov, B. A. Kniehl, and A. V. Kotikov, "Ultrahigh-energy neutrino-nucleon deep-inelastic scattering and the Froissart bound," *Phys. Rev. Lett.* **106** (2011) 231802, 1105.2829.

[400] I. Romero and O. A. Sampayo, "Leptoquarks signals in KM**3 neutrino telescopes," *JHEP* **05** (2009) 111, 0906.5245.

[401] S. R. Klein and A. Connolly, "Neutrino Absorption in the Earth, Neutrino Cross-Sections, and New Physics," in *Proceedings, Community Summer Study 2013: Snowmass on the Mississippi (CSS2013): Minneapolis, MN, USA, July 29-August 6, 2013*, 2013. 1304.4891.

[402] B. Dutta, Y. Gao, T. Li, C. Rott, and L. E. Strigari, "Leptoquark implication from the CMS and IceCube experiments," *Phys. Rev. D* **91** (2015) 125015, 1505.00028.

[403] S. R. Klein, *Probing high-energy interactions of atmospheric and astrophysical neutrinos*, ch. 4, pp. 75–107. World Scientific. ISBN: 978-981-3275-01-0, 2020. 1906.02221.

[404] V. Bertone, R. Gauld, and J. Rojo, "Neutrino Telescopes as QCD Microscopes," *JHEP* **01** (2019) 217, 1808.02034.

[405] A. Connolly, R. S. Thorne, and D. Waters, "Calculation of High Energy Neutrino-Nucleon Cross Sections and Uncertainties Using the MSTW Parton Distribution Functions and Implications for Future Experiments," *Phys. Rev. D* **83** (2011) 113009, 1102.0691.

[406] FASER Collaboration, H. Abreu *et al.*, "Technical Proposal: FASERnu," 2001.03073.

[407] V. B. Valera, M. Bustamante, and C. Glaser, "The ultra-high-energy neutrino-nucleon cross section: measurement forecasts for an era of cosmic EeV-neutrino discovery," 2204.04237.

[408] D. Seckel, "Neutrino photon reactions in astrophysics and cosmology," *Phys. Rev. Lett.* **80** (1998) 900–903, hep-ph/9709290.

[409] S. R. Klein, S. A. Robertson, and R. Vogt, "Nuclear effects in high-energy neutrino interactions," *Phys. Rev. C* **102** (2020) 015808, 2001.03677.

[410] N. Song, S. W. Li, C. A. Argüelles, M. Bustamante, and A. C. Vincent, "The Future of High-Energy Astrophysical Neutrino Flavor Measurements," *JCAP* **04** (2021) 054, 2012.12893.

[411] C. A. Argüelles, T. Katori, and J. Salvado, "New Physics in Astrophysical Neutrino Flavor," *Phys. Rev. Lett.* **115** (2015) 161303, 1506.02043.

[412] R. W. Rasmussen, L. Lechner, M. Ackermann, M. Kowalski, and W. Winter, "Astrophysical neutrinos flavored with Beyond the Standard Model physics," *Phys. Rev. D* **96** (2017) 083018, 1707.07684.

[413] J. G. Learned and S. Pakvasa, "Detecting tau-neutrino oscillations at PeV energies," *Astropart. Phys.* **3** (1995) 267–274, hep-ph/9405296.

[414] S. Pakvasa, W. Rodejohann, and T. J. Weiler, "Flavor Ratios of Astrophysical Neutrinos: Implications for Precision Measurements," *JHEP* **02** (2008) 005, 0711.4517.

[415] M. Bustamante, A. M. Gago, and J. Jones Perez, "SUSY Renormalization Group Effects in Ultra High Energy Neutrinos," *JHEP* **05** (2011) 133, 1012.2728.

[416] M. Bustamante, A. M. Gago, and C. Pena-Garay, "Energy-independent new physics in the flavour ratios of high-energy astrophysical neutrinos," *JHEP* **04** (2010) 066, 1001.4878.

[417] P. Mehta and W. Winter, "Interplay of energy dependent astrophysical neutrino flavor ratios and new physics effects," *JCAP* **1103** (2011) 041, 1101.2673.

[418] I. M. Shoemaker and K. Murase, "Probing BSM Neutrino Physics with Flavor and Spectral Distortions: Prospects for Future High-Energy Neutrino Telescopes," *Phys. Rev. D* **93** (2016) 085004, 1512.07228.

[419] M. C. Gonzalez-Garcia, M. Maltoni, I. Martinez-Soler, and N. Song, "Non-standard neutrino interactions in the Earth and the flavor of astrophysical neutrinos," *Astropart. Phys.* **84** (2016) 15–22, 1605.08055.

[420] M. Ahlers, M. Bustamante, and S. Mu, "Unitarity Bounds of Astrophysical Neutrinos," *Phys. Rev. D* **98** (2018) 123023, 1810.00893.

[421] M. Bustamante and S. K. Agarwalla, "Universe's Worth of Electrons to Probe Long-Range Interactions of High-Energy Astrophysical Neutrinos," *Phys. Rev. Lett.* **122** (2019) 061103, 1808.02042.

[422] P. Coloma, P. A. N. Machado, I. Martinez-Soler, and I. M. Shoemaker, "Double-Cascade Events from New Physics in Icecube," *Phys. Rev. Lett.* **119** (2017) 201804, 1707.08573.

[423] E. Bertuzzo, S. Jana, P. A. N. Machado, and R. Zukanovich Funchal, "Dark Neutrino Portal to Explain MiniBooNE excess," *Phys. Rev. Lett.* **121** (2018) 241801, 1807.09877.

[424] E. Bertuzzo, S. Jana, P. A. Machado, and R. Zukanovich Funchal, "Neutrino Masses and Mixings Dynamically Generated by a Light Dark Sector," *Phys. Lett. B* **791** (2019) 210–214, 1808.02500.

[425] P. Ballett, S. Pascoli, and M. Ross-Lonergan, "U(1)' mediated decays of heavy sterile neutrinos in MiniBooNE," *Phys. Rev. D* **99** (2019) 071701, 1808.02915.

[426] S.-F. Ge, M. Lindner, and W. Rodejohann, "Atmospheric Trident Production for Probing New Physics," *Phys. Lett. B* **772** (2017) 164–168, 1702.02617.

[427] B. Zhou and J. F. Beacom, "Neutrino-nucleus cross sections for W-boson and trident production," *Phys. Rev. D* **101** (2020) 036011, 1910.08090.

[428] B. Zhou and J. F. Beacom, "W -boson and trident production in TeV–PeV neutrino observatories," *Phys. Rev. D* **101** (2020) 036010, 1910.10720.

[429] J. F. Beacom, N. F. Bell, D. Hooper, S. Pakvasa, and T. J. Weiler, "Decay of high-energy astrophysical neutrinos," *Phys. Rev. Lett.* **90** (2003) 181301, hep-ph/0211305.

[430] P. Baerwald, M. Bustamante, and W. Winter, "Neutrino Decays over Cosmological Distances and the Implications for Neutrino Telescopes," *JCAP* **1210** (2012) 020, 1208.4600.

[431] M. Bustamante, J. F. Beacom, and K. Murase, "Testing decay of astrophysical neutrinos with incomplete information," *Phys. Rev. D* **95** (2017) 063013, 1610.02096.

[432] P. B. Denton and I. Tamborra, "Invisible Neutrino Decay Could Resolve IceCube's Track and Cascade Tension," *Phys. Rev. Lett.* **121** (2018) 121802, 1805.05950.

[433] M. Bustamante, "New limits on neutrino decay from the Glashow resonance of high-energy cosmic neutrinos," *arXiv e-prints* (2020) 2004.06844.

[434] A. Abdullahi and P. B. Denton, "Visible Decay of Astrophysical Neutrinos at IceCube," *Phys. Rev. D* **102** (2020) 023018, 2005.07200.

[435] MiniBooNE Collaboration, A. A. Aguilar-Arevalo *et al.*, "Significant Excess of ElectronLike Events in the MiniBooNE Short-Baseline Neutrino Experiment," *Phys. Rev. Lett.* **121** (2018) 221801, 1805.12028.

[436] S. Parke and M. Ross-Lonergan, "Unitarity and the three flavor neutrino mixing matrix," *Phys. Rev. D* **93** (2016) 113009, 1508.05095.

[437] V. Brdar, J. Kopp, and X.-P. Wang, "Sterile Neutrinos and Flavor Ratios in IceCube," *JCAP* **1701** (2017) 026, 1611.04598.

[438] C. A. Argüelles *et al.*, "Sterile neutrinos in astrophysical neutrino flavor," *JCAP* **02** (2020) 015, 1909.05341.

[439] D. Colladay and V. A. Kostelecky, "Lorentz violating extension of the Standard Model," *Phys. Rev. D* **58** (1998) 116002, hep-ph/9809521.

[440] V. A. Kostelecky and M. Mewes, "Lorentz and CPT violation in neutrinos," *Phys. Rev. D* **69** (2004) 016005, hep-ph/0309025.

[441] D. Hooper, D. Morgan, and E. Winstanley, "Lorentz and CPT invariance violation in high-energy neutrinos," *Phys. Rev. D* **72** (2005) 065009, hep-ph/0506091.

[442] V. A. Kostelecky and N. Russell, "Data Tables for Lorentz and CPT Violation," *Rev. Mod. Phys.* **83** (2011) 11, 0801.0287.

[443] A. Kostelecky and M. Mewes, "Neutrinos with Lorentz-violating operators of arbitrary dimension," *Phys. Rev. D* **85** (2012) 096005, 1112.6395.

[444] P. W. Gorham *et al.*, "Implications of ultra-high energy neutrino flux constraints for Lorentz-invariance violating cosmogenic neutrinos," *Phys. Rev. D* **86** (2012) 103006, 1207.6425.

[445] E. Borriello, S. Chakraborty, A. Mirizzi, and P. D. Serpico, "Stringent constraint on neutrino Lorentz-invariance violation from the two IceCube PeV neutrinos," *Phys. Rev. D* **87** (2013) 116009, 1303.5843.

[446] F. W. Stecker and S. T. Scully, "Propagation of Superluminal PeV IceCube Neutrinos: A High Energy Spectral Cutoff or New Constraints on Lorentz Invariance Violation," *Phys. Rev. D* **90** (2014) 043012, 1404.7025.

[447] L. A. Anchordoqui *et al.*, "End of the cosmic neutrino energy spectrum," *Phys. Lett. B* **739** (2014) 99, 1404.0622.

[448] G. Tomar, S. Mohanty, and S. Pakvasa, "Lorentz Invariance Violation and IceCube Neutrino Events," *JHEP* **11** (2015) 022, 1507.03193.

[449] G. Amelino-Camelia, D. Guetta, and T. Piran, "Icecube Neutrinos and Lorentz Invariance Violation," *Astrophys. J.* **806** (2015) 269.

[450] J. Liao and D. Marfatia, "IceCube's astrophysical neutrino energy spectrum from CPT violation," *Phys. Rev. D* **97** (2018) 041302, 1711.09266.

[451] L. A. Anchordoqui, C. A. Garcia Canal, H. Goldberg, D. Gomez Dumm, and F. Halzen, "Probing leptoquark production at IceCube," *Phys. Rev. D* **74** (2006) 125021, hep-ph/0609214.

[452] G. Amelino-Camelia, J. R. Ellis, N. E. Mavromatos, D. V. Nanopoulos, and S. Sarkar, "Tests of quantum gravity from observations of gamma-ray bursts," *Nature* **393** (1998) 763, astro-ph/9712103.

[453] M. C. Gonzalez-Garcia, F. Halzen, and M. Maltoni, "Physics reach of high-energy and high-statistics icecube atmospheric neutrino data," *Phys. Rev. D* **71** (2005) 093010, hep-ph/0502223.

[454] L. A. Anchordoqui *et al.*, "Probing Planck scale physics with IceCube," *Phys. Rev. D* **72** (2005) 065019, hep-ph/0506168.

[455] J. L. Bazo, M. Bustamante, A. M. Gago, and O. G. Miranda, "High energy astrophysical neutrino flux and modified dispersion relations," *Int. J. Mod. Phys. A* **24** (2009) 5819, 0907.1979.

[456] J. S. Diaz, A. Kostelecky, and M. Mewes, "Testing Relativity with High-Energy Astrophysical Neutrinos," *Phys. Rev. D* **89** (2014) 043005, 1308.6344.

[457] F. W. Stecker, S. T. Scully, S. Liberati, and D. Mattingly, "Searching for Traces of Planck-Scale Physics with High Energy Neutrinos," *Phys. Rev. D* **91** (2015) 045009, 1411.5889.

[458] J. Ellis, N. E. Mavromatos, A. S. Sakharov, and E. K. Sarkisyan-Grinbaum, "Limits on Neutrino Lorentz Violation from Multimessenger Observations of TXS 0506+056," *Phys. Lett.* **B789** (2019) 352–355, 1807.05155.

[459] R. Laha, "Constraints on neutrino speed, weak equivalence principle violation, Lorentz invariance violation, and dual lensing from the first high-energy astrophysical neutrino source TXS 0506+056," *Phys. Rev. D* **100** (2019) 103002, 1807.05621.

[460] Z.-Y. Wang, R.-Y. Liu, and X.-Y. Wang, "Testing the equivalence principle and Lorentz invariance with PeV neutrinos from blazar flares," *Phys. Rev. Lett.* **116** (2016) 151101, 1602.06805.

[461] V. A. Kostelecky and M. Mewes, "Lorentz and CPT violation in the neutrino sector," *Phys. Rev. D* **70** (2004) 031902, hep-ph/0308300.

[462] C. A. Argüelles, A. Kheirandish, and A. C. Vincent, "Imaging Galactic Dark Matter with High-Energy Cosmic Neutrinos," *Phys. Rev. Lett.* **119** (2017) 201801, 1703.00451.

[463] F. Capozzi, I. M. Shoemaker, and L. Vecchi, "Neutrino Oscillations in Dark Backgrounds," *JCAP* **1807** (2018) 004, 1804.05117.

[464] Y. Farzan and S. Palomares-Ruiz, "Flavor of cosmic neutrinos preserved by ultralight dark matter," *Phys. Rev. D* **99** (2019) 051702, 1810.00892.

[465] S. Pandey, S. Karmakar, and S. Rakshit, "Interactions of Astrophysical Neutrinos with Dark Matter: A model building perspective," *JHEP* **01** (2019) 095, 1810.04203.

[466] J. Alvey and M. Fairbairn, "Linking Scalar Dark Matter and Neutrino Masses with IceCube 170922A," *JCAP* **07** (2019) 041, 1902.01450.

[467] S. Koren, "Neutrino – Dark Matter Scattering and Coincident Detections of UHE Neutrinos with EM Sources," *JCAP* **09** (2019) 013, 1903.05096.

[468] K.-Y. Choi, J. Kim, and C. Rott, "Constraining dark matter-neutrino interactions with IceCube-170922A," *Phys. Rev. D* **99** (2019) 083018, 1903.03302.

[469] N. Klop and S. Ando, "Effects of a neutrino-dark energy coupling on oscillations of high-energy neutrinos," *Phys. Rev. D* **97** (2018) 063006, 1712.05413.

[470] X. He, G. C. Joshi, H. Lew, and R. Volkas, "NEW Z-prime PHENOMENOLOGY," *Phys. Rev. D* **43** (1991) 22–24.

[471] X.-G. He, G. C. Joshi, H. Lew, and R. Volkas, "Simplest Z-prime model," *Phys. Rev. D* **44** (1991) 2118–2132.

[472] R. Foot, X. He, H. Lew, and R. Volkas, "Model for a light Z-prime boson," *Phys. Rev. D* **50** (1994) 4571–4580, hep-ph/9401250.

[473] K. C. Y. Ng and J. F. Beacom, "Cosmic neutrino cascades from secret neutrino interactions," *Phys. Rev. D* **90** (2014) 065035, 1404.2288. [Erratum: Phys. Rev. D 90, 089904 (2014)].

[474] K. Ioka and K. Murase, "IceCube PeV–EeV neutrinos and secret interactions of neutrinos," *PTEP* **2014** (2014) 061E01, 1404.2279.

[475] M. Ibe and K. Kaneta, "Cosmic neutrino background absorption line in the neutrino spectrum at IceCube," *Phys. Rev. D* **90** (2014) 053011, 1407.2848.

[476] A. Kamada and H.-B. Yu, "Coherent Propagation of PeV Neutrinos and the Dip in the Neutrino Spectrum at IceCube," *Phys. Rev. D* **92** (2015) 113004, 1504.00711.

[477] A. DiFranzo and D. Hooper, "Searching for MeV-Scale Gauge Bosons with IceCube," *Phys. Rev. D* **92** (2015) 095007, 1507.03015.

[478] K. Murase and I. M. Shoemaker, "Neutrino Echoes from Multimessenger Transient Sources," *Phys. Rev. Lett.* **123** (2019) 241102, 1903.08607.

[479] K. J. Kelly and P. A. N. Machado, "Multimessenger Astronomy and New Neutrino Physics," *JCAP* **1810** (2018) 048, 1808.02889.

[480] M. Bustamante, C. A. Rosenstroem, S. Shalgar, and I. Tamborra, "Bounds on secret neutrino interactions from high-energy astrophysical neutrinos," *Phys. Rev. D* **101** (2020) 123024, 2001.04994.

[481] C. P. de los Heros, "The Quest for Dark Matter with Neutrino Telescopes," in *in Neutrino Astronomy, T. Gaisser and A. Karle, eds. Chapter 11.*, pp. 155–171. World Scientific, 2017. 1511.03500.

[482] D. J. H. Chung, P. Crotty, E. W. Kolb, and A. Riotto, "On the Gravitational Production of Superheavy Dark Matter," *Phys. Rev. D* **64** (2001) 043503, hep-ph/0104100.

[483] D. J. H. Chung, E. W. Kolb, and A. Riotto, "Superheavy dark matter," *Phys. Rev. D* **59** (1999) 023501, hep-ph/9802238.

[484] D. J. H. Chung, E. W. Kolb, and A. Riotto, "Nonthermal supermassive dark matter," *Phys. Rev. Lett.* **81** (1998) 4048–4051, hep-ph/9805473.

[485] I. V. Moskalenko, T. A. Porter, and A. W. Strong, "Attenuation of VHE gamma rays by the Milky Way interstellar radiation field," *Astrophys. J.* **640** (2006) L155–L158, astro-ph/0511149.

[486] IceCube Collaboration, M. G. Aartsen *et al.*, "Search for neutrinos from decaying dark matter with IceCube," *Eur. Phys. J.* **C78** (2018) 831, 1804.03848.

[487] M. Pospelov, A. Ritz, and M. B. Voloshin, "Secluded WIMP Dark Matter," *Phys. Lett. B* **662** (2008) 53–61, 0711.4866.

[488] R. K. Leane, K. C. Y. Ng, and J. F. Beacom, "Powerful Solar Signatures of Long-Lived Dark Mediators," *Phys. Rev. D* **95** (2017) 123016, 1703.04629.

[489] M. Ardid, I. Felis, A. Herrero, and J. A. Martìnez-Mora, "Constraining Secluded Dark Matter models with the public data from the 79-string IceCube search for dark matter in the Sun," *JCAP* **1704** (2017) 010, 1701.08863.

[490] IceCube Collaboration, M. G. Aartsen *et al.*, "Searches for Relativistic Magnetic Monopoles in IceCube," *Eur. Phys. J.* **C76** (2016) 133, 1511.01350.

[491] S. Kopper, *Search for Exotic Double Tracks with the IceCube Neutrino Telescope*. PhD thesis, Wuppertal U., 2016.

[492] L. A. Anchordoqui, M. M. Glenz, and L. Parker, "Black Holes at IceCube Neutrino Telescope," *Phys. Rev. D* **75** (2007) 024011, hep-ph/0610359.

[493] J. I. Illana and M. Masip, *TeV Gravity Searches*, pp. 267–291. World Scientific, 2020. 2001.05195.

[494] J. I. Illana, M. Ahlers, M. Masip, and D. Meloni, "Exotic physics with ultrahigh energy cosmic rays," *Acta Phys.Polon.* **B38** (2007) 3357–3364, 0710.0584.

[495] J. Illana, M. Masip, and D. Meloni, "TeV gravity at neutrino telescopes," *Phys. Rev. D* **72** (2005) 024003, hep-ph/0504234.

[496] I. F. Albuquerque, G. Burdman, and Z. Chacko, "Direct detection of supersymmetric particles in neutrino telescopes," *Phys. Rev. D* **75** (2007) 035006, hep-ph/0605120.

[497] M. M. Reynoso and O. A. Sampayo, "New physics with IceCube," *Phys. Rev. D* **76** (2007) 033003, hep-ph/0703076.

[498] I. F. Albuquerque and S. R. Klein, "Supersymmetric and Kaluza-Klein Particles Multiple Scattering in the Earth," *Phys. Rev. D* **80** (2009) 015015, 0905.3180.

[499] S. Schonert, T. K. Gaisser, E. Resconi, and O. Schulz, "Vetoing atmospheric neutrinos in a high energy neutrino telescope," *Phys. Rev. D* **79** (2009) 043009, 0812.4308.

[500] T. K. Gaisser, K. Jero, A. Karle, and J. van Santen, "Generalized self-veto probability for atmospheric neutrinos," *Phys. Rev. D* **90** (2014) 023009, 1405.0525.

[501] IceCube Collaboration, M. Aartsen *et al.*, "Measurement of South Pole ice transparency with the IceCube LED calibration system," *Nucl. Instrum. Meth. A* **711** (2013) 73–89, 1301.5361.

[502] IceCube Collaboration, M. Aartsen *et al.*, "Energy Reconstruction Methods in the IceCube Neutrino Telescope," *JINST* **9** (2014) P03009, 1311.4767.

[503] IceCube Collaboration, D. Heinen *et al.*, "An Acoustic Calibration System for the IceCube Upgrade," *PoS* **ICRC2019** (2020) 1030, 1909.02047.

[504] IceCube Collaboration, W. Kang, C. Tönnis, and C. Rott, "The camera system for the IceCube Upgrade," *PoS* **ICRC2019** (2020) 928, 1908.07734.

[505] IceCube-Gen2 Collaboration, A. Omeliukh *et al.*, "Optimization of the optical array geometry for IceCube-Gen2," *PoS* **ICRC2021** (2021) 1184, 2107.08527.

[506] J. van Santen, "IceCube-Gen2: the next-generation neutrino observatory for the South Pole," *PoS* **ICRC2017** (2017) 991.

[507] IceCube Collaboration, R. Abbasi *et al.*, "IceTop: The surface component of IceCube," *Nucl. Instrum. Meth. A* **700** (2013) 188–220, 1207.6326.

[508] G. A. Askaryan, "Excess negative charge of an electron-photon shower and its coherent radio emission," *JETP* **14** (1962) 441.

[509] J. Alvarez-Muniz, A. Romero-Wolf, and E. Zas, "Practical and accurate calculations of Askaryan radiation," *Phys. Rev. D* **84** (2011) 103003, 1106.6283.

[510] D. Saltzberg *et al.*, "Observation of the Askaryan effect: Coherent microwave Cherenkov emission from charge asymmetry in high-energy particle cascades," *Phys. Rev. Lett.* **86** (2001) 2802–2805, hep-ex/0011001.

[511] P. W. Gorham *et al.*, "Accelerator measurements of the Askaryan effect in rock salt: A Roadmap toward teraton underground neutrino detectors," *Phys. Rev. D* **72** (2005) 023002, astro-ph/0412128.

[512] ANITA Collaboration, P. W. Gorham *et al.*, "Observations of the Askaryan effect in ice," *Phys. Rev. Lett.* **99** (2007) 171101, hep-ex/0611008.

[513] Pierre Auger Collaboration, A. Aab *et al.*, "Probing the radio emission from air showers with polarization measurements," *Phys. Rev. D* **89** (2014) 052002, 1402.3677.

[514] P. Schellart *et al.*, "Polarized radio emission from extensive air showers measured with LOFAR," *JCAP* **10** (2014) 014, 1406.1355.

[515] LOFAR Collaboration, O. Scholten *et al.*, "Measurement of the circular polarization in radio emission from extensive air showers confirms emission mechanisms," *Phys. Rev. D* **94** (2016) 103010, 1611.00758.

[516] L. D. Landau and I. Pomeranchuk, "Limits of applicability of the theory of bremsstrahlung electrons and pair production at high-energies," *Dokl. Akad. Nauk Ser. Fiz.* **92** (1953) 535–536.

[517] A. B. Migdal, "Bremsstrahlung and pair production in condensed media at high-energies," *Phys. Rev.* **103** (1956) 1811–1820.

[518] J. Alvarez-Muniz, A. Romero-Wolf, and E. Zas, "Cherenkov radio pulses from electromagnetic showers in the time-domain," *Phys. Rev. D* **81** (2010) 123009, 1002.3873.

[519] L. Gerhardt and S. R. Klein, "Electron and Photon Interactions in the Regime of Strong LPM Suppression," *Phys. Rev. D* **82** (2010) 074017, 1007.0039.

[520] S. I. Dutta, M. H. Reno, I. Sarcevic, and D. Seckel, "Propagation of muons and taus at high-energies," *Phys. Rev. D* **63** (2001) 094020, hep-ph/0012350.

[521] D. García-Fernández, A. Nelles, and C. Glaser, "Signatures of secondary leptons in radio-neutrino detectors in ice," *Phys. Rev. D* **102** (2020) 083011, 2003.13442.

[522] C. Glaser, D. García-Fernández, and A. Nelles, "Prospects for neutrino-flavor physics with in-ice radio detectors," *PoS* **ICRC2021** (2021) 1231.

[523] S. Stjärnholm, O. Ericsson, and C. Glaser, "Neutrino direction and flavor reconstruction from radio detector data using deep convolutional neural networks," *PoS* **ICRC2021** (2021) 1055.

[524] S. Barwick, D. Besson, P. Gorham, and D. Saltzberg, "South Polar in situ radio-frequency ice attenuation," *J. Glaciol.* **51** (2005) 231–238.

[525] I. Kravchenko, D. Besson, and J. Meyers, "In situ index-of-refraction measurements of the South Polar firn with the RICE detector," *Journal of Glaciology* **50** (2004) 522–532.

[526] S. W. Barwick *et al.*, "Observation of classically 'forbidden' electromagnetic wave propagation and implications for neutrino detection," *JCAP* **1807** (2018) 055, 1804.10430.

[527] ARA Collaboration, P. Allison *et al.*, "Measurement of the real dielectric permittivity ϵ_r of glacial ice," *Astropart. Phys.* **108** (2019) 63–73, 1712.03301.

[528] I. Kravchenko *et al.*, "Rice limits on the diffuse ultrahigh energy neutrino flux," *Phys. Rev. D* **73** (2006) astro-ph/0601148.

[529] ARA Collaboration, J. Kelley, M.-Y. Lu, D. Seckel, Y. Pan, and D. Z. Besson, "Observation of two deep, distant (1.4, 4)km impulsive RF transmitters by the Askaryan Radio Array (ARA).," *PoS* **ICRC2017** (2018) 1030.

[530] ARIANNA Collaboration, A. Anker *et al.*, "Neutrino vertex reconstruction with in-ice radio detectors using surface reflections and implications for the neutrino energy resolution," *JCAP* **1911** (2019) 030, 1909.02677.

[531] J. A. Aguilar *et al.*, "Reconstructing the neutrino energy for in-ice radio detectors: A study for the Radio Neutrino Observatory Greenland (RNO-G)," *Eur. Phys. J. C* **82** (2022) 147, 2107.02604.

[532] I. Plaisier, S. Bouma, and A. Nelles, "Reconstructing the arrival direction of neutrinos in deep in-ice radio detectors," *Eur. Phys. J. C* **83** (2023) 443, 2302.00054.

[533] C. Glaser *et al.*, "NuRadioReco: A reconstruction framework for radio neutrino detectors," *Eur. Phys. J.* **C79** (2019) 464, 1903.07023.

[534] ARIANNA Collaboration, C. Glaser, "Neutrino direction and energy resolution of Askaryan detectors," *PoS* **ICRC2019** (2020) 899, 1911.02093.

[535] ARIANNA Collaboration, S. Barwick *et al.*, "Capabilities of ARIANNA: Neutrino Pointing Resolution and Implications for Future Ultra-high Energy Neutrino Astronomy," *PoS* **ICRC2021** (2021) 1151.

[536] C. Glaser, S. McAleer, S. Stjärnholm, P. Baldi, and S. W. Barwick, "Deep-learning-based reconstruction of the neutrino direction and energy for in-ice radio detectors," *Astropart. Phys.* **145** (2023) 102781, 2205.15872.

[537] A. Vieregg, K. Bechtol, and A. Romero-Wolf, "A Technique for Detection of PeV Neutrinos Using a Phased Radio Array," *JCAP* **02** (2016) 005, 1504.08006.

[538] J. Avva *et al.*, "Development Toward a Ground-Based Interferometric Phased Array for Radio Detection of High Energy Neutrinos," *Nucl. Instrum. Meth. A* **869** (2017) 46–55, 1605.03525.

[539] ARA Collaboration, P. Allison *et al.*, "Design and performance of an interferometric trigger array for radio detection of high-energy neutrinos," *Nucl. Instrum. Meth. A* **930** (2019) 112–125, 1809.04573.

[540] ARIANNA Collaboration, R. Rice-Smith, "Assessing the Background Rate due to Cosmic Ray Core Scattering from Internal Reflection Layers in the South Pole Ice Cap," July, 2022.

[541] K. D. de Vries *et al.*, "The cosmic-ray air-shower signal in Askaryan radio detectors," *Astropart. Phys.* **74** (2016) 96–104, 1503.02808.

[542] ARIANNA Collaboration, S. W. Barwick *et al.*, "Radio detection of air showers with the ARIANNA experiment on the Ross Ice Shelf," *Astropart. Phys.* **90** (2017) 50–68, 1612.04473.

[543] Arianna Collaboration, A. Anker *et al.*, "Measuring the polarization reconstruction resolution of the ARIANNA neutrino detector with cosmic rays," *JCAP* **04** (2022) 022, 2112.01501.

[544] S. Barwick and C. Glaser, "Radio Detection of High Energy Neutrinos in Ice," *to be published in Neutrino Physics and Astrophysics, edited by F. W. Stecker, in the Encyclopedia of Cosmology II, edited by G. G. Fazio, World Scientific Publishing Company, Singapore* (2022) 2208.04971.

[545] IceCube Collaboration, A. Haungs *et al.*, "A Scintillator and Radio Enhancement of the IceCube Surface Detector Array," *EPJ Web Conf.* **210** (2019) 06009, 1903.04117.

[546] IceCube-Gen2 Collaboration, F. G. Schroeder *et al.*, "The Surface Array planned for IceCube-Gen2," *PoS* **ICRC2021** (2021) 407, 2108.00364.

[547] IceCube Collaboration, R. Abbasi *et al.*, "First air-shower measurements with the prototype station of the IceCube surface enhancement," *PoS* **ICRC2021** (2021) 314, 2107.08750.

[548] IceCube Collaboration, R. Abbasi *et al.*, "Hybrid cosmic ray measurements using the IceAct telescopes in coincidence with the IceCube and IceTop detectors," *PoS* **ICRC2021** (2021) 276, 2108.05572.

[549] IceCube-Gen2 Collaboration, L. Classen, M. Kossatz, A. Kretzschmann, S. Lindner, and D. Shuklin, "The mDOM - A multi-PMT digital optical module for the IceCube-Gen2 neutrino telescope," *PoS* **ICRC2017** (2018) 1047.

[550] IceCube Collaboration, L. Classen, A. Kappes, and T. Karg, "A multi-PMT Optical Module for the IceCube Upgrade," *PoS* **ICRC2019** (2019) 855, 1908.10802.

[551] IceCube Collaboration, R. Abbasi *et al.*, "D-Egg: a Dual PMT Optical Module for IceCube," 2212.14526.

[552] IceCube-Gen2 Collaboration, S. Shimizu, S. Yoshida, A. Stoessl, and A. Ishihara, "Overview and performance of the D-Egg optical sensor for IceCube-Gen2," *PoS* **ICRC2017** (2018) 1051.

[553] ARA Collaboration, P. Allison *et al.*, "Design and Initial Performance of the Askaryan Radio Array Prototype EeV Neutrino Detector at the South Pole," *Astropart. Phys.* **35** (2012) 457–477, 1105.2854.

[554] ARIANNA Collaboration, S. W. Barwick *et al.*, "Design and Performance of the ARIANNA HRA-3 Neutrino Detector Systems," *IEEE Trans. Nucl. Sci.* **62** (2015) 2202–2215, 1410.7369.

[555] ARIANNA Collaboration, S. W. Barwick *et al.*, "A First Search for Cosmogenic Neutrinos with the ARIANNA Hexagonal Radio Array," *Astropart. Phys.* **70** (2015) 12–26, 1410.7352.

[556] RNO-G Collaboration, J. A. Aguilar *et al.*, "Design and Sensitivity of the Radio Neutrino Observatory in Greenland (RNO-G)," *JINST* **16** (2021) P03025, 2010.12279.

[557] S.-H. Wang *et al.*, "TAROGE-M: Radio Observatory on Antarctic High Mountain for Detecting Near-Horizon Ultra-High Energy Air Showers," *PoS* **ICRC2021** (2021) 1173.

[558] PUEO Collaboration, Q. Abarr *et al.*, "The Payload for Ultrahigh Energy Observations (PUEO): a white paper," *JINST* **16** (2021) P08035, 2010.02892.

[559] IceCube Collaboration, M. Kauer *et al.*, "The Scintillator Upgrade of IceTop: performance of the prototype array," *PoS* **ICRC2019** (2019) 309.

[560] IceCube-Gen2 Collaboration, F. Schröder *et al.*, "Physics Potential of a Radio Surface Array at the South Pole (ARENA 2018)," in *Acoustic and Radio EeV Neutrino Detection Activities (ARENA 2018) Catania, Italy, June 12-15, 2018*, 2018. 1811.00599.

[561] E. de Lera Acedo, N. Razavi-Ghods, N. Troop, N. Drought, and A. J. Faulkner, "SKALA, a log-periodic array antenna for the SKA-low instrument: design, simulations, tests and system considerations," *Experimental Astronomy* **39** (2015) 567–594.

[562] E. de Lera Acedo, N. Drought, B. Wakley, and A. Faulkner, "Evolution of SKALA (SKALA-2), the log-periodic array antenna for the SKA-low instrument," *2015 International Conference on Electromagnetics in Advanced Applications (ICEAA)* (2015) 839–843.

[563] E. de Lera Acedo, A. Faulkner, and J. Bij de Vaate, "SKA low frequency aperture array," in *2016 United States National Committee of URSI National Radio Science Meeting (USNC-URSI NRSM)*, pp. 1–2, 2016.

[564] T. Kittler, *Simulation and Reconstruction of Muon Tracks with the "multi-PMT Digital Optical Module" in Comparison to the "PINGU Digital Optical Module" for*

the IceCube-Gen2 High-Energy Array. PhD thesis, Erlangen - Nuremberg U., 2020.

[565] IceCube Collaboration, M. Aartsen *et al.*, "Atmospheric and astrophysical neutrinos above 1 TeV interacting in IceCube," *Phys. Rev. D* **91** (2015) 022001, 1410.1749.

[566] Pierre Auger Collaboration, A. Aab *et al.*, "Energy Estimation of Cosmic Rays with the Engineering Radio Array of the Pierre Auger Observatory," *Phys. Rev. D* **93** (2016) 122005, 1508.04267.

[567] Pierre Auger Collaboration, A. Aab *et al.*, "Measurement of the Radiation Energy in the Radio Signal of Extensive Air Showers as a Universal Estimator of Cosmic-Ray Energy," *Phys. Rev. Lett.* **116** (2016) 241101, 1605.02564.

[568] M. Gottowik, C. Glaser, T. Huege, and J. Rautenberg, "Determination of the absolute energy scale of extensive air showers via radio emission: systematic uncertainty of underlying first-principle calculations," *Astropart. Phys.* **103** (2018) 87–93, 1712.07442.

[569] P. Allison *et al.*, "Long-baseline horizontal radio-frequency transmission through polar ice," *JCAP* **2020** (2020) 009, 1908.10689.

[570] ARIANNA Collaboration, A. Anker *et al.*, "Targeting ultra-high energy neutrinos with the ARIANNA experiment," *Adv. Space Res.* **64** (2019) 2595–2609, 1903.01609.

[571] RNO-G Collaboration, J. A. Aguilar *et al.*, "Energy reconstruction with the Radio Neutrino Observatory Greenland (RNO-G)," *PoS* **ICRC2021** (2021) 1033.

[572] ARA Collaboration, M.-Y. Lu, "Radio-interferometric Neutrino Reconstruction for the Askaryan Radio Array," *EPJ Web Conf.* **135** (2017) 05003.

[573] ARIANNA Collaboration, A. Anker *et al.*, "Probing the angular and polarization reconstruction of the ARIANNA detector at the South Pole," *JINST* **15** (2020) P09039, 2006.03027.

[574] LOPES Collaboration, W. D. Apel *et al.*, "The wavefront of the radio signal emitted by cosmic ray air showers," *JCAP* **1409** (2014) 025, 1404.3283.

[575] LOFAR Collaboration, A. Corstanje *et al.*, "The shape of the radio wavefront of extensive air showers as measured with LOFAR," *Astropart. Phys.* **61** (2015) 22–31, 1404.3907.

[576] C. Welling, C. Glaser, and A. Nelles, "Reconstructing the cosmic-ray energy from the radio signal measured in one single station," *JCAP* **10** (2019) 075, 1905.11185.

[577] IceCube Collaboration, M. G. Aartsen *et al.*, "Time-Integrated Neutrino Source Searches with 10 Years of IceCube Data," *Phys. Rev. Lett.* **124** (2020) 051103, 1910.08488.

[578] P. B. Price, K. Woschnagg, and D. Chirkin, "Age vs depth of glacial ice at South Pole," *Geophysical Research Letters* **27** (2000) 2129–2132, https://agupubs.onlinelibrary.wiley.com/doi/pdf/10.1029/2000GL011351.

[579] M. Aartsen *et al.*, "South pole glacial climate reconstruction from multi-borehole laser particulate stratigraphy," *Journal of Glaciology* **59** (2013) 1117–1129.

[580] M. Ackermann *et al.*, "Optical properties of deep glacial ice at the south pole," *Journal of Geophysical Research: Atmospheres* **111** (2006) https://agupubs.onlinelibrary.wiley.com/doi/pdf/10.1029/2005JD006687.

[581] P. B. Price and L. Bergström, "Optical properties of deep ice at the south pole: scattering," *Appl. Opt.* **36** (1997) 4181–4194.

[582] R. Abbasi *et al.*, "In-situ estimation of ice crystal properties at the South Pole using LED calibration data from the IceCube Neutrino Observatory," *The Cryosphere Discussions* **2022** (2022) 1–48.

[583] IceCube Collaboration, M. G. Aartsen *et al.*, "Measurement of South Pole ice transparency with the IceCube LED calibration system," *Nucl. Instrum. Meth. A* **711** (2013) 73–89, 1301.5361.

[584] IceCube Collaboration, "South pole ice temperature data," 2020.

[585] P. B. Price *et al.*, "Temperature profile for glacial ice at the south pole: Implications for life in a nearby subglacial lake," *Proceedings of the National Academy of Sciences* **99** (2002) 7844–7847.

[586] B. H. Hills *et al.*, "Geophysics and Thermodynamics at South Pole Lake Indicate Stability and a Regionally Thawed Bed," *Geophysical Research Letters* **49** (2022).

[587] N. Heyer and C. Glaser, "First-principle calculation of birefringence effects for in-ice radio detection of neutrinos," *Eur. Phys. J. C* **83** (2023) 124, 2205.06169.

[588] S. Babinec *et al.*, "Feasibility of Renewable Energy for Power Generation at the South Pole," 2306.13552.

[589] IceCube Collaboration, R. Abbasi *et al.*, "Calibration and Characterization of the IceCube Photomultiplier Tube," *Nucl. Instrum. Meth. A* **618** (2010) 139–152, 1002.2442.

[590] IceCube Collaboration, R. Abbasi *et al.*, "The IceCube Data Acquisition System: Signal Capture, Digitization, and Timestamping," *Nucl. Instrum. Meth. A* **601** (2009) 294–316, 0810.4930.

[591] S. Kleinfelder, "Gigahertz waveform sampling and digitization circuit design and implementation," *IEEE Transactions on Nuclear Science* **50** (2003) 955–962.

[592] M. A. U. Elorrieta, " Studies on dark rates induced by radioactive decays of the multi-PMT digital optical module for future IceCube extensions ," Master's thesis, Westfälische Wilhelms-Universität Münster, 2017.

[593] LIGO, Virgo Collaborations, B. P. Abbott *et al.*, "Gravitational Waves and Gamma-Rays from a Binary Neutron Star Merger: GW170817 and GRB 170817A," *Astrophys. J. Lett.* **848** (2017) L13, 1710.05834.

[594] IceCube Collaboration, A. Achterberg *et al.*, "First Year Performance of The IceCube Neutrino Telescope," *Astropart. Phys.* **26** (2006) 155–173, astro-ph/0604450.

[595] IceCube Collaboration, M. G. Aartsen *et al.*, "All-sky Search for Time-integrated Neutrino Emission from Astrophysical Sources with 7 yr of IceCube Data," *Astrophys. J.* **835** (2017) 151, 1609.04981.

[596] IceCube Collaboration, N. M. B. Amin, "Implementation of IceTop data in the IceCube Realtime Alert System," *J. Phys. Conf. Ser.* **2156** (2021) 012217.

[597] IceCube Collaboration, D. Soldin, "Cosmic Ray Measurements with IceCube and IceTop," in *21st International Symposium on Very High Energy Cosmic Ray Interactions*, 8, 2022. 2208.01911.

[598] IceCube Collaboration, R. Abbasi *et al.*, "D-Egg: a dual PMT optical module for IceCube," *JINST* **18** (2023) P04014, 2212.14526.

[599] W. Kang and C. Tönnis and C. Rott, "The camera system for the IceCube Upgrade," *PoS* **ICRC2019** (2019) 928.

[600] IceCube Collaboration, C. Fruck, F. Henningsen, and C. Spannfellner, "The POCAM as self-calibrating light source for the IceCube Upgrade," *PoS* **ICRC2019** (2020) 908, 1908.09600.

[601] IceCube Collaboration, M. Rongen and D. Chirkin, "Advances in IceCube ice modelling & what to expect from the Upgrade," *JINST* **16** (2021) C09014, 2108.03291.

[602] R. Jacobel, "Radar studies of internal stratigraphy and bed topography along the us itase-ii traverse," *U.S. Antarctic Program (USAP) Data Center* (2010).

[603] G. Paxman *et al.*, "Subglacial Geology and Geomorphology of the Pensacola-Pole Basin, East Antarctica," *Geochemistry, Geophysics, Geosystems* **20** (2019).

[604] L. Greenler *et al.*, "Modeling hole size, lifetime and fuel consumption in hot-water ice drilling," *Annals of Glaciology* **55(68)** (2014) 115–123.

[605] IceCube Collaboration, R. Abbasi *et al.*, "Calibration and Characterization of the IceCube Photomultiplier Tube," *Nucl. Instrum. Meth. A* **618** (2010) 139–152, 1002.2442.

[606] IceCube Collaboration, R. Abbasi *et al.*, "Design and performance of the multi-PMT optical module for IceCube Upgrade," *PoS* **ICRC2021** (2021) 1070, 2107.11383.

[607] GEANT4 Collaboration, S. Agostinelli *et al.*, "GEANT4–a simulation toolkit," *Nucl. Instrum. Meth. A* **506** (2003) 250–303.

[608] IceCube-Gen2 Collaboration, P. Peiffer and D. Hebecker, "Overview and Performance of the Wavelength-shifting Optical Module (WOM) for IceCube-Gen2," *PoS* **ICRC2017** (2018) 1052.

[609] IceCube Collaboration, J. Rack-Helleis *et al.*, "The Wavelength-shifting Optical Module (WOM) for the IceCube Upgrade," *PoS* **ICRC2021** (2021) 1038, 2107.10194.

[610] C. Rott, S. In, F. Retière, and P. Gumplinger, "Enhanced photon traps for hyper-kamiokande," *Journal of Instrumentation* **12** (2017) P11021.

[611] ANITA Collaboration, P. W. Gorham *et al.*, "The Antarctic Impulsive Transient Antenna Ultra-high Energy Neutrino Detector Design, Performance, and Sensitivity for 2006-2007 Balloon Flight," *Astropart. Phys.* **32** (2009) 10, 0812.1920.

[612] B. T. Zhang and K. Murase, "Ultrahigh-energy cosmic-ray nuclei and neutrinos from engine-driven supernovae," *Phys. Rev. D* **100** (2019) 103004, 1812.10289.

[613] C. Glaser and S. W. Barwick, "An improved trigger for Askaryan radio detectors," *PoS* **ICRC2021** (2021) 1050.

[614] J. A. Aguilar *et al.*, "Triboelectric backgrounds to radio-based polar ultra-high energy neutrino (UHEN) experiments," *Astropart. Phys.* **145** (2023) 102790.

[615] ARA Collaboration, P. Allison *et al.*, "A low-threshold ultrahigh-energy neutrino search with the Askaryan Radio Array," 2202.07080.

[616] C. Deaconu *et al.*, "Measurements and Modeling of Near-Surface Radio Propagation in Glacial Ice and Implications for Neutrino Experiments," *Phys. Rev. D* **98** (2018) 043010, 1805.12576.

[617] TAROGE, Arianna Collaborations, S.-H. Wang *et al.*, "TAROGE-M: radio antenna array on antarctic high mountain for detecting near-horizontal ultra-high energy air showers," *JCAP* **11** (2022) 022, 2207.10616.

[618] J. Beise and C. Glaser, "Simulation study for an in-situ calibration system for the measurement of the snow accumulation and the index-of-refraction profile for radio neutrino detectors," *JINST* **18** (2023) P01036, 2205.00726.

[619] ARIANNA Collaboration, A. Nelles, "Cosmic-ray detection with and novel reconstruction algorithms for the ARIANNA experiment," *PoS* **ICRC2019** (2020) 366.

[620] IceCube-Gen2 Collaboration, S. Bouma *et al.*, "Direction reconstruction performance for IceCube-Gen2 Radio," *PoS* **ICRC2023** (2023) 1045.

[621] S. A. Kleinfelder, E. Chiem, and T. Prakash, "The SST Fully-Synchronous Multi-GHz Analog Waveform Recorder with Nyquist-Rate Bandwidth and Flexible Trigger Capabilities," in *2014 IEEE Nuclear Science Symposium and Medical Imaging Conference and 21st Symposium on Room-Temperature Semiconductor X-ray and Gamma-ray Detectors*, 5, 2015. 1505.07085.

[622] J. M. Roberts *et al.*, "LAB4D: A Low Power, Multi-GSa/s, Transient Digitizer with Sampling Timebase Trimming Capabilities," *Nucl. Instrum. Meth. A* **925** (2019) 92–100, 1803.04600.

[623] E. Oberla, J. Porter, and J. Stahoviak, "PSEC4A : A 10 GSa/s Waveform Sampling ASIC with Multi-Event Buffering Capability." https://indico.cern.ch/event/697988/contributions/3056053/attachments/1720190/2776726/TWEPP_Porter_poster_163.pdf, 2018.

[624] IceCube-Gen2 Collaboration, R. Abbasi *et al.*, "Sensitivity studies for the IceCube-Gen2 radio array," *PoS* **ICRC2021** (2021) 1183, 2107.08910.

[625] E. Y. Chiem, *Multi-Gigahertz Synchronous Sampling and Triggering (SST) Circuit with Picosecond Timing Resolution*. PhD thesis, UC, Irvine, 2017.

[626] IceCube Collaboration, E. Blaufuss, T. Kintscher, L. Lu, and C. F. Tung, "The Next Generation of IceCube Real-time Neutrino Alerts," *PoS* **ICRC2019** (2020) 1021, 1908.04884.

[627] A. Fedynitch, F. Riehn, R. Engel, T. K. Gaisser, and T. Stanev, "Hadronic interaction model sibyll 2.3c and inclusive lepton fluxes," *Phys. Rev. D* **100** (2019) 103018, 1806.04140.

[628] IceCube Collaboration, R. Abbasi *et al.*, "Density of GeV Muons Measured with IceTop," *PoS* **ICRC2021** (2021) 342, 2107.09583.

[629] Pierre Auger Collaboration, S. Müller, "Direct Measurement of the Muon Density in Air Showers with the Pierre Auger Observatory," *EPJ Web Conf.* **210** (2019) 02013.

[630] H. V. Cane, "Spectra of the non-thermal radio radiation from the galactic polar regions," *Mon. Not. R. Astron. Soc.* **189** (1979) 465–478.

[631] Pierre Auger Collaboration, J. Bellido, "Depth of maximum of air-shower profiles at the Pierre Auger Observatory: Measurements above $10^{17.2}$ eV and Composition Implications," *PoS* **ICRC2017** (2018) 506.

[632] A. Corstanje *et al.*, "Depth of shower maximum and mass composition of cosmic rays from 50 PeV to 2 EeV measured with the LOFAR radio telescope," *Phys. Rev. D* **103** (2021) 102006, 2103.12549.

[633] Telescope Array Collaboration, R. U. Abbasi *et al.*, "The Cosmic-Ray Composition between 2 PeV and 2 EeV Observed with the TALE Detector in Monocular Mode," *Astrophys. J.* **909** (2021) 178, 2012.10372.

[634] J. Matthews, "A Heitler model of extensive air showers," *Astropart. Phys.* **22** (2005) 387–397.

[635] B. Flaggs, A. Coleman, and F. G. Schröder, "Studying the mass sensitivity of air-shower observables using simulated cosmic rays," 2306.13246.

[636] Pierre Auger Collaboration, A. Aab *et al.*, "The Pierre Auger Observatory Upgrade - Preliminary Design Report," 1604.03637.

[637] "IceCube Neutrino Observatory weather." https://icecube.wisc.edu/pole/weather/. Accessed: 2021-12-15.

[638] B. V. Aswathi, A. Haungs, T. Huege, and F. G. Schröder, "PeVatron search using radio measurements of extensive air showers at the south pole," *Journal of Physics: Conference Series* **1342** (2020) 012006.

[639] United States Antarctic Program, "Field manual - comms." https://www.usap.gov/USAPgov/travelAndDeployment/documents/FieldManual-Comms.pdf.

[640] IceCube Collaboration, M. Oehler and R. Turcotte-Tardif, "Development of a scintillation and radio hybrid detector array at the South Pole," *PoS* **ICRC2021** (2021) 225.

[641] Times Microwave Systems, *LMR-240 Flexible Low Loss Communications Coax*.

[642] Times Microwave Systems, *LMR-400 Flexible Low Loss Communications Coax*.

[643] S. Ritt, R. Dinapoli, and U. Hartmann, "Application of the DRS chip for fast waveform digitizing," *Nucl. Instrum. Meth. A* **623** (2010) 486–488.

[644] IceCube Collaboration, M. Aartsen and et al., "Design and performance of the first iceact demonstrator at the south pole," *Journal of Instrumentation* **15** (2020) T02002–T02002.

[645] S. Funk *et al.*, "Target: A digitizing and trigger asic for the cherenkov telescope array," *AIP Conference Proceedings* **1792** (2017) 080012, https://aip.scitation.org/doi/pdf/10.1063/1.4969033.

[646] M. Karus *et al.*, "Ground Calibration of MAPMT and SiPM for JEM-EUSO," *PoS* **ICRC2015** (2016) 612.

[647] K. Mulrey *et al.*, "Calibration of the LOFAR low-band antennas using the Galaxy and a model of the signal chain," *Astropart. Phys.* **111** (2019) 1–11, 1903.05988.

[648] M. Renschler, *A Prototype Radio Detector for the IceCube Surface Enhancement*. PhD thesis, Karlsruher Institut für Technologie (KIT), 2020.

[649] IceCube-Gen2 Collaboration, J. L. Kelley and C. Wendt, "Evolution of the IceCube data acquisition system for IceCube-Gen2," *JINST* **16** (2021) C09017.

[650] M. Lipiński, T. Włostowski, J. Serrano, and P. Alvarez, "White Rabbit: A PTP application for robust sub-nanosecond synchronization," in *2011 IEEE International Symposium on Precision Clock Synchronization for Measurement, Control and Communication*, pp. 25–30, IEEE, 2011.

[651] J. Serrano *et al.*, "The white rabbit project," in *Proc. 12th Int. Conf. on Accelerator and Large Experimental Physics Control Systems (ICALEPCS'09)*, pp. 93–95, JACoW Publishing, Oct., 2009.

[652] P. P. M. Jansweijer, H. Z. Peek, and E. De Wolf, "White Rabbit: Sub-nanosecond timing over Ethernet," *Nucl. Instrum. Meth. A* **725** (2013) 187–190.

[653] IEEE, "IEEE Standard for a Precision Clock Synchronization Protocol for Networked Measurement and Control Systems," *IEEE Std 1588-2008 (Revision of IEEE Std 1588-2002)* (2008) 1–269.

[654] ITU-T, "Timing and synchronization aspects in packet networks - amendment 2." https://www.itu.int/rec/T-REC-G.8261-202010-I!Amd2/en. Rec. G.8261 (2020).

[655] IceCube Collaboration, M. Kauer, T. Huber, D. Tosi, and C. Wendt, "The Scintillator Upgrade of IceTop: Performance of the prototype array," *PoS* **ICRC2019** (2021) 309, 1908.09860.

[656] https://www.unavco.org/projects/project-support/polar/remote/power/power.html.

[657] D. Z. Besson, D. M. Kennedy, K. Ratzlaff, and R. Young, "Design, Modeling and Testing of the Askaryan Radio Array South Pole Autonomous Renewable Power Stations," *Nucl. Instrum. Meth. A* **763** (2014) 521–532, 1403.1253.

[658] R. Abbasi *et al.*, "A Convolutional Neural Network based Cascade Reconstruction for the IceCube Neutrino Observatory," *JINST* **16** (2021) P07041, 2101.11589.

[659] ANITA Collaboration, "AnitaAnalysisFramework." https://github.com/anitaNeutrino/AnitaAnalysisFramework.

[660] ARA Collaboration, "AraRoot: ARA data access framework." https://github.com/ara-software/AraRoot.

[661] J. C. Díaz-Vélez *et al.*, "Snowmass2021 - letter of interest: Icecube and icecube-gen2 simulation." https://www.snowmass21.org/docs/files/summaries/CompF/SNOWMASS21-CompF2_CompF1-041.pdf. Accessed 2022-01-17.

[662] M. G. Aartsen *et al.*, "The IceProd Framework: Distributed Data Processing for the IceCube Neutrino Observatory," *arXiv e-prints* (2013) arXiv:1311.5904, 1311.5904.

[663] ARA Collaboration, P. Allison *et al.*, "First Constraints on the Ultra-High Energy Neutrino Flux from a Prototype Station of the Askaryan Radio Array," *Astropart. Phys.* **70** (2015) 62–80, 1404.5285.

[664] B. Hokanson-Fasig, "PyREx: A Python package for Askaryan radio neutrino experiments," 2022. https://github.com/bhokansonfasig/pyrex.

[665] M. D. Wilkinson *et al.*, "The FAIR Guiding Principles for scientific data management and stewardship," *Scientific Data* **3** (2016) 160018.

[666] E. Dart *et al.*, "The Science DMZ: a network design pattern for data-intensive science," *SC '13: Proceedings of the International Conference on High Performance Computing, Networking, Storage and Analysis* (2013) 1–10.

[667] `https://www.trustedci.org`.

[668] L. Peters, "Untersuchung des Einflusses der Unsicherheiten der Geometriekalibration auf die Richtungsrekonstruktion in IceCube," Master's thesis, RWTH Aachen University, 2019.

[669] IceCube Collaboration, J. Borowka, C. Günther, D. Heinen, S. Zierke, *et al.*, "The Acoustic Module for the IceCube Upgrade," *PoS* **ICRC2021** (2021) 1059, `2108.05631`.

[670] IceCube Collaboration, D. Heinen *et al.*, "An Acoustic Calibration System for the IceCube Upgrade," 2021.

[671] R. Abbasi *et al.*, "Measurement of acoustic attenuation in south pole ice," *Astroparticle Physics* **34** (2011) 382–393.

[672] M. Ackermann, J. Ahrens, *et al.*, "Optical properties of deep glacial ice at the south pole," *Journal of Geophysical Research* **111** (2006).

[673] IceCube Collaboration, M. Rongen, D. Chirkin, *et al.*, "A novel microstructure based model to explain the IceCube ice anisotropy," in *Proceedings of 37th International Cosmic Ray Conference — PoS(ICRC2021)*, Sissa Medialab, July, 2021.

[674] IceCube Collaboration, M. Rongen and D. Chirkin, "Advances in icecube ice modelling & what to expect from the upgrade," *Journal of Instrumentation* **16** (2021) C09014.

[675] R. C. Bay, P. B. Price, G. D. Clow, and A. J. Gow, "Climate logging with a new rapid optical technique at Siple Dome," *Geophys. Res. Lett.* **28** (2001) 4635–4638.

[676] N. E. Bramall, R. C. Bay, K. Woschnagg, R. A. Rhode, and P. B. Price, "A deep high-resolution optical log of dust, ash, and stratigraphy in South Pole glacial ice," *Geophys. Res. Lett.* **32** (2005) L21815.

[677] IceCube Collaboration, M. G. Aartsen *et al.*, "South Pole glacial climate reconstruction from multi-borehole laser particulate stratigraphy," *J. Glaciol.* **59** (2013) 1117–1128.

[678] M. Rongen, R. C. Bay, and S. Blot, "Observation of an optical anisotropy in the deep glacial ice at the geographic South Pole using a laser dust logger," *Cryosphere* **14** (2020) 2537–2543.

[679] D. Chirkin and M. Rongen, "An improved mapping of ice layer undulations for the IceCube Neutrino Observatory," *PoS (in preparation)* **ICRC2023** (2023).

[680] IceCube Collaboration, M. Rongen, "Measuring the optical properties of IceCube drill holes," *EPJ Web Conf.* **116** (2016) 06011.

[681] R. Abbasi, M. Ackermann, *et al.*, "A calibration study of local ice and optical sensor properties in IceCube," *PoS* **ICRC2021** (2021) 1023.

[682] IceCube Collaboration, A. Ishihara and A. Kiriki, "Calibration LEDs in the IceCube Upgrade D-Egg modules," *PoS* **ICRC2019** (2020) 923, 1908.10780.

[683] M. A. Unland Elorrieta, *Development, simulation, and characterisation of a novel multi-PMT optical module for IceCube Upgrade with emphasis on detailed understanding of photomultiplier performance parameters*. PhD thesis, Universität Münster, July, 2023.

[684] IceCube Collaboration, W. Kang and J. Lee and G. Roellinghoff and C. Rott and C. Tönnis, "Camera Calibration for the IceCube Upgrade and Gen2," *PoS* **ICRC2021** (2021) 1064, 2107.12186.

[685] T. M. Jordan *et al.*, "Modelling ice birefringence and oblique radio wave propagation for neutrino detection at the South Pole," *Annals Glaciol.* **61** (2020) 84, 1910.01471.

[686] J. Nam *et al.*, "Development of drone-borne aerial calibration pulser system for radio observatories of ultra-high energy air showers," *PoS* **ICRC2021** (2021) 283.

[687] S. Prohira *et al.*, "HiCal 2: An instrument designed for calibration of the ANITA experiment and for Antarctic surface reflectivity measurements," *Nucl. Instrum. Meth. A* **918** (2019) 60–66, 1710.11175.

[688] Radar Echo Telescope Collaboration, S. Prohira *et al.*, "Modeling in-ice radio propagation with parabolic equation methods," *Phys. Rev. D* **103** (2021) 103007, 2011.05997.

[689] A. Connolly, "Impact of biaxial birefringence in polar ice at radio frequencies on signal polarizations in ultrahigh energy neutrino detection," *Phys. Rev. D* **105** (2022) 123012, 2110.09015.

[690] I. Kravchenko, D. Besson, A. Ramos, and J. Remmers, "Radio frequency birefringence in south polar ice and implications for neutrino reconstruction," *Astroparticle Physics* **34** (2011) 755–768.

[691] D. Z. Besson, I. Kravchenko, and K. Nivedita, "Polarization angle dependence of vertically propagating radio-frequency signals in south polar ice," *Astroparticle Physics* **144** (2023) 102766.

[692] Tunka-Rex, LOPES Collaborations, W. D. Apel *et al.*, "A comparison of the cosmic-ray energy scales of Tunka-133 and KASCADE-Grande via their radio

extensions Tunka-Rex and LOPES," *Phys. Lett. B* **763** (2016) 179–185, 1610.08343.

[693] K. Mulrey, "Cross-calibrating the energy scales of cosmic-ray experiments using a portable radio array," *PoS* **ICRC2021** (2021) 414.

[694] A. Nelles *et al.*, "Calibrating the absolute amplitude scale for air showers measured at LOFAR," *JINST* **10** (2015) P11005, 1507.08932.

[695] Pierre Auger Collaboration, A. Aab *et al.*, "Energy Estimation of Cosmic Rays with the Engineering Radio Array of the Pierre Auger Observatory," *Phys. Rev. D* **93** (2016) 122005, 1508.04267.

[696] P. A. Bezyazeekov *et al.*, "Measurement of cosmic-ray air showers with the Tunka Radio Extension (Tunka-Rex)," *Nucl. Instrum. Meth. A* **802** (2015) 89–96, 1509.08624.

[697] LOPES Collaboration, W. D. Apel *et al.*, "Final results of the LOPES radio interferometer for cosmic-ray air showers," *Eur. Phys. J. C* **81** (2021) 176, 2102.03928.

[698] Pierre Auger Collaboration, A. Aab *et al.*, "Calibration of the logarithmic-periodic dipole antenna (LPDA) radio stations at the Pierre Auger Observatory using an octocopter," *JINST* **12** (2017) T10005, 1702.01392.

[699] LOPES Collaboration, W. D. Apel *et al.*, "Improved absolute calibration of LOPES measurements and its impact on the comparison with REAS 3.11 and CoREAS simulations," *Astropart. Phys.* **75** (2016) 72–74, 1507.07389.